ABSTRACT

Title Of Dissertation:	**THE USE OF VARIABLE CELESTIAL X-RAY SOURCES FOR SPACECRAFT NAVIGATION**
	Suneel Ismail Sheikh Doctor of Philosophy, 2005
Dissertation Directed By:	Professor Darryll J. Pines Department of Aerospace Engineering University of Maryland

Accurate control and guidance of spacecraft require continuous high performance three-dimensional navigation solutions. Celestial sources that produce fixed radiation have demonstrated benefits for determining location near Earth and vehicle attitude. Many interplanetary navigation solutions have also relied on Earth-based radio telescope observations and substantial ground processing.

This dissertation investigates the use of variable celestial sources to compute an accurate navigation solution for autonomous spacecraft operation and presents new methodologies for determining time, attitude, position, and velocity. A catalogue of X-ray emitting variable sources has been compiled to identify those that exhibit characteristics conducive to navigation. Many of these sources emit periodic signals that are stable and predictable, and all are located at vast distances such that the signal visibility is available throughout the solar system and beyond. An important subset of these sources is pulsar stars. Pulsars are rapidly rotating neutron stars, which generate

pulsed radiation throughout the electromagnetic spectrum with periods ranging from milliseconds to thousands of seconds.

A detailed analysis of several X-ray pulsars is presented to quantify expected spacecraft range accuracy based upon the source properties, observation times, and X-ray photon detector parameters. High accuracy time transformation equations are developed, which include important general relativistic corrections. Using methods that compare measured and predicted pulse time of arrival within an inertial frame, approaches are presented to determine absolute and relative position, as well as corrections to estimated solutions. A recursive extended Kalman filter design is developed to incorporate the spacecraft dynamics and pulsar-based range measurements.

Simulation results demonstrate that absolute position determination depends on the accuracy of the pulse phase measurements and initial solutions within several tens of kilometers are achievable. The delta-correction method can improve this position solution to within 100 m MRSE and velocity to within 10 mm/s RMS using observations of 500 s and a 1-m^2 detector. Comparisons to recorded flight data obtained from Earth-orbiting X-ray astrophysics missions are also presented.

Results indicate that the pulsed radiation from variable celestial X-ray sources presents a significant opportunity for developing a new class of navigation system for autonomous spacecraft operation.

THE USE OF VARIABLE CELESTIAL X-RAY SOURCES FOR SPACECRAFT NAVIGATION

By

Suneel Ismail Sheikh

Dissertation submitted to the Faculty of the Graduate School of the
University of Maryland, College Park, in partial fulfillment
of the requirements for the degree of
Doctor of Philosophy
2005

Advisory Committee:
Professor Darryll J. Pines, Chair
Associate Professor David L. Akin
Dr. N. Glenn Creamer
Dr. Robert A. Nelson
Professor John E. Osborn
Assistant Professor Benjamin Shapiro

Dedication

I dedicate this dissertation and its research to those who have gone on before me
and had such a great influence on all that I have done.

My Dad:
Dr. Hyder Ismail Sheikh (FRCS)

My Grandparents:
Haji Ismail Ibrahim Sheikh (Bhaisaheb)
James and Annie Duncan
Mae and George Waller

My Grandparents-In-Law:
Ella Gahler
Wallace Thul

My Grandparents-In-Friends:
Robert and Lorraine Rowe

I also dedicate this dissertation to the two women
who have given me life and made it worth living.

My Mum:
Joan Mary Duncan Sheikh Bauder

My Wife:
Kristen Louise Thul Sheikh

Acknowledgements

"If I have seen further than others,

it is by standing upon the shoulders of giants."

– Isaac Newton 1675

For anyone as fortunate as I am to have reached this point in life, you realize it could only have been done by the support, love, and friendship of many people. Although everyone we meet during our lives influences us in some manner, some do more than others. Some shape our lives, others enrich it. From some, we have so many great memories we could never forget them, while others, unfortunately, I could not forget if I tried. It is therefore with great respect and admiration (and yes, a little bit of fun) I acknowledge the persons below who have contributed significantly to my life experience. Yes, the list is long, but for this I feel privileged. Many more could be added and to those I say, "thank you".

To my Mom, Joan, who has provided me so much. Her biggest gifts were the freedom to explore and learn all that I could, and the encouragement to chase after my dreams. During all this, she has always been there to support me whenever I felt too low to carry on. Her own life lessons for me were always the most influential. Her love for my father and stories about him only make me wish we all could have known him longer. It is his success and struggles through life that have delivered me to this point in my life.

To my brothers and sisters, who gave me my fondest memories and inspirations: My big sister, Neena, you have been an incredible inspiration to me through all you have accomplished in your challenging life. For those of you who have had the pleasure of

arguing with an older sister, you know that you always lose. Brady Bunch vs. Star Trek, the battle continues… But I was "allowed" to see enough of my shows that it kept me wanting more. Maybe this drove my interest in space, since I never knew when I would get a chance to see it. To my brother, Kiran, it was all those play times in our youth, and not so youth, that shaped me today. Launches in the rocket house, cutting lawns, fixing Karmann Ghias and Suzukis, all our adventures, they all taught me. A great brother to us all. To my younger sister, Tiffani, I will always remember that bright blonde hair chasing after "squeels", singing to the Muppets, and giggling. Your passion to help others has impressed us all. To my youngest brother Courtney, the most mischievous one: throwing snowballs at cars when you couldn't even see over the snow bank, climbing the camel hills, playing soccer, and watching the Packers. Your globetrotting has made us all envious, but very proud. To my newest brother, Scott, for all the enjoyable Mac OS and Packers talk and ideas. To my upcoming new sister, Heather, buckle up, you are in for one hell of a ride!

To the new generation of our family: Tianna, it has been wonderful watching you grow into a beautiful young woman, literally from the day you were born. I always enjoy hearing what you are up to next. To Seth and Zach, those two smiling bundles I met wearing matching baby tuxedo outfits, "and the ball poppas loose"! To Chanel, originally the quiet one, but now is the loudest with your passion and goals for the future. Graham, who has astounded us all with his drawing skills and knowledge of cars and computers, I am looking forward to riding in one of your designs that Seth and Zach have built! And to Duncan, our newest, welcome to our family and I will definitely have some secrets about your Mum when you are ready!

To my “newer” family: Tom, Janet, and Amy Thul, and of course, Nanny (Ella Gahler) and Grandpa (Wally Thul). You welcomed me into your family with big open arms, and helped us so much while we were here. I am most thankful to you for letting me take your daughter and sister away for a while. Can’t wait for all the family RV trips.

To my family in England: Eric, Pearl, Theresa, John, Yvonne, Mario, Alexandra, and Horatio. Thank you for all the great memories and potential dreams of another life. Of course, I must include Hazel and Myles Jackson as our extended family, for all the times they took care of us after our long journeys.

To my family in India: All my father’s sisters and their families, I wish we knew each other better. Haider Noorani and family, a great friend of my father’s, who has always kept in touch. Also, Uncle Razak (Bom-Bom) for giving us a piece of my father’s history.

To my friends at a young age across the globe: My Edmonton pals, including Ian Leonard, Scott McKerchar, Kate Rogers, and the Coulters. To my Reading pals, including Chris Hiester, Peter Cress, David Solinger, Gary Miller, Eddie Brown, the Taylor gang, and Anna Mae Adams. To all my Green Bay pals on Rowe Lane (what a crew!). To Chris Schultz, who became a life long friend (will you ever eat another popsicle?). All your friendships and memories have supported me through this journey.

Many of my early teachers were incredibly influential in my beginning years. To Mrs. Lines, Mrs. Grainger, and Mrs. Priebe, who helped me through some difficult times. To Mr. Bruce Gehret, whose gift of a globe of the Earth has always helped keep the world around me in perspective. Who could forget those pants that (Crazy) Ray Greisinger wore for physics and chemistry? He knew we were laughing, but surprisingly we were all still paying attention. Or Jeff Parish’s red eyes … yeah, he was “tired”. Or how about all the stories of bears by Peter Bonkowski? Never again was Calculus as interesting. My language teachers of Ginny Giguere and Mary Schwartz. I learned that writing could take you places you may never go but can still imagine. My guidance counselor, Marlyn Gilbert, who also enjoyed woodworking and was always so encouraging. He was as depressed at losing those scholarships as I was. To Russ Holdiman, a really great man who understood wood like no one else, and the antics of young boys in shop class. When are we going parachuting? Thanks for all you taught me and for being a friend to us all.

To my professors at University of Minnesota, including Chester Miracle and George Brauer (red tongue and "what is infinity like?"). This is where I learned the most.

To all my friends in my early college years, especially Stuart Bale, Philip Price, Chris Sietz, Larry Leon, Sean McNamee, Neil Simmons, Jay Larson, Jason Hinze, and the whole third floor "Tower" and "Reno" friends. My, those were formative years. To Joe Wallerius, I shared lots of laughter and fun with his brothers and family. Thanks for all the rides to and from Green Bay. You also taught me that its ok to go backwards for a while once you've reached your limit, and this is not such a bad thing, could be the smartest move you ever make! To John Siebenshuh, memories of listening to music late at night for Mechanical drawing, the long drive to CA, and lots of Mountain Dew. You taught me that I should enjoy life, and one can *never* have enough electronics ("I've got to have more watts!"). We met the night of freshman orientation, man those people dancing were hosers (Joe, we're looking your way). To David Schnorenberg, watching you work you're a** off and still get up at 4 am, just so you could make your dreams come true. Always wondered how hard one could kick Pumpkinhead's door without being expelled – it helps being the teacher's pet! Who will move across the country next?

To the Stanford "B" Team: John Siebenshuh, Greg Augenstein, David Schleicher, Jerry Yen, and Daryl Kabashigawa. You are all on my "A" list … 8). Also to my lab and homework partners, Mike Prior and Clark Cohen, couldn't have done it without you. You all told me the PhD wasn't worth it – can't say you are all wrong, but glad you convinced me not go back to our alma matter.

To Dave Wahlstedt and all the woebegone members of "Dave's House for WE", including Paul Felix ("1st Ave. Man!"), Chris Okey, Craig, Carleton, and Vance. Robes were always at 8:00. Still remains the longest time I ever spent in one house my whole life. Also to the Sunday morning football crew – on those fields I learned one can never play enough sports, watch sports, or start fantasy games about sports.

To my traveling partners and oh, so many wild nights: Michael Carroll, Missy Fisher, Lori Sorensen, Ada Farnell, and Jody Sorensen. Good times …

To Alex Case and Paul Samanant. Much wisdom imparted with large quantities of libation. The three of us hit almost every Sexorama night there ever was. Too much fun. Glad Honeywell never found out we went out five nights a week!

To all my Honeywell co-workers, many who became good friends, Mario Ignagni (taught me so much about Kalman filters), Larry Vallot (still one of the brightest persons I know), Scott Snyder (hey, Tom Cruise? … 8), Erik Lindquist (late night comrade), Tony Case (Tetris anyone?), Bill Volna ("Can I borrow your camera?"), Alan Touchberry, Mahesh Jeerage, Brian Schipper, Jennifer Sly, Rich Olson, Ron Quinn, Valerie McKay, Dave Lowry, and all the members of the Navigation section and those in MN, FL, AZ, and NM. To my friend Tricia Syke, who was always there to help me get through tough times by making me laugh at something crazy (moo!).

A big thanks goes to Jeff Dinsmore, the best flight instructor, and the Honeywell Flying Club. Learning to fly has only deepened my interest in engineering.

To Holly Paige, thanks for keeping Kristen busy while I was always gone. Our house and lawn have always appreciated your care.

To John Drake for helping us fix our house up. To our renters, thanks for helping us over the years. To our neighbors, Janet, Fred, Greg, Stephanie, Ed, Richard, and the Hernandez family ("the Christo-kids"), who made lots of many interesting memories.

To the Space Systems Laboratory, including David Akin (thanks for the office and the advice!!), Mary Bowden, Ella Atkins, and Rob Sanner (you taught me so much). I would not have made it here without the support and friendship of my peers in the lab: Craig Carignan, Sarah Hall, Dave Hart, Glen Henshaw, Mike Perna, Brian Roberts, Stephen Roderick, Brook Sullivan, and all the rest. Keejoo Lee and all the fellow students in the Manufacturing building made graduate life completely tolerable.

My Teaching Assistant buddies: Joe Schultz (Go Packers! Beat the Vikings!!), Ryan Lee (who went through hell during our time together, but came out the other side a better man), Igor Alonso-Portillo (who could ever forget this smiling character?), and Marc Gervais (I still hear Igor weeping). To my study partner, Jim Simpson, who got me through a lot of long homeworks. Thanks for all the friendship you have shown over these years, making Kristen and I feel at home. To Ken Wallace, who inspired us all with his flights at Top Gun – you are our Ace, and I wish we could have done more research together. To Yannick Pennecot, Sylvan (Woody), Maria Ribera, and Ramon. Igor and Yannick never ceased to keep me from laughing at their antics (if Ella only knew …).

To my football buddies at Maryland: Falcon Rankins, Ashish Purekar, Karthikeyan Duraisamy ("Super Safety"), Sean Guerra, Michel Santos, Michael Brigley, and all the rest. Was a great break from the research routine. Glad we did it for Swami.

Also to the Engineering Graduate Student Council: it has been an honor and a privilege to work with all of you. Keep up the great work!

Special thanks go to all in the Aerospace Engineering Department, who have helped me along in many simple and a few difficult situations, including Bryan Hill (always full of good advice – at least "full" of something …), Patricia Baker (who is really kind to Kristen and I and always interested about our personal lives here in Maryland – a great "mother" figure to all us displaced students), Becky Sarni, Debora Chandler, and all.

I owe a lot of my success here at Maryland to Dr. William Fourney, our Department Chairman. He has been a friend, mentor, and sage my entire time here. I am grateful for all he has done for me, which is quite a lot. Thanks for encouraging me all along the way.

To my friends and colleagues at the Naval Research Laboratory, who collaborated in much of this research, Kent Wood, Paul Ray, Michael Wolff, Michael Lovellette, Zachary (Wiz) Fewtrell, Jon Determan, Daryl Yentis, and Lev Titarchuk. I really owe a large debt of gratitude to Kent Wood for giving us the opportunity to investigate pulsars and navigation with his USA experiment data. Paul taught me everything I know about X-ray pulsars, and I never could have done it without his help. I must also thank Liam Healy for all his orbit determination help, Glenn Creamer for his helpful filtering discussions, and Robert Nelson for his enlightening insights on relativity.

Much of this research would never have been accomplished without the astronomers and astrophysicists who tirelessly observed these sources and discovered their unique

characteristics. I really appreciate the helpful discussions from David Nice, Saul Rappaport, Christopher Reynolds, Cole Miller, Charles Misner, and Deepto Chakrabarty during my studies. Yong Kim's early work catapulted my cataloguing efforts.

We were able to survive through this research with the significant contributions of the Metropolitan Washington DC Chapter of the ARCS Foundation. We enjoyed meeting all the members and their curious nature, on science and our lives.

My work succeeded through the wonderful contributions of Dr. Edna Hokenson. She has turned her sacrifice into something really special. It has been an honor to be awarded the grant in Gus' name. We will all miss her lovely smile, laugh, and thoughts on life.

To my advisor, Darryll Pines, who took a chance on a lonely, frustrated soul. Tremendous amounts of encouragement, support, and friendship don't even begin to describe all that you have given me. My future will always be bright after all you taught me. Really enjoyed all the late evening discussions, surprisingly little about our research. Don't ever let your "creative energy" become extinguished.

And of course most importantly, to my beautiful wife, Kristen. *Thank you for everything* only starts to express what you have provided. I could not have ever made it without you here to share the joys and frustrations. The experience was worth it all, especially having my best friend beside me. Looking forward to a wonderful long future together – where are we off to next?

And lastly, to all those slogging at their research late at night while all their buddies are out drinking. Keep it up, and take a break when you have to. Remember the journey itself is the reward.

Table of Contents

List of Tables

List of Figures

List of Abbreviations

AGN	–	Active Galactic Nuclei
APSR	–	Accretion-Powered Pulsar
ARGOS	–	Advanced Research and Global Observation Satellite
ATNF	–	Australian Telescope National Facility
AXP	–	Anomalous X-ray Pulsar
BCRS	–	Barycentric Celestial Reference System
BH	–	Black Hole
BHC	–	Black Hole Candidate
BV	–	Binary Variable star
CCD	–	Charge-Coupled Device
CS	–	Coronal Star
CV	–	Cataclysmic Variable star
CXC	–	Chandra X-ray Center
DBS	–	Direct Broadcast Satellite
Dec	–	Declination
DSN	–	Deep Space Network
DXB	–	Diffuse X-ray Background
ECI	–	Earth Centered Inertial
ESA	–	European Space Agency (European Union)
ET	–	Ephemeris Time
FK5	–	Fifth Fundamental Catalogue
FOV	–	Field Of View

FW10	–	Full-Width 10% Maximum
FWHM	–	Full-Width Half Maximum
GC	–	Globular Cluster
GCVS	–	General Catalogue of Variable Stars
GDOP	–	Geometric Dilution Of Precision
GEO	–	Earth (related)
GEO	–	Geosynchronous Earth Orbit
GLONASS	–	Global Navigation Satellite System
GPS	–	Global Positioning System
GRE	–	Galactic Ridge Emission
GSFC	–	Goddard Space Flight Center
GXC	–	Galaxy Cluster
HEAO	–	High Energy Astronomy Observatory
HEASARC	–	High Energy Astrophysics Science Archive Research Center
HMXB	–	High-Mass X-ray Binary
ICRF	–	International Celestial Reference Frame
INS	–	Isolated Neutron Star
ITRF	–	International Terrestrial Reference Frame
J2000	–	Epoch year 2000, JD 2451545.0 TDB
JAXA	–	Japan Aerospace Exploration Agency
JD	–	Julian Date
LAGEOS	–	Laser Geodynamics Satellite
LEO	–	Low Earth Orbit

LHS	–	Left Hand Side
LMC	–	Large Magellanic Cloud
LMXB	–	Low-Mass X-ray Binary
LORAN	–	Long-range Radio Navigation
LRO	–	Lunar Reconnaissance Orbiter
MEO	–	Medium Earth Orbit
MJD	–	Modified Julian Day
MPSR	–	Millisecond Period Pulsar
MRSE	–	Mean Radial Spherical Error
NASA	–	National Aeronautics and Space Administration (USA)
NDB	–	Non-Directional Beacon
NKF	–	Navigation Kalman Filter
NORAD	–	North American Aerospace Defense Command
NRAO	–	National Radio Astronomy Observatory
NRL	–	Naval Research Laboratory
NS	–	Neutron Star
NSF	–	National Science Foundation
OMEGA	–	Optimized Method for Estimating Guidance Accuracy
PDOP	–	Position Dilution Of Precision
PNT	–	Post-Newtonian Time
PPN	–	Parameterized Post-Newtonian
PPT3	–	Position and Partials as functions of Time Version 3
PRN	–	Pseudorandom Noise

PSPC – Position Sensitive Proportional Counter

PSR – Pulsar

RA – Right Ascension

RAC – Radial, Along-Track, and Cross-Track

RHS – Right Hand Side

RMS – Root Mean Square

ROSAT – Röntgen Satellite

RPSR – Rotation-Powered Pulsar

RS CVn – RS Canum Venaticorum type star

SAO – Smithsonian Astrophysical Observatory

SAO – Special Astrophysical Observatory (Russia)

SC – Spacecraft

SDP4 – Simplified Deep Space Perturbations Number 4

SGP4 – Simplified General Perturbations Number 4

SGR – Soft Gamma Repeater

SMC – Small Magellanic Cloud

SNR – Signal-to-Noise Ratio

SNR – Supernova Remnant

SSB – Solar System Barycenter

SSPS – Solar System Positioning System

TAI – International Atomic Time

TCB – Barycentric Coordinate Time

TCG – Geocentric Coordinate Time

TDB	–	Barycentric Dynamical Time
TDOA	–	Time Difference Of Arrival
TDOP	–	Time Dilution Of Precision
TDT	–	Terrestrial Dynamical Time
TLE	–	Two-Line Element
TOA	–	Time-Of-Arrival
TT	–	Terrestrial Time
URA	–	User Range Accuracy
USA	–	Unconventional Stellar Aspect experiment
USA	–	United States of America (also U.S.)
UT	–	Universal Time
UTC	–	Coordinated Universal Time
VLBI	–	Very Long Baseline Interferometer
VOR	–	VHF Omni-directional Radio Range
WD	–	White Dwarf star
XB	–	X-ray Binary
XNAVSC	–	X-ray Navigation Source Catalogue
XPSR	–	X-ray Pulsar
XTE	–	Rossi X-ray Timing Explorer

Chapter 1 Introduction

"I must go down to the seas again, to the lonely sea and the sky,

And all I ask is a tall ship and a star to steer her by …"

– *Sea-Fever*, John Masefield 1902

1.1 Motivation

This quote from Masefield's early 20^{th} Century poem reflects the perspective of a traveler's ambition to plot a course over Earth's oceans and steer one's vessel towards its destination. This yearning of humankind to explore their surroundings has always been directly related to their ability to determine a path to follow along their journey, with the eventual goal of returning home. As their skill to precisely determine dependable paths has developed, the evolution of human's capability to safely traverse their environment has progressed. Although unique discoveries are often unveiled through deviations off an intended path, whether planned or unplanned, reliable routes and methods to maintain one's location and speed along these routes have promoted humankind's expansion over its livable globe.

The essence of exploration has three components: navigation, guidance, and control. Navigation is the art of determining one's location and orientation relative to the intended destination. Guidance is the art of determining the optimal path to follow to arrive at a destination based upon one's current location. Control is the art of directing one's vehicle to follow the optimal path.

Since navigation is the crucial first step in the process of beginning any journey, and is the method of verifying the location along an intended path, substantial capabilities have been created for this process while on Earth. As humans continue their reach about and beyond their tiny planet into the space environment where there are yet many unknowns, methods of advancing the capability of navigation must continue. Therefore, investigating new methods to improve the ability to navigate while in space aids current day exploration, and may eventually advance this capability in all environments.

1.1.1 Navigation on Earth

The development of navigation methods and tools has been continual since humans first ventured out of sight and safety of their local refuge. Land-based navigation over Earth has been accomplished with acceptable accuracy for thousands of years. Humans are well adapted to identifying *landmarks* to maintain a reference to their location. Methods of *triangulation* with respect to multiple landmarks allow refined location estimation. As these landmarks were recorded, the creation of maps assisted travel over foreign lands. Methods to determine speed over the terrain were eventually developed, as well as determining the orientation of a vessel with respect to known fixed objects or the planet's magnetic poles. Map reading and processes of *dead reckoning* assisted many successful journeys.

However, when humans ventured to travel over the seas and oceans, many of these fixed visual cues were no longer available once land slipped past the visible horizon.

New methods of navigating needed to be devised. Although some cultures adapted quicker than others, many sought the use of celestial objects as points of reference for navigating the featureless oceans. As observed from Earth's surface, the motions of the Sun, Moon, planets, and stars initially provided the concept of *time*, as their periodic motions formed the concept of a *celestial clock*. As long as one could look up and recognize a celestial object above the horizon, a reference to time, and eventually to location, could be computed. Early Polynesians traveled thousands of miles across open oceans using only the knowledge of the motion of stars, the existence of sea swells, and the appearance of certain birds and sea creatures. This information was handed down orally from one generation to the next, often simply in the form of a song [92]. The great distances these seafarers traveled with regular repeatability proved that these simple objects and their reported characteristics could provide sufficient navigation information.

All celestial objects, including the Sun, Moon, planets, and stars, came to be widely used for many centuries as sources for positional reference markers. Using catalogued celestial almanac data the observation of visible stars provided navigators on Earth a means to determine location information relative to observation stations fixed on Earth. The chief drawback of *celestial-based navigation*, however, was the restricted viewing times and the limited visibility of these objects due to inclement weather. However, as methods of utilizing these objects have matured over time, in addition to the development of instrumented time clocks, or *chronometers*, the performance of navigation methods has improved.

Determining latitude over Earth via inclination of celestial objects above the horizon proved simpler than computing longitude. Accurate, all-weather methods of navigation across vast ocean longitudes was not accomplished with sufficient accuracy and repeatability until chronometers improved in accuracy within the 1800s [197]. The use of the chronometer allowed navigators to compare the local observed time to the time at a known fixed location in order to determine the change in longitude with respect to the known location. The use of these instruments eventually replaced many proposed schemes that utilized celestial-based clocks. The time comparison method required knowledge of time at a known reference location, which typically meant transporting multiple timepieces, one for local time and one for reference time. If instead this information could be broadcast to a user, the complexity of the user's equipment would be reduced.

In addition to chronometers, local navigation beacons were created to assist navigation relative to a specific location. Optical lighthouses were established, which produced periodic flashes of light, to warn mariners of potential dangerous shorelines, as well as provide an estimate of distance to the fixed lighthouse location. Radio-based navigation beacons, such as LORAN, NDB, OMEGA, and VOR, were developed once radio communication was invented. These systems provide distance and direction information to both sea craft and aircraft for improved navigation accuracy, although the data communicated by these navigation beacons to vehicles has limited range and many beacons are necessary to cover a large geographical area.

Recognizing the need for all-weather, systematic time comparisons and range determination, during 1960-1980 the United States military developed a timing system which has grown into what is known today as the Global Position System (GPS) [156, 157]. A constellation of satellites orbiting Earth broadcast time and data information for users to receive and process in order to compute time, position, velocity, and attitude over Earth. These human-made *celestial objects* achieve similar, but greatly improved, reference information that the Sun, Moon, planets, and visible stars provided to early history navigators. GPS has developed into a useful utility for Earth-bound users. In addition to the U.S. GPS system, the existing Russian Global Navigation Satellite System (GLONASS) [177] and the future European Union planned Galileo system provide worldwide time and navigation information to users on or near Earth.

The term *navigation* has advanced to signify the process of determining position, velocity, attitude, and attitude-rate of a vehicle specified at a certain time or times. Navigation systems that provide this data for a vehicle include components that measure internal characteristics of the vehicle's motion as well as sensors that derive information from external sources to maintain accurate computed motion.

1.1.2 Navigation in Space

Human's ability to travel has progressed to the point of allowing exploration outside Earth's atmosphere into the outer space environment. With this new setting in which to explore, new methods for determining navigation information for vessels in space have been devised. Several descriptive terms have developed that distinguish between the various types of navigation used for spacecraft missions:

- *Orbit Determination*: Process of determining the orbit of vehicle or object through repeated and/or successive observations of the vehicle or object from Earth ground stations. Observational measurements are combined to produce the best estimate of orbit state dynamics of vehicles.

- *Orbit Propagation*: Process of propagating the state dynamics of a vehicle or object in orbit using models of force acting upon the vehicle or object. The state dynamics are numerically or analytically integrated to produce the best estimate of position and velocity.
- *Orbit Navigation*: Process of determining the vehicle or object state data by utilizing external sensors to measure the vehicle's navigation state, including time, position, velocity, acceleration, attitude, and attitude rate. Includes the blending of external sensor data with internal sensor data to produce high accuracy navigation solutions for a vehicle. The navigation solution is generated autonomously by the vehicle and its sensors, and may be verified using a ground-based orbit determination solution.

Navigation of vehicles above and beyond Earth's surface has gained significantly from knowledge of the navigation methods developed on Earth. For example, many satellites orbiting Earth and spacecraft traveling through the solar system have relied on celestial sources to successfully complete their missions. Additionally, celestial source navigation systems have been augmented with human-made systems to further increase spacecraft navigation performance. To date, many methods have been used to compute the navigation information of spacecraft that have traveled around Earth, through the solar system, and beyond the solar system's outer planets, as far as the heliopause.

Exploration between Earth, its Moon, and other solar system planets has been largely successful. Most missions have encountered their target object with relatively good accuracy, sufficient enough to carry out their mission. Navigating and controlling vehicles within Earth-orbits or towards their planetary destinations is still a challenge however, requiring accurate ground-based tracking of a vehicle to correct any solution discrepancies. Since spacecraft in orbit about a central mass follow a predictable, often stable, path that can be estimated using the propagation of the vehicle's dynamics, an analytical solution of a spacecraft trajectory can be studied prior to launch. However, unmodelled or unforeseen disturbances may perturb the vehicle from the orbit path and eventually an orbit propagator's position error grows to an unacceptable level for vehicle guidance or control. Orbit determination methods using observations of the spacecraft from Earth ground stations can detect these deviations of the vehicle from the predicted path and can update the estimation of the orbital elements. Alternatively, vehicles can perform the navigation function with onboard sensors in order to detect these disturbances and correct its own solution. Whether the navigation solution is produced via ground station observations or onboard systems, various types of sensors have been developed to support the navigation function.

Knowledge of time onboard a spacecraft is important for various operations, such as process timing for payload functions, communications, and for determining locations of local bodies using ephemeris data. Time has been determined using a clock on-board the spacecraft, or through periodic computer updates from ground control stations. Therefore, an accurate clock has become a fundamental component of most spacecraft navigation systems. For example, in order to track radio signals from Earth at accuracies of a few tenths of a meter, a clock with nanosecond accuracy over several hours is needed [128]. This tracking accuracy requires the clock to be stable within one part in 10^{13}. Just as early chronometers helped improve navigation over Earth's ocean, more accurate chronometers assist navigation through the solar system. Atomic clocks available for spacecraft applications provide high accuracy references and are typically accurate to within one part in 10^9-10^{15} over a day.

Attitude determination of spacecraft is necessary in order to properly orient payloads with respect to their intended targets. Onboard gyroscopes can sense the spacecraft's rotation rate relative to an inertial frame and once initialized can provide attitude and attitude rate information to the vehicle. Sensors that measure Earth's magnetic field, magnetometers, and Earth horizon sensors can also be used to orient Earth-orbiting satellites relative to an Earth frame. Celestial objects including the Sun and stars are also used for attitude determination. Sun sensors, star cameras, and star trackers are often used for many spacecraft missions due to their high accuracy from these distant stellar objects.

The extremely large distances to the stars in the Milky Way galaxy and other galaxies essentially create the illusion that the stars are stationary with respect to a coordinate frame fixed to Earth. Therefore, the rotation and/or translation of a spacecraft with respect to the apparently *fixed* background of stars allows the measurement of attitude, attitude rate, and to some extent, position. However, just as the solar system rotates, so does the Milky Way rotate and the Galaxy translates with respect to neighboring galaxies. Hence, although these distant objects seem stationary, they are speeding away or towards the solar system continually at all times. Fortunately, the motion of the stars is very slow compared to many other measurements of time such that for the vast majority of applications this motion can be considered negligible.

Similar to methods developed on Earth to triangulate a position relative to identifiable landmarks, it is conceivable to use persistent starlight as markers for triangulating spacecraft position [17]. The large distances to these objects, however, does not produce large changes in line-of-sight angles even with significant position changes of spacecraft within the solar system. Typically only unit directions to these objects and their relative directions to other solar system objects are utilized. In addition to small angular changes due to the extreme distances to these objects, there is no method of determining *when* the visible light was sent from these stars, thus determining range information from an individual star to triangulate a spacecraft's position is problematic.

During the instance of *occultation*, or when a known celestial body passes in front of a selected star, the relative position information to a known object can be deduced directly from starlight [17]. If the atmosphere of a local body is in view, measurements of spacecraft range from the body can be produced by the refraction of starlight as a stellar object passes behind the body's atmosphere [68]. Both of these methods require a local body to be in view, accurate models of the body's atmosphere to be available, and the spacecraft must be near to the body such that multiple measurements can be produced.

Although there are substantial benefits of celestial-based navigation, most space vehicle operations have relied heavily on Earth-based navigation solutions to complete their task [89, 128, 221]. Radar range and optical tracking methods have been the predominant system for tracking and maintaining continuous orbit determination of spacecraft [16, 219, 221]. In order to compute the position of a spacecraft, radar range systems compute the range, range-rate, and/or the angular orientation angles to the spacecraft relative to the radial direction from a radar tracking station. This is achieved primarily through the reflection of signals transmitted from an Earth observing station by the space vehicle structure and measurement of the transmitted signal round-trip time. Accuracies on the order of a few meters or less in range and fractions of mm/s in range-rate are possible, although the remaining two axes of position typically have much larger error [89]. Early demonstrations using these tracking systems on the Vikings spacecraft missions to Mars showed positional accuracies to within 50 km, and projected accuracies of hundreds of kilometers at the outer planets [128].

Although a ground-based tracking system requires no active hardware on the spacecraft itself, it does require extensive ground operations and careful analysis of the measured data against an electromagnetically noisy background environment. By processing multiple radar measurements over time, the vehicle's orbit parameters can be computed. The position of the vehicle can be propagated ahead in time using standard orbital mechanics that includes known models of solar system object's gravitational potential field and any known disturbance or perturbations effects, such as object body atmospheric drag. This propagated orbit determination solution is then compared to subsequent radar measurements and the orbit solution is corrected for any computed errors. This process continues until a satisfactory orbit solution converges to within the expedition's required parameters. However, vehicle maneuvers or any unanticipated disturbances will affect the trajectory of the vehicle. Without exact knowledge of these maneuver dynamics or disturbance effects, it is necessary for the propagation and radar measurement comparison to continue throughout the flight.

As a spacecraft moves further away from Earth observation stations, the error increases in radar-ranging solutions of spacecraft orbit data. To achieve the necessary range determination, the radar system requires knowledge of the observation station's position on Earth to great accuracy, which necessitates sophisticated surveys of each ground antenna [89]. An additional limitation is the accuracy of known positional information of the solar system objects [89]. This solar system ephemeris data has continually improved with new observations and spacecraft flybys. However, even with this precise station and ephemeris knowledge, the vehicle position measurement can only be accurate to a finite angular accuracy. The transmitted radar beam, along with the reflected signal, travels in a cone of uncertainty. This uncertainty degrades the position knowledge in the transverse direction of the vehicle as a linear function of distance. As the vehicle gets more distant, any fixed angular uncertainty reduces the knowledge of vehicle position, especially in the two transverse axes relative to the range direction. These axes are *along-track* of the vehicle's velocity and *cross-track*, or perpendicular, to the vehicle's velocity and radial direction.

Alternatively, many spacecraft, including those traveling into deep space or on interplanetary missions, have employed active transmitters to be used for orbit determination purposes [89]. The radial velocity is measured at a receiving station by measuring the Doppler shift in the frequency of the transmitted signal. The spacecraft essentially receives a *ping* from an observation station on Earth and re-transmits the signal back to Earth. Although improvements in the radial direction range and range-rate measurements are made utilizing such system, transverse axes errors still exist, and this method has errors that also grow with distance. The Deep Space Network (DSN) assists navigation of vehicles far from Earth by determining range and range-rate along the line-of-sight from the ground radar station to the vehicle [88]. Three locations, located roughly 120° apart, at Goldstone (California, USA), Madrid (Spain), and Canberra (Australia) can provide continuous observation of vehicle missions. Although accurate radial position can be determined, DSN requires extensive ground operations and scheduling to coordinate the observations. Even utilizing interferometry, by using the difference between multiple signals compared at two ranging stations, the angular uncertainty can grow significantly for distant spacecraft. Total position accuracies on the order of 1 to 10 km per AU of distance from Earth are achievable using interferometric measurements of the Very Long Baseline Interferometer (VLBI) through the DSN [89].

Optical tracking measurements for spacecraft position and orbit determination are completed in a similar fashion as radar tracking [16]. Optical tracking uses the visible light reflected off a vehicle to determine its location. Some optical measurements require a photograph to be taken and the vehicle's position is calculated after analysis of the photograph and comparison to a fixed star background. Real-time measurements using such systems are typically not easily achieved. Additionally, optical measurements are limited by favorable weather and environmental conditions.

Since many missions have concentrated on planetary observation, augmentation to the ranging navigation system can be made within the vicinity of the investigated planet. By taking video images of the planet and comparing to known planetary parameters (such as diameter and position with respect to other objects), the video images can determine position of the spacecraft relative to the planet [17]. Often the objective is to orbit the planet, thus only relative positioning is primarily required for the final phase of the flight. Based upon solar system dynamics, it is possible to predict a planetary object's location within the solar system's coordinate frame to high accuracy over time. Using the determined relative position information and the objects inertial location, a spacecraft can consequently determine its absolute position.

Typically, combinations of Earth-based radar ranging and on-vehicle planet imaging are required to produce accurate navigation solutions for deep space missions to another planet. This method of navigation still requires human interaction and interpretation of data. Additionally, as radar-ranging system errors grow as the distance from Earth increases, accurate orbit determination to the outer planets becomes progressively more complex due to the required finer pointing accuracy of ground antennas. Vehicles that process planetary images to improve radar-ranging solutions have complicated vehicle subsystems and increased cost. This imaging process also requires planets to be sufficiently close along the vehicle's trajectory in order to be photographed.

For vehicles operating in space near Earth, the current Global Positioning System (GPS) – and similar human-developed systems – can provide a *complete* navigation solution comprised of referenced time, position, velocity, attitude, and attitude rate [156, 157]. The GPS system produces signals from multiple transmitting satellites that allow a receiver to determine its position from the ranges to each transmitting satellites. However, these satellite systems have limited scope for operation of vehicles relatively far from Earth. Unpredictably, these systems may have their service interrupted through malfunction or unforeseen circumstances.

Table 1-1 through Table 1-3 provide a summary of sensors and methods used to determine spacecraft time, attitude, and position. Estimates of performance for each system are provided.

Table 1-1. Spacecraft Time Determination Methods and Comparisons [48, 49, 221].

Method	Advantages	Disadvantages	Performance
Computer-Counters (ex. Crystal Oscillators)	- Measures intervals	- No absolute time	- Stable to 1 part in 10^{10} per orbit - About 100 μs within GMT
Ground-based Time Tagging	- Timing handled by ground operations	- Extensive ground tracking and communication	- 2.5 - 25 μs
Atomic Clocks	- High accuracy	- Expensive - Weight	- Stable to 1 part in 10^{14} per year
GPS	- High accuracy	- Visibility - Requires system maintenance	- ≤ 40 ns (95%) (SPS)

Table 1-2. Spacecraft Attitude Determination Methods and Comparisons [107, 221].

Method	Advantages	Disadvantages	Operating Range	Performance
Horizon Sensor - Scanner - Fixed Head	- Infrared sensing of Earth limb	- Low operating range	LEO	<0.1° to 0.25°
Magnetometer	- Simple, reliable, lightweight	- Uses Earth magnetic field - Requires separation from payload	LEO	0.5° to 3°
GPS	- High accuracy - Full nav solution	- Requires GPS system maintenance - Signal multipath	LEO (< GPS orbit)	0.3° to 0.5° (requires antenna separation)
Sun Sensor	- Can use data from observing payload	- Requires unobstructed view of Sun	LEO to Interplanetary	0.005° to 3°
Inertial Measurement Unit (gyros and accelerometers)	- Angular rate data and acceleration	- Requires external aiding	LEO to Interplanetary	Gyro drift rate: 0.003°/hr to 1°/hr Accel linearity: 1 to 5 $\times 10^{-6}$ g/g^2
Star Sensor - Camera - Tracker/Mapper	- High accuracy	- Moderate to High Cost	LEO to Interplanetary	0.0003° to 0.01°

Table 1-3. Spacecraft Position Determination Methods and Comparisons [107, 221].

Method	Advantages	Disadvantages	Operating Range	Performance
Landmark or Ground Object Tracking	- Can use data from observing payload	- Landmark detection may be difficult - May have geometry singularities	LEO	5 km
Stellar Refraction (Horizon Crossings)	- Could be autonomous for attitude and position - Uses attitude-sensing hardware	- Fairly new concept	LEO	150 m - 1 km
TDRS Tracking System	- NASA spacecraft - High accuracy - Same hardware for tracking & data	- Not autonomous - Mostly NASA missions	LEO	50 m
Satellite Crosslinks	- Can use satellite crosslink hardware	- Unique to each satellite constellation - Only relative position (no absolute) - Potential problems with system deployment and S/C failures	LEO	50 m (in theory)
GPS	- High accuracy - Full nav solution: time, attitude, position and velocity	- Requires GPS system maintenance	LEO to MEO (< GPS)	15 m-100 m (in LEO)
Star/Moon Sextant	- Could be autonomous for attitude and position	- Fairly new concept - Heavy and high power	LEO to GEO	250 m
Sun, Earth & Moon Observer	- Could be autonomous for attitude and position - Uses attitude-sensing hardware	- Flight tested - Initialization and convergence depend on geometry	LEO to GEO	100 m-400 m (in LEO)
Ground-based Tracking Systems	- Traditional approach - Method well established	- Accuracy depends on station coverage - Not autonomous, operation intensive	LEO to Interplanetary	1 - 100 km

1.1.3 Future Space Navigation Architectures

As exploration of the solar system continues, methods of increasing the navigation performance while reducing the system complexity are attractive to many expeditions. With the benefits of a complete navigation solution provided by the GPS system for near-Earth applications navigation and the accuracy provided by range measurements from radar system for deep space missions by DSN, it is necessary to investigate methods that could provide a complete, accurate navigation solution throughout the solar system, and perhaps even interstellar and eventually intergalactic regimes.

On a larger scale, conceiving a GPS-like human developed and controlled system that encompasses the entire solar system it not unimaginable. For example, a *solar system positioning system* (SSPS) could be created. This would require transmitting spacecraft to be deployed throughout the solar system in orbits either inclined to the ecliptic plane of the solar system, perhaps outside the orbit of Jupiter or Pluto, or in halo orbits above or below the ecliptic plane in order to provide sufficient coverage for operations to all planets. However, it can be quickly realized that the cost in development and operation of such a system would be tremendous. This type of system could only be justified once travel between Earth and other planets becomes commonplace.

Alternatively, local system constellations could be deployed, such as a GPS-like system about the Moon, the Earth-Moon system, or Mars and its moons. These types of local systems would allow communication as well as navigation to be performed by the orbiting spacecraft. Even though only a few satellites would be necessary in these local system constellations, the deployment and operations cost would still be significant. Since the ground control segment of the GPS system provides a significant role in maintaining the accuracy of that system, similar control segments would be required for these GPS-like systems, which would utilize extensive resources back on Earth.

With the newly proposed missions for humans to explore the Moon and Mars [5], these types of local system constellations would support navigation in orbits about these bodies and on their surfaces. However, unless these beacons can produce powerful, omni-directional signals, the interplanetary trajectory phase of these missions would still require radar-tracking based navigation from Earth. A single system that could support both phases of these mission would be much more attractive.

A less complex method than local satellite constellations about each body may be to place several navigation beacons on planetary or moon surfaces throughout the solar system, effectively creating a ranging system spread across the system with adequate visibility. The remotely operated beacons could aid spacecraft along their journeys to different planets. Unfortunately, the cost of even operating these remote beacons is still prohibitive, and the need for such beacons would have to grow substantially to be considered.

1.1.3.1 Autonomous Operation

As the cost of vehicle operations continues to increase, spacecraft navigation is evolving away from Earth-based solutions towards increasingly autonomous methods [58, 68]. Autonomous operations of spacecraft require the determination of a complete navigation solution in order to control itself towards its destination, without the interaction or assistance of human operations. Using onboard and external sensors, the vehicle's navigation system internally computes its own navigation and guidance information. Any deviations from its planned path would be detected, reported, and corrected without input from the ground mission control. Although not necessarily fully *independent* operation, using absolutely no oversight from mission control, this autonomous operation would reduce the control segment's labor-intensive operations for vehicle control, especially for constellations of multiple spacecraft or formations of spacecraft.

For near-Earth operations, using GPS can aid autonomous navigation for spacecraft that can receive sufficient signals from these satellites. Until a SSPS system is realized, the question remains whether there are any other possible methods for near-Earth and interplanetary navigation that can be used in a similar manner as GPS is used today. Celestial-based systems, which use sources at great distance from Earth, remain attractive for complementing existing systems and for developing future navigation systems that could operate in an autonomous mode.

1.2 Previous Research

1.2.1 Variable Celestial Sources

Celestial sources have proven to be significant aids for navigation throughout history, although the majority of sources used have been the fixed, persistent visible radiation stars. Those sources that produce variable, or modulated, intensity of radiation, referred to as *variable celestial sources*, have also been discovered and observed for the past few centuries [61]. Astronomical observations have revealed several classes of variable celestial objects that produce signals that vary in intensity throughout the electromagnetic spectrum, including those that emit in the high energy bands of X-ray and gamma-rays [2, 38].

Of the different variable source types, individual stars that have a uniquely identifiable signal and whose signals are periodic and predictable, can be utilized in a different manner for navigation purposes than the persistent sources. Chapter 2 provides additional detail on the discovery of these variable sources, as well as the various types. It will be shown that those sources that emit X-ray radiation are attractive for spacecraft navigation applications.

A particularly unique class of variable celestial sources is pulsars. It is theorized that pulsars are rotating neutron stars [13, 14, 155]. Neutron stars are formed when a class of stars collapse, and from conservation of angular momentum, as the stars become smaller, or more compact, they rotate faster. For certain types of pulsars, the rotation can be extremely stable. No two neutron stars have been formed in exactly the same manner, thus their periodic signatures are unique. Because many pulsars provide signals that are unique, periodic, and extremely stable, they can assist navigation by providing a method to triangulate position from their signals. Pulsars were first discovered in the radio band by Bell and Hewish in 1967 [80]. Pulsars have been observed in the radio, visible, X-ray, and gamma-ray bands of the electromagnetic spectrum.

Most variable celestial sources, including pulsars, are extremely distant from the solar system, which provides good visibility of their signal near Earth as well as throughout the solar system. However, unlike the transmitting satellites within the GPS or GLONASS systems, the distances of the celestial sources cannot be measured such that direct range measurements from each source can be determined. Rather, indirect range measurement along the line-of-sight to a pulsar from a reference location to a spacecraft can be computed. Thus, precise direction information to each source at a selected time epoch as well as any motion of the source over time is essential for accurate navigation. Existing catalogues of these variable celestial objects exist, which can assist the identification of sources that would support the navigation endeavor. However, improvements or additional accuracy of the recorded data will most likely be required for future use.

1.2.2 History of Pulsar-Based Navigation

Since their discovery by Bell and Hewish, early observers of the stable, periodic signals from pulsars recognized the potential of these stars to provide a high quality celestial clock. In 1971, Reichley, Downs, and Morris proposed using pulsar signals as a clock for Earth-based systems [167]. Pulse timing resolution of fractions of a millisecond from pulsars was achievable during that early research [168]. The stability of these sources were shown to be quite stable once long term observations were produced [167]. In 1980, details of methods to determine pulse time of arrivals from pulsar signals were provided by Downs and Reichley based upon decade-long observations made using NASA's DSN [51]. Presentations by Allan, Matsakis, Taylor, and others in the 1980s and 1990s, demonstrated that several pulsars match the quality of atomic clocks [7, 127]. Indeed, due to their measured stabilities, pulsars have been considered as celestial time standards. As discussed above, some form of time synchronization is typically utilized for accurate navigation, and improved performance can be achieved by using higher quality clocks. Thus it was soon conjectured that pulsars could also be used as clocks for navigation.

In 1974, Downs presented a method of navigation for orbiting spacecraft based upon radio signals from a pulsar [50]. This method proposed developing omni directional antennae to be placed on a spacecraft to record pulsar signal phase and create a three-dimensional position fix. Three to nine antennas of pyramidal shape that are 2 m on a side would be required for full sky coverage. Based on the 27 proposed radio pulsars for navigation and their achievable signal quality over integration time of 24 hours, position accuracy on the order of 150 km was projected to be attainable. The method assumed that no ambiguities in the phase cycles would exist if existing navigation schemes were employed in parallel with the pulsar position determination method. No relativistic effects of the pulse time transfer between a spacecraft and the inertial origin were considered. Although today's accuracy of existing navigation methods has surpassed the accuracy of the method proposed by Downs, this introductory paper on pulsar navigation provided the original basis for succeeding research.

Both the radio and optical signatures from pulsars have limitations that may reduce their effectiveness for spacecraft navigation. Wallace, in 1988, discussed the issues related to using celestial sources that produce radio emission, including pulsars, for navigation applications on Earth [218]. He states that neighboring celestial objects including the Sun, Moon, Jupiter, and close stars, as well as distance objects such as radio galaxies, quasars, and the galactic diffuse emissions, are broadband radio sources that could obscure weak pulsar signals. It is expected that radio-based systems would require large antennas to detect sources, which would be impractical for most spacecraft. Furthermore, the low signal intensity from radio pulsars would require long signal integration times for an acceptable signal-to-noise ratio as demonstrated by Downs and others [50, 51]. The small population of pulsars with detected optical pulsations (only five isolated pulsars [185]) severely limits an optical pulsar-based navigation system. Since optical pulsars are also dim sources, large aperture telescopes are required to collect sufficient photons. Any nearby bright visible sources would require precise pointing and significant processing to detect these pulsars.

During the 1970s, astronomical observations within the X-ray band of 1–20 keV (2.5×10^{17}–4.8×10^{18} Hz) yielded pulsars with X-ray signatures. In 1981, Chester and

Butman proposed using pulsars emitting in the X-ray band as an improved option for Earth satellite navigation [40]. They listed 17 known X-ray pulsars that could provide good signal coverage. Although lacking supporting analysis, sensors on the order of 0.1 m^2 were proposed, which would be significantly smaller than the antennas or telescopes required for radio or optical observations. Their proposed navigation method compares the pulse time of arrivals from pulsars between a distant spacecraft and a satellite in orbit about Earth. Using this difference in arrival times, they projected that positional accuracy on the order of 150 km after one full day of measurements could be computed. Although their analysis did not produce immediate motivation for implementing such a pulsar-based system, X-ray emitting sources present a significant benefit to spacecraft applications, primarily through their utilization of smaller sized detectors. Also, there are fewer X-ray sources to contend with and many are unique signatures, which do not get obscured by closer celestial objects.

In 1993, Wood proposed studying a comprehensive approach to X-ray navigation covering attitude, position, and time, as part of the NRL-801 experiment for the Advanced Research and Global Observation Satellite (*ARGOS*) [229]. This study included utilizing X-ray sources other than pulsars. Attitude was proposed to be determined in a similar manner as existing visible star cameras. Position of a vehicle was to be determined using the occultation of a source behind Earth's or the Moon's limb, and accuracy on the order of tens of meters was forecast. Timekeeping was also presented as a potential from X-ray sources, and accuracy approaching 30 μs over different timescales was promoted. As part of the Naval Research Laboratory's (NRL) development effort for this experiment, Hanson produced a thesis in 1996 on the subject of X-ray navigation

[72]. This work included a detailed description of spacecraft attitude determination based upon the two-axis gimbaled detector. Comparison studies to data collected by the *HEAO-1* spacecraft [233] showed attitude accuracies on order of 0.1-0.01 degrees using either a single or dual detector. Hanson's thesis also presented autonomous timekeeping using X-ray sources, including the implementation of a phase-locked loop to maintain accurate time aboard a spacecraft.

From 1999–2000, NRL's Unconventional Stellar Aspect (USA) experiment onboard the *ARGOS* satellite provided a platform for pulsar-based spacecraft navigation experimentation [166, 231, 232, 234, 235]. The X-ray data from this experiment was initially used to demonstrate the concept of attitude determination [232]. The proportional counter detector portion of this experiment ended prematurely due to the loss of gas within the detector chambers, the leak was theorized to be created by a micrometeorite strike. Research efforts, including this dissertation, are continuing to demonstrate position determination and timekeeping using the recorded data from this flight experiment. A summary, in chronological order, of significant contributions to the theoretical prediction, discovery, and observations of pulsars is provided in Table 1-4. Elaboration of these contributions, as well as other relevant references, is continued throughout the following chapters of this dissertation. Table 1-5 summarizes, in chronological order, contributions into the investigation of using pulsars as accurate, periodic beacons in space for vehicle navigation. Since the discovery of pulsars, a significant amount of research has been done with respect to navigation in general. However as seen in these tables, only recent limited introductory analysis on solving the three-dimensional position solution for spacecraft using pulsars has been attempted.

Table 1-4. Contributions to Pulsar Astronomy and Timing Research.

Year	Name	Description	Refs.
1916	Einstein	The general theory of relativity	[53]
1930s	Various	Theoretical predictions of neutron stars	[13, 14, 155]
1930s	Chandrasekhar	Theories on stellar structure and atmospheres	[37]
1967	Bell, Hewish, et al.	Discovery of radio pulsars	[80]
1977	Manchester & Taylor	Detailed overview of pulsars	[118]
1980	Downs & Reichley	Techniques for measuring pulse arrival times	[51]
1983	Murray	Pulsar astrometry and timing	[140]
1986	Hellings	Relativistic effects in pulsar timing	[15, 79]
1987	Allan	Showed comparison of pulsars & atomic clocks	[7]
1992	Taylor	Pulsar timing and relativistic gravity	[204]
1997	Matsakis, Taylor & Eubanks	New statistic for pulsar & clock stabilities	[127]
1998	Lyne & Graham-Smith	Overview of pulsar astronomy	[114]

Table 1-5. Contributions to Pulsar Navigation Research.

Year	Name	Description	Refs.
1974	Downs	Proposed using radio pulsars for spacecraft navigation	[50]
1981	Chester & Butman	Suggested X-ray pulsars for interplanetary navigation	[40]
1988	Wallace	Investigated "radio stars" for all-weather Earth navigation	[218]
1993	Wood	Proposed X-ray pulsars for near Earth orbit navigation	[229]
1996	Hanson	Doctoral thesis on X-ray navigation: attitude and time	[72]
1999	USA Experiment	Earth orbit attitude determination using X-ray sources	[166, 231, 232]

1.3 Overview of Contributions

This dissertation research pursued an in depth analysis of the use of pulsars, specifically those emitting X-ray radiation, for navigation of spacecraft. The original contribution of this dissertation research consists of the first comprehensive study of all aspects of spacecraft navigation using variable celestial sources. This includes reviewing previously proposed methods of navigation using these types of sources; investigating the types and number of sources that can support high accuracy navigation; determining the accuracy of pulse measurements of individual and groups of sources; developing new methods of computing time, attitude, position, and velocity; and demonstrating the expected performance of these methods using recorded and simulated data.

An X-ray celestial source catalogue has been created to support this research. Via thorough research of existing catalogues and individual source papers, this new catalogue identifies candidate sources for navigation. A quality figure of merit is derived to rank individual sources that benefit time and position determination. To support the pulse timing analysis, a study of the comparison of pulse arrival times at the visible, radio, and X-ray energy ranges for the Crab Pulsar was produced. This work demonstrated that each energy range has a unique arrival time, and identified several issues with absolute timing of photon arrivals for X-ray astronomy missions.

A detailed derivation of the time transfer equations between an orbiting spacecraft and the solar system barycenter has been developed. These equations are used to transfer the arrival time of a pulse on a spacecraft to the inertial origin or pulse model definition location. This derivation has identified a potential discrepancy with existing pulsar timing equations.

Numerous original algorithms and analysis were generated during this research effort. The time of arrival accuracy is identified using a method based upon the signal-to-noise ratio of an observation of an individual source and its characteristics as identified in the source catalogue. Range accuracy based upon this time of arrival accuracy and the geometric dilution of precision of a set of sources is determined. Algorithms used to determine the absolute or relative position to a known location have been produced. These algorithms provide a method to resolve the phase cycle ambiguities due to the unknown location of the vehicle, whereas most previous methods have assumed external information to determine the ambiguous number of phase cycles between a detector and the pulse model location. These algorithms essentially solve the *lost-in-space* problem for spacecraft, without requiring any external assistance. Algorithms to recursively correct estimated position and velocity based upon sequential pulsar range measurements have been developed. This approach compares the measured to the predicted arrival time of a pulse signal, and differences are converted to range corrections. Simulated results of the operation of these algorithms have been presented, and empirical validation of the concept has been presented based upon recorded data. These new algorithms also provide a scheme to correct vehicle clock time. Methods to determine vehicle attitude have also been produced, as extensions to the presented methods of position and time determination.

1.4 Dissertation Overview

This dissertation is separated into four major sections. The first section, Chapter 2, introduces variable celestial sources, including the different types, their emission mechanisms, and radiation at different wavelengths. The second section, Chapters 3 and 4, describes modeling and timing of pulses from variable celestial sources. The third section, Chapters 5 through 9, provides a detailed description of the various methods of navigation using variable celestial sources developed during this research. The fourth section is the Appendices that provide the source catalogue and supporting material for the descriptions within the various Chapters.

Chapter 2 presents an overview of the variable celestial sources. It presents the physics and mechanisms for the variable intensity radiation produced by the objects. A discussion is provided on which of the sources are most conducive for navigation, including the selection of X-ray emitting sources as opposed to those that produce radio or visible radiation. A detailed discussion is provided on pulsars, including the different pulsar types. Challenges for navigation due to the characteristics of these variable sources are identified. A catalogue of X-ray sources is provided to assist in the selection of source candidates for navigation. Important properties of sources within the catalogue are graphed in plots. An important subset of these sources, those with periods on the order of milliseconds, is analyzed in further detail.

Chapter 3 discusses the identification and modeling of pulses from variable celestial sources. Methods to produce profiles of pulses are provided, as well as the development of models used to predict the time of arrival of individual pulses. The measured stability of pulses from several objects is provided in order to demonstrate their predictability. A detailed method is presented for determining pulse time of arrival accuracy based upon the acquired signal relative to its projected noise. This method is used to provide the determination of accuracy of range measurements computed between a pulse detector and the identified location of the pulse model. During the investigation of this research, a preliminary analysis of the pulse arrival times at different wavelengths was pursued, and this analysis is presented at the end of this Chapter. Chapter 4 discusses the methods of time transformation between spacecraft clock measured time and inertial time standards. The various time standards used within the framework of navigation using these celestial sources are presented. Conversion from spacecraft clock proper time to coordinate time is discussed for near-Earth and interplanetary applications. The time transfer equation between the location of the spacecraft and the solar system barycenter is presented in detail. This transfer is the primary measurement equation used within many of the navigation schemes presented. A discussion is provided of how this transfer equation is related to existing pulsar-timing equations.

Chapter 5 gives a broad overview introduction into the methods of navigation using variable celestial sources. These include methods of time, attitude, velocity, and position determination. A description of a navigation system using these sources is provided. Chapter 6 provides the methods and algorithms for determining absolute position based upon measurements from variable celestial sources. The observable values and their errors, as well as differences of these values that can be computed, are presented in detail. Methods to compute solution accuracy based upon an observed set of sources are supplied. A simulation of the absolute position algorithms is described, and their performance is demonstrated for several orbit scenarios. Chapter 7 discusses the details of the scheme to correct an estimate of position and velocity. The necessary algorithms and accurate measurement equations are developed. An experimental validation of this method is provided using actual measured data from the NRL USA experiment. Chapter 8 presents the methods and algorithms necessary to implement sequential measurements of pulse observations with the dynamics of an orbiting spacecraft. The Kalman filter measurement models for both first-order and higher-order implementations are discussed. Results from simulations of these algorithms and discussions about the filter's performance are provided. Chapter 9 concludes the dissertation, identifying future work to be continued in the pursuit of the navigation goals using these celestial sources.

There are several appendices that support the content within this dissertation. Appendix A lists necessary supplementary data for use in various analyses throughout the text. Appendix B provides details on the X-ray catalogue created to support this navigation effort. Appendix C lists time of arrival observations data used by the analysis in Chapter 7 and orbital elements of the investigated spacecraft. Appendix D provides an overview of the Kalman filter related equations to support the discussion of Chapter 8. Appendix E identifies several known types of X-ray source detectors that could be utilized for spacecraft applications, including known advantages and disadvantages of each type.

Chapter 2 Variable Celestial Sources

"Twinkle, twinkle, little star. How I wonder what you are …"

– Jane Taylor 1806

The celestial sources that are utilized in this investigated method of spacecraft navigation are variable in their output intensity. A detailed description of these types of sources is provided below, including the physical mechanisms that produce the variable signal and the different types of electromagnetic radiation emitted by these sources. It will be shown that sources within the X-ray band of the electromagnetic spectrum possess perhaps the most advantageous characteristics for navigation. The different types of X-ray sources are presented, along with details of a newly created catalogue of the objects, which can be used to select candidate variable sources for navigation.

2.1 Variable Intensity Sources

The known Universe is filled with numerous celestial objects that emit copious amounts of radiation. During the daytime, the solar system's Sun is the singular bright, intense visible object in the sky. In contrast, as seen in the night sky, multitudes of objects emit, or reflect, radiation within the solar system, across the Galaxy, and beyond.

A momentary flicker, or *twinkle*, of these objects may occasionally be seen. This is due to the light from these sources being attenuated in Earth's atmosphere or passing too close to a nearby object. However, mostly the light from these sources appears to be relatively constant. Although it appears that all sources produce *fixed* amounts of radiation, celestial objects exist whose intensity of their emissions vary over time. The variation in brightness of many of these objects is quite regular, or periodic. Hence these objects are referred to as *variable* objects, or *variable stars*. It is these objects that hold promise in creating a new navigation system for spacecraft.

Bright, fixed stars, with their continuous, steady, or *persistent* emission of radiation have been excellent navigation aides for travels across Earth's globe, as well as for some spacecraft traveling in the solar system. Existing star cameras and star trackers use persistent celestial sources to determine the attitude of the vehicle within an inertial frame to high accuracy. These sensors have also been occasionally used to determine position of a spacecraft relative to a planetary body. These systems rely on the nature of these sources that their signal is constant, or invariable, such that database searches can identify viewed objects through their visible magnitude and relative position to nearby sources. Once the characteristic parameters of these persistent objects are entered into a database, it is expected that only minor updates in position would ever be required.

However, variable celestial objects possess very different characteristics when compared to persistent sources. At a given instance, the intensity of the variable object fluctuates with respect to its observation at a later time. Many of the variable sources exhibit highly regular variations in intensity, although there are some variable sources that have irregular or inconsistent outbursts of energy. The variability of these sources provides a periodic signal that assists in the prompt identification of each specific source, since most of these signatures are of unique period and strength.

There are far fewer variable sources that have been detected and catalogued than the visible persistent stars. Approximately 38,500 visible variable sources have been catalogued versus the many millions of persistent sources [179]. The discovery of these types of sources was made only in recent history. The first variable source discovered was the super nova (*stella nova*, or *new star*) within the constellation Cassiopeia by Tycho Brahe and W. Schuler in 1572 [62]. Shortly thereafter in 1596, the variable red giant star Mira (Omicron Ceti) in the constellation Cetus was discovered by David Fabricius; however, its periodicity was not established until 1638 by Holwarda [82, 175].

With their natural periodic signals, these variable sources possess similar navigation qualities of *navigation beacons*, or *lighthouses*, used by ocean-going vessels. Once a lighthouse upon the shore is identified, by using the known rotation frequency and color of the signal beacon one can determine the coarse range and heading estimates from the ship to the lighthouse. With the varying signal intensity due to the rotation, it is possible to ensure the detection of a lighthouse near the horizon, as opposed to a fixed signal that may be interrupted or obscured, such as by waves on the surface of the ocean, shoreline obstructions, or atmospheric effects. The use of the variable celestial sources for spacecraft utilizes these same concepts as lighthouses on Earth for three-dimensional navigation through space.

2.1.1 Variation Physics

The variation of the signal intensity from these sources is due to either an *intrinsic* or *extrinsic* physical mechanism [179]. Intrinsic forms of producing this variability are due to the object itself and its internal characteristics. Extrinsic methods are due to the external environment acting upon the source, which therefore varies the output of the source's radiation.

Intrinsic mechanisms include the two major classifications of *pulsating* and *eruptive* types [2, 179]. *Pulsating variable* sources show variability due to their expanding and contracting surfaces, which can be detected during observation. This shape-change can either be in a radial or non-radial manner. *Eruptive variable* stars fluctuate due to violent thermonuclear outbursts within their coronae or chromospheres. These sources typically have irregular outbursts and flaring characteristics.

Extrinsic mechanisms include the three major classifications of *rotating stars*, *eclipsing binaries*, and *cataclysmic variables* [2, 179]. *Rotating stars* produce variable radiations due to the rotation about their axes with respect to an observer. Hot, bright spots on their surfaces can become visible once per rotation. Alternatively, charged particles from the surrounding region about the star can be accelerated outward along the star's magnetic axis, which sweeps around the rotation axis and becomes visible once per rotation. *Eclipsing binaries* are sources that are eclipsed by their binary companions along the line-of-sight to an observer. As sources are eclipsed, their intensity diminishes until the eclipse is completed. *Cataclysmic variables* are explosive sources [44]. Their variation is produced by thermonuclear effects in their surface layers (*novae*), within their cores (*super novae*), or from processes that emulate nova outbursts (*nova-like*). Many of these types of cataclysmic sources are within binary systems.

There exist many sub-classifications of these variable star types discussed above [179]. Primarily, these sub-types depend upon a specific star's evolutionary process and unique characteristics of mass, rotation rate, and surrounding environment. Figure 2-1 provides a classification hierarchy of variable celestial sources.

2.1.2 Source Types Conducive to Navigation

The variable celestial sources, presented in the previous sections and Figure 2-1, are unique objects that possess interesting capabilities for spacecraft navigation. Some of the types are more conducive to different aspects of navigation. As with any system, however, there are advantages and disadvantages of selecting a specific source type for each navigation aspect.

It will be shown in the following chapters that in order to determine or update time, position, and/or velocity of a spacecraft it is beneficial to utilize sources that are intense, or bright, sources, such that detectors need not be too large; are stable, periodic signatures, such that models can be developed to predict their behavior; and have narrow, sharp pulse profiles, such that the arriving pulses are quickly and easily identified. Of the various types of variable celestial sources, the *eruptive* and *cataclysmic* types do not clearly match these criteria since although their outbursts may be intense, they are typically hard to predict because of their unstable or irregular nature. The *pulsating* variable type sources do not produce sufficient signal variation to create narrow pulse profiles, and few are intense sources. The most advantageous sources for these methods of navigation are the *rotating* and *eclipsing binary* types, since typically these source's signatures are periodic and many are stable. These types are not bright sources, so some compensation must be made in detector design.

Of the rotating source types, pulsar stars, those generating pulsed emission through the rotation of their magnetospheres or by the accretion of matter from a companion, are exceptional variable celestial sources for navigation. Many of these objects have stable periodic signatures, and enough signal intensity so that practical systems can be developed to use pulsars for spacecraft time, position, and velocity determination.

For navigation systems that utilize variable celestial sources for spacecraft attitude determination, any of the source types can be considered candidates as long as their radiation is sufficiently bright and produces a recognizable image on the system's detector. Some of the sources that are not appropriate for position or time may be suitable candidates for attitude determination.

2.1.3 Variable Source Radiation

The variation in intensity that is observed from these sources is due to the varying amount of electromagnetic radiation that arrives at an observer's location. The different sources types can emit radiation throughout the electromagnetic spectrum. A majority of the variable celestial sources emit in the visible, or optical, band of the spectrum [179]. However, many of the sources have been shown to emit one or more of the radio, infrared, visible (optical), ultraviolet, X-ray, and gamma-ray bands of the spectrum.

Figure 2-2 provides a simple representation of the electromagnetic spectrum, along with the wavelength, frequency, and energy per photon associated with each band [18, 108]. Figure 2-3 provides images of the Crab Nebula and its pulsar in multiple spectrum wavelengths. This specific source produces variable radiation across the electromagnetic spectrum. Many variable sources produce radiation in multiple bands; however, the intensity and pulse shape of the radiation is typically not the same in each band. Figure 2-4 shows the pulse profiles observed from several sources across the electromagnetic spectrum. The difference in pulse shapes between sources across the spectrum is evident.

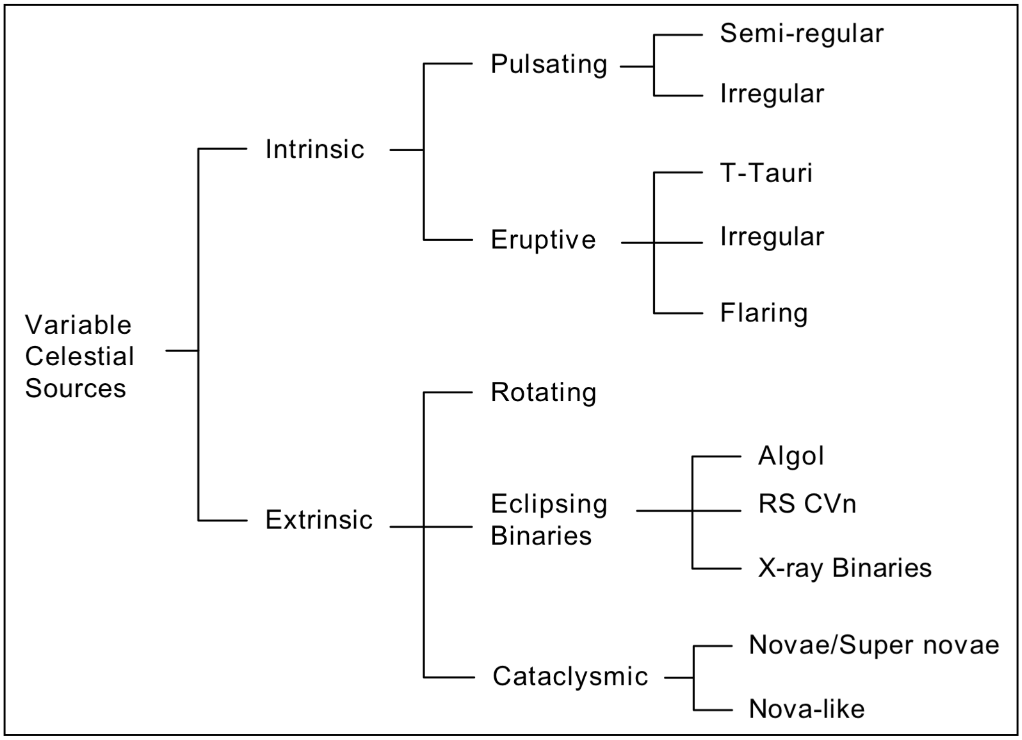

Figure 2-1. Variable celestial source classifications.

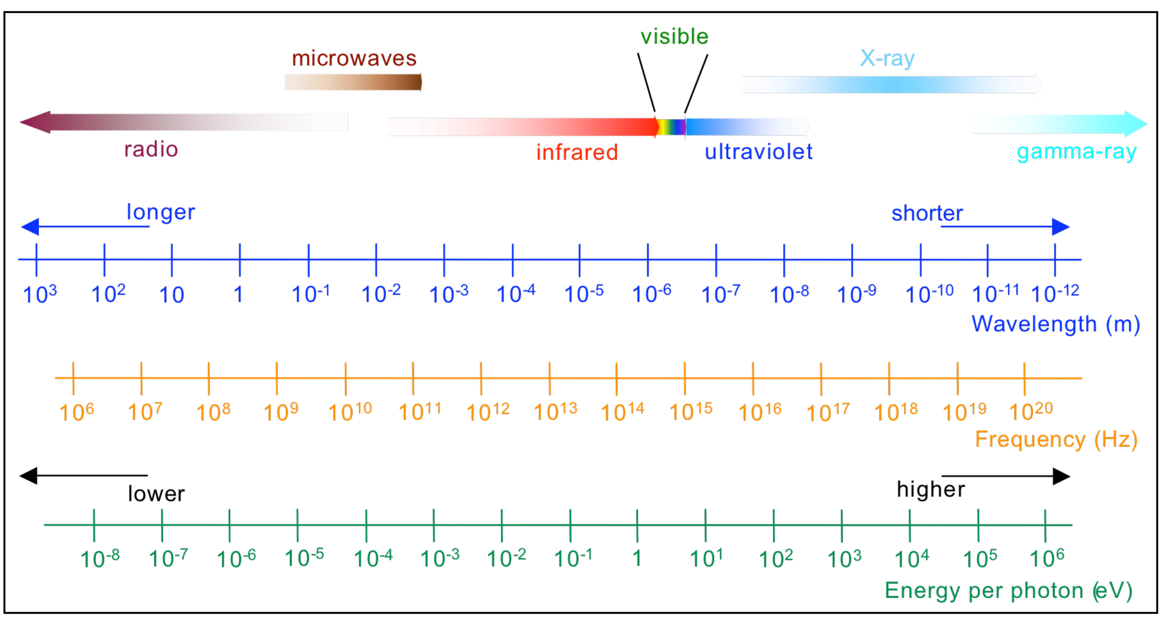

Figure 2-2. Electromagnetic spectrum.

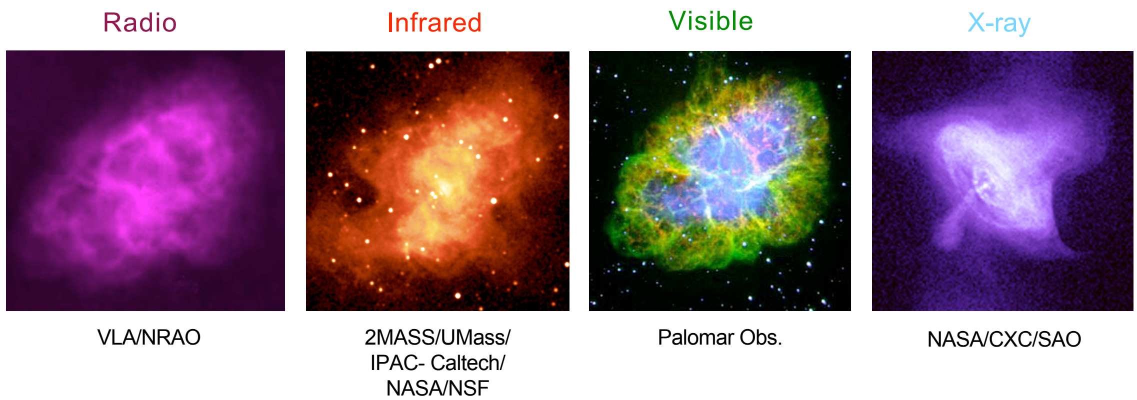

Figure 2-3. Crab Nebula and Pulsar across electromagnetic spectrum.

(Courtesy of identified observatories [147]).

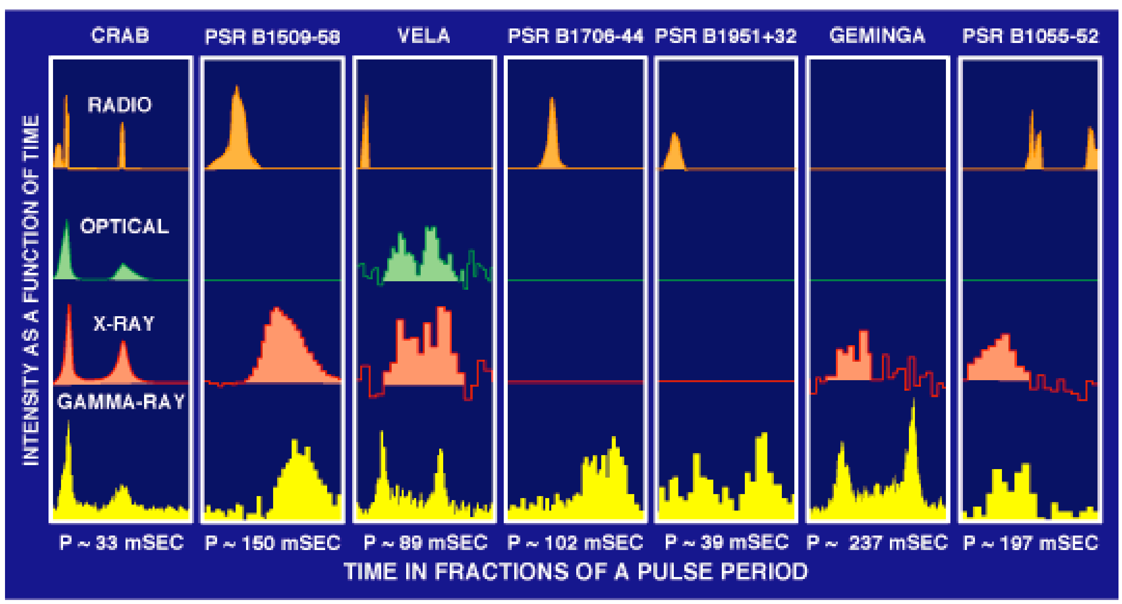

Figure 2-4. Pulse profiles from various sources across electromagnetic spectrum.

(Courtesy of D.J. Thompson (NASA/GSFC) [211]).

As the wavelength of each band within the spectrum changes, different methods of detecting these signals are required for observation. Radio and infrared wavelengths would typically utilize a type of antenna, whereas the visible band could use a standard telescope. The X-ray and gamma-ray bands would require specialized detectors to capture and record the high-energy photons within these bands. Appendix E provides descriptions of several X-ray detector types.

2.1.4 Radio and Visible Sources

By far the most studied variable sources are those that emit radiation within the radio and visible bands. This is primarily due to the ability of these longer wavelengths of the electromagnetic spectrum to penetrate Earth's atmosphere, thus allowing early observers to make measurements at their observatories. Although variable sources have been found to emit in shorter wavelengths (implying higher frequency and higher photon energy), these discoveries were not made until instruments were taken above Earth's signal absorbing atmosphere.

There are numerous radio celestial sources that have been detected [77]. Many of these sources produce variable radiation in the radio band. Radio sources can be detected via large dish-type antennas on the order of tens to hundreds of meters in diameter. Examples of these include the National Radio Astronomy Observatory's (NRAO) Telescope 85-3 at 26 m diameter or the Robert C. Byrd Green Bank Telescope at 100 m diameter [154], the National Astronomy and Ionosphere Center's (NAIC) Arecibo Observatory's Radio telescope at 305 m diameter [142], or the Russian Academy of Science's Special Astrophysical Observatory (SAO) Radio Astronomical Telescope Academy Nauk (RATAN-600) at 576 m diameter [181]. The Australia Telescope

National Facility (ATNF) has recently completed the most comprehensive radio pulsar study to date in their Parkes Multibeam Pulsar Survey. This survey has increased the number of known radio pulsars from 558 [208] to over 1400 [81, 119].

The General Catalogue of Variable Stars (GCVS) presents a detailed classification of sources known and measured to produce variable radiation [178, 179]. These list all optically visible sources, with a total of 38,525 sources currently catalogued. Many are faint sources and require powerful optical telescopes to view them. Examples of these are NASA's orbiting Hubble Space Telescope at 2.4 m in diameter [143], the California Institute of Technology's Palomar Observatory Hale Telescope at 5 m in diameter [30], and the SAO Big Telescope Alt-azimuthal (BTA) telescope at 6 m in diameter [180].

2.1.4.1 Navigation Issues with Radio and Visible Sources

Selecting a wavelength to observe variable sources and utilize their information within a navigation system can be a challenge due to all the options described above. Ideally, one would choose to select the best source candidates for high navigation performance. However, since these candidates may only be ideal in *different* wavelengths, a navigation system would be required to have sensors that could detect across multiple wavelengths. Multiple detector types are typically impractical for spacecraft systems due to their extra power and weight requirements. Selecting one type of detector is more advantageous for spacecraft operations.

Variable sources that emit in the radio band are certainly one consideration for a navigation system. There are numerous radio sources, as well as a significant number of radio emitting rotating stars [12, 77]. However, at the radio frequencies that these variable sources emit (~100 MHz to few GHz) and with their faint emissions, radio-based systems would require antennas 20 m in diameter or larger to detect sources. For most spacecraft this size of an appendage would severely impact design, operation, and cost [69, 107]. Some celestial objects are broadband radio sources that could obscure weak pulsar signals at a spacecraft's detector [218]. With these neighboring radio sources and the low signal intensity from radio pulsars, a navigation system based upon radio may require significantly long signal integration times to produce an acceptable signal-to-noise ratio from each source.

Similarly, limitations exist with the optical variable sources. Given the number of variable sources presented by the GCVS catalog suggests there should be an ample number of candidates for navigation. However, this large number of sources can also be a hindrance, since many sources increases the complexity of the identification process. If bright persistent visible stars exist nearby a variable source, precise telescope pointing and significant signal processing would be required to detect the source's signal variation in order to not be overwhelmed by the nearby source. As is shown in the visible band of the Crab Nebula in Figure 2-3 many sources are visible within a close proximity of the Crab Pulsar. Observing dim, visible variable sources requires a large aperture optical telescope to collect sufficient photons. Smaller spacecraft could not afford the extra mass of these observatories. However, perhaps the most detrimental aspect of creating a navigation system based upon optical variable sources is the very small population of pulsars with detected optical pulsations. To date, there are only five faint, isolated pulsars observed in the visible band [185].

Therefore, even with the advantages of numerous, studied sources, the radio and visible bands appear not to be the proper choice for selecting variable source candidates.

2.2 Variable Celestial X-ray Sources

Although the sources that emit in the radio and visible bands suffer from significant disadvantages when applied to spacecraft navigation, these disadvantages diminish for the sources that emit in the X-ray band. The primary advantage for spacecraft navigation using X-ray types of variable sources is that smaller sized detectors can be utilized. This offers significant savings in power and mass for spacecraft development and operations. It will be shown in Chapter 3 that detectors on the order of one to several square-meters can be effectively utilized to perform the navigation function. Other important advantages of X-ray sources include being unique and widely distributed. This makes the identification of these sources less complex. The image of the Crab Nebula and its pulsar in Figure 2-3 shows that the pulsar can be much more easily identified as the unique source in the image without all the clutter of extra sources as can be seen in the infrared and visible band images.

Because of the potential smaller detector size and their unique identification, variable celestial X-ray emitting sources were chosen as the primary source candidates for this research in spacecraft navigation. This section describes the types of X-ray sources, specifically the X-ray pulsars that are well suited for navigation purposes. Due to the characteristics of these sources, some potential challenges of using these sources for navigation are also presented.

2.2.1 X-ray Source Types

In order to utilize these types of sources for navigation, it is important to understand the characteristics and quantity of all X-ray sources. The X-ray sky contains several types of celestial objects that can be used for various aspects of spacecraft navigation.

Variable X-ray objects employ an array of energy sources for their X-ray emissions. Table 2-1 presents a brief description of the various types of X-ray sources. Although all variable emission sources are excellent candidates for time, position, and/or velocity determination, those objects that produce persistent, non-pulsating X-ray flux may be good candidates for attitude determination.

Figure 2-5 presents a hierarchy of X-ray source classification. The many different X-ray source types can be categorized as either a *simple*, often solitary, object; a *compound* set of objects; an *extended* object, generally a large, complex object; and an *extragalactic* object, which includes much of the X-ray background. The *compact objects* of white dwarf stars, neutron stars, and black holes are sources of significant mass but relatively small radius when compared to most other stars.

Although the maximum value may be defined higher (as shown in Appendix A), X-ray sources essentially emit within the 0.1–200 keV energy band of the electromagnetic spectrum. The wavelengths and frequencies of such sources are 1.24×10^{-8}–6.20×10^{-12} m and 2.4×10^{16}–4.8×10^{18} Hz, respectively. A *soft* range of X-rays can be considered within the range of 0.1–10 keV, and a *hard* range of 10–200 keV. However, there is often great flexibility in the definition of these soft and hard ranges.

The primary measurement from these X-ray sources is the high energy photons emitted by the source. The rate of arrival of these photons can be measured in terms of *flux* of radiation, or number of photons per unit area per unit time. Given the energy range of photons being observed, the total number of photons can be converted to energy, such that the received energy flux is in terms of energy per unit area per unit time. Typical units for these measurements of flux are photons/cm^2/s or ergs/cm^2/s.

Table 2-1. Description of Various X-ray Source Types [145, 227].

Source	Acronym	Description
Active Galactic Nuclei	AGN	Accretion onto central black hole produces X-ray emissions.
Algol	---	Triple variable star system (named after first in class, Algol).
Atoll Sources	---	Quasi-periodic sources, neutron stars with weak magnetic field.
Binary Variable	BV	Binary variable star system.
Black Hole Candidates	BHC	Sources with indication of a black hole.
Cataclysmic Variables	CV	White dwarf stars accreting material from a binary companion.
Coronal Stars	CS	X-ray emission generated in the coronae of active stars.
Diffuse X-ray Background	DXB	Background X-ray radiation.
Galactic Ridge Emission	GRE	Diffuse X-ray emission extending along the Galactic plane.
Galaxy Clusters	GXC	X-ray emission from hot intracluster gas trapped near center.
Globular Cluster	GC	Vast collection of stars with X-ray emission from within cluster.
Neutron Star	NS	Compact star, either isolated or in binary system.
Pulsar	PSR	Neutron star emitting pulsed radiation.
RS CVn	---	Binary variable star, no mass transfer (first: Canes Venaticorum).
Soft Gamma Repeaters	SGR	Highly magnetized neutron stars, occasional burst of gamma rays.
Supernova Remnant	SNR	X-ray emissions of heated remnant material of supernova explosion.
White Dwarfs	WD	Cores of stars after exhausted all their elements.
Z Sources	---	Quasi-periodic sources, neutron stars with strong magnetic field.

2.2.1.1 X-ray Background

The diffuse X-ray background is an appreciably strong signal that is observed when viewing the X-ray sky. The X-ray background is largely composed of two components, *soft* and *hard* [38]. The *soft* component is for energies less that 1.0 keV, and is produced by the glow of stars and clouds of hot gases within approximately 100 parsecs of the Sun. It is referred to as the *galactic X-ray background*. This galactic component of the X-ray background has a detectable spatial structure, and is based upon the strong sources within the Milky Way galaxy. The *hard* component of the X-ray background is for energies greater than 1.0 keV. This component is produced by the many sources outside the Milky Way galaxy, and is largely isotropic in structure.

Measures of the X-ray background radiation must be considered when observing a source. Variable X-ray sources must emit more radiation than this background signal in order for it to be detectable. This background signal can be considered *noise* within the detected X-ray flux from a source. Acceptable *signal-to-noise* (SNR) ratios of these source signals are essentially the magnitude of the received X-ray flux above the expected X-ray background level for a certain location in the sky.

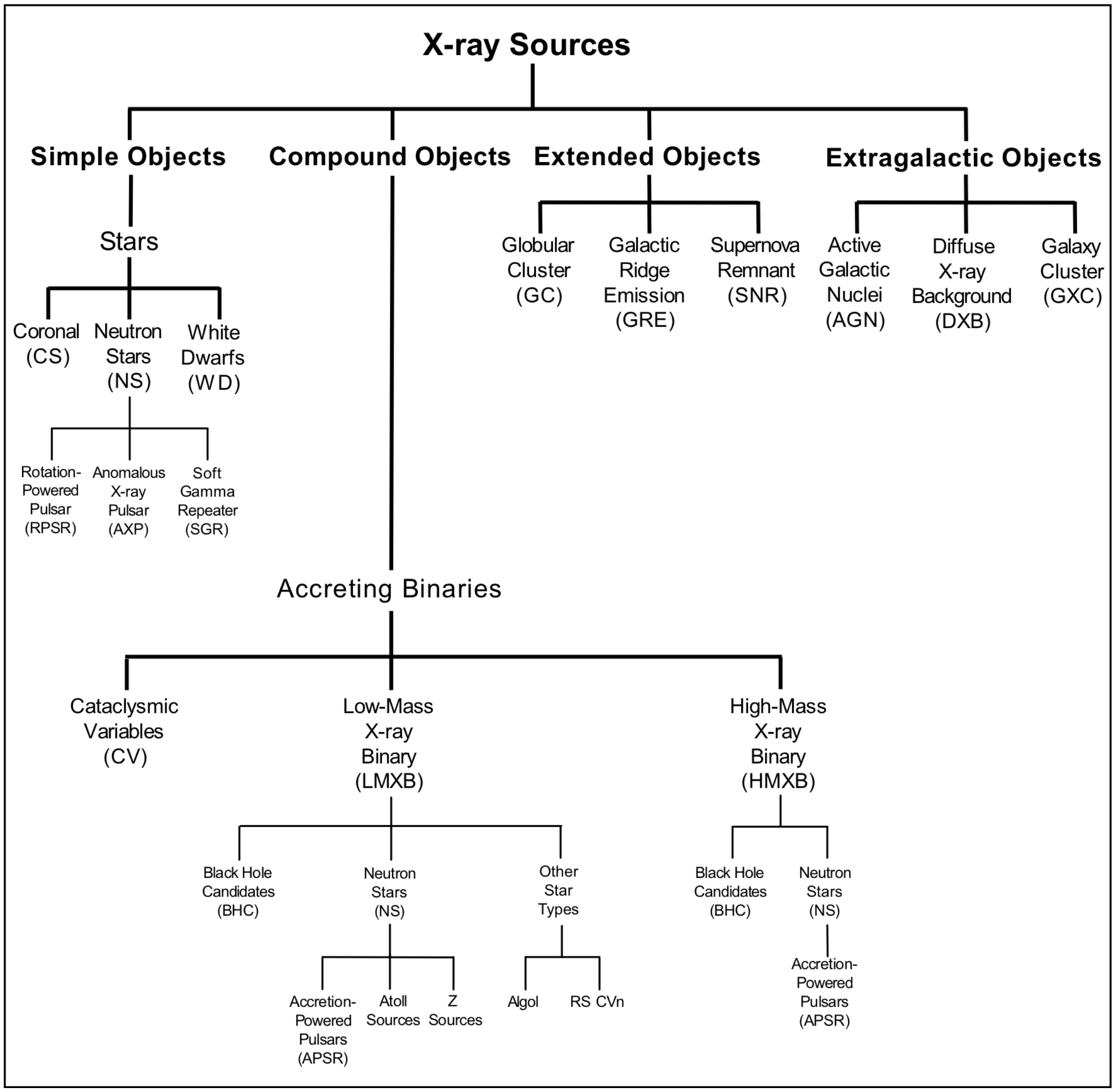

Figure 2-5. X-ray source type classifications.

2.2.2 X-ray Pulsars

This section provides detailed discussions on the pulsar stars; including their evolution, discovery, and details on the various types of these variable sources.

2.2.2.1 Neutron Stars

Theories of general relativity and stellar structure project the evolution of a star as it progresses through its life cycle [37, 53]. These theories predict that upon their collapse, stars with insufficient mass to create a *black hole,* objects with such immense gravitational fields that even light cannot escape*,* produce several types of ultra-dense, compact objects. Two such proposed objects are *white dwarf* (WD) stars and *neutron stars* (NS) [13, 14, 155]. These objects are the result of a massive star that has exhausted its nuclear fuel and undergone a core-collapse resulting in a *supernova* explosion. For those with remaining material after the supernova of near 1.4 solar masses, the stellar remnant collapses onto itself to form a neutron star.

The resulting neutron star is a small, extremely dense object that is roughly 10 km in radius. This small, compact object is an equilibrium configuration in which its nuclear effects provide support against the strong gravity. To reach this allowed equilibrium configuration the stellar constituents must be adjusted by reactions that force free electrons together with protons to form neutrons, hence the name *neutron* stars. It is postulated that a neutron star is composed of a solid outer crust of neutron-rich nuclei a few tenths of kilometer thick surrounding a superfluid core.

Conservation of angular momentum during the collapse phase of the stellar remnant greatly increases the rotation rate of the neutron star. Young, newly born neutron stars typically rotate with periods on the order of tens of milliseconds, while energy dissipation eventually slows down older neutron stars to periods on the order of several seconds. Unique aspects of this rotation are that it can be extremely stable and predictable.

2.2.2.1.1 Pulsar Discovery

In 1967, Cambridge University graduate student Jocelyn Bell and her supervisor Professor Anthony Hewish discovered radio pulsations during a survey of scintillation phenomena due to interplanetary plasma in the radio frequency of 81.5 MHz [80]. Among the expected random noise emerged a signal having a period of 1.337 seconds and constant to better than one part in 10^7. Because of the extreme stability in the periodic signature, it was first conjectured that it could not be a natural signal (thus the original term of LGM, for *little green men*, was phrased for these objects). However, once the discovery conferred with stellar theory, it was soon realized that these objects were rotating neutron stars, *pulsars*, pulsating at radio frequencies.

Since their discovery, pulsars have been found to emit throughout the radio, infrared, visible, ultraviolet, X-ray, and gamma-ray energies of the electromagnetic spectrum. With their periodic radiation and wide distribution, pulsars appear to act as natural beacons, or *celestial lighthouses*, on an intergalactic scale.

2.2.2.2 Rotation-Powered Pulsars

Many X-ray pulsars are *rotation-powered* pulsars (RPSR). The energy source of these neutron stars is the stored rotational kinetic energy of the star itself. The X-ray pulsations occur due to two types of mechanisms, either *magnetospheric* or *thermal* emissions [38]. Some neutron stars can emit using both types of mechanisms.

Neutron stars harbor immense magnetic fields [25]. Under the influence of these strong fields, charged particles are accelerated along the field lines to very high energies.

As these charged particles move in the star's strong magnetic field, powerful beams of electromagnetic waves are radiated out from the magnetic poles. X-rays, as well as other forms of radiation, can be produced within this magnetospheric emission. If the neutron star's spin axis is not aligned with its magnetic field axis, then an observer will sense a *pulse* of electromagnetic radiation as the magnetic pole sweeps across the observer's line-of-sight to the star.

Alternatively, pulsed X-ray radiation can be sensed as hot spots on the rotating neutron stars cross the line-of-sight to the observer. After their formation following a supernova explosion, neutron stars are extremely hot. As they age, local areas on the surface of these stars cool at different rates, leaving some locations hotter than others. The thermal energy in these hot areas causes electrons to accelerate, collide with other particles, and radiate electromagnetic energy.

Since no two neutron stars are formed in exactly the same manner or have the same geometric orientation relative to Earth, the pulse frequency and shape produce a unique, identifying signature for each pulsar.

Figure 2-6 provides a diagram of a neutron star with its distinct spin and magnetic axes. These objects may exist either as an isolated neutron star (ISN), with no local companion objects, or as a component of a multiple star system [215]. Figure 2-3 shows an X-ray image of the Crab Nebula and Pulsar (PSR B0531+21) taken by NASA's *Chandra X-ray Observatory*. The pulsar can be seen as a distinct object within the Nebula. Figure 2-7 provides an X-ray image from *Chandra* of the Vela rotation-powered pulsar (PSR B0833–45).

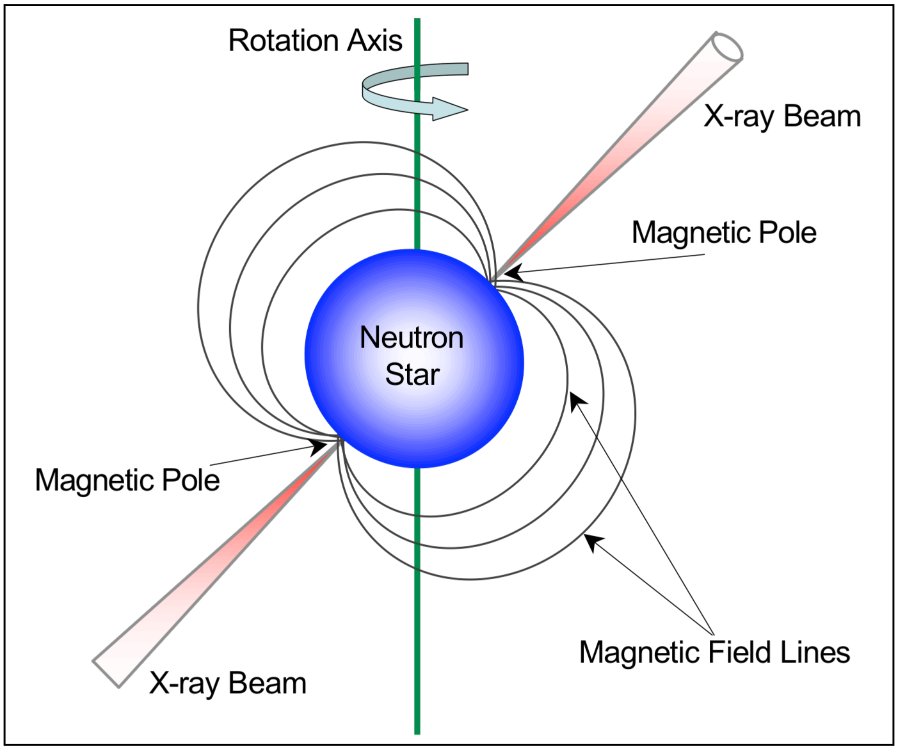

Figure 2-6. Diagram of pulsar with distinct rotation and magnetic axes.

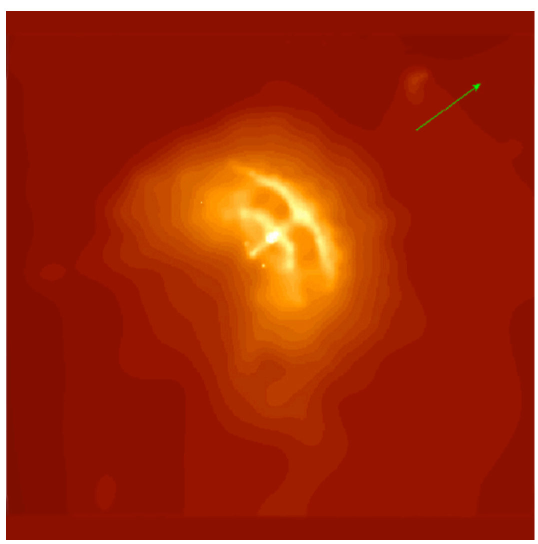

Figure 2-7. Vela Pulsar (PSR B0833–45) X-ray image taken by *Chandra* observatory.

(NASA/PSU/G.Pavlov et al. [146])

2.2.2.3 Accretion-Powered Pulsars

Accretion-powered pulsars (APSR) are neutron stars in binary systems where material is being transferred from the companion star onto the neutron star. This flow of material is channeled by the magnetic field of the neutron star onto the poles of the star, which creates hot spots on the star's surface. The pulsations are a result of the changing viewing angle of these hot spots as the neutron star rotates. These types of pulsars are subdivided into those with a companion of certain mass.

A pulsar that produces X-ray radiation and orbits a high-mass companion exists in what is referred to as a High-Mass X-ray Binary (HMXB) system. The companion object is typically 10–30 solar masses in size. These objects are immense in comparison to the small neutron star. A portion of the strong stellar wind produced by the companion star is absorbed, or accreted, by the neutron star. X-ray radiation is produced by the pulsar as it travels through the stellar wind in its orbit about its companion star [38]. Figure 2-8 provides a conceptual diagram of a HMXB system.

Alternatively, neutron stars can inhabit systems with companion objects of much lower mass, perhaps of size less than one solar mass. These systems are referred to as Low-Mass X-ray Binary (LMXB) systems. The stellar wind of these lower mass companions is much smaller. However, the gravitational potential of the neutron star is sufficient to attract matter from the companion object. The process of accretion transfers mass from the companion onto the neutron star producing a large *accretion disk* surrounding the neutron star [100]. X-rays are created as matter from the accretion disk is transfer onto the neutron star [38]. Figure 2-9 shows a conceptual diagram of a LMXB system.

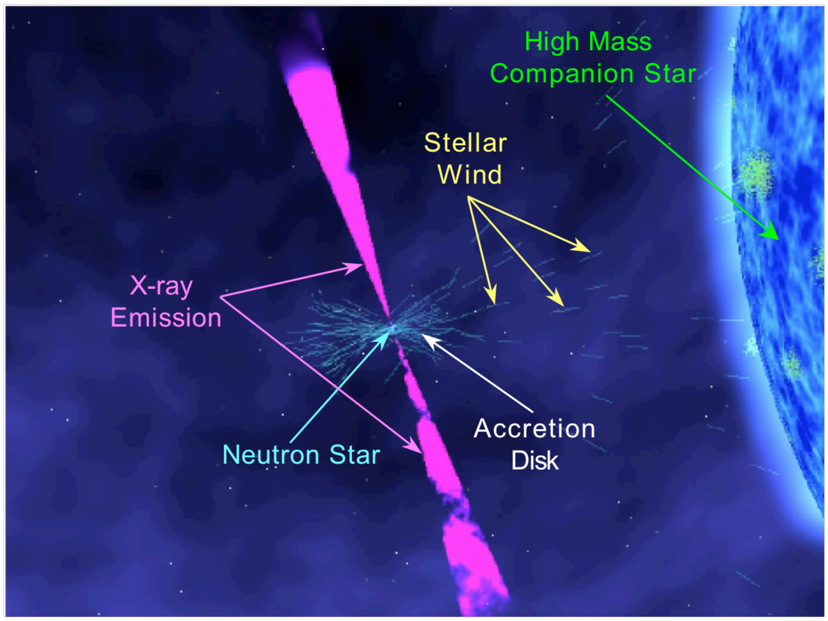

Figure 2-8. High-mass X-ray binary system.

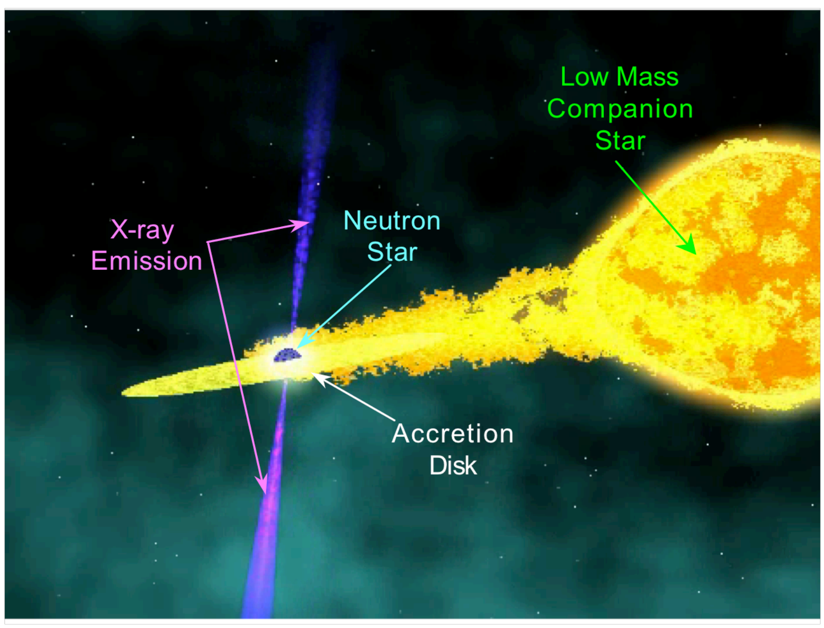

Figure 2-9. Low-mass X-ray binary system.

Although pulsars within binary systems can produce significant amounts of X-ray flux, the pulsations of these types of pulsars are more complex. This is due to the combined effects of both the rotating neutron star and the orbit of the star about its companion. Also, along the line-of-sight to an observer, the companion can eclipse the neutron star and its signal. These eclipsing binary systems introduce additional signal complexity.

2.2.2.4 Anomalous X-ray Pulsars

A smaller population of X-ray pulsars is those sources that are powered by the decay of their immense magnetic fields. The magnetic field strength of these sources is approximately 10^{13}–10^{15} Gauss [210]. For comparison, the magnetic field strength of the Sun is approximately 50 Gauss [221]. These *anomalous X-ray pulsars* (AXP) have similarities to the soft gamma repeater (SGR) sources. *Magnetars*, neutron stars with incredibly immense magnetic fields (> 10^{14} Gauss) are assumed to be part of this pulsar type [52, 210].

2.2.3 Navigation Challenges with X-ray Sources

All celestial sources that emit sufficient detectable X-ray photons can be implemented in some manner within the spacecraft navigation scheme. Of the various X-ray sources that exist, X-ray pulsars, including rotation-powered and accretion-powered types that produce predictable pulsations, possess the most desirable characteristics for determining time and position. However, several issues complicate their utilization for navigation solutions.

Pulsars that emit in multiple electromagnetic wavelengths do not necessarily have the same temporal signature in all observable bands. Studies have compared pulsars at visible, radio, and X-ray bands, and show that the pulse arrival times are dissimilar across different bands, as is evident from Figure 2-4. While a vast majority of pulsars are detectable at radio wavelengths, only a subset are seen at the visible, X-ray, and gamma-ray wavelengths. As X-ray and gamma rays are difficult to detect on the ground due to the absorption of these wavelengths by Earth's atmosphere, observations in these bands must be made above the atmosphere. The highly energetic photons emitted by the source must be detected by pointing the X-ray detector at the source, or by waiting until the source enters the field of view (FOV) of the detector. In addition, many X-ray sources are faint and require sensitive instruments to be detected. The Crab Pulsar (PSR B0531+21) is the brightest rotation-powered pulsar in the X-ray band, yielding ~9.9×10^{-9} ergs/cm^2/s of X-ray energy flux in the 2–10 keV band. The next brightest rotation-powered pulsars are over an order of magnitude fainter than the Crab Pulsar (ex. PSR B1509-58 and *SAX* J1846-0258) [158]. Due to the faintness of these sources, long observation times are required to produce acceptable SNR values. Multiple detectors may be necessary if many independent measurements are required within a given processing time span.

Most bright X-ray sources, although located within the Galaxy, are still very far from the solar system. The distances to X-ray sources cannot be determined to an accuracy that would allow absolute range determination between the source and a detector. However, the angular position in the sky can be determined with high precision, and this direction knowledge can be used in determining a navigation solution. These sources are not truly fixed in the celestial sky, as they have *proper–motion*, or radial and transverse motion relative to the solar system. However, the source's displacement from this proper–motion is very small compared to typical source observation durations. Many sources are clustered along the Milky Way galactic plane; hence there are a limited number of bright sources that could provide off-plane triangulation for three-dimensional position determination.

Although pulsars are uniquely recognizable due to their different pulse shapes, a single pulse from a specific pulsar is not directly identifiable. Thus, a navigation system that updates position using the fraction of the phase cycle within a pulse must either have an *a priori* estimate of position to approximately align phase within a pulse, or must use additional methods to correctly identify which specific pulse is detected. The stability of pulse arrival must also be considered when creating models to predict pulse arrival times. Sources with large period derivatives must have their models updated if a long time has elapsed since the last model definition. Models that are effective for sufficiently long durations, thus requiring infrequent updates, are desirable from stable sources. Databases that contain precise models should be maintained and distributed frequently to allow users to create accurate measurements.

Though nearly all rotation-powered pulsars are constant in intensity, many accreting pulsars and most other X-ray source classes often exhibit highly aperiodic variability in intensity that may compromise their usefulness for precise time and position determination [214]. Those in binary systems introduce more complex signal processing and pulse arrival time determination than isolated sources. Many accreting sources are unsteady, or *transient*, sources. This phenomenon of reduced X-ray emission for some duration is due primarily to stellar physics [223]. The recurrence times of transient sources are often unpredictable. Sources that exhibit transient characteristics cannot be used as continuously detectable navigation source candidates. High intensity signals lasting for short periods, X-ray *flares* and X-ray *bursts*, are occasionally detected from some sources [109]. Since neutron stars are believed to contain a solid crust and a superfluid interior, exchanges of angular momentum between the two materials can cause unpredictable *star-quakes*. These events can significantly alter the spin rates of these stars, and create timing *glitches* in the periodicity of the source. The diffuse X-ray background would be present in all observations, and this would add to any noise present in the detector system.

A navigation system that utilizes pulsed emissions from pulsars would have to address the faintness, phase cycle, transient, flaring, bursting, and glitching aspects of these sources, in addition to the presence of the noise from the X-ray background, in order to successfully produce solutions.

2.3 X-ray Source Catalogue

To support the use of these types of objects for spacecraft navigation, a catalogue of variable celestial X-ray sources has been assembled. Gathering all the data for these sources into one collective set allows the analysis of each source for its potential as a candidate for navigation purposes.

This section describes the assembled X-ray Navigation Source Catalogue (XNAVSC) in further detail. A brief discussion is provided on the types of X-ray astronomy missions pursued to discover new objects. Many of these missions produced lists of their observed sources and characteristics, which can be merged together with other mission's data. A description of how and where the sources for the catalogue were collected is presented. The types of parameters recorded for each source is discussed. Information and overall statistics about the catalogue are also provided. Additionally, Appendix B of this document provides a detailed listing of the XNAVSC.

2.3.1 X-ray Source Survey Missions

The issues raised in the previous sections require careful analysis of X-ray sources in order to develop a working spacecraft navigation system with sufficient performance. To accomplish this analysis, the identification of X-ray sources that have been discovered and characterized is required.

The first non-solar cosmic X-ray source, Scorpius X-1 (B1617-155), was detected in June 1962 using Geiger counters onboard a rocket at a 230 km altitude [45, 66, 67]. Since this discovery, numerous balloon, rocket, and satellite borne instruments have surveyed the sky. Different X-ray missions have observed the X-ray sky in various energy ranges, depending on instrument characteristics or mission goals.

Table 2-2 provides a list of missions designed for X-ray source discovery and survey. During its mission in the late 1970s, *HEAO-1* detected 842 sources within the 0.2–10 keV range [233]. The German X-ray observatory *ROSAT* in 2000 completed the latest comprehensive all-sky survey of the X-ray sky [216, 217]. This mission detected 18,806 bright sources (above 0.05 X-ray photon counts/s in the 0.1–2.4 keV range), and a significant number of sources, 105,924 objects, in its faint all-sky X-ray survey.

2.3.2 Selection of Sources

The sources within the XNAVSC were collected from many different existing catalogues and individual source description papers, as well as existing Internet web sites that provide databases on X-ray sources. The complete listing of the catalogue's references is provided in Appendix B. At the beginning of this research, no single definitive existing catalogue could provide all the information for these sources. Either the databases or articles concentrated on a specific type of X-ray source, they were too general in format with insufficient parameter detail, or they listed only detailed information on a small subset of sources. Thus, it was necessary to collect all the source information into one database such that it could be accessed for source evaluation and selection.

There are several major contributors to this catalogue, which either assisted the beginning formulation of this collection or provided additional detail on a large number of sources. Table 2-3 provides a summary of these major contributors, listed in order of the number of sources in their catalogues. Of these, the NASA High Energy Astrophysics Science Archive Research Center (HEASARC) X-ray Master Catalog [78] and the *ROSAT* Catalogs [216, 217] contain the most numerous sources. Special acknowledgement is made to the X-ray source tables generated by Dr. Yong Kim [99]. This major contribution was significant for the beginning development of the XNAVSC.

Since the X-ray pulsars are of significant interest for navigation, the listing of radio emitting pulsars is important to study since radio pulsars are often later observed to also emit X-ray radiation. Table 2-4 provides a list of the primary radio pulsar catalogues referred to while assembling the XNAVSC.

Table 2-2. X-ray Source Survey and Discovery Missions [75].

Mission Name	Mission Operation	Energy Range (keV)
ORS 3	July 1965 – Sep 1965	0.8 – 12
OSO 3	Mar 1967 – Nov 1969	7.7 – 210
Vela 5B	May 1969 – June 1979	3 – 750
Vela 6A	Apr 1970 – Mar 1972	3 – 12
Vela 6B	Apr 1970 – Jan 1972	3 – 12
UHURU	Dec 1970 – Mar 1973	2 – 20
OSO-7	Sep 1971 – July 1974	1 – 10,000
Copernicus	Aug 1972 – Feb 1981	0.5 – 10
Skylab	May 1973 – July 1979	0.1 – 0.3
ANS	Aug 1974 – June 1977	0.1 – 30
Ariel V	Oct 1974 – Mar 1980	0.3 – 40
Salyut-4	Jan 1975 – Feb 1977	0.2 – 9.6
SAS-3	May 1975 – Apr 1979	0.1 – 60
OSO-8	June 1975 – Sep 1978	0.15 – 1,000
Apollo-Soyuz	July 1975	0.6 – 10
HEAO-1	Aug 1977 – Jan 1979	0.2 – 10,000
Einstein	Nov 1978 – Apr 1981	0.2 – 20
Hakucho	Feb 1979 – Apr 1985	0.1 – 100
P78-1	Feb 1979 –Sep 1985	3 – 10
Tenma	Feb 1983 – Nov 1985	0.1 – 60
Astron	Apr 1983 – June 1989	2 – 25
EXOSAT	May 1983 – Apr 1986	0.05 – 20
Spacelab 1	Nov 1983 – Dec 1983	2 – 30
Spartan 1	June 1985	1 – 12
Spacelab 2	July 1985 – Aug 1985	2.5 – 25
Ginga	Feb 1987 – Nov 1991	1 – 500
Kvant	Apr 1987 – Oct 1989	2 – 200
Granat	Dec 1989 – Nov 1998	2 – 100,000
BBXRT	Dec 1990	0.3 – 12
ROSAT	June 1990 – Feb 1999	0.1 – 2.5
EURECA	Aug 1992 – July 1993	6 – 150
DXS	Jan 1993	0.15 – 0.28
ASCA	Feb 1993 – Mar 2001	0.4 – 10
Rossi XTE	Dec 1995 – Present	2 – 250
IRS-P3	May 1996 – June 2000	2 – 18
BeppoSAX	Apr 1996 – Apr 2002	0.1 – 300
USA	May 1999 – Nov 2000	1 – 15
Chandra	July 1999 – Present	0.1 – 10
XMM-Newton	Dec 1999 – Present	0.1 – 15
HETE-2	Oct 2000 – Present	0.5 – 400
Swift	Nov 2004 – Present	0.2 – 150

Table 2-3. Major Contributors to the XNAVSC.

Authors	Reference	X-ray Source Types	Number of Listed Sources
NASA HEASARC X-ray Catalog	[78]	All	> 100,000
ROSAT (Voges et al.)	[216]	Faint Sources	105,924
ROSAT (Voges et al.)	[217]	Bright Sources	18,806
Yong Kim Tables	[99]	All	881
HEAO A-1 (Wood et al.)	[233]	All	842
Ritter & Kolb	[174]	CV, LMXB, & Related	414
Meliani	[129]	All	226
Liu, van Paradijs, & van den Heuvel	[111]	LMXB & AXP	158
Astronomical Almanac	[1]	All	135
Liu, van Paradijs, & van den Heuvel	[110]	HMXB	130
NRL USA	[230]	All	90
Singh, Drake, & White	[196]	RS CVn & Algol	88
XTE (ASM) & *BATSE*	[139]	APSR & AXP	88
Corbet et al.	[43]	XPSR in SMC	47
Majid, Lamb, & Macomb	[116]	XPSR in SMC	46
Possenti et al.	[158]	RPSR	41
Mereghetti	[131]	APSR & AXP	34
Becker & Trümper	[19]	RPSR	27
Freire et al.	[60]	XPSR in 47 Tucanae	20
Grindlay et al.	[70]	XPSR in 47 Tucanae	17
Becker & Trümper	[20]	MPSR	10
White & Zhang	[222]	MPSR	10
Kuiper & Hermsen	[105]	MPSR	3

Table 2-4. Radio Pulsar Catalogues.

Authors	Reference	Number of Radio Pulsars
ATNF Pulsar Catalogue	[12]	1412
Lyne & Graham-Smith	[114]	733
Princeton University Pulsar Catalog	[159]	706
Taylor, Manchester, & Lyne	[208]	558
Manchester & Taylor	[118]	149

2.3.2.1 Source Selection Criteria

Sources were selected from the catalogues of Table 2-3 as well as the individual source papers listed in Appendix B. Duplicate source listings from different catalogs were not repeated in the XNAVSC. The number of available X-ray sources is significantly larger than the number of sources listed in the XNAVSC. This is due to the selection criteria for the sources in the XNAVSC.

Firstly, in order for a source to be selected to the XNAVSC, it must have a well-determined position. Position knowledge on the order of fractions of arcseconds in RA and Dec will be shown to be important in Chapters 3 and 4, thus only sources with good position knowledge were added to the catalogue.

Secondly, only sources with measured X-ray radiation flux were retained. Sources with unmeasured flux either identify a faint source (too faint to be adequately computed by a mission) or are not well defined. The amount of flux produced by a source is critical for its evaluation as a navigation candidate.

Thirdly, if a source had a measured pulse frequency, or orbital period in a binary system, determined within the X-ray band, these sources were retained. As mentioned previously, pulsars, either rotation-powered or accretion-powered, are the predominant sources for time and position determination. Thus, to be considered as candidates, sources should have measured X-ray flux, and preferably pulsed flux.

2.3.3 X-ray Catalogue Parameters

The XNAVSC is separated into three main lists, the *Simple List*, the *Detailed List*, and the *2–10 keV Energy List*. The data parameters of each of these lists are discussed below.

2.3.3.1 Catalogue Simple List

The first list, referred to as the *Simple List*, provides a simplified listing of all the sources in the database. Many objects that have been discovered by a mission and then rediscovered by subsequent missions have multiple names associated with them. This can be incredibly confusing when trying to determine which source is presented. The XNAVSC retains a source based upon its measured position, and not its name. For a source that has multiple names, the common ones from various missions are collected in this *Simple List*. The Simbad Astronomical Database was referred to for both additional names and position verification [35].

Many individual sources are named by their measured position in the format of *Right Ascension±Declination*. If a source has a measured position associated with the B1950 inertial frame, then the position name is typically pre-appended by a "B" (*B-name*); for those measured in the J2000 inertial frame, they are pre-appended by a "J" (*J-name*). Many sources, but not all, are pre-appended by either their type, such as *PSR* for Pulsar or *SNR* for Super Nova Remnant, or by their discoverer mission experiment name, such as *SAX* for BeppoSAX or *XTE* for Rossi X-ray Timing Explorer. The Right Ascension (RA) is typically broken into two numeral of hours and two numerals of minutes; however seconds are sometimes included by using fractions of minutes. For Declination (Dec) two numeral of degrees and two numerals of arcminutes are used; although arcseconds can be included by using fractions of arcminutes. For example, the Crab Nebula pulsar is RA (B1950) = 05hr 3min and Dec (B1950) = +21° 58min, thus its name is often presented as PSR B0531+21. The naming convention for these sources follows the International Astronomical Unions Recommendations for Nomenclature of celestial objects [86].

To simplify source nomenclature, and to provide a specific source reference within the database, the XNAVSC creates a name of *Jhhmm±ddmm* for all of its sources, based upon the J2000 inertial position of RA and Dec. In many cases, this name matches the common name of the source, but for those sources whose refined position location does not match the original discoverer's position and name, the XNAVSC name may deviate slightly from the common name. Caution should be taken, as these XNAVSC names are not intended to rename sources, rather to provide a single consistent naming convention throughout the database and to provide a catalogue reference for checking for repeated source listings. The *Simple List* specifically identifies this correlation between the database J-name of an object and its more common names.

The *Simple List* also provides a listing of an object's type. The object type follows the hierarchy of Figure 2-5. The order of the objects within the *Simple List* is in the order of their installation into the database.

2.3.3.2 Catalogue Detailed List

The second list, the *Detailed List,* provides all the characteristic parameters of a source. This is broken into six major areas: *Name and Type*, *Position*, *Energy*, *Stability*, *Periodicity*, and *Reference*. Each of these areas is discussed in further detail below. The objects in the *Detailed List* follow the same order as the *Simple List*.

The *Name and Type* section provides the catalogue specific J-name and its B-name, if it exists. It also provides the object's type, as well as object class and sub-class. These categories follow the same hierarchy of Figure 2-5.

The *Position* section provides the J2000 inertial frame RA and Dec, as well as any known uncertainties in these values. The Galactic Longitude (LII) and Latitude (BII) are provided, which are transformed values from the recorded RA and Dec values. These longitude and latitude values represent a sphere of the Milky Way galaxy, with the Galactic plane forming the equator of this sphere. The value of the distance to the source is reported in units of kiloparsecs (1 parsec = 3.262 light years = 3.086×10^{16} m). Distances to these sources can only be currently determined on the order of a fraction of a kiloparsec, so these values represent coarse distance measurements. The *z-distance* to the source is also reported, or its distance above the galactic plane. The measured proper motion of the source is also reported and must be considered if precise position location of a source is required at a particular observation time.

The *Energy* section reports the measured X-ray flux of each source and parameters related to this flux. For the XNAVSC, the flux is separated into two sections of *Soft* X-rays, those with measured energies < 4.5 keV, and *Hard* X-rays, those with energies > 4.5 keV. Survey missions use unique instruments that are designed to measure the arrival of photons at different energies as shown in Table 2-2. Thus, the measured flux of sources is dependent on the mission that observed it. Some sources have X-ray flux measured in both Soft and Hard X-ray energies, while others have measured flux in only one band or the other. The *Neutral Hydrogen Column Density* (n_H), is the amount of hydrogen atoms per unit area along the direction to the source. This value, along with the *photon index*, is used to convert the number of photon counts from a mission instrument for an object into energy flux.

The measured *pulsed fraction*, p_f, is also recorded. This important parameter is used in determining the accuracy of a pulse time of arrival in Chapter 3. The pulsed fraction is the ratio of the pulsed flux to the mean flux, quantifying the amount of flux that is pulsed from a source [27]. To compute the pulsed fraction the *X-ray flux*, F_x, from a source can be determined as a function of the phase cycle of a pulse profile, as,

$$F_x = F_x(\Phi); \quad 0 \le \Phi \le 1 \tag{2.1}$$

The minimum flux is defined as the minimum value of flux over this cycle as,

$$F_{x_{\min}} = \min\left[F_x(\Phi)\right]; \quad 0 \le \Phi \le 1 \tag{2.2}$$

The *pulsed flux*, $F_{x_{pulsed}}$, is the difference over the phase cycle of the pulse profile between the measured flux and the minimum flux, as in

$$F_{x_{pulsed}} = \int_0^1 \left[F_x(\Phi) - F_{x_{\min}} \right] d\Phi \tag{2.3}$$

The mean flux over this cycle can be computed using,

$$F_{x_{mean}} = \int_0^1 \left[F_x(\Phi) \right] d\Phi \tag{2.4}$$

Therefore, the pulsed fraction is,

$$p_f = \frac{F_{x_{pulsed}}}{F_{x_{mean}}} \tag{2.5}$$

The *pulse width*, W, is another important parameter in the arrival time analysis, and two forms of this width are listed in the XNAVSC. The 50% width of the pulse profile, or Full-Width Half-Maximum (FWHM) is provided, as well as the width at 10% of the peak intensity, or Full-Width 10% Maximum (FW10). Figure 2-10 provides a diagram of a pulse profile along with the identification of these pulse widths. If the magnetic field strength is estimated of the source, this value is also recorded.

The *Stability* section defines the characteristics about the known stability of the source rotation and signal. The source is either characterized as a known steady periodic or transient signal. If the source produces X-ray bursts, or has any known timing glitches, these are also noted. For those sources existing in binary systems, this is highlighted to alert the user of the potential additional complexity in determining pulse time of arrivals from the signal of these sources.

The *Periodicity* section provides data on the known pulse cycles and binary orbit parameters. The pulse period, P, is the time interval between pulses. Any known first,

$\dot{P}$, and second, $\ddot{P}$, order period derivatives are provided. The epoch, or time, of the determination of this period and its derivatives is recorded. The characteristic age, τ_C, is computed using its definition of,

$$\tau_C = \frac{P}{2\dot{P}} \tag{2.6}$$

This term provides a measure of the rate of slow down in the rotation rate, as well as a representative age of the object [118]. If a source is a component of a binary system, then its orbital period in that system is provided.

The *Reference* section of the Detailed List provides information about the references utilized for the catalogued data.

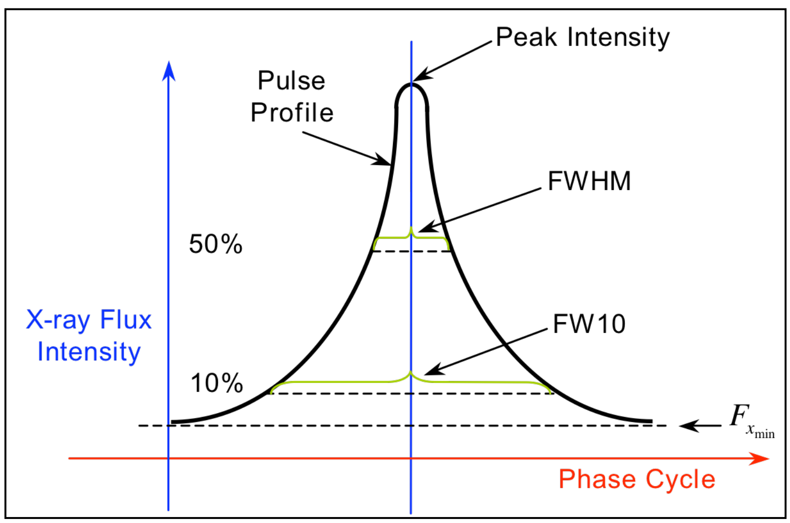

Figure 2-10. Pulse profile and widths.

2.3.3.3 Catalogue 2–10 keV Energy List

The third list, the *2–10 keV Energy List,* of the XNAVSC provides additional information on the X-ray flux from a source. The reported measured flux from each source is provided from the *Detailed List*. However, since many of these sources have been measured at different X-ray energy bands, it is difficult to draw immediate comparisons between the sources. It is easier to make these comparisons if flux from each source is determined in the exact same band. Thus to facilitate these comparisons, all the fluxes are converted into the same 2–10 keV energy band. Various methods have been employed to make these conversions, such as the reported conversion rates from source references or the PIMMS mission count energy conversion software tool from NASA HEASARC [76].

Although analyses can be pursued using these similar band flux values, caution should be exercised when quoting these values. Although X-ray flux may be measured in a band higher or lower than the 2–10 keV, there is no guarantee that the source will actually produce similar radiation within this specific band.

2.3.4 X-ray Catalogue Data Characteristics

The XNAVSC is designed to provide a listing of celestial X-ray sources that are candidates for use in spacecraft navigation. This section provides an overview of the sources and their data characteristics from the catalogue as a whole. Table 2-5 provides the total number of catalogued sources as of this publication contained in the XNAVSC. Table 2-6 through Table 2-11 provide a breakdown of each major source object type into their classes and sub-classes. Appendix B provides additional information on source classification and XNAVSC data description.

Figure 2-11 provides a plot of all the sources within the XNAVSC database. This figure is presented in Galactic longitude and latitude, where the equator of the plot is along the Galactic plane. X-ray sources exist throughout the X-ray sky, as is evident from Figure 2-11, although the clustering near the Galactic plane is clear. Distances to X-ray objects range from several to thousands of parsecs. Most sources are detected within the

Galaxy, however as many as 45 pulsars are located outside the Galaxy in the Large and Small Magellanic Clouds (LMC and SMC, respectively) – two irregular dwarf galaxies near Galactic coordinates 80°W–33°S and 60°W–45°S [56]. Figure 2-12 provides this same information using Right Ascension and Declination coordinates for the sources. Figure 2-13 and Figure 2-14 provide views of these source plotted along Galactic longitude and latitude globes, viewed from opposite orientations. Plots of each of the major source object type of NS, LMXB, HMXB, CV, and other types are provided in plots of Figure 2-15 through Figure 2-24. Most types show a distinct distribution mainly centered along the Galactic plane, especially the HMXB sources. However, the plot in Figure 2-22 shows that CV sources are much more equally distributed throughout three-dimensional space.

Table 2-5. Sources Within the XNAVSC Database.

Object	Number of Sources
Low-Mass X-ray Binary	290
High-Mass X-ray Binary	152
Cataclysmic Variable	141
Neutron Star	95
Other Type	67
Unknown Type	8
Active Galactic Nuclei	6
Total	**759**

Table 2-6. LMXB Sources Within the XNAVSC Database.

Object	Sub-Totals	Number of Sources
Algol		30
Black Hole Candidate		5
Neutron Star		91
Accretion-Powered Pulsar	9	
Binary Pulsar	10	
Unknown NS Type	72	
RS CVn		82
Unknown LMXB Type		82
Total		**290**

Table 2-7. HMXB Sources Within the XNAVSC Database.

Object	Sub-Totals	Number of Sources
Black Hole Candidate		3
Neutron Star		95
Accretion-Powered Pulsar	62	
Binary Pulsar	28	
Unknown NS Type	5	
Unknown HMXB Type		54
Total		**152**

Table 2-8. CV Sources Within the XNAVSC Database.

Object	Number of Sources
CV, AM	2
CV, D	3
CV, DN	15
CV, IP	29
CV, N	18
CV, NL	3
CV, P	43
CV, RN	1
CV, S	6
CV, U	5
CV, X	1
CV, Z	3
Unknown CV Type	12
Total	**141**

Table 2-9. NS Sources Within the XNAVSC Database.

Object	Number of Sources
Anomalous X-ray Pulsar	11
Rotation-Powered Pulsar	68
Soft Gamma Repeater	3
Unknown NS Type	13
Total	**95**

Table 2-10. AGN Sources Within the XNAVSC Database.

Object	Number of Sources
Seyfert 2 Type	5
Unknown AGN Type	1
Total	**6**

Table 2-11. Other Sources Within the XNAVSC Database.

Object	Number of Sources
Black Hole Candidate	5
Magnetar	1
Binary Pulsar	6
BY	9
CHRM	1
FK	1
Pre-Cataclysmic Binary	1
Quasar	1
Super Soft X-ray Source	3
T-Tauri	24
VXS	1
Wolf-Rayet	2
White Dwarf	3
WU	6
WUM	3
Total	**67**

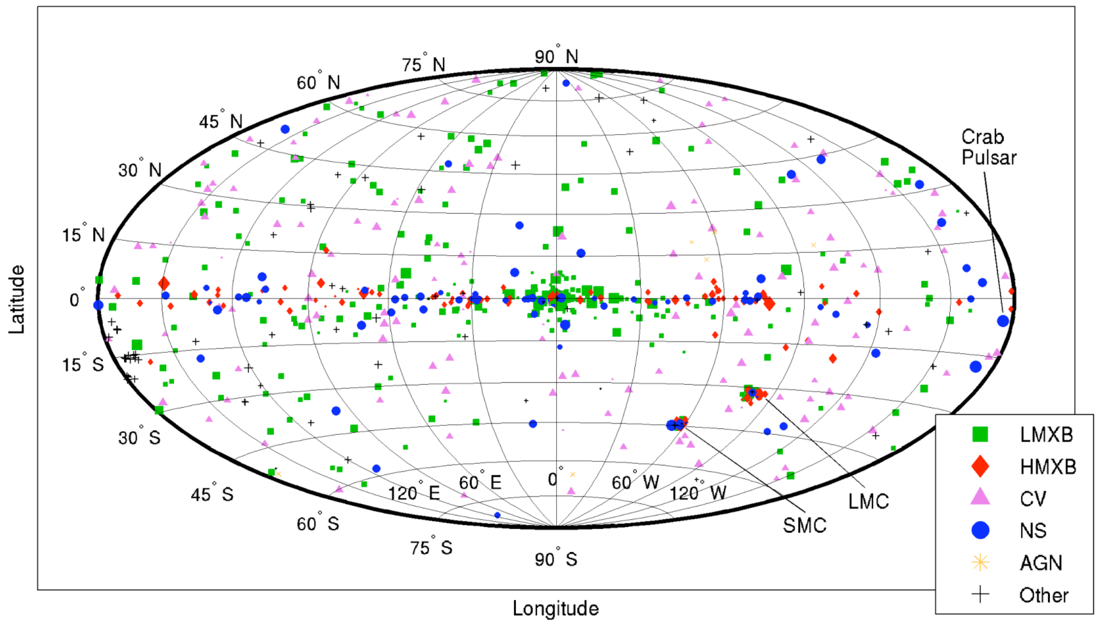

Figure 2-11. Plot of X-ray sources from XNAVSC in Galactic longitude and latitude.

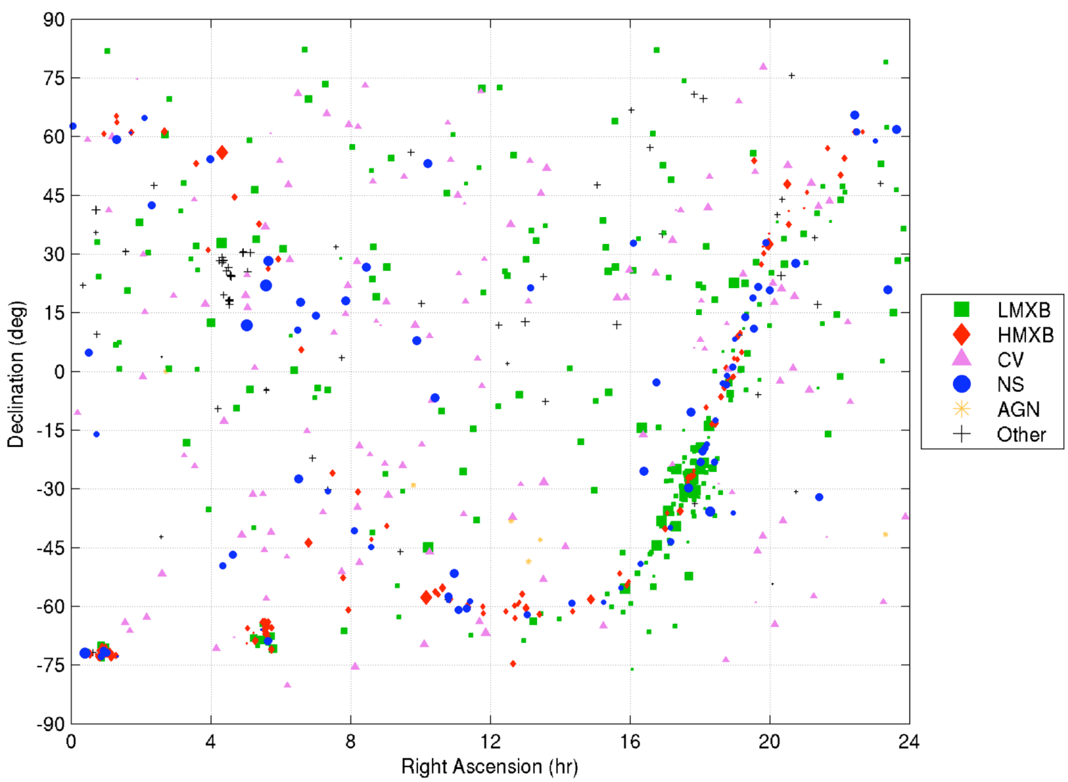

Figure 2-12. Plot of X-ray sources from XNAVSC in Right Ascension and Declination.

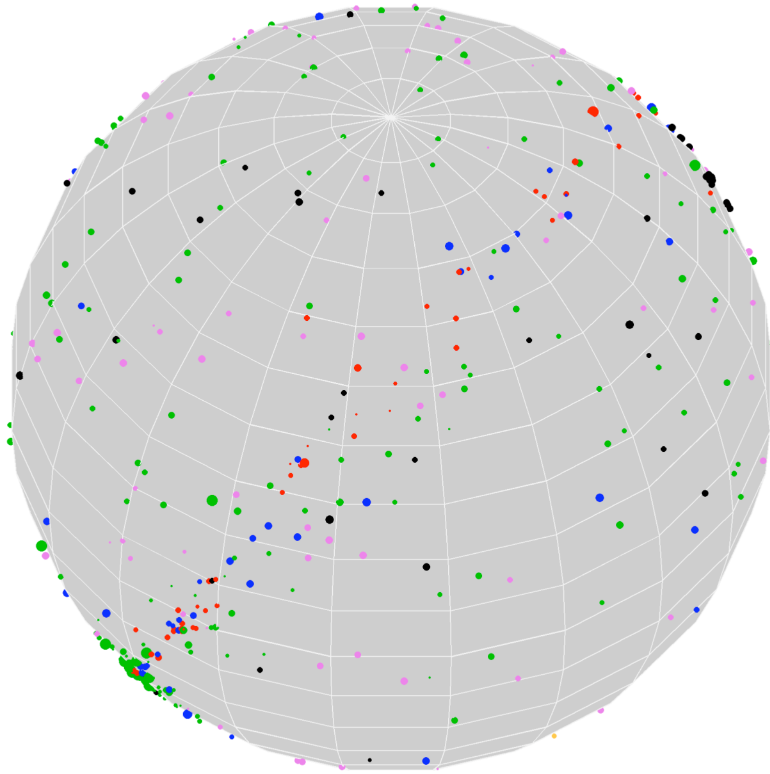

Figure 2-13. Plot of X-ray sources along globe viewed from 45° RA and 45° Dec.

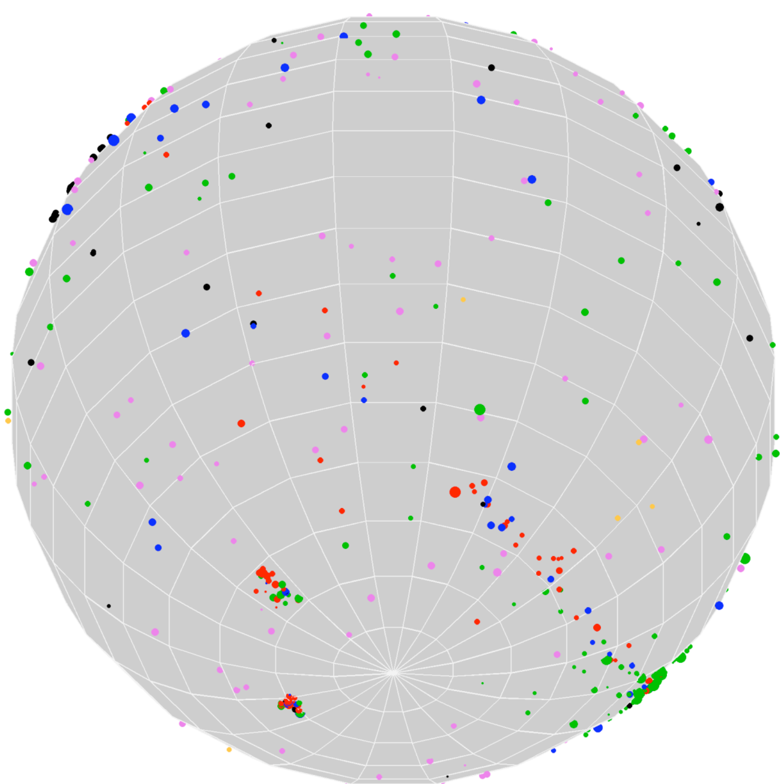

Figure 2-14. Plot of X-ray sources along globe viewed from -45° RA and 225° Dec.

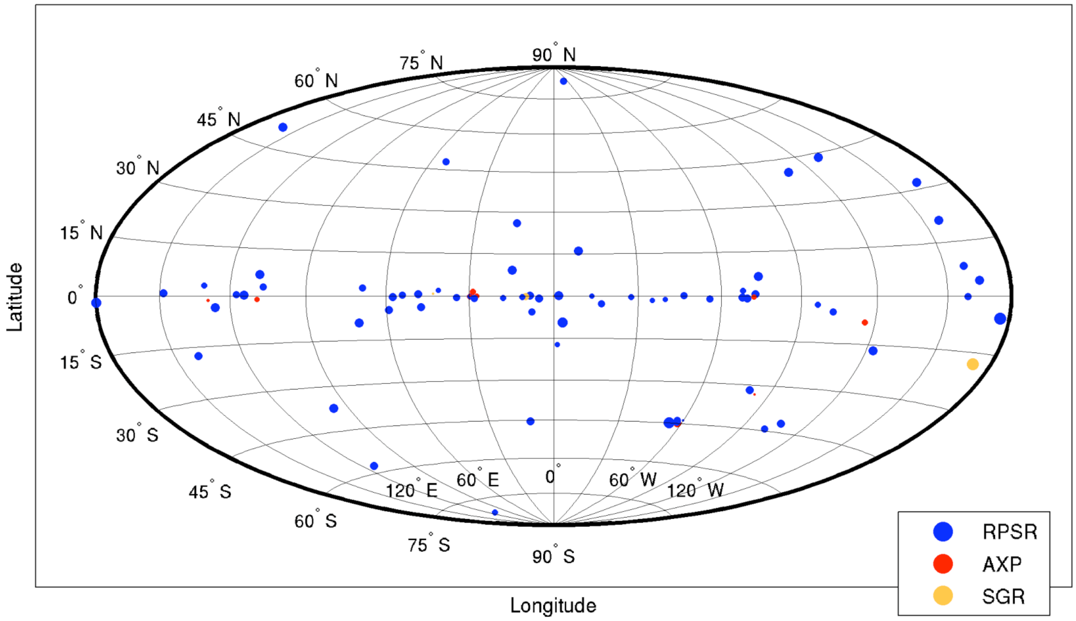

Figure 2-15. Plot of neutron star sources in Galactic longitude and latitude.

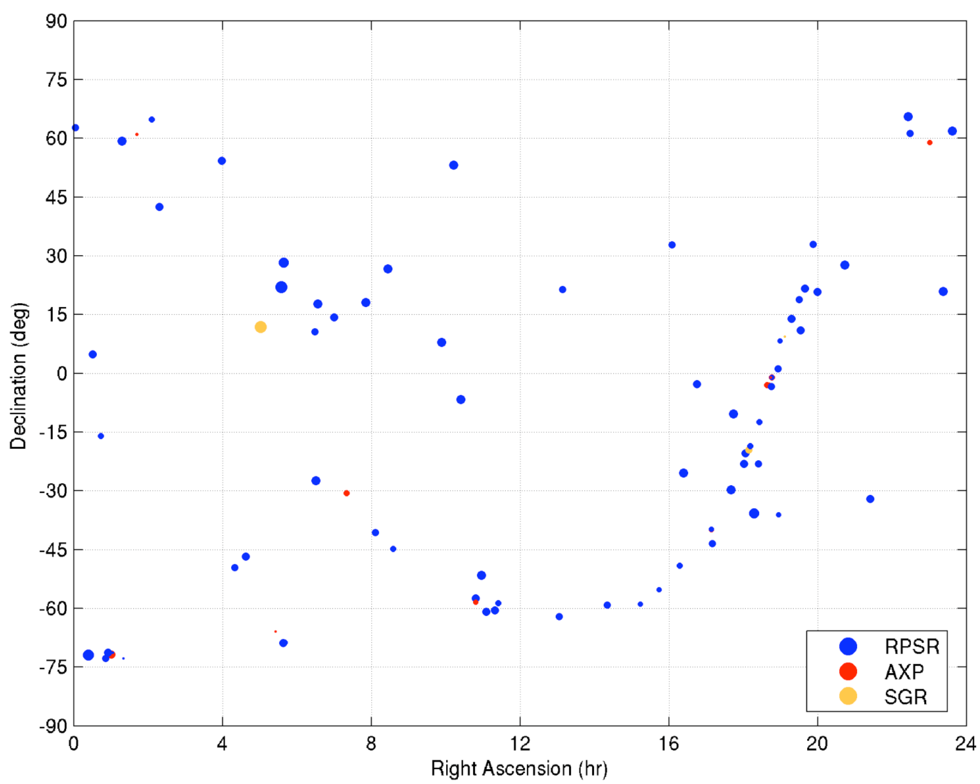

Figure 2-16. Plot of neutron star sources in Right Ascension and Declination.

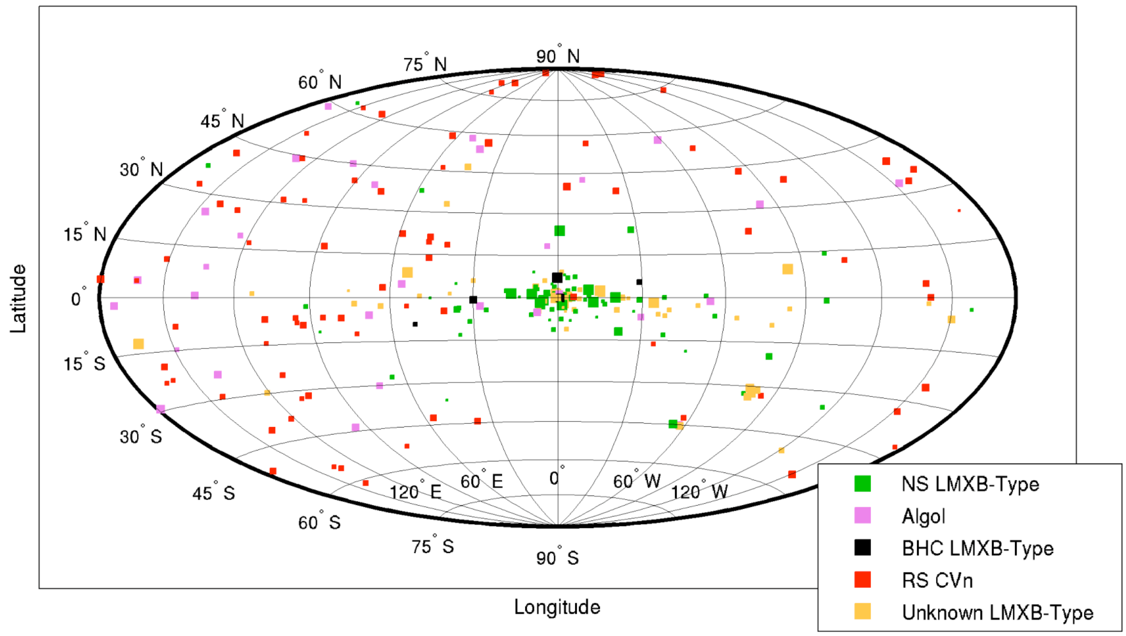

Figure 2-17. Plot of LMXB sources in Galactic longitude and latitude.

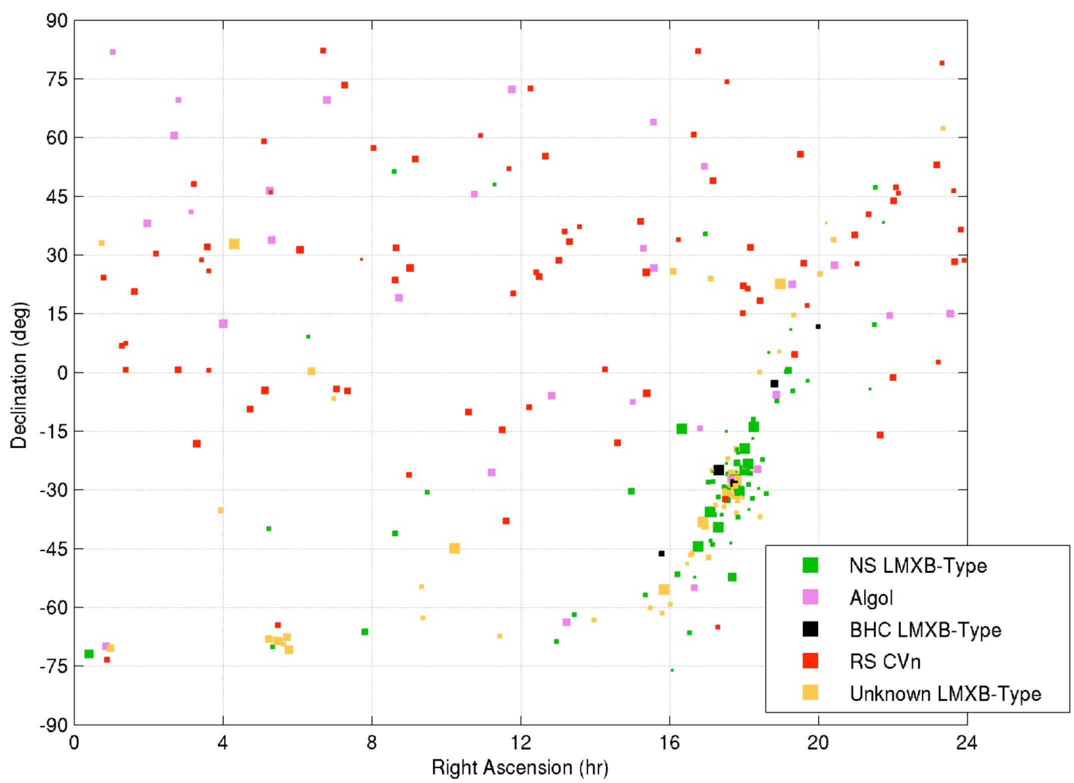

Figure 2-18. Plot of LMXB sources in Right Ascension and Declination.

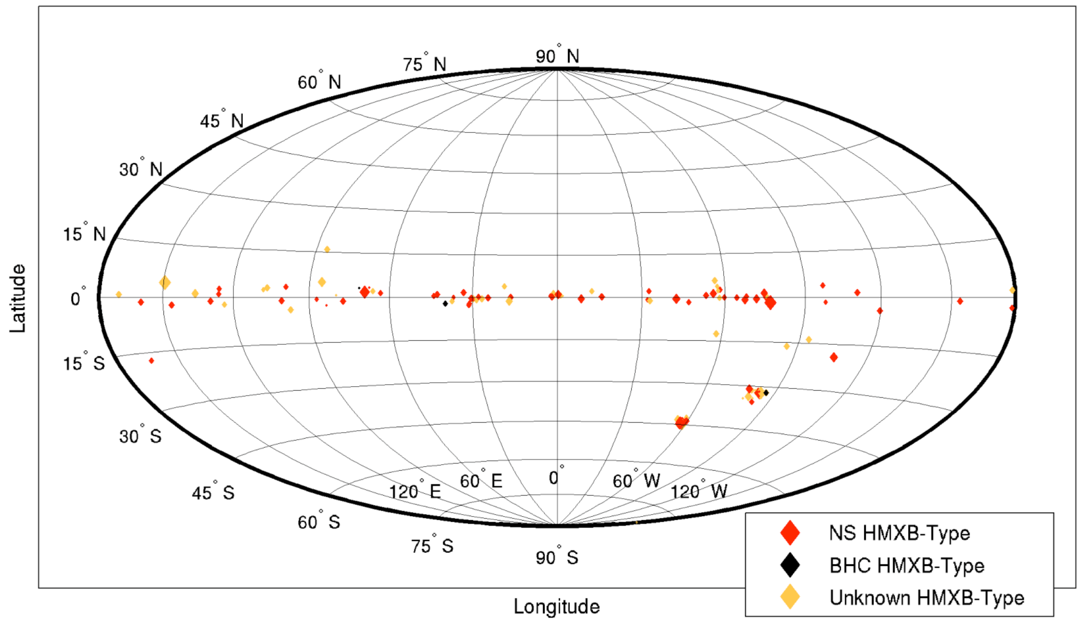

Figure 2-19. Plot of HMXB sources in Galactic longitude and latitude.

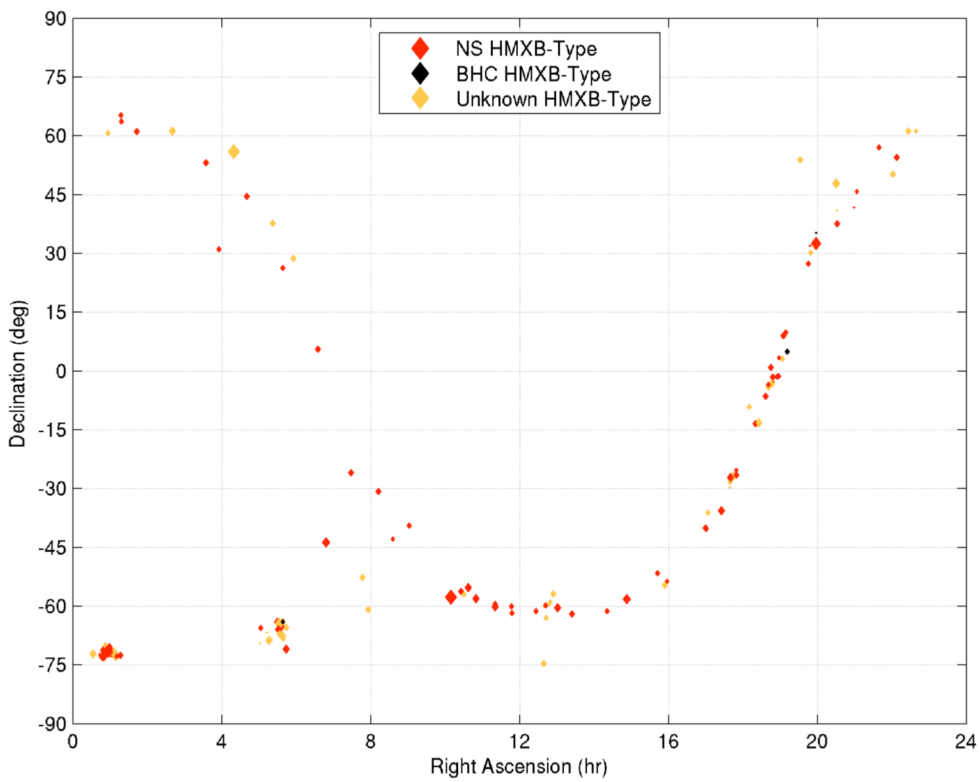

Figure 2-20. Plot of HMXB sources in Right Ascension and Declination.

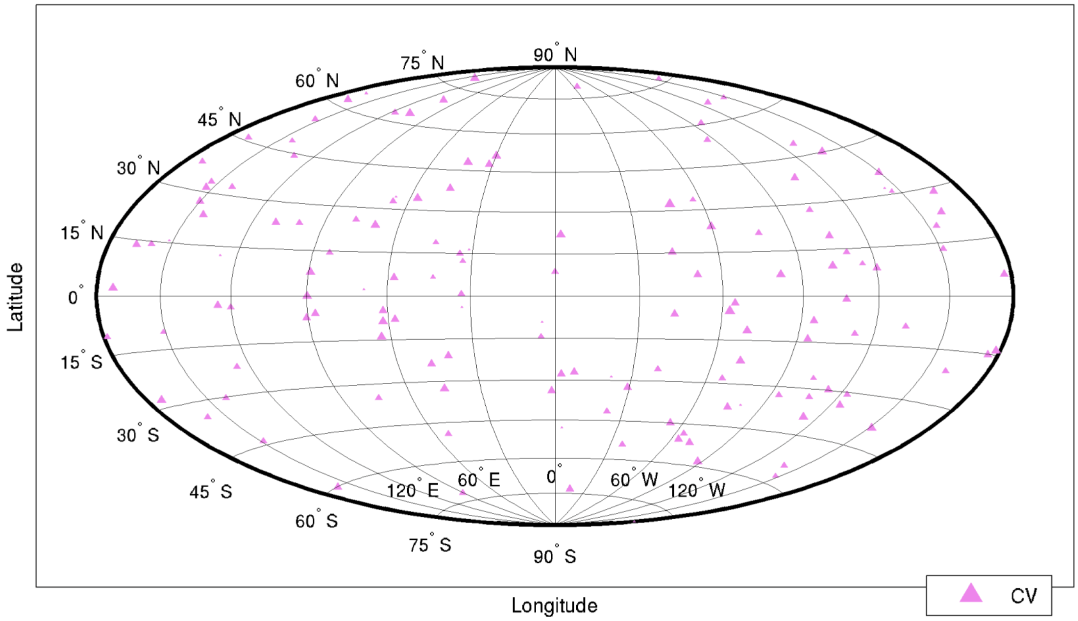

Figure 2-21. Plot of CV sources in Galactic longitude and latitude.

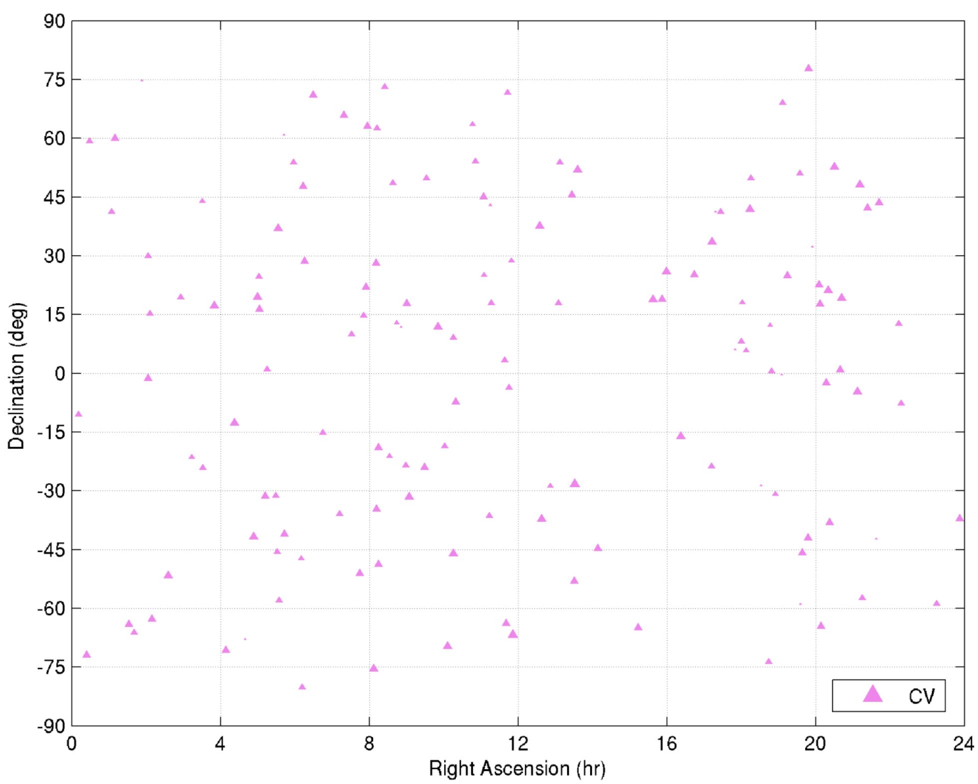

Figure 2-22. Plot of CV sources in Right Ascension and Declination.

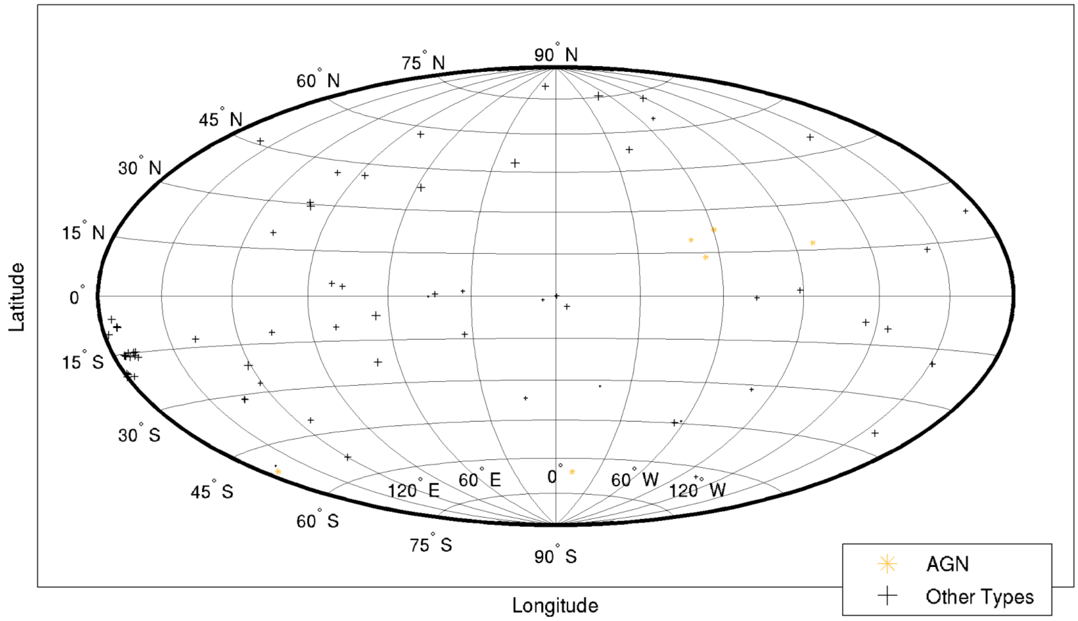

Figure 2-23. Plot of AGN and other types of sources in Galactic longitude and latitude.

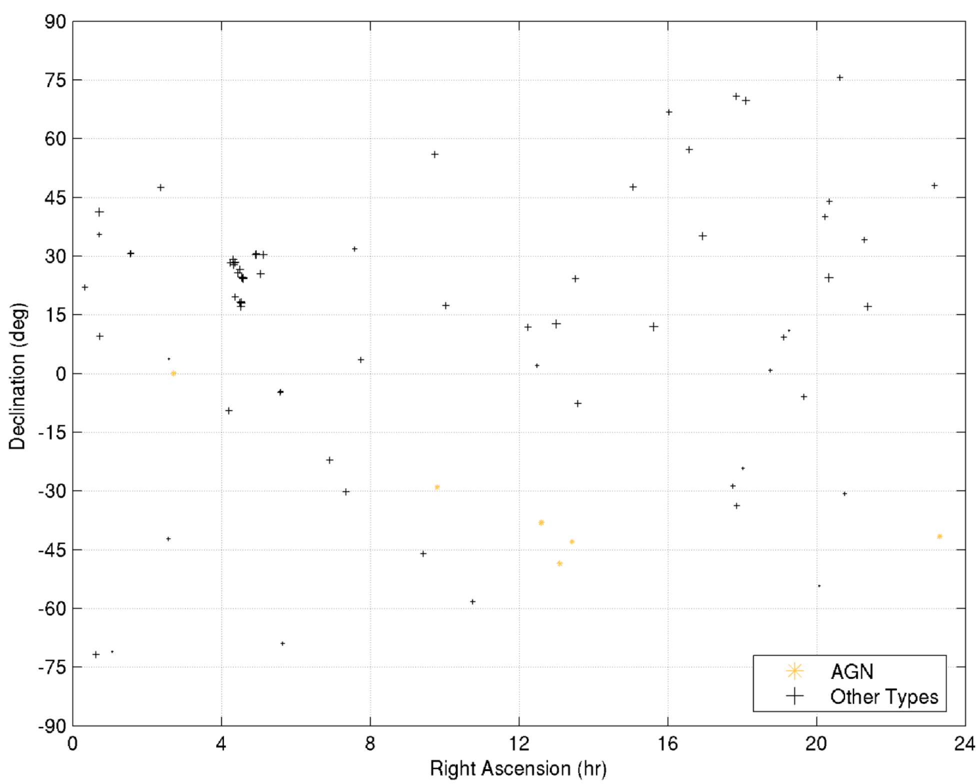

Figure 2-24. Plot of AGN and other source types in Right Ascension and Declination.

2.3.4.1 X-ray Catalogue Data Analysis

Information about the nature and physics of the X-ray sources can be determined by analyzing the data parameters from the XNAVSC. This section discusses several plots of these parameters.

Figure 2-25 provides a plot of the period derivative of sources versus their measured period. Although there is some spread in the data points, generally it can be seen that period derivative gets larger as the period increases. The period derivative is an indicator of the stability of the source, and is used in Chapter 3 for developing pulse time of arrival models. As the period derivative increases, it becomes more difficult to predict the arrival of a pulse since the period changes more quickly over time. However, it can be see in this figure the many of the fastest rotation period sources, on the order of several milliseconds, are also the sources with the most near-fixed rotation rate since the period derivative is so small. Due to their fast periods and stable signatures, these types of sources are attractive candidates for time and position determination. Pulse periods range from 0.00156 to 10 seconds for the rotation-powered pulsars, and from 0.0338 to 10,000 seconds for accretion-powered pulsars. Figure 2-26 provides the second period derivative for the sources that have these reported values.

For those sources that have reported period and first period derivative values, Figure 2-27 provides a plot of the characteristic age of the source versus its period. The characteristic age of many of the shortest period sources is 10^7–10^{11} yr. The plot in Figure 2-28 shows the strength of a source's magnetic field versus its period. Although there are several exceptions, the plot shows that the period generally increases for larger magnetic fields, and that the fastest rotating sources have field strengths on the order of 10^8-10^{10} Gauss.

The X-ray radiation flux measured for each source versus its rotation period is plotted in Figure 2-29. Flux intensity is important for the detection of a source, as well as its use in producing a time and position solution in navigation. This plot show that several sources emit large amounts of X-ray flux (~10^{-2} ph/cm^2/s and higher) while rotating at rates faster than 100 Hz. The plot in Figure 2-30 shows this X-ray flux versus the magnetic field strength of the source. Due to the spread of values, stronger magnetic fields do not necessarily indicate greater flux intensity. However, for the sub-group of NS sources as the magnetic field increases, the X-ray flux also tends to rise.

The pulsed fraction of the signal intensity for each source versus its rotation period is plotted in Figure 2-31. The range of pulsed fraction from a few percent to nearly 100 % indicates the variety of pulsed components of the signals. Figure 2-32 provides a plot of pulse width (FWHM) of each source versus its rotation period. Very little data on this parameter is presented in the published catalogues, as this figure indicates, thus data analysis usually estimates this value.

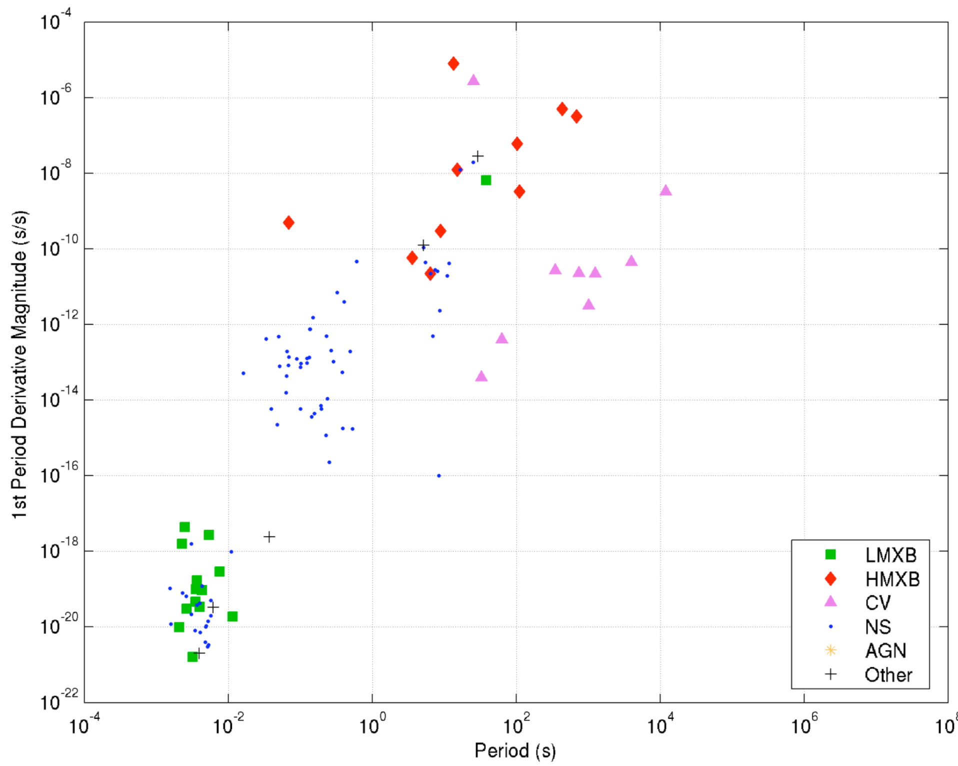

Figure 2-25. First period derivative versus period for sources in the XNAVSC.

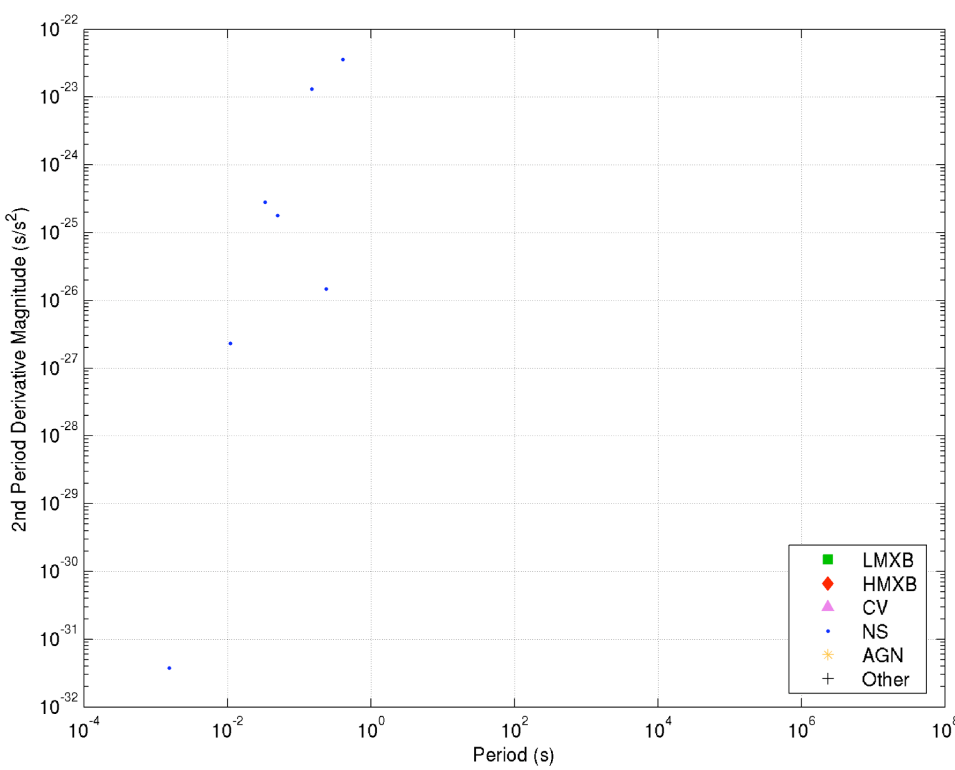

Figure 2-26. Second period derivative versus period for sources in the XNAVSC.

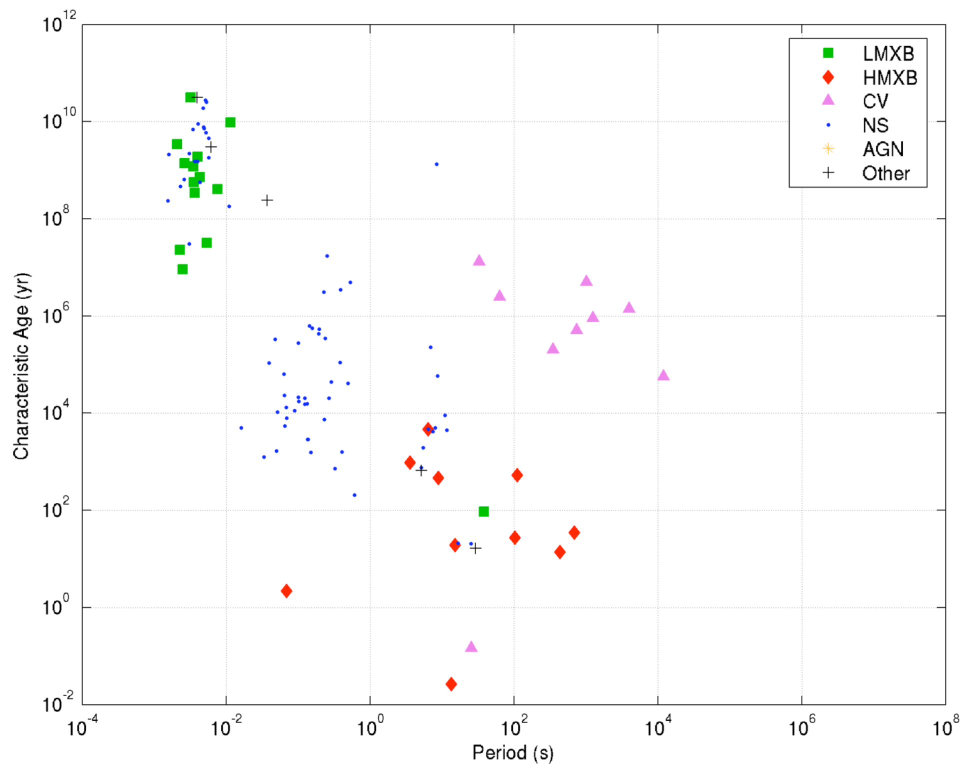

Figure 2-27. Characteristic age versus period for sources in the XNAVSC.

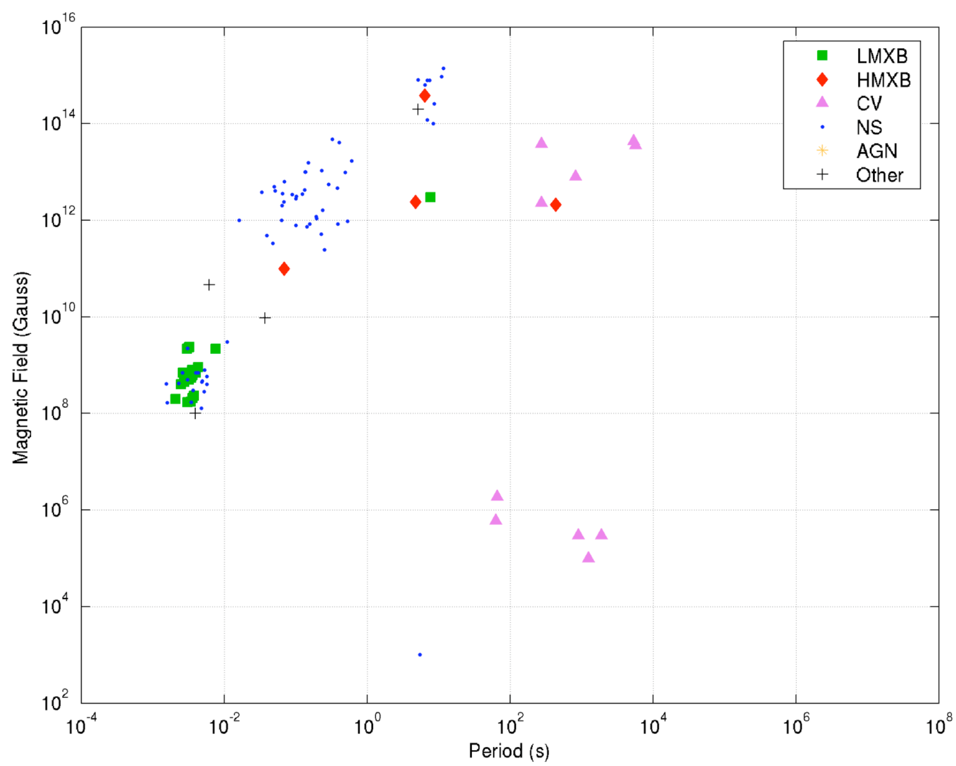

Figure 2-28. Magnetic field versus period for sources in the XNAVSC.

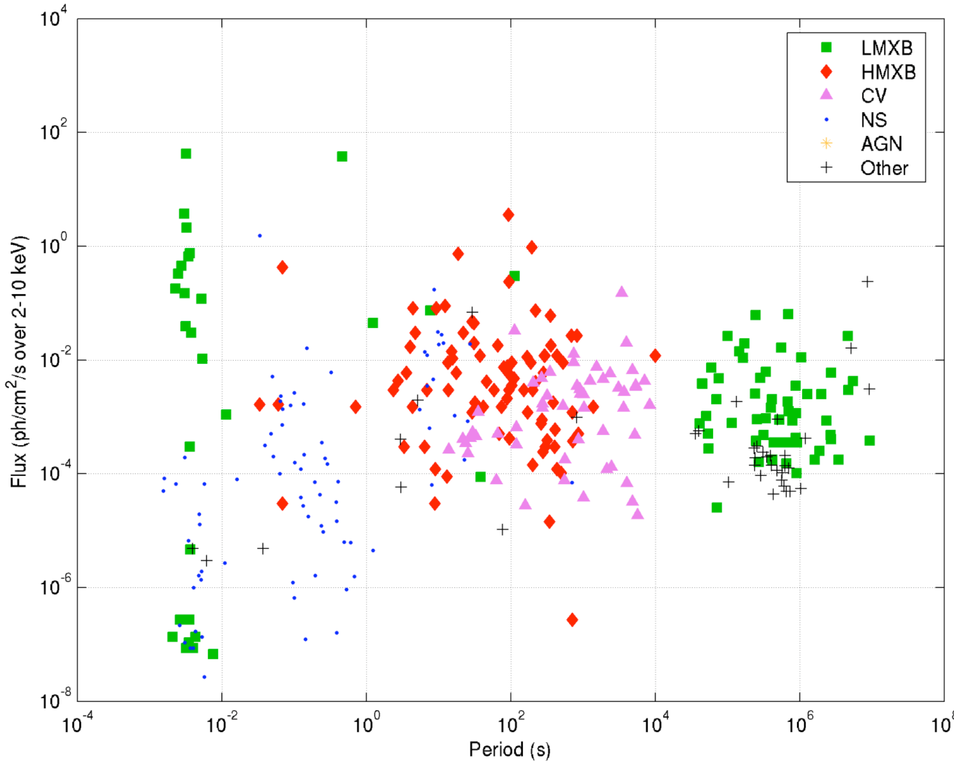

Figure 2-29. X-ray flux versus period for sources in the XNAVSC.

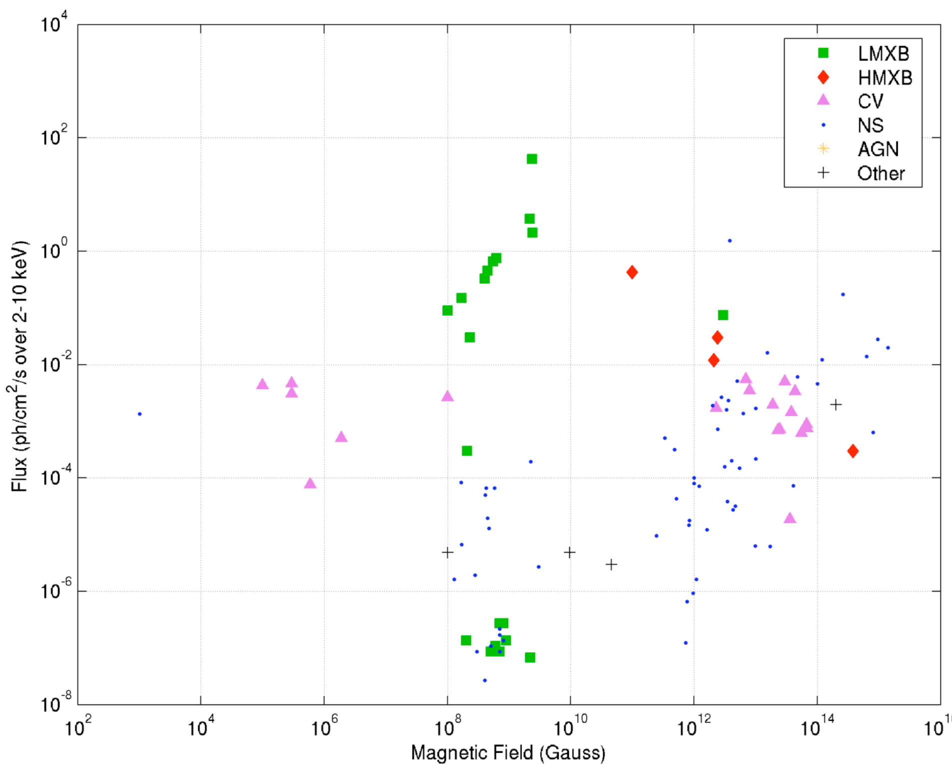

Figure 2-30. X-ray flux versus magnetic field for sources in the XNAVSC.

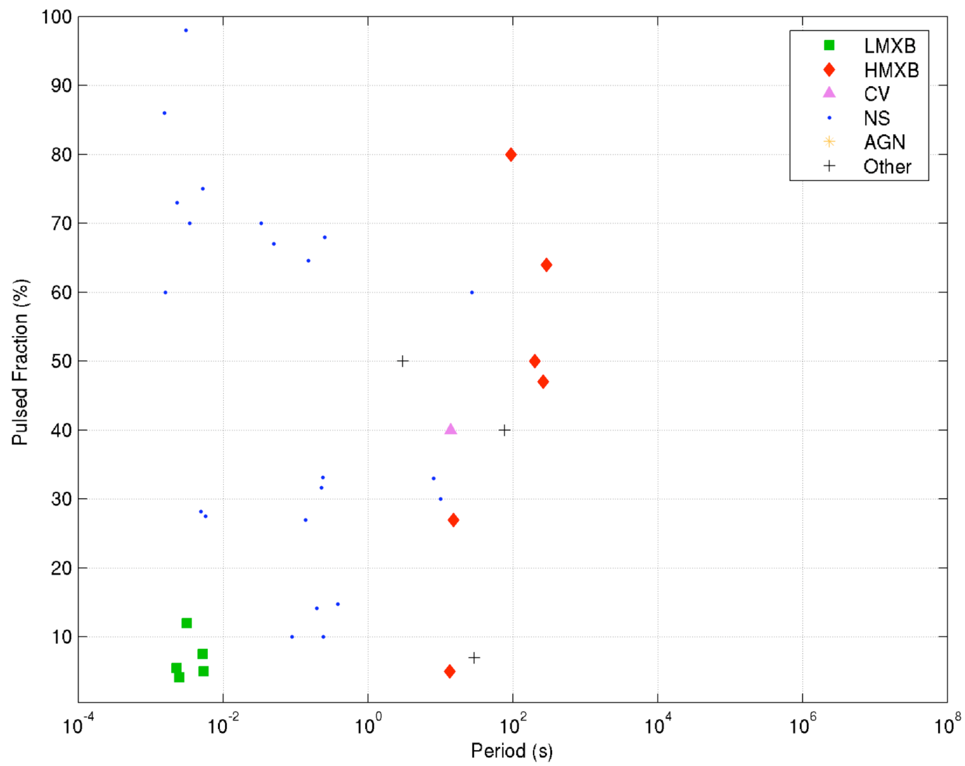

Figure 2-31. Pulsed fraction versus period for sources in the XNAVSC.

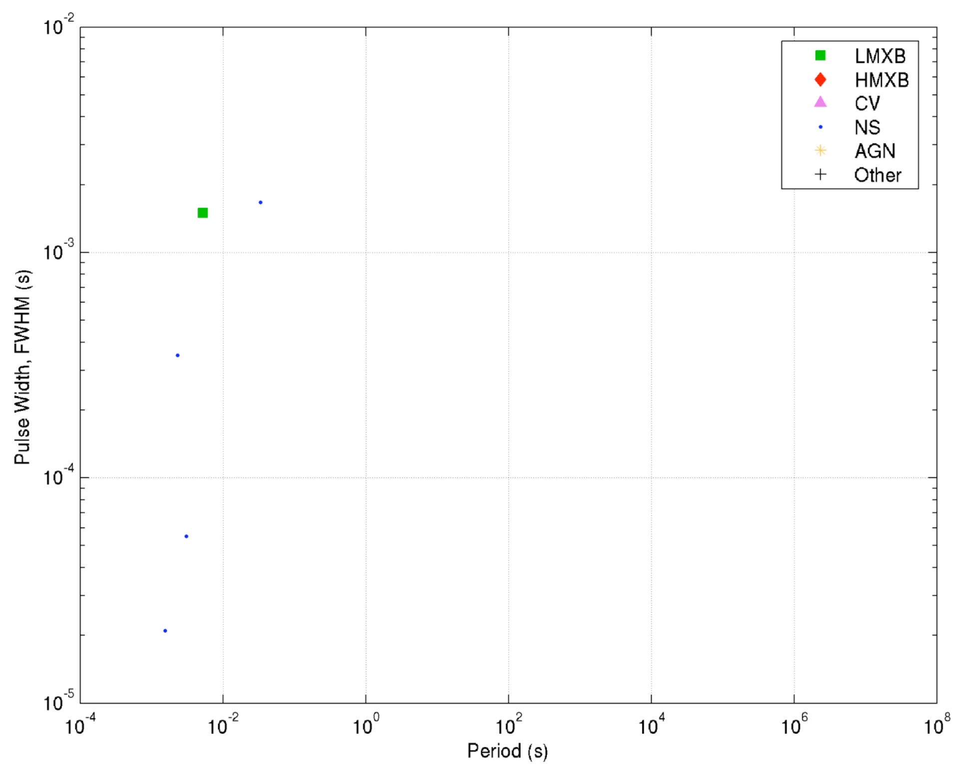

Figure 2-32. Pulse width (FMHW) versus period for sources in the XNAVSC.

2.3.4.2 X-ray Millisecond Sources

As the previous section illustrates, a very important sub-category of sources that can be used for spacecraft navigation is those sources that have rotation periods on the order of several milliseconds. Many of these sources rotate at speeds greater than 100 Hz, and several of these sources are intense X-ray flux emitters. Therefore, their study is key to understanding the capability of X-ray sources for position and time determination.

Table 2-12 provides a listing of the names and periods of the millisecond sources from the XNAVSC with periods shorter than 0.02 s, arranged in order of increasing period. Figure 2-33 provides a graph of these 48 sources plotted in Galactic coordinates. Several of these sources are referred to as *millisecond pulsars* (MPSR), those whose period in on the order of several milliseconds. These pulsars are assumed to be older neutron stars that have been recycled, and through the process of accretion have significantly increased their rotation rates [24, 223]. Many exist in X-ray binary (XB) systems, however some are isolated neutron stars [102, 103]. The fastest rotating known source is PSR B1937+21, which has a period of 0.001558 s [151]. Since the sources located in 47 Tucanae have very close positions, they appear as a single point on this plot.

Figure 2-34 provides the period derivative versus period for these millisecond period sources from the XNAVSC. This plot shows that many of these sources have very stable periods, as their derivatives are small ($<10^{-17}$ s/s). This provides additional support for the use of these sources in navigation, since accurate models can be created for these sources to predict the arrival of pulses from these sources. Figure 2-35 shows the X-ray flux versus period for these sources. Several of the LMXB type millisecond sources have high flux, thus can be more easily identified by detectors developed for navigation.

Table 2-12. Millisecond Period Sources in XNAVSC Database.

Source Names	Source Type	Period (s)	Reference
PSR B1937+21	RPSR	0.00156	[105, 151, 158]
PSR B1957+20, Black Widow Pulsar	RPSR	0.00160	[19, 20, 159]
PSR J0023-7203J; 47 Tuc J	LMXB	0.00210	[60, 70]
XTE J1751-305	LMXB	0.00230	[64, 121, 125, 134]
PSR J0218+4232	RPSR	0.00232	[19, 20, 105, 151, 158, 159]
Sax J1808.4-3658; XTE J1808-369	LMXB	0.00249	[36, 111, 225, 226]
PSR J0024-7204F; 47 Tuc F	RPSR	0.00262	[60, 70]
PSR J0024-7204O; 47 Tuc O	LMXB	0.00264	[60, 70]
4U 1728-34	LMXB	0.00276	[111, 222]
4U 1758-25	LMXB	0.00303	[111, 222]
PSR B1821-24	RPSR	0.00305	[19, 105, 151, 158, 159]
PSR J0024-7204N; 47 Tuc N	RPSR	0.00305	[60, 70]
4U 0614+091; 1H 0610+091	LMXB	0.00305	[111, 222]
XTE J1814-338	LMXB	0.00318	[104, 122, 200]
PSR J0024-7204H; 47 Tuc H	LMXB	0.00321	[60, 70]
Sco X-1; B1617-155	LMXB	0.00323	[111, 222]
4U 1813-14	LMXB	0.00327	[111, 222]
4U 1743-29; 1H 1744-293	LMXB	0.00340	[222]
4U 1636-53; 1H 1636-536	LMXB	0.00345	[111, 222]
PSR J0751+1807	RPSR	0.00347	[19, 20, 158, 159]
PSR J0024-7204I; 47 Tuc I	LMXB	0.00348	[60, 70]
PSR J0024-7205E; 47 Tuc E	LMXB	0.00354	[60, 70]
4U 1820-30; 1H 1820-303	LMXB	0.00363	[111, 222]
4U 1908+005	LMXB	0.00364	[111, 222]
PSR J1740-5340	LMXB	0.00365	[47, 60, 70]
PSR J0023-7205M; 47 Tuc M	RPSR	0.00368	[60, 70]
KS 1731-260	LMXB	0.00380	[111, 222]
PSR J2019+2425	Binary Pulsar	0.00393	[19]
PSR J0024-7204Q; 47 Tuc Q	LMXB	0.00403	[60, 70]
PSR J0024-7204G; 47 Tuc G	RPSR	0.00404	[60, 70]
PSR J1744-1134	RPSR	0.00407	[158]
PSR J0024-7203U; 47 Tuc U	LMXB	0.00434	[60, 70]
PSR J0024-7204L; 47 Tuc L	RPSR	0.00435	[60, 70]
PSR J2322+2057	RPSR	0.00480	[19]
PSR J0030+0451	RPSR	0.00487	[158]
PSR J2124-33	RPSR	0.00493	[19, 158, 159]
PSR J1024-0719	RPSR	0.00516	[158]
PSR J1012+5307	RPSR	0.00525	[19, 20, 158, 159]
XTE J1807-294	LMXB	0.00525	[33, 101, 123, 124]
PSR J0024-7204D; 47 Tuc D	RPSR	0.00536	[60, 70]
XTE J0929-314	LMXB	0.00540	[64, 169]
PSR J0437-4715	RPSR	0.00575	[19, 158, 159]
PSR J0023-7204C; 47 Tuc C	RPSR	0.00576	[60, 70]
PSR B1257+12	Binary Pulsar	0.00620	[19]
PSR J0024-7204T; 47 Tuc T	LMXB	0.00759	[60, 70]
PSR B1620-26	RPSR	0.01108	[19]
PSR 1744-24A	LMXB	0.01156	[152]
PSR J0537-6910	RPSR	0.01611	[158]

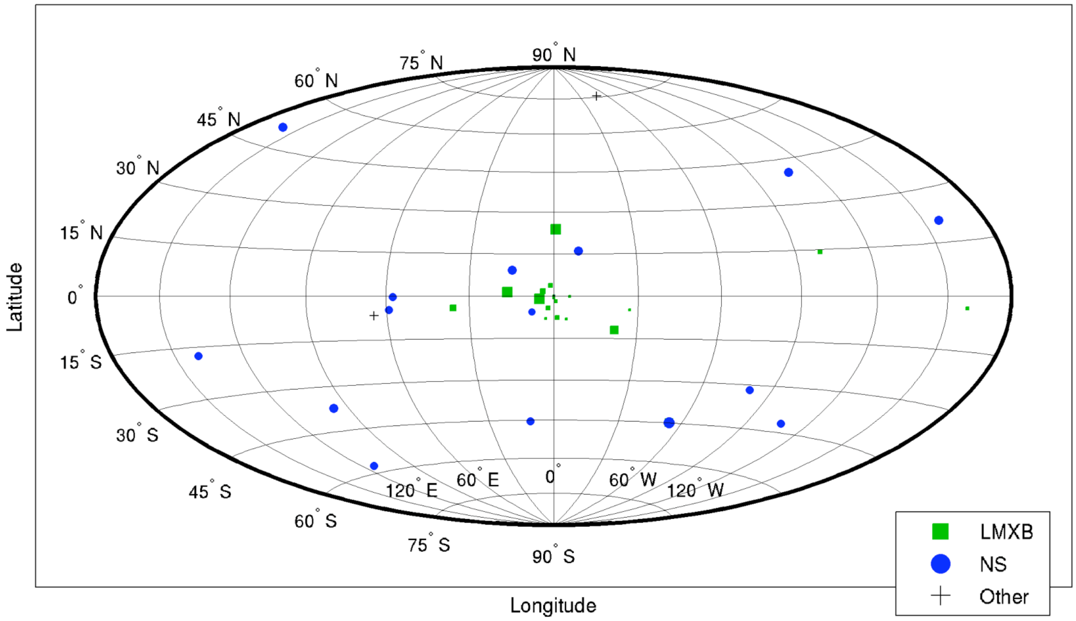

Figure 2-33. Millisecond period sources from the XNAVSC.

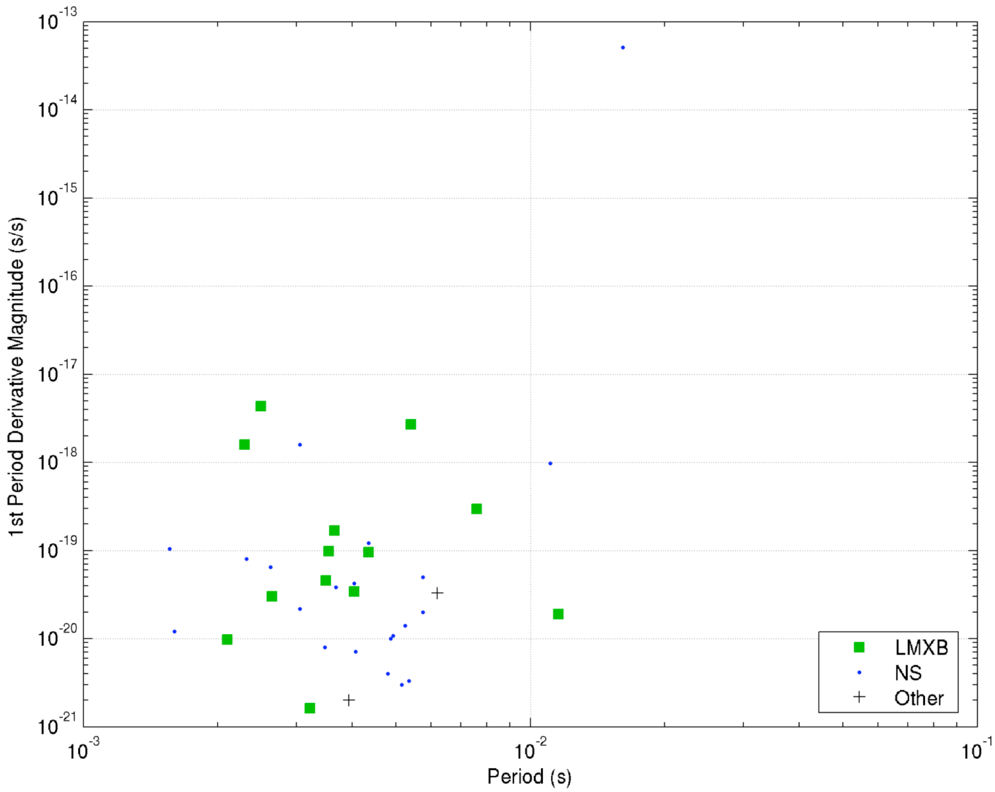

Figure 2-34. First period derivative versus period for millisecond period sources.

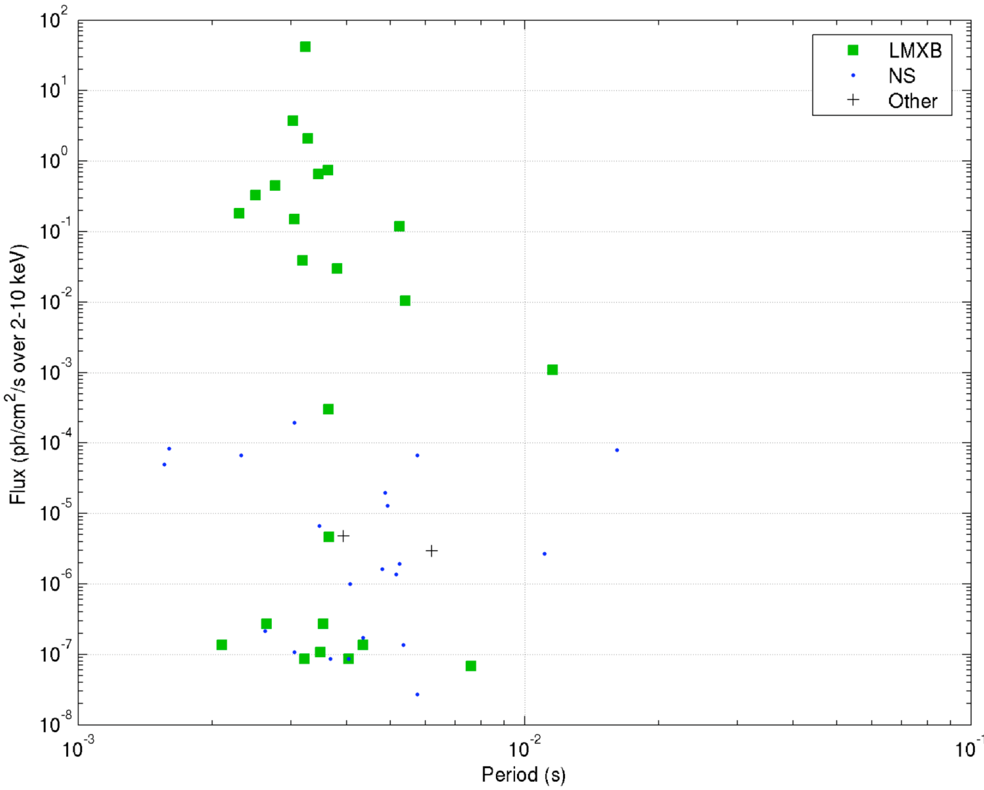

Figure 2-35. X-ray flux versus period for millisecond sources.

Chapter 3 Pulse Identification, Characterization, and Modeling

"You may delay, but time will not."

– Benjamin Franklin

The cyclic emissions generated by variable celestial sources offer measurable signals that can be exploited within a navigation system. To utilize these signals, they must be detectable, such that sensors can be developed that can determine the arrival of the emissions from each individual unique source; the signals must be able to be characterized, such that the necessary parameters distinctive to a specific source can be resolved and be used to identify each source as data are recorded; and the signals must be able to be modeled, such that methods can be created to predict the future arrival time of the signals at a given location.

This Chapter presents methods for assembling the received photons from these sources into a signal that can be utilized for navigation. The *Pulse Profile* section describes the pulse detection and profile creation processes. The *Pulse Timing Models* section provides descriptions of how models are created using the signal detection, as well as a discussion of the pulse stability that has been shown from long duration observations of several sources. The *Pulse Arrival Time Measurement Accuracy* section presents an analysis on how to determine the accuracy of a measured arrival time based upon the SNR value of a specific observation. The final section on *Arrival Time Comparison* discusses the issue of comparing pulse arrival times across different energy wavelengths, and how this may affect pulse modeling.

3.1 Pulse Profile

From the variety of variable celestial sources described in Chapter 2, the emission mechanisms and the reception of these signals within the solar system produces an equal diversity of pulse signals. The *profile* of each pulse is a representation of the characteristics of the pulse. Pulse profiles vary in terms of shape, size, cycle length, and intensities. Some sources produce sharp, impulsive, high intensity profiles, while others produce sinusoidal, elongated profiles. Although many sources produce a single, identifiable pulse, other pulse profiles contain sub-pulses, or inter-pulses that are evident within the signal [114, 118].

Replicating the pulse profile from the detected X-ray photons provides information about the source's characteristics, the arrival time of the pulse, and data that can be utilized for navigation. This section provides methods to reproduce the pulse profile so that this information can be extracted from the source's signal.

3.1.1 Photon Detection and Timing

At X-ray energy wavelengths, the measured components of the emitted signal from a source are the individual photons released in a source's energy discharge. The observed profile is created via the detection of these photons from the source as they arrive at the navigation system's detector.

The first step in generating the pulse profile is to detect the onset of photons from a source above the nominal X-ray background signal. Appendix E provides a description of several types detector designs that have been successfully demonstrated on spacecraft missions to detect X-ray photons. Typically a grid of material detects a photon within two-dimensional array, providing a measurement of energy produced by the photon and the approximate location of the photon detection event within the detector's field-of-view (FOV) [59]. Each photon provides a quantized unit of energy that is released within the detector grid. Photon energy magnitude and the number of photons received per unit time provide indications that a source has been detected.

To observe a source, an X-ray detector is initially aligned along the line-of-sight to the chosen source. Once photon events from this source are positively identified, components within the detector system record the time of arrival of each individual X-ray photon with respect to the system's clock to high precision. For accurate systems, this has been demonstrated to the order of one microsecond photon event timing resolution. Future designs will attempt to resolve the photon timing to even greater precision.

During the total observation time of a specific source, a large number of photons, N_{ph}, will have each of their arrival times recorded. The measured individual photon arrival times from τ_0 to τ_{N-1} must then be converted from the detector's system clock to their equivalent time in an inertial frame, t_0 to t_{N-1}. This conversion provides an alignment of the photon's arrival time into a frame that is not moving with respect to the observed source. The methods of time transfer necessary for this alignment is discussed in detail within Chapter 4 and is a crucial component of successful pulse profile development, as well as a central algorithm within the time and position determine processes discussed in later chapters.

3.1.2 Profile Creation

The N_{ph} number of photons detected within a given observation spans numerous pulse cycles if the observation time is much greater than the pulse cycle period. Each photon is a component of an individual pulse, and detecting a single photon does not immediately provide an indication of a given pulse. The photon event data are essentially a table of arrival times for these N_{ph} photons. To create the pulse profile, these photons must be assembled together to align their arrival times with respect to one individual pulse.

The process of assembling all the measured photon events into a pulse profile is referred to as *epoch folding*, or averaging synchronously all the photon events with the expected pulse period of the source. A *binned pulse profile* is constructed by dividing the expected pulse phase into M equal bins and dropping each of the N_{ph} recorded photon events into the appropriate phase bin. The bins can be either created within the time domain or the frequency domain. Through the folding process, for sources that produce identifiable pulse signatures, some phase bins within the pulse cycle length will accumulate more photon events than others. The resulting histogram over the pulse cycle length renders the profile of the pulse from the source. Thus, the pulse profile is a representation of the phase average of multiple detected pulses from a source.

Once produced, characteristics of the pulse can be determined from a profile, or set of profiles. These characteristics include pulse amplitude above the averaged signal and number and shape of peaks. Variability in parameters such as period length and noise, as well as continuity of pulsed emission can be determined. The unique characteristics of each source's pulse profile aids in the identification process of the source.

3.1.2.1 Pulse Profile Template

To assist an individual pulse time of arrival measurement, pulse profiles with very high signal-to-noise ratio (SNR) can be created. These *standard profile template*s are produced similarly to observation profiles using epoch folding. However, these templates utilize much longer observation times and possibly multiple observations folded together in order to gain a high SNR value. These templates often present a much clearer representation of the pulse profile, as the noise on this signal is reduced through the repeated observations.

Figure 3-1 shows a standard pulse template for the Crab Pulsar (PSR B0531+21) in the X-ray band (1–15 keV) created using multiple observations with the USA experiment onboard the *ARGOS* vehicle. The intensity of the profile is a ratio of count rate relative to average count rate. This image shows two cycles of the pulsar's pulse for clarity. The Crab Pulsar's pulse is comprised of one main pulse and a smaller secondary sub-pulse with lower intensity amplitude. The phase of the main peak of pulse within this template has been aligned to a phase equal to zero. This was chosen so that arrival times correspond to the peak of the main pulse.

Contrasting this image, Figure 3-2 shows an observation profile of the Crab Pulsar produced using a shorter observation close to the same epoch as the standard template. This observation has not been aligned for zero phase, as was done for the standard template. This image shows that standard observation contains significant amounts of noise when compared to the standard pulse template of Figure 3-1.

As another example, Figure 3-3 shows a two-cycle image of the pulse profile of PSR B1509–58 created using data from the *RXTE* spacecraft. This profile shows that the pulse from this pulsar is a broad sinusoidal shape, and only one single peak per period is clearly visible. The image shows quantization within the curvature of the pulse shape. In order to be used as a pulse template, folding with additional data would be needed to reduce the noise within the profile.

3.1.3 Pulse Arrival Time Measurement

The fundamental measurable quantity for time and position determination within a variable source-based navigation system is the arrival time of an observed pulse at the detector. It is necessary to determine the time of arrival (TOA) of the pulse so that navigation algorithms can compare the measured TOA to the expected TOA and use the information accordingly.

A pulse TOA measurement is initiated by observing a source for multiple pulse periods and producing an epoch folded profile, as described in the previous section. Prior to this observation, it is assumed a standard pulse template defined at a specified epoch has been created and is available for comparison to the observed profile. The observed profile, $p(t)$, will differ from the template profile, $s(t)$, by several factors. Typically the observed pulse will vary by a shift of time origin, Δt_S, a bias, b, a scale factor, k, and

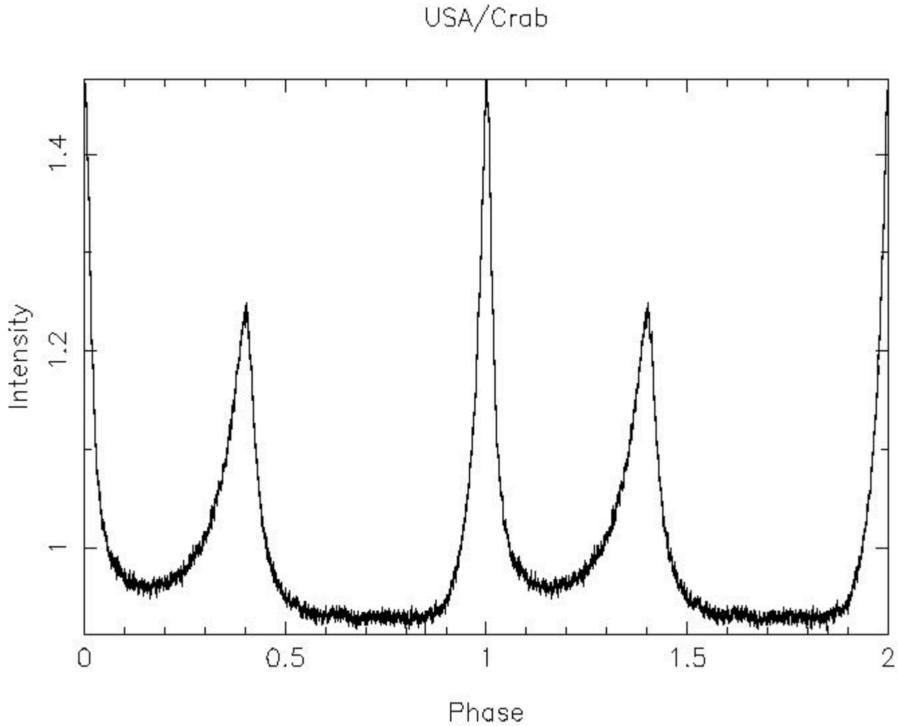

Figure 3-1. Crab Pulsar standard pulse template. Period is about 33.5 milliseconds (epoch 51527.0 MJD).

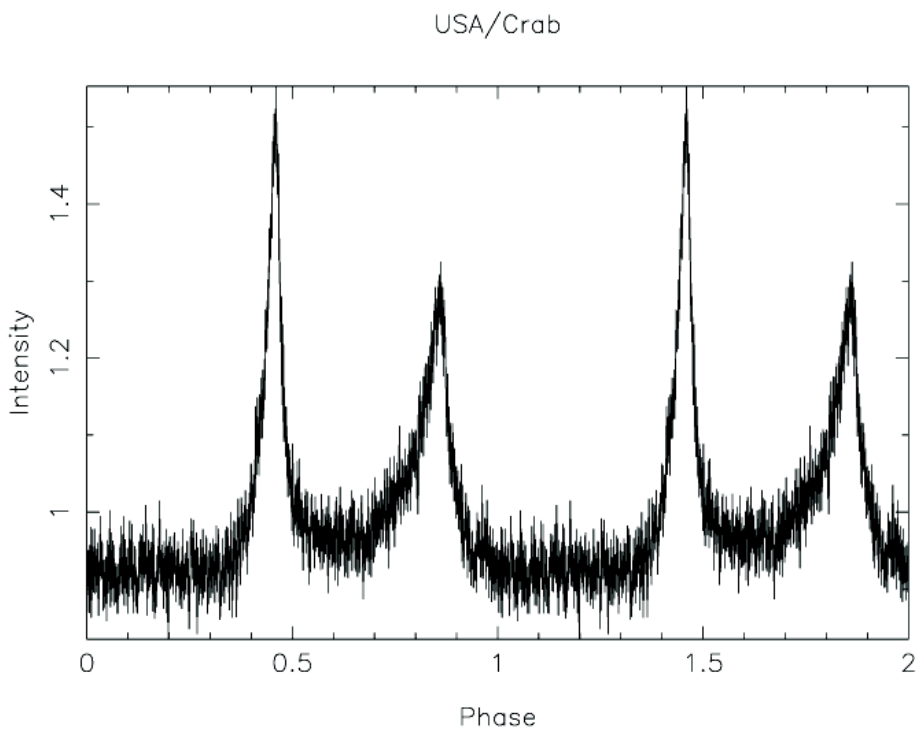

Figure 3-2. Crab Pulsar observation profile.

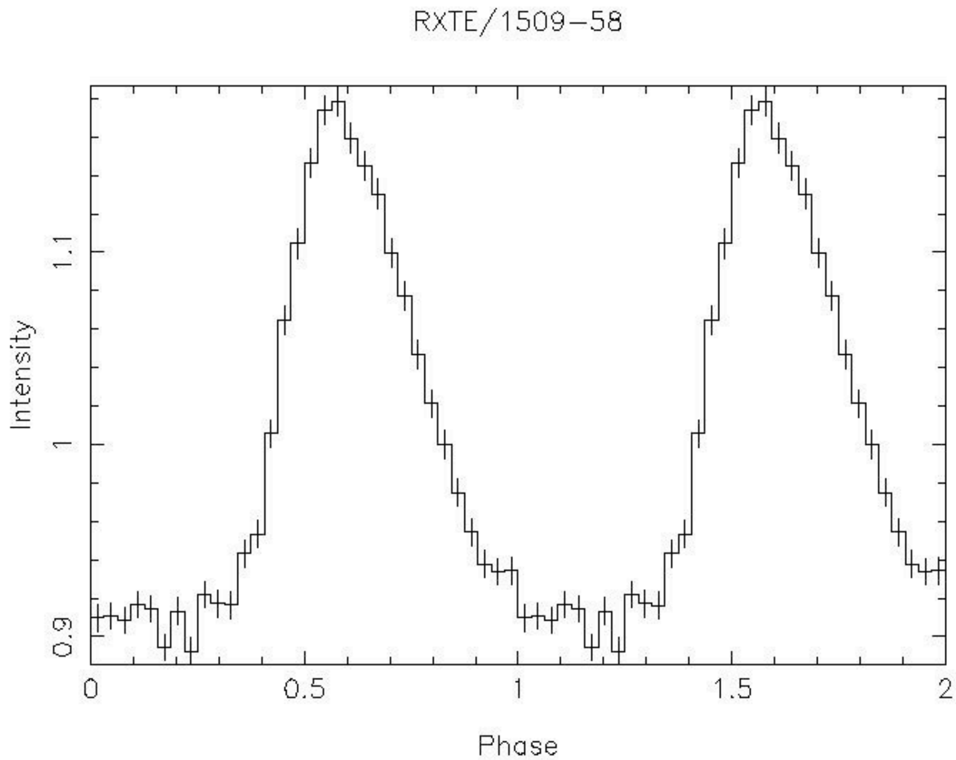

Figure 3-3. PSR 1509-58 pulsar standard pulse template. Period is about 150.23 milliseconds (epoch 48355.0 MJD).

random noise $\eta(t)$ [204, 205]. The relationship between the observed profile and the standard template profile is given by,

$$p(t) = b + k\left[s(t - \Delta t_S)\right] + \eta(t) \tag{3.1}$$

For X-ray observations that records individual photon events, Poisson counting statistics typically dominates the random noise in this expression.

The objective of the observed and template profile comparison process is to determine the constant values of bias, scale factor, and particularly the time shift in Eq. (3.1). The time shift necessary to align the peaks of within the two profiles is added to the start time of the observation to produce the TOA of the first pulse within this particular observation.

The discrete Fourier transforms of the two profiles can be compared using the method described by Taylor [204]. After converting time to phase of the pulse period, this process measures the phase offset of the observed profile with respect to the high SNR standard profile template. This is based upon the assumption that, after averaging a sufficiently large number of pulses, a pulse profile recorded in the same energy range is invariant with time. The template can be aligned with an arbitrary point in the profile as phase zero, but two conventions are commonly used. Either the peak of the main pulse can be aligned as the zero phase point, or the profile can be aligned such that the phase of the fundamental component of its Fourier transform is zero. Although it reduces to the former in the case of a single-symmetric pulse profile, the latter method using the fundamental component is preferred because it is more precise and generally applicable. This method also allows for simpler construction of standard templates by measuring the phase of the fundamental Fourier component, applying a fractional phase shift to the profile, and summing many observations to produce the template.

An estimate of the accuracy of the TOA measurement can be computed as an outcome of this comparison process. This estimate provides an assessment on the quality of the TOA measurement, and can be useful in the navigation algorithms. Although the time domain could be used to determine the computed time shift, Taylor's method is preferred as its error estimate in the TOA measurement can be expressed independent of the photon event sampling time interval.

3.2 Pulse Timing Models

The pulsed emission from variable celestial sources arrives within the solar system with sufficient regularity that the arrival of each pulse can be modeled. These models predict when specific pulses from the sources will arrive within the solar system. For navigation, these models can be used as a method to predict when pulses are expected to arrive at an observing station.

These models provide information about the characteristics of the sources, including their period duration, and the rate of change of this duration. Using this information, elements of the evolution and nature of a source can be determined. After a source's model has been produced, new observations of the source can be conducted and results compared against the model. As discussed in the previous section, the process of pulse epoch folding uses the expected pulse period from these models to create accurate pulse profiles, which are in turn used to compute accurate TOAs.

For navigation, it is necessary to have a database of predetermined pulse timing models for all sources planned to be used within the system to avoid requiring this information to be determined during a spacecraft's mission. Many sources already have well determined models, as was shown in Chapter 2. These external observations and models provide a significant resource for developing this navigation system. As an example, the Jodrell Bank Observatory performs daily radio observations of the Crab Pulsar, and publishes a monthly ephemeris report [115]. This published report lists model parameters that describe the pulsar's timing behavior since the beginning of their observations in May 1988. Information similar to this would need to be maintained for all sources and continually provided to the navigation system onboard a vehicle.

3.2.1 Frequency and Period Forms of Models

Pulse timing models are often represented as the total accumulated phase of the source's signal as a function of time. A starting cycle number, $\Phi_0 = \Phi(t_0)$, can be arbitrarily assigned to the pulse that arrives at a fiducial time, t_0, and all subsequent pulses can be numbered incrementally from this first pulse. Assigning a cycle number to individual pulses is necessary since the celestial sources do not directly provide this information. The total phase of arriving pulses, Φ, is measured as the sum of the fractions of the period, or phase fraction, ϕ, and the accumulated whole value cycles, N. These can be expressed as functions of time as,

$$\Phi(t) = \phi(t) + N(t) \tag{3.2}$$

From a chosen reference time, t_0, the phase fraction varies from 0 to 1 for each pulse period whereas the number of whole value cycles continue to increase. Thus, the total phase, Φ, has both periodic and secular effects from these two components.

The total phase can be specified at a specific location using a pulsar phase model of,

$$\Phi(t) = \Phi(t_0) + f[t - t_0] + \frac{\dot{f}}{2}[t - t_0]^2 + \frac{\ddot{f}}{6}[t - t_0]^3 \tag{3.3}$$

Eq. (3.3) is known as the *pulsar spin equation*, or *pulsar spin down law* [114, 118]. In this equation, the observation time, t, is in *coordinate time*, discussed in more detail in Chapter 4. The model in Eq. (3.3) uses pulse frequency, f, and its derivatives. From the relationship of frequency and period, their derivatives can be computed simply as [114],

$$f = \frac{1}{P}; \qquad P = \frac{1}{f}$$
$$\dot{f} = -\frac{\dot{P}}{P^2}; \qquad \dot{P} = -\frac{\dot{f}}{f^2} \tag{3.4}$$
$$\ddot{f} = \frac{2\dot{P}^2}{P^3} - \frac{\ddot{P}}{P^2}; \qquad \ddot{P} = \frac{2\dot{f}^2}{f^3} - \frac{\ddot{f}}{f^2}$$

Using Eqs. (3.3) and (3.4), the pulse timing models can also be represented using pulse period, P, (also angular velocity $\Omega = 2\pi f$) as,

$$\Phi(t) = \Phi(t_0) + \frac{1}{P}[t - t_0] - \frac{\dot{P}}{2P^2}[t - t_0]^2 + \left(\frac{\dot{P}^2}{3P^3} - \frac{\ddot{P}}{6P^2}\right)[t - t_0]^3 \tag{3.5}$$

The specific model parameters for a particular object are generated through repeated observations of the source until a parameter set is created that adequately fits the observed data. The accuracy of the model prediction depends on the quality of the known timing model parameters and on the intrinsic noise of the pulsar rotation [114, 194].

Since the pulse phase depends on the time when it is measured as well as the position in space where it is measured, the location of where the model is valid must be supplied in addition to the parameters that define the model for accurate pulsar timing. Typically, this location is chosen as the solar system barycenter (SSB), however, other locations can be utilized as long as this is declared along with the model.

The pulsar phase model of Eq. (3.3), or (3.5), allows the determination of the phase of a pulse signal at a future time t, relative to a reference epoch t_0, at a specified position in space. Thus, it is possible to predict when any peak amplitude of a pulsar signal is expected to arrive at a given location. The model shown in Eq. (3.3) utilizes pulse frequency and two of its derivatives (equivalently, Eq. (3.5) uses period and its two derivatives); however, any number of derivatives may be required to accurately model a particular pulsar's timing behavior. Additionally, sources that are components of multiple star systems, such as binary systems, require parameters that include the periodic orbits of the source within the systems. It is necessary to have precise models in order to accurately predict the pulse arrival times. However, as long as these parameters can be sufficiently determined, any source with detectable pulsations can be used in the time and position determination scheme.

3.2.2 Pulsar Timing Stability

The accuracy of the pulse timing models depends significantly on whether the intrinsic nature of the source or the extrinsic effects acting on the source continues to match the model's predicted rotation rates. As some pulsars have been observed for many years, it has been shown that the stability of their spin rates compares well to the quality of today's atomic clocks [7, 96, 112, 113, 127, 163].

An accurate timer or clock is important to many spacecraft sub-systems and is often a fundamental component to the spacecraft navigation system. Figure 3-4 presents the stability of several of today's atomic clocks [127]. Atomic clocks provide high accuracy references and are typically accurate to one part in 10^9-10^{15} in stability over a day. Figure 3-5 plots the stability of two well studied pulsars, PSR B1937+21 and PSR B1855+09 in the radio band [95]. Figure 3-6 provides both sets of this data on the same plot [112]. The metric used here for comparing the signal stability from these clocks and pulsars is computed using *third* differences, $\sigma_z(t)$, or third-order polynomial variations – as opposed to *second* differences for the standard clock Allan variance statistic – of clock and pulsar timing residuals [6, 127]. This metric is sensitive to variations in frequency drift rate of atomic clocks and pulsars; the standard Allan variance is sensitive to variations in frequency drift. With this metric and these plots, it can be seen that some pulsars approach the stability of today's atomic clocks for the long term (on the order of one or more years). For the short term (on the order of days to a year), these pulsars match the stability of a few of today's atomic clocks, with more accurate atomic clocks having improved stability in this short term. With these long term comparisons, the high quality stability of these variable celestial sources has led some researchers to consider new time standards based upon these sources [163, 167, 203].

Older pulsars, particularly those that have undergone a long period of accretion in a binary system that spins them up to a millisecond period, have extremely stable and predictable rotation rates. The plots in Figure 3-5 and Figure 3-6 use data from radio pulsars, however, PSR B1937+21 is also detected in the X-ray band. Its X-ray stability is expected to be similar, or perhaps better because of a reduction of propagation effects from the interstellar medium effect on X-ray photons. Figure 3-5 and Figure 3-6 demonstrate that several pulsars compare well to typical atomic clock stabilities. This stability assures that the pulse timing models created for these sources will sufficiently predict arrival times of pulses, such that a navigation system can use these predictable pulse observations for either correcting time or position on the spacecraft.

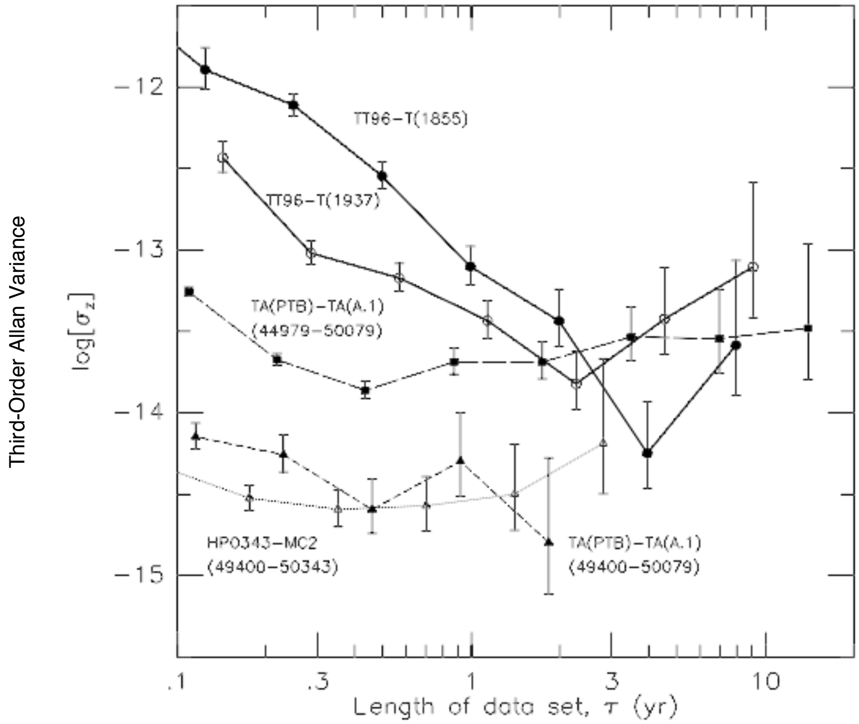

Figure 3-4. Stability of several atomic clocks
(Courtesy of Matsakis, Taylor, and Eubanks [127]).

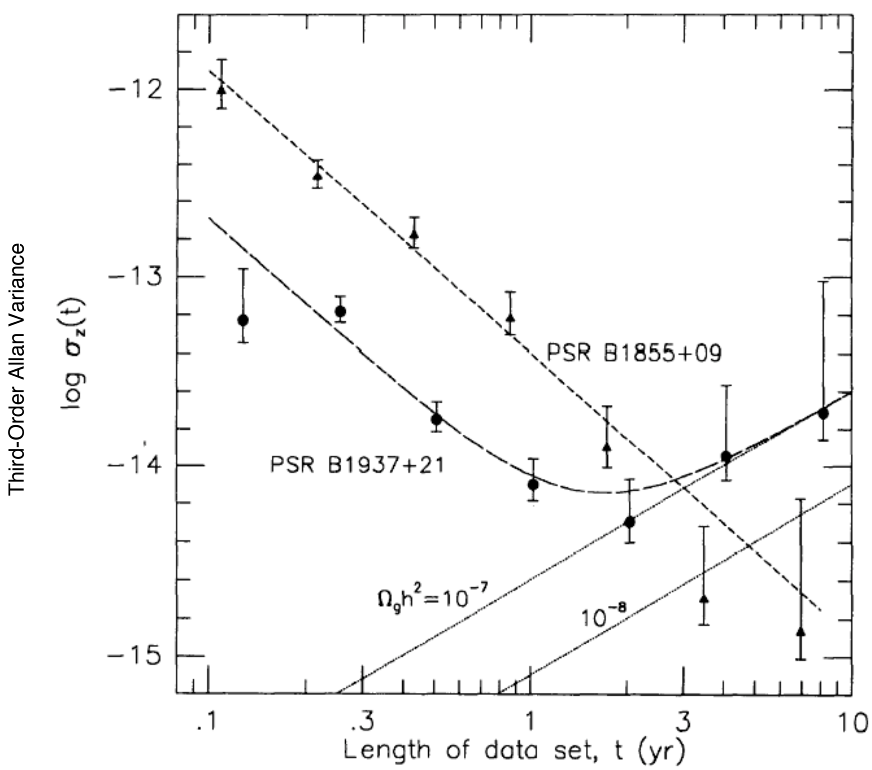

Figure 3-5. Stability of two pulsars (Courtesy of Kaspi, Taylor, and Ryba [96]).

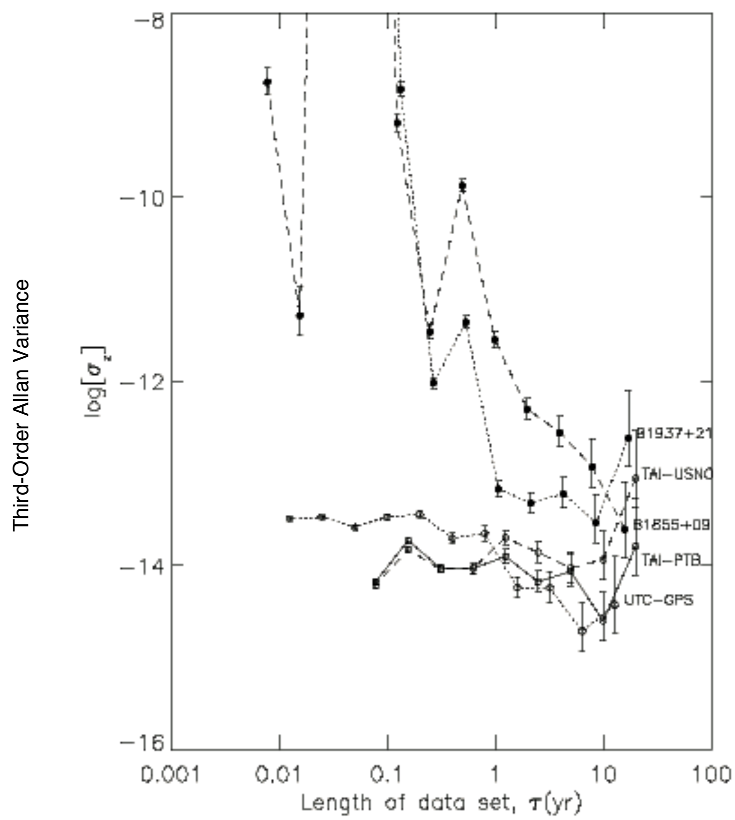

Figure 3-6. Stability of atomic clocks and pulsars (Courtesy of Lommen [112]).

3.3 Pulse Arrival Time Measurement Accuracy

Once pulse profiles and timing models are provided, pulse TOAs can be computed. An important aspect of this arrival time measurement for navigation is its estimated accuracy. This estimation is used to weight the processing of each TOA either in a batch estimation process or Kalman filter implementation to improve solutions of spacecraft navigation data as presented in Chapters 6 through 8. This section provides discussion on the methods used to compute TOA accuracy and demonstrates these methods using pulsar observations and characteristics.

3.3.1 Pulse Profile Fourier Transform Analysis

It is important to determine the TOA with an accuracy that is determined by the SNR of the profile, and not by the choice of the phase bin size. A standard cross-correlation analysis does not allow this to be easily achieved. However, the method given by Taylor [204] is independent of bin size and can be implemented into a navigation system. The technique employs the time shifting property of Fourier transform signal pairs. The Fourier transform of a function shifted by an amount Δt_S is the Fourier transform of the original function multiplied by a phase factor of $e^{2\pi i f \Delta t_S}$, where f is frequency of the signal. Since the observed profile differs from the template by the constant values of the bias, the scale factor, the time shift, and random noise, as in Eq. (3.1), it is straightforward to transform both the profile and the template into the Fourier domain. The parameters in Eq. (3.1) are then determined by a standard least squares fitting method. Chi-squared tests are pursued to minimize the fitting statistics for determining these observation and template profile comparison model parameters. The final measured TOA of the pulse is then determined by adding the fitted offset Δt_S to the recorded start time of the data set t_0.

Chapter 7 and Appendix C provide sample observations made by the NRL USA experiment of the Crab Pulsar. Measurements produced using this Fourier transform analysis are provided, along with estimated accuracies based upon this method. Using this experiment's data, TOAs on the order of a few microseconds are computed. As is explained in Chapters 4 and 7, if all the TOA measurement error is assumed to be directly related to spacecraft position, then these errors convert to a couple of kilometers of range error along the Crab Pulsar's unit direction.

Possible future enhancements to this Fourier transform method may include improved parameter-fitting methods. The description of the comparison of the observed and template profiles of Eq. (3.1) can be implemented within a Kalman filter. This implementation approach could incorporate higher order parameters and additional system dynamics, such as detector motion, in order to compute additional model parameters and produce covariance estimates of the TOA accuracy. A Kalman filter may allow analysis at the individual photon level, as opposed to the full pulse profile analysis used here. New research should be considered to determine if new approaches to determining parameter models might generate improved results.

3.3.2 SNR From Source Characteristics Analysis

The method presented by Taylor [204] creates a computation of TOA accuracy based upon the observed profile characteristics compared to the template profile. This method does not provide an immediate assessment of a source based upon its known characteristics of a source's energy flux and pulsations.

An alternative method is presented here for assessing a specific X-ray source's characteristics that are used to produce high accuracy TOAs. This method uses the computation of the SNR of a source. An added benefit of this analysis is that enhanced implementations could incorporate the efficiency of a detector.

The pulsed signal component from a source is determined by the number of photons that are received through the detector area, A, during the observation time, Δt_{obs}. The source parameter of pulsed fraction, p_f, defines the percentage of the source flux that is pulsed. The *duty cycle*, d, of a pulse is the fraction that the width of the pulse, W, spans the pulse period, P, or

$$d = \frac{W}{P} \tag{3.6}$$

The noise of the pulsed signal is comprised of a fraction of both the background radiation flux and the total observed flux from this source. The background flux and the non-pulsed component of the signal contribute to the noise during the duty cycle of the pulse. The pulsed signal contribution to the noise exists throughout the full pulse period. Using this interpretation of signal noise, the SNR can be determined from the source due to the observed X-ray photon flux, F_X, and the X-ray background radiation flux, B_X. This ratio relates the pulsed component of the signal source photon counts, $N_{S_{pulsed}}$, to the one-sigma error in detecting this signal as [59, 161],

$$\begin{aligned} SNR = \frac{N_{S_{pulsed}}}{\sigma_{noise}} &= \frac{N_{S_{pulsed}}}{\sqrt{\left(N_B + N_{S_{non-pulsed}}\right)_{duty\,cycle} + N_{S_{pulsed}}}} \\ &= \frac{F_X A p_f \Delta t_{obs}}{\sqrt{\left[B_X + F_X\left(1 - p_f\right)\right]\left(A \Delta t_{obs} d\right) + F_X A p_f \Delta t_{obs}}} \end{aligned} \tag{3.7}$$

For a given observation, the TOA accuracy can be determined from the one-sigma value of the pulse and the SNR via,

$$\sigma_{TOA} = \frac{\frac{1}{2} W}{SNR} \tag{3.8}$$

In this equation, the one-sigma value of the pulse has been estimated as one-half the pulse width (or Half-Width Half Maximum, HWHM), which assumes the pulse shape is approximately Gaussian and the full width is equal to two-sigma. The TOA accuracy represents the resolution of the arrival time of a pulse based upon a single observation.

A TOA measurement can be used to determine range of the detector from a chosen reference location along the line-of-sight to the pulsar. The accuracy of the range measurement can be computed using c to represent the speed of light as,

$$\sigma_{RANGE} = c\,\sigma_{TOA} \tag{3.9}$$

3.3.2.1 Required Observation Time For TOA Accuracy

Based upon the SNR calculation of Eq. (3.7), the required observation time to achieve specific range accuracy in Eq. (3.9) can be determined. This process is useful for evaluating candidate sources, by initially selecting sources that can produce high accuracy range measurements in short observation spans. This section presents pulsar sources of both RPSR and XB types along with their catalogued characteristics, and determines their potential for producing good range measurements.

One analysis method is to solve Eq. (3.8) in terms of Δt_{obs} using the relationship for SNR from Eq. (3.7). This produces an expression of,

$$\Delta t_{obs} = \frac{W^2 \left\{ \left[B_X + F_X \left(1 - p_f \right) \right] d + F_X p_f \right\}}{4 \sigma_{TOA}^2 F_X^2 p_f^2 A} \tag{3.10}$$

By selecting a desired TOA accuracy and knowing the parameters for a specific source, Eq. (3.10) can be used to determine the amount of observation time required to attain this accuracy. Alternatively, a set of observation times can be chosen and the accuracy from Eq. (3.8) or (3.9) can be computed based upon these time and source parameters. This second method is presented in further detail below.

Table 3-1 and Table 3-2 provide source parameters for 25 RPSRs from the XNAVSC. These sources were chosen to have high flux output and short rotation periods, and are listed based upon increasing period length. Similarly, Table 3-3 and Table 3-4 provide source parameters for 25 sources in X-ray binary systems, including several APSRs, Atoll, and Z sources, also listed in increasing period. The data for all these sources is reported in the XNAVSC, and its associated reference catalogues and papers. However, since not all parameters for these sources are provided by these references, several of the values of pulsed fraction and pulse width have to be estimated. These estimates are created based upon reported values from corresponding similar types of pulsars. Pulsed fraction was chosen to be 10% if not reported. For sources with pulse periods greater than 0.1 s, the pulse width was set to 0.0182 times the period. For sources with periods less than 0.1 s, the pulse width for RPSRs was set to 5% of period, and the pulse width of XBs was set to 20% of period. These conservative estimated values were chosen based upon similar sources with known data and to avoid labeling a source with unknown characteristics as a highly potential navigation candidate.

For this TOA accuracy analysis, a common X-ray background rate of 0.005 ph/cm^2/s (3×10^{-11} erg/cm^2/s) over 2–10 keV energy range was used for all sources. This representative background rate is a conservative value, and for this analysis is considered fixed throughout the celestial sky. Choosing two detector areas of 1-m^2 and 5-m^2, Eqs. (3.7) and (3.9) were utilized for varying observation times in order to determine a source's achievable range measurement accuracy.

The plots of Figure 3-7 and Figure 3-8 provide range accuracies for the RPSRs with a 1-m^2 and 5-m^2 detector, respectively. These plots show the top ten sources from the data in Table 3-1 and Table 3-2 that produce the best range accuracies. Values of SNR > 2 are shown on the plots for each source. These plots show that several sources achieve range accuracies better than 1 km within 1000 s of observation. These plots show that although increasing the detector area collects additional X-ray background radiation, larger detector areas can improve the range accuracy of each source.

Using the data for XBs from Table 3-3 and Table 3-4, the plots in Figure 3-9 and Figure 3-10 show the achievable range measurement accuracies for SNR > 2 and 1-m^2 and 5-m^2 detector areas, respectively. The ten XB sources from these tables with the best range accuracies are shown in these plots. Within 1000 s of observation, all the ten sources produce better than 1 km accuracies for either size detector.

Comparing RPSR to XB sources from these figures, there are several XBs that could provide good, or higher, range accuracy based upon these table parameters. Although these XB sources introduce additional complexity in their timing models, their potential for producing accurate range measurements cannot be ignored. However, additional investigation of these sources must be pursued to determine the true values of pulsed fraction and pulse width in order to make an improved assessment of all these sources.

The plots of these figures allow unlimited SNR values. However, limits may exist of the maximum SNR attainable for a given source. Thus, Rappaport [161] suggests limiting the SNR to a maximum value of 1000 for all sources. Based upon this limitation, a low-pass filter for SNR of the following can be used for this limit,

$$SNR_{filtered} = \frac{1000 SNR}{1000 + SNR} \tag{3.11}$$

The plots in Figure 3-11 and Figure 3-12 provided the range accuracies based upon this filtered SNR values for RPSRs and XBs, respectively. Both these plots use a 1-m^2 detector area. In Figure 3-11, several RPSRs have reduced achievable range accuracy due to the limitation on SNR, and no further observation time would improve these values. In Figure 3-12, all the XBs have this reduced range accuracy due to SNR limits.

The listings in Table 3-5 and Table 3-6 provide the range accuracies for the top 10 RPSRs and XBs for a 1-m^2 detector. These tables provide data for the unlimited and limited SNR scenarios over a range of 500 s, 1000 s, and 5000 s observation lengths. Navigation methods can use these range accuracy values from the sources in order to weight each measurement from individual sources.

The analysis presented here assumes an area for a theoretical detector with perfect efficiency, no internal losses or noise, and no background rejection. Each source is assumed in this analysis to produce a single, identifiable pulse shape per pulse period, and the pulse period is assumed to be accurate over the observation duration. It assumes that sources have no intrinsic noise, as it is not yet well understood how this noise will directly affect the range accuracy. However, a conservative estimate of X-ray background noise was chosen in part to incorporate the effects of the pulsar signal noise, and other errors that may not be fully modeled in the above equations. For sources with well-modeled signals, their range accuracy may improve if the true X-ray background present near that source is implemented in the SNR and range accuracy equations. Further source investigation must be pursued to verify the specific SNR limitation for each source. Limitations on the SNR may also be included due to a specific detector's viewable area and photon detection and timing efficiency, which may reduce the range accuracy for some sources.

Table 3-1. List of Rotation-Powered Pulsar Position and References.

Name	Galactic Longitude (deg)	Galactic Latitude (deg)	Distance (kpc)	References
PSR B1937+21	57.51	-0.29	3.60	[105, 151, 158]
PSR B1957+20	59.20	-4.70	1.53	[19, 20, 159]
PSR J0218+4232	139.51	-17.53	5.70	[19, 20, 105, 151, 158, 159]
PSR B1821–24	7.80	-5.58	5.50	[19, 105, 151, 158, 159]
PSR J0751+1807	202.73	21.09	2.02	[19, 20, 158, 159]
PSR J0030+0451	113.14	-57.61	0.23	[158]
PSR J2124–3358	10.93	-45.44	0.25	[19, 158, 159]
PSR J1012+5307	160.35	50.86	0.52	[19, 20, 158, 159]
PSR J0437–4715	253.39	-41.96	0.18	[19, 158, 159]
PSR J0537-6910	279.55	-31.76	47.30	[158]
PSR B0531+21	184.56	-5.78	2.00	[19, 158, 159]
PSR B1951+32	68.77	2.82	2.50	[19, 158, 159]
PSR B1259–63	304.18	-0.99	2.00	[19, 159]
PSR B0540–69	279.72	-31.52	47.30	[19, 90, 158, 159]
PSR J1811-1926	11.18	-0.35	7.80	[158]
PSR J0205+6449	130.72	3.08	2.60	[158]
PSR J1420-6048	313.54	0.23	2.00	[158]
PSR J1617-5055	332.50	-0.28	4.50	[158]
PSR B0833–45	263.55	-2.79	0.25	[19, 158, 159]
PSR B1823–13	18.00	-0.69	4.12	[19, 158, 159]
PSR B1706–44	343.10	-2.68	1.82	[19, 158, 159]
PSR J1124-5916	292.04	1.75	4.80	[31, 158]
PSR J1930+1852	54.10	0.27	5.00	[32]
PSR B1509–58	320.32	-1.16	4.30	[19, 158, 159]
PSR J1846-0258	29.71	-0.24	19.00	[131, 158]

Table 3-2. List of Rotation-Powered Pulsar Periodicity and Pulse Attributes.

Name	Period (s)	Flux (2–10 keV) ($ph/cm^2/s$)	Pulsed Fraction (%)	Pulse Width (FWHM) (s)
PSR B1937+21	0.00156	4.99E-05	86.0	0.000021
PSR B1957+20	0.00160	8.31E-05	60.0	0.000080 [a]
PSR J0218+4232	0.00232	6.65E-05	73.0	0.000350
PSR B1821–24	0.00305	1.93E-04	98.0	0.000055
PSR J0751+1807	0.00347	6.63E-06	70.0	0.00017 [a]
PSR J0030+0451	0.00487	1.96E-05	10 [a]	0.00024 [a]
PSR J2124–3358	0.00493	1.28E-05	28.2	0.00025[a]
PSR J1012+5307	0.00525	1.93E-06	75.0	0.00026 [a]
PSR J0437–4715	0.00575	6.65E-05	27.5	0.00029 [a]
PSR J0537-6910	0.01611	7.93E-05	10 [a]	0.00081 [a]
PSR B0531+21	0.03340	1.54E+00	70.0	0.001670
PSR B1951+32	0.03953	3.15E-04	10 [a]	0.0020 [a]
PSR B1259–63	0.04776	5.10E-04	10 [a]	0.0024 [a]
PSR B0540–69	0.05037	5.15E-03	67.0	0.0025 [a]
PSR J1811-1926	0.06467	1.90E-03	10 [a]	0.0032 [a]
PSR J0205+6449	0.06568	2.32E-03	10 [a]	0.0033[a]
PSR J1420-6048	0.06818	7.26E-04	10 [a]	0.0034 [a]
PSR J1617-5055	0.06934	1.37E-03	10 [a]	0.0035 [a]
PSR B0833–45	0.08929	1.59E-03	10.0	0.0045 [a]
PSR B1823–13	0.10145	2.63E-03	10 [a]	0.0018 [a]
PSR B1706–44	0.10245	1.59E-04	10 [a]	0.0019 [a]
PSR J1124-5916	0.13531	1.70E-03	10 [a]	0.0025 [a]
PSR J1930+1852	0.13686	2.16E-04	27.0	0.0025 [a]
PSR B1509–58	0.15023	1.62E-02	64.6	0.0027 [a]
PSR J1846-0258	0.32482	6.03E-03	10 [a]	0.0059 [a]

[a] Estimated value. Refer to text.

Table 3-3. List of X-ray Binary Source Position and References.

Name	Type	Galactic Longitude (deg)	Galactic Latitude (deg)	Distance (kpc)	References
XTE J1751-305	LMXB	359.18	-1.91	8	[64, 121, 125, 134]
SAX J1808.4-3658	LMXB	355.39	-8.15	4	[36, 111, 225, 226]
B1728-337	LMXB	354.30	-0.15	—	[111, 222]
B1758-250	LMXB	5.08	-1.02	—	[111, 222]
B0614+091	LMXB	200.88	-3.36	—	[111, 222]
XTE J1814-338	LMXB	358.75	-7.59	8	[104, 122, 200]
B1617-155	LMXB	359.09	23.78	—	[111, 222]
B1813-140	LMXB	16.43	1.28	—	[111, 222]
B1636-536	LMXB	332.92	-4.82	—	[111, 222]
B1820-303	LMXB	2.79	-7.91	—	[111, 222]
B1908+005	LMXB	35.72	-4.14	—	[111, 222]
B1731-260	LMXB	1.07	3.66	—	[111, 222]
XTE J1807-294	LMXB	1.94	-4.27	8	[33, 101, 123, 124]
XTE J0929-314	LMXB	260.10	14.21	6	[64, 169]
PSR B1744-24A	LMXB	3.84	1.70	—	[152]
PSR J0635+0533	HMXB	206.15	-1.04	—	[110]
1E 1024.0-5732	HMXB	284.52	-0.24	—	[110]
AO 0538-66	HMXB	276.86	-31.87	50	[141]
GRO J1744-28	LMXB	0.04	0.30	—	[111]
B0115-737	HMXB	300.41	-43.56	—	[110]
B1656+354	LMXB	58.15	37.52	—	[111]
GRO J1750-27	HMXB	2.37	0.51	—	[110]
B1119-603	HMXB	292.09	0.34	8.5	[110]
PSR B1627-673	LMXB	321.79	-13.09	—	[64, 111]
GRO J1948+32	HMXB	67.48	3.28	—	[110]

Table 3-4. List of X-ray Binary Source Periodicity and Pulse Attributes.

Name	Period (s)	Flux (2–10 keV) ($ph/cm^2/s$)	Pulsed Fraction (%)	Pulse Width (FWHM) (s)
XTE J1751-305	0.00230	1.81E-01	5.50	0.00046 [a]
SAX J1808.4-3658	0.00249	3.29E-01	4.10	0.00050 [a]
B1728-337	0.00276	4.49E-01	10 [a]	0.00055 [a]
B1758-250	0.00303	3.74E+00	10 [a]	0.00061 [a]
B0614+091	0.00305	1.50E-01	10 [a]	0.00061 [a]
XTE J1814-338	0.00318	3.88E-02	12.00	0.00064 [a]
B1617-155	0.00323	4.19E+01	10 [a]	0.00065 [a]
B1813-140	0.00327	2.10E+00	10 [a]	0.00065 [a]
B1636-536	0.00345	6.58E-01	10 [a]	0.00069 [a]
B1820-303	0.00363	7.48E-01	10 [a]	0.00073 [a]
B1908+005	0.00364	2.99E-04	10 [a]	0.00073 [a]
B1731-260	0.00380	2.99E-02	10 [a]	0.00076 [a]
XTE J1807-294	0.00525	1.18E-01	7.50	0.0015
XTE J0929-314	0.00540	1.05E-02	5.00	0.0011 [a]
PSR B1744-24A	0.01156	1.09E-03	10 [a]	0.0023 [a]
PSR J0635+0533	0.03380	1.65E-03	10 [a]	0.0068 [a]
1E 1024.0-5732	0.06100	1.65E-03	10 [a]	0.012 [a]
AO 0538-66	0.06921	4.27E-01	10 [a]	0.014 [a]
GRO J1744-28	0.46700	3.80E+01	10 [a]	0.0085 [a]
B0115-737	0.71600	1.50E-03	10 [a]	0.013 [a]
B1656+354	1.24000	4.49E-02	10 [a]	0.023 [a]
GRO J1750-27	4.45000	8.08E-02	10 [a]	0.081 [a]
B1119-603	4.81793	2.99E-02	10 [a]	0.088 [a]
PSR B1627-673	7.70000	7.48E-02	10 [a]	0.14 [a]
GRO J1948+32	18.70000	7.31E-01	10 [a]	0.34 [a]

[a] Estimated value. Refer to text.

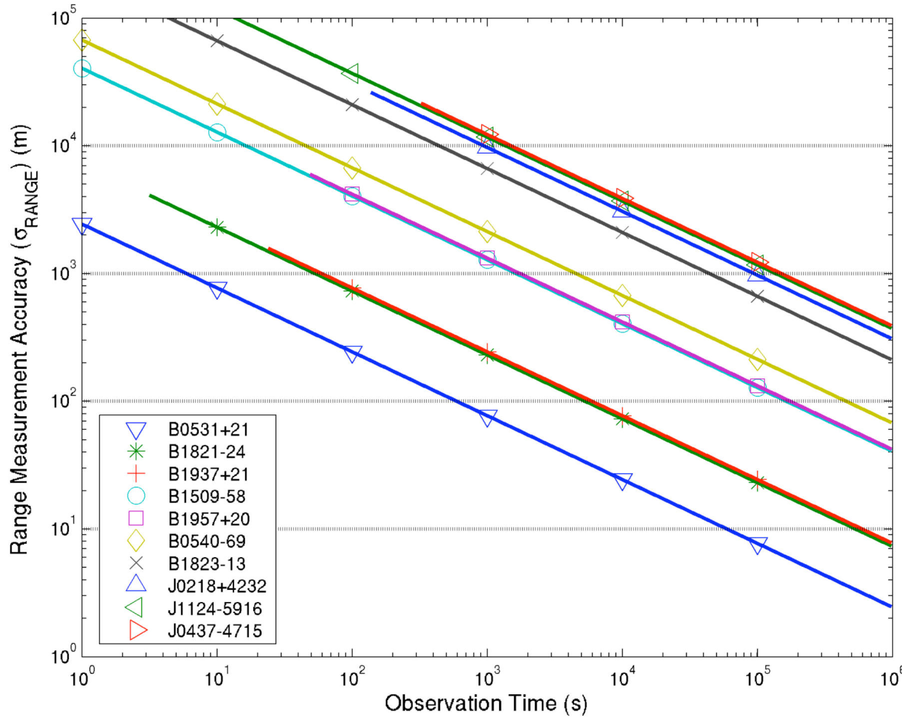

Figure 3-7. Range measurement accuracies using RPSRs versus observation time [Area = 1 m^2, X-ray background = 0.005 ph/cm^2/s (2–10 keV)].

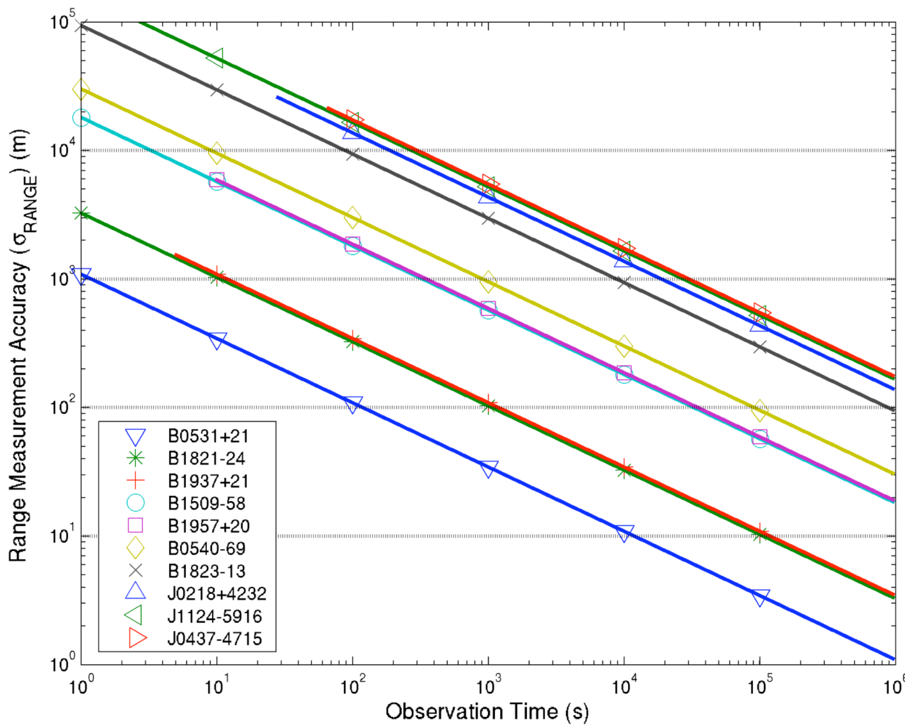

Figure 3-8. Range measurement accuracies using RPSRs versus observation time [Area = 5 m^2, X-ray background = 0.005 ph/cm^2/s (2–10 keV)].

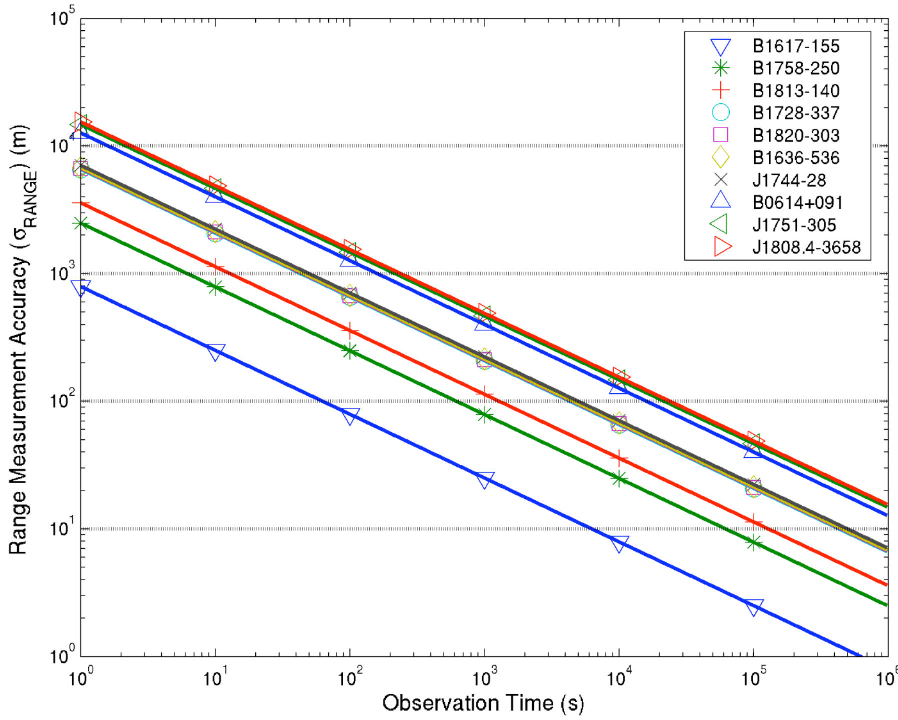

Figure 3-9. Range measurement accuracies using XBs versus observation time [Area = 1 m^2, X-ray background = 0.005 ph/cm^2/s (2–10 keV)].

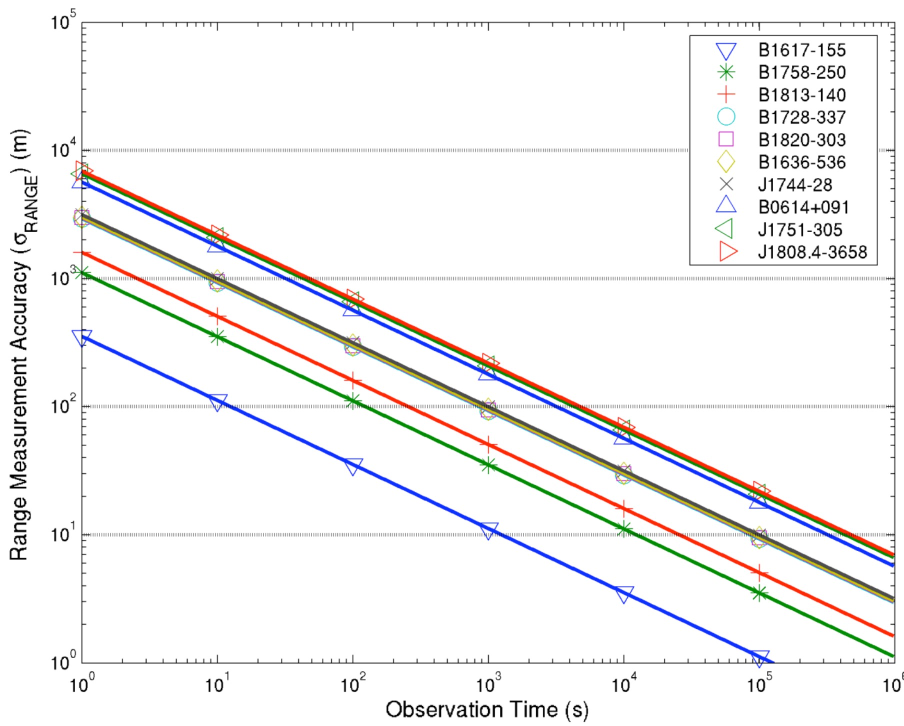

Figure 3-10. Range measurement accuracies using XBs versus observation time [Area = 5 m^2, X-ray background = 0.005 ph/cm^2/s (2–10 keV)].

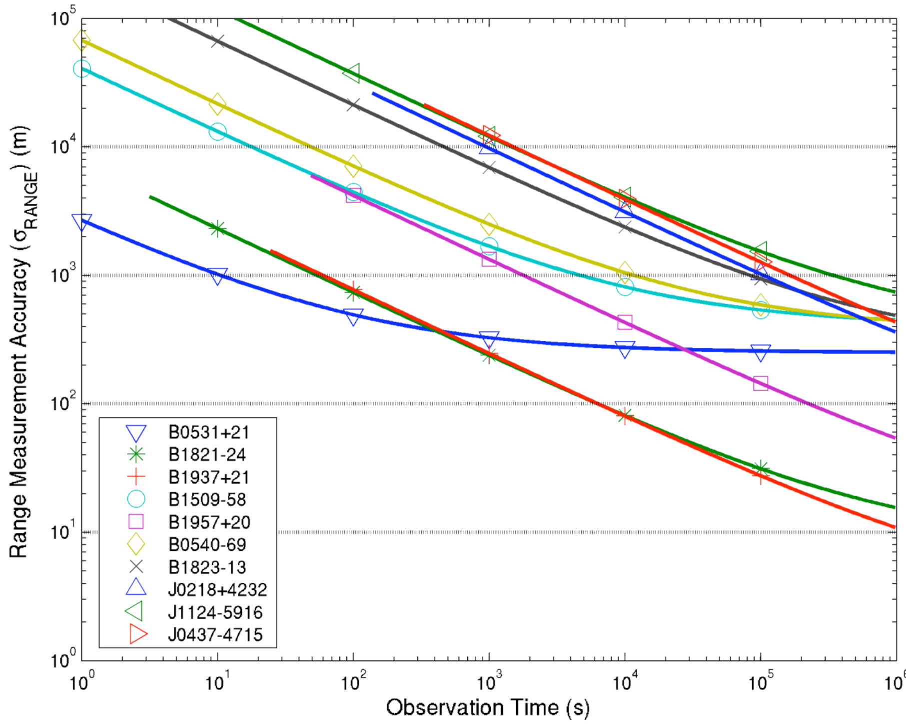

Figure 3-11. Range measurement accuracies using RPSRs, with SNR limited to 1000 [Area = 1 m^2, X-ray background = 0.005 ph/cm^2/s (2–10 keV)].

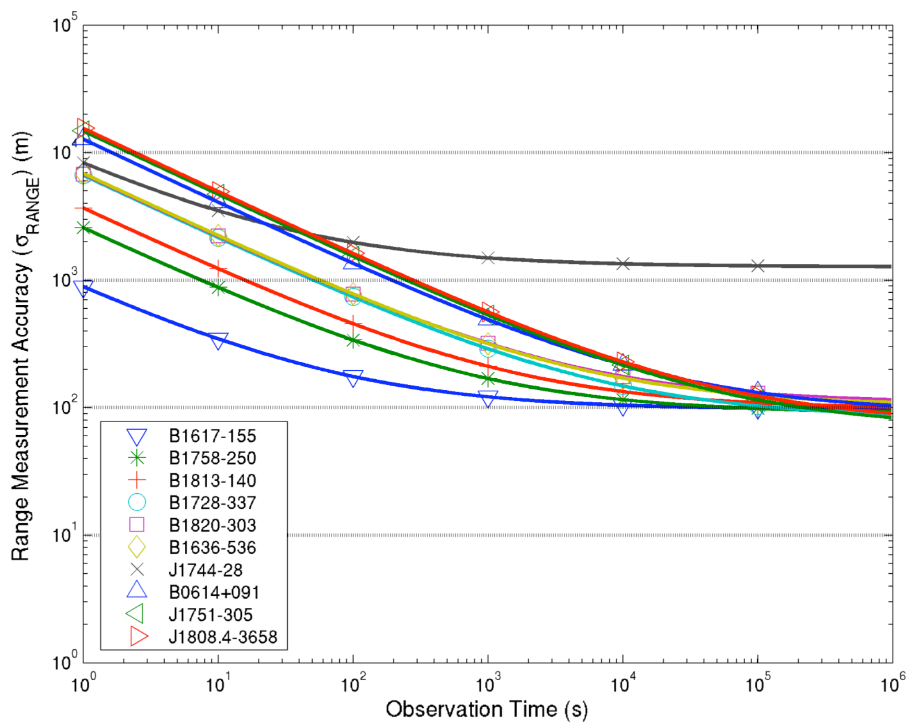

Figure 3-12. Range measurement accuracies using XBs, with SNR limited to 1000 [Area = 1 m^2, X-ray background = 0.005 ph/cm^2/s (2–10 keV)].

Table 3-5. RPSR Range Measurement Accuracy Values (1-m² Detector).

Name	σ_{RANGE} Range Measurement Accuracy (m) No SNR Limit			σ_{RANGE} Range Measurement Accuracy (m) SNR Limit of 1000		
	500 s	**1000 s**	**5000 s**	**500 s**	**1000 s**	**5000 s**
PSR B0531+21	109	77.9	34.8	359	328	285
PSR B1821–24	325	233	104	334	241	112
PSR B1937+21	344	247	110	347	250	113
PSR B1509–58	1807	1294	578	2217	1704	988
PSR B1957+20	1866	1336	597	1877	1348	609
PSR B0540–69	3007	2153	962	3384	2531	1339
PSR B1823–13	9367	6708	2996	9644	6985	3273
PSR J0218+4232	13701	9812	4383	13754	9865	4435
PSR J1124-5916	16485	11805	5273	16854	12174	5642
PSR J0437–4715	17293	12384	5532	17336	12427	5575

Table 3-6. XB Range Measurement Accuracy Values (1-m² Detector).

Name	σ_{RANGE} Range Measurement Accuracy (m) No SNR Limit			σ_{RANGE} Range Measurement Accuracy (m) SNR Limit of 1000		
	500 s	**1000 s**	**5000 s**	**500 s**	**1000 s**	**5000 s**
B1617-155	35.4	25.3	11.3	132	122	108
B1758-250	111	79.5	35.5	202	170	126
B1813-140	160	115	51.2	258	213	149
B1728-337	293	210	93.7	376	293	177
B1820-303	298	214	95.4	407	322	204
B1636-536	302	216	96.7	406	320	200
GRO J1744-28	315	226	101	1589	1500	1375
B0614+091	565	404	181	656	496	272
XTE J1751-305	657	470	210	726	539	279
SAX J1808.4-3658	690	494	221	764	569	295

3.3.3 X-ray Source Figure of Merit

Based upon the SNR calculation in Eq. (3.7) and the TOA accuracy of Eq. (3.8), an algorithmic representation to assess each source can be created. This figure of merit (FOM) for each source can be computed to assist identifying X-ray sources with potential to provide good timing and range accuracy.

The FOM can be computed by squaring the TOA accuracy Eq. (3.8) to produce,

$$\left(\sigma_{TOA}\right)^2 = \frac{\frac{1}{4}W^2}{SNR^2} = \frac{W^2 B_X d}{4\left(F_X p_f\right)^2 A\Delta t_{obs}} + \frac{W^2 F_X\left[\left(1-p_f\right)d + p_f\right]}{4\left(F_X p_f\right)^2 A\Delta t_{obs}} \tag{3.12}$$

By assuming that the X-ray background rate, a given detector area, and fixed observation time are nearly constant for this calculation, these common terms can be ignored in developing a general FOM expression for all sources. Using Eq. (3.12) and only the terms that a unique to each source, this FOM, Q_X, can be represented as,

$$Q_X = \frac{F_X p_f^2}{W^2\left[p_f + \frac{W}{P}\left(1-p_f\right)\right]} \tag{3.13}$$

Using this X-ray variable celestial source FOM provides a means to evaluate and rank sources that provide high accuracy timing and range. Although this FOM is not dimensionless, it can be normalized with respect to the value of a reference candidate. Normalizing by the $Q_{X_{Crab}}$ value for the Crab Pulsar (PSR B0531+21),

Table 3-7 and Table 3-8 provide the rank of the sources of the ten best RPSR and XB sources from the previous section. The sources in these tables are listed in increasing pulse period. Though it lacks the full representation of signal noise from the SNR equation, the listed ranking based upon the FOM calculations compares well with the ranking based upon the plots of the full range accuracy equation. Although there are a few RPSRs that have slightly different rankings from each method, the XBs match perfectly. Thus, the FOM computation of Eq. (3.13) provides an efficient, quick calculation for evaluating sources.

Highly ranked sources have large flux, large pulsed fraction, short duty cycles, and narrow pulse widths, which can produce accurate timing and range estimates in Eq. (3.9). The FOM of Eq. (3.13) does not include X-ray background flux. If background flux needs to be included in the source evaluation, then a FOM based upon Eq. (3.12) must be investigated.

A simpler form of this metric could be used for even quicker source evaluations. The simple form of this figure of merit ignores the pulsed fraction component of the signal and is evaluated as,

$$Q_X = \frac{F_X p_f^2}{W^2} \tag{3.14}$$

However, this simpler form has less accuracy of predicting source quality than the FOM in Eq. (3.13). Although the FOM of Eq. (3.13) is recommended, using either of these forms of the X-ray source quality FOM provides a means to evaluate and list hierarchically the catalogued sources. Then those sources that are expected to provide high accuracy timing and position can be chosen for further investigation.

Table 3-7. RPSR FOM Rankings (1-m^2 Detector).

Name	$Q_X/Q_{X_{Crab}}$ FOM Ratio	Q_x - Based Ranking	Plot-Based Ranking
PSR B1937+21	0.26	2	3
PSR B1957+20	0.020	4	5
PSR J0218+4232	0.00099	7	8
PSR B1821–24	0.17	3	2
PSR J0437–4715	0.00052	8	10
PSR B0531+21	1.00	1	1
PSR B0540–69	0.0014	6	6
PSR B1823–13	0.00018	9	7
PSR J1124-5916	0.00006	10	9
PSR B1509–58	0.0037	5	4

Table 3-8. XB FOM Rankings (1-m^2 Detector).

Name	$Q_X/Q_{X_{Crab}}$ FOM Ratio	Q_x - Based Ranking	Plot-Based Ranking
XTE J1751-305	0.028	9	9
SAX J1808.4-3658	0.025	10	10
B1728-337	0.14	4	4
B1758-250	0.96	2	2
B0614+091	0.038	8	8
B1617-155	9.50	1	1
B1813-140	0.46	3	3
B1636-536	0.13	6	6
B1820-303	0.13	5	5
GRO J1744-28	0.12	7	7

3.3.4 Source Selection Criteria

An important property of candidate sources is their ability to provide an accurate TOA within acceptable observation duration. From the current X-ray catalog, it is possible to determine which are viable candidates for use in a navigation system. Not all sources can be used however, due to their individual characteristics or due to lack of sufficient parameter information. There are 759 sources in the current catalog, which includes 459 sources within binary systems and 8 with known glitches.

From the TOA accuracy models from either the Taylor Fourier transform method or the source FOM based upon observation SNR, sources with certain characteristics provide improved ability for time and position determination within a navigation scheme. Perhaps the two most important criteria of a source are its well-determined position location and its high X-ray flux output. Additionally, sources with fast pulse periods and with pulse shapes that feature sharp, narrow peaks provide additional benefits during a given observation. Sources that are stable over long durations such that pulse-timing models predict accurately the arrival of pulses within the solar system are also attractive. For these types of navigation solutions, it is necessary to seek out sources that match these criteria.

Of the sources listed in the current catalog, for accurate and efficient time and position determination, sources could be deselected based upon the following criteria:

- Choose only those sources with defined pulse timing models.
- Choose only those sources with period less than 10000 seconds.
- Choose all those with detected flux over specified energy range.
- Remove all bursters (49 bursters)

The above selection process results in 247 remaining sources. Of these remaining, there are 129 sources with measured flux above 0.001 ph/cm^2/s (2–10 keV), and 57 sources with measured flux above 0.01 ph/cm^2/s (2–10 keV).

Removing all the 175 sources with known transient signals from the catalogue further reduces the number of available candidates. There are 27 sources that remain with measured flux above 0.01 ph/cm^2/s (2–10 keV) after removing the sources with transient characteristics. Many of the accreting pulsars in Table 3-3 and Table 3-4 are known transient sources. If the potential benefits of all these sources were ignored however, the ability to pursue spacecraft navigation using variable celestial sources would diminish.

Signals from transient sources could be utilized when the source is producing sufficient X-ray flux to be detected. Time spans when these sources produce high flux can last for days to months, thus a navigation system that can provide fast updates to the source almanac data may allow the limited use of these sources. In order to make use of all sources, continual monitoring and database updates must be maintained for this navigation system.

Some of the sources from the current catalog lack available parameter information. As investigation into these sources continues, the parameters can be included in the database and the sources reconsidered as potential navigation candidates.

3.4 Arrival Time Comparison

Sources that emit pulsed radiation in multiple wavelengths do not necessarily produce the exact same signal in each band, as discussed in Chapter 2. During this research, a study was pursued using observed data to determine whether the measured pulse TOAs agree across the radio, visible, and X-ray bands for the Crab Pulsar [164, 165, 187]. This section presents results from this study, as well as a discussion about potential consequences of these results. The methods used to compute the measured TOAs follow the Fourier transform method of Section 3.3.

There are four sets of observation station data used in this study. These are the following:

- Radio: Jodrell Bank Observatory, Jodrell Bank Pulsar Group (Crab Pulsar Monthly Ephemeris data and Reference Notes) (610 MHz and 1396 MHz observations) [115].

- Visible: Palomar Observatory, optical telescope [30].
- X-ray: *RXTE* Satellite, Guest Observer Facility, NASA Goddard Space Flight Center (GFSC) [144].
- X-ray: USA Experiment by NRL aboard the *ARGOS* vehicle.

The radio data supplied by Mark Roberts of the Jodrell Bank Observatory provided the pulse-timing model, as well as the radio telescope observations for the months of November and December 1999 and January 2000. A few observations were provided by Dae Sik Moon using the optical telescope at Palomar Observatory during this same time span. Also during these months, the USA experiment and the RXTE spacecraft completed observations.

Using the data furnished by each observation station, the measured pulse arrival times were fitted to a model using the Princeton TEMPO pulsar timing package [206, 207]. This software program provides a means to compare all the measured TOAs in each observation wavelength to one another. TEMPO reads a file of arrival times, transfers the observed arrival times to the SSB inertial frame if needed, and completes a least squares fit to a pulse timing model [8]. The output of this package is *timing residuals*, or differences between the measured and predicted pulse TOAs.

A plot of the TOA residuals for these four data sets during the three months is provided in Figure 3-13. The green asterisks are the fiducial arrival times published in the Jodrell Bank Monthly Ephemeris for November, December and January [115]. The red crosses and cyan triangles represent the Jodrell Bank radio TOAs at 610 MHz and 1396 MHz respectively. The radio data represent the baseline for comparison to the other wavelengths. The pulse timing model based upon the Jodrell Bank Observatory monthly pulsar ephemeris was chosen to fit all of the provided radio observations [115]. The model used in this plot is $f =$ 29.84670409339285200 Hz, $\dot{f} =$ = -3.746098445932E-10 Hz/s, and $\ddot{f} =$ = 1.019126284E-20 Hz/s^2, with epoch of 51527.0 MJD. The dispersion measure of the interstellar medium used in the radio observations is 56.767 pc/cm^3.

With more data available during the selected time span, the USA X-ray data appears to follow the general shape and trends of the radio data. However, it can be seen from Figure 3-13 that both the *RXTE* and the USA data are offset from the radio data. More significantly, however, the *RXTE* and USA data sets are not offset by the same amount. Computing these offsets using the JUMP option within the TEMPO program, Figure 3-14 provides an overlay plot of the *RXTE*, USA, optical data, and radio data. From this plot, it can be seen that all different measurement types follow the same general trend over the time span.

Table 3-9 lists the computed offsets and the estimated error for the observed data compared to the radio data. Since the *RXTE* leads the radio data by 533 μs while the USA data lags the radio data by 108 μs, no definitive conclusion can be reached about X-ray versus radio signal transmission of the Crab Pulsar. Since these observations were made with overlapping X-ray energy bands and contemporaneously, some kind of calibration or analysis error must be responsible for the difference. The single optical observation also leads the radio data, by 253 μs. With only one observation point however, it is difficult to draw any conclusions from this data set at this point.

Table 3-9. Offset of X-ray and Optical Data from Radio Data for Crab Pulsar.

Measurement Station	Offset from Jodrell Bank Radio Data (μs)	Computed Error in Offset (μs)
RXTE	+533	±28
USA	-108	±23
Palomar	+253	±125

3.4.1 TOA Comparison Discussion

Although no immediate conclusions can be drawn about the TOA differences between the radio and X-ray observations, some remarks can be discussed, especially about the potential differences in the two X-ray measurement sets from USA and RXTE. These are discussed in further detail below and must be further considered for future navigation system implementations.

3.4.1.1 Absolute Time Stamp Errors

An absolute systematic timing error could exist within either spacecraft's system. An undiscovered, constant time stamp error in photon event timing could be present. These errors are naturally much more difficult to discover since the relative timing for each instrument will be accurate.

It has been assumed that the absolute time of the photon events from each station has been calibrated to the same absolute reference. However, if references or calibrations to the same absolute time reference are incorrect, this may explain some of the computed offset between stations. The Jodrell Bank Observatory, the NRL USA experiment, and Palomar Observatory all claim to accurately calibrate their system clock using GPS as their absolute time reference. The GPS system has a civilian timing accuracy of about 40 ns [49].

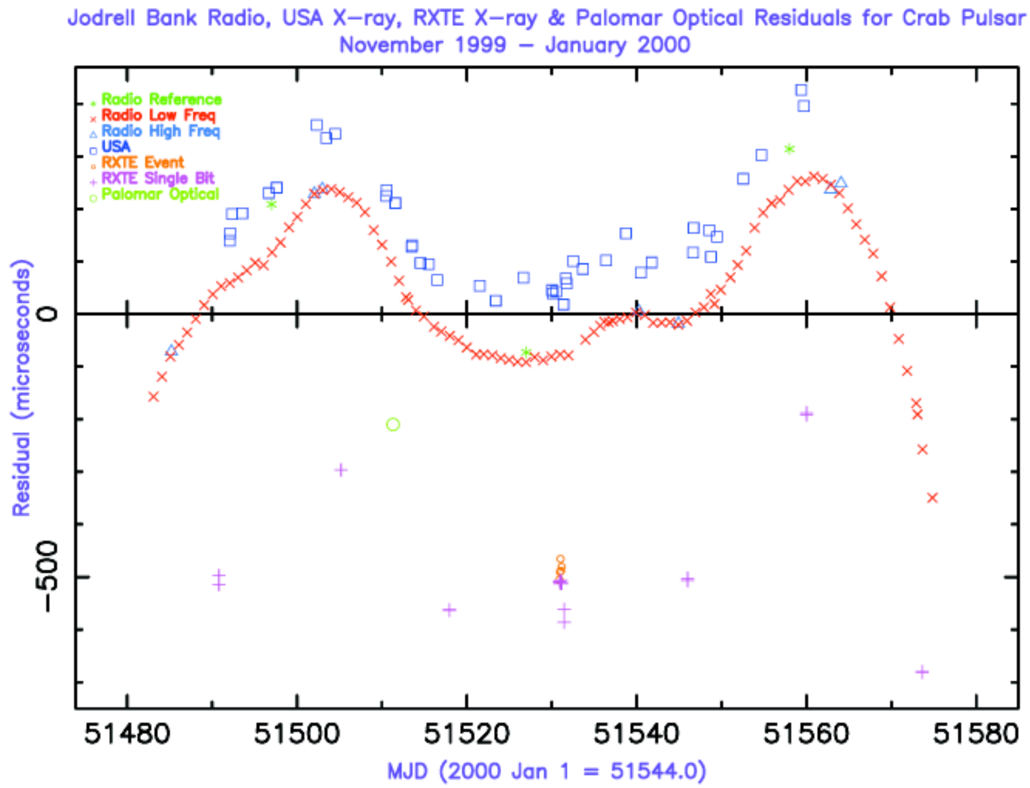

Figure 3-13. Radio, X-ray, and optical Crab Pulsar TOA residual comparisons.

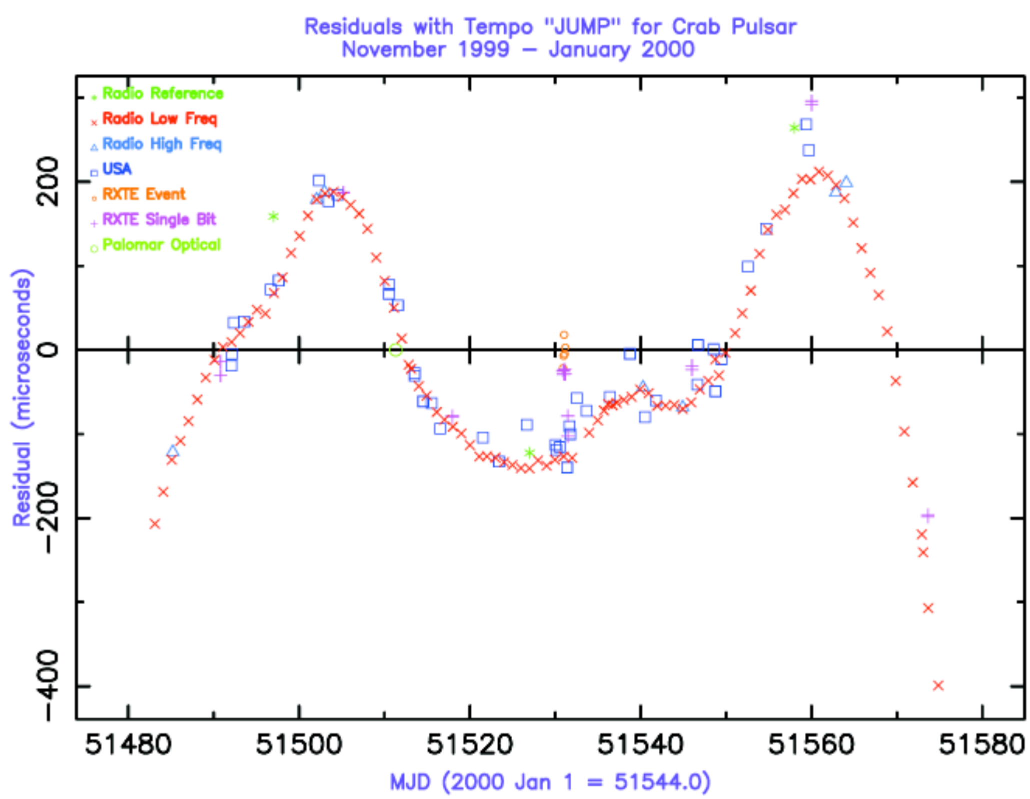

Figure 3-14. Comparison plot with offsets in TOA residuals removed.

The *RXTE* satellite uses its Missions Operation Center to calibrate its clock, and additionally verifies the clock via cosmic sources. The quoted accuracy of this timing is 5 or 8 μs [144]. Since, the *ARGOS* mission was known to have navigational errors as discussed in Chapter 7, potential timing errors may be present also if its GPS receiver produced inaccurate absolute time and passed these on to the USA experiment.

3.4.1.2 Spacecraft Position Errors

The Earth-fixed observatories, Jodrell Bank and Palomar, use their known coordinates relative to Earth center and solar system data from the JPL DE200 ephemeris to complete the time transfer task for accurate pulse timing. The Earth-orbiting observatories, the USA and *RXTE* experiments, must provide an accurate orbit position solution to complete the time transfer task. Position errors within the navigation solution of each of these spacecraft would produce inaccurate pulse TOA calculations. However, position error on the order of 100 km is necessary to produce a timing error of 33 μs. It is unlikely this magnitude of position error would not be discovered during each spacecraft's mission, unless position errors were significant in the along-track direction of the orbit. The navigation errors discussed in Chapter 7 for the *ARGOS* could contribute to some of the USA experiment timing offset.

3.4.1.3 Software Processing Errors

Although all attempts were made to minimize the number of different software analysis packages used in this data processing, it is possible that the few separate packages could handle the *RXTE* and USA X-ray data differently and introduce a time offset. Future studies could make similar comparisons with other pulsars that have been observed nearly simultaneously by both experiments. Computed time offsets with these new data may identify issues with the analysis programs.

3.4.1.4 Pulsar Position and Model Errors

Pulsar position and pulse timing models may be in error by some amount. The quoted position by the Jodrell Bank Observatory was used for all data processing. Any error in this position would be consistent throughout all measurement station data processing. A standard pulse model was also used for each measurement set processing. It is evident in Figure 3-14 that there is variation in the time residuals of all sets of data. Removing some of this variation by using higher order model parameters, however, does not affect the offset between each measurement station. Higher order terms only act to *flatten* the residual plot of each respective set, but does not adjust the offset. This variation is probably due to the Crab Pulsar's rotational instabilities during the observing time span and is consistent within each measurement station set.

3.4.1.5 Energy Range Differences

The two X-ray experiments used slightly different energy ranges for their observations. If the pulse profile had significant energy dependence, this may account for some of the time offset. The USA experiment observed the source within the 1–15 keV band, while the RXTE single-bit data observed within the 2–15 keV band. However, RXTE data at the higher band of 15–60 keV shows little change in the TOA offset for this experiment, which may indicate no energy dependence on the signal exists for the Crab Pulsar.

3.4.1.6 Dispersion Measurement Errors

The radio wavelength emissions from variable celestial sources is delayed by the ionized gas of the interstellar medium [114, 118]. A *dispersion measure*, DM, of this delay can be estimated, or computed, using multiple radio wavelength observations. Error in this computed value could account for some of the offset error between the radio and X-ray observations. However, the DM of the Crab Pulsar varies by about 0.01 pc/cm^3 per month [164, 165]. An error of this magnitude would cause an offset of 110 μs in the 610 MHz data. However, the multi-wavelength observations by Jodrell Bank Observatory in Figure 3-13 do not have this significant offset between the two radio observations. Thus, DM does not fully explain the radio and X-ray observation offsets.

Chapter 4 Time Transformation and Time of Arrival Analysis

"The only reason for time is so that everything doesn't happen at once."

– Albert Einstein

Timing the arrival of photons from the celestial sources is the fundamental measurable component within a variable celestial source-based navigation system. Accuracy of this timing is critical for a high performance navigation system. An onboard pulsar-based navigation system would be comprised of a detector and instrumentation to detect arriving photons, a high performance clock or oscillator (such as an atomic clock), and a computer to facilitate the data collection and recording. Once recorded, the arrival time of these photons must be transformed to an appropriate time frame so that pulse profiles may be established. The comparison of pulse arrival times to existing pulse timing models requires the transfer of time to the location where the model is defined.

The first order analysis presented in the previous Chapters represents an estimate of TOA accuracies that produce spacecraft position estimates. This Chapter presents detailed time conversion and transfer techniques to insure high accuracy TOA measurements. These time transfer methods include relativistic corrections in order to produce timing resolution of pulse photons on the order of a few nanoseconds.

4.1 *Inertial Coordinate Reference Systems*

In order to compute accurate arrival times of pulses, measurements must be made relative to an inertial frame – a frame unaccelerated with respect to the pulsars [15, 79, 113, 137, 138, 201, 202, 209]. This frame represents the three-dimensional inertial position coordinates as well as the fourth dimension of coordinate time. Most observations of variable celestial sources have been made on Earth for radio wavelength sources, or on a spacecraft moving about Earth for X-ray wavelength sources. The data collected while in these moving frames must be first transformed into an inertial frame and subsequently transferred to where the pulse model is defined.

Options exist for inertial coordinate frames that can be used for accurate pulse timing, and several are presented below. Appendix A also provides lists of time scales and standards that may be used for pulse timing.

4.1.1 Parameterized Post-Newtonian Frame

The parameterized post-Newtonian (PPN) coordinate system is one framework for reference time and inertial position [135, 153, 170-173, 228]. This system is useful for general relativistic analysis, and can be used as a tool in studying pulse arrival times. The Post-Newtonian time (PNT) can be used as the time coordinate within this system.

4.1.2 Solar System Barycenter Frame

The solar system barycenter (SSB) frame is a more suitable coordinate system for spacecraft navigation than the PPN. This is a common inertial reference system chosen for many pulsar observations and simplifies some of the general relativistic equations used for high accuracy time transfer.

The SSB frame is referred to as the International Celestial Reference Frame (ICRF) and its axes are aligned with the equator and equinox of epoch J2000 [183]. The origin of this ICRF frame is the position of the center of mass for the whole solar system, or barycenter. The Sun and Jupiter are the primary contributors to this location, with all other planets, moon, and asteroids contributing only secondary effects. Due to the large mass of the Sun, the barycenter position is very near the surface of the Sun. The center of the Sun rotates around this barycenter position with a period equal to the ~12 yr orbit period of Jupiter.

For operations and measurement of pulsar timing within the solar system, the effects of Earth's motion on detectors must also be removed to produce accurate models. Two time scales exist which support solar system timing, and each have their origin at the SSB. These are the *Temps Coordonnée Barycentrique* (TCB, Barycentric Coordinate Time) and the *Temps Dynamique Barycentrique* (TDB, Barycentric Dynamical Time) [23, 183]. Many current pulsar observations are computed using the TDB time scale. Recent improvements in time-ephemeris models may prove that the TCB scale produces increased pulsar model accuracy [87].

4.1.3 Terrestrial Time Standards

Earth-based telescopes can reference their observations to specific epochs by initially using terrestrial time standards, such as *Temps Atomique International* (TAI, International Atomic Time) or Coordinated Universal Time (UTC). These times are then often converted to Earth-based coordinate time of either Terrestrial Time (TT) [once referred to as Terrestrial Dynamical Time], or *Temps Coordonnée Géocentrique* (TCG, Geocentric Coordinate Time). TCG is the coordinate time scale with respect to Earth's center, and TCG differs from TT by a scaling factor [183]. Standard corrections can then be applied to convert recorded terrestrial time to TCB or TDB [57, 63, 87, 183, 199].

For spacecraft in operation near-Earth or within the solar system, additional corrections must be applied to transform the spacecraft's clock time to these inertial reference times. These correction methods are discussed in the following sections.

4.2 Proper Time to Coordinate Time

To produce an accurate navigation system, the effects on time measured by a clock in motion and within a gravitational potential field must be considered. The general relativistic theory of gravity provides a method for precisely comparing the time measured by a spacecraft's clock to a barycentric standard time reference, such as TCB or TDB.

Reference standard time, referred to as *coordinate time*, is the time measured by a standard clock at rest (fixed or not moving) in the inertial frame and not under the influence of gravity (located at *infinite distance*) [148, 156]. The spacecraft clock, although often very precise, does not truly measure perfect coordinate time. Corrections must be applied to account for the vehicle's motion, as well as different gravitational perturbations, so that the clock's measured time can be compared to other known time standards. A spacecraft's clock, while in motion and at a different gravitational potential than the standard reference clock, measures *proper time*, or the time a clock measures its detected events as it travels along a four-dimensional spacetime path [156, 220].

The following sections provide methods to transform spacecraft proper time to coordinate time, for both near-Earth and interplanetary mission applications.

4.2.1 Spacetime Interval

The four dimensions of the spacetime coordinate frame can be generalized to

$$\left\{x^0, x^1, x^2, x^3\right\} = \{ct, x, y, z\} \tag{4.1}$$

In this representation, the superscripts on the generalized coordinates, x, are indices, not exponents. The coordinate ct represents the dimension related to time, and $\{x, y, z\}$ represent the spatial coordinates.

The path taken by a light ray or particle in four-dimensional spacetime is referred to as a *world line*. A *geodesic path* is the path between two points a light ray or particle takes while in free fall within a gravitational field. For a particle, the geodesic path is typically the shortest path between the two points. For a light ray, these paths have zero spacetime length and are referred to as *null geodesics*. Generally within a gravitational field these geodesics have some curvature in space [148, 149, 156]. In the theory of general relativity, this notion of a *spacetime interval* in curved space is invariant with respect to arbitrary transformations of coordinates. This spacetime interval can be defined as [148, 149, 156, 220],

$$ds = \sqrt{\sum_{\alpha=0}^{3} \sum_{\beta=0}^{3} g_{\alpha\beta} dx^{\alpha} dx^{\beta}} \tag{4.2}$$

In this definition, the metric $g_{\alpha\beta} = g_{\alpha\beta}(ct, x, y, z)$ is a function of the time and spatial coordinates, and the elements of $g_{\alpha\beta}$ form a symmetric, covariant tensor that defines the geometry of spacetime. The dx^i terms are the differentials of the spacetime coordinates and define the path of an object through spacetime. In this representation, the Greek indices α and β range from 0 to 3 and the Latin indices of i and j range from 1 to 3 [148, 149, 220]. Eq. (4.2) can be expanded using these definitions as,

$$ds^2 = \sum_{\alpha=0}^{3}\sum_{\beta=0}^{3} g_{\alpha\beta} dx^{\alpha} dx^{\beta} = g_{00}c^2 dt^2 + 2\sum_{j=1}^{3} g_{0j} cdtdx^j + \sum_{i=1}^{3}\sum_{j=1}^{3} g_{ij} dx^i dx^j \tag{4.3}$$

For Minkowski's flat space of special relativity (absence of gravity), the symmetric tensor is simply the four terms of $g_{00} = -1,\ g_{11} = g_{22} = g_{33} = 1$, with all other terms equal to zero [148]. Since the spacetime interval is invariant with respect to arbitrary coordinate transformations its value remains constant for these transformations. Thus, the proper time measured by a clock, τ, as it moves along a world line, is related to the invariant spacetime interval and the coordinate time in special relativity via,

$$ds^2 = -c^2 d\tau^2 = -c^2 dt^2 + dx^2 + dy^2 + dz^2 \tag{4.4}$$

From the theory of general relativity the relationship for the spacetime interval with clock proper time and coordinate time is general with respect to the geometry of spacetime from Eq. (4.3) as,

$$ds^2 = -c^2 d\tau^2 = -g_{00}c^2 dt^2 + 2\sum_{j=1}^{3} g_{0j} cdtdx^j + \sum_{i=1}^{3}\sum_{j=1}^{3} g_{ij} dx^i dx^j \tag{4.5}$$

In a weak-gravitational field and nearly flat space, which is appropriate for the solar system, a Post-Newtonian metric tensor is suitable and can be expressed to linear order of the total gravitational potential within the system. Therefore, the spacetime interval relationship of Eq. (4.3) has been shown of the order $O(1/c^2)$ to be [148, 149],

$$ds^2 = -c^2 d\tau^2 = -\left(1 - \frac{2U}{c^2}\right)c^2 dt^2 + \left(1 + \frac{2U}{c^2}\right)\left(dx^2 + dy^2 + dz^2\right) \tag{4.6}$$

The total gravitational potential, U, acting on the spacecraft clock is the sum of the gravitational potentials of all the bodies in the solar system, and is defined in the positive sense $\left(U = GM/r + \text{higher order terms}\right)$.

The total speed, v, of the spacecraft's local frame through the solar system can be written as,

$$v^2 = \left(\frac{dx}{dt}\right)^2 + \left(\frac{dy}{dt}\right)^2 + \left(\frac{dz}{dt}\right)^2 \tag{4.7}$$

Using this expression for speed, the spacetime interval of Eq. (4.6) can be divided by dt^2 to yield,

$$\left(\frac{ds}{dt}\right)^2 = -c^2\left(\frac{d\tau}{dt}\right)^2 = -\left(1 - \frac{2U}{c^2}\right)c^2 + \left(1 + \frac{2U}{c^2}\right)v^2 \tag{4.8}$$

Taking the square root of the terms in Eq. (4.8) the relationship between proper time of the spacecraft's clock and coordinate time can be established. Through a binomial series expansion for the square root terms and retaining only terms of $O(1/c^2)$ yields the two expressions,

$$d\tau = \left[1 - \frac{U}{c^2} - \frac{1}{2}\left(\frac{v}{c}\right)^2\right]dt \tag{4.9}$$

$$dt = \left[1 + \frac{U}{c^2} + \frac{1}{2}\left(\frac{v}{c}\right)^2\right]d\tau \tag{4.10}$$

These expressions are valid with a maximum error of 10^{-12} s [137]. The expression in Eq. (4.9) demonstrates that a moving clock is slowed by the relativity concept of *time dilation*, as $d\tau$ is smaller than the elapsed coordinate time dt [148].

By integrating Eq. (4.10) a solution of the coordinate time relative to the proper time can be determined for a spacecraft clock. Integrating Eq. (4.10) over time yields,

$$\int_{t_0}^{t} dt = (t - t_0) = \int_{\tau_0}^{\tau} \left[1 + \frac{U}{c^2} + \frac{1}{2}\left(\frac{v}{c}\right)^2 \right] d\tau = (\tau - \tau_0) + \int_{\tau_0}^{\tau} \left[\frac{U}{c^2} + \frac{1}{2}\left(\frac{v}{c}\right)^2 \right] d\tau \qquad (4.11)$$

Various methods have been employed to solve this remaining integral, including near-Earth applications [9, 10, 156, 157], a vector-based solution using positions of various planetary bodies relative to the SSB [137, 138], and a solution for an Earth-based ground telescope and its clock used for pulsar timing [15, 79].

4.2.2 Near-Earth Mission Applications

Eq. (4.11) is the general conversion equation for clocks in motion. This equation can be solved based upon knowledge of the spacecraft's orbit type. The speed of an Earth-orbiting spacecraft with respect to inertial space can be related to the inertial velocity of Earth, $\mathbf{v}_E$, and the relative spacecraft velocity, $\dot{\mathbf{r}}_{SC/E}$, using,

$$v^2 = \left(\mathbf{v}_E + \dot{\mathbf{r}}_{SC/E}\right) \cdot \left(\mathbf{v}_E + \dot{\mathbf{r}}_{SC/E}\right) \qquad (4.12)$$

This expression can also be represented as,

$$v^2 = \left(\mathbf{v}_E \cdot \mathbf{v}_E\right) + 2\left[\frac{d}{dt}\left(\mathbf{v}_E \cdot \mathbf{r}_{SC/E}\right) - \frac{d}{dt}\left(\mathbf{v}_E\right) \cdot \mathbf{r}_{SC/E}\right] + \left(\dot{\mathbf{r}}_{SC/E} \cdot \dot{\mathbf{r}}_{SC/E}\right) \qquad (4.13)$$

The total gravitational potential acting at the spacecraft's location within the solar system, U_{SS}, can be expressed as the sum gravitation potential of Earth, U_E, acting at the spacecraft's position relative to Earth, and the total potential due to all other solar system bodies, U_{SS-E}. This can be presented as,

$$U = U_{SS}\left(\mathbf{r}_{SC}\right) = U_E\left(\mathbf{r}_{SC/E}\right) + U_{SS-E}\left(\mathbf{r}_E + \mathbf{r}_{SC/E}\right) \qquad (4.14)$$

Using the substitutions for speed and gravitational potential from Eqs. (4.13) and (4.14), as well as expressing the magnitude of a vector as $r = \|\mathbf{r}\| = (\mathbf{r} \cdot \mathbf{r})^{\frac{1}{2}}$, the conversion of proper time of an Earth-orbiting spacecraft clock to coordinate time is,

$$(t - t_0) = (\tau - \tau_0) + \int_{\tau_0}^{\tau} \frac{1}{c^2} \begin{bmatrix} U_E(\mathbf{r}_{SC/E}) + U_{SS-E}(\mathbf{r}_E) \\ \frac{1}{2}(r_{SC/E})^2 + \frac{1}{2}(v_E)^2 \end{bmatrix} d\tau + \frac{1}{c^2}(\mathbf{v}_E \cdot \mathbf{r}_{SC/E}) \tag{4.15}$$

The gravitational potential for non-Earth bodies has been expanded in this expression, and terms involving Earth acceleration cancel with one of the expanded terms [137, 209]. The integral term can be replaced by the standard corrections based upon planetary ephemeredes [137, 183]. Additional correction terms are required if comparisons of the proper time of a spacecraft clock are made with reference to the proper time read by a clock on Earth's surface, the *geoid* [149]. The third term on the right-hand side is often referred to as the *Sagnac effect* and is the correction applied to elapsed time of a light signal in a rotating reference frame, in this case the spacecraft's clock in orbit about Earth [156].

These relativistic effects upon clocks in orbit about Earth are appreciable and cannot be ignored if accurate time comparison is required. For example, the net secular relativistic effect on the clocks of GPS satellites amount to 38.6 μs per day (equivalent to 11.6 km in range error) [148, 149]. Ignoring this significant value would eventually produce large navigation error in GPS-based solutions.

4.2.3 Interplanetary Mission Applications

For a spacecraft in orbit about another planetary body, Eq. (4.15) can be represented using the body's absolute velocity, $\mathbf{v}_{PB}$, and spacecraft's relative position, $\mathbf{r}_{SC/PB}$, as,

$$\left(t-t_0\right)=\left(\tau-\tau_0\right)+\int_{\tau_0}^{\tau}\frac{1}{c^2}\begin{bmatrix}U_{PB}\left(\mathbf{r}_{SC/PB}\right)+U_{SS-PB}\left(\mathbf{r}_{PB}\right)\\ \frac{1}{2}\left(r_{SC/PB}\right)^2+\frac{1}{2}\left(v_{PB}\right)^2\end{bmatrix}d\tau+\frac{1}{c^2}\left(\mathbf{v}_{PB}\cdot\mathbf{r}_{SC/PB}\right) \quad (4.16)$$

This would be useful for example for applications of spacecraft in orbit around Mars or within the Jovian system.

For spacecraft on heliocentric orbits, the velocity term can be converted using the *vis-viva* energy, or energy integral, equation of the orbit [17, 213]. The integral can then be directly evaluated using the eccentric anomaly angle, E, such that,

$$\left(t-t_0\right)=\left(\tau-\tau_0\right)\left[1-\frac{\mu_S}{2c^2a}\right]+\frac{2}{c^2}\sqrt{a\mu_S}\left(E-E_0\right) \quad (4.17)$$

In this equation, $\mu_S\left(=GM_S\right)$ is the Sun's gravitational parameter (and the primary gravitational influence), and a is the semi-major axis of the heliocentric orbit. Using additional descriptions of the Keplerian orbit parameters and how they relate to time, this expression may also be written as [148, 156, 188],

$$\left(t-t_0\right)=\left(\tau-\tau_0\right)\left[1+\frac{3\mu_S}{2c^2a}\right]+\frac{2}{c^2}\left(\mathbf{r}\cdot\mathbf{v}-\mathbf{r}_0\cdot\mathbf{v}_0\right) \quad (4.18)$$

4.3 Time Transfer To Solar System Barycenter

As discussed in the Chapter 3, once a pulsar's model is defined, in order for this model to be utilized by another observer, the coordinate time scale and the valid location for this model must be stated. The common frame utilized is the SSB coordinate frame and either the TCB or TDB time scales. The models are often described to be valid at the origin of the SSB frame. In order to compare a measured pulse arrival time at a remote observation station with the predicted time at the SSB origin, the station must project arrival times of photons by its detector onto the SSB origin. This comparison requires time to be transferred from the observation station, or spacecraft, to the SSB. Alternatively, the SSB pulse-timing model could be transferred to another known location. For example, at a given time instance, the pulse timing model could be transferred to Earth's center, in order to create pulse arrival time comparisons with the position of Earth.

To accurately transfer time from one location to another, geometric and relativistic effects must be included in this transfer. These effects account for the difference in light ray paths from a source to the detector's location and to the model's location. These light ray paths can be determined using the existing theory of general relativity and the effects of the solar system [171-173]. The discussion below describes a method of transferring detected arrival times to the SSB origin.

4.3.1 First Order Time Transfer

Figure 4-1 shows the relationship of pulses from a pulsar as they arrive into the solar system relative to the SSB inertial frame and a spacecraft orbiting Earth. The positions of the spacecraft, $\mathbf{r}$, and the center of Earth, $\mathbf{r}_E$, with respect to the SSB are shown, as well as the unit direction to the pulsar, $\hat{\mathbf{n}}$. From the known angular positions of the celestial objects, the line-of-sight to the pulsar can be determined relative to the SSB inertial coordinate system.

Figure 4-2 depicts a simple representation of the position of the spacecraft relative to the origin, as well as the range of the spacecraft from the origin along the line-of-sight vector to the pulsar $(\hat{\mathbf{n}} \cdot \mathbf{r})$. Using the Right Ascension, α, and Declination angles, δ, of the pulsar's position, the line-of-sight unit vector $\hat{\mathbf{n}}$ to the pulsar can be computed as,

$$\hat{\mathbf{n}} = \cos(\delta)\cos(\alpha)\,\hat{\mathbf{i}} + \cos(\delta)\sin(\alpha)\,\hat{\mathbf{j}} + \sin(\delta)\,\hat{\mathbf{k}} \tag{4.19}$$

Since the pulsar is so distant from the origin within the solar system, first order analysis allows the line-of-sight from the origin to the pulsar to be assumed parallel with the line-of-sight from the spacecraft to the pulsar. Therefore, the spacecraft measured pulse-timing differences between the spacecraft and the origin (or another reference observation station) represents a measure of the spacecraft's position offset along the direction towards the pulsar. Figure 4-3 provides a diagram of this offset time and distance between the spacecraft and the origin. Using the spacecraft's position relative to the SSB, the offset of time a pulsar signal arrives at a spacecraft compared to the arrival time of the same pulse at the SSB to *first order* is,

$$t_{SSB} = t_{SC} + \frac{\hat{\mathbf{n}} \cdot \mathbf{r}}{c} \tag{4.20}$$

In this representation, t_{SSB} is the coordinate time of the pulse TOA at the SSB, t_{SC} is the coordinate time of the pulse TOA at the spacecraft, and c is the speed of light. Since many pulsars are so distant from Earth, in this simple expression, the unit direction to the pulsars may be considered constant throughout the solar system. However, parallax and any apparent proper–motion should be included when determining the direction of closer pulsars.

To transfer time from the spacecraft to the barycenter, the simple geometric relationship of Eq. (4.20) determines the time offset as,

$$\Delta t = t_{SSB} - t_{SC} = \frac{\hat{\mathbf{n}} \cdot \mathbf{r}}{c} \tag{4.21}$$

This expression also represents the time of arrival difference between the two locations.

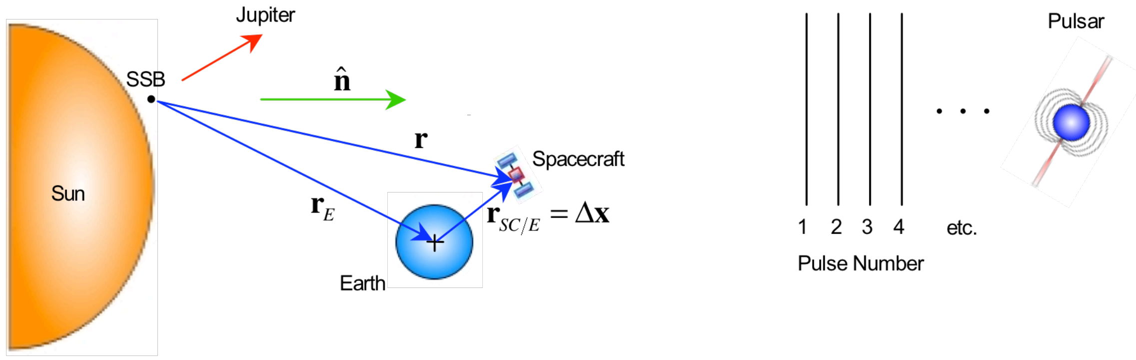

Figure 4-1. Position of spacecraft upon pulse arrival within solar system.

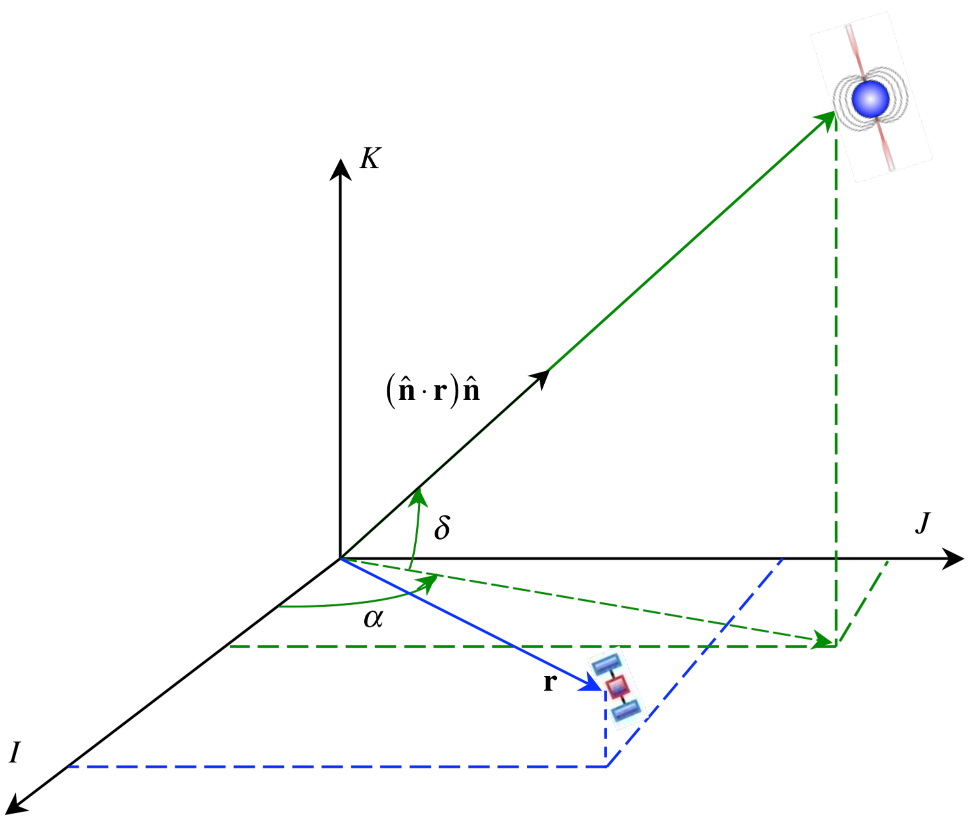

Figure 4-2. The unit direction to a pulsar and the position of a spacecraft [50].

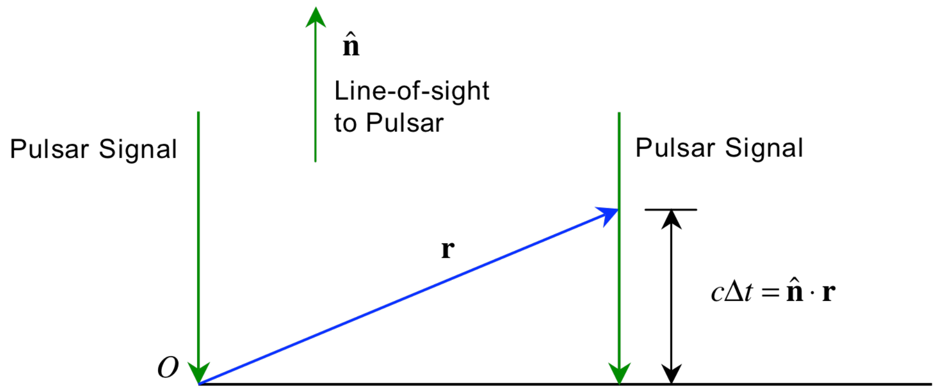

Figure 4-3. Spacecraft position offset distance in direction of pulsar signal.

4.3.2 Higher Order Time Transfer

A time transfer equation with improved accuracy over Eq. (4.21) can be created using theory the general relativity, which provides a method of accurately transferring time data within an inertial frame. The equations from this theory relate the emission time of photons that emanate from a source to their arrival time at a station and define the path of the photons traveling through curved spacetime [15, 79, 140].

The goal of a pulsar-based navigation system would be in part to provide accurate position information of the spacecraft. This could only be accomplished by accurately timing pulsar signals and then correctly transferring this time to the SSB. If a performance goal of the navigation system is to provide accurate position information on the order of 300 meters or less, then the system must accurately time pulses to at least 1 μs ($\approx 300 \;\mathrm{m}/c$). The relativistic effects on time transfer neglected in Eq. (4.21) account from tens to thousands of nanoseconds thus must be included to achieve this time and position determination goal. Thus, general and special relativistic effects on a clock in motion relative to an inertial frame and within a gravitational potential field must be considered. A derivation of these effects on time is provided below, and follows the models of Hellings, Moyer, Murray, and others [15, 79, 126, 137, 138, 140], which are specific to Earth-based ground telescopes and their use for pulsar timing analysis.

From the theory of general relativity, the solar system can be estimated as a weak-gravitational field and nearly flat space. Within this type of system, the spacetime interval, ds, which is invariant with respect to arbitrary transformations of coordinates to order $O(1/c)$, is given by Eq. (4.6).

An individual pulse is composed of an assemblage of photons from a variable celestial source. Each single photon travels along a light ray path, or *world line*. For electromagnetic signals, this world line takes the path of a *null geodesic,* as the photon travels from the emitting source to the receiving location of an observer [148, 156]. Transfer of time can be accomplished by using the light ray path between these two locations. Along this null geodesic the spacetime interval equals zero, or $ds = 0$ [148]. Therefore the time coordinate relates to the path coordinates using Eq. (4.6) as,

$$c^2 dt^2 = \frac{1 + \frac{2U}{c^2}}{1 - \frac{2U}{c^2}} \left(dx^2 + dy^2 + dz^2 \right) \tag{4.22}$$

Using a binomial expansion, this relationship is valid to order $O(1/c^2)$ as,

$$cdt = \left(1 + \frac{2U}{c^2} \right) \sqrt{dx^2 + dy^2 + dz^2} \tag{4.23}$$

Considering a single pulse from a source, the transmission time of one photon is related to the reception, or observed, time of the photon by the distance along the path this photon has traveled. Figure 4-4 presents a diagram of a emitting source and the observation of the photon at a spacecraft near Earth. The vector to the source from the

Sun is $\mathbf{D}$, the position of the spacecraft relative to the Sun is $\mathbf{p}$, and the line-of-sight from the spacecraft to the pulsar is $\hat{\mathbf{n}}_{SC}$. Since a pulse is an ensemble of these photons, by measuring the arrival times of all the photons within a pulse period, the arrival time of the pulse peak can be determined.

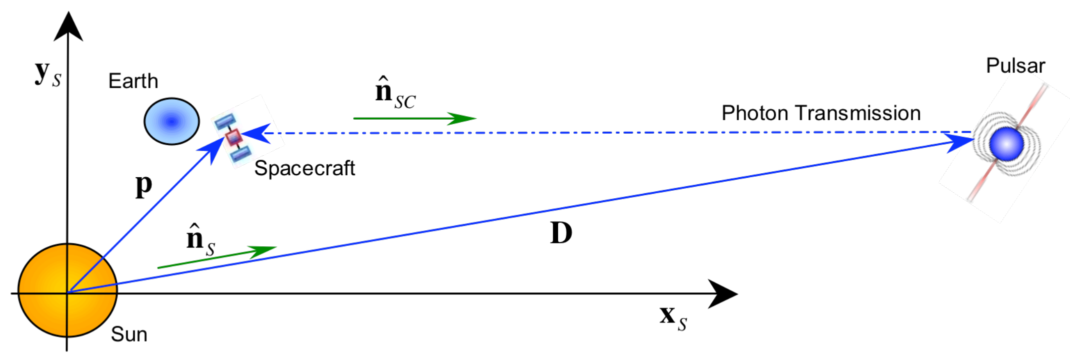

Figure 4-4. Light ray path arriving from distant pulsar to spacecraft within solar system.

By integrating Eq. (4.23), an algorithm can be developed to determine when the N^{th} pulse is received at the spacecraft at time, t_{SC_N}, relative to when it was transmitted from the pulsar at time, t_{T_N}. This is represented as,

$$c\int_{t_{T_N}}^{t_{SC_N}} dt = \int_{D_x}^{p_x} \left(1+\frac{2U}{c^2}\right)\left[1+\frac{dy^2}{dx^2}+\frac{dz^2}{dx^2}\right]^{\frac{1}{2}} dx \tag{4.24}$$

In this expression, p_x and D_x are the x-axis components of the $\mathbf{p}$ and $\mathbf{D}$ vectors of Figure 4-4, respectively. The solution to this equation depends on the null geodesic light ray path and the gravitational potential of bodies along this path.

For a pulse arriving into the solar system, the integrated solution between a pulsar and an observation spacecraft is [15, 79, 113, 126, 170-173, 188],

$$\left(t_{SC_N} - t_{T_N}\right) = \frac{1}{c}\hat{\mathbf{n}}_{SC} \cdot \left(\mathbf{D}_N - \mathbf{p}_N\right) - \sum_{k=1}^{PB_{SS}} \frac{2GM_k}{c^3} \ln\left|\frac{\hat{\mathbf{n}}_{SC} \cdot \mathbf{p}_{N_k} + p_{N_k}}{\hat{\mathbf{n}}_{SC} \cdot \mathbf{D}_{N_k} + D_{N_k}}\right|$$
$$+ \frac{2\mu_S^2}{c^5 {D_{N_y}}^2} \left\{ \begin{aligned} &\hat{\mathbf{n}}_{SC} \cdot \left(\mathbf{D}_N - \mathbf{p}_N\right)\left[\left(\frac{\left(\hat{\mathbf{n}}_{SC} \cdot \mathbf{D}_N\right)}{D_N}\right)^2 + 1\right] \\ &+ 2\left(\hat{\mathbf{n}}_{SC} \cdot \mathbf{D}_N\right)\left(\frac{p_N}{D_N} - 1\right) \\ &+ D_{N_y}\left(\arctan\left(\frac{p_{N_x}}{D_{N_y}}\right) - \arctan\left(\frac{D_{N_x}}{D_{N_y}}\right)\right) \end{aligned} \right\} \tag{4.25}$$

In this equation, $\mathbf{p}_N$ represents position of the spacecraft when it receives the N^{th} pulse from the pulsar relative to the center of the Sun (not the SSB). The first term on the right hand side of Eq. (4.25) is the geometric separation between the source and the observer. The second term is the summation of *Shapiro* delay effects of all the bodies within the solar system [184]. This summation term is taken over all planetary bodies in the solar system, PB_{SS}. The terms $\mathbf{p}_{N_k}$ and $\mathbf{D}_{N_k}$ are the respective positions of the spacecraft and the source relative to the k^{th} planetary body in the solar system. The third large term in this equation is the deflection of the light ray path of the pulse due to the Sun, which is the primary influencing gravitational force within the solar system. This term is typically a small value (< 1 ns).

Similarly, the elapsed time of the pulse travel between the emission of the N^{th} pulse from the pulsar and the SSB origin can be computed using Eq. (4.24). However, the position of the SSB origin relative to the Sun, $\mathbf{b}_N$, and the direction to the pulsar from the SSB, $\hat{\mathbf{n}}_{SSB}$, are used instead of the corresponding values for the spacecraft. The term $\mathbf{b}_{N_k}$ is the position of the SSB relative to the k^{th} planetary body. This elapsed time can be represented as,

$$\left(t_{SSB_N} - t_{T_N}\right) = \frac{1}{c}\hat{\mathbf{n}}_{SSB}\cdot\left(\mathbf{D}_N - \mathbf{b}_N\right) - \sum_{k=1}^{PB_{SS}} \frac{2GM_k}{c^3}\ln\left|\frac{\hat{\mathbf{n}}_{SSB}\cdot\mathbf{b}_{N_k} + b_{N_k}}{\hat{\mathbf{n}}_{SSB}\cdot\mathbf{D}_{N_k} + D_{N_k}}\right|$$
$$+\frac{2\mu_S^2}{c^5 D_{N_{y_{SSB}}}^2}\left\{\begin{aligned} &\hat{\mathbf{n}}_{SSB}\cdot\left(\mathbf{D}_N - \mathbf{b}_N\right)\left[\left(\frac{\left(\hat{\mathbf{n}}_{SSB}\cdot\mathbf{D}_N\right)}{D_N}\right)^2 + 1\right] \\ &+ 2\left(\hat{\mathbf{n}}_{SSB}\cdot\mathbf{D}_N\right)\left[\frac{b_N}{D_N} - 1\right] \\ &+ D_{N_{y_{SSB}}}\left[\arctan\left(\frac{b_{N_x}}{D_{N_{y_{SSB}}}}\right) - \arctan\left(\frac{D_{N_{x_{SSB}}}}{D_{N_{y_{SSB}}}}\right)\right] \end{aligned}\right\} \tag{4.26}$$

In order to compare the pulse arrival time at the spacecraft relative to the arrival time at the SSB, time must be transferred from the spacecraft to the SSB. This time transfer can be accomplished by differencing the transmit time of the N^{th} pulse from a pulsar, t_{T_N}, to its arrival at each of the spacecraft, t_{SC_N}, and the SSB, t_{SSB_N}, as in

$$\left(t_{SSB_N} - t_{T_N}\right) - \left(t_{SC_N} - t_{T_N}\right) = t_{SSB_N} - t_{SC_N} \tag{4.27}$$

Figure 4-5 presents a diagram of the positions of the pulsar, the spacecraft, and the SSB with respect to the Sun. The time transfer relates t_{SC_N} and t_{SSB_N}, as well as the relative position between these two locations, $\mathbf{r}$.

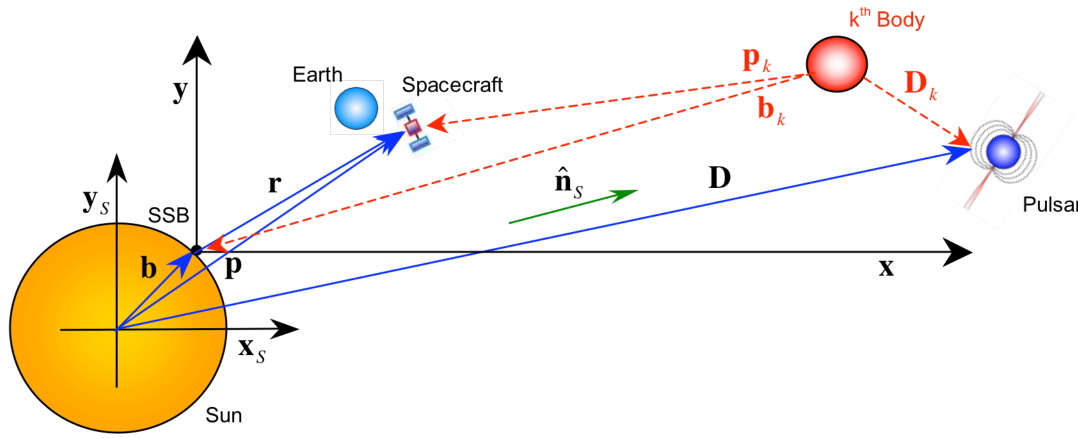

Figure 4-5. Spacecraft position relative to Sun and SSB origin.

Differencing Eq. (4.25) from Eq. (4.26) yields the necessary transfer time of Eq. (4.27) between the spacecraft and the SSB,

$$
\begin{aligned}
\left(t_{SSB}-t_{SC}\right) = {} & \frac{1}{c}\hat{\mathbf{n}}_{SSB}\cdot\left(\mathbf{D}-\mathbf{b}\right)-\frac{1}{c}\hat{\mathbf{n}}_{SC}\cdot\left(\mathbf{D}-\mathbf{p}\right) \\
& -\sum_{k=1}^{PB_{SS}}\frac{2GM_k}{c^3}\ln\left|\frac{\hat{\mathbf{n}}_{SSB}\cdot\mathbf{b}_k+b_k}{\hat{\mathbf{n}}_{SSB}\cdot\mathbf{D}_k+D_k}\right|+\sum_{k=1}^{PB_{SS}}\frac{2GM_k}{c^3}\ln\left|\frac{\hat{\mathbf{n}}_{SC}\cdot\mathbf{p}_k+p_k}{\hat{\mathbf{n}}_{SC}\cdot\mathbf{D}_k+D_k}\right| \\
& +\frac{2\mu_S^2}{c^5D_{y_{SSB}}^2}\left\{\begin{aligned}&\hat{\mathbf{n}}_{SSB}\cdot\left(\mathbf{D}-\mathbf{b}\right)\left[\left(\frac{\left(\hat{\mathbf{n}}_{SSB}\cdot\mathbf{D}\right)}{D}\right)^2+1\right]+2\left(\hat{\mathbf{n}}_{SSB}\cdot\mathbf{D}\right)\left[\frac{b}{D}-1\right]\\&+D_{y_{SSB}}\left[\arctan\left(\frac{b_x}{D_{y_{SSB}}}\right)-\arctan\left(\frac{D_{x_{SSB}}}{D_{y_{SSB}}}\right)\right]\end{aligned}\right\} \\
& -\frac{2\mu_S^2}{c^5D_y{}^2}\left\{\begin{aligned}&\hat{\mathbf{n}}_{SC}\cdot\left(\mathbf{D}-\mathbf{p}\right)\left[\left(\frac{\left(\hat{\mathbf{n}}_{SC}\cdot\mathbf{D}\right)}{D}\right)^2+1\right]+2\left(\hat{\mathbf{n}}_{SC}\cdot\mathbf{D}\right)\left(\frac{p}{D}-1\right)\\&+D_y\left(\arctan\left(\frac{p_x}{D_y}\right)-\arctan\left(\frac{D_x}{D_y}\right)\right)\end{aligned}\right\}
\end{aligned}
\tag{4.28}
$$

In this expression, the subscript for the N^{th} pulse received at each location has been dropped for clarity. Eq. (4.28) is the full high accuracy time transfer equation between the spacecraft and the SSB, and should be accurate to sub-nanosecond if all terms are retained.

4.3.2.1 Simplified Analytical Time Transfer

Simplifications to algorithm of Eq. (4.28) can still produce accurate time transfer. These simplifications reduce the computational complexity of the algorithm, but also reduce the accuracy to the order of a few nanoseconds or microseconds.

The first simplification can be neglecting the difference in the light ray bending effect terms. Since these terms from Eqs. (4.25) and (4.26) are small (< 1 ns), the difference of these two small values can be effectively ignored.

The proper-motion of the emitting source can also be included for the change of the pulsars location from its position, $\mathbf{D}_0$, at the emission of the 0^{th} pulse, t_{T_0}, and it position, $\mathbf{D}_N$, of the N^{th} pulse, t_{T_N} [79]. Assuming a constant value of proper motion, $\mathbf{V}$, and that the difference in transmission time $\left(t_{T_N} - t_{T_0}\right)$ is equal to the difference in reception time $\left(t_{SC_N} - t_{SC_0}\right)$, the pulsar position can be represented as,

$$\mathbf{D}_N = \mathbf{D}_0 + \mathbf{V}\left(t_{T_N} - t_{T_0}\right) \approx \mathbf{D}_0 + \mathbf{V}\left(t_{SC_N} - t_{SC_0}\right) = \mathbf{D}_0 + \mathbf{V}\Delta t_N \tag{4.29}$$

If the line-of-sight to the emitting source is considered constant within the solar system, then the direction becomes $\hat{\mathbf{n}}_{SC} \approx \hat{\mathbf{n}}_{SSB} \approx \hat{\mathbf{n}}_S \approx \hat{\mathbf{n}} \approx \mathbf{D}_0 / D_0$. Using the position of the SSB origin relative to the Sun's center as $\mathbf{b}$, the position of the spacecraft relative to the SSB as $\mathbf{r}$ (such that $\mathbf{p} = \mathbf{b} + \mathbf{r}$), then these simplifications modify the time transfer equation to relate t_{SC} and t_{SSB}, to the following,

$$
\left(t_{SSB}-t_{SC}\right)=\frac{1}{c}\left[\begin{array}{l}
\hat{\mathbf{n}}\cdot\mathbf{r}-\dfrac{r^2}{2D_0}+\dfrac{\left(\hat{\mathbf{n}}\cdot\mathbf{r}\right)^2}{2D_0}+\dfrac{\mathbf{r}\cdot\mathbf{V}\Delta t_N}{D_0}-\dfrac{\left(\hat{\mathbf{n}}\cdot\mathbf{V}\Delta t_N\right)\left(\hat{\mathbf{n}}\cdot\mathbf{r}\right)}{D_0}\\
+\dfrac{\left(\hat{\mathbf{n}}\cdot\mathbf{r}\right)}{D_0^2}\left[\left(\mathbf{r}\cdot\mathbf{V}\Delta t_N\right)-\dfrac{r^2}{2}\right]+\dfrac{\left(\hat{\mathbf{n}}\cdot\mathbf{V}\Delta t_N\right)\left(r^2\right)}{2D_0^2}-\dfrac{\left(\hat{\mathbf{n}}\cdot\mathbf{V}\Delta t_N\right)\left(\mathbf{r}\cdot\mathbf{V}\Delta t_N\right)}{D_0^2}\\
-\dfrac{\left(\mathbf{b}\cdot\mathbf{r}\right)}{D_0}+\dfrac{\left(\hat{\mathbf{n}}\cdot\mathbf{b}\right)\left(\hat{\mathbf{n}}\cdot\mathbf{r}\right)}{D_0}\\
+\dfrac{\left(\hat{\mathbf{n}}\cdot\mathbf{r}\right)}{D_0^2}\left[-\left(\mathbf{b}\cdot\mathbf{r}\right)-\dfrac{b^2}{2}+\left(\mathbf{b}\cdot\mathbf{V}\Delta t_N\right)\right]\\
+\dfrac{\left(\hat{\mathbf{n}}\cdot\mathbf{b}\right)}{D_0^2}\left[-\left(\mathbf{b}\cdot\mathbf{r}\right)-\dfrac{r^2}{2}+\left(\mathbf{r}\cdot\mathbf{V}\Delta t_N\right)\right]+\dfrac{\left(\hat{\mathbf{n}}\cdot\mathbf{V}\Delta t_N\right)\left(\mathbf{b}\cdot\mathbf{r}\right)}{D_0^2}
\end{array}\right]
+\sum_{k=1}^{PB_{SS}}\frac{2GM_k}{c^3}\ln\left|\frac{\hat{\mathbf{n}}\cdot\mathbf{r}_k+r_k}{\hat{\mathbf{n}}\cdot\mathbf{b}_k+b_k}+1\right| \tag{4.30}
$$

Ignoring all terms of order $O\left(1/D_0^2\right)$ yields a time transfer algorithm of,

$$
\left(t_{SSB}-t_{SC}\right)=\frac{1}{c}\left[\begin{array}{l}
\hat{\mathbf{n}}\cdot\mathbf{r}-\dfrac{r^2}{2D_0}+\dfrac{\left(\hat{\mathbf{n}}\cdot\mathbf{r}\right)^2}{2D_0}+\dfrac{\mathbf{r}\cdot\mathbf{V}\Delta t_N}{D_0}-\dfrac{\left(\hat{\mathbf{n}}\cdot\mathbf{V}\Delta t_N\right)\left(\hat{\mathbf{n}}\cdot\mathbf{r}\right)}{D_0}\\
-\dfrac{\left(\mathbf{b}\cdot\mathbf{r}\right)}{D_0}+\dfrac{\left(\hat{\mathbf{n}}\cdot\mathbf{b}\right)\left(\hat{\mathbf{n}}\cdot\mathbf{r}\right)}{D_0}
\end{array}\right]
+\sum_{k=1}^{PB_{SS}}\frac{2GM_k}{c^3}\ln\left|\frac{\hat{\mathbf{n}}\cdot\mathbf{r}_k+r_k}{\hat{\mathbf{n}}\cdot\mathbf{b}_k+b_k}+1\right| \tag{4.31}
$$

Since the values of proper motion, $\mathbf{V}$, are typically small, such that $\mathbf{D}_0 >> \mathbf{V}\Delta t_N$, and the Sun imposes the primary gravitational field within the solar system, the expression in Eq. (4.31) may be further simplified as,

$$
\left(t_{SSB}-t_{SC}\right)=\frac{\hat{\mathbf{n}}\cdot\mathbf{r}}{c}+\frac{1}{2cD_0}\left[\left(\hat{\mathbf{n}}\cdot\mathbf{r}\right)^2-r^2+2\left(\hat{\mathbf{n}}\cdot\mathbf{b}\right)\left(\hat{\mathbf{n}}\cdot\mathbf{r}\right)-2\left(\mathbf{b}\cdot\mathbf{r}\right)\right]
+\frac{2\mu_S}{c^3}\ln\left|\frac{\hat{\mathbf{n}}\cdot\mathbf{r}+r}{\hat{\mathbf{n}}\cdot\mathbf{b}+b}+1\right| \tag{4.32}
$$

In Eq. (4.32), ignoring the effects of the outer planets can have errors as large as 200 ns depending on the photon's flight path [79]. This simplified time transfer equation is accurate to about roughly 10 μs with respect to the full equation of Eq. (4.28).

The first term on the right-hand side of Eq. (4.32) is the first order *Doppler delay*, and represents the simple geometric time delay between these two locations. The second term is due to the effects of parallax. Together these two terms are referred to as *Roemer delay*. The last term is the Sun's *Shapiro delay* effect, which is the additional time delay from the curved light ray path due to the Sun's gravity field [184]. The interstellar medium dispersion measure term, appearing as a correction to this equation for all radio observations, is considered zero (~10^{-3} nanoseconds) for high frequency X-ray radiation [114, 118]. Eq. (4.32) requires accurate solar system ephemeris information to provide the SSB location and the Sun's gravitational parameter. If the relativistic effects and terms of order $O\left(1/D_0\right)$ are ignored, Eq. (4.32) reduces to the first order approximation of Eq. (4.21).

Using any of the simplified expressions from Eq. (4.30), (4.31), or (4.32) provides a method to transfer time from the spacecraft's position to the SSB position. When using one of these equations to operate within a navigation system, it is important to consider reference time scales, pulsar phase timing model definitions, and desired accuracy in order to insure correct time transfer results.

Since pulse timing models could be described at any known location, such as Earth–center, Earth–Moon barycenter, Mars–center, even other spacecraft locations, it may be necessary to implement time transfer to locations other than the SSB. These equations can be used to transfer time between the spacecraft and another reference position, by replacing the position of the SSB's origin, $\mathbf{b}$, with the new reference position (ex. $\mathbf{r}_E$, if the model is defined at Earth–center). Thus, these expressions provide a method to accurately compare the arrival time of a pulse at the spacecraft with those of pulsar timing models that can be defined at any known location within the solar system.

Time transfer is an important aspect for accurate navigation using variable celestial sources. However, as can be seen in these equations, this time transfer requires knowledge, or an estimate, of detector position in order to be implemented. It will be shown in Chapters 6 through 8 that this dilemma can still be addressed in order to determine spacecraft position.

4.3.2.2 Numerical Accuracy of Time Transfer Expressions

The equations of time transfer in the solar system of Eqs. (4.28), (4.30), (4.31), and (4.32) provide decreasing complexity of computation, however, these also produce diminishing accuracy. Depending on the performance required by a specific application, the algorithm with adequate accuracy should be utilized.

Table 4-1 provides a summary of the comparison of accuracy among the four time transfer algorithms. For this comparison, the specific position in the orbit of the *ARGOS* vehicle was chosen at time = 2451538.96769266 JD, and the results are only valid for this specific location. The single source used in this analysis was the Crab Pulsar, along with its proper motion of μ_α = -17 mas/yr and μ_δ = 7 mas/yr and a distance of 2 kpc [34]. A value of Δt_N = 100 days was selected as a representation of the elapsed time between the measured $\mathbf{D}_0$ and the current time.

From this table it can be seen that for this specific instance and position in space, the difference between the simplified expression of Eq. (4.32) and the full expression of Eq.

(4.28) is about 5.3 μs. The values in the fourth row of this table show that by adding the Shapiro delay effect of all the bodies in the solar system, instead of considering only the Sun's effect, accounts for as much as 10 ns of difference. The reported error of 200 ns by Hellings [79] of ignoring all solar system planets is realistic when considering another point in the vehicle's orbit, where Jupiter's or other large planet's position would create a greater effect on the delay. Table 4-2 lists the values of the terms within the simplified expression of Eq. (4.32). For this specific instance, the values in the table shows that the geometric delay term provides the majority of the time transfer, whereas the Shapiro delay term accounts for nearly 51 μs of correction.

In order to produce the results of these tables it was required to utilize *variable precision arithmetic* to compute the differences between large and small values. This was implemented to avoid the potential numerical truncation, which ignores small remainders, when using fixed double precision. It is recommended that at least quadruple precision (128 bits of floating point representation) be used if any of the Eqs. (4.28) through (4.31) are implemented. Since Eq. (4.32) does not require any of these types of computations for near-Earth applications, this equation could be implemented using double precision (64 bit), however this assessment should be verified when data is collected from deep space missions.

A full study should be further pursued to determine the accuracy of the time transfer algorithms at different times, implying different locations of the spacecraft, Sun, and planetary bodies, and different celestial sources. This comprehensive study should further assess the performance of these algorithms. Although it may be desired to utilize the algorithm with the assumed best performance, Eq. (4.28), the limitations of this expression include the required accurate knowledge of source position. Unfortunately, no observed source has three-dimensional position knowledge that would allow this equation to be truly applicable.

Table 4-1. Time Transfer Algorithm Accuracy Comparison.

Algorithm	Difference from Eq. (4.28)	Difference from Preceding Algorithm
Eq. (4.28)	---	---
Eq. (4.30)	-3.59 μs	-3.59 μs
Eq. (4.31)	-3.59 μs	+0.71 ps
Eq. (4.31) with $\Delta t_N = 0$	-5.32 μs	-1.73 μs
Eq. (4.32)	-5.31 μs	+9.43 ns

Table 4-2. Simplified Time Transfer Algorithm Component Contributions.

Term	Value (s)
$\dfrac{\hat{\mathbf{n}} \cdot \mathbf{r}}{c}$	+481.221740080369
$\dfrac{1}{2cD_0}\left[(\hat{\mathbf{n}} \cdot \mathbf{r})^2 - r^2\right]$	-0.000000019854
$\dfrac{1}{2cD_0}\left[2(\hat{\mathbf{n}} \cdot \mathbf{b})(\hat{\mathbf{n}} \cdot \mathbf{r}) - 2(\mathbf{b} \cdot \mathbf{r})\right]$	+0.000000001493
$\dfrac{2\mu_S}{c^3} \ln\left\lvert \dfrac{\hat{\mathbf{n}} \cdot \mathbf{r} + r}{\hat{\mathbf{n}} \cdot \mathbf{b} + b} + 1 \right\rvert$	+0.000050898463
Total	481.221790960471

4.3.3 Pulse Arrival Time Comparison Summary

The preceding sections provide methods to time observed pulsar pulses and compare this time to pulse prediction models. This section provides a summary of how to implement this pulse comparison in a manner that would be utilized by a pulsar-based navigation system. A navigation system would include of a sensor that would detect pulsar pulse photons at the spacecraft, a clock onboard the vehicle that would time the photons' arrival, and a database of known timing models for pulsars.

Table 4-3 provides the steps necessary to complete time transfer of observed pulsar data and comparison to pulsar phase timing models. In order to compute a pulse TOA and compare this measured TOA to the predicted TOA of a timing model, all time measurements must be converted to in inertial coordinate time frame, such as TCB or TDB. Also, all pulses must be timed as if they would arrive at the inertial frame's origin, such as the SSB.

Table 4-3. Pulse Time Transfer and Comparison Process.

Process	Steps
Photon Arrival in TDB	• Collect and time pulsar X-ray photons at the spacecraft's detector using onboard clock. • Correct spacecraft clock proper time to SSB coordinate system TDB time using standard corrections and spacecraft velocity effects.
Time Transfer to Barycenter	• Using spacecraft position and velocity and gravitational potential of solar system, correct measured photon TDB arrival time for offset of vehicle from SSB origin.
TOA Measurement and Offset	• Coherently fold photons into an observed pulse profile. • Compare observed pulse profile to standard template profile of pulsar to determine measured TOA of detected pulse, as it would arrive at SSB origin. • Using pulsar-timing mode, compare predicted TOA of pulse closest to measured TOA to determine difference in pulse arrival time.

4.4 Pulsar Timing Analysis Equations

Previous astrophysical researchers have pursued the timing analysis of pulsar signals. Much of the previous work was concerned only with observations made by telescopes on Earth's surface, and the corrections to the clocks at those stations necessary to compute accurate pulse TOA comparison. This section presents an overview of these previous results, as well as a discussion about the relationships of these previous algorithms to the time transfer equations presented above.

Hellings and Backer [15, 79], and Murray [140] present the most detailed discussion on pulsar signal timing analysis. Hellings derivation in [79] builds upon the relativistic work accomplished by Richter and Matzner [170-173]. The accuracy of the resulting algorithm is stated as ≤ 100 ns. Both these analyses only determine the coordinate arrival time of a photon at the observation station on Earth, but could be applicable to spacecraft if the spacecraft's position is substituted for Earth position.

There have been several other articles on the development of photon arrival timing for pulsar pulse timing [22, 94, 95, 113, 162, 206]. All have presented simplified SSB transfer equations for Earth-fixed clocks based upon the work by Hellings, Backer, and Murray. All directly relate to radio telescope observations, thus include the additional effects of the interstellar dispersion measure. Taylor and Weisberg state the terms of the proper time and relativistic effects, whereas others leave these as generalized terms in their equations [206]. If only the Roemer delay and part of the Shapiro delay terms are considered, most of these simplified transfer expression match well with the transfer equations derived in the previous sections.

There are several papers that present the timing of pulsars that exist within binary systems [28, 54, 74]. Binary system pulsars add additional complexity to their timing models, as well as considerations of the additional relativistic effects produced by the companion star's mass. The Shapiro delay terms in these systems can be represented similarly as the isolated pulsar sources. However these papers present considerations of only the time-varying portion of the Shapiro delay effects, and do not create a time difference between the pulse arrival at Earth-based telescopes and the SSB.

Hellings Eq. (32) [79] is the same as Eq. (4.25), and is similar to the equations presented by Murray [140]. A time transformation algorithm is then derived based upon this equation. However this algorithm is not the difference between the arrival times at the SSB and the observation station, but rather the actual arrival time of the photons at the observation station. This results in equations for both Hellings and Murray that retain the full position of the pulsar, $\mathbf{D}$, and the transmission time, t_{T_N}. Since these cannot be determined to the accuracy required by the pulsar timing analysis or are unknown, new terms are introduced to the algorithm in order to gather these unknown terms into values that can be effectively ignored within pulsar timing analysis. The term that Hellings introduces is the 0^{th} order pulse TOA into the solar system as (Hellings uses the symbol for transmission time as $T = t_T$),

$$t_{SC_0} = t_{T_0} + \frac{1}{c}\left(\hat{\mathbf{n}}_{SC_0} \cdot \mathbf{D}_0\right) - \sum_{k=1}^{PB_{SS}} \frac{2GM_k}{c^3} \ln\left|\frac{1}{\hat{\mathbf{n}}_{SC} \cdot \mathbf{D}_{N_k} + D_{N_k}}\right| \tag{4.33}$$

Ignoring the last term in Eq. (4.25), Hellings arrival time equation becomes the following using Eq. (4.25) and (4.33),

$$\begin{aligned}\left(t_{SC_N} - t_{SC_0}\right) = \left(t_{T_N} - t_{T_0}\right) + \frac{1}{c}\hat{\mathbf{n}}_{SC} \cdot \left(\mathbf{D}_N - \mathbf{D}_0\right) - \frac{1}{c}\left(\hat{\mathbf{n}}_{SC} \cdot \mathbf{p}_N\right) \\ - \sum_{k=1}^{PB_{SS}} \frac{2GM_k}{c^3} \ln\left|\hat{\mathbf{n}}_{SC} \cdot \mathbf{p}_{N_k} + p_{N_k}\right|\end{aligned} \tag{4.34}$$

Implementing the proper motion expression of Eq. (4.29), this expression becomes Hellings' Eq. (46), except that Hellings replaces the observations station's Sun relative position, $\mathbf{p}$, with its SSB relative position, $\mathbf{r}$.

Although this time transformation equation presented in Eq. (4.34) is used currently for many pulsar data analyses and may be sufficient for spacecraft clock applications, the differences between this method and the derivations presented in the previous section should be considered. The derivation of the relativistic light ray paths used in the timing derivations in the previous section and by Hellings from Richter and Matzner are developed for the frames that are centered at the Sun, not the SSB [170-173]. Thus, simple replacement of the relative position from the Sun to the relative position from the SSB may not be valid. Since the transmission times from the pulsar, t_{T_N} and t_{T_0}, are unknown, these have to be ignored when using Eq. (4.34). The 0^{th} order pulse TOA, t_{SC_0}, cannot be directly measured, only estimated.

But perhaps the largest issue with utilizing these existing pulsar analysis equations is due to their computational errors at the location of the SSB origin. From Figure 4-4, if the spacecraft were hypothetically at the center of the Sun approximated as a point mass, then there would be no bending effects of the light ray path and only the geometric elapsed time between the pulsar and the spacecraft would exist. For a spacecraft hypothetically located at the SSB origin, the time transfer equation between the vehicle and the origin should produce zero time difference. However, replacing $\mathbf{p}$ with its SSB relative position $\mathbf{r}$ in Eq. (4.34) and setting $\mathbf{r} = \mathbf{0}$ for the SSB origin, the Shapiro delay term becomes undefined in this expression currently used by many pulsar-timing analyses. However, in the newly derived transfer Eqs. (4.30), (4.31), or (4.32), the Shapiro delay term correctly is computed as zero in this scenario.

The fundamental difference is that pulsar timing analysis equations of Hellings, Backer, and Murray determine the photon TOA with respect to the pulsar as in Eq. (4.25) by ignoring the unknown transmission time, whereas the time transfer Eq. (4.28) uses the measured TOA of a photon and projects this arrival time to the SSB origin. Further analysis may be required in order to determine how to resolve these discrepancies.

Chapter 5 Variable Celestial Source-Based Navigation

"We shall not cease from exploration, and the end of all our exploring will be to arrive where we started and know the place for the first time."

– T. S. Eliot

5.1 Navigation

Having investigated and developed the relevant physics, modeling, and analysis that characterize variable celestial sources in the preceding four chapters, it is necessary to determine how the measured data can be used to determine a navigation solution for spacecraft. Various techniques can be employed to facilitate the use of the periodic signals from these sources. An overview of the concepts for determining components of a full navigation solution is provided in this chapter.

As identified in Chapter 1, *navigation* is the process of determining when, where, and the orientation of a person or vehicle in relation to a fixed reference object. The *time determination* process solves for the accurate absolute time at a given instance, or *epoch*. *Position determination* is the process that solves for the location of the vehicle. *Attitude determination* is the process of determining the orientation of the vehicle with respect to a chosen to set of reference coordinate axes. Additionally, navigation may include determining the velocity of the vehicle, or the direction and speed of its current motion. These processes determine the state of the vehicle at a given instance. Once resolved, the navigation information can be utilized to guide the vehicle to its planned destination.

In order to pursue their intended mission, spacecraft utilize navigation information for assisting the computation of the optimal guidance path required to achieve its target orbit or rendezvous with an object. Once the necessary path has been calculated, the control of the vehicle can be implemented via spacecraft maneuvers, which may include re-orientation and/or impulsive engine thrusts [93, 195, 224]. Precise control is necessary so that the vehicle will accurately maintain its position and attitude along the intended path. Navigation updates computed as the vehicle traverses the path identifies any necessary corrections that are fed back into this navigation, guidance, and control processing loop.

A navigation system that can determine position in an *absolute navigation* sense can determine where a vehicle is at any instance, without necessarily requiring any *a priori* information about its location or motion. Methods that provide a user with absolute position information are critical for many applications, including situations where a spacecraft is *lost-in-space*, or when no position information is known at all. However, determining position in a *relative navigation* sense, such that a spacecraft can maneuver with respect to a target planet or other vehicle is also useful for many applications.

Celestial navigation is the process of navigation based upon the positions of persistent radiation celestial objects. This dissertation provides information on how to determine a navigation solution of a spacecraft utilizing the signals of celestial sources whose signal intensities *vary* periodically. Most of the discussion is presented with respect to time, position, and velocity determination, although aspects of attitude determination are presented in limited scope.

Chapters 3 and 4 have provided models and methods to compare the measured pulse TOA from a variable celestial source to a predicted TOA within an inertial frame. This Chapter provides additional discussion on how these comparisons can be used for each aspect of spacecraft navigation. Chapters 6 through 8 provide further details on the specific methods of absolute, relative, and delta-correction position determination, as well as empirical and simulated examples to demonstrate performance.

5.2 Time Determination

It has been shown that an accurate clock is a fundamental component of a spacecraft navigation system. The plots in Chapter 3 show that the stability of the pulses from several pulsars match the stability of several of today's atomic clocks over the long term. The signal from these pulsars can be used to stabilize an onboard spacecraft clock. Therefore, perhaps the most significant benefit of pulsars is to provide accurate atomic clock quality time based solely upon celestial observation [127, 167]. Detecting pulsations from celestial sources does not provide a direct measurement of absolute time; however, the stable pulsations can adjust the drift of spacecraft's clocks to maintain accurate time.

A method of correcting clock time using a *phase-locked loop* can be implemented [72]. As shown in Figure 5-1, within this feedback loop, the phase difference between the local clock's oscillator and the reference signal from the pulsar is driven towards zero. Using repeated pulsar observations, the phase differences are continuously computed and any local clock errors are removed. However, this method must coordinate the measured pulsar phase information with the velocity of the vehicle and potentially the orbital dynamics information, as phase shifts are present in the signal from pulsars as the vehicle moves toward or away from the source in its orbit.

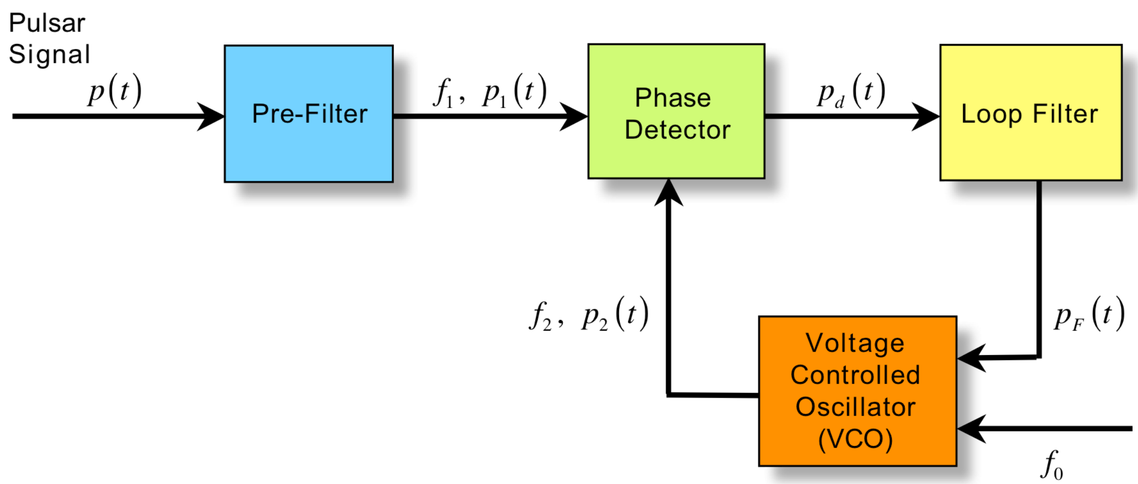

Figure 5-1. Phase-locked loop for clock adjustment [72].

Alternatively, individual pulse arrival times can be used to correct clock time. The offset between the measured pulse arrival time and the predicted arrival time provides a measure of the error within a spacecraft clock. This assumes that most, if not all, of the offset is timing error. Using the model of the spacecraft clock's expected behavior, such as clock drift or known effects due to temperature variations, the measured pulse arrival time offset can adjust the clock's output accordingly.

For example, given initial estimates of clock bias, b_C, scale factor, k_C and jitter, j_C, a filter that incorporates the dynamics of these parameters, such as a Kalman filter, can be created to update these clock parameter values. The true time, τ_T, can be represented using the spacecraft clock time, τ_C, and a reference time, τ_0, by the following,

$$\tau_T = \tau_C + b_C + k_C\left(\tau_C - \tau_0\right) + \frac{1}{2} j_C\left(\tau_C - \tau_0\right)^2 + \eta_C\left(\tau\right) \tag{5.1}$$

The measurement provided to the filter would be the difference between the true time and the measured clock time, and this relates to these parameters where noise is ignored as the following,

$$\delta\tau = \tau_T - \tau_C \cong \tau_P - \tau_C = b_C + k_C\left(\tau_C - \tau_0\right) + \frac{1}{2} j_C\left(\tau_C - \tau_0\right)^2 \tag{5.2}$$

In this representation and within the filter, the true time is estimated using the predicted pulse arrival time, τ_P, from one or several pulsars.

The clock model dynamics and measurement could be further incorporated into a Kalman filter that includes other navigation states, such as vehicle position and velocity. Accurate time determination using the relativistic effects presented in Chapter 4 requires position and velocity information. Incorporating time determination within this larger Kalman filter design allows these processes to be combined and operated simultaneously. Chapter 8 provides additional discussion on estimating clock parameters within a Kalman filter.

5.3 Attitude Determination

Determining attitude of a spacecraft can be accomplished using pulsar observations through several methods. Much of the discussion throughout this dissertation has concentrated on celestial sources that produce variable intensity signals. However, for attitude determination persistent, or non-variable, X-ray sources provide equally good candidates that can be identified due to their specific characteristics of flux and image. Chapter 2 identifies several types of X-ray celestial sources with low variability in their intensity. The orientation of the image of these nearly persistent sources provides a method to determine the attitude of the detector. Pulsars are also potential source candidates for attitude determination, as long as their pulse signal can be identified during the observation time window. The methods suggested here for these sources are similar to the processes employed by existing optical star cameras and trackers except that X-ray wavelengths are measured instead of visible wavelengths.

Assuming a static, or fixed, detector on a spacecraft, attitude of the vehicle can be determined by detecting a source in the sensor's FOV and comparing the resulting signal against a database of known X-ray source characteristics, profiles, and images. Once the source is identified, its image on the detector plane determines angles within the sensor coordinate frame. The line-of-sight to the source is known in inertial frame coordinates, and the sensor to inertial frame transformation provides vehicle attitude. A detector pointed randomly in the sky will either detect a recognizable source or the X-ray background. For detected signals above the background level, comparisons can be made which will help determine which, if any, source is in the FOV of the detector. For a static detector it may take some time for a detectable source to enter its FOV, which will depend on vehicle rotation rate and FOV size. Because X-rays are very short wavelength, they cast sharp shadows such that diffraction is not the limiting factor for attitude determination. The achieved accuracy depends on the detector area, acceptable integration time, detector position resolution, and detector mask scale and distance. Plausible systems could achieve attitude accuracies of arcminutes to arcseconds depending on the particular design. Once a pulsar is detected and identified, however, the pulsar location information provides a means of determining the sensor's, and hence the vehicle's, attitude. The line-of-sight to the pulsar will be known in inertial frame coordinates, and once detected by the sensor, the sensor to inertial frame transformation provides vehicle attitude. Very slowly rotating spacecraft could also use this type of attitude determination process. Attitude rate information may also be derived by observing the slew of the image of a source across the detector's FOV [72].

Alternatively, a gimbaled sensor system can be used to scan various X-ray source locations in the sky to hasten the process of detecting a suitable source [72]. However, a gimbaled system requires a high performance drive and control system in order to maintain fine pointing resolution while on a moving platform, which may impact vehicle design.

The USA experiment used a two-axis gimbal system to point its detector to desired source locations [72, 166, 232]. During its mission, the USA experiment was used to detect an offset in the roll axis of the host *ARGOS* satellite by sweeping the detector past a known source. Since the vehicle's navigation system attitude solution was incorrect by a small amount, the source detection did not occur at the expected attitude. By adjusting the values of roll and yaw of the *ARGOS* vehicle, the USA detector was then re-oriented and again pointed at the known source. This process was continued until satisfactory source detection occurred based upon determined gimbals and vehicle attitude. This iterative, or feedback, method could be employed for attitude determination systems.

5.4 Velocity Determination

Various mission applications may require knowledge of a vehicle's velocity, or speed and direction. For instance, when a spacecraft requires an orbital maneuver, the velocity of the vehicle is used to determine the appropriate point in its orbit to accomplish the rocket firing. A straightforward method to determine a spacecraft's velocity is to accumulate a sequence of position estimates using any of the methods described within this dissertation using variable sources. The velocity can then be computed using the difference of successive position estimates divided by the time interval between estimates. Thus by determining the differential of position over time, vehicle velocity can be established. Since position determination inherently contains noise from the pulse measurements, this differentiation process will amplify this noise in the system, which reduces the accuracy of the velocity calculation. This position derivative method may have only limited use, such as a verification technique, or for start-up mode in a lost-in-space scenario.

Velocity may also be determined using a pulsar's signal Doppler shift. Because pulsars transmit pulse signals that are periodic in nature, as a spacecraft moves toward or away from the source, Doppler effects will be present in the measured pulsar signal. Second-order and higher Doppler effects may be significant depending on the pulsar signal and vehicle motion. Measuring the pulse frequency from a pulsar and comparing this to its expected model can determine the Doppler shift. The Doppler shift can then be converted to speed along the line-of-sight to the pulsar. Assembling measurements from several pulsars allows full three-dimensional velocity to be determined. Whereas some processes will attempt to minimize the Doppler effect by selecting sources that are perpendicular to the vehicle's plane of motion, this velocity determination method pursues sources that produce the maximum Doppler effect. Higher order relativistic Doppler effects should also be included for increased accuracy [148, 149].

For systems that evaluate pulse cycle ambiguities, the triple difference calculation can also produce an estimate of spacecraft velocity. This method is presented in Chapter 6 [189]. Although this method may amplify measurement noise as in the position-differenced method above, once accurate pulse cycles are known, only the cycle phase measurements are processed. These types of measurements will most likely have less noise than full position estimates.

5.5 Position Determination

Given the unique, periodic signatures of pulsars, it is possible to determine position of a spacecraft. The position, or location, of the vehicle is determined with respect to a desired inertial frame. Position knowledge is necessary for spacecraft mission operations such as verifying the correct trajectory path, scheduling observations of science objectives on planetary bodies, rendezvousing with other spacecraft of orbiting bodies, etc. The success of these operations typically depends on the achievable position knowledge accuracy.

This section discusses several possible methods using variable celestial sources for computing the position of a spacecraft. The two methods of occultation and pulsar-elevation are similar to existing visible source celestial navigation methods. However, these methods offer an advantage over optical systems since X-ray signals are difficult to blind in a conventional manner. A major disadvantage of these methods is their requirement of having another celestial body simultaneously in view with a pulsar. Due to the characteristics of the body, detectors in different wavelengths, such as visible, may be required to detect both the body and the pulsar at the same time.

Two new methods are presented based upon the periodic pulse generated by these celestial objects. In these methods, pulse-timing differences between the spacecraft and the reference origin provide a measure of the spacecraft's position offset along the direction towards the source. These methods use accurate pulse TOA measurements from these sources, which requires coordinate time conversion and the barycenter offset corrections to be applied as presented in Chapter 4. However, these corrections require spacecraft position knowledge in order to be correctly implemented. This requirement of position information presents a dilemma if trying to resolve spacecraft position. Resolution of this dilemma is discussed in these methods described below. Additionally, the process of position determination may require the additional navigation components of time, attitude, and velocity to be determined. However, this depends on the type of detectors that are implemented within the navigation system and their available FOV.

Although the SSB provides one inertial coordinate frame and reference origin, it is also useful for mission operations to also relate vehicle position to Earth's position. Several of the methods discussed here can produce position relative to Earth. Methods for determining position of spacecraft on interplanetary trajectories or missions about other planets can be extended from these Earth-based methods.

5.5.1 Source Occultation Method

Occultation of an X-ray source by Earth's limb provides position information for Earth-orbiting spacecraft [17, 229]. As a vehicle revolves about Earth in its orbit, X-ray sources move behind the limb and then reappear on the other side. The time spent behind Earth represents a chord length of Earth's disc. Knowing the source position and Earth's dimensions, it is possible to determine the position of the vehicle relative to Earth.

In the Earth-limb occultation method, a detector on the spacecraft is pointed towards Earth's limb and sources are observed as they pass behind the limb. A short duration of occultation can be interpreted as either a source only grazing Earth's limb, or the spacecraft is far from Earth such that Earth's disc creates only a very small area in the detector's FOV. A long duration of occultation can be interpreted as a source traversing the full diameter of the occultation disc, or the spacecraft is so close to Earth that its disc nearly covers the detector's FOV. Expected visibility durations can be computed using the visibility algorithms of Chapter 8. Figure 5-2 provides a diagram of a pulsar being occulted by Earth as the viewer moves along an orbit path.

Constituents of Earth's atmosphere absorb X-ray photons from these sources. Thus, knowledge of Earth's atmosphere is required since the X-ray signals would begin to be absorbed by the atmosphere as the source passes close to the limb [231]. The science of aeronomy must be used in this method, as information about the constituents of the atmospheric regions can be studied. Alternatively, this occultation method could be used about any planetary body that occults the visibility of a pulsar. The body must have known dimensional parameters, positional ephemeredes, and atmospheric elements to be a good candidate for this method.

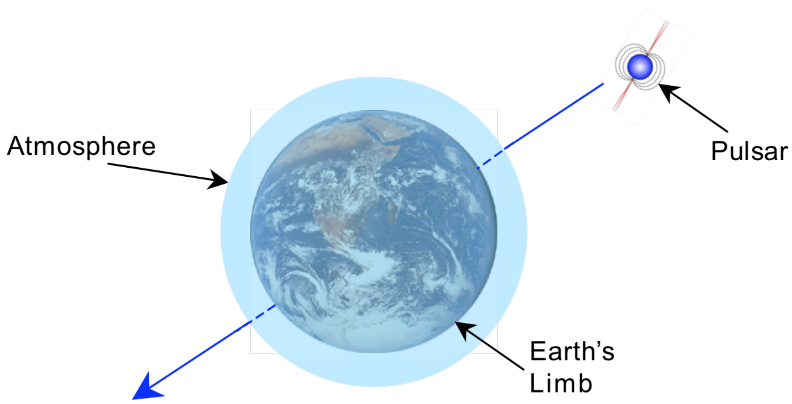

Figure 5-2. Occultation of pulsar due to Earth's disc and atmosphere.

5.5.2 Source Elevation Method

A vehicle with known inertial attitude can point its detector in the direction of a chosen X-ray source. By simultaneously observing a reference planetary body, elevation angles between the source and reference body, as well as the apparent diameter of the body, can be used to determine the range of the detector relative to the body [17]. Nearly persistent X-ray sources, as well as identifiable pulsars are candidates for this method, and multiple sources are required for full position determination.

Figure 5-3 shows a diagram of this method, where γ_E is the apparent angular diameter of Earth, and A_E is the measured angle from the line-of-sight to a pulsar with respect to the spacecraft, $\hat{\mathbf{n}}$, and the edge of Earth's limb. Using the known radius of Earth, R_E, the range of the spacecraft from Earth can be represented as,

$$r_{SC/E} = \frac{R_E}{\sin(\gamma_E)} \tag{5.3}$$

This component of this spacecraft position along the pulsar's line-of-sight from the spacecraft is related to the full position by the following,

$$\hat{\mathbf{n}} \cdot \mathbf{r}_{SC/E} = -r_{SC/E} \cos\left(A_E + \gamma_E\right) \tag{5.4}$$

It can be seen from Figure 5-3 that the two angles are functions of the spacecraft's distance from Earth, as $\gamma_E = \gamma_E\left(\rho_{SC/E}\right)$ and $A_E = A_E\left(\rho_{SC/E}\right)$. Differentiating these expressions with respect to the spacecraft position vector, solutions for components of the position vector can be computed [17]. Adding measurements with other pulsars and other celestial bodies, such as the Moon shown in Figure 5-3, allows determination of the full three-dimensional position vector. Since this method determines relative position with respect to the planetary body, absolute vehicle position can be determined by using the knowledge of absolute position of the body.

Sensors that can detect objects within multiple wavelengths may be required for this method – X-ray for the source and optical for the planetary bodies. However, Earth and the Moon are bright in X-ray wavelengths on their sun-lit sides, which may allow an X-ray-only system. The simultaneous observation of multiple objects within the FOV requires a complex system of detectors and processing. This method may only be useful when orbiting a planetary body, as during interplanetary trajectories planetary bodies may not be adequately viewable.

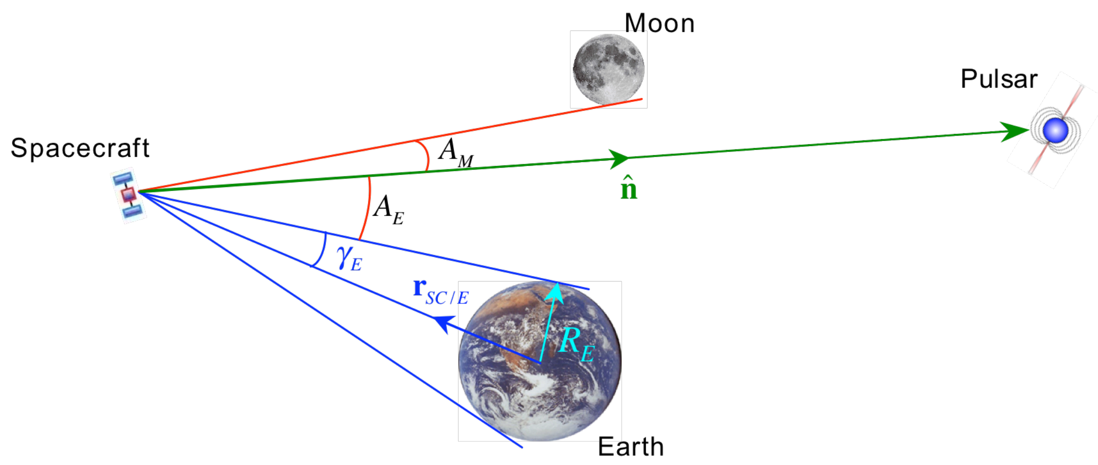

Figure 5-3. Spacecraft position with respect to Earth and elevation of pulsar.

5.5.3 Absolute Position Determination

An onboard navigation system that can operate in an absolute, or *cold-start,* mode is very desirable for many spacecraft applications. In this mode, the navigation system generates a complete three-dimensional position solution using its equipment and source measurements. This type of system does not require assistance from external navigation systems, such as DSN or GPS. Absolute position determination allows a spacecraft to navigate and guide itself to its intended target with complete autonomy. It is also very advantageous after abnormal circumstances, such as a computer reset or vehicle power failure.

To determine absolute position from variable celestial sources it is necessary to determine which specific integer phase cycle, or pulse period, is being detected at a certain time. A celestial source does not uniquely identify each of its pulses, so techniques must be developed to identify a detected pulse relative to a chosen reference pulse. By tracking the phase of several pulsars and including the pulsar line-of-sight directions, it is possible to determine the unique set of cycles that satisfies the combined information to compute absolute position relative to the inertial origin. The cycle identification, or resolution, process determines the numbered cycle through its selection criteria and testing. Once it is determined which specific cycle is detected, then range between the origin and the spacecraft can be determined along a source's unit direction.

Multiple simultaneous pulsar observations may be required for this process. Successive observations should be corrected for time differences, and may be used if vehicle motion is relatively small between observations. This identification process is similar to the GPS *integer cycle ambiguity-resolution* method. Offering an advantage over GPS, pulsars can provide many different cycle lengths, some very small (few milliseconds) to very large (many thousand of seconds). These diverse cycle lengths assist the pulse integer cycle resolution method. Chapter 6 provides an in depth study and analysis of the absolute position determination process using variable celestial sources.

5.5.4 Relative Position Determination

As important as determining the absolute position of a spacecraft, resolving its *relative* position with respect to another known object (other spacecraft, observation station, planetary body, etc.) can be equally important. This method allows relative navigation with respect to this object in the object's frame of reference, without requiring full inertial positional knowledge.

An advantage of this method is that only relative position differences or range differences may be needed for this application instead of a full three-dimensional solution. Also, techniques similar to those used for absolute position determination can be implemented within this method. The computation of the number of integer phase cycles between the spacecraft and the known object can determine the range between the two positions. Since this would typically be a shorter distance than the range between the spacecraft and the inertial origin, the cycle resolution process in this relative position method may be simpler due to the fewer number of cycle candidates. Chapter 6 provides further detail on the algorithms for relative navigation position determination.

5.5.5 Delta-Correction To Position Solution

A more subtle but equally important method of position determination is the correction of an existing, approximate position solution. These *delta-correction* techniques are used to update, or correct, a working solution of position such that improved solutions are produced. Various schemes can be implemented to produce an approximate solution. These include onboard orbit propagators, range measurements from DSN, other position determination methods described above such as source occultation, source elevation, absolute, and relative navigation. The signals emitted by variable celestial sources can then measure the error within the estimated solution, such that successive measurements refine the estimated solution to an acceptable level of accuracy.

Spacecraft launched on predictable trajectories or on known orbits around planetary bodies with few anticipated disturbances can utilize the methods of the delta-correction techniques to assure the computed path is accurate. Additionally, time and velocity components of navigation can be updated through the same delta-correction techniques.

Chapters 7 and 8 provide additional description of this technique, as well as a simulation study that presents the expected navigation performance based upon this method.

5.6 *Variable Celestial Source-based Navigation System Description*

A navigation system based upon the signals of variable celestial sources, including pulsars, would be comprised of a sensor to detect pulsar photons at the spacecraft, a clock onboard the vehicle to time the photons' arrival, and a database of known timing models for pulsars. Once a pulsar is identified and a pulse TOA is determined, this information can be utilized to update or determine attitude, velocity, time, and/or position. Figure 5-4 presents a simplified data processing flow chart using pulse TOA measurements.

The necessary sequence of navigation solution determination is the following:

- Time Determination – Needed to align pulse information, select appropriate pulse models, ensure accurate photon event time tagging. Pulse timing can update clock estimates.
- Attitude Determination – Necessary to determine orientation of spacecraft and detector gimbal angles to place pulsar within FOV of detector. Determines if vehicle is rotating or tumbling at an acceptable rate.
- Velocity Determination – Determines direction and speed of vehicle. Assists with selecting sources perpendicular to vehicle path to decrease Doppler effects.
- Position Determination – Determines instantaneous position of vehicle. Used to improve estimates of position and velocity. Interrelated with accurate time determination and time transformation.

For a spacecraft that has no navigation solution, or for a start-up or calibration mode of the navigation system, the system must progress through this sequence to complete the full navigation solution. The order of time and attitude determination could be interchanged depending on the criticality of mission operations, or if time were already provided by onboard clock or an external provider. The methods described in this dissertation show that the determination of the navigation components of time and position are coupled. Independent methods of determining each of the components are desirable, and future research may provide alternative options for their computation.

In order for this navigation system to operate correctly, the system must provide continuous output of time, as this is the most fundamental component for navigation using the methods presented here. A free-running clock that is started upon initialization from an external reference and is independent of the spacecraft sub-systems may be required. This would be especially important after unforeseen circumstances such as a vehicle power failure, or a computer processing system reset.

Figure 5-5 provides a diagram of the schematics for a pulsar-based navigation system for a spacecraft. Various detector types could be used in this system. Appendix E provides descriptions of these detectors that could be used for X-ray source-based navigation. Additional instrumentation may be required for each type of detector in order to reduce the effects of the X-ray background and successfully time the arrival of each photon. Since most designs are planar arrays of detector components, the detector could be mounted upon a one-axis or two-axis gimbaled system to provide continuous viewing of a source independent of the vehicle's motion or current attitude. This may require additional power, processing, and gimbal sensors to maintain the fine alignment of detector with the source, but the benefits of increased performance and viewing potential would offset these disadvantages. If multiple detectors are integrated into a single system, future designs may not require the detector to incorporate a gimbaled system for pointing.

Since a complete spacecraft navigation system is rarely comprised of only a single detector or sensor, many spacecraft utilize complementary and redundant components to enhance the overall navigation solution. External sensors such as GPS or DSN could be used when available. Onboard sensors such as atomic clocks, gyros, and accelerometers would increase overall autonomy. Sensors historically used for spacecraft navigation such as magnetometers, sun sensors, horizon sensors could aid these onboard sensors. Other types of celestial navigation sensors, such as optical star cameras and trackers could supplant navigation information when necessary or provide a traditional backup system [221]. Blending of all the navigation sensor's data could be accomplished within a central navigation Kalman filter. Upon producing its best solution, the navigation system would pass this solution onto the vehicle's guidance and control system to ensure the intended trajectory path and mission objectives are being met.

The navigation system would include a database of source ephemeris and characteristic data to be used as needed. Thus, maintenance of this database would be provided by an external entity, most likely the entire astronomical community. As new sources are discovered, the database could be updated via communication by the spacecraft's ground operations, or perhaps an orbiting base station that periodically broadcasts up-to-date source information.

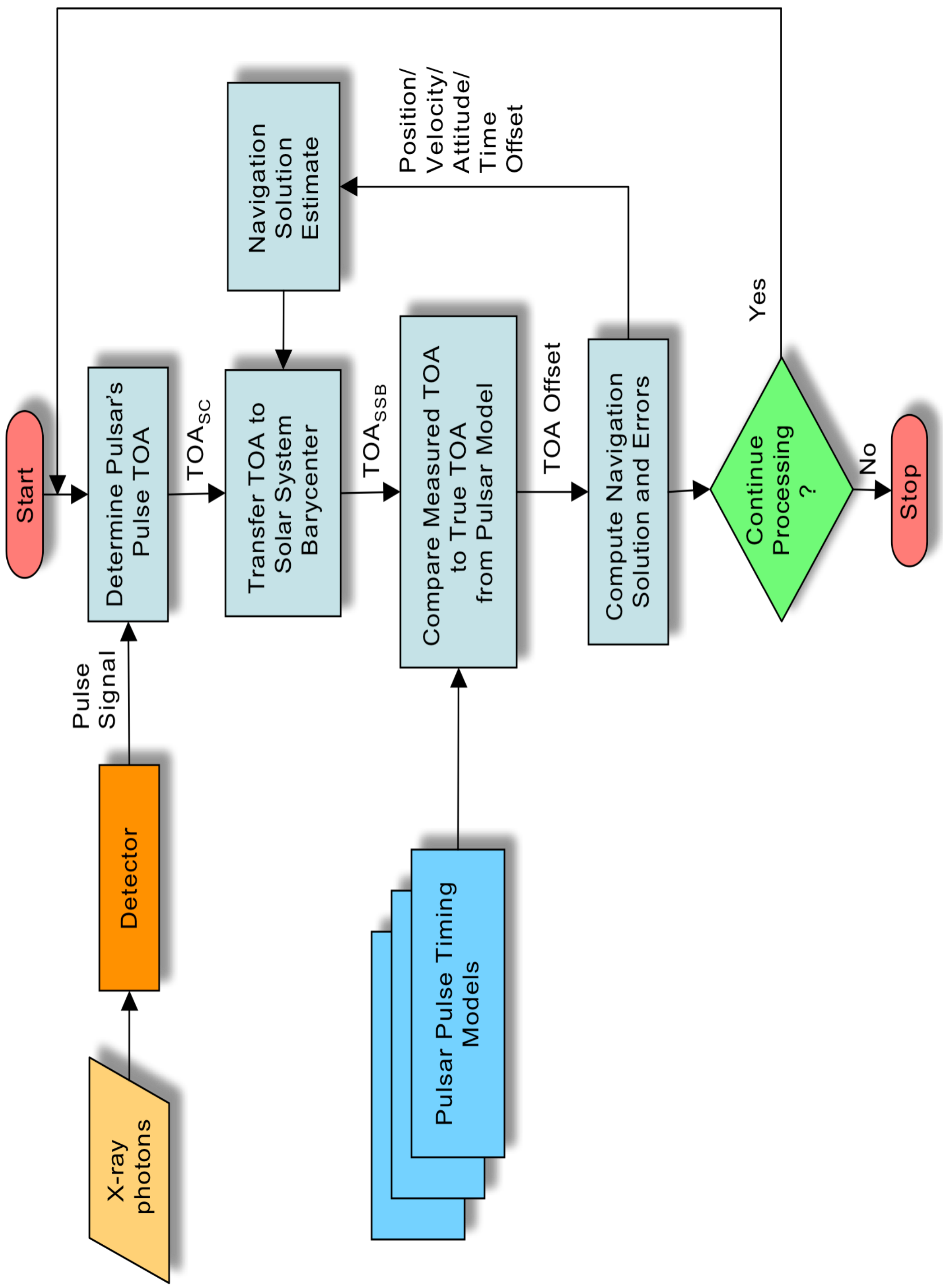

Figure 5-4. Pulsar-based navigation system data processing flowchart.

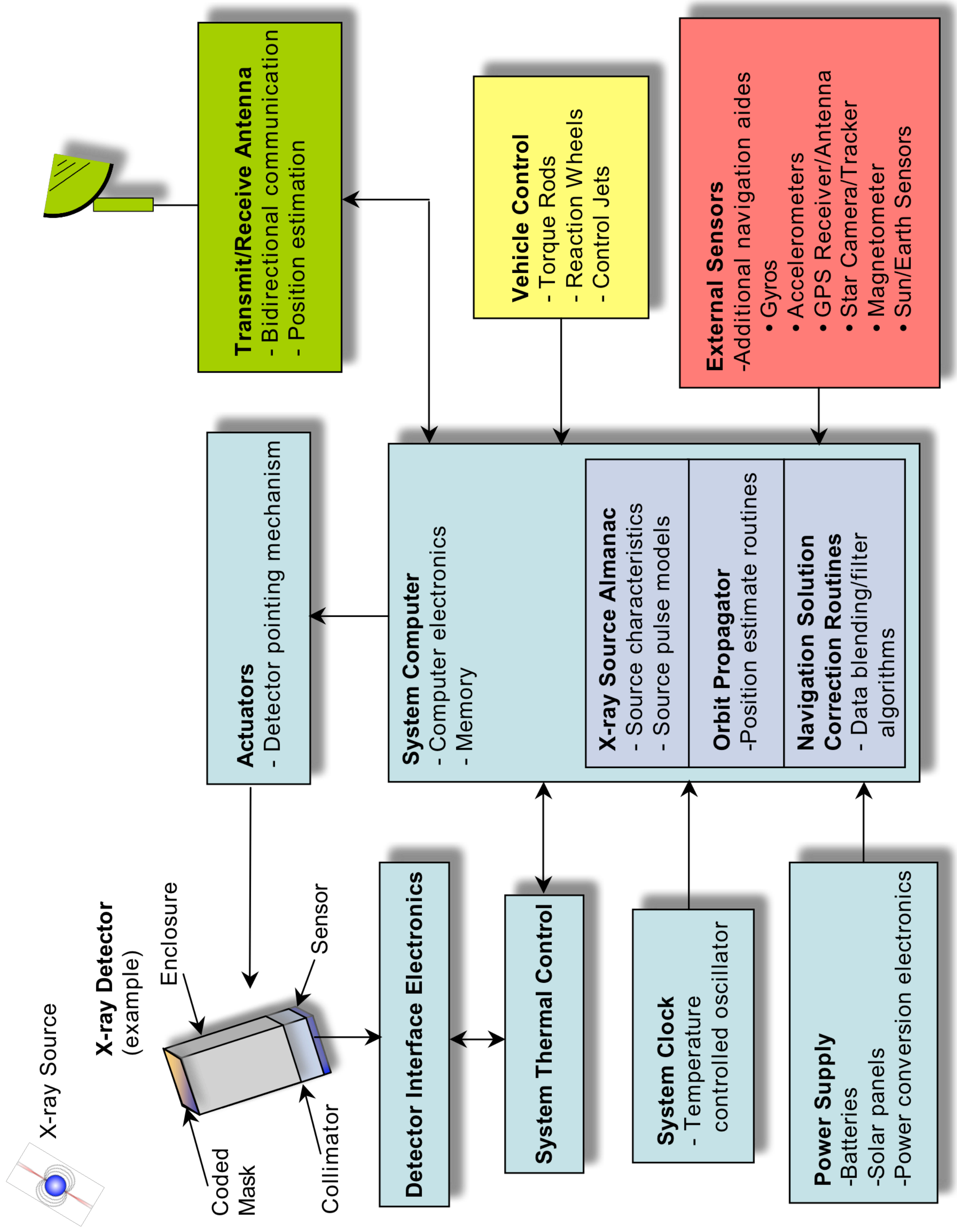

Figure 5-5. Navigation system schematic.

Chapter 6 Absolute and Relative Position Determination

"Each thing is of like form from everlasting and comes round again in its cycle."

– Marcus Aurelius

6.1 Description

The absolute position of an object is its three-dimensional location specified in an inertial frame. Determining the absolute position of a spacecraft allows the vehicle to immediately recognize its relationship to other nearby objects, allows the vehicle to safely control itself around potential obstacles, and most importantly assists the vehicle in pursuing its intended mission. Navigation systems that can report the absolute position of the vehicle to its guidance and control systems provide increased vehicle autonomy, safety, and reliability.

Various existing methods solve for absolute position of a user, include using fixed visible star references; map reading; time references; Earth-bound navigation system such as LORAN or OMEGA; and Earth-orbiting systems, such as GPS, GLONASS, and the proposed European Galileo system. Via the radio signal provided by the GPS or GLONASS systems, users can triangulate their location from the accurate range measurements between the user and the known locations of the orbiting, transmitting satellites. These systems have shown to provide impressive navigation accuracies for time, position, velocity, and attitude [156, 157]. However, limitations do exist for these systems, including limited signal visibility and availability, low source signal strengths, and these systems only operate near-Earth, since the primary function of these systems is to provide for Earth-bound users. For applications far from Earth, or where GPS/GLONASS signals are unattainable, different methods of determining absolute position determination is necessary.

In this Chapter, it is shown that variable celestial sources, including pulsars, can be utilized to determine accurate absolute position [189, 193]. In order to utilize sources for absolute position determination, the specific pulse cycle received from a source must be identified. Methods are developed to show how the unknown, or *ambiguous*, number of pulse cycles can be determined. Once any unknown cycles are resolved, absolute position of a user can be produced with respect to a reference frame origin. An important attribute of this method is that it is applicable to all regions of space. The method is valid throughout the solar system, as well as further into the Milky Way galaxy, and perhaps beyond, as long as sufficient measurements can be processed to solve for the ambiguous pulse cycles.

The determination of unknown cycles for variable celestial sources, or *pulse phase cycle ambiguity resolution* process, is in some manner similar to the methods used in GPS/GLONASS navigation systems, including particularly those used for surveying and differential positioning systems. However, the ambiguity resolution process for variable celestial sources is unique in many ways from the GPS/GLONASS systems, including the following:

- Antennas vs. Models: GPS/GLONASS systems use multiple antennas and receivers to determine cycle ambiguities measured between the antenna locations. Pulsar-based systems would primarily use the measured pulse arrival at a detector and compare this to the expected arrival time produced by a model at another location in order to determine absolute position of the detector. No detector is physically located at the model's location. A relative positioning system, however, may be able to use multiple detectors at different locations to determine the offset of each detector relative to one another.
- Different Frequencies: The GPS system currently uses one, or perhaps two, cycle periods, or frequencies, to complete its ambiguity resolution process. Each pulsar, however, has a unique signature, thus each cycle period can be quite different. The pulsar-based ambiguity resolution process must evaluate each different signal and utilize this different period length. These many different pulse cycle lengths, some very small (few milliseconds) to very large (many thousands of seconds), can assist the cycle ambiguity resolution process.
- Availability and Control: The GPS and GLONASS systems are developed and maintained by humans. The satellites within each system are bound to an Earth-orbit and their signal strength primarily allows for near-Earth observations. Celestial sources have been developed and maintained by the Universe. Although control of these sources is unavailable, their immense

distance and high signal strength allow them to provide usable signals throughout the Milky Way galaxy and beyond.

- Multiple Wavelength Observations: Radio band emissions from these celestial sources can be received in space and on Earth's surface. X-ray emissions from these sources are absorbed by Earth's atmosphere, thus use of this wavelength is limited to space or planetary body applications. A pulsar-based navigation system can use the different wavelengths of these sources, anywhere from radio through gamma-ray bands. Different pulse detection methods and hardware may be required in different wavelength bands.

- Range vs. No Range Measurements: The GPS/GLONASS methods make use of direct measurements of range between the orbiting satellite and the receiving antenna through the accurate time tagging of data from the satellites. Celestial sources, however, are very distant from the solar system and these distances are not known to sufficient accuracy. These sources do not provide labeled time information with their signal, thus no direct measurement of range is made from these sources.

- Carrier Wave vs. Signal Pulse: The GPS/GLONASS cycles are determined from the radio wavelength *carrier* wave combined with the *code* signal. Pulsars emit pulses directly at a specified frequency. Although the carrier signal from pulsars could be monitored, the pulse cycles themselves are used in the ambiguity resolution process.

- Phase Rate vs. Doppler Effects: GPS/GLONASS receivers can accurately track the carrier wave of the signal transmitted from the orbiting satellites.

> Thus, measurements of carrier phase rate can be used in GPS/GLONASS cycle ambiguity resolution. Since the carrier wave is not directly tracked from pulsars, this phase rate cannot be measured. However, it may be possible to determine the rate of change of pulse phase as the detector is in motion due any observed signal Doppler effect.

Alternatively, this navigation process can be applied to determine the position relative to another translating or rotating object. The process of *relative navigation* is similar to absolute navigation in that it determines information relative to another object. However, in the relative navigation case, this object may or may not be fixed. For example, absolute navigation of a ship on Earth's oceans determines the vehicle's location – such as latitude, longitude, and perhaps altitude – at a given time with respect to the fixed Earth coordinate system. However, relative navigation of this ship would apply in the case of a tugboat approaching the vessel in order to match its speed and direction. These examples also apply to spacecraft in orbit. On a heliocentric orbit, absolute navigation of a spacecraft would include determining the exact position of the vehicle at a given instance with respect to the solar system barycenter (SSB) inertial reference frame. Relative navigation of this same spacecraft would be the process of determining the position offset of a sister spacecraft as the two vehicles maneuver in coordinated flight to accomplish their intended mission.

Both the absolute and relative navigation processes are different from navigation process that use either integrated vehicle motion, *a priori* navigation information, or an estimate of vehicle navigation data. These processes use estimates of navigation values, and new measurements are generated to refine, or update, the estimated values in order to determine a more accurate complete navigation solution. Since no initial estimate is required for absolute, or relative, navigation, many applications benefit from these directly available solutions.

This Chapter provides details of the methods and algorithms to determine the phase cycle ambiguities from pulsars. The following section on *Observables and Errors* provides a description of quantities that are measured from variable celestial sources. Errors that can be significant in this process are also presented. It also discusses the issue of creating pulse profiles and determining pulse TOA without accurate or unknown position knowledge. The section on *Measurement Differences* computes all the necessary differences that are used in the process of computing absolute position. The *Search Space and Cycle Ambiguity Resolution* section describes how to assemble the candidate cycle search space and then test individual candidate cycles in order to determine the most probable location for the user. Various techniques that can be implemented in this resolution process are provided. The *Relative Position* section discusses the use of these navigation techniques for applications where relative position information is required, instead of absolute information. The section on *Solution Accuracy* provides computations that provide estimates of the accuracy of the navigation solution, including methods that help choose optimal sets of sources. The final section of *Numerical Simulation* discusses results of the performance of the described algorithms.

6.2 Observables and Errors

Variable celestial sources emit periodic radiation that can be detected using various methods. Each source produces a unique signal. Due to the stability of the emission mechanisms of the sources, the arrival time of this pulsed radiation is often predictable.

For a pulse arriving into the solar system to the position of the spacecraft relative to the Sun center, $\mathbf{p}$, the relationship of the transmission time, t_T, to the reception time, $t_{R_{SC}}$, is the following from Chapter 4 [188, 192, 193],

$$\left(t_{R_{SC}} - t_T\right) = \frac{1}{c}\hat{\mathbf{n}}_{SC} \cdot \left(\mathbf{D} - \mathbf{p}\right) - \sum_{k=1}^{PB_{SS}} \frac{2GM_k}{c^3} \ln\left|\frac{\hat{\mathbf{n}}_{SC} \cdot \mathbf{p}_k + p_k}{\hat{\mathbf{n}}_{SC} \cdot \mathbf{D}_k + D_k}\right| + \frac{2\mu_S^2}{c^5 {D_y}^2}\left\{\begin{array}{l} \hat{\mathbf{n}}_{SC} \cdot \left(\mathbf{D} - \mathbf{p}\right)\left[\left(\dfrac{\left(\hat{\mathbf{n}}_{SC} \cdot \mathbf{D}\right)}{D}\right)^2 + 1\right] + 2\left(\hat{\mathbf{n}}_{SC} \cdot \mathbf{D}\right)\left(\dfrac{p}{D} - 1\right) \\ + D_y\left(\arctan\left(\dfrac{p_x}{D_y}\right) - \arctan\left(\dfrac{D_x}{D_y}\right)\right) \end{array}\right\} \tag{6.1}$$

For the discussion in this Chapter, the second and third terms in Eq. (6.1) can be combined together into a single parameter, $RelEff$, which represents all the relativistic effects along the light ray path such that,

$$\left(t_{R_{SC}} - t_T\right) = \frac{1}{c}\hat{\mathbf{n}}_{SC} \cdot \left(\mathbf{D} - \mathbf{p}\right) + \frac{1}{c} RelEff \tag{6.2}$$

6.2.1 Range Measurement

The range, ρ, from the source to the observer can be computed from the transmit and receive times of Eq. (6.2) as the following,

$$\rho = c\left(t_{R_{SC}} - t_T\right) \tag{6.3}$$

Using the representation of these times from Eq. (6.2), range can also be expressed in terms of the position vectors as,

$$\rho = \hat{\mathbf{n}}_{SC} \cdot (\mathbf{D} - \mathbf{p}) + RelEff \tag{6.4}$$

The unit vector along the direction from the observer to the source can be written in terms of the pulsar and observer positions as,

$$\hat{\mathbf{n}}_{SC} = \frac{\mathbf{D} - \mathbf{p}}{\|\mathbf{D} - \mathbf{p}\|} \tag{6.5}$$

Using this representation for unit direction, the range from Eq. (6.4) becomes,

$$\rho = \|\mathbf{D} - \mathbf{p}\| + RelEff \tag{6.6}$$

The range vector is defined to be in the direction from the source to the observer. Since the magnitude of a vector is equal to the magnitude of the opposite direction vector, or $\|\mathbf{x}\| \equiv \|-\mathbf{x}\|$, Eq. (6.6) can be more properly stated as the following,

$$\rho = \|\mathbf{p} - \mathbf{D}\| + RelEff \tag{6.7}$$

This form of the equation will be utilized because of the choice of the direction of the range vectors, and will be shown in more detail in the following *Measurement Differences* section.

Eqs. (6.3), (6.4), and (6.7) represent the total path length, or range, that a pulse must travel from a source to the observer. If the observer's position and the source position vectors are accurately known, then the range can be directly determined from Eq. (6.4). Conversely, if a range *measurement* can be computed between the source and the observer along with using knowledge of the source position, rearranging Eq. (6.4) or (6.7) allows a portion of the observer's position relative to the Sun to be computed. Thus any method that can provide an absolute range measurement can contribute to determining observer position.

An absolute range measurement can be computed using Eq. (6.3), if the transmission and reception times are known for an individual pulse, and this measurement could be applied to Eq. (6.4) to determine observer position. However, any measurement system that attempts to use transmission and reception times is limited primarily by the major complication that pulsars do not provide a means to determine *when* an individual pulse was transmitted. Thus, although the reception time can be measured, the transmission time, t_T, is unknown. Contrastingly, navigation system such as GPS, GLONASS and Earth-bound systems provide the signal transmission time, which allows direct computation of range between a user and the transmitting satellite or station. Nonetheless, as will be shown, enough information is provided such that observer position can still be determined using measurements from pulsars.

6.2.1.1 Range Measurement Error

Within a navigation system, the range *measurement*, $\tilde{\rho}$, will differ from the *true* range, ρ, by some error amount, $\delta\rho$. The relationship of the true and measured range can be written as,

$$\rho = \tilde{\rho} + \delta\rho \tag{6.8}$$

In terms of measured, or estimated, transmit and reception time for the i^{th} pulsar, the measured range from Eq. (6.3) is,

$$\tilde{\rho}_i = c\left(\tilde{t}_{R_{SC_i}} - \tilde{t}_{T_i}\right) \tag{6.9}$$

The measured range using transmit and receive time will differ from the true range by several errors, including station clock and signal timing errors at the observer's station,

δt_{SC}, intrinsic timing model errors or unknowns for a specific pulsar, δT_i, and range measurement noise, η_i. Assuming that these errors behaving linearly with respect to the measurement, the true range can be represented as the sum of the measurement and its errors as,

$$\rho_i = c\left(\tilde{t}_{R_{SC_i}} - \tilde{t}_{T_i}\right) + c\delta t_{SC} + c\delta T_i + \eta_i \tag{6.10}$$

Similarly, in terms of measured, or estimated, source and observer position for the i^{th} pulsar, the measured range from Eq. (6.7) is,

$$\tilde{\rho}_i = \left\|\tilde{\mathbf{p}} - \tilde{\mathbf{D}}_i\right\| + \widetilde{RelEff}_i \tag{6.11}$$

This form of measured range will differ from the true range by several errors, including observer position error, $\delta\mathbf{p}$, and source position error, $\delta\mathbf{D}_i$, along the direction to the source, relativistic effects error, $\delta RelEff_i$, as well as range measurement noise. If these errors sum linearly with the measurement, then the true range is represented as,

$$\rho_i = \left\|\tilde{\mathbf{p}} - \tilde{\mathbf{D}}_i\right\| + \widetilde{RelEff}_i + \left\|\delta\mathbf{p}\right\| + \left\|\delta\mathbf{D}_i\right\| + \delta RelEff_i + \eta_i \tag{6.12}$$

The range measurement of Eq. (6.11) uses the magnitude of the geometric difference between the source and the observer. Alternatively, the estimate of line-of-sight direction to the source can be used from Eq. (6.5), such that the measured range is,

$$\tilde{\rho}_i = \tilde{\mathbf{n}}_{SC_i} \cdot \left(\tilde{\mathbf{D}}_i - \tilde{\mathbf{p}}\right) + \widetilde{RelEff}_i \tag{6.13}$$

The errors for this equation include those from Eq. (6.12) and the additional effect of the line-of-sight error, $\delta\tilde{\mathbf{n}}_{SC_i}$, such that the true range is,

$$\begin{aligned}\rho_i = \tilde{\mathbf{n}}_{SC_i} \cdot \left(\tilde{\mathbf{D}}_i - \tilde{\mathbf{p}}\right) + \widetilde{RelEff}_i + \tilde{\mathbf{n}}_{SC_i} \cdot \delta\mathbf{D}_i + \tilde{\mathbf{n}}_{SC_i} \cdot \delta\mathbf{p} \\ + \delta\tilde{\mathbf{n}}_{SC_i} \cdot \left(\tilde{\mathbf{D}}_i - \tilde{\mathbf{p}}\right) + \delta RelEff_i + \eta_i\end{aligned} \tag{6.14}$$

It has been assumed that these representative errors sum linearly. Any non-linear error effects that may prove significant must be included appropriately, which may complicate processing.

6.2.2 Phase Measurement

Variable celestial sources produce pulsed radiation that arrives periodically at a detector. It is this periodic nature of these sources that make them valuable as navigation beacons. Since the periodicity of these sources is stable, it is possible to identify individual pulse cycles. At any given measurement time however, the peak of the pulse, or other identifying structure of the pulse, may not be detected. Instead, a certain instance within the pulse cycle will be measured, which can be represented as the *phase* of the cycle, or the fraction of the pulse period often measured in dimensionless units from zero to one. As presented in Chapter 3, at a given measurement time, a series of cycles can be represented as the total cycle phase, Φ. This total cycle phase is the sum of the fraction of a pulse, ϕ, plus an integral number, N, of full integer cycles that have accumulated since a chosen initial time. Thus, total cycle phase can be written as,

$$\Phi = \phi + N \tag{6.15}$$

The phase of a cycle, or series of elapsed cycles, emanating from the source and arriving at the observer is related to the range between the source and observer by the wavelength, λ, of the cycle,

$$\rho = \lambda\Phi = \lambda\phi + \lambda N \tag{6.16}$$

Therefore, if the number of cycles plus the fraction of the current pulse could be determined between the pulsar and the observer, the range can be computed from Eq. (6.16). This equation provides an alternative method of determining range, rather than using transmit and receive time in Eq. (6.3) or source and receiver positions as in Eq. (6.4). However, celestial sources provide no identifying information with each pulse, so that there is no direct method of determining which *specific* cycle is being detected at any given time. As an example of this relationship, Figure 6-1 provides a diagram of a train of pulse cycles and shows the association of phase and range along certain points relative to the origin.

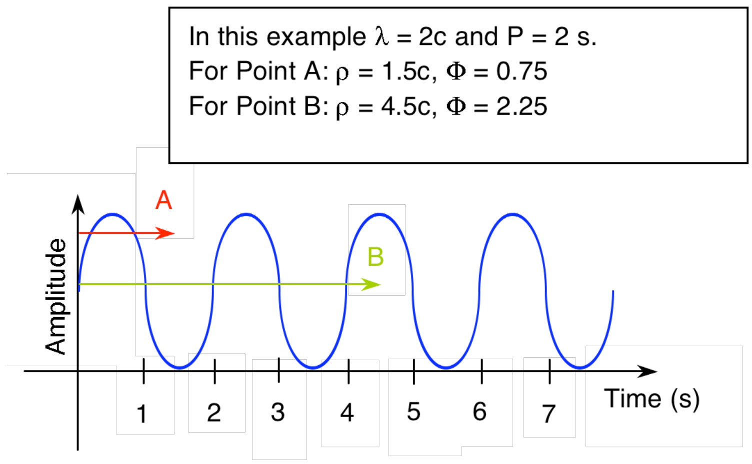

Figure 6-1. Range and phase measurement along a train of pulse cycles.

6.2.2.1 Phase Measurement Error

The total measured cycle phase, $\tilde{\Phi}$, of a celestial source pulse from a detector system will differ from the true phase, Φ, by any phase error, $\delta\Phi$, unresolved within the system, such as,

$$\Phi = \tilde{\Phi} + \delta\Phi \tag{6.17}$$

This phase error can be separated into errors, $\delta\phi$ and δN, within the measured fraction of phase, $\tilde{\phi}$, and the measured number of full cycles, $\tilde{N}$, respectively as,

$$\phi + N = \tilde{\phi} + \tilde{N} + \delta\phi + \delta N \tag{6.18}$$

Using Eqs. (6.11) and (6.16), the measured phase fraction and cycle number relate to the measured source and observer position as,

$$\lambda_i \tilde{\boldsymbol{\Phi}}_i = \lambda_i \left(\tilde{\phi}_i + \tilde{N}_i \right) = \left\| \tilde{\mathbf{p}} - \tilde{\mathbf{D}}_i \right\| + \widetilde{RelEff}_i \tag{6.19}$$

Since the measurement of phase is directly related to the timing of arriving pulses and the distance to the source, the combined effects of the errors from the range measurement of Eqs. (6.10) and (6.12), along with the specific phase measurement noise error, β_i, relate the true phase to the measured phase by the following,

$$\begin{aligned} \lambda_i \boldsymbol{\Phi}_i &= \lambda_i \left(\phi_i + N_i \right) \\ &= \left\| \tilde{\mathbf{p}} - \tilde{\mathbf{D}}_i \right\| + \widetilde{RelEff}_i + c\delta t_{SC} + c\delta T_i + \left\| \delta \mathbf{p} \right\| + \left\| \delta \mathbf{D}_i \right\| + \delta RelEff_i + \beta_i \end{aligned} \tag{6.20}$$

The measured phase can also be computed in terms of the source line-of-sight as in Eq. (6.13) to produce,

$$\lambda_i \tilde{\boldsymbol{\Phi}}_i = \lambda_i \left(\tilde{\phi}_i + \tilde{N}_i \right) = \tilde{\mathbf{n}}_{SC_i} \cdot \left(\tilde{\mathbf{D}}_i - \tilde{\mathbf{p}} \right) + \widetilde{RelEff}_i \tag{6.21}$$

By including the line-of-sight errors from Eq. (6.14), the true phase can be represented as the following,

$$\begin{aligned} \lambda_i \boldsymbol{\Phi}_i &= \lambda_i \left(\phi_i + N_i \right) \\ &= \tilde{\mathbf{n}}_{SC_i} \cdot \left(\tilde{\mathbf{D}}_i - \tilde{\mathbf{p}} \right) + \widetilde{RelEff}_i + c\delta t_{SC} + c\delta T_i + \tilde{\mathbf{n}}_{SC_i} \cdot \delta \mathbf{D}_i + \tilde{\mathbf{n}}_{SC_i} \cdot \delta \mathbf{p} \\ &\quad + \delta \tilde{\mathbf{n}}_{SC_i} \cdot \left(\tilde{\mathbf{D}}_i - \tilde{\mathbf{p}} \right) + \delta RelEff_i + \beta_i \end{aligned} \tag{6.22}$$

6.2.3 Pulse Arrival Time Determination

As discussed previously in Chapters 3 and 4, accurate determination of the pulse arrival time from a pulsar requires time at the detector to be transferred to the SSB and compared to a pulsar-timing model. Utilizing a clock onboard a spacecraft, the timing of photons can be directly determined as these arrive at the detector. In order to create a pulse profile for model comparison, each photon arrival time must be transferred to the model's defined location, in most cases this is chosen as the SSB. However, this time transfer requires knowledge of the spacecraft's position. In the absolute position determination process, it is assumed that no prior knowledge of the spacecraft's position is available, thus the time transfer cannot be implemented as previously presented.

The methods of determining absolute position rely on the difference of range or phase between the spacecraft and the model's defined location. If this location is far from the spacecraft, then many pulse cycles will exist between the two locations. If this location is relatively close to the spacecraft, then it is possible that only a fraction of a pulse cycle exists between the two locations. But in order to calculate these differences, the photon arrival times at the detector must be transferred to this location.

For spacecraft orbiting Earth, one method to avoid accumulating pulse cycles between the vehicle's detector and the SSB is to use pulsars with large periods. Using sources with periods greater than 500 sec $\left(\approx 1AU/c\right)$ ensures there is only one cycle between the SSB and Earth.

Long period pulses, however, also require longer observation time, which may be detrimental to spacecraft operations if a fast absolute position solution is required. An improved method for ensuring that only a few cycles exist between the spacecraft and the pulse model location is to keep the model's defined location *close* to the spacecraft. For spacecraft orbiting Earth, or near-Earth, better pulse model locations would be at the geocenter (Earth-center) or the Earth-Moon barycenter. Although these locations are not truly inertial locations, compensations in the pulse models as well as short observation times would allow these locations to be used. Alternatively, any location near the spacecraft could be used for the model location. For example, a spacecraft orbiting Mars or Jupiter could use the center of those planets or their system's barycenter. These methods require redefining existing pulsar timing models defined at the SSB to these new locations.

Creating pulse profiles with varying assumptions of position knowledge demonstrates the effects of position on profile accuracy. Figure 6-2 provides a high SNR template plot of the pulse cycle of the Crab pulse detected using the NRL USA experiment. The clarity of the pulse is evident from this profile. Figure 6-3 shows the profile results of an observation of the Crab Pulsar made by the USA experiment with time transferred from the spacecraft to the SSB. This observation was made on December 19, 1999, starting at 08:54:05.78 AM and lasting for 483.57 seconds. To create this image, the navigation system onboard the vehicle provides one second updates on the vehicle position and velocity and this information was used to transfer time to the SSB.

If however, spacecraft navigation data were unknown, then this time transfer could not be completed accurately. A starting assumption could be made that the vehicle was located at the geocenter. Figure 6-4 provides a diagram of the same Crab Pulsar observation that uses Earth's center location as the position to transfer time to the SSB. The pulse shape is altered when compared to either the template in Figure 6-2 or the barycentered observation in Figure 6-3. The noise within the pulse has grown. Assuming no knowledge of spacecraft position, Figure 6-4 provides the Crab Pulsar observation using no time transfer at all. Pulse shape is significantly altered, with pulse height intensity being reduced, as well as obviously substantial noise increase. These effects are due to ignoring the spacecraft's position and motion within the inertial frame when computing the photon arrival time.

Table 6-1 provides a summary of the calculated pulse TOA values for these observations. These TOAs were computed by comparing the observed pulsed to the high signal-to-noise template of Figure 6-2. Choosing the geocenter as the location of the pulse detector and transferring this arrival time to the SSB results in a TOA difference of 0.0188 s. This value is less than the pulse period of 0.0335 s, and less than the maximum possible time difference between the geocenter and the 833 km altitude orbit of the *ARGOS* spacecraft of 0.024 s $\left[=\left(833+6378\right)/c\right]$. An improved comparison could be created by developing a pulse arrival-timing model that exists at the geocenter. Then the difference of the pulse arrival time at the spacecraft to the predicted arrival time at the geocenter could be made, instead of the distant SSB. The pulse cycle wavelength is 10,043 km $\left(=0.0335*c\right)$, thus the *ARGOS* vehicle orbit will remain within ±one cycle with respect to the geocenter.

Using the known actual position of the spacecraft, the true time difference between the spacecraft and the geocenter is 0.0167 s $\left(=\hat{\mathbf{n}}\cdot\mathbf{r}_{SC/E}/c\right)$. The difference between this true time difference and the measured TOA difference assuming the vehicle is at the geocenter is 0.0021 s (= 0.0188 – 0.0167). This corresponds to either 630 km of position error along the line-of-sight to the Crab Pulsar, or 6.3% of phase difference for a Crab Pulsar pulse cycle. Thus, by assuming that the spacecraft is at the geocenter creates at Crab TOA measurement that computes a range estimate with error less than 10% of the *ARGOS* orbit radius of 7213 km. Appendix C presents additional sets of data and shows several phase error values.

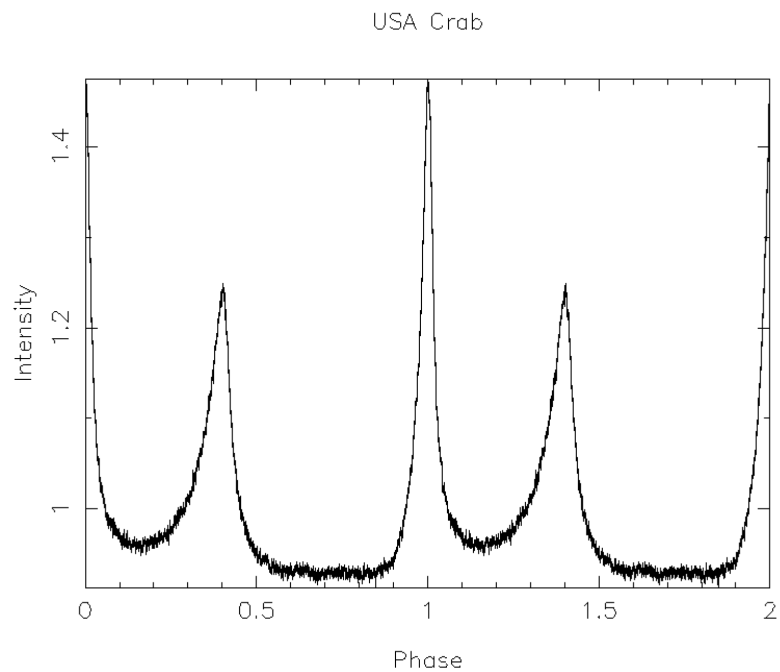

Figure 6-2. High signal-to-noise profile template of two pulses from Crab Pulsar.

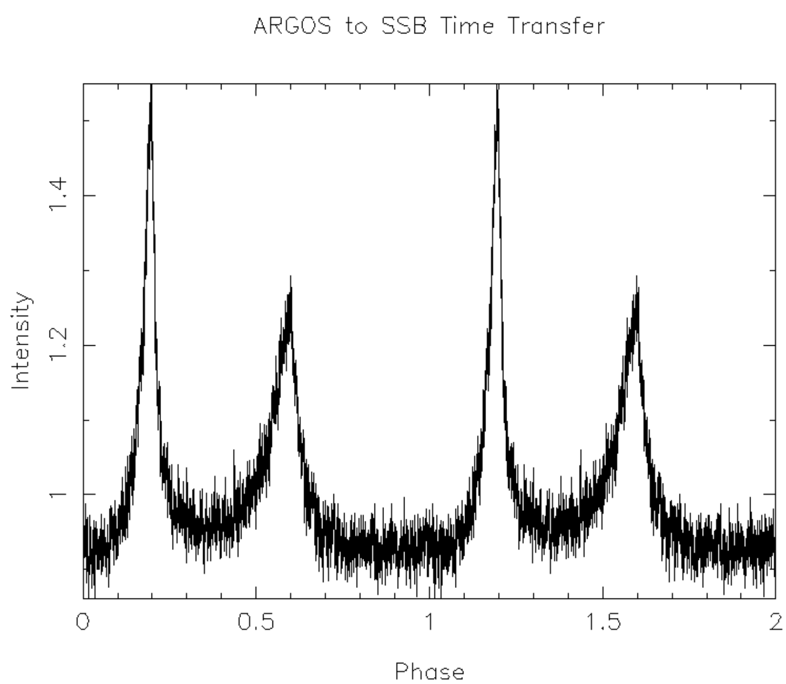

Figure 6-3. Crab Pulsar profile with photon arrival times transferred from *ARGOS* position to SSB.

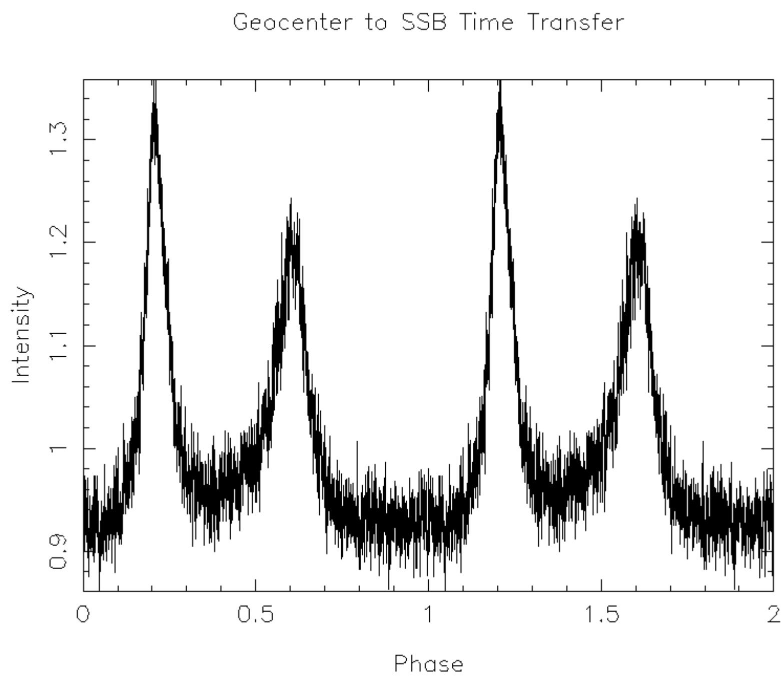

Figure 6-4. Crab Pulsar profile with photon arrival times transferred from geocenter to SSB.

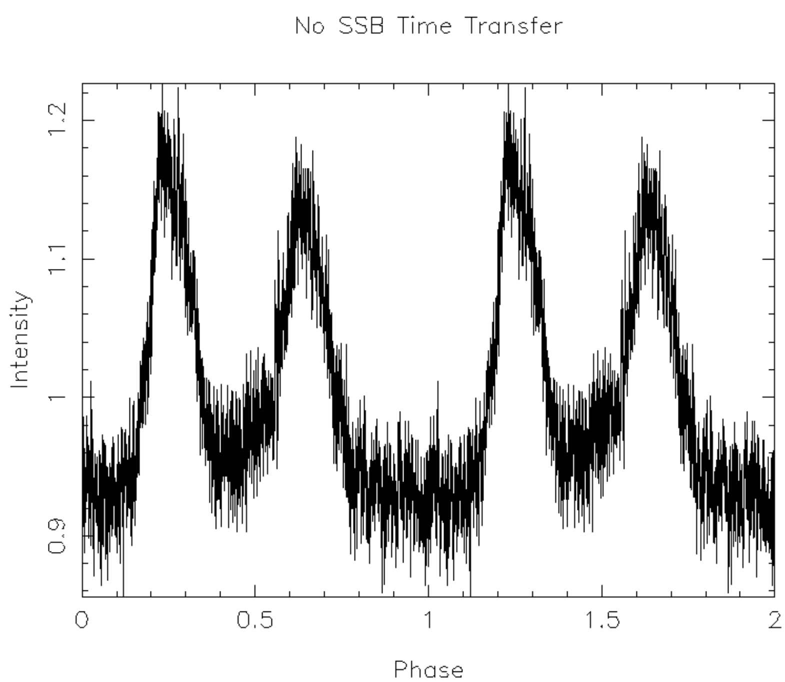

Figure 6-5. Crab Pulsar profile with no time transfer on photon arrival times.

Table 6-1. TOA Calculations and Differences for Crab Pulsar Observation.

Time Transfer	TOA (MJD)	TOA Error (10^{-6} s)	TOA Difference wrt SC to SSB (s)	TOA Difference wrt GEO to SSB (s)
From SC to SSB	51531.3772976203982	9.98	---	-0.0188
From GEO to SSB	51531.3772974026506	7.93	0.0188	---
None	51531.3716434666494	15.98	488.5189	488.5001

If a spacecraft is moving in a plane perpendicular, or nearly perpendicular, to the direction to a pulsar, then arriving pulses will not be affected by the vehicle's motion. However, with motion towards or away from the pulsar, the pulses, as well as the folded pulse profile, would be affected by the Doppler effect produced by the motion. If a folded profile is corrected for this motion by transferring the individual photon arrival times to the SSB, then clear profiles are evident, as in Figure 6-2 or Figure 6-3. If a profile is not corrected to the inertial origin and created only at the vehicle's location, the Doppler effect essentially smears, or distorts, the folded profile. Figure 6-5 provides an image of a Crab Pulsar observation at the *ARGOS* vehicle with no SSB time transfer when the vehicle's motion is close to perpendicular to the pulsar line-of-sight. This motion implies the dot product of the direction and spacecraft velocity is small. For the observation in Figure 6-5 $\hat{\mathbf{n}} \cdot \mathbf{v}_{SC/E} = 0.13\,\text{km/s}$. Figure 6-6 provides an image of another observation on January 3, 2000 at 16:50:00 when the spacecraft's motion distorts the profile due to a higher Doppler effect. In the observation of Figure 6-6 $\hat{\mathbf{n}} \cdot \mathbf{v}_{SC/E} = -4.8\,\text{km/s}$. In order to create TOA measurements for use in the following sections, only observations should be utilized when the vehicle's motion is primarily within this perpendicular plane or for sections of the orbit where the Doppler effect is reduced. Thus, a measure of this Doppler effect must be considered when creating pulse TOAs at the vehicle with no correction to the SSB. It is obvious from these images that the pulse height intensity and shape gives a measure of this profile distortion and presumably the measurement of the size of the Doppler effect.

Creating an iterative scheme involving observations may improve the absolute position determination process. If the first iteration assumes the vehicle is at some predefined location, such as the geocenter, then the TOA differences can be used to correct some of this position estimate. Subsequent iterations of the same observations using these corrected position estimates could further remove position error until a solution is determined that satisfies all observations from different pulsars.

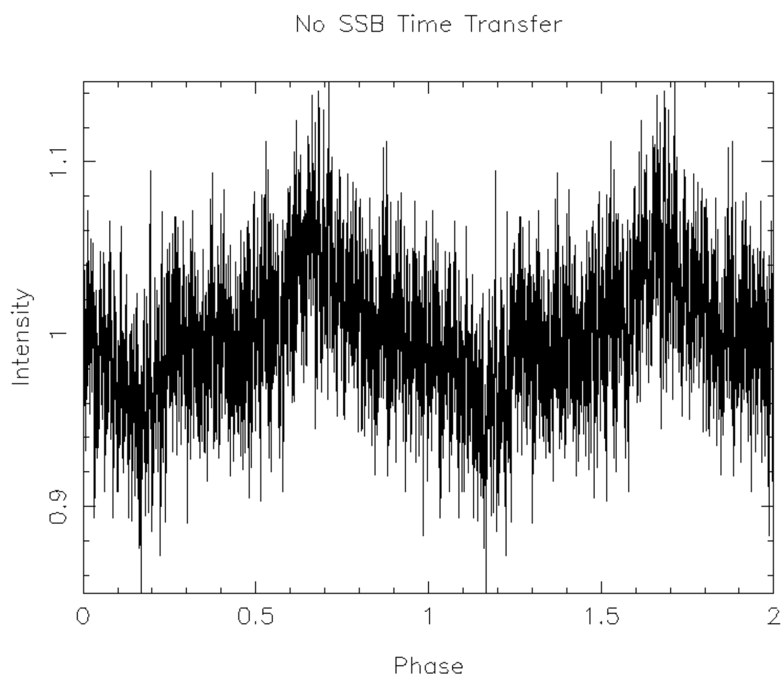

Figure 6-6. Second Crab Pulsar profile with no time transfer on photon arrival times. Profile is distorted due to Doppler effect on pulses arriving at vehicle.

6.3 Measurement Differences

In order to compute the absolute position of a detector using variable celestial sources, it is necessary to determine which specific pulse is arriving at the detector from a source. Since sources do not identify any of the pulses that they emit, specific pulses must be identified by the way a set of pulses coordinate with respect to the orientation of a set of pulsars.

Figure 6-7 shows the arrival of pulses at a spacecraft from three pulsars. At any given instance, there is only one unique set of pulses from this group of pulsars that solves for the exact location of the vehicle. By identifying this set of pulses, the position of the vehicle can be determined.

Due to the significant distances between the celestial sources and the solar system, the pulse waves that arrive into the system are assumed to be planar, not spherical. Ignoring the spherical effects of the wave propagation is only significant if the spacecraft and location of the model used for comparison are very far apart.

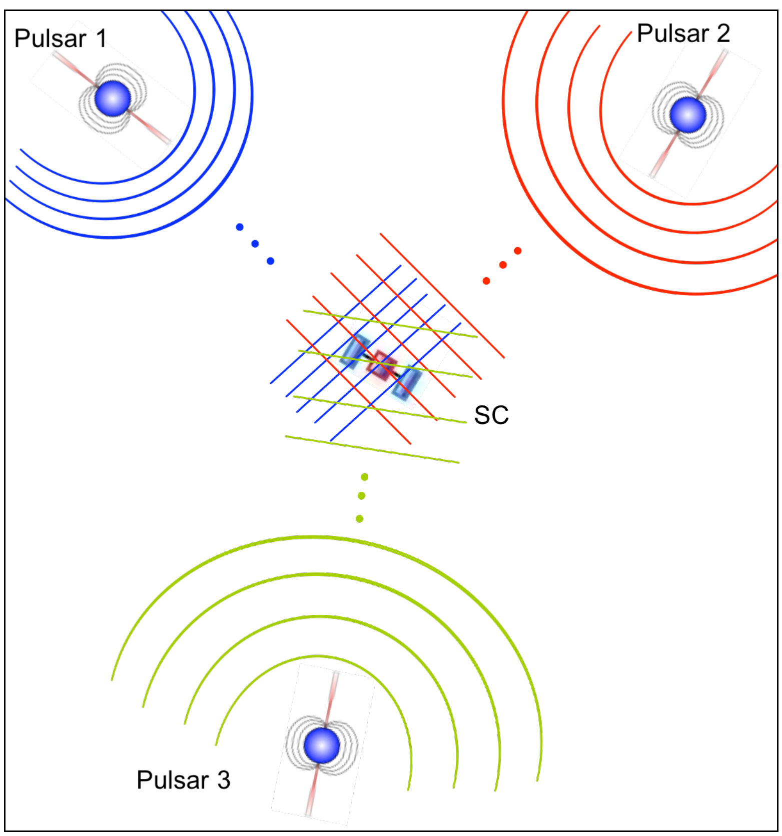

Figure 6-7. Pulse arrivals from individual pulsars at spacecraft location.

Since no identifying information is provided with each pulse from a pulsar, determining which specific pulse is arriving at a given instance is not possible. However, by choosing a pulse-timing model at a known location, it is possible to identify the set of *differences* in pulses between the spacecraft and the known location. For a single pulsar, a measured difference can be created with the pulse arrival time at the detector and the predicted arrival time at the known location. The difference in these values immediately identifies a set of candidate positions along the line-of-sight to the pulsar. These candidate locations are the value of measured fraction of pulse phase plus or minus multiple whole value pulse cycle lengths. Only one unique position satisfies measured differences from a set of pulsars; and once this unique position is identified, the correct set of differenced cycles are immediately determined.

Alternatively, a *phase cycle ambiguity search space* can be created, either by choosing these search spaces based upon a preferred geometry, or by selecting a maximum number of search cycles to be considered. All the candidate cycles that exist within this search space can be tested to determine whether the corresponding location satisfies the measured phase differences.

This method of position determination is similar to the navigation concept of *Time Difference of Arrival* (TDOA). In TDOA, the difference of two sets of time arrival measurements is used to determine the optimum location that satisfies specified criteria. However, in most TDOA concepts, two detectors or sensors are used to measure the source's signal, and data from these two systems are differenced. Contrastingly, in the celestial source methods described below, one of the detectors in the TDOA configuration is replaced by a model of pulse arrival that is defined to exist at a specified location, thus there is only one actual detector in the system. In these methods, no data needs to be transmitted between the detector and the model location. Using a supplied pulsar almanac containing these models, the navigation system on the spacecraft can compute the entire absolute position. This is a true absolute positioning system, since the navigation system's detector needs only to observe celestial source data, and determine its location within a given inertial frame. Although two detectors could be used for the absolute positioning system and data communicated between them, this would be more correctly represented as a *relative* positioning system.

Several types of measurement differences are described below. The *Single Difference* is the difference between the measured phase at the detector and the phase predicted at a model location for a single pulsar. The *Double Difference* is the subtraction of two single differences from two separate pulsars. The *Triple Difference* is the subtraction of two double differences between two separate time epochs. The benefits of computing these differences include removing immeasurable errors, with higher order differences removing additional errors. The complexity of using higher order differences includes requiring more observable sources to produce solutions, which may take additional observation time.

6.3.1 Single Difference

Measurements of the pulsed radiation from variable celestial sources can be differenced with the predicted arrival time from a pulse-timing model. The pulse-timing model is defined at a specific location within an inertial frame. Any specified location can be used, however, the most common location is the SSB origin. For the examples shown below, the location of Earth within the SSB inertial frame will be used for illustrative purposes. Many spacecraft missions are in Earth orbit, or are for near-Earth applications. Although Earth is used for these examples, any known location in the solar system can be used, such as the Moon, Mars, Pluto, etc. In addition, the known location of another spacecraft or base station may be utilized.

The single difference removes any values common to both the spacecraft and the model location. Primarily it removes the pulsar distance, which is often not known to any great accuracy.

Measurement differences can be created using measured range from the source or measured cycle phase. Primarily, since range measurements are difficult to compute from celestial sources, the phase measurements will be used to compute spacecraft position. However, the range measurement algorithms are provided to help illustrate the methods described here. The errors that are expected to be present in an actual navigation system are also identified and are shown within the difference computations.

6.3.1.1 Range Single Difference

The range vectors between the pulsar source and Earth and between the pulsar and the spacecraft are shown in Figure 6-8. The source is assumed to be extremely far away from the solar system. Consequently the difference in these range vectors provides an estimate of the offset between Earth and the spacecraft, $\Delta\mathbf{x}$.

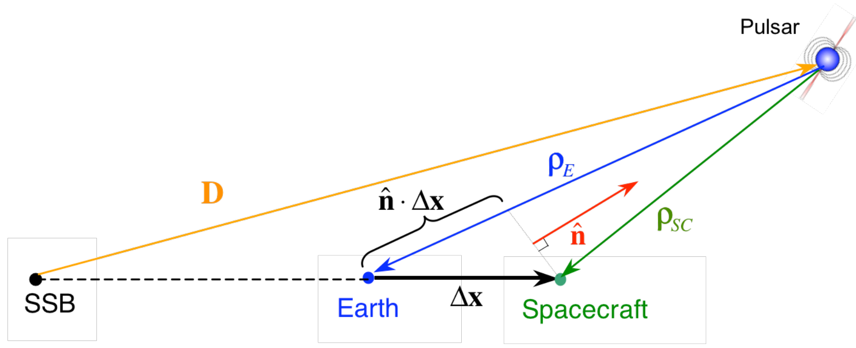

Figure 6-8. Range vectors from single pulsar to Earth and spacecraft locations.

6.3.1.1.1 Geometric-Only

Considering only the geometric representation from Figure 6-8, the position of the spacecraft relative to Earth can be represented using the spacecraft's position, $\mathbf{r}_{SC}$, and Earth's position, $\mathbf{r}_E$, within the SSB inertial frame as,

$$\Delta\mathbf{x} = \Delta\mathbf{r} = \mathbf{r}_{SC/E} = \mathbf{r}_{SC} - \mathbf{r}_E \tag{6.23}$$

This position can also be represented by the range vectors from the i^{th} celestial source as,

$$\Delta\mathbf{x} = \Delta\boldsymbol{\rho}_i = \boldsymbol{\rho}_{SC_i} - \boldsymbol{\rho}_{E_i} \tag{6.24}$$

Within the SSB inertial frame, the line-of-sight, or unit direction, to the source can very nearly be considered as a constant, due to the extreme distances to the sources. Thus the unit direction to the source can be represented using its known position within the inertial frame. The unit direction is in the opposite direction from the source to either the spacecraft or Earth as,

$$\hat{\mathbf{n}}_i = \frac{\mathbf{D}}{D} \approx -\hat{\boldsymbol{\rho}}_{SC_i} \approx -\hat{\boldsymbol{\rho}}_{E_i} \tag{6.25}$$

The range vector can be represented using its magnitude and direction, as $\|\boldsymbol{\rho}\| = \rho$, or $\boldsymbol{\rho} = \rho\hat{\boldsymbol{\rho}}$. Using the unit direction from Eq. (6.25), the difference in range magnitude represents the spacecraft's position along the line-of-sight to the pulsar as,

$$\Delta\rho_i = \rho_{E_i} - \rho_{SC_i} = \hat{\mathbf{n}}_i \cdot \Delta\mathbf{x} \tag{6.26}$$

It is important to note the distinction between symbols for the range vector difference, $\Delta\boldsymbol{\rho}_i$, from Eq. (6.23) and the range magnitude difference, $\Delta\rho_i$, from Eq. (6.26). Since the line-of-sight from the SSB to the source is in opposite direction with respect to the range vectors, the range vector difference is in opposite sense as the range magnitude difference. This is clear from the diagram in Figure 6-8.

6.3.1.1.2 Relativistic Effects

As was discussed in the *Observables and Errors* section above, the relativistic effects on the path of a photon from the source to either the spacecraft or Earth cannot be considered negligible if accurate position determination is required. With the addition of these effects, the range difference using Eq. (6.7) becomes,

$$\begin{aligned}\Delta\rho_i = \rho_{E_i} - \rho_{SC_i} &= \left[\|\mathbf{r}_E - \mathbf{D}_i\| + RelEff_{E_i}\right] - \left[\|\mathbf{r}_{SC} - \mathbf{D}_i\| + RelEff_{SC_i}\right] \\ &= \left[\|\mathbf{r}_E - \mathbf{D}_i\| - \|\mathbf{r}_{SC} - \mathbf{D}_i\|\right] + \left[RelEff_{E_i} - RelEff_{SC_i}\right]\end{aligned} \tag{6.27}$$

The position magnitude difference in the first term of Eq. (6.27) can be represented as,

$$\begin{aligned}\begin{bmatrix}\|\mathbf{r}_E - \mathbf{D}_i\| \\ -\|\mathbf{r}_{SC} - \mathbf{D}_i\|\end{bmatrix} &= \left(\mathbf{r}_E \cdot \mathbf{r}_E - 2\mathbf{r}_E \cdot \mathbf{D}_i + \mathbf{D}_i \cdot \mathbf{D}_i\right)^{\frac{1}{2}} \\ &\quad - \left(\mathbf{r}_{SC} \cdot \mathbf{r}_{SC} - 2\mathbf{r}_{SC} \cdot \mathbf{D}_i + \mathbf{D}_i \cdot \mathbf{D}_i\right)^{\frac{1}{2}} \\ &= \mathbf{D}_i\left(\frac{r_E^2}{D_i^2} - \frac{2\mathbf{r}_E \cdot \mathbf{D}_i}{D_i^2} + 1\right)^{\frac{1}{2}} - \mathbf{D}_i\left(\frac{r_{SC}^2}{D_i^2} - \frac{2\mathbf{r}_{SC} \cdot \mathbf{D}_i}{D_i^2} + 1\right)^{\frac{1}{2}}\end{aligned} \tag{6.28}$$

Using a binomial expansion of the square root terms and the line-of-sight simplification from Eq. (6.25) produces,

$$\begin{aligned}\begin{bmatrix}\|\mathbf{r}_E-\mathbf{D}_i\|\\ -\|\mathbf{r}_{SC}-\mathbf{D}_i\|\end{bmatrix} &\approx \mathbf{D}_i\left[1+\frac{1}{2}\left(\frac{r_E^2}{D_i^2}-\frac{2\mathbf{r}_E\cdot\mathbf{D}_i}{D_i^2}\right)\right]\\ &\quad -\mathbf{D}_i\left[1+\frac{1}{2}\left(\frac{r_{SC}^2}{D_i^2}-\frac{2\mathbf{r}_{SC}\cdot\mathbf{D}_i}{D_i^2}\right)\right]+O\left(1/D_i^2\right)\\ &\approx \frac{1}{2D_i}\left(r_E^2-r_{SC}^2\right)+\left(\mathbf{r}_{SC}\cdot\frac{\mathbf{D}_i}{D_i}-\mathbf{r}_E\cdot\frac{\mathbf{D}_i}{D_i}\right)+O\left(1/D_i^2\right)\\ &\approx \hat{\mathbf{n}}_i\cdot\left(\mathbf{r}_{SC}-\mathbf{r}_E\right)+\frac{1}{2D_i}\left(r_E^2-r_{SC}^2\right)+O\left(1/D_i^2\right)\end{aligned} \tag{6.29}$$

Therefore the range difference expression can be simplified from Eq. (6.27) as,

$$\Delta\rho_i \approx \hat{\mathbf{n}}_i\cdot\left(\mathbf{r}_{SC}-\mathbf{r}_E\right)+\frac{1}{2D_i}\left(r_E^2-r_{SC}^2\right)+\left[RelEff_{E_i}-RelEff_{SC_i}\right]+O\left(1/D_i^2\right) \tag{6.30}$$

A further simplification that the second term of Eq. (6.30) is small in most cases yielding,

$$\Delta\rho_i \approx \hat{\mathbf{n}}_i\cdot\Delta\mathbf{x}+\left[RelEff_{E_i}-RelEff_{SC_i}\right]+O\left(1/D_i\right) \tag{6.31}$$

The expression for the single difference in Eqs. (6.30) or (6.31) shows the main reason for its implementation. The poorly determined and very inaccurate pulsar position vector, $\mathbf{D}_i$, has been removed from the equations. Thus spacecraft position computations no longer rely on the measurement of range directly from the pulsar. From these expressions, the range difference is only related to both the spacecraft position difference and the difference in relativistic effects to order $O\left(1/D_i\right)$.

6.3.1.1.3 Range Single Difference Measurement with Errors

Actual measurements made within the navigation system will contain some errors. Thus the true range difference is a function of the actual measured values and their errors. From the range expression of Eq. (6.12), the range difference becomes,

$$
\begin{aligned}
\Delta\rho_i &= \left[\left\|\tilde{\mathbf{r}}_E - \tilde{\mathbf{D}}_i\right\| + \widetilde{RelEff}_{E_i} + \left\|\delta\mathbf{r}_E\right\| + \left\|\delta\mathbf{D}_{E_i}\right\| + \delta RelEff_{E_i} + \eta_{E_i}\right] \\
&\quad - \left[\left\|\tilde{\mathbf{r}}_{SC} - \tilde{\mathbf{D}}_i\right\| + \widetilde{RelEff}_{SC_i} + \left\|\delta\mathbf{r}_{SC}\right\| + \left\|\delta\mathbf{D}_{SC_i}\right\| + \delta RelEff_{SC_i} + \eta_{SC_i}\right] \\
&= \left[\left\|\tilde{\mathbf{r}}_E - \tilde{\mathbf{D}}_i\right\| - \left\|\tilde{\mathbf{r}}_{SC} - \tilde{\mathbf{D}}_i\right\|\right] + \left[\widetilde{RelEff}_{E_i} - \widetilde{RelEff}_{SC_i}\right] + \left[\left\|\delta\mathbf{r}_E\right\| - \left\|\delta\mathbf{r}_{SC}\right\|\right] \\
&\quad + \left[\left\|\delta\mathbf{D}_{E_i}\right\| - \left\|\delta\mathbf{D}_{SC_i}\right\|\right] + \left[\delta RelEff_{E_i} - \delta RelEff_{SC_i}\right] + \left[\eta_{E_i} - \eta_{SC_i}\right]
\end{aligned}
\tag{6.32}
$$

From the representation of the first term in Eq. (6.32) from Eq. (6.29), the range single difference can be estimated as,

$$
\begin{aligned}
\Delta\rho_i &\approx \hat{\mathbf{n}}_i \cdot \Delta\mathbf{x} + \left[\widetilde{RelEff}_{E_i} - \widetilde{RelEff}_{SC_i}\right] + \left[\left\|\delta\mathbf{r}_E\right\| - \left\|\delta\mathbf{r}_{SC}\right\|\right] \\
&\quad + \left[\left\|\delta\mathbf{D}_{E_i}\right\| - \left\|\delta\mathbf{D}_{SC_i}\right\|\right] + \left[\delta RelEff_{E_i} - \delta RelEff_{SC_i}\right] + \left[\eta_{E_i} - \eta_{SC_i}\right]
\end{aligned}
\tag{6.33}
$$

6.3.1.2 Phase Single Difference

The phase of the arriving pulse from a celestial source can be differenced between the spacecraft and a known model location, similar to the range difference created above. The phase difference represents the fraction of cycle phase, or fraction of phase plus a fixed number of integer cycles, from an arriving pulse between the spacecraft and the model location. Figure 6-9 provides a diagram of arriving pulses from a single celestial source at a spacecraft and Earth. By measuring the phase difference, the spacecraft's position with respect to Earth along the line-of-sight to the source is determined. Using multiple measured phase differences from different sources provides a method of determining the spacecraft's three-dimensional position with respect to Earth in an inertial frame.

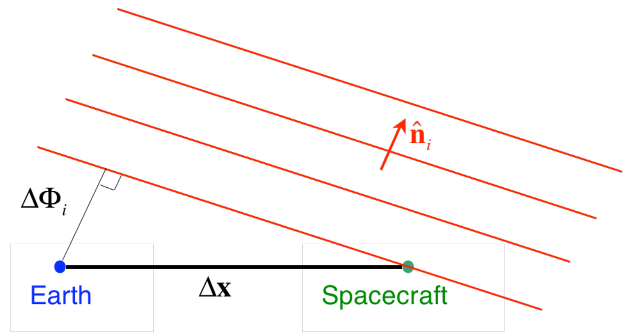

Figure 6-9. Phase difference for individual pulses arriving at the spacecraft and Earth.

6.3.1.2.1 Geometric-Only

Phase difference is directly related to range difference when the wavelength, λ_i, of the cycle is included. From Figure 6-8 and Figure 6-9, the geometric relationship of phase with respect to range from a source can be expressed as,

$$\begin{aligned}\Delta\rho_i &= \rho_{E_i} - \rho_{SC_i} \\ &= \lambda_i \Delta\Phi_i = \lambda_i\left(\Delta\phi_i + \Delta N_i\right) = \lambda_i\left[\left(\phi_{E_i} - \phi_{SC_i}\right) + \left(N_{E_i} - N_{SC_i}\right)\right]\end{aligned} \tag{6.34}$$

The geometric relationship of phase with respect to spacecraft position is then

$$\lambda_i \Delta\Phi_i = \lambda_i\left(\Delta\phi_i + \Delta N_i\right) = \hat{\mathbf{n}}_i \cdot \Delta\mathbf{x} \tag{6.35}$$

6.3.1.2.2 Relativistic Effects

Analogous to the range calculations, improved accuracy is attained when the relativistic effects on the light ray paths from the source are included. From Eq. (6.27), the phase difference becomes,

$$\begin{aligned}\lambda_i \Delta\Phi_i &= \lambda_i\left(\Delta\phi_i + \Delta N_i\right) \\ &= \left[\left\|\mathbf{r}_E - \mathbf{D}_i\right\| - \left\|\mathbf{r}_{SC} - \mathbf{D}_i\right\|\right] + \left[RelEff_{E_i} - RelEff_{SC_i}\right]\end{aligned} \tag{6.36}$$

If the simplifications to the first term are included as was considered in Eqs. (6.29) and (6.31), and the line-of-sight is included from Eq. (6.25), this phase difference becomes,

$$\lambda_i \Delta\Phi_i = \lambda_i\left(\Delta\phi_i + \Delta N_i\right) \approx \hat{\mathbf{n}}_i \cdot \Delta\mathbf{x} + \left[RelEff_{E_i} - RelEff_{SC_i} \right] + O\left(1 \big/ D_i \right) \qquad (6.37)$$

6.3.1.2.3 Phase Single Difference Measurement with Errors

Actual phase measurements made at the detector of a spacecraft will contain errors, similar to an actual range measurement. Referring to the measurement errors for phase from Eq. (6.20), the phase difference calculation is related to these errors as,

$$\begin{aligned}
\lambda_i \Delta\Phi_i &= \lambda_i\left(\Delta\phi_i + \Delta N_i\right) \\
&= \left[\left\| \tilde{\mathbf{r}}_E - \tilde{\mathbf{D}}_i \right\| - \left\| \tilde{\mathbf{r}}_{SC} - \tilde{\mathbf{D}}_i \right\| \right] + \left[\widetilde{RelEff}_{E_i} - \widetilde{RelEff}_{SC_i} \right] + \left[c\delta t_E - c\delta t_{SC} \right] \\
&\quad + \left[c\delta T_i - c\delta T_i \right] + \left[\left\| \delta\mathbf{r}_E \right\| - \left\| \delta\mathbf{r}_{SC} \right\| \right] + \left[\left\| \delta\mathbf{D}_{E_i} \right\| - \left\| \delta\mathbf{D}_{SC_i} \right\| \right] \\
&\quad + \left[\delta RelEff_{E_i} - \delta RelEff_{SC_i} \right] + \left[\beta_{E_i} - \beta_{SC_i} \right]
\end{aligned} \qquad (6.38)$$

It should be noted from Eq. (6.38) that the term involving pulsar intrinsic model error, $c\delta T_i$, cancels when computing a phase single difference. This is significant since any model errors that exist in the pulse-timing model for a specific pulsar do not affect the computation of position when using a phase difference. With the additional simplification of the first term on the right hand side of Eq. (6.38) using Eq. (6.29), the phase single difference equation becomes,

$$\begin{aligned}
\lambda_i \Delta\Phi_i &= \lambda_i\left(\Delta\phi_i + \Delta N_i\right) \\
&\approx \hat{\mathbf{n}}_i \cdot \Delta\mathbf{x} + \left[\widetilde{RelEff}_{E_i} - \widetilde{RelEff}_{SC_i} \right] + \left[c\delta t_E - c\delta t_{SC} \right] + \left[\left\| \delta\mathbf{r}_E \right\| - \left\| \delta\mathbf{r}_{SC} \right\| \right] \\
&\quad + \left[\left\| \delta\mathbf{D}_{E_i} \right\| - \left\| \delta\mathbf{D}_{SC_i} \right\| \right] + \left[\delta RelEff_{E_i} - \delta RelEff_{SC_i} \right] + \left[\beta_{E_i} - \beta_{SC_i} \right]
\end{aligned} \qquad (6.39)$$

Alternatively, the geometric representation of phase can be stated in terms of the line-of-sight and its related errors from Eq. (6.22), as,

$$
\begin{aligned}
\lambda_i \Delta\Phi_i &= \lambda_i \left(\Delta\phi_i + \Delta N_i\right) \\
&\approx \left[\tilde{\mathbf{n}}_{E_i} \cdot \left(\tilde{\mathbf{D}}_i - \tilde{\mathbf{r}}_E\right) - \tilde{\mathbf{n}}_{SC_i} \cdot \left(\tilde{\mathbf{D}}_i - \tilde{\mathbf{r}}_{SC}\right)\right] + \left[\widetilde{RelEff}_{E_i} - \widetilde{RelEff}_{SC_i}\right] \\
&\quad + \left[c\delta t_E - c\delta t_{SC}\right] + \left[\left(\tilde{\mathbf{n}}_{E_i} - \tilde{\mathbf{n}}_{SC_i}\right) \cdot \delta\mathbf{D}_i\right] + \left[\tilde{\mathbf{n}}_{E_i} \cdot \delta\mathbf{r}_E - \tilde{\mathbf{n}}_{SC_i} \cdot \delta\mathbf{r}_{SC}\right] \\
&\quad + \left[\delta\hat{\mathbf{n}}_{E_i} \cdot \left(\tilde{\mathbf{D}}_i - \tilde{\mathbf{r}}_E\right) - \delta\hat{\mathbf{n}}_{SC_i} \cdot \left(\tilde{\mathbf{D}}_i - \tilde{\mathbf{r}}_{SC}\right)\right] \\
&\quad + \left[\delta RelEff_{E_i} - \delta RelEff_{SC_i}\right] + \left[\beta_{E_i} - \beta_{SC_i}\right]
\end{aligned}
\tag{6.40}
$$

With the additional assumption that the line-of-sight is constant throughout the solar system such that $\tilde{\mathbf{n}}_i \approx \tilde{\mathbf{n}}_{E_i} \approx \tilde{\mathbf{n}}_{SC_i}$, the above representation can be simplified to the following,

$$
\begin{aligned}
\lambda_i \Delta\Phi_i &= \lambda_i \left(\Delta\phi_i + \Delta N_i\right) \\
&\approx \tilde{\mathbf{n}}_i \cdot \Delta\mathbf{x} + \left[\widetilde{RelEff}_{E_i} - \widetilde{RelEff}_{SC_i}\right] + \left[c\delta t_E - c\delta t_{SC}\right] + \left[\tilde{\mathbf{n}}_i \cdot \left(\delta\mathbf{r}_E - \delta\mathbf{r}_{SC}\right)\right] \\
&\quad + \left[\delta\hat{\mathbf{n}}_i \cdot \Delta\mathbf{x}\right] + \left[\delta RelEff_{E_i} - \delta RelEff_{SC_i}\right] + \left[\beta_{E_i} - \beta_{SC_i}\right]
\end{aligned}
\tag{6.41}
$$

The fourth term on the right hand side of Eq. (6.41) is related to the error in spacecraft position, or $\left(\delta\mathbf{r}_E - \delta\mathbf{r}_{SC}\right) \cong \delta\Delta\mathbf{x}$. If the position of Earth is accurately known, then the error in Earth position is effectively zero, or $\delta\mathbf{r}_E \approx 0$. Thus, this expression simplifies directly to spacecraft position error.

An interesting observation is that the *delta-correction position* method of Chapter 7 [192, 193], can be implemented utilizing Eq. (6.41). Using phase single difference measurements and an estimate of spacecraft position, $\Delta\tilde{\mathbf{x}}$, Eq. (6.41) can be used to solve for any unknown spacecraft position error, $\delta\mathbf{r}_{SC}$.

6.3.2 Double Difference

The primary benefit of the single difference computation is the removal of the poorly known pulsar position vector, $\mathbf{D}_i$ from the computations. Implementing a *double difference* can provide additional benefits. A double difference is the subtraction of two single differences from two separate pulsars. This difference removes values that are common to both pulsars, such as navigation system dependent values. However, double differences require observations from multiple sources to be conducted contemporaneously, such that the pulse arrival time measurements from these sources are computed simultaneously and at the same position of the spacecraft. Otherwise, methods must be employed to adjust arrival times for observations made at different times to the same time epoch. This may require multiple detectors to be integrated into a single system for full absolute position determination.

6.3.2.1 Range Double Difference

The range double difference is computed between these two sources, the i^{th} and j^{th} pulsars. The diagram in Figure 6-10 shows the arriving pulses from two pulsars into the solar system.

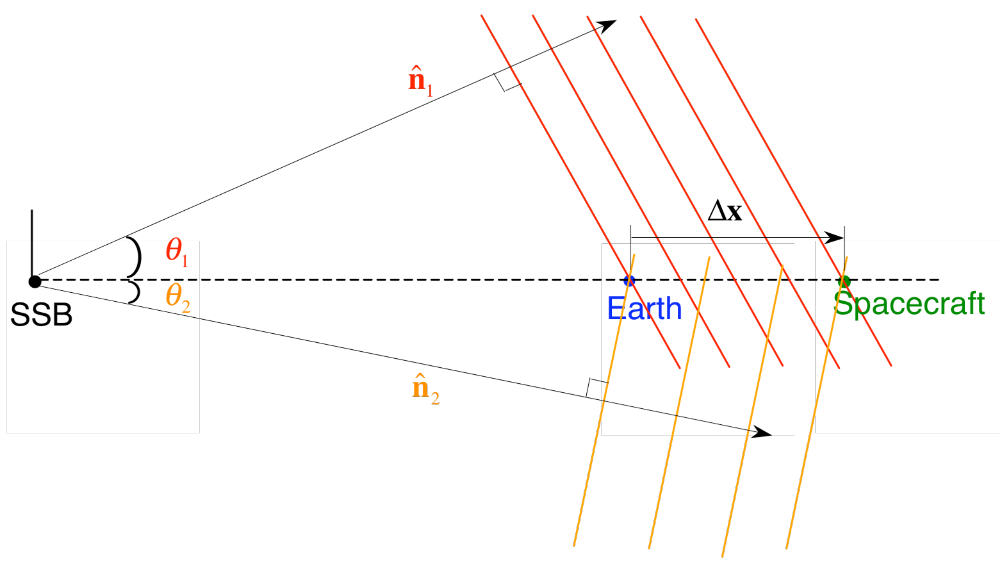

Figure 6-10. Pulse plane arrivals within solar system from two separate sources.

6.3.2.1.1 Geometric-Only

If only the geometric relationship for two pulsar range vectors and the spacecraft position is considered as in Figure 6-8 and Figure 6-10, the range vector double difference can be expressed as,

$$\nabla\Delta\boldsymbol{\rho}_{ij} = \Delta\boldsymbol{\rho}_i - \Delta\boldsymbol{\rho}_j = \left(\boldsymbol{\rho}_{SC_i} - \boldsymbol{\rho}_{E_i}\right) - \left(\boldsymbol{\rho}_{SC_j} - \boldsymbol{\rho}_{E_j}\right) \tag{6.42}$$

In this expression, the symbol ∇ is used to represent a double difference, and should not be misinterpreted as the gradient operator. From the representation of a range vector single difference from Eq. (6.24) it can be seen that the range vector double difference equals zero, or,

$$\nabla\Delta\boldsymbol{\rho}_{ij} = \Delta\boldsymbol{\rho}_i - \Delta\boldsymbol{\rho}_j = \Delta\mathbf{x} - \Delta\mathbf{x} = 0 \tag{6.43}$$

Although the double range vector difference is zero, this is not true of the double range (scalar) difference. Since the line-of-sight vectors are different for each pulsar, the double range difference is not zero. Instead, in a purely geometric-sense, the range double difference using Eq. (6.26) is the following,

$$\nabla\Delta\rho_{ij} = \left(\rho_{E_i} - \rho_{SC_i}\right) - \left(\rho_{E_j} - \rho_{SC_j}\right) = \left(\hat{\mathbf{n}}_i - \hat{\mathbf{n}}_j\right) \cdot \Delta\mathbf{x} \tag{6.44}$$

6.3.2.1.2 Relativistic Effects

Including the effects of relativity on the light ray path for range single differences as in Eq. (6.31), the range double difference for two pulsars becomes,

$$\nabla\Delta\rho_{ij} \approx \left(\hat{\mathbf{n}}_i - \hat{\mathbf{n}}_j\right) \cdot \Delta\mathbf{x} + \left[\Delta RelEff_i - \Delta RelEff_j\right] + O\left(\frac{1}{D_i} - \frac{1}{D_j}\right) \tag{6.45}$$

6.3.2.1.3 Range Double Difference Measurement with Errors

Including the measurement errors for the range single differences, the double difference between two pulsars from Eq. (6.32) becomes,

$$\begin{aligned}\nabla\Delta\rho_{ij} = &\begin{bmatrix}\left\|\tilde{\mathbf{r}}_E - \tilde{\mathbf{D}}_i\right\| - \left\|\tilde{\mathbf{r}}_{SC} - \tilde{\mathbf{D}}_i\right\| \\ -\left\|\tilde{\mathbf{r}}_E - \tilde{\mathbf{D}}_j\right\| + \left\|\tilde{\mathbf{r}}_{SC} - \tilde{\mathbf{D}}_j\right\|\end{bmatrix} + \left[\widetilde{\Delta RelEff}_i - \widetilde{\Delta RelEff}_j\right] + \begin{bmatrix}\left\|\delta\mathbf{r}_E\right\| - \left\|\delta\mathbf{r}_{SC}\right\| \\ -\left\|\delta\mathbf{r}_E\right\| + \left\|\delta\mathbf{r}_{SC}\right\|\end{bmatrix} \\ &+\begin{bmatrix}\left\|\delta\mathbf{D}_{E_i}\right\| - \left\|\delta\mathbf{D}_{SC_i}\right\| \\ -\left\|\delta\mathbf{D}_{E_j}\right\| + \left\|\delta\mathbf{D}_{SC_j}\right\|\end{bmatrix} + \left[\Delta\delta RelEff_i - \Delta\delta RelEff_j\right] + \begin{bmatrix}\eta_{E_i} - \eta_{SC_i} \\ -\eta_{E_j} + \eta_{SC_j}\end{bmatrix}\end{aligned} \tag{6.46}$$

This expression can be further simplified, since the terms involving Earth location error and spacecraft position error cancel, to produce,

$$\begin{aligned}\nabla\Delta\rho_{ij} = &\begin{bmatrix}\left(\left\|\tilde{\mathbf{r}}_E - \tilde{\mathbf{D}}_i\right\| - \left\|\tilde{\mathbf{r}}_E - \tilde{\mathbf{D}}_j\right\|\right) \\ -\left(\left\|\tilde{\mathbf{r}}_{SC} - \tilde{\mathbf{D}}_i\right\| - \left\|\tilde{\mathbf{r}}_{SC} - \tilde{\mathbf{D}}_j\right\|\right)\end{bmatrix} + \left[\widetilde{\Delta RelEff}_i - \widetilde{\Delta RelEff}_j\right] \\ &+\begin{bmatrix}\left(\left\|\delta\mathbf{D}_{E_i}\right\| - \left\|\delta\mathbf{D}_{E_j}\right\|\right) \\ -\left(\left\|\delta\mathbf{D}_{SC_i}\right\| - \left\|\delta\mathbf{D}_{SC_j}\right\|\right)\end{bmatrix} + \left[\Delta\delta RelEff_i - \Delta\delta RelEff_j\right] + \left[\Delta\eta_i - \Delta\eta_j\right]\end{aligned} \tag{6.47}$$

If the line-of-sight vectors are utilized instead, as in Eq. (6.33), then this range double difference becomes,

$$\begin{aligned}\nabla\Delta\rho_{ij} = &\left(\hat{\mathbf{n}}_i - \hat{\mathbf{n}}_j\right)\cdot\Delta\mathbf{x} + \left[\widetilde{\Delta RelEff}_i - \widetilde{\Delta RelEff}_j\right] \\ &+\begin{bmatrix}\left(\left\|\delta\mathbf{D}_{E_i}\right\| - \left\|\delta\mathbf{D}_{E_j}\right\|\right) \\ -\left(\left\|\delta\mathbf{D}_{SC_i}\right\| - \left\|\delta\mathbf{D}_{SC_j}\right\|\right)\end{bmatrix} + \left[\Delta\delta RelEff_i - \Delta\delta RelEff_j\right] + \left[\Delta\eta_i - \Delta\eta_j\right]\end{aligned} \tag{6.48}$$

The range double difference of Eqs. (6.47) and (6.48) involve differences of small values. It is likely that in practical situations many, if not all, of the differences other than spacecraft position and noise can be ignored.

6.3.2.2 Phase Double Difference

As was shown for range, double phase differences can be calculated for the i^{th} and j^{th} pulsars. Figure 6-11 provides a diagram of the phase single difference for two pulsars, which can be subtracted from one another to produce a phase double difference.

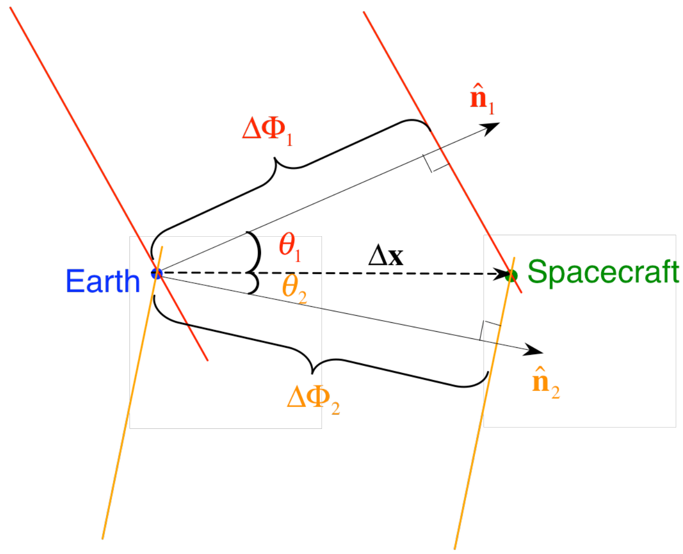

Figure 6-11. Phase difference at the spacecraft and Earth from two sources.

6.3.2.2.1 Geometric-Only

The total phase double difference is composed of the fractional phase double difference and the integer cycle double difference, and is given by,

$$\nabla\Delta\Phi_{ij} = \Delta\Phi_i - \Delta\Phi_j = \nabla\Delta\phi_{ij} + \nabla\Delta N_{ij} = \left(\Delta\phi_i + \Delta N_i\right) - \left(\Delta\phi_j + \Delta N_j\right) \tag{6.49}$$

From Figure 6-9 and Figure 6-11, the geometric relationship of phase with respect to spacecraft position is

$$\lambda_i \Delta\Phi_i - \lambda_j \Delta\Phi_j = \lambda_i \left(\Delta\phi_i + \Delta N_i\right) - \lambda_j \left(\Delta\phi_j + \Delta N_j\right) = \left(\hat{\mathbf{n}}_i - \hat{\mathbf{n}}_j\right) \cdot \Delta\mathbf{x} \tag{6.50}$$

or, by dividing through by cycle wavelength,

$$\nabla\Delta\Phi_{ij} = \nabla\Delta\phi_{ij} + \nabla\Delta N_{ij} = \left(\frac{\hat{\mathbf{n}}_i}{\lambda_i} - \frac{\hat{\mathbf{n}}_j}{\lambda_j}\right)\cdot\Delta\mathbf{x} \tag{6.51}$$

6.3.2.2.2 Relativistic Effects

Analogous to the range calculations, improved accuracy is attained by including the relativistic effects on the light ray paths from the source. From Eq. (6.36), the phase difference becomes,

$$\begin{aligned}\lambda_i\Delta\Phi_i - \lambda_j\Delta\Phi_j &= \lambda_i\left(\Delta\phi_i + \Delta N_i\right) - \lambda_j\left(\Delta\phi_j + \Delta N_j\right)\\ &= \begin{bmatrix}\left\|\mathbf{r}_E - \mathbf{D}_i\right\| - \left\|\mathbf{r}_{SC} - \mathbf{D}_i\right\| \\ -\left\|\mathbf{r}_E - \mathbf{D}_j\right\| + \left\|\mathbf{r}_{SC} - \mathbf{D}_j\right\|\end{bmatrix} + \left[\Delta RelEff_i - \Delta RelEff_j\right]\end{aligned} \tag{6.52}$$

If the simplifications to the first term are included as was considered in Eq. (6.37) and the line-of-sight is included from Eq. (6.25), this phase double difference becomes,

$$\begin{aligned}\lambda_i\Delta\Phi_i - \lambda_j\Delta\Phi_j &= \lambda_i\left(\Delta\phi_i + \Delta N_i\right) - \lambda_j\left(\Delta\phi_j + \Delta N_j\right)\\ &\approx \left(\hat{\mathbf{n}}_i - \hat{\mathbf{n}}_j\right)\cdot\Delta\mathbf{x} + \begin{bmatrix}\Delta RelEff_i \\ -\Delta RelEff_j\end{bmatrix} + O\left(\frac{1}{D_i} - \frac{1}{D_j}\right)\end{aligned} \tag{6.53}$$

or, by dividing through by cycle wavelength this becomes,

$$\begin{aligned}\nabla\Delta\Phi_{ij} &= \nabla\Delta\phi_{ij} + \nabla\Delta N_{ij}\\ &\approx \left(\frac{\hat{\mathbf{n}}_i}{\lambda_i} - \frac{\hat{\mathbf{n}}_j}{\lambda_j}\right)\cdot\Delta\mathbf{x} + \left[\frac{\Delta RelEff_i}{\lambda_i} - \frac{\Delta RelEff_j}{\lambda_j}\right] + O\left(\frac{1}{\lambda_i D_i} - \frac{1}{\lambda_j D_j}\right)\end{aligned} \tag{6.54}$$

6.3.2.2.3 Phase Double Difference Measurement with Errors

Actual phase measurements made at the detector of a spacecraft will contain errors, similar to an actual range measurement. From Eq. (6.38), the phase double difference equation becomes,

$$
\begin{aligned}
\lambda_i \Delta\Phi_i - \lambda_j \Delta\Phi_j &= \lambda_i\left(\Delta\phi_i + \Delta N_i\right) - \lambda_j\left(\Delta\phi_j + \Delta N_j\right) \\
&\approx \left(\hat{\mathbf{n}}_i - \hat{\mathbf{n}}_j\right)\cdot \Delta\mathbf{x} + \left[\Delta\widetilde{RelEff}_i - \Delta\widetilde{RelEff}_j\right] + \begin{bmatrix} c\delta t_E - c\delta t_{SC} \\ -c\delta t_E + c\delta t_{SC} \end{bmatrix} \\
&+ \begin{bmatrix} \left\|\delta\mathbf{r}_E\right\| - \left\|\delta\mathbf{r}_{SC}\right\| \\ -\left\|\delta\mathbf{r}_E\right\| + \left\|\delta\mathbf{r}_{SC}\right\| \end{bmatrix} + \begin{bmatrix} \left\|\delta\mathbf{D}_{E_i}\right\| - \left\|\delta\mathbf{D}_{SC_i}\right\| \\ -\left\|\delta\mathbf{D}_{E_j}\right\| + \left\|\delta\mathbf{D}_{SC_j}\right\| \end{bmatrix} \\
&+ \left[\Delta\delta RelEff_i - \Delta\delta RelEff_j\right] + \left[\Delta\beta_i - \Delta\beta_j\right]
\end{aligned}
\tag{6.55}
$$

Observing the terms within Eq. (6.55), the spacecraft and Earth time errors cancel, as well as the spacecraft and Earth position errors. Removing these terms yields,

$$
\begin{aligned}
\lambda_i \Delta\Phi_i - \lambda_j \Delta\Phi_j &= \lambda_i\left(\Delta\phi_i + \Delta N_i\right) - \lambda_j\left(\Delta\phi_j + \Delta N_j\right) \\
&\approx \left(\hat{\mathbf{n}}_i - \hat{\mathbf{n}}_j\right)\cdot \Delta\mathbf{x} + \begin{bmatrix} \Delta\widetilde{RelEff}_i \\ -\Delta\widetilde{RelEff}_j \end{bmatrix} + \begin{bmatrix} \left\|\delta\mathbf{D}_{E_i}\right\| - \left\|\delta\mathbf{D}_{SC_i}\right\| \\ -\left\|\delta\mathbf{D}_{E_j}\right\| + \left\|\delta\mathbf{D}_{SC_j}\right\| \end{bmatrix} \\
&+ \begin{bmatrix} \Delta\delta RelEff_i \\ -\Delta\delta RelEff_j \end{bmatrix} + \left[\Delta\beta_i - \Delta\beta_j\right]
\end{aligned}
\tag{6.56}
$$

In terms of double phase difference, the Eq. (6.55) becomes,

$$
\begin{aligned}
\nabla\Delta\Phi_{ij} &= \nabla\Delta\phi_{ij} + \nabla\Delta N_{ij} \\
&\approx \left(\frac{\hat{\mathbf{n}}_i}{\lambda_i} - \frac{\hat{\mathbf{n}}_j}{\lambda_j}\right)\cdot \Delta\mathbf{x} + \left[\frac{\Delta\widetilde{RelEff}_i}{\lambda_i} - \frac{\Delta\widetilde{RelEff}_j}{\lambda_j}\right] + \left[\left(c\delta t_E - c\delta t_{SC}\right)\left(\frac{1}{\lambda_i} - \frac{1}{\lambda_j}\right)\right] \\
&+ \begin{bmatrix} \dfrac{\left\|\delta\mathbf{D}_{E_i}\right\| - \left\|\delta\mathbf{D}_{SC_i}\right\|}{\lambda_i} \\ -\dfrac{\left\|\delta\mathbf{D}_{E_j}\right\| - \left\|\delta\mathbf{D}_{SC_j}\right\|}{\lambda_j} \end{bmatrix} + \left[\left(\left\|\delta\mathbf{r}_E\right\| - \left\|\delta\mathbf{r}_{SC}\right\|\right)\left(\frac{1}{\lambda_i} - \frac{1}{\lambda_j}\right)\right] \\
&+ \left[\frac{\Delta\delta RelEff_i}{\lambda_i} - \frac{\Delta\delta RelEff_j}{\lambda_j}\right] + \left[\frac{\Delta\beta_i}{\lambda_i} - \frac{\Delta\beta_j}{\lambda_j}\right]
\end{aligned}
\tag{6.57}
$$

Alternatively, the geometric representation of phase can be stated in terms of the line-of-sight and its related errors from Eq. (6.41) such that the phase double difference becomes,

$$
\begin{aligned}
\lambda_i \Delta\Phi_i - \lambda_j \Delta\Phi_j &= \lambda_i \left(\Delta\phi_i + \Delta N_i\right) - \lambda_j \left(\Delta\phi_j + \Delta N_j\right) \\
&\approx \left(\tilde{\mathbf{n}}_i - \tilde{\mathbf{n}}_j\right)\cdot \Delta\mathbf{x} + \begin{bmatrix} \Delta\widetilde{RelEff}_i \\ -\Delta\widetilde{RelEff}_j \end{bmatrix} + \left[\left(\tilde{\mathbf{n}}_i - \tilde{\mathbf{n}}_j\right)\cdot\left(\delta\mathbf{r}_E - \delta\mathbf{r}_{SC}\right)\right] \\
&\quad + \left[\left(\delta\hat{\mathbf{n}}_i - \delta\hat{\mathbf{n}}_j\right)\cdot\Delta\mathbf{x}\right] + \begin{bmatrix} \Delta\delta RelEff_i \\ -\Delta\delta RelEff_j \end{bmatrix} + \left[\Delta\beta_i - \Delta\beta_j\right]
\end{aligned} \tag{6.58}
$$

If this is represented as phase only, this expression becomes,

$$
\begin{aligned}
\nabla\Delta\Phi_{ij} &= \nabla\Delta\phi_{ij} + \nabla\Delta N_{ij} \\
&\approx \left(\frac{\tilde{\mathbf{n}}_i}{\lambda_i} - \frac{\tilde{\mathbf{n}}_j}{\lambda_j}\right)\cdot\Delta\mathbf{x} + \left[\frac{\Delta\widetilde{RelEff}_i}{\lambda_i} - \frac{\Delta\widetilde{RelEff}_j}{\lambda_j}\right] + \left[\left(c\delta t_E - c\delta t_{SC}\right)\left(\frac{1}{\lambda_i} - \frac{1}{\lambda_j}\right)\right] \\
&\quad + \left[\left(\frac{\tilde{\mathbf{n}}_i}{\lambda_i} - \frac{\tilde{\mathbf{n}}_j}{\lambda_j}\right)\cdot\left(\delta\mathbf{r}_E - \delta\mathbf{r}_{SC}\right)\right] + \left[\left(\frac{\delta\hat{\mathbf{n}}_i}{\lambda_i} - \frac{\delta\hat{\mathbf{n}}_j}{\lambda_j}\right)\cdot\Delta\mathbf{x}\right] \\
&\quad + \left[\frac{\Delta\delta RelEff_i}{\lambda_i} - \frac{\Delta\delta RelEff_j}{\lambda_j}\right] + \left[\frac{\Delta\beta_i}{\lambda_i} - \frac{\Delta\beta_j}{\lambda_j}\right]
\end{aligned} \tag{6.59}
$$

For most practical systems, the phase double difference of Eqs. (6.55) or (6.58) are very beneficial, since the time errors cancel in these representations. However, some applications may only produce direct phase double difference measurements in which case there would be no alternative but to use Eqs. (6.57) or (6.59). However, in these equations the time errors do not cancel, so all terms must be retained for accurate position determination.

6.3.3 Triple Difference

The triple difference is created by subtracting two double differences over time. This difference removes any values that are not time dependent. For a static system or when measurements are made over fairly short difference in time, many of the time independent terms will cancel.

6.3.3.1 Range Triple Difference with Errors

The triple difference for range can be computed from Eq. (6.48) at time t_1 and t_2 as,

$$\begin{aligned}\nabla\Delta\rho_{ij}(t_2)-\nabla\Delta\rho_{ij}(t_1) &\cong \{\hat{\mathbf{n}}_i-\hat{\mathbf{n}}_j\}\cdot\left[\Delta\mathbf{x}(t_2)-\Delta\mathbf{x}(t_1)\right]+\begin{bmatrix}\nabla\Delta RelEff_{ij}(t_2)\\ -\nabla\Delta RelEff_{ij}(t_1)\end{bmatrix}\\ &+\begin{bmatrix}\nabla\Delta\delta RelEff_{ij}(t_2)\\ -\nabla\Delta\delta RelEff_{ij}(t_1)\end{bmatrix}+\left[\nabla\Delta\eta_{ij}(t_2)-\nabla\Delta\eta_{ij}(t_1)\right]\end{aligned} \tag{6.60}$$

This representation of Eq. (6.60) assumes that the triple difference of pulsar position error, with respect to Earth and the spacecraft, is negligible. The triple difference of the relativistic effect and its errors can also be considered to be very small, so for most applications the range triple difference can be stated as,

$$\nabla\Delta\rho_{ij}(t_2)-\nabla\Delta\rho_{ij}(t_1) \cong \{\hat{\mathbf{n}}_i-\hat{\mathbf{n}}_j\}\cdot\left[\Delta\mathbf{x}(t_2)-\Delta\mathbf{x}(t_1)\right]+\begin{bmatrix}\nabla\Delta\eta_{ij}(t_2)\\ -\nabla\Delta\eta_{ij}(t_1)\end{bmatrix} \tag{6.61}$$

6.3.3.2 Phase Triple Difference with Errors

Similarly as with range described above, a phase triple difference can be computed using Eq. (6.57). If all the triple differences with respect to relativity effects and its errors, time errors on Earth and the spacecraft, and position errors are considered negligible, then the phase triple difference can be written as,

$$\begin{aligned}\nabla\Delta\Phi_{ij}(t_2)-\nabla\Delta\Phi_{ij}(t_1) &= \left[\nabla\Delta\phi_{ij}(t_2)-\nabla\Delta\phi_{ij}(t_1)\right]+\left[\nabla\Delta N_{ij}(t_2)-\nabla\Delta N_{ij}(t_1)\right]\\ &\approx \left\{\frac{\hat{\mathbf{n}}_i}{\lambda_i}-\frac{\hat{\mathbf{n}}_j}{\lambda_j}\right\}\cdot\left[\Delta\mathbf{x}(t_2)-\Delta\mathbf{x}(t_1)\right]\\ &+\left[\frac{\Delta\beta_i(t_2)-\Delta\beta_i(t_1)}{\lambda_i}-\frac{\Delta\beta_j(t_2)-\Delta\beta_j(t_1)}{\lambda_j}\right]\end{aligned} \tag{6.62}$$

If the time difference is short enough, and the phase cycle is long enough, then the integer cycle will not change between measurements and the integer cycle triple difference from

Eq. (6.62) will be zero, or $\left[\nabla\Delta N_{ij}(t_2)-\nabla\Delta N_{ij}(t_1)\right]=0$. This simplifies the expression, and spacecraft position can be determined using only the fractional phase measurements.

6.3.4 Velocity Measurement

An interesting aspect of the triple differences is that by subtracting values over time this difference introduces the potential for spacecraft velocity determination. Rewriting Eq. (6.62) with the time difference between t_1 and t_2 as

$$\begin{aligned}\left[\frac{\nabla\Delta\Phi_{ij}(t_2)-\nabla\Delta\Phi_{ij}(t_1)}{t_2-t_1}\right]&=\left[\frac{\nabla\Delta\phi_{ij}(t_2)-\nabla\Delta\phi_{ij}(t_1)}{t_2-t_1}\right]+\left[\frac{\nabla\Delta N_{ij}(t_2)-\nabla\Delta N_{ij}(t_1)}{t_2-t_1}\right]\\&\approx\left\{\frac{\hat{\mathbf{n}}_i}{\lambda_i}-\frac{\hat{\mathbf{n}}_j}{\lambda_j}\right\}\cdot\left[\frac{\Delta\mathbf{x}(t_2)-\Delta\mathbf{x}(t_1)}{t_2-t_1}\right]\\&\quad+\left[\frac{\Delta\beta_i(t_2)-\Delta\beta_i(t_1)}{\lambda_i\{t_2-t_1\}}-\frac{\Delta\beta_j(t_2)-\Delta\beta_j(t_1)}{\lambda_j\{t_2-t_1\}}\right]\end{aligned} \tag{6.63}$$

Spacecraft velocity can be introduced as,

$$\Delta\dot{\mathbf{x}}=\frac{\Delta\mathbf{x}(t_2)-\Delta\mathbf{x}(t_1)}{t_2-t_1} \tag{6.64}$$

Creating similar derivatives for phase double difference and phase noise, the triple difference of Eq. (6.63) becomes,

$$\nabla\Delta\dot{\Phi}_{ij}=\nabla\Delta\dot{\phi}_{ij}+\nabla\Delta\dot{N}_{ij}\approx\left\{\frac{\hat{\mathbf{n}}_i}{\lambda_i}-\frac{\hat{\mathbf{n}}_j}{\lambda_j}\right\}\cdot\Delta\dot{\mathbf{x}}+\left[\frac{\Delta\dot{\beta}_i}{\lambda_i}-\frac{\Delta\dot{\beta}_j}{\lambda_j}\right] \tag{6.65}$$

If a system is developed that is able to determine phase measurements over time, a spacecraft velocity measurement could be completed using Eq. (6.65). If the integer cycle velocity term zero, or $\nabla\Delta\dot{N}_{ij}=0$, then the spacecraft velocity can be determined directly from the fractional phase velocity.

6.4 Search Space and Cycle Ambiguity Resolution

The previous section provided methods to determine the position of a spacecraft with respect to a known location. These methods rely on measuring the phase of an arriving pulse at a detector and comparing this to the phase predicted to arrive at the reference location. The predicted phase is determined using a pulse-timing model. However, comparing measured and predicted phase of a single pulse does not determine absolute position unless the number of full pulse cycles between these two locations is also known. Since the number of integer phase cycles is not observable in the pulse measurement from a pulsar, or they are *ambiguous*, additional methods must be developed that resolve these ambiguous cycles so that true absolute position can be determined.

This section describes the *pulse phase cycle ambiguity resolution* processes. These processes rely on the fact that for a given fully determined set of phase measurements from separate pulsars, there is one unique position in three-dimensional space that satisfies all the measurements. Thus, there is only one fully unique set of cycles that satisfies the position and phase measurements. Once this set of cycles is identified, the three-dimensional position can be determined by adding the fractional portion and integer number of phase cycles that are present between the spacecraft and the reference location.

A solution for the cycle sets can be generated through direct solution methods. These methods use a linear combination of a subset of measurements. Given enough measurements, solutions can be created for the unique set of cycles and the absolute position. However, since the phase measurements and the position produce an under-determined system (more unknowns than equations), some method of intelligently guessing some of the unknowns may need to be implemented.

The solution cycle set may also be selected from a *search space*, or three-dimensional geometry that contains an array of candidate cycle sets. Each set within a chosen search space is processed and the likelihood of each set being the unique solution is tested. Individual candidates that satisfy processing tests are retained for further evaluation. Using sufficient measurements from enough pulsars – or by using multiple measurements from a single pulsar – allows a unique cycle set within the search space to be chosen as the most likely set for the absolute position of the spacecraft. Testing each candidate set of cycles within a large search space can be computationally intensive and may require large processing time. Methods that help reduce the search space, or more quickly remove unlikely candidates from the space, are a benefit to the computations. Additionally, multiple tests of the candidate sets, which help identify likely candidates, improve the efficiency of the selection process.

In an actual navigation system, errors that are present within the system will cause the candidate selection process to be less accurate. Within the direct solution methods, errors may cause incorrect cycle sets to be identified. Within the search space methods, errors cause multiple candidate sets to be retained until the correct solution can be identified. Utilizing aggressive candidate tests may incorrectly label a set of cycles as the chosen solution, since this set may pass all the tests. Often, this set of cycles will appear to be correct given the measurements, but will eventually become obviously incorrect once additional measurement processing is available. For deep space vehicles, or vehicles orbiting Earth, this incorrect navigation solution may have disastrous effects on the spacecraft's mission. All attempts must be made to insure that i) selection methods guarantee that the correct solution is a potential solution, ii) the true candidate set lies within the chosen search space, iii) test criteria must account for measurement noise within the system, and iv) any chosen set of cycles must be continually monitored to insure its validity.

The GPS and GLONASS systems utilize similar search space and integer cycle ambiguity resolution techniques as the ones described below [3, 4, 73, 85, 106]. The basis of the techniques used for these human-made systems can be applied to the methods using variable celestial sources. However, due to the variety of types of sources and pulse cycles, the techniques for celestial sources are more complex.

The following sections describe methods on setting up the cycle determination process, generating a valid search space if needed, and resolving phase cycle ambiguities. Various options exist for search space geometry and cycle test characteristics. The methods described below provide a broad overview of these options.

6.4.1 Search Space

Resolving the ambiguous cycles that exist from the phase measurements often requires generating a search space of possible integer phase cycle combinations. Each candidate cycle set is then tested for its validity and accuracy. It is assumed that only one unique set of cycles correctly solves the phase measurements and position location, as well as passes the entire candidate set tests. However, if insufficient measurements are available, or the given measurements have large errors, then a unique set may not be solvable, and only several possible cycle sets may be identified. Creating a sufficient search space is critical for accurate cycle identification and position determination.

The search space is typically symmetrical about its origin. The origin, or center point, of the search space can be chosen depending on the application and would often be chosen as the model location. Since most pulsar timing models exist at the SSB, the barycenter is a potential choice as the search space origin. For spacecraft missions studying the solar system's planets, especially inner planets, the SSB is an appropriate option for the origin. For spacecraft operating in orbit about Earth or within the Earth-Moon system, the geocenter – or in some cases the Earth-Moon barycenter – is a more useful choice for the search space origin. When a spacecraft is known to be orbiting a planetary body, choosing this body as the origin of the search space significantly reduces the size of the search space rather than the choice of the SSB as origin. Candidate cycles can exist within the search space on either side of the origin, unless some prior knowledge allows the removal of candidates from one side of the origin. The search space could be shifted with respect to the origin if information regarding its shape can be determined.

For spacecraft that have failed for some reason and must implement absolute position navigation in order to solve the vehicle's lost-in-space problem, a better choice for the search space origin is the vehicle's last known position. This position would need to be stored in backup memory onboard the vehicle. This provides the ambiguity resolution process and its search space definition a much more accurate representation of where the vehicle *could* be, rather than starting the process entirely over and using a distant reference location as the origin.

In an operational sense, any known location can be utilized as the search space origin, since only known locations are valid for defining the pulse timing model. The choice of the origin should be made in the most prudent manner given the vehicle's situation and application.

Figure 6-12 shows a diagram of a candidate cycle search space in two dimensions. The SSB, Earth, and spacecraft positions are shown, and arriving pulse phase planes are diagramed arriving from four different pulsars. The spherical geometry search space is shown as centered about Earth. The only candidate set of cycles within the search space that has all phase planes crossing in one location is the true location of the spacecraft.

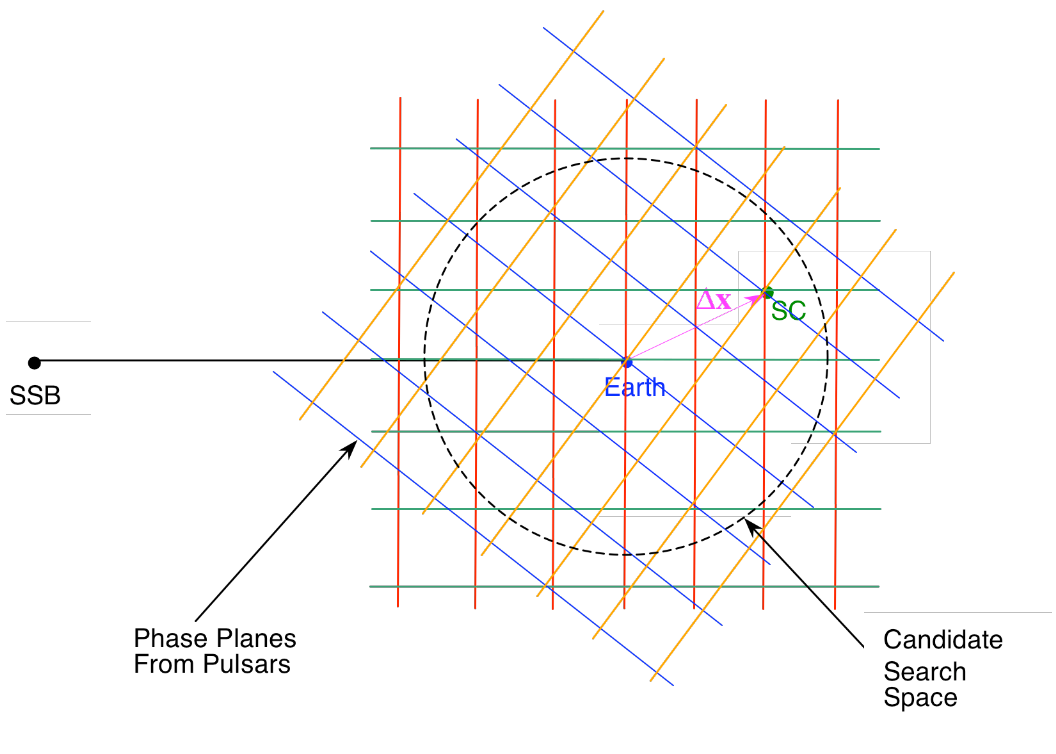

Figure 6-12. Phase cycle candidate search space, centered about Earth.

There are three methods presented below for generating a search space.

- Geometrical Space: A straightforward method of developing a cycle search space is to place a three dimensional geometrical boundary about the origin. Options for shapes include a sphere of specified radius, a cube of specified dimensions, or an ellipsoid, perhaps about the planet's equatorial plane. The dimensions of this geometry, centered about the origin, define the candidate cycles along the line-of-sight vector to each pulsar. The search space candidate sets are selected such that they lie within this geometrical boundary.

- Phase Cycle Space: A search space can be defined as a fixed number of cycles along the line-of-sight to a pulsar. The number of cycles considered can be specific to each pulsar. For example, a choice of ten cycles on each side of the origin could be selected for a pulsar. If the pulse cycle length from each pulsar is sufficiently different, care must be taken in order to ensure that the true cycle set is maintained within the created search space.
- Covariance Space: Given a set of pulsar phase measurements and the corresponding measurement noise associated with each measurement, a search space can be created that is defined by the covariance matrix of the measurements. The covariance matrix will skew the search space based on the magnitudes of the errors. This method is similar to the *Geometrical Space* method, however the *Covariance Space* shape is ellipsoidal oriented along the eigenvectors of the covariance matrix [4].

Once a search space has been generated, it is possible to reduce the number of sets to be searched by removing those sets that are known to exist inside any planetary bodies. The spacecraft could not be physically located inside these bodies, so there is no need to test these candidate sets. Sets that define a position within the Sun, Earth, or any planetary body, can be immediately removed from the search space. For applications in planetary orbits, such as low-Earth orbits, this may significantly reduce the number of searchable candidates.

6.4.2 Cycle Candidates

The candidate cycle sets within a search space are defined by the single, double, or triple differences as developed in the *Measurement Differences* section. Given a set of phase measurements, from predicted phase arrivals at a known model reference location and detected arrivals at the spacecraft position, then there is only one set of phase cycles that uniquely defines the combination of this data. The search space essentially contains an array of cycles defined to be in the vicinity of this true set. Each possible cycle combination within this search space can be identified in the array and tested to determine whether accurate spacecraft position has been resolved.

As an example, the phase single difference of Eq. (6.35) defines the relationship between fractional phase difference, $(\Delta\phi_i)$, phase integer cycle difference, (ΔN_i), and spacecraft position, $(\Delta\mathbf{x})$, for a single pulsar. If the phase difference is measured and the integer cycle difference is known *a priori*, then the spacecraft position along the line-of-sight to that pulsar, $(\hat{\mathbf{n}}_i \cdot \Delta\mathbf{x})$, is directly known from this equation. However, if ΔN_i is not known *a priori*, and supposing a search space of ten cycles is chosen, then each of the ten different cycles could be selected as the potential cycle value that defines the spacecraft location. By utilizing measurements from additional pulsars, each set of potential cycles from each pulsar can be processed to establish which set uniquely solves for the combination of phase measurements and spacecraft location.

This process could easily be extended for double or triple differences by using Eqs. (6.51) and (6.62) respectively. If the phase double differences are measured, then there exists one set of cycle double differences that solves for the unique spacecraft location. Appropriately, a search space that contains the entire array of possible cycle double differences can be generated, and each combination of cycles within this space can be tested for its validity.

Figure 6-13 shows an elementary two-dimensional search space generated from two orthogonally located pulsars. Several phase cycle single differences are labeled, such as $(\Delta N_1, \Delta N_2) = (2,2)$ and $(\Delta N_1, \Delta N_2) = (-2,-1)$. The true spacecraft position happens to be located at the intersection of phase planes 1 and 2, or $(\Delta N_1, \Delta N_2) = (1,2)$.

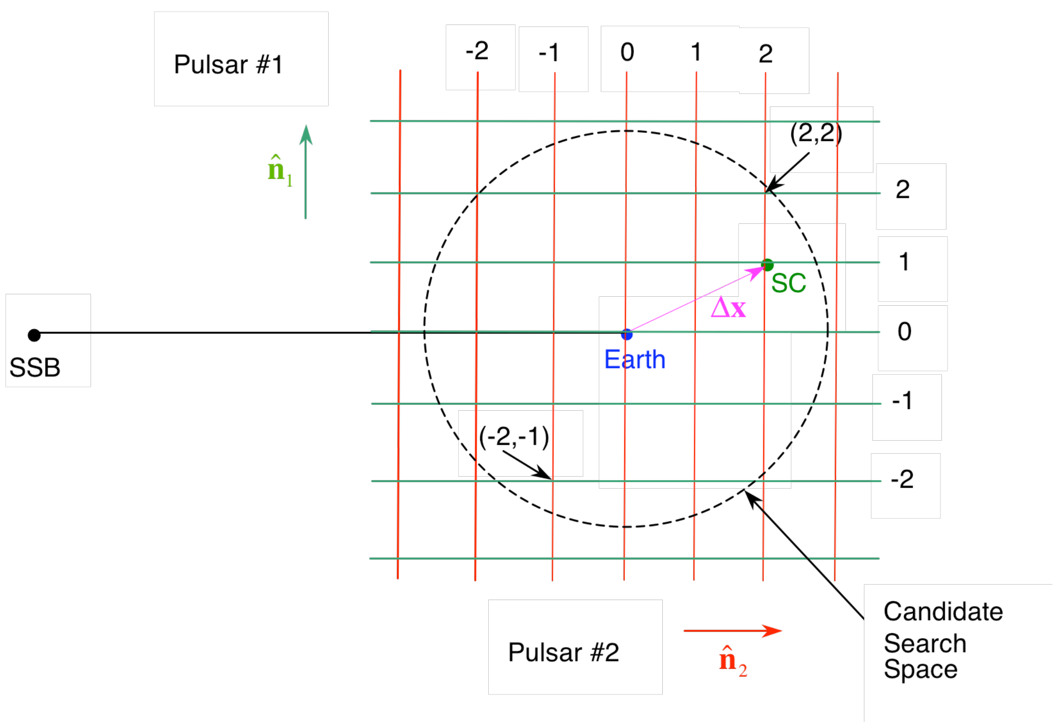

Figure 6-13. Phase cycle search space, containing candidate cycle sets, centered about Earth.

6.4.3 Cycle Ambiguity Resolution

Accurate spacecraft absolute position determination requires precise phase measurements at the spacecraft detectors, thorough pulse timing models at the base reference location, and exact knowledge of the ambiguous phase cycles between the spacecraft and the reference location. The phase cycle ambiguity resolution process determines these unknown phase cycles, which match the measured phase data.

Three resolution methods are presented. Each method has advantages for specific applications, and some require less processing than the others. The *Batch*, or *Least Squares*, method directly solves for cycle ambiguities based upon input measurements. Processing is fairly simple, but requires intelligent pre-processing, and inaccurate measurements can lead to widely erroneous results. The *Floating-Point Kalman Filter* method generates a floating-point estimate of the integer cycle ambiguity set as produced by the observing Kalman filter (or similar observation filter). Somewhat process intensive, this method may require large amounts of measurement data, spread over time, in order to resolve the correct ambiguity set. The *Search Space Array* method exhaustively tests each potential cycle set that exists within a generated search space. Although process intensive if large amount of candidate sets exist within a search space, with the use of well-chosen selection tests this method can typically correctly resolve the cycle ambiguities. Further detail on each processing method is provided below.

6.4.3.1 Batch (Least Squares) Resolution

This *Batch* method assembles a set of phase measurements from separate pulsars to simultaneously and instantly solve for spacecraft position and phase cycle ambiguities. A straightforward *Least Squares* solution can be implemented, or perhaps enhanced

Weighted Least Squares method, which uses weights based upon the phase measurement accuracies.

To sufficiently solve for the three-dimensional position and cycle ambiguities, some intelligent pre-processing of pulsar data must be implemented. This is required since even with measurements from several pulsars, the linear system of equations is under-determined (more unknowns than available equations). Reducing the number of unknown variables is necessary to create a fully determined system.

Any of the single, double, or triple differences may be implemented into this *Batch* resolution process. Additionally, system errors may also be determined. However, adding the estimation of error terms increases the number of unknowns.

From the phase single difference Eq. (6.35), the equation may be placed in linear form for a single pulsar as,

$$\Delta\phi_i = \begin{bmatrix} \dfrac{\hat{\mathbf{n}}_i}{\lambda_i} & -1 \end{bmatrix} \begin{bmatrix} \Delta\mathbf{x} \\ \Delta N_i \end{bmatrix} \tag{6.66}$$

Small errors that may exist for this equation have been ignored. This single equation has one measurement, $\Delta\phi_i$, and four unknowns – three from the position vector, $\Delta\mathbf{x}$, and one from the single-phase cycle unknown, ΔN_i. Assembling phase measurements from k pulsars, this equation becomes,

$$\begin{bmatrix} \Delta\phi_1 \\ \Delta\phi_2 \\ \cdot \\ \cdot \\ \cdot \\ \Delta\phi_k \end{bmatrix} = \begin{bmatrix} \frac{\hat{\mathbf{n}}_1}{\lambda_1} & -1 & 0 & \cdot & \cdot & \cdot & 0 \\ \frac{\hat{\mathbf{n}}_2}{\lambda_2} & 0 & -1 & 0 & \cdot & \cdot & 0 \\ \cdot & \cdot & & \cdot & & & \cdot \\ \cdot & \cdot & & & \cdot & & \cdot \\ \cdot & 0 & \cdot & \cdot & 0 & -1 & 0 \\ \frac{\hat{\mathbf{n}}_k}{\lambda_k} & 0 & \cdot & \cdot & \cdot & 0 & -1 \end{bmatrix} \begin{bmatrix} \Delta\mathbf{x} \\ \Delta N_1 \\ \Delta N_2 \\ \cdot \\ \cdot \\ \cdot \\ \Delta N_k \end{bmatrix} \tag{6.67}$$

This system has k equations and $k+3$ unknowns, which is an under-determined system. At least three unknowns must be estimated prior to attempting to solve this equation. Any prior knowledge that allows an estimate of enough unknowns to reduce the system to be fully determined is useful.

The selection of certain pulsars may support reducing the number of cycle unknowns. When trying to determine spacecraft position, the knowledge of the vehicle's mission may provide insight to estimates of its locations. For example, consider a spacecraft within a geosynchronous orbit of Earth (radius = 42,200 km). If observation pulsars are selected that have a cycle period of greater than 0.28 s (= 2*42,200/c), then these specific pulsars have no known cycle ambiguities within the potential orbit radius. Only one cycle exists within this distance. Since a phase difference measurement may have ambiguous sign, it may also be wise to test at least one single cycle difference $(\Delta N = 1)$ for these specific pulsars. Choosing a minimum of three pulsars with large enough period allows prior estimation of their cycle differences. With these three values already known, the system of equation becomes,

$$
\begin{bmatrix} \Delta\phi_1 \\ \Delta\phi_2 \\ \cdot \\ \cdot \\ \Delta\phi_{k-3} \\ \Delta\phi_{k-2}+\Delta N_{k-2} \\ \Delta\phi_{k-1}+\Delta N_{k-1} \\ \Delta\phi_k+\Delta N_k \end{bmatrix} = \begin{bmatrix} \dfrac{\hat{\mathbf{n}}_1}{\lambda_1} & -1 & 0 & \cdot & \cdot & \cdot & 0 \\ \dfrac{\hat{\mathbf{n}}_2}{\lambda_2} & 0 & -1 & 0 & \cdot & \cdot & 0 \\ \cdot & \cdot & & & & \cdot & \cdot \\ \cdot & \cdot & & & & \cdot & 0 \\ \dfrac{\hat{\mathbf{n}}_{k-3}}{\lambda_{k-3}} & 0 & & & & 0 & -1 \\ \dfrac{\hat{\mathbf{n}}_{k-2}}{\lambda_{k-2}} & 0 & \cdot & \cdot & \cdot & \cdot & 0 \\ \dfrac{\hat{\mathbf{n}}_{k-1}}{\lambda_{k-1}} & 0 & \cdot & \cdot & \cdot & \cdot & 0 \\ \dfrac{\hat{\mathbf{n}}_k}{\lambda_k} & 0 & \cdot & \cdot & \cdot & \cdot & 0 \end{bmatrix} \begin{bmatrix} \Delta\mathbf{x} \\ \Delta N_1 \\ \Delta N_2 \\ \cdot \\ \cdot \\ \cdot \\ \Delta N_{k-3} \end{bmatrix} \tag{6.68}
$$

This new system of equations now has k equations and k unknowns. This new system can be solved by rewriting the system in full vector form as,

$$
[\Delta\boldsymbol{\phi}] = H \begin{bmatrix} \Delta\mathbf{x} \\ \Delta\mathbf{N} \end{bmatrix} \tag{6.69}
$$

The H matrix, composed of the terms from Eq. (6.69), is referred to as the *measurement matrix*. This new system can be solved using methods of *Least Squares* as the following,

$$
\begin{bmatrix} \Delta\mathbf{x} \\ \Delta\mathbf{N} \end{bmatrix} = \left(H^T H\right)^{-1} \left(H^T\right) [\Delta\boldsymbol{\phi}] \tag{6.70}
$$

Additionally, a weighting matrix, W, representing the covariance estimate of accuracies for each measurement can be implemented as,

$$
[\Delta\boldsymbol{\phi}] = WH \begin{bmatrix} \Delta\mathbf{x} \\ \Delta\mathbf{N} \end{bmatrix} \tag{6.71}
$$

The solution to this weighted equation is then,

$$
\begin{bmatrix} \Delta\mathbf{x} \\ \Delta\mathbf{N} \end{bmatrix} = \left[(WH)^T (WH)\right]^{-1} (WH)^T [\Delta\boldsymbol{\phi}] \tag{6.72}
$$

Thus, using either Eqs. (6.70) or (6.72), a *Batch* solution of vehicle position and unknown cycle ambiguities can be determined. This method is relatively simple to generate and limited processing is required. Instant position and cycle value results are available once sufficient measurements are created. This process can be extended to use the error equation for a phase single difference of Eq. (6.41), however, unless methods are provided to estimate these additional errors, more equations (or measurements) are required to solve for the additional unknown variables.

Alternatively, this *Batch* process can be extended to utilize the phase double or triple differences. As shown previously, creating double or triple differences reduce the errors associated with each phase measurement. However, these additional differences reduce the number of equations within a system. For a system of k measurements, a double difference system has only $k-1$ equations with $k+2$ unknowns, and a triple difference system has only $k-2$ equations with $k+1$ unknowns. Additional methods of estimating unknowns must be created for these higher order difference systems.

6.4.3.2 Floating-Point Kalman Filter Resolution

In this *Floating-Point Kalman Filter* resolution method, an analytical filter is developed that estimates the state variables of spacecraft position and phase cycle using measurements of phase differences. A Kalman filter is a recursive state estimator that relies on adequate models of the behavior of each state variable over time, the state *dynamics*, and sufficient representation of the relationship of the state variables with respect to the observed measurements [29, 65]. Process noise associated with the state dynamics and measurement noise associated with each measurement are incorporated into the Kalman filter process. Estimates of state variables and the error covariance matrix associated with the state variables are products of this filter. The error covariance matrix provides an estimate of the accuracy of the state estimation during the filter processing.

The *Floating-Point Kalman Filter* is created such that the spacecraft position and the cycle ambiguities are treated as state variables. The phase differences are provided as measurements to the filter. The dynamics of each state can be represented over time using any prior knowledge of their dynamics, or if the measurements are produced over a sufficiently short amount of time, the state dynamics can be treated as *static* (not changing due to time). This type of filter could incorporate triple difference measurements using Eq. (6.65) to determine spacecraft velocity as well as position. This would assist with any unknown vehicle dynamics. Although the phase cycle differences are integer values, these terms are estimated as floating-point (real) values within the *Floating-Point Kalman Filter* [3]. Once sufficient measurements have been processed such that the values remain stable, these floating-point estimates can be rounded to the nearest integer.

The *Floating-Point Kalman Filter* resolution method provides processing of sequential measurements as they become available, as opposed to the *Batch* processing technique, which is implemented all at once. However, since there are many pulsars that can be observed, and coordinating the differences between them all can be a bookkeeping challenge, this method is process intensive.

The *Floating-Point Kalman Filter* could be implemented as an error-state filter, where state variables are the associated errors of whole states (such as error in position rather than position). Since some errors may be non-linear, the *extended* form of the Kalman filter algorithms would be implemented.

6.4.3.3 Search Space Array Resolution

The previous methods solve directly for cycle ambiguities as a consequence of their processing. The *Search Space Array* method selects a candidate set of cycles and determines whether this set provides an accurate position solution. This method must exhaustively test all possible candidates for the most likely set, and is consequently process intensive. However, testing all possible candidate sets within a generated search space assures that the correct solution set will be tested, rather than potentially never being evaluated by the previous methods. As was mentioned previously in the *Search Space* section, intelligent search space creation will help reduce the exhaustive processing by limiting the number of candidate sets, while still attempting to insure the correct solution lies within the search space.

As shown in Figure 6-12 and Figure 6-13, the search space is essentially a geometric grid of candidate cycles from each observed pulsar. Every possible grid point must be evaluated within the search space in order to determine which point is the most likely candidate cycle set for the combined pulse phase difference measurements and the spacecraft position.

In order to evaluate each candidate cycle set, a comprehensive test, or series of tests, of the candidate's validity and accuracy must be performed. From Eq. (6.35), for a phase single difference from one pulsar, using the measured phase difference, $\Delta\phi_i$, and a chosen set of cycle differences, $\Delta\tilde{N}_i$, the spacecraft position along the line-of-sight for the pulsar can be solved for using,

$$\hat{\mathbf{n}}_i \cdot \Delta\tilde{\mathbf{x}} = \lambda_i\left(\Delta\phi_i + \Delta\tilde{N}_i\right) \tag{6.73}$$

Given a set of at least three pulsars, the measurements can be assembled as,

$$\begin{bmatrix} \hat{\mathbf{n}}_1 \\ \hat{\mathbf{n}}_2 \\ \hat{\mathbf{n}}_3 \end{bmatrix} \Delta\tilde{\mathbf{x}} = H\Delta\tilde{\mathbf{x}} = \begin{bmatrix} \lambda_1\left(\Delta\phi_1 + \Delta\tilde{N}_1\right) \\ \lambda_2\left(\Delta\phi_2 + \Delta\tilde{N}_2\right) \\ \lambda_3\left(\Delta\phi_3 + \Delta\tilde{N}_3\right) \end{bmatrix} \tag{6.74}$$

The spacecraft position can then be solved for using,

$$\Delta\tilde{\mathbf{x}} = \left[\left(H^T H\right)^{-1} H^T\right] \begin{bmatrix} \lambda_1\left(\Delta\phi_1 + \Delta\tilde{N}_1\right) \\ \lambda_2\left(\Delta\phi_2 + \Delta\tilde{N}_2\right) \\ \lambda_3\left(\Delta\phi_3 + \Delta\tilde{N}_3\right) \end{bmatrix} \tag{6.75}$$

Using this value for spacecraft position, any additional pulsars $\left(j > 3\right)$ can have their cycle ambiguities directly solved for by

$$\Delta\tilde{N}_j = round\left(\frac{\hat{\mathbf{n}}_j}{\lambda_j} \cdot \Delta\tilde{\mathbf{x}} - \Delta\phi_j\right) \tag{6.76}$$

where the $round$ function rounds the floating-point expression within the parentheses to the nearest integer.

A *residual test* can be determined using these new estimated cycle ambiguities as,

$$v_j = \frac{\hat{\mathbf{n}}_j}{\lambda_j} \cdot \Delta\tilde{\mathbf{x}} - \Delta\phi_j - \Delta\tilde{\mathbf{N}}_j \tag{6.77}$$

If more than one additional observed pulsar is available, then a vector of these residual tests can be produced,

$$\mathbf{v} = \begin{bmatrix} v_j \\ v_{j+1} \\ \cdot \\ \cdot \\ \cdot \\ v_k \end{bmatrix} = \begin{bmatrix} \frac{\hat{\mathbf{n}}_j}{\lambda_j} \cdot \Delta\tilde{\mathbf{x}} - \Delta\phi_j - \Delta\tilde{N}_j \\ \frac{\hat{\mathbf{n}}_{j+1}}{\lambda_{j+1}} \cdot \Delta\tilde{\mathbf{x}} - \Delta\phi_{j+1} - \Delta\tilde{N}_{j+1} \\ \cdot \\ \cdot \\ \cdot \\ \frac{\hat{\mathbf{n}}_k}{\lambda_k} \cdot \Delta\tilde{\mathbf{x}} - \Delta\phi_k - \Delta\tilde{N}_k \end{bmatrix} \tag{6.78}$$

The magnitude of this residual vector provides an estimate of the quality of the computed spacecraft position, $\Delta\tilde{\mathbf{x}}$,

$$\sigma_v = norm(\mathbf{v}) \tag{6.79}$$

Each candidate set within a search space can be evaluated using this test statistic, σ_v. If a chosen set does not match well with the measured phase difference and spacecraft position, then the value of residual σ_v will be large. Likewise, if the chosen set does match well, then the differences for each extra observable pulsar from Eq. (6.78) will be small and consequently, the magnitude of the residual vector will be small. A threshold for this residual magnitude can be chosen in order to remove many, if not all, of the candidate sets other than the specific candidate set that represents the true spacecraft position. If several candidate sets remain below a chosen threshold, additional measurements from pulsars can help to eliminate wrong candidate sets. Eventually, after enough measurements have been processed, the true candidate set will be identified and the absolute position of the spacecraft will be determined. For some cases, the vector of residual tests can be computed using all available sources instead of just those with index $j > 3$, which may give further information about which candidate sets can be discarded.

As was shown within the *Batch* resolution process, weighting of individual pulsars can be used to help determine an estimated vehicle position. Adding a weighting matrix to Eq. (6.74), the spacecraft position solution of Eq. (6.75) becomes,

$$\Delta\tilde{\mathbf{x}} = \left[(WH)^T (WH) \right]^{-1} (WH)^T \begin{bmatrix} \lambda_1 \left(\Delta\phi_1 + \Delta\tilde{N}_1 \right) \\ \lambda_2 \left(\Delta\phi_2 + \Delta\tilde{N}_2 \right) \\ \lambda_3 \left(\Delta\phi_3 + \Delta\tilde{N}_3 \right) \end{bmatrix} \tag{6.80}$$

Weights may also be included in the residual calculation of Eq. (6.78). Incorporating weights into these measurements may be necessary if a subset of pulsars is more accurately measurable than the remaining pulsars.

The residual vector defined in Eq. (6.78) can be extended to include double and/or triple phase and cycle differences. The sections describing these differences have shown that errors are reduced when using higher order differences. However, because these higher order differences are evaluated using differences of close or similar values, developing a test statistic threshold that sufficiently removes unwanted candidate sets and retains the correct candidate set becomes increasingly difficult. Care must be exercised in choosing a good statistic threshold. In order to augment this issue, *combined-order* systems, where candidate set evaluation is performed at multiple levels of differences can assist in selecting the correct cycle set. For example a combined-order system incorporating both first and second differences may help to identify the correct cycle set.

Additional tests may be created that help remove unwanted candidate sets. If any dynamics of the vehicle is known during an observation time, this information can determine how future cycles behave with respect to current cycle estimates. Comparing the *Batch* method results to the *Search Space Array* results, using the assumed correct set of cycles, can be an additional test of cycle and spacecraft position validity.

6.5 Relative Position

The preceding sections developed methods to determine a spacecraft's absolute position within an inertial frame. Choosing a known reference location within this frame, the offset position with respect to this location is determined from these methods. The spacecraft's absolute position is then the sum of the reference position and the offset position. Some applications, however, may only require knowledge of *relative position*, or the position relative to a location that may or may not be fixed. This relative, or *base station*, location may be the position of another vehicle or any object that the spacecraft uses as a relative reference. Since this base station's relative location may not be known by the spacecraft at any given instance, the location of this relative object must be transmitted to the spacecraft when measurements are needed. This requires communication between the base station and the spacecraft.

If the base station also has a detector, similar to the spacecraft, then direct phase measurement differences can be implemented instead of using a pulse-timing model. If a pulse-timing model is used, the base station must transmit its location so that the inertial-based timing model can be transferred to the base station's location. If full detector information can be transmitted from the base station, then a model is not required, since direct phase differences can be calculated.

Figure 6-14 provides a diagram of the relative navigation concept with a base station spacecraft and a single remote spacecraft. Communication between the remote spacecraft and the base station, as well as contemporaneously measured pulse arrival times, allows relative navigation of the vehicles.

This relative navigation system requires more processing due to the extra communication and because the system is a dynamically operating system versus a static base station. Time alignment of measurement date is crucial and often complicated. This type of navigation has similarities to the processes of differential or relative GPS navigation, where one receiver station transmits its information to another station in order to determine relative position and velocity information [156].

Relative navigation is useful for applications such as multiple spacecraft formation flying, a spacecraft docking with another vehicle, or a rover operating on a planetary body with respect to its lander's base station. Alternatively, a base station satellite can be placed in Earth orbit and be used to monitor and update pulsar ephemeris information. Ideal locations for these base stations may include geosynchronous orbits, Sun-Earth and Earth-Moon Lagrange points, or solar-system halo orbits. Once new or updated pulsar data is computed, the base station could broadcast this information to all operational spacecraft. Those spacecraft within the base station's vicinity and within communication contact can use the station's information to compute a relative position solution. This method may provide improved accuracy over the absolute position method, since the base station can provide real-time updates of pulse models. If accurate base station navigation information is known, then computing a relative navigation solution with respect to the base station also allows the spacecraft to compute its own absolute position.

For spacecraft operating in near-vicinity to one another, linear approximations to their relative equations of motions can provide additional simplifications to this relative navigation process. The Clohessy-Wiltshire-Hill equations describe this motion between two orbiting vehicles when their distance apart is small and they have similar orbit parameters [41]. Using these linear equations in addition to the simultaneous range measurements from the two vehicles can benefit the relative navigation methods.

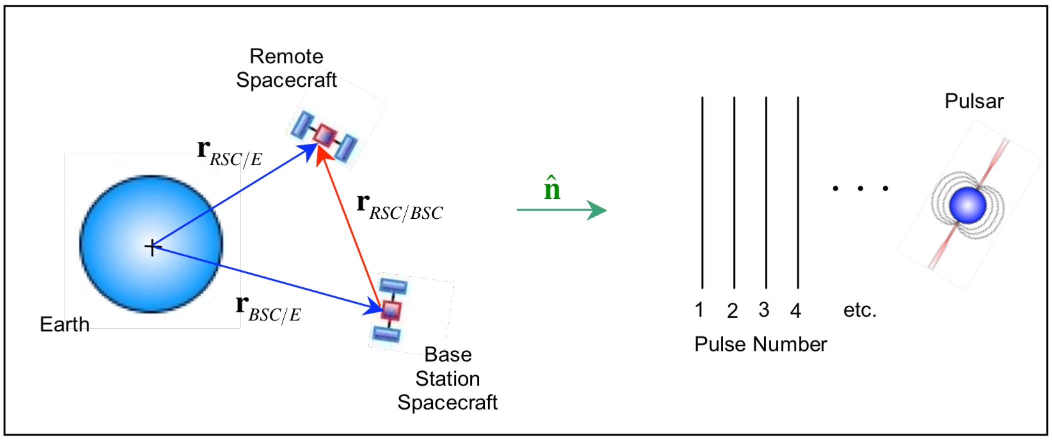

Figure 6-14. Position of remote spacecraft relative to base station spacecraft.

6.5.1 Vehicle Attitude Determination

An interesting potential application of relative position determination is the calculation of the position of two pulsar detectors affixed to the same spacecraft. Determining the position of one detector relative to another on the vehicle could allow an alternative method of determining the attitude, or orientation, of the vehicle. A significant advantage of this method is that no integer cycle ambiguity resolution is required, since even the fastest pulsar period is much larger than any previously developed spacecraft (pulse period = 0.00156 s => 467 km), thus the detectors are always within a cycle of each other. Additionally, the separation between the two detectors can be determined when installed on the vehicle, reducing the unknown relative position in the above ambiguity resolution processes. Once the phase difference can be determined for the same pulse at each detector, only the angle, θ, along the line-of-sight to the pulsar needs to be determined.

Similar to Figure 6-9, Figure 6-15 illustrates the orientation of the baseline, L_{AB}, between two detectors, detectors A and B, mounted on the same spacecraft relative to the incoming pulse planes from a pulsar. The angle is related to the phase difference and the baseline length as,

$$\sin(\theta) = \frac{\Delta\Phi_i}{L_{AB}} \tag{6.81}$$

The baseline between the two detectors and the error in determining the relative position determines the potential accuracy of such an attitude system. Assuming the pulse time of arrival can be determined to within 1 ns for each detector, then attitude accuracy of 0.5° requires a baseline length of 33 m. Future spacecraft, such as solar sails, may be able to accommodate detectors spaced this far apart.

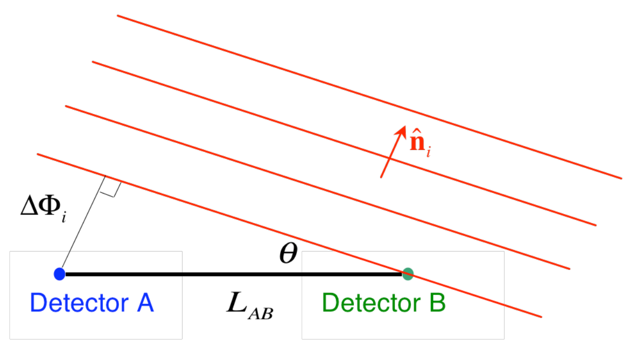

Figure 6-15. Orientation of two detectors on spacecraft relative to pulsar.

Unlike GPS and GLONASS, it is difficult to track the carrier signal of pulsars. This may be possible at the radio wavelengths, but would be complicated at the visible and X-ray wavelengths since only individual photons are detected. Thus, this attitude determination would only be computed occasionally when TOA measurements are produced. Blending this data with other onboard attitude sensors, such as gyros, could enhance a spacecraft's navigation performance.

6.6 Solution Accuracy

Upon the computation of a position solution, providing an estimate of its accuracy is important for many operations. This accuracy estimate provides a measure of how close the solution is with regards to the true solution. The *Floating-Point Kalman Filter* and *Search Space Array* methods provide accuracy estimates as part of their processing. Several additional methods determining position accuracy estimates are discussed in this section. These concepts allow an assessment of the quality of the computations.

6.6.1 Position Covariance

The covariance of position (the cov function for short) uses the *expectation operator*, E, as

$$\mathrm{covariance}(position) = \mathrm{cov}(position) = E\left(\Delta\mathbf{x} \cdot \Delta\mathbf{x}^T\right) \tag{6.82}$$

The relationship of position to the measured range to each pulsar is from Eq. (6.26) as,

$$\Delta\rho_i = \lambda_i \Delta\Phi_i = \hat{\mathbf{n}}_i \cdot \Delta\mathbf{x} \tag{6.83}$$

Creating a vector of these measurements from j pulsars, Eq. (6.83) becomes,

$$\overrightarrow{\Delta\rho} = \begin{bmatrix} \hat{\mathbf{n}}_1 \\ \hat{\mathbf{n}}_2 \\ \cdot \\ \cdot \\ \cdot \\ \hat{\mathbf{n}}_j \end{bmatrix} \Delta\mathbf{x} = H\Delta\mathbf{x} \tag{6.84}$$

A word of caution, the symbol $\overrightarrow{\Delta\rho}$ is used here to represent a vector of range measurements, not to become confused with the range difference vector, $\Delta\boldsymbol{\rho}$, of Eq. (6.24).

Using the pseudo-inverse of the *line-of-sight measurement matrix*, H, the covariance of position with respect to the range measurements is,

$$\operatorname{cov}(position) = E\left(\Delta\mathbf{x}\cdot\Delta\mathbf{x}^T\right) = \left\{\left(H^T H\right)^{-1} H^T\right\} E\left[\overrightarrow{\Delta\rho}\cdot\overrightarrow{\Delta\rho}^T\right]\left\{\left(H^T H\right)^{-1} H^T\right\}^T \tag{6.85}$$

With the relationship between the range measurement and the phase measurement as listed in Eq. (6.35), the position covariance can also be expressed from the phase measurement expectations as,

$$\operatorname{cov}(position) = \left\{\left(H^T H\right)^{-1} H^T\right\} E\left[\overrightarrow{\lambda\Delta\Phi}\cdot\overrightarrow{\lambda\Delta\Phi}^T\right]\left\{\left(H^T H\right)^{-1} H^T\right\}^T \tag{6.86}$$

where $\overrightarrow{\lambda\Delta\Phi}$ is the vector of phase measurements and their cycle wavelengths.

Unlike the GPS system, which assumes the same variance for each range measurement from all the similar satellites, each pulsar is assumed to have specific difference accuracy for its measurement. Hence, each measurement will have a unique variance. This is primarily due to the unique pulse cycle length and timing model for each pulsar. However, these measurements are assumed to be uncorrelated, with zero mean, such that $E\left[\Delta\rho_i \cdot \Delta\rho_j\right]=0;\ i \neq j$, or $E\left[\lambda_i\Delta\Phi_i \cdot \lambda_j\Delta\Phi_j\right]=0;\ i \neq j$. Thus the expectations matrix for the range measurements can be expressed as the diagonal matrix,

$$E\left[\overline{\Delta\rho} \cdot \overline{\Delta\rho}^T\right]=\begin{bmatrix} \sigma_{\rho_1}^2 & 0 & \cdot & \cdot & \cdot & 0 \\ 0 & \sigma_{\rho_2}^2 & & & & \cdot \\ \cdot & & \cdot & & & \cdot \\ \cdot & & & \cdot & & \cdot \\ \cdot & & & & \cdot & 0 \\ 0 & \cdot & \cdot & \cdot & 0 & \sigma_{\rho_k}^2 \end{bmatrix} \tag{6.87}$$

Similarly, the expectations matrix for phase can be represented as,

$$E\left[\overline{\lambda\Delta\Phi} \cdot \overline{\lambda\Delta\Phi}^T\right]=\begin{bmatrix} \lambda_1^2\sigma_{\Phi_1}^2 & 0 & \cdot & \cdot & \cdot & 0 \\ 0 & \lambda_2^2\sigma_{\Phi_2}^2 & & & & \cdot \\ \cdot & & \cdot & & & \cdot \\ \cdot & & & \cdot & & \cdot \\ \cdot & & & & \cdot & 0 \\ 0 & \cdot & \cdot & \cdot & 0 & \lambda_j^2\sigma_{\Phi_k}^2 \end{bmatrix} \tag{6.88}$$

The values of each variance would be created based upon the accuracy of the measured pulsar pulse arrival time. It may also be related to the cycle period and the pulse width.

It is expected that each pulsar would typically have a unique variance. However, if a system were created such that the variance was the same value for each measurement, then the position covariance would be simplified to either,

$$\begin{aligned} \operatorname{cov}(position) &= \left\{\left(H^T H\right)^{-1} H^T\right\} E\left[\overline{\Delta\rho} \cdot \overline{\Delta\rho}^T\right]\left\{\left(H^T H\right)^{-1} H^T\right\}^T \\ &= \sigma_\rho^2\left(H^T H\right)^{-1} \end{aligned} \tag{6.89}$$

or, in terms of phase,

$$\begin{aligned} \operatorname{cov}(position) &= \left\{\left(H^T H\right)^{-1} H^T\right\} E\left[\overline{\lambda\Delta\Phi} \cdot \overline{\lambda\Delta\Phi}^T\right]\left\{\left(H^T H\right)^{-1} H^T\right\}^T \\ &= \sigma_\Phi^2 diag\left(\lambda_1^2, \lambda_2^2, \ldots, \lambda_j^2\right)\left(H^T H\right)^{-1} \end{aligned} \tag{6.90}$$

This simplification relies on the symmetric matrix identity of $\left(H^T H\right)^{-1} = \left\{\left(H^T H\right)^{-1}\right\}^T$. It is more than likely this assumption of the same accuracy of range measurement for each pulsar is not valid. Pulsars are very unique; no two emit the same signal. Thus, it is expected that specific variances for each range must be considered as in Eq. (6.87) and as phase in Eq. (6.88).

6.6.1.1 Including Spacecraft Clock Error

If spacecraft clock error, δt_{SC}, is also considered as an error that is observable from the pulsar range measurements, then this error can be included in the state vector. The equation for range measurements can be modified for this additional error as,

$$\overline{\Delta\rho} = \begin{bmatrix} \hat{\mathbf{n}}_1 & 1 \\ \hat{\mathbf{n}}_2 & 1 \\ \cdot & \cdot \\ \cdot & \cdot \\ \cdot & \cdot \\ \hat{\mathbf{n}}_j & 1 \end{bmatrix} \begin{bmatrix} \Delta\mathbf{x} \\ c\delta t_{sc} \end{bmatrix} = H'\Delta\mathbf{x}' \tag{6.91}$$

In this equation, H' is the modified measurement matrix, and $\Delta\mathbf{x}'$ is new state vector that includes both spacecraft position and spacecraft clock error. From the error equations discussed in the *Measurement Differences* section, any errors could be included in the state vector, as long the correct modifications to the measurement matrix are implemented and these errors are observable. The analysis for position covariance described above can be implemented using this new model equation of Eq. (6.91). Alternatively, phase measurements could be utilized instead of range measurements, as presented in previous discussions.

6.6.2 Geometric Dilution of Precision

The *Geometric Dilution of Precision* (GDOP) is an expression of the accuracy of the estimated position [156]. GDOP is based upon the covariance matrix of the estimated errors of the position solution. This parameter is often used in GPS position accuracy estimates, and some of the algorithms used for GPS apply to pulsars, although modifications shown above for the position covariance are required. In the GPS system, the range accuracy from each GPS satellite is often assumed constant, thus the range covariance matrix reduces to a constant value multiplied by an identity matrix. The GPS-specific GDOP can then be represented as a scalar quantity. For a pulsar-based system, range measurements to each pulsars are most likely unique to each pulsar, thus the simplification in GPS cannot be realized within a pulsar-based system. Nonetheless, the position accuracy can still be estimated using the computed variance. The pulsar-based navigation system GDOP is then no longer a scalar value, but rather a direct estimate of position accuracy.

The position covariance matrix of Eq. (6.89) or (6.90) are 3x3 matrices, since the state vector is composed of position. This covariance matrix can be represented as,

$$\operatorname{cov}(position) = E\left(\Delta\mathbf{x} \cdot \Delta\mathbf{x}^T\right) = C = \begin{bmatrix} \sigma_x^2 & \sigma_x\sigma_y & \sigma_x\sigma_z \\ \sigma_y\sigma_x & \sigma_y^2 & \sigma_y\sigma_z \\ \sigma_z\sigma_x & \sigma_z\sigma_y & \sigma_z^2 \end{bmatrix} \tag{6.92}$$

The GDOP can be computed from the trace of this matrix. With this representation, a GDOP from a pulsar-based system has units of position, not a simple scalar unitless quantity as in GPS, and is represented as,

$$GDOP_{PSR} = \sqrt{trace(C)} = \sqrt{\sigma_x^2 + \sigma_y^2 + \sigma_z^2} \tag{6.93}$$

If the error state covariance matrix is developed to include spacecraft clock error, as shown in Eq. (6.91), then the covariance matrix is represented as,

$$\mathrm{cov}\left(position\right) = E\left(\Delta\mathbf{x}'\cdot\Delta\mathbf{x}'^{T}\right) = C' = \begin{bmatrix} \sigma_x^2 & \sigma_x\sigma_y & \sigma_x\sigma_z & \sigma_x\sigma_t \\ \sigma_y\sigma_x & \sigma_y^2 & \sigma_y\sigma_z & \sigma_y\sigma_t \\ \sigma_z\sigma_x & \sigma_z\sigma_y & \sigma_z^2 & \sigma_z\sigma_t \\ \sigma_t\sigma_x & \sigma_t\sigma_y & \sigma_t\sigma_z & \sigma_t^2 \end{bmatrix} \tag{6.94}$$

The GDOP for this system is again based upon the trace of the covariance matrix, but this now includes the variance due to clock error,

$$GDOP_{PSR} = \sqrt{trace\left(C'\right)} = \sqrt{\sigma_x^2 + \sigma_y^2 + \sigma_z^2 + \sigma_t^2} \tag{6.95}$$

The *position dilution of precision* (PDOP) can be determined from this system by considering only the position related states as,

$$PDOP_{PSR} = \sqrt{trace\left(C_{3x3}^{'}\right)} = \sqrt{\sigma_x^2 + \sigma_y^2 + \sigma_z^2} \tag{6.96}$$

The *time dilution of precision* (TDOP) is directly computed by the time variance in this matrix and also has units of position,

$$TDOP_{PSR} = \sigma_t \tag{6.97}$$

The measured GDOP provides a description of how well the set of chosen pulsars will compute an accurate three-dimensional position, based upon the covariance matrix of the estimated position errors. If pulsars are chosen from only one portion of the sky, the measurement matrix will skew the observations towards this direction and will not produce a good three-dimensional solution. If pulsars are chosen that are distributed correctly in the sky, then no preferred direction will be skewed by the measurement matrix and a good three-dimensional solution will result. Lower values of GDOP indicate more favorable pulsar distribution. Thus various sets of pulsars can be chosen and their associated GDOP will determine which is the more appropriate set for processing. This GDOP value may prove very useful when choosing pulsars for the *Batch* resolution process, since a good distribution of pulsars improves this solution.

6.6.2.1 Example GDOP Values

Using the unit direction for position and range measurement accuracy from the Table 3.5 and Table 3.6, after 1000 seconds of observation, the GDOP for the top ten RPSRs and top ten APSRs is 9.22 km for a 1-m^2 detector. Using the top four of each RPSRs and APSRs the GDOP reduces to 1.04 km for this size detector. If only the four pulsars PSR B0531+21, PSR B1937+21, PSR B1617-155, and PSR B1758-250 are considered due to their good geometrical distribution and range variance, the GDOP improves to 0.37 km for 1-m^2. If the observation time is increased to 5000 seconds for these four pulsars, the GDOP further improves to 0.17 km for a 1-m^2 detector. If the three top RPSRs of PSR B0531+21, PSR B1821-24, and PSR B1937+21 are utilized, the GDOP for a 500 s observation is 2.0 km and for a 1000 s observation is 1.4 km.

Since the value of $A \cdot \Delta t_{obs}$ is constant throughout the SNR expressions of Chapter 3, system design tradeoffs can be considered for detector area versus observation time. For example, the SNR produces the same range variance, and consequently the same GDOP, for a 1-m^2 detector observing for 5000 seconds as a 5-m^2 detector observing for 1000 seconds. However, other mitigating factors, such as power usage, may need to be considered in this type of study. Most of the RPSRs in Table 3.5 all lie in the lower latitudes of the Galactic sphere. Sources above the Galactic equator may be considered for improved geometrical distribution.

6.7 Numerical Simulation

In order to test the methods presented above for determination of absolute position of a spacecraft, a simulation of the algorithms has been developed. A description of this simulation and results of several test cases are presented. The current implementation of the simulation concentrates on determining the position of vehicles orbiting Earth. However, the simulation is also designed for relative position determination between two vehicles and for position determination of spacecraft orbiting different bodies.

6.7.1 Simulation Description

To study the performance of the absolute position determination methods, the simulation was developed to compute position of vehicles near-Earth. The geocenter was chosen as the reference location, instead of the SSB. The choice was made primarily to reduce the size of the search space, since the distance between Earth and the spacecraft is much smaller than the distance between the SSB and the spacecraft and therefore fewer cycle candidates.

The intent of the simulation is to determine the unknown integer pulse cycles of the total phase difference from each source between the geocenter reference location and the true location of the spacecraft. A search space is created to identify candidate sets of integer cycles that would produce the most likely position of the spacecraft based upon the measured fractional pulse phase differences between geocenter and the spacecraft.

The simulation creates a geometrical search space using a reasonable distance from Earth for a specific spacecraft. The search space is in the form of a spherical shell and is centered about the geocenter. The bounds of the shells are defined by a minimum radius, such as the radius of Earth, and a maximum radius, such as several times the expected orbit radius of the vehicle. Only sets of candidate integer cycles that compute position within these bounds are considered acceptable and processed within the simulation. Since each candidate set within the search space must be investigated, the processing time becomes significant with a large number of sets. Any technique that can initially remove incorrect candidates reduces the processing time, however these techniques must assure that the correct solution set is not discarded.

A set of ten variable sources was selected using their geometrical distribution, availability, and range measurement accuracy as reported in Chapter 3. These sources and some of their characteristics are listed in Table 6-2. It was assumed that each source could be observed simultaneously for duration of 1000 s. This assumption would require multiple detectors acting in unison to produce pulse phase measurements from each source at the same time. Otherwise, a separate scheme must be chosen to align the phase measurements to the same epoch and spacecraft position. Since position is unknown to the vehicle processing, a source's pulse arrival time was computed assuming the detector was located at the geocenter. However, as shown in Section 6.2.3, since the vehicle's detector is not actually located at the geocenter, but rather at its true location, the detector will measure a pulse TOA that is likely different in phase from the predicted TOA of a pulse-timing model located at the geocenter. The true phase difference is in terms of both fractional phase cycle and an integer number of cycles, although since the number of cycles is unknown, only the fractional phase portion of the difference can be measured.

Table 6-2. Sources Used By Absolute Position Simulation.

Source Name	Period (s)	Cycle Wavelength (km)	σ_{RANGE} after 1000 s (km)
PSR B0531+21	0.03340	10013.1	0.078
PSR B1937+21	0.00156	467.7	0.247
PSR J0218+4232	0.00232	695.5	9.812
B1636-536	0.00345	1034.3	0.216
B1758-250	0.00303	908.4	0.080
PSR B1821–24	0.00305	914.4	0.233
B1820-303	0.00363	1088.2	0.214
PSR B1823–13	0.10145	30413.9	6.708
PSR J1124-5916	0.13531	40564.9	11.81
PSR B1509–58	0.15023	45037.8	1.294

To simulate the measurement error within a phase measurement, the magnitude of the contribution of between 5% and 10% of fractional phase plus the range measurement accuracy from Table 6-2 divided by cycle wavelength is determined. For each source's observation, the total error is multiplied by a normalized random number. This span of error was selected based upon the Crab Pulsar observation by the USA experiment discussed in section 6.2.3 and Appendix C, where the geocenter is the assumed position. Within the simulation, this measurement error was added to the true phase value for each source, and was provided to the position determination algorithm for processing.

There are two main processing loops within the simulation that implements a combined order system. A phase double difference loop and a phase single difference loop are used. Within the double difference loop, the first four sources from Table 6-2 (the shaded rows) are used along with each combination of their integer cycle candidates in the defined search space to compute a position offset from the geocenter as in Eq. (6.54). The sources were selected due to their short cycle wavelengths and their good GDOPs. The computed position from this set of four sources is verified to exist within the search space. This position is then used to compute a residual as in Eq. (6.78) for each of the six remaining sources from the table. The magnitude of this residual is compared to a test statistic threshold value. The set of candidate cycles that pass the residual threshold test are recorded and passed to the single difference loop.

The second loop within the simulation computes a position based upon the phase measurements and all the search space candidates that passed the double difference residual test. This new position is first verified to exist within the defined search space. Those positions that pass the search space geometry test are then used along with their phase measurements and candidate cycles to compute a single difference residual vector for all ten sources. Those candidate sets that pass a single difference threshold residual test are recorded. For many runs of the simulation, the set of cycles that computes the smallest single difference residual is the set that computes the correct spacecraft position.

For some cases, there are several single differenced candidate sets that compute residuals that are smaller than the candidate set of the true solution. This is due to the amount of phase error measured by the system. For some candidate sets, large phase errors can create solutions that although having small residuals their position solutions are incorrect. In these situations, additional tests must be pursued to determine which solution is the correct one. Otherwise, another complete observation and processing of the algorithm can be pursued. The new data should expose those incorrect solution sets and help identify the correct solution from both observations.

Although geocentric operations are demonstrated here, it is projected that the simulation would work equally well for selenocentric, Mars-centered, or other planetary body-centered orbiting spacecraft. The position information of that planetary body is required for correct operation in these instances. For interplanetary missions, where typically only SSB-centered simulations could be pursued, additional intelligence of the spacecraft's trajectory must be gathered to assist in reducing the size of the search space. Alternatively, longer cycle wavelength sources could be utilized within the scheme to reduce the number of candidate cycles that could exist over these long distances.

6.7.2 Simulation Results

Several test cases have been investigated using this simulation. Presented below are simulations of the absolute position determination of spacecraft in the *ARGOS*, GPS, and geosynchronous orbits. Each case has a specifically defined search space. The dimensions of each search space are provided in Table 6-3. For the *ARGOS* and GPS orbit, spherical shells are created for the search space, since these spacecraft could be anywhere within this three-dimensional region. For the geosynchronous orbit, the DirecTV 2 spacecraft was chosen to represent satellites in this orbit. Within this geosynchronous orbit, the spherical shell search spaces are truncated along the z-axis, since these vehicles would most likely remain close to the equator. This table also presents the selected threshold values for the double difference and single difference residual tests used in the simulation. Orbit data of each spacecraft's orbit is provided by the NORAD Two-Line Element (TLE) sets [83, 97]. Appendix C provides a listing of these sets for each vehicle. The chosen epoch that defines the position of the vehicle within its orbit is provided in Table 6-3.

Table 6-4 presents example simulation results for determining the correct set of cycle candidates within the *ARGOS* spacecraft orbit. With 5% of phase measurement error and using the *ARGOS* orbit radius of 7218 km, there are initially 245125 candidates that are investigated. Of these candidates, only 44966 sets remain within the defined search space shell. Using the threshold value from Table 6-3, only 30 candidates remain after the double difference residual test. Using the all sources to define the single difference position solution, only 19 candidates remain within the search space region. After the single differenced residual test only 4 candidates remain. Of these four candidates, the set with the smallest value from the single difference residual test is the correct solution. With 10% of phase measurement error similar reduction in candidate sets are evident. However, four potential candidate sets have a single difference residual that is smaller than the set that computes the true position solution. These five sets would need to be monitored or re-evaluated to determine which one is the correct solution.

Table 6-3. Simulated Orbit Search Space And Threshold Data.

Spacecraft Orbit	Epoch (JD)	Search Space (km)	Double Difference Residual Threshold	Single Differenced Residual Threshold
ARGOS	2451538.967692660	$R_{min} = R_{Earth}$ $R_{max} = 13200$	5% Phs Err: 0.20 10% Phs Err: 0.25	5% Phs Err: 0.20 10% Phs Err: 0.25
GPS BIIA-16 PRN-01	2453345.820344930	$R_{min} = 20025$ $R_{max} = 33375$	5% Phs Err: 0.20 10% Phs Err: 0.20	5% Phs Err: 0.20 10% Phs Err: 0.25
DirecTV 2 (DBS 2)	2453372.624232230	$R_{min} = 31500$ $R_{max} = 52500$ $z_{max} = \pm 10000$	5% Phs Err: 0.20 10% Phs Err: 0.25	5% Phs Err: 0.20 10% Phs Err: 0.25

Due to the 5% of phase measurement error and the phase measurement accuracy, the correct set of pulse candidates produce a position solution that has a magnitude of 118 km of error with respect to the true position. Although at first this may appear to be a large position error, since the vehicle was initially assumed to exist at the center of Earth at the start of this process, the error in position has been significantly improved. To improve the position solution even further, several options could be pursued. Using the new estimated position, the simulation could re-run. This new position would improve the accuracy of the pulse time transfer to the SSB, and consequently would reduce the pulse phase measurement error for each source. With reduced phase measurement error, and selecting sources with short cycle wavelengths and best GDOPs, the updated position estimate should have reduced error. Methods such as this iterative process refine the estimated position solution. Techniques such as this could also be used to investigate the remaining five candidate sets for the 10% phase measurement error case.

Table 6-4. Example Simulation Results For *ARGOS* Spacecraft.

Integer Cycle Candidate Set Characteristics	**5% Phase Measurement Error**	**10% Phase Measurement Error**
# Initial Total Candidates	245125	245125
# Found Within Search Space Shell	44966	44974
# Pass Double Difference Residual Test	30	90
# Found Within Search Space Shell	19	60
# Pass Single Difference Residual Test	4	12
# Candidates with Single Difference Residual Less than True Candidate Set	0	4
Magnitude of Position Error for Correct Candidate Set (km)	118	235

Table 6-5 presents the simulation results for the GPS orbit. Since the search space region is much larger than in the ARGO orbit case, there are many more initial candidate sets that must be investigated. However, this large number of candidates is quickly reduced when tested to exist within the search space region and tested against the double difference residual threshold. For this specific run, with the 5% phase error the correct solution is identified with the smallest single difference residual. For the 10% phase error case, although all ten remaining candidates other than the true solution have residuals less than the true set, only two other solutions compute an orbit radius within 500 km of the true GPS orbit. Table 6-6 presents the simulation results for the DirecTV 2 orbit. There are a significant number of potential candidates at the start of the simulation, however, only a few percent of these exist within the search space shell. For the 10% phase error case, although 14 candidates remain after the single difference case, only one other candidate than the true candidate set has an orbit radius within 500 km of the actual radius.

Table 6-5. Example Simulation Results For GPS Spacecraft.

Integer Cycle Candidate Set Characteristics	5% Phase Measurement Error	10% Phase Measurement Error
# Initial Total Candidates	3429153	3429153
# Found Within Search Space Shell	758025	757894
# Pass Double Difference Residual Test	400	475
# Found Within Search Space Shell	290	343
# Pass Single Difference Residual Test	10	11
# Candidates with Single Difference Residual Less than True Candidate Set	0	10
Magnitude of Position Error for Correct Candidate Set (km)	158	313

Table 6-6. Example Simulation Results For DirecTV 2 Spacecraft.

Integer Cycle Candidate Set Characteristics	5% Phase Measurement Error	10% Phase Measurement Error
# Initial Total Candidates	20326119	20326119
# Found Within Search Space Shell	1184081	1183802
# Pass Double Difference Residual Test	407	1126
# Found Within Search Space Shell	182	507
# Pass Single Difference Residual Test	11	34
# Candidates with Single Difference Residual Less than True Candidate Set	0	14
Magnitude of Position Error for Correct Candidate Set (km)	176	352

The algorithms and results presented in this chapter demonstrate the potential of using differenced phase measurements to compute spacecraft absolute position. By determining the correct phase cycle set for the observed pulses from a set of pulsars, the range estimates between a reference location and the spacecraft can be computed for each observation. The several techniques discussed select the correct cycle set from a group of candidate sets. Combining the range estimates and the line-of-sight direction to each pulsar provides an approach to determine the full three-dimensional absolute position within an inertial coordinate system. The accuracy of the position solution depends on the error of each phase measurement. As the simulation results show, choosing a search space origin close to the estimated position reduces the number of candidates that must be investigated, and may also help reduce the amount of phase measurement error.

The set of sources chosen for this simulation were primarily selected based upon their geometrical distribution and range measurement accuracy. Other sources could also be selected to either include additional measurements within the processing or replace any of those sources that do not achieve their predicted performance. Future investigations of the simulation would choose alternative sets of sources to analyze their absolute position determination performance.

For various applications, the position solution produced by this method may be sufficient for the vehicle to complete its mission. For those applications that require additional accuracy, this method can be used in an iterative process to yield improved solutions. Once the initial correct cycle set is determined, the process of creating pulse profiles from photons and determining the pulse arrival times could be recomputed using the new position solution. This would reduce the phase measurement errors further and would produce improved range estimates. These new range estimates would consequently produce a position solution with greater accuracy. Iterative processes such as these would help produce solutions with sufficient accuracy for most applications. Alternatively, the solution produced by this absolute position determination process could be utilized as the initial conditions for a numerical orbit propagation routine, which could then be corrected over time using the concepts that are presented in Chapters 7 and 8.

Determining absolute position with no *a priori* information using the signals emitted by these variable celestial sources will prove to be a significant resource for future spacecraft navigation systems. As new detector systems are developed that can view multiple sources at once, the results demonstrated show that this technique would benefit a wide variety of spacecraft operations.

Chapter 7 Delta-Correction of Position Estimate

"An approximate answer to the right problem is worth a good deal more than an exact answer to an approximate problem."

– John Tukey

Determining absolute position with no prior knowledge of vehicle position or velocity information is useful for many situations. However, navigation can often be interpreted as the process of *improving* an estimate of the current state information of a vehicle. If an estimate is sufficiently accurate and provides enough information to safely guide and control the vehicle, then the navigation system's role is to maintain this accuracy, or continually improve the solution over time. This Chapter describes the methods used to improve an estimate of the position and velocity state information using the measured pulse arrival times from variable celestial sources.

7.1 Concept Description

7.1.1 Estimated Position

Given a navigation solution of time, position, and velocity, a spacecraft can predict this state information using its known dynamics through the process of onboard orbit propagation. External forces acting on the spacecraft, such as gravity, atmospheric drag, and solar pressure, as well as thrusting forces due to the vehicle's own engines, can be used as models to propagate the state dynamics.

If these force and perturbation models are sufficiently accurate, forward propagation of the state dynamics can correctly predict the navigation state of the vehicle at a future time. However, small model errors or unmodelled disturbances can significantly affect the state prediction. Higher order gravitational potential, fluctuating drag, and varying solar radiation pressure effects that are not accounted for in the dynamics models can alter the known state of the vehicle such that large prediction errors can result. Especially with the periodic nature of spacecraft orbits, any incorrectly modeled effects can cause errors to grow without bounds, such that predicted orbits will not match the true orbit of the vehicle.

Variable celestial sources provide the necessary signal to create updates to the estimates of onboard navigation solutions. Since these sources are significantly distant from the solar system, they provide signal coverage for much greater regions than the near-Earth designed systems of GPS and GLONASS. The processing concepts rely on measuring of pulse time arrivals from the sources and comparing the measured times to the predicted arrival times from pulse timing models. Although this comparison process is similar to those completed in the algorithms of Chapter 6 for absolute position determination, in this concept reasonable estimates of position and velocity are utilized within the processing algorithms and updates to these estimates are generated.

This method of creating an update to an estimated navigation solution is referred to as the *delta-correction* method, as the product of this method is a delta, or small offset, correction to an estimated solution. Some authors refer to this technique as a *differential-correction* method [16, 17, 55, 160, 213]. However, due to the current popularity of *differential corrections* for GPS systems [156], it was chosen to avoid the confusion between these dissimilar concepts. In differential GPS, it is assumed a receiver and its antenna are located at some known location and GPS satellite and atmospheric corrections are broadcast from this receiver to local users. In the delta-correction variable celestial source method only algorithmic models are provided at a known location and stored within the spacecraft's database. There is no detector located at the model's location that broadcasts its model information. However, referring to this described method as a *differential correction from pulsars* concept is not entirely incorrect.

7.1.2 Algorithms

Pulsar signals received at a spacecraft are offset from those arriving at the SSB primarily by the distance between the SSB and the spacecraft. If accurate detector position is known, then the time offset of the arriving pulses between the detector and the SSB can be calculated. Conversely, if accurate time is known such that pulses are accurately measured at the detector, then the position offset of the detector and the SSB can be computed by comparing the pulse measurement with that predicted by the pulsar-timing model. The pulse timing models defined in Chapter 3 predict the arrival of individual pulses at the SSB.

As it moves away from the SSB, a spacecraft sensor will detect a pulse at a time relative to the predicted arrival time based upon the pulse-timing model. A direct comparison of the arrival time at the spacecraft to the same pulse's arrival time at the SSB is accomplished using the time transfer equations of Chapter 4. These equations require accurate knowledge of the spacecraft's position and velocity in order to be implemented correctly. If, however, the spacecraft position is in error by some amount, using the time transfer equations to transform the detected pulse time from the spacecraft to the SSB will result in some offset in the comparison of pulse arrival times. If the spacecraft position is not known whatsoever, then the time transfer equations cannot be utilized. Pulses can still be detected and timed at the spacecraft's detector, but timing can only be made relative to the spacecraft itself.

In the *delta-correction* scheme, estimated values of spacecraft position and velocity are utilized within the time transfer equation to create the best estimates of pulse arrival times at the SSB. The estimated values can come from a variety of potential methods. Other external navigation sensors onboard the spacecraft could provide these estimates, Sensors such as GPS or GLONASS could directly provide periodic position and velocity values when those system's satellites are visible to the spacecraft's receiving antenna. Star camera and trackers could also be utilized to provide estimated position values. Data telemetry from ground stations using the DSN could also provide position and velocity estimates. Any complementing external method that provides estimated values could be used within this scheme.

However, additional spacecraft operations autonomy is provided if a high fidelity onboard orbit propagator is implemented within the vehicle's navigation system in order to provide a continuous estimate of the vehicle's dynamics during a pulsar observation. The implementation of onboard orbit propagators will be presented in more detail in Chapter 8. Using an approximate set of starting values for position and velocity, orbit propagators can provide the necessary information to transfer spacecraft pulse time of arrival to the SSB.

From an estimated position, $\tilde{\mathbf{r}}$, the detected pulse arrival times at the spacecraft are transferred to the SSB origin via the time transfer equations. A range comparison along the line-of-sight to the pulsar is created by differencing the measured arrival time to the predicted arrival time from the pulse-timing model. The discrepancy in these values provides a contribution to the estimate of the offset position, $\delta\mathbf{r}$, between the true position of the vehicle and the estimated position. Referring to Figure 7-1, the error in position will relate to the computed time offset of a pulse along the line-of-sight to the pulsar. Using pulsars at different locations provides line-of-sight measurements in each pulsar's direction. Combining measurements from different pulsars solves for the full position offset in three dimensions. The following sections provide details on methods to compute the range differences for varying degrees of complexity in the time transfer equations.

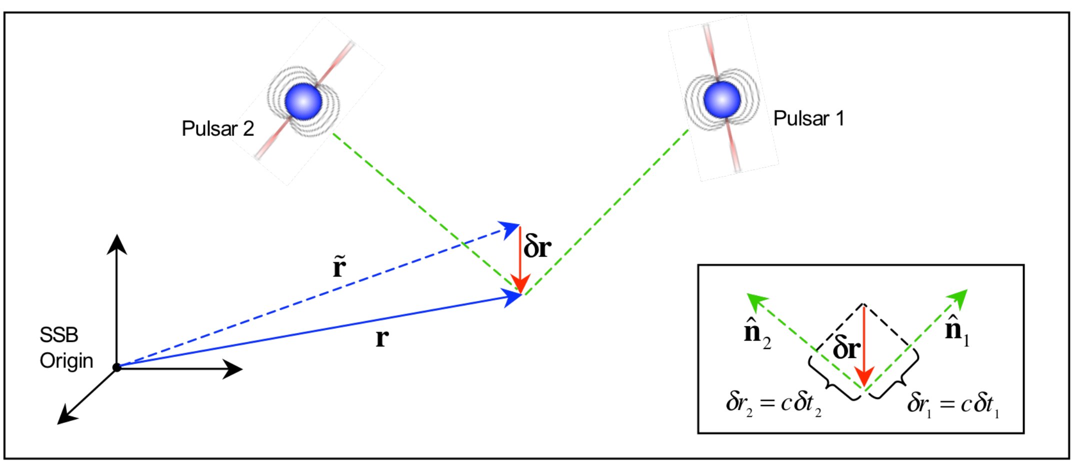

Figure 7-1. Estimated position error relative to the signal received from two pulsars.

7.1.2.1 First Order Measurement

The position error, or offset, $\delta\mathbf{r}$, can be defined as the difference of true and estimated position as,

$$\delta\mathbf{r} = \mathbf{r} - \tilde{\mathbf{r}} \tag{7.1}$$

The error in spacecraft observation time of the pulse is the difference between the true and estimated arrival time at the spacecraft and can be represented as,

$$\delta t_{SC} = t_{SC} - \tilde{t}_{SC} \tag{7.2}$$

The error in the pulse arrival time at the SSB is the difference between the true and estimated arrival times, and can be represented as,

$$\delta t_{SSB} = t_{SSB} - \tilde{t}_{SSB} \tag{7.3}$$

The pulse TOA measured at the spacecraft, t_{SC}, can be transferred to its arrival time at the SSB, t_{SSB}. To first order from Chapter 4, this transfer has been shown to be the following for the i^{th} pulsar,

$$t_{SSB} = t_{SC} + \frac{\hat{\mathbf{n}}_i \cdot \mathbf{r}}{c} \tag{7.4}$$

Eq. (7.4) assumes perfect TOA measurement at the spacecraft, as well as absolute knowledge of the direction to the pulsar and the spacecraft position. If position is only an estimated value, and potentially some uncertainty in the spacecraft measured TOA, then this equation becomes an estimated value as,

$$\tilde{t}_{SSB} = \tilde{t}_{SC} + \frac{\hat{\mathbf{n}}_i \cdot \tilde{\mathbf{r}}}{c} \tag{7.5}$$

The true pulse TOA at its arrival at the SSB can be predicted via the pulse-timing model. Using t_{SSB} to represent the true predicted TOA at the SSB, then the two representations of TOA from the model and TOA from the spacecraft measurement in

Eqs. (7.4) and (7.5), respectively, can be differenced to produce the offset in TOA arrival. Using Eqs. (7.3) through (7.5) this offset is expressed as,

$$\delta t_{SSB} = t_{SSB} - \tilde{t}_{SSB} = \left(t_{SC} + \frac{\hat{\mathbf{n}}_i \cdot \mathbf{r}}{c} \right) - \left(\tilde{t}_{SC} + \frac{\hat{\mathbf{n}}_i \cdot \tilde{\mathbf{r}}}{c} \right) \tag{7.6}$$

From the error expressions for position and spacecraft observation TOA of Eqs. (7.1) and (7.2) respectively, the error in position can be expressed as a function of SSB pulse TOA offset and spacecraft observation error as,

$$c\delta t_{SSB} - c\delta t_{SC} = \hat{\mathbf{n}}_i \cdot \delta \mathbf{r} \tag{7.7}$$

Assuming there is no measurable error within the spacecraft's direct observation of the photons used to create the pulse profile then δt_{SC} can be assumed negligible. Thus, any determined difference between the predicted TOA from the timing model and the measured pulse TOA can be expressed as range offset of the spacecraft along the unit direction to the pulsar, or,

$$c\delta t_{SSB} = \hat{\mathbf{n}}_i \cdot \delta \mathbf{r} \tag{7.8}$$

This is the fundamental observable within the *delta-correction* scheme. This equation is used to correct the estimated position of the spacecraft due to the observed measured pulse TOA.

7.1.2.1.1 Position Offset Relative to Earth

The position offset computed above pertains to the position relative to the inertial location of the defined pulse model, typically taken as the SSB origin. Most operational spacecraft utilize position relative to Earth in their navigation systems. The time transfer expression from Eq. (7.4) can be expressed in terms of Earth position and the spacecraft relative position to Earth as,

$$t_{SSB} - t_{SC} = \frac{\hat{\mathbf{n}}_i \cdot \mathbf{r}}{c} = \frac{\hat{\mathbf{n}}_i}{c} \cdot \left(\mathbf{r}_E + \mathbf{r}_{SC/E} \right) \tag{7.9}$$

Using the estimated value of this relative position, $\tilde{\mathbf{r}}_{SC/E}$, the error in this value, $\delta\mathbf{r}_{SC/E}$, is related to the true value as,

$$\mathbf{r}_{SC/E} = \tilde{\mathbf{r}}_{SC/E} + \delta\mathbf{r}_{SC/E} \tag{7.10}$$

The error expression of Eq. (7.7) can be expanded using Eqs. (7.9) and (7.10) such that,

$$c\delta t_{SSB} - c\delta t_{SC} - \hat{\mathbf{n}}_i \cdot \delta\mathbf{r}_E = \hat{\mathbf{n}}_i \cdot \delta\mathbf{r}_{SC/E} \tag{7.11}$$

The known Earth position could be provided by standard ephemeris tables (ex. JPL ephemeris data). If planetary ephemeris data is assumed without error, such that $\boldsymbol{\delta}\mathbf{r}_E = \mathbf{0}$, then $\delta\mathbf{r} = \delta\mathbf{r}_{SC/E}$, and Eq. (7.11) reverts to Eq. (7.7).

7.1.2.1.2 Simple One-Dimensional Example

Figure 12 illustrates how *delta-correction* scheme is visualized along a one-dimensional pulse train from a pulsar. This simple example uses the first order terms of the pulse timing model and Eqs. (7.5), and (7.7) to demonstrate how a new estimate of position is computed based upon the predicted and actual arrival times of a detected pulse.

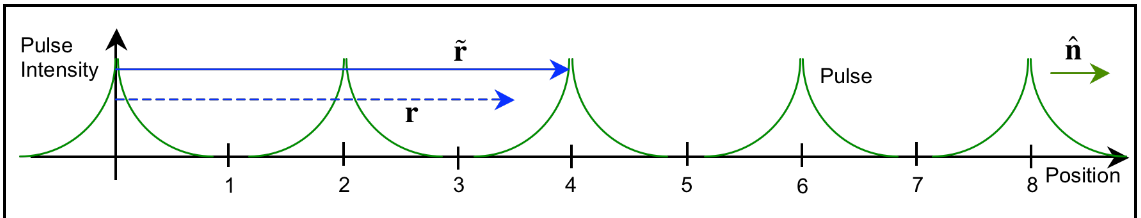

- To simplify this example, normalize position and time units such that $c = 1$.
- Phase pulse: $\Phi = \Phi_0 + \frac{1}{P}\left(t_{SSB} - t_0\right) \approx \frac{1}{P} t_{SSB}$, where choosing $\Phi_0 = 0$ and $t_0 = 0$.
- Assume $\tilde{\mathbf{r}} = 4$ at $\tilde{t}_{SC} = 4$, then $\tilde{t}_{SSB} = \tilde{t}_{SC} + \frac{\hat{\mathbf{n}} \cdot \tilde{\mathbf{r}}}{c} = 4 + 4 = 8$.
- From $\Phi = \frac{1}{P} t_{SSB} = \frac{8}{2} = 4$ equals whole value => pulse arriving at origin now ($\delta t_{SSB} = 0$).
- However, actual position is $\mathbf{r} = 3.5$, thus measure actual pulse quarter-cycle later, $\delta t_{SC} = 0.5$.
- Compute position error: $\delta t_{SSB} - \delta t_{SC} = \frac{\hat{\mathbf{n}} \cdot \delta \mathbf{r}}{c}$ => $\delta r = 0 - 0.5 = -0.5$.
- Update position estimate: $\mathbf{r} = \tilde{\mathbf{r}} + \delta \mathbf{r} = 4 - 0.5 = 3.5$.

Figure 7-2. One-dimensional position estimate error example.

Although the SSB origin is used as the model location within these equations, the methods works equally well for any reference model location. Thus if pulse timing models were provided at the geocenter, then time transfer could be implemented between the spacecraft and the geocenter, and the delta-correction scheme could produce position offsets directly for the vehicle's estimated position relative to Earth's center. If the pulse model was defined at the location of another spacecraft, then this scheme could also produce the relative position offset between the two spacecrafts.

7.1.2.2 Higher Order Measurement

The previous section presents methods to determine the error in an estimate of position based upon the first order expressions of time transfer. However, as was discussed in Chapter 4, higher order relativistic terms should be included in order to accurately transfer time from a spacecraft to the SSB. Although the previous section demonstrates the basic correction methods of this scheme, an actual navigation system would need to use the full time transfer equations for high accuracy. Additional considerations for improving the accuracy of the delta-correction measurement include numbering the individual pulses received at the detector from a reference value to correctly identify pulses for comparison, and accounting for any modeling uncertainties and measurement noise within the entire system.

A high accuracy time transfer equation between the spacecraft coordinate time and the SSB coordinate time is provided in Chapter 4. Slight modification of this expression by assuming the Sun is the primary gravitational effect in the Shapiro delay term produces the following time transfer equation,

$$t_{SSB} = t_{SC} + \frac{1}{c}\begin{bmatrix} \hat{\mathbf{n}}\cdot\mathbf{r} - \dfrac{r^2}{2D_0} + \dfrac{(\hat{\mathbf{n}}\cdot\mathbf{r})^2}{2D_0} + \dfrac{\mathbf{r}\cdot\mathbf{V}\Delta t_N}{D_0} \\ -\dfrac{(\hat{\mathbf{n}}\cdot\mathbf{V}\Delta t_N)(\hat{\mathbf{n}}\cdot\mathbf{r})}{D_0} - \dfrac{(\mathbf{b}\cdot\mathbf{r})}{D_0} + \dfrac{(\hat{\mathbf{n}}\cdot\mathbf{b})(\hat{\mathbf{n}}\cdot\mathbf{r})}{D_0} \end{bmatrix} + \frac{2\mu_S}{c^3}\ln\left|\frac{\hat{\mathbf{n}}\cdot\mathbf{r}+r}{\hat{\mathbf{n}}\cdot\mathbf{b}+b}+1\right| \quad (7.12)$$

Using an estimated position and its error from Eq. (7.1) this time transfer equation becomes,

$$c(t_{SSB} - t_{SC}) = \hat{\mathbf{n}}\cdot(\tilde{\mathbf{r}}+\delta\mathbf{r}) + \frac{1}{D_0}\begin{bmatrix} \dfrac{1}{2}\left[\hat{\mathbf{n}}\cdot(\tilde{\mathbf{r}}+\delta\mathbf{r})\right]^2 - \dfrac{1}{2}\left\|\tilde{\mathbf{r}}+\delta\mathbf{r}\right\|^2 \\ +(\tilde{\mathbf{r}}+\delta\mathbf{r})\cdot\mathbf{V}\Delta t_N - (\hat{\mathbf{n}}\cdot\mathbf{V}\Delta t_N)\left[\hat{\mathbf{n}}\cdot(\tilde{\mathbf{r}}+\delta\mathbf{r})\right] \\ -\mathbf{b}\cdot(\tilde{\mathbf{r}}+\delta\mathbf{r}) + (\hat{\mathbf{n}}\cdot\mathbf{b})\left[\hat{\mathbf{n}}\cdot(\tilde{\mathbf{r}}+\delta\mathbf{r})\right] \end{bmatrix}$$
$$+\frac{2\mu_S}{c^2}\ln\left|\frac{\left[\hat{\mathbf{n}}\cdot(\tilde{\mathbf{r}}+\delta\mathbf{r})\right]+\left\|\tilde{\mathbf{r}}+\delta\mathbf{r}\right\|}{\hat{\mathbf{n}}\cdot\mathbf{b}+b}+1\right| \quad (7.13)$$

The terms involving the position error can be linearized such that,

$$\left[\hat{\mathbf{n}}\cdot(\tilde{\mathbf{r}}+\delta\mathbf{r})\right]^2 = (\hat{\mathbf{n}}\cdot\tilde{\mathbf{r}})^2 + 2(\hat{\mathbf{n}}\cdot\tilde{\mathbf{r}})(\hat{\mathbf{n}}\cdot\delta\mathbf{r}) + (\hat{\mathbf{n}}\cdot\delta\mathbf{r})^2 \quad (7.14)$$

$$\left\|\tilde{\mathbf{r}}+\delta\mathbf{r}\right\|^2 = (\tilde{\mathbf{r}}+\delta\mathbf{r})\cdot(\tilde{\mathbf{r}}+\delta\mathbf{r}) = \tilde{\mathbf{r}}\cdot\tilde{\mathbf{r}} + 2\tilde{\mathbf{r}}\cdot\delta\mathbf{r} + \delta\mathbf{r}\cdot\delta\mathbf{r} \quad (7.15)$$

$$\ln\left|\frac{\left[\hat{\mathbf{n}}\cdot(\tilde{\mathbf{r}}+\delta\mathbf{r})\right]+\|\tilde{\mathbf{r}}+\delta\mathbf{r}\|}{\hat{\mathbf{n}}\cdot\mathbf{b}+b}+1\right| = \ln\left|\frac{\hat{\mathbf{n}}\cdot\tilde{\mathbf{r}}+\tilde{r}}{\hat{\mathbf{n}}\cdot\mathbf{b}+b}+1\right| + \left[\frac{\hat{\mathbf{n}}\cdot\delta\mathbf{r}+\frac{\tilde{\mathbf{r}}}{\tilde{r}}\cdot\delta\mathbf{r}}{(\hat{\mathbf{n}}\cdot\tilde{\mathbf{r}}+\tilde{r})+(\hat{\mathbf{n}}\cdot\mathbf{b}+b)}\right]+H.O.T \tag{7.16}$$

In Eq. (7.16), the higher-order terms $(H.O.T)$ are functions of $(\delta\mathbf{r})^2$ and higher.

Assuming second-order and higher terms are negligible in Eqs. (7.14)-(7.16), the linearized expression of Eq. (7.13) becomes,

$$\begin{aligned} &c(t_{SSB}-t_{SC})-(\hat{\mathbf{n}}\cdot\tilde{\mathbf{r}})-\frac{1}{D_0}\begin{bmatrix}\frac{1}{2}(\hat{\mathbf{n}}\cdot\tilde{\mathbf{r}})^2-\frac{1}{2}\tilde{r}^2\\ +(\tilde{\mathbf{r}}\cdot\mathbf{V}\Delta t_N)-(\hat{\mathbf{n}}\cdot\mathbf{V}\Delta t_N)(\hat{\mathbf{n}}\cdot\tilde{\mathbf{r}})\\ -(\mathbf{b}\cdot\tilde{\mathbf{r}})+(\hat{\mathbf{n}}\cdot\mathbf{b})(\hat{\mathbf{n}}\cdot\tilde{\mathbf{r}})\end{bmatrix}-\frac{2\mu_S}{c^2}\ln\left|\frac{\hat{\mathbf{n}}\cdot\tilde{\mathbf{r}}+\tilde{r}}{\hat{\mathbf{n}}\cdot\mathbf{b}+b}+1\right| \\ &=\hat{\mathbf{n}}\cdot\delta\mathbf{r}+\frac{1}{D_0}\begin{bmatrix}(\hat{\mathbf{n}}\cdot\tilde{\mathbf{r}})(\hat{\mathbf{n}}\cdot\delta\mathbf{r})-\tilde{\mathbf{r}}\cdot\delta\mathbf{r}\\ +(\mathbf{V}\Delta t_N)\cdot\delta\mathbf{r}-(\hat{\mathbf{n}}\cdot\mathbf{V}\Delta t_N)(\hat{\mathbf{n}}\cdot\delta\mathbf{r})\\ -(\mathbf{b}\cdot\delta\mathbf{r})+(\hat{\mathbf{n}}\cdot\mathbf{b})(\hat{\mathbf{n}}\cdot\delta\mathbf{r})\end{bmatrix}+\frac{2\mu_S}{c^2}\left[\frac{\hat{\mathbf{n}}\cdot\delta\mathbf{r}+\frac{\tilde{\mathbf{r}}}{\tilde{r}}\cdot\delta\mathbf{r}}{(\hat{\mathbf{n}}\cdot\tilde{\mathbf{r}}+\tilde{r})+(\hat{\mathbf{n}}\cdot\mathbf{b}+b)}\right]\end{aligned} \tag{7.17}$$

The LHS of Eq. (7.17) can be further simplified by noting that the terms with estimated position produce the estimated arrival time at the SSB, $\tilde{t}_{SSB}$. The difference between this estimated value and the predicted arrival time is expressed as in Eq. (7.3). Including the potential error in spacecraft timing, Eq. (7.17) can be written as,

$$\begin{aligned} c(\delta t_{SSB}-\delta t_{SC}) &= \hat{\mathbf{n}}\cdot\delta\mathbf{r}+\frac{1}{D_0}\begin{bmatrix}(\hat{\mathbf{n}}\cdot\tilde{\mathbf{r}})(\hat{\mathbf{n}}\cdot\delta\mathbf{r})-\tilde{\mathbf{r}}\cdot\delta\mathbf{r}\\ +(\mathbf{V}\Delta t_N)\cdot\delta\mathbf{r}-(\hat{\mathbf{n}}\cdot\mathbf{V}\Delta t_N)(\hat{\mathbf{n}}\cdot\delta\mathbf{r})\\ -(\mathbf{b}\cdot\delta\mathbf{r})+(\hat{\mathbf{n}}\cdot\mathbf{b})(\hat{\mathbf{n}}\cdot\delta\mathbf{r})\end{bmatrix} \\ &\quad+\frac{2\mu_S}{c^2}\left[\frac{\hat{\mathbf{n}}\cdot\delta\mathbf{r}+\frac{\tilde{\mathbf{r}}}{\tilde{r}}\cdot\delta\mathbf{r}}{(\hat{\mathbf{n}}\cdot\tilde{\mathbf{r}}+\tilde{r})+(\hat{\mathbf{n}}\cdot\mathbf{b}+b)}\right]\end{aligned} \tag{7.18}$$

It is noted that the RHS of Eq. (7.18) is a linear expression with respect to the position offset, $\delta\mathbf{r}$. This representation assumes a straightforward measurement from a recognizable singular source. Additional complexity is added if binary pulsar observations are incorporated, and these extra terms must be added through the time transfer equations [28].

7.1.2.2.1 Spacecraft Proper Time

The coordinate time used for the spacecraft observation time in the above equations is composed of the spacecraft's accurate clock time, or proper time, τ_{SC}, and the standard corrections from this proper time to standard coordinate time. As discussed in Chapter 4, spacecraft clocks must also be corrected for their motion within the inertial frame. Using $StdCorr_E$ to represent the standard corrections for terrestrial bound clocks, the coordinate time of spacecraft orbiting Earth can be represented as,

$$t_{SC} = \tau_{SC} + StdCorr_E + \frac{1}{c^2}\left(\mathbf{v}_E \cdot \mathbf{r}_{SC/E}\right) \tag{7.19}$$

For spacecraft using an estimated position, then the spacecraft's position relative to Earth can be represented by this estimate and its error as in Eq. (7.10). The coordinate time equation from Eq. (7.19) then becomes,

$$t_{SC} = \tau_{SC} + StdCorr_E + \frac{1}{c^2}\left(\mathbf{v}_E \cdot \tilde{\mathbf{r}}_{SC/E}\right) + \frac{1}{c^2}\left(\mathbf{v}_E \cdot \delta\mathbf{r}_{SC/E}\right) \tag{7.20}$$

Utilizing estimated values for spacecraft proper time, this expression can be rewritten as,

$$\delta t_{SC} = \delta\tau_{SC} + \frac{1}{c^2}\left(\mathbf{v}_E \cdot \delta\mathbf{r}_{SC/E}\right) \tag{7.21}$$

Eq. (7.21) assumes no errors in the coordinate time standard corrections, or Earth ephemeris data; however, these errors could also be included if considered relevant. This equation could be added to Eq. (7.18) if spacecraft proper time is necessary to use in this expression instead of spacecraft coordinate time.

7.1.2.3 Multiple Measurements

The measurement equations presented in the previous sections provide estimates of range error along the unit direction to an observed pulsar. If the full three-dimensional position offset is desired, then measurements from multiple pulsars located in different directions must be blended together.

Since Eq. (7.18) is a linear function of the offset position, it can be rewritten in vector form as,

$$c\left(\delta t_{SSB} - \delta t_{SC}\right) = \mathbf{A} \cdot \delta \mathbf{r} \tag{7.22}$$

The vector $\mathbf{A} = \mathbf{A}\left(\tilde{\mathbf{r}}, \hat{\mathbf{n}}, \mathbf{D}_0, \mathbf{V}, \mathbf{b}, \Delta t_N, \mu_S\right)$ is composed of the terms from Eq. (7.18). This linear expression in Eq. (7.22) can be assembled for *k* different pulsars to create a matrix of observations,

$$\begin{bmatrix} c\left(\delta t_{SSB} - \delta t_{SC}\right)_1 \\ c\left(\delta t_{SSB} - \delta t_{SC}\right)_2 \\ \cdot \\ \cdot \\ \cdot \\ c\left(\delta t_{SSB} - \delta t_{SC}\right)_k \end{bmatrix} = \begin{bmatrix} \mathbf{A}_1^T \\ \mathbf{A}_2^T \\ \cdot \\ \cdot \\ \cdot \\ \mathbf{A}_k^T \end{bmatrix} \delta \mathbf{r} \tag{7.23}$$

The LHS of Eq. (7.23) is computed using the models presented above. The difference in SSB pulse arrival times is computed using the predicted arrival time from the pulse-timing model and the measured time computed using the estimated position to transfer the arrival time at the spacecraft. The difference in spacecraft time is determined through any known errors in the spacecraft clock, proper time conversion, and photon timing.

Eq. (7.23) can be solved directly through a batch method such at *Least Squares*, where the inverse of the $\mathbf{A}$ matrix multiplied by the time differences computes the position offset. Repeating this measurement process refines the position estimate over time. However, creating these time differences for multiple pulsars requires the observations to be detected simultaneously such that the same position error is valid for all the observations. This requires detectors, or multiple detectors, that can track multiple pulsars. Although this type of system would be beneficial for navigation, many vehicles may only be able to accommodate one detector. With only one detector producing one measurement per pulsar, vehicle motion that is significant during the time span between the measurements must be addressed in an implementation of this *delta-correction* method for full three-dimensional position offset determination. A Kalman filter that incorporates vehicle dynamics and a measurement model from Eq. (7.18) can be used to blend sequential observations with vehicle motion to successfully update the estimate of vehicle position. Chapter 8 describes this type of implementation using an extended Kalman filter, along with providing examples of various orbits.

7.1.2.4 Expected Performance

To assess the potential performance of a pulsar-based navigation system, it is necessary to understand the error sources inherent to the system. If no errors in modeling or measurement are present, then Eq. (7.23) solves directly for accurate position offsets. However, errors do remain which limit the performance of this system. The magnitude of these errors must be considered when evaluating the determined position offset. Errors within each of the terms in this equation include the following;

- δt_{SSB}: The SSB time difference contains errors due to pulsar timing models and time transfer.
- δt_{SC}: The spacecraft time difference contains system level timing errors and pulse signal timing errors.

- $\mathbf{A}$: The observation matrix contains errors in the approximations to the relativistic time transfer effects, as well as pulsar position uncertainty and planetary ephemeris accuracy.

A phase cycle ambiguity may still be present in these equations if the estimate of position has large error. The *delta-correction* scheme equations relate the fraction of a cycle to the difference in predicted and measured time. This method does not identify which *specific* cycle is being detected. It is important to have an initial estimate of the accuracy of the estimated position prior to using this scheme so that it can be determined if more than a fraction of phase cycle could exist.

In deriving the observations used within the *delta-correction* method, the time equations were linearized with respect to position error, clock error, and pulsar timing error. This linearization did not include all error sources, namely errors in pulsar position and proper–motion. Adding pulsar position error and considering only first order effects from Eq. (7.7), the position error equation becomes,

$$c\left(\delta t_{SSB} - \delta t_{SC}\right) - \delta\hat{\mathbf{n}}_i \cdot \tilde{\mathbf{r}} = \tilde{\mathbf{n}}_i \cdot \delta\mathbf{r} \tag{7.24}$$

Using only the first order terms is valid in this analysis since the remaining terms are several orders of magnitude smaller [note the division by either pulsar distance or multiples of speed of light in Eq. (7.18)].

Navigation system performance with respect to the SSB can be established using Eq. (7.24) based upon projected estimates of error sources. The second term of the LHS of Eq. (7.24) shows that if pulsar position is not determined to high accuracy, then this system's performance degrades as distance increases away from the SSB. For pulsars with poorly determined position, this error growth due to distance is similar to those of

Earth-based radar range systems. Table 7-1 provides theoretical estimates of position performance using Eq. (7.24) for a pulsar-based navigation system centered at the SSB origin using the *delta-correction* scheme. The Total Timing Error column includes the sum of the SSB differenced pulse arrival time errors, system clock errors and pulsar timing errors. The first and second rows of Table 7-1 represent the current technology from today's sensors and measured pulsar positions and timing models. If the goal of this system were to provide meter-level position accuracy of spacecraft, pulsar position knowledge to less than 0.0001 arcseconds and pulse timing to less than 0.1 microseconds would be required for missions near Earth. If improvements can be made to current day values, the performance of the method could reach the levels of GPS performance for near-Earth applications, and any continued improvements would generate this type of performance for operations throughout the solar system.

The expression of Eq. (7.24) and values in Table 7-1 are appropriate for solar system missions. Inertial frames at the barycenter of other star systems, or the galactic center, would be appropriate for interstellar missions. However, the same performance degradation would exist as vehicles travel further from the frame's origin.

Table 7-1. Delta-Correction Method Performance Within Solar System.

Detector Position	Total Timing Error (10^{-6}s)	Pulsar Position Error (arcsec)	Position Accuracy From SSB
1 AU	10	0.01	< 10 km
1 AU	1	0.001	< 1 km
1 AU	0.1	0.0001	< 0.1 km
10 AU	10	0.001	< 10 km
10 AU	1	0.0001	< 1 km
10 AU	0.1	0.00001	< 0.1 km

7.2 Experimental Validation of Method

The preceding sections describe the delta-correction scheme for updating an estimate of a navigation system's position solution. These finite corrections can be used to improve the overall navigation solution, and maintain a level of accuracy that can ensure mission success. This section presents empirical data used to validate this concept, as well as descriptions of the accuracy of the data and the position solution.

7.2.1 USA Experiment Description

Most of the X-ray survey missions presented in Chapter 2 did not provide enhanced photon arrival timing resolution as well as precise spacecraft position and velocity information in order to thoroughly test the delta-correction method with actual data. However, the NRL USA experiment onboard the *ARGOS* spacecraft was partially designed to investigate the use of pulsars for navigation. Thus the data it provides can be used to begin to investigate the capability of the *delta-correction* methods.

The USA experiment was a collimated proportional counter telescope comprised of two detectors mounted on the aft section of the *ARGOS* vehicle [166, 229, 231, 232, 234, 235]. The experiment's parameters are provided in Table 7-2. The *ARGOS* vehicle was three-axis stabilized and nadir-pointing. The vehicle was placed in a sun synchronous, circular orbit of 840 km altitude. Although the experiment was comprised of two detectors, only one detector was used during a given observation. The experiment operated from May 1, 1999 through November 16, 2000, when its gas for the detector was depleted due to a leak, suspected to be produced by a micrometeorite strike. Figure 7-3 provides an image of the USA experiment, with its X-ray detector mounted on the *ARGOS* satellite.

Table 7-2. USA Experiment Parameters [72, 166, 232].

Two Detectors:	1000 cm^2 each, effective area
Field Of View:	1.2° x 1.2° (collimated) (FWHM)
Mass:	245.2 kg
Power:	~50 W
Energy Range:	1 – 15 keV
Energy Resolution:	0.17 (1 keV @ 5.9 keV)
Background Rejection:	Five-sided cosmic ray veto
Field Of Regard:	2π sr
Two-Axis Gimbaled System:	~3.6°/min (track), ~20°/min (slew)
Data Time Tagging:	32 μs timing resolution, GPS receiver provided time

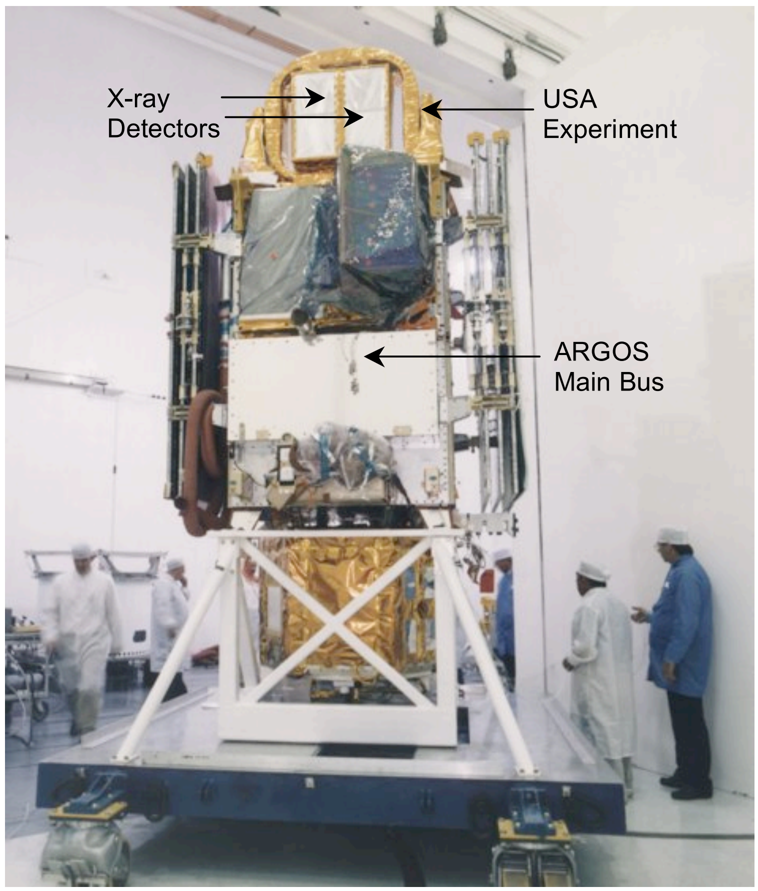

Figure 7-3. NRL's USA experiment onboard *ARGOS* spacecraft [Courtesy of NRL].

7.2.2 USA Detector Crab Pulsar Observations

The USA experiment's detector was pointed to observe the Crab Pulsar for multiple observations during December 1999. Table 7-3 provides the Crab Pulsar ephemeris values used for this experiment as provided by the Jodrell Band Observatory, through their monthly ephemeris updates [115]. The observation data were recorded, including time-tagged X-ray photon detection events and *ARGOS* satellite one-second navigation values. Using the Crab Pulsar pulse period, the recorded observation data were folded to produce an observed profile.

Table 7-3. Crab Pulsar (PSR B0531+21) Ephemeris Data [115].

Parameter	Value
Right Ascension (J2000)	$05^h34^m31.972^s$
Declination (J2000)	22°00'52.069"
Galactic Longitude	184.5575°
Galactic Latitude	-5.7843°
Distance (kpc)	2.0
Frequency (Hz)	29.8467040932
Period (s)	0.0335045369458
Frequency Derivative (Hz/s)	-3.7461268×10^{-10}
Period Derivative (s/s)	4.2052296×10^{-13}
Epoch of Ephemeris (MJD)	51527.0000001373958

Prior to these specific observations, several separate observations of the Crab Pulsar were folded to produce a standard template profile with a high SNR. The observed profiles and the template profile were then compared as described in Chapter 3 to produce observation TOAs. The measured pulse TOA represents the arrival time of the peak of the first pulse within the observation window. The error in the TOA was also computed, and represents the uncertainty in aligning the observed and template profiles [204].

In the process of computing the pulse TOA, an analysis tool was used to transfer the spacecraft's recorded photon arrival time to their arrival time at the SSB using an expression similar to Eq. (7.12), expect the pulsar distance, D_0, and proper-motion, $\mathbf{V}\Delta t_N$, as well as the barycenter position, $\mathbf{b}$, are ignored in this tool. Since the photon timing resolution was on the order of microseconds, interpolation of the 1 Hz navigation data was used to produce spacecraft positions at each photon arrival time. Thus, the computed TOA is the arrival time at the SSB of the measured pulse detected at the USA detector using the *ARGOS* navigation data to complete the time transfer.

Computed offsets from estimated spacecraft position can now be derived from the difference between the predicted and measured pulse arrival times. If the assumption is made that any time difference is based solely upon vehicle position offset in the direction of the pulsar, the error in position can be deduced from this pulsar pulse comparison as in Eq. (7.18). The computed offset is the delta-correction for range along the unit direction to the Crab Pulsar. Table 7-4 provides a list of recorded observations; their corresponding position offset determination, and estimated accuracies. Position corrections of several kilometers along the line-of-sight to the Crab Pulsar are produced, with estimated accuracies on the order of two kilometers.

Table 7-4. Computed Position Offsets from Crab Pulsar Observations.

Observation Date (Dec. 1999)	Duration (s)	Observed Pulse Cycles	TOA Difference (10^{-6} s)	TOA Estimated Error (10^{-6} s)	Position Offset (km)	Estimated Offset Error (km)
21st	446.7	13332	53.75	5.8	16.1	1.8
24th	695.9	20770	-31.02	5.2	-9.3	1.6
26th	421.7	12586	-37.16	6.3	-11.1	1.9

7.2.3 Delta-Position Truth Comparisons

To assess the validity of the computed position offsets in Table 7-4, it is necessary to know the exact position of the *ARGOS* vehicle. This truth information can then be compared to the solutions created by correcting the estimated position of the navigation system. Unfortunately, a reference truth position of *ARGOS* was not available at the time of these 1999 observations. However, an external estimation of vehicle position was studied during January 2000. This parallel study conducted by NRL using a ground-based navigation system concluded that the navigation system onboard *ARGOS* had errors between 5 and 15 km. It has been speculated that much of this position error is due to errors within the navigation system software, as during the *ARGOS* mission it was determined that the spacecraft's GPS receiver and clock were faulty. Correction solutions were required every four hours to update the spacecraft's onboard orbit propagation algorithm.

Further investigation is being conducted to determine why this navigation position error existed. With these magnitudes of position error discovered for January 2000, it is likely that they existed for the observations completed during late December 1999, which could account for much of the position offset determined from the measured TOAs. Future studies are planned to simulate pulsar measurements and *ARGOS* orbit propagation, in order to help investigate the *ARGOS* navigation issues.

Although the lack of absolute truth data does not allow direct evaluation of the measurements, basic assessments of the computed position offsets can be provided. The two main computations in this experiment include the position offset calculation and its estimated accuracy. Factors that limit the position offset calculation include pulsar timing model inaccuracies, calibration errors in the USA experiment timing system, photon time binning of 32 μs in the USA data collection mode, and pulsar position errors. The reported accuracy of the Crab Pulsar timing model parameters is 60 μs for the month of December 1999 and is likely a large contributor to the measured position offset [115]. Although the USA experiment was designed to maintain a 32-μs photon bin timing accuracy, fractions of the bin size were used to improve the time resolution of arriving photons. From the range measurement accuracies reported in Chapter 3, for a 0.1 m^2 detector, σ_{RANGE} = 0.1 km for the Crab Pulsar after 500 seconds of observation. Although this ideal computation of position accuracy is a few times less than the calculated values in Table 7-4, several of the above mentioned issues likely contribute to the measured error. Future studies on *ARGOS* navigation data will also attempt to understand this discrepancy between theoretical accuracy and recorded data accuracy to determine whether system errors or pulsar model errors dominate.

Chapter 8 Recursive Estimation of Position and Velocity

"Big results require big ambitions."

– Heraclitus

A range measurement of a spacecraft relative to an inertial reference location can be computed based upon a pulse TOA from a single celestial source, as demonstrated in Chapter 7. However, the portion of range measured along the line-of-sight to the source does not compute full three-dimensional position of the vehicle. Nonetheless, in a manner similar to orbit determination, which uses sequential measurements of range and/or range-rate by ground stations of a spacecraft to compute its orbit solution, the dynamics of the vehicle can be blended with the pulsar-based range measurements to allow an onboard navigation system to systematically compute a full position and velocity solution.

The blending of spacecraft state dynamics and pulse range measurement has been implemented within a Kalman filter technique [65, 91]. This filter, referred to as the Navigation Kalman filter (NKF), recursively incorporates pulse TOA measurements with an estimate of the orbit state. These estimated states are based upon a numerically propagated position and velocity solution [42, 55, 71, 93, 136, 190, 191, 195, 212, 213, 224]. A discussion is provided on the dynamics of the filter states, as well as how the dynamics are used within the filter. Methods to implement various measurement models within the filter are also provided. A simulation of the NKF and pulsar-based TOA measurements is presented, along with performance results of spacecraft position determination using these techniques. Appendix D describes the fundamentals of processing navigation information through the dynamics and observations within a Kalman filter, and should be referred to as a supplement to the descriptions within this chapter.

8.1 Kalman Filter Dynamics

8.1.1 Spacecraft Orbit Navigation States

The specific dynamics of the NKF used to integrate pulsar-based range measurements along a spacecraft's flight path is described in detail within this section [189, 191]. A spacecraft in orbit about a central body will follow a stable, often predictable, path if left unperturbed from its motion. The dynamics of the spacecraft can be expressed in analytical form, which in turn can be used within the filter's time propagation routines.

8.1.1.1 State Dynamics

The states used by the NKF to describe the spacecraft dynamics are three-dimensional inertial frame position and velocity. These primary states are the absolute values, or *whole-values*, of each parameter. The state vector, $\mathbf{x}$, has six states, and is composed of the three element position vector, $\mathbf{r} = \mathbf{r}_{SC} = \left\{ r_x, r_y, r_z \right\}$, and the three element velocity vector, $\mathbf{v} = \mathbf{v}_{SC} = \left\{ v_x, v_y, v_z \right\}$. The states are represented in vector form as,

$$\mathbf{x} = \begin{bmatrix} \mathbf{r} \\ \mathbf{v} \end{bmatrix} = \begin{bmatrix} r_x \\ r_y \\ r_z \\ v_x \\ v_y \\ v_z \end{bmatrix} \tag{8.1}$$

In a general form, the dynamics of the state variables can be presented as

$$\dot{\mathbf{x}}(t) = \vec{f}\left(\mathbf{x}(t), \mathbf{u}(t), t\right) + \boldsymbol{\eta}(t) \tag{8.2}$$

In this equation, $\vec{f}$ is a function that describes the dynamics of each state in terms of the state vector, $\mathbf{x}(t)$, any control inputs, $\mathbf{u}(t)$, and the noise associated with the state dynamics, $\boldsymbol{\eta}(t)$. The dynamics may be non-linear with respect to the states with this expression.

To determine the natural dynamics of a spacecraft, noise can be initially ignored $\left(\boldsymbol{\eta}(t) \approx \mathbf{0}\right)$ and no control inputs are commanded $\left(\mathbf{u}(t) \approx \mathbf{0}\right)$. With vehicle acceleration, $\mathbf{a}$, being the time derivative of velocity and velocity, $\mathbf{v}$, being the time derivative of position, the time derivative of the state vector from Eq. (8.1) is therefore represented as,

$$\dot{\mathbf{x}} = \vec{f}\left(\mathbf{x}(t), t\right) = \begin{bmatrix} \dot{\mathbf{r}} \\ \dot{\mathbf{v}} \end{bmatrix} = \begin{bmatrix} \mathbf{v} \\ \mathbf{a} \end{bmatrix} = \begin{bmatrix} v_x \\ v_y \\ v_z \\ a_x \\ a_y \\ a_z \end{bmatrix} \tag{8.3}$$

This may also be written as,

$$\begin{aligned} \dot{\mathbf{r}}(t) &= \mathbf{v}(t) \\ \dot{\mathbf{v}}(t) &= \ddot{\mathbf{r}}(t) = \mathbf{a}(t) \end{aligned} \tag{8.4}$$

The dynamics of Eq. (8.3) represents a first-order system. From Newton's second law of dynamics [150], the relationship between the vehicle's dynamics and the external forces acting on the vehicle is the following,

$$\mathbf{a} = \frac{1}{m}\sum \mathbf{F}_{ext} \tag{8.5}$$

where $\mathbf{a}$ is the acceleration of the vehicle, m is the mass of the vehicle, and $\sum \mathbf{F}_{ext}$ is the sum of all external forces applied to the vehicle [this should not be confused with the Jacobian matrix $\mathbf{F}(t)$ for the error-state dynamics later in this chapter and Appendix D]. Once an initial condition is known, such as,

$$\mathbf{x}(t_0) = \mathbf{x}_0 = \begin{bmatrix} \mathbf{r}_0 \\ \mathbf{v}_0 \end{bmatrix} \tag{8.6}$$

and the acceleration on the vehicle is determined from Eq. (8.5), the state dynamics of Eqs. (8.3) and (8.6) completely defines the motion of the spacecraft.

If an analytical expression for the integral of Eq. (8.3) can be determined, then the vehicle state can be directly computed for any future time, t. However, the full dynamics of a spacecraft is a complex expression due to the multiple high order effects, and it is difficult to determine an accurate analytical solution. Thus, the dynamics of the spacecraft, along with its initial condition, are typically numerically integrated in order to determine the vehicle's state at some future time.

The six translational state elements of position and velocity of a spacecraft expressed as Eq. (8.3) is one possible representation for the dynamics. An alternative method is the utilization of *Keplerian* elements that describe a specific orbit of a spacecraft [117]. An advantage of this representation is that except for the element of time the remaining five classical Keplerian elements are nearly constant, and once determined to high accuracy can define a vehicle's orbit with high performance. However, a significant disadvantage of using these Keplerian elements as state variables is that these elements are only valid for one specific orbit. This may be useful for a spacecraft that is launched and placed in a set orbit, with no mission operations deviating from that orbit. However, if a spacecraft's mission requires it to maneuver at some point, such as merely changing its location along the orbit track or possibly altering its entire orbit shape, the six inertial states of position and velocity are much more suitable for these types of mission operations. Also, if a vehicle does not operate along a definable Keplerian orbit, the position and velocity states are more appropriate for this motion. An example of this motion is a group of spacecraft flying in formation, where the leader is in a Keplerian orbit, but its followers must maintain non-Keplerian orbits to remain in the desired formation.

To adequately represent a spacecraft's orbit about a central body, the following acceleration effects are considered for the succeeding analysis: central two-body acceleration effects; non-spherical gravitational potential effects from the central body; atmospheric drag effects if the spacecraft is close enough to the central body's atmosphere; and any appreciable third-body gravitational potential effects. The total acceleration on a spacecraft is the sum of these effects as,

$$\mathbf{a}_{total} = \ddot{\mathbf{r}} = \mathbf{a}_{two-body} + \mathbf{a}_{non-spherical} + \mathbf{a}_{drag} + \mathbf{a}_{third-body} + \mathbf{a}_{H.O.T} \tag{8.7}$$

These contributing effects are presented in further detail below. In this equation, $\mathbf{a}_{H.O.T}$ represents all *higher-order terms* that may affect acceleration (such as solar radiation pressure, albedo, Earth tidal, etc.) but are nominally considered negligible compared to the remaining effects.

8.1.1.1.1 Two-Body

The effect of the acceleration of a spacecraft about a central massive body, where the mass of the body is much greater than the spacecraft, $m_{body} \gg m_{SC}$, is the standard expression of,

$$\mathbf{a}_{two-body} = -\frac{\mu}{r^3}\mathbf{r} = -\frac{\mu}{r^2}\hat{\mathbf{r}} \tag{8.8}$$

In this equation, μ is the gravitational parameter of the central body, where $\mu = Gm_{body}$ and G is the universal gravitational constant.

8.1.1.1.2 Non-Spherical Gravitational Potential

The gravitational acceleration of Eq. (8.8) assumes a uniformly spherical gravitational field emanating from the point-mass central body. Many planets, moons, as well as the Sun, actually do not have uniformly distributed material within their body's spheres. Thus, the true gravitational field is not spherical for these objects. Additional terms must be added to the simple two-body spherical approximation in order to more accurately represent these gravity fields. These terms often are presented as *Legendre* polynomials whose coefficients define the spherical harmonics of the field, whose *degree* and *order* define the resolution of the field. These polynomials can be categorized as *zonal* terms (only terms parallel to a body's equator, and reflect a body's oblateness), *sectorial* terms (for lumps of mass distributed in a body's longitudinal direction), and *tesseral* terms (for mass lumps distributed in various sections of the body's sphere) [213]. These non-spherical gravity effects on a body are a function of the spacecraft's position within the field, and can be represented as,

$$\mathbf{a}_{non-spherical} = \vec{g}\left(\text{Non-spherical gravity}, \mathbf{r}\right) \tag{8.9}$$

The specific non-spherical gravity model used in the NKF for Earth-orbiting spacecraft uses the J_2 through J_6 zonal terms of Earth's gravity. Although many higher-order harmonic representations exist for Earth, this simple zonal model has been shown to be sufficient for most of the NKF's analysis. These gravitational potential terms only depend on the z-axis position, which does not require the computation to be affected by the rotation of Earth fixed axes relative to inertial axes. Using $\sin d = r_z / r$ and the radius of Earth, R_E, the acceleration can be represented as the following, [55, 213, 221]

$$a_{non-spherical_x} = -\frac{\mu}{r^3} r_x \begin{bmatrix} 1 + J_2 \left(\frac{R_E}{r} \right)^2 \frac{3}{2} \left(1 - 5 \sin^2 d \right) \\ + J_3 \left(\frac{R_E}{r} \right)^3 \frac{5}{2} \left(3 - 7 \sin^2 d \right) \sin d \\ - J_4 \left(\frac{R_E}{r} \right)^4 \frac{5}{8} \left(3 - 42 \sin^2 d + 63 \sin^4 d \right) \\ - J_5 \left(\frac{R_E}{r} \right)^5 \frac{3}{8} \left(35 - 210 \sin^2 d + 231 \sin^4 d \right) \sin d \\ + J_6 \left(\frac{R_E}{r} \right)^6 \frac{1}{16} \begin{pmatrix} 35 - 945 \sin^2 d \\ +3465 \sin^4 d - 3003 \sin^6 d \end{pmatrix} \end{bmatrix} \tag{8.10}$$

$$a_{non-spherical_y} = \frac{r_y}{r_x} a_{non-spherical_x} \tag{8.11}$$

$$a_{non-spherical_z} = -\frac{\mu}{r^3} r_z \begin{bmatrix} 1 + J_2 \left(\frac{R_E}{r}\right)^2 \frac{3}{2}\left(3 - 5\sin^2 d\right) \\ +J_3 \left(\frac{R_E}{r}\right)^3 \frac{5}{2}\left(6 - 7\sin^2 d\right)\sin d \\ -J_4 \left(\frac{R_E}{r}\right)^4 \frac{5}{8}\left(15 - 70\sin^2 d + 63\sin^4 d\right) \\ -J_5 \left(\frac{R_E}{r}\right)^5 \frac{3}{8}\left(105 - 315\sin^2 d + 231\sin^4 d\right)\sin d \\ +J_6 \left(\frac{R_E}{r}\right)^6 \frac{1}{16}\begin{pmatrix} 245 - 2205\sin^2 d \\ +4851\sin^4 d - 3003\sin^6 d \end{pmatrix} \end{bmatrix} + \frac{\mu}{r^2}\left[J_3 \left(\frac{R_E}{r}\right)^3 \frac{3}{2} - J_5 \left(\frac{R_E}{r}\right)^5 \frac{15}{8} \right] \tag{8.12}$$

8.1.1.1.3 Drag

As a spacecraft orbits about a central body, the atmosphere that extends above the body's surface can produce drag upon the vehicle. This drag retards the motion of the vehicle. This effect, acting tangentially to the vehicle's orbit along the negative velocity direction, reduces the velocity of the spacecraft. With prolonged exposure to this drag effect, enough speed can be reduced such that the spacecraft will no longer be able to maintain its orbit, and the gravitational forces will dominate the vehicle's motion such that it eventually drops out of orbit onto the body's surface.

The acceleration effect due to drag can be written as

$$\mathbf{a}_{drag} = -\frac{1}{2}\frac{C_D A_{SC}}{m_{SC}}\rho_{ATM} \mathrm{v}_r \mathbf{v}_r = -\frac{1}{2}\frac{C_D A_{SC}}{m_{SC}}\rho_{ATM} \mathrm{v}_r^2 \hat{\mathbf{v}}_r \tag{8.13}$$

In this expression, C_D is the coefficient of drag due to the shape of the vehicle, A_{SC} is the cross-sectional area of the spacecraft that impinges on the oncoming atmosphere, and m_{SC} is the mass of the spacecraft. Together, these terms can be grouped as

$B = m_{SC} / C_D A_{SC}$, which is referred to as the *ballistic coefficient* of the vehicle. The density of the atmosphere is represented as ρ_{ATM}. This term is often expressed as either an exponential function with respect to altitude of the spacecraft above the body's surface, or a table of values dependent on altitude. For Earth-orbiting spacecraft, the NKF utilizes the Harris-Priester Earth atmosphere model [136].

The velocity used in Eq. (8.13) is the velocity of the spacecraft relative to the atmosphere. Since the atmosphere typically rotates along with the body's surface, this relative velocity is the spacecraft's velocity corrected for the atmosphere's rotation rate as [136],

$$\mathbf{v}_r = \mathbf{v} - \boldsymbol{\omega}_E \times \mathbf{r} \tag{8.14}$$

8.1.1.1.4 Third-Body Gravitational Effects

Spacecraft orbiting a central body are dominated by the gravitational effect of this body upon the vehicle. However, all gravitational effects from any nearby body, no matter how small, are actually acting upon the vehicle. Over time, these third-body gravitational effects can alter the motion of the vehicle, and if ignored, can cause the estimated vehicle state to accumulate significant errors. Thus, any body that could potentially act upon a spacecraft's orbit should be considered within the vehicle dynamics. The acceleration effects acting on the vehicle due to a third-body can be represented as [136],

$$\mathbf{a}_{third-body} = -\mu_{3^{rd}\,body} \left(\frac{\mathbf{r}_{SC/3^{rd}\,body}}{r^3_{SC/3^{rd}\,body}} + \frac{\mathbf{r}_{3^{rd}\,body/Main-body}}{r^3_{3^{rd}\,body/Main-body}} \right) \tag{8.15}$$

In this equation, $\mu_{3^{rd}\,body}$ is the gravitational parameter of the third-body acting on the vehicle, $\mathbf{r}_{SC/3^{rd}\,body}$ is the inertial frame position of the spacecraft with respect to the third-body, and $\mathbf{r}_{3^{rd}\,body/Main-body}$ is the position of the third-body with respect to the central main body that the vehicle is orbiting.

For spacecraft orbiting Earth, the two primary additional perturbing third-bodies are the Moon and the Sun. The third-body effect from the Moon can be represented from Eq. (8.15) as,

$$\mathbf{a}_{Moon} = -\mu_{Moon}\left(\frac{\mathbf{r}_{SC/Moon}}{r_{SC/Moon}^{3}} + \frac{\mathbf{r}_{Moon/Earth}}{r_{Moon/Earth}^{3}}\right) \tag{8.16}$$

Since the position of the spacecraft with respect to the Moon is not typically directly computed, the vectorial representation of this vector can be expanded using the known state position of the spacecraft with respect to Earth and the well known position of the Moon with respect to Earth, such that,

$$\mathbf{r}_{SC/Moon} = \mathbf{r}_{SC/Earth} - \mathbf{r}_{Moon/Earth} \tag{8.17}$$

The third body gravitational effect due the Moon can thus be represented using Eq. (8.17) as,

$$\mathbf{a}_{Moon} = -\mu_{Moon}\left(\frac{\left(\mathbf{r}_{SC/Earth} - \mathbf{r}_{Moon/Earth}\right)}{\left\|r_{SC/Earth} - r_{Moon/Earth}\right\|^{3}} + \frac{\mathbf{r}_{Moon/Earth}}{r_{Moon/Earth}^{3}}\right) \tag{8.18}$$

Although the Sun is much further away from Earth than the Moon, its gravity field is massive enough such that it should be considered as a third-body effect for Earth-orbiting spacecraft. Due to the Sun, the third-body acceleration expressions are represented as,

$$\mathbf{a}_{Sun} = -\mu_{Sun}\left(\frac{\mathbf{r}_{SC/Sun}}{r_{SC/Sun}^3} + \frac{\mathbf{r}_{Sun/Earth}}{r_{Sun/Earth}^3}\right) \tag{8.19}$$

$$\mathbf{a}_{Sun} = -\mu_{Sun}\left(\frac{\left(\mathbf{r}_{SC/Earth} - \mathbf{r}_{Sun/Earth}\right)}{\left\| r_{SC/Earth} - r_{Sun/Earth} \right\|^3} + \frac{\mathbf{r}_{Sun/Earth}}{r_{Sun/Earth}^3}\right) \tag{8.20}$$

To assure numerical stability of these third-body expressions the magnitude term of $\left\| r_{SC/Earth} - r_{3^{rd}\,body/Earth} \right\|^3$ is often expanded in Taylor series form. The magnitude of the third-body position is often significantly greater than the magnitude of the spacecraft's position with respect to Earth, such that $r_{3^{rd}\,body/Earth} \gg r_{SC/Earth}$. Expanding this difference in Taylor series doesn't require the computation of the potentially erroneous difference of a small value minus a large value [136]. The NKF uses the direct forms of these equations as in Eqs. (8.18) and (8.20) since double precision calculations are used throughout the analysis. If less precision is used for these computations, Taylor series expansion should be considered.

8.1.2 Orbit State Transition Matrix

The NKF is implemented as an *extended* Kalman filter, due to the non-linear state dynamics as shown above. Although the navigation states are the ultimate product of this filter, the terms processed within the NKF filter are the errors associated with each element of the state vector. These error-states, $\delta\mathbf{x}$, can be represented based upon the true states, $\mathbf{x}$, and the estimated states, $\tilde{\mathbf{x}}$, as,

$$\mathbf{x} = \tilde{\mathbf{x}} + \delta\mathbf{x} \tag{8.21}$$

Necessary for error-state and error-covariance processing within the NKF is the proper representation of the state transition matrix, $\mathbf{\Phi}$. The primary definition of this matrix is from the following expression, where it is used to determine the values of the error-state, $\delta\mathbf{x}$, at a future time, t.

$$\delta\mathbf{x} = \mathbf{\Phi}(t,t_0)\delta\mathbf{x}_0 \tag{8.22}$$

The state transition matrix is found by solving the integral of the following expressions,

$$\begin{aligned} \dot{\mathbf{\Phi}}(t,t_0) &= \mathbf{F}(t)\mathbf{\Phi}(t,t_0) \\ \mathbf{\Phi}(t_0,t_0) &= \mathbf{I} \end{aligned} \tag{8.23}$$

8.1.2.1 State Jacobian Matrix

The Jacobian matrix, $\mathbf{F}(t)$, is defined as the derivative of the dynamics of the states with respect to it states, as in,

$$\mathbf{F}(t) = \frac{\partial\vec{f}(\tilde{\mathbf{x}})}{\partial\mathbf{x}} \tag{8.24}$$

Determining the Jacobian matrix is necessary in order to solve for the state transition matrix in Eq. (8.23). Thus, the dynamics of the states from Eq. (8.2) must be known or estimated in order to complete this differentiation.

The dynamics of the navigation states from Eq. (8.3) are the following,

$$\vec{f}(\mathbf{x}(t),\mathbf{u}(t),t) = \begin{bmatrix} \dot{\mathbf{r}} \\ \dot{\mathbf{v}} \end{bmatrix} = \begin{bmatrix} \mathbf{v} \\ \mathbf{a} \end{bmatrix} \tag{8.25}$$

From Eq. (8.24), to determine the dynamics of the errors of these states, the Jacobian matrix can be determined as,

$$\mathbf{F}(t) = \frac{\partial\vec{f}(\tilde{\mathbf{x}})}{\partial\mathbf{x}} = \frac{\partial}{\partial\mathbf{x}}\begin{bmatrix} \mathbf{v} \\ \mathbf{a} \end{bmatrix} = \begin{bmatrix} \frac{\partial\mathbf{v}}{\partial\mathbf{r}} & \frac{\partial\mathbf{v}}{\partial\mathbf{v}} \\ \frac{\partial\mathbf{a}}{\partial\mathbf{r}} & \frac{\partial\mathbf{a}}{\partial\mathbf{v}} \end{bmatrix} \tag{8.26}$$

From the known definition of the states from Eqs. (8.1) and (8.4), the first row elements of Eq. (8.26) can be simplified as,

$$\frac{\partial \mathbf{v}}{\partial \mathbf{r}} = \mathbf{0}_{3\text{x}3};\ \frac{\partial \mathbf{v}}{\partial \mathbf{v}} = \mathbf{I}_{3\text{x}3} \tag{8.27}$$

The second row elements depend entirely upon the acceleration of the spacecraft, and cannot be immediately simplified. Thus, using Eq. (8.27), the Jacobian matrix for spacecraft dynamics can be expressed as,

$$\mathbf{F}(t) = \begin{bmatrix} \mathbf{0}_{3\text{x}3} & \mathbf{I}_{3\text{x}3} \\ \dfrac{\partial \mathbf{a}}{\partial \mathbf{r}} & \dfrac{\partial \mathbf{a}}{\partial \mathbf{v}} \end{bmatrix} \tag{8.28}$$

8.1.2.1.1 Acceleration Derivatives

Using the acceleration expressions from Eqs. (8.7)-(8.20), the derivatives with respect to position and velocity can be determined for each of the gravitational, drag, and third-body effects. Since position, velocity, and acceleration are all three-element vectors, taking their derivative requires the derivative to be determined from each vector element. In matrix form, this is determined as,

$$\frac{\partial \mathbf{a}}{\partial \mathbf{r}} = \begin{bmatrix} \dfrac{\partial a_x}{\partial r_x} & \dfrac{\partial a_x}{\partial r_y} & \dfrac{\partial a_x}{\partial r_z} \\ \dfrac{\partial a_y}{\partial r_x} & \dfrac{\partial a_y}{\partial r_y} & \dfrac{\partial a_y}{\partial r_z} \\ \dfrac{\partial a_z}{\partial r_x} & \dfrac{\partial a_z}{\partial r_y} & \dfrac{\partial a_z}{\partial r_z} \end{bmatrix};\ \frac{\partial \mathbf{a}}{\partial \mathbf{v}} = \begin{bmatrix} \dfrac{\partial a_x}{\partial v_x} & \dfrac{\partial a_x}{\partial v_y} & \dfrac{\partial a_x}{\partial v_z} \\ \dfrac{\partial a_y}{\partial v_x} & \dfrac{\partial a_y}{\partial v_y} & \dfrac{\partial a_y}{\partial v_z} \\ \dfrac{\partial a_z}{\partial v_x} & \dfrac{\partial a_z}{\partial v_y} & \dfrac{\partial a_z}{\partial v_z} \end{bmatrix} \tag{8.29}$$

where $\mathbf{a} = \{a_x, a_y, a_z\}$, $\mathbf{r} = \{r_x, r_y, r_z\}$, and $\mathbf{v} = \{v_x, v_y, v_z\}$.

The following vector differential identities are useful when deriving these acceleration derivatives,

$$\frac{\partial r}{\partial \mathbf{r}} = \hat{\mathbf{r}} \tag{8.30}$$

$$\frac{\partial}{\partial \mathbf{r}}\left(r^n\right) = nr^{n-2}\mathbf{r}^T \tag{8.31}$$

$$\frac{\partial \mathbf{r}}{\partial \mathbf{r}} = \mathbf{I}_{3x3} \tag{8.32}$$

$$\frac{\partial}{\partial \mathbf{r}}\left(\mathbf{r}^T\mathbf{v}\right) = \mathbf{v} \tag{8.33}$$

In these equations, $r = \|\mathbf{r}\|$, $\hat{\mathbf{r}}$ is the unit direction of $\mathbf{r}$ such that $\hat{\mathbf{r}} = \mathbf{r}/r$, and $\mathbf{r}^T\mathbf{v}$ is the scalar value *inner product* of vectors $\mathbf{r}$ and $\mathbf{v}$ $\left(\mathbf{r}^T\mathbf{v} = \mathbf{r}\cdot\mathbf{v} = r_x v_x + r_y v_y + r_z v_z\right)$.

8.1.2.1.2 Two-Body

For the two-body acceleration effect from Eq. (8.8), the position derivative is straightforward to determine using the identities of Eqs. (8.30)-(8.33) [120, 213],

$$\frac{\partial \mathbf{a}_{two-body}}{\partial \mathbf{r}} = \frac{\mu}{r^3}\left(3\hat{\mathbf{r}}\hat{\mathbf{r}}^T - \mathbf{I}_{3x3}\right) \tag{8.34}$$

In this equation, $\hat{\mathbf{r}}\hat{\mathbf{r}}^T$ is the *outer-product* of this vector and produces a 3x3 matrix. Since the two-body acceleration is independent of spacecraft velocity, this derivative is zero, or,

$$\frac{\partial \mathbf{a}_{two-body}}{\partial \mathbf{v}} = \mathbf{0}_{3x3} \tag{8.35}$$

8.1.2.1.3 Non-Spherical Gravitational Potential

For higher-order non-spherical gravitational potential effects, the derivative of the spacecraft acceleration due to position from Eq. (8.9) is,

$$\frac{\partial \mathbf{a}_{non-spherical}}{\delta \mathbf{r}} = \frac{\partial}{\delta \mathbf{r}}\left(\vec{g}\right) \tag{8.36}$$

Due to the recursive nature of the typical gravity field harmonics for higher-order representations, various analytical methods exist to represent the derivative of Eq. (8.36) [46, 130, 236].

For the most accurate representation of the effects due to the non-spherical gravity, the derivatives of all terms used in the dynamics should be computed. However, contributions to the derivative of total acceleration with respect to the highest-order terms are usually not significant. Instead, it is often sufficient to only consider the primary contributors and ignore the remaining terms. This is often a trade-off when considering algorithm computation time versus precision.

In the NKF used for pulsar-based navigation, only the zonal terms of Earth's gravity are considered in the dynamics of Earth-orbiting spacecraft. Up to zonal degree six, J_6, is considered, with zero order. However, for the Jacobian matrix, currently only degree two, J_2, is considered in the acceleration derivative since the higher order terms compute only small effects. This can be expressed as [120],

$$\frac{\partial \mathbf{a}_{non-spherical}}{\partial \mathbf{r}} = \frac{\mu}{r^3}\left[\frac{3}{2}J_2\left(\frac{R_{Earth}}{r}\right)^2\right]\left\{\begin{array}{l} 5\hat{\mathbf{r}}\hat{\mathbf{r}}^T\left[1-7\left(\hat{\mathbf{n}}^T\hat{\mathbf{r}}\right)^2\right]-\left[1-5\left(\hat{\mathbf{n}}^T\hat{\mathbf{r}}\right)^2\right]\mathbf{I}_{3\text{x}3} \\ +10\left(\hat{\mathbf{n}}^T\hat{\mathbf{r}}\right)\left[\hat{\mathbf{r}}\hat{\mathbf{n}}^T+\hat{\mathbf{n}}\hat{\mathbf{r}}^T\right]-2\hat{\mathbf{n}}\hat{\mathbf{n}}^T \end{array}\right\} \quad (8.37)$$

If degree three or higher, or order greater than zero, should be incorporated into the harmonics for improved accuracy, then the derivatives of these terms should also be included in Eq. (8.36).

Since the gravity field from Eq. (8.36) is independent of velocity, this derivative is zero, or,

$$\frac{\partial \mathbf{a}_{non-spherical}}{\partial \mathbf{v}} = \mathbf{0}_{3\text{x}3} \quad (8.38)$$

8.1.2.1.4 Drag

The expression for drag acceleration effects on a spacecraft is complex, as Eq. (8.13) suggests. It is a function of position and velocity, since the intermediate term of density is a function of position, and relative velocity a function of both. The derivatives must use the chain-rule for differentiation to determine the complete formulas [136]. These can be expressed initially as,

$$\frac{\partial \mathbf{a}_{drag}}{\partial \mathbf{r}} = -\frac{1}{2B}\frac{\partial \rho_{ATM}}{\partial \mathbf{r}} \mathrm{v}_r \mathbf{v}_r - \frac{\rho_{ATM}}{2B}\frac{\partial}{\partial \mathbf{r}}\left(\mathrm{v}_r \mathbf{v}_r\right) \tag{8.39}$$

$$\frac{\partial \mathbf{a}_{drag}}{\partial \mathbf{v}} = \frac{\partial \mathbf{a}_{drag}}{\partial \mathbf{v}_r}\frac{\partial \mathbf{v}_r}{\partial \mathbf{v}} = -\frac{\rho_{ATM}}{2B}\left[\frac{\partial}{\partial \mathbf{v}_r}\left(\mathrm{v}_r \mathbf{v}_r\right)\right]\frac{\partial \mathbf{v}_r}{\partial \mathbf{v}} \tag{8.40}$$

The derivative of density with respect to position can be approximated using the differences of the table values for density, or

$$\frac{\partial \rho_{ATM}}{\partial \mathbf{r}} \approx \frac{\partial \rho_{ATM}}{\partial r}\frac{\partial r}{\partial \mathbf{r}} \cong \frac{\Delta \rho_{ATM}}{\Delta r}\hat{\mathbf{r}} \tag{8.41}$$

The Δ terms can be computed using values close to the computed altitude, h, of the specified position $\left(r = R_E + h\right)$, as,

$$\frac{\Delta \rho_{ATM}}{\Delta r} = \frac{\rho_{ATM\,2} - \rho_{ATM\,1}}{r_2 - r_1} \tag{8.42}$$

The derivative of relative velocity with respect to position magnitude can be expressed from Eq. (8.14) as,

$$\frac{\partial \mathbf{v}_r}{\partial \mathbf{r}} = \frac{\partial}{\partial \mathbf{r}}\left(\mathbf{v} - \boldsymbol{\omega}_E \times \mathbf{r}\right) = \frac{\partial \mathbf{v}}{\partial \mathbf{r}} - \frac{\partial}{\partial \mathbf{r}}\left(\left\{\boldsymbol{\omega}_E\right\}\mathbf{r}\right) = -\left\{\boldsymbol{\omega}_E\right\}\mathbf{I}_{3x3} \tag{8.43}$$

In Eq. (8.43), $\left\{\boldsymbol{\omega}_E\right\}$ represents the skew-symmetric representation of the Earth rotation matrix as,

$$\{\boldsymbol{\omega}_E\} = \begin{bmatrix} 0 & -\omega_z & \omega_y \\ \omega_z & 0 & -\omega_x \\ -\omega_y & \omega_x & 0 \end{bmatrix} \tag{8.44}$$

The derivative of the relative velocity terms in Eq. (8.39) with respect to position can be rewritten as,

$$\frac{\partial}{\partial \mathbf{r}}\left(\mathrm{v}_r \mathbf{v}_r\right) = \frac{\partial}{\partial \mathbf{v}_r}\left(\mathrm{v}_r \mathbf{v}_r\right)\frac{\partial \mathbf{v}_r}{\partial \mathbf{r}} = \left(\hat{\mathbf{v}}_r \mathbf{v}_r + \mathrm{v}_r \mathbf{I}_{3x3}\right)\frac{\partial \mathbf{v}_r}{\partial \mathbf{r}} \tag{8.45}$$

Using the representation in Eq. (8.43), this expression becomes,

$$\frac{\partial}{\partial \mathbf{r}}\left(\mathrm{v}_r \mathbf{v}_r\right) = -\left(\hat{\mathbf{v}}_r \mathbf{v}_r + \mathrm{v}_r \mathbf{I}_{3x3}\right)\{\boldsymbol{\omega}_E\} \tag{8.46}$$

Thus, using Eqs. (8.41) and (8.45), the derivative of acceleration with respect to position from Eq. (8.39) is,

$$\frac{\partial \mathbf{a}_{drag}}{\partial \mathbf{r}} = -\frac{1}{2B}\frac{\Delta \rho_{ATM}}{\Delta r}\mathrm{v}_r \hat{\mathbf{r}}\mathbf{v}_r^T + \frac{\rho_{ATM}}{2B}\left(\frac{\mathbf{v}_r \mathbf{v}_r^T}{\mathrm{v}_r} + \mathrm{v}_r \mathbf{I}_{3x3}\right)\{\boldsymbol{\omega}_E\} \tag{8.47}$$

The derivative of relative velocity with respect to velocity can be represented as,

$$\frac{\partial \mathbf{v}_r}{\partial \mathbf{v}} = \frac{\partial}{\partial \mathbf{v}}\left(\mathbf{v} - \boldsymbol{\omega}_E \times \mathbf{r}\right) = \frac{\partial \mathbf{v}}{\partial \mathbf{v}} - \frac{\partial}{\partial \mathbf{v}}\left(\{\boldsymbol{\omega}_E\}\mathbf{r}\right) = \mathbf{I}_{3x3} - \mathbf{0} = \mathbf{I}_{3x3} \tag{8.48}$$

The derivative of acceleration with respect to relative velocity using Eq. (8.40) is expressed as,

$$\frac{\partial \mathbf{a}_{drag}}{\partial \mathbf{v}_r} = -\frac{\rho_{ATM}}{2B}\left[\frac{\partial}{\partial \mathbf{v}_r}\left(\mathrm{v}_r \mathbf{v}_r\right)\right] = -\frac{\rho_{ATM}}{2B}\left[\frac{\mathbf{v}_r \mathbf{v}_r^T}{\mathrm{v}_r} + \mathrm{v}_r \mathbf{I}_{3x3}\right] \tag{8.49}$$

Thus, the derivative of acceleration with respect to velocity is the combination of Eqs. (8.48) and (8.49) as,

$$\frac{\partial \mathbf{a}_{drag}}{\partial \mathbf{v}} = -\frac{\rho_{ATM}}{2B}\left[\frac{\mathbf{v}_r \mathbf{v}_r^T}{\mathrm{v}_r} + \mathrm{v}_r \mathbf{I}_{3x3}\right] \tag{8.50}$$

8.1.2.1.5 Third-Body

The derivative of acceleration due to third-body acceleration effects can be computed using the following notational simplifications of $\mathbf{r} = \mathbf{r}_{SC/Main-body}$ and $\mathbf{s} = \mathbf{r}_{3^{rd}\,body/Main-body}$ from Eq. (8.15) such that [136],

$$\mathbf{a}_{third-body} = -\mu_{3^{rd}\,body}\left(\frac{\mathbf{r}-\mathbf{s}}{\|\mathbf{r}-\mathbf{s}\|^3} + \frac{\mathbf{s}}{s^3}\right) \tag{8.51}$$

The derivation with respect to position yields,

$$\begin{aligned} \frac{\partial \mathbf{a}_{third-body}}{\partial \mathbf{r}} &= -\mu_{3^{rd}\,body}\left[\frac{\partial}{\partial \mathbf{r}}\left(\frac{\mathbf{r}}{\|\mathbf{r}-\mathbf{s}\|^3}\right) - \frac{\partial}{\partial \mathbf{r}}\left(\frac{\mathbf{s}}{\|\mathbf{r}-\mathbf{s}\|^3}\right) + \frac{\partial}{\partial \mathbf{r}}\left(\frac{\mathbf{s}}{s^3}\right)\right] \\ &= -\mu_{3^{rd}\,body}\left[\frac{1}{\|\mathbf{r}-\mathbf{s}\|^3}\mathbf{I}_{3x3} - \frac{3}{\|\mathbf{r}-\mathbf{s}\|^5}(\mathbf{r}-\mathbf{s})(\mathbf{r}-\mathbf{s})^T\right] \end{aligned} \tag{8.52}$$

This partial derivative must be computed for each of the third-body perturbations that are considered within the dynamics.

Since this acceleration effect is independent of velocity, the derivative with respect to velocity is zero, or,

$$\frac{\partial \mathbf{a}_{third-body}}{\partial \mathbf{v}} = \mathbf{0}_{3x3} \tag{8.53}$$

8.1.2.2 State Transition Matrix Integration

Using the above representations for the partial derivatives of acceleration the terms for the Jacobian matrix in Eq. (8.28) can be assembled as,

$$\frac{\partial \mathbf{a}}{\partial \mathbf{r}} = \frac{\partial \mathbf{a}_{two-body}}{\partial \mathbf{r}} + \frac{\partial \mathbf{a}_{non-spherical}}{\delta \mathbf{r}} + \frac{\partial \mathbf{a}_{drag}}{\partial \mathbf{r}} + \sum_{i}^{PB_{SS}} \frac{\partial \mathbf{a}_{i^{th}\ third-body}}{\partial \mathbf{r}} \tag{8.54}$$

$$\frac{\partial \mathbf{a}}{\partial \mathbf{v}} = \frac{\partial \mathbf{a}_{drag}}{\partial \mathbf{v}} \tag{8.55}$$

In Eq. (8.54), the third-body gravitational potential effects are summed over all the bodies within the solar system (PB_{SS}). In the NKF, only the Moon and Sun are currently considered for Earth-orbiting spacecraft. Drag is the only perturbing force that is a function of velocity, thus the only term in Eq. (8.55).

The partial derivatives of acceleration can then be placed in the Jacobian matrix in Eq. (8.28). The best estimated values of the navigation states are considered in this matrix, such that $\mathbf{F} = \mathbf{F}(\tilde{\mathbf{r}}, \tilde{\mathbf{v}})$. This matrix can then be used in the numerical integration of Eq. (8.23) in order to determine the current state transition matrix used for time propagation of the error-states and error-covariances.

8.1.3 Covariance Matrix Dynamics

The expectations of the error-states and the noise of the k^{th} step in a discrete system are represented as,

$$\mathbf{P}_k = E\left[\delta\mathbf{x}_k \delta\mathbf{x}_k^T\right] \tag{8.56}$$

$$\mathbf{Q}_k = E\left[\boldsymbol{\omega}_k \boldsymbol{\omega}_k^T\right] \tag{8.57}$$

The *covariance matrix*, $\mathbf{P}$, is symmetric and provides a representation of the statistical uncertainty in the error-states, $\delta\mathbf{x}$ [65]. The $\mathbf{Q}$ matrix is referred to as the *process noise* matrix for the system, and is related to how well the dynamics of the state variables are known. A Kalman filter interprets high process noise as poor knowledge of the dynamics by maintaining a high estimate of the state covariances. The noise of the individual error states, $\boldsymbol{\omega}$, is assumed to be uncorrelated with respect to time (*white noise*), and assumed to be uncorrelated with respect to the states such that $E\left[\delta\mathbf{x}_k \boldsymbol{\omega}_k^T\right] = \mathbf{0}$. (Note that the process noise, $\boldsymbol{\omega}_k$, should not be confused with the symbol for Earth rotation rate, $\boldsymbol{\omega}_E$, above). The discrete form of the dynamics of the covariance matrix can be represented as [65],

$$\mathbf{P}_{k+1}^{-} = \mathbf{\Phi}_k \mathbf{P}_k \mathbf{\Phi}_k^T + \mathbf{\Gamma}_k \mathbf{Q}_k \mathbf{\Gamma}_k^T \tag{8.58}$$

From the dynamics of Eq. (8.2), the matrix $\mathbf{\Gamma}$ is identity. Eqs. (8.21) and (8.58) represent the *time update* (*a priori*) of the NKF.

8.2 Kalman Filter Measurement Models

The time propagation of the NKF error-states provides predicted estimates of the errors as the spacecraft progresses through its motion. The dynamics defined in the previous section assures this prediction is produced in its most accurate manner. However, any errors that exist within the system, such as initial errors in the estimated states, dynamic modeling errors, or unforeseen disturbances, will cause the estimated dynamics solution to remain in error with respect to the true solution. In order to correct any errors in these states, it is necessary to utilize external observations and process these through the filter. Thus, with high-quality time propagation and correcting measurement updates, over time the filter produces the most accurate state solution possible.

The NKF utilizes range measurements produced by the observation of pulses from pulsars. These range measurements are blended with error-state dynamics of position and velocity such that any errors in these states are determined. This section describes the methods used to incorporate the range measurement from pulsars into the NKF elements so that the measurement updates can proceed in an optimal manner. Both first order and higher-order measurement methods are presented for pulsars based upon the fidelity of the pulsar knowledge and pulse timing accuracy.

Similar to the state dynamics, the observations may also have a non-linear relationship with respect to the whole-value states. Thus the measurement, $\mathbf{y}$, has the following representation,

$$\mathbf{y}(t) = \vec{h}\left(\mathbf{x}(t), t\right) + \boldsymbol{\nu}(t) \tag{8.59}$$

In this expression, $\vec{h}$ is a non-linear function of the state vector, and perhaps time. The measurement noise associated with each observation is represented as $\boldsymbol{\nu}$.

In order to assemble the observations in terms of the error-states of the NKF, a measurement difference, $\mathbf{z}$, between the measurement and its estimate from Eq. (8.59) is computed [65]. To first order, this difference is computed as,

$$\begin{aligned} \mathbf{z}(t) = \mathbf{y}(t) - \vec{h}(\tilde{\mathbf{x}}) &= \frac{\partial \vec{h}(\tilde{\mathbf{x}})}{\partial \mathbf{x}} \delta\mathbf{x} + \boldsymbol{\nu}(t) \\ &= \mathbf{H}(\tilde{\mathbf{x}}) \delta\mathbf{x} + \boldsymbol{\nu}(t) \end{aligned} \tag{8.60}$$

This measurement difference, $\mathbf{z}(t)$, is referred to as the *measurement residual*, and $\mathbf{H} = \partial\vec{h}/\partial\mathbf{x}$ is the *measurement matrix* of measurement partial derivatives with respect to the states [65]. This can be represented in discrete form as,

$$\mathbf{z}_{k+1} = \mathbf{H}_{k+1} \delta\mathbf{x}_{k+1} + \boldsymbol{\nu}_{k+1} \tag{8.61}$$

A *measurement update* (*a posteriori*) of the state vector estimates and the covariance matrix is produced using [29, 65],

$$\tilde{\mathbf{x}}_{k+1}^{+} = \tilde{\mathbf{x}}_{k+1}^{-} + \mathbf{K}_{k+1_{opt}} \mathbf{z}_{k+1} \tag{8.62}$$

$$\mathbf{P}_{k+1}^{+} = \left(\mathbf{I} - \mathbf{K}_{k+1_{opt}} \mathbf{H}_{k+1}\right) \mathbf{P}_{k+1}^{-} \tag{8.63}$$

This update process uses the optimal Kalman gain, $\mathbf{K}_{opt}$, which can be computed based upon the time update of the covariance matrix, the measurement matrix, and the expectations of the measurement noise, $\mathbf{R} = E\left[\mathbf{v}\mathbf{v}^{\mathrm{T}}\right]$ [91]. In discrete form this optimal gain is written as,

$$\mathbf{K}_{k+1_{opt}} = \mathbf{P}_{k+1}^{-}\mathbf{H}_{k+1}^{T}\left(\mathbf{H}_{k+1}\mathbf{P}_{k+1}^{-}\mathbf{H}_{k+1}^{T} + \mathbf{R}_{k+1}\right)^{-1} \tag{8.64}$$

Within the NKF, individual measurements are evaluated prior to a measurement update to remove those out-lying measurements that may potentially corrupt the filter's solution. Using a measurement residual test (Appendix D), the NKF verifies each measurement is five times less than the innovations as computed by the filter.

8.2.1 Pulsar Range Measurement

The range measurement for a spacecraft with respect to a reference location is produced by comparing the measured pulse TOA at the spacecraft to its predicted TOA at the reference location. Any difference in the measured and predicted TOA values is assumed to be a result of errors in the estimated vehicle position, as it is assumed that any additional errors within the system (ex. photon arrival time tagging, spacecraft clock errors, process delays) have already been accounted for in the measurement TOA, and the pulse model is as accurate as possible.

A direct comparison of the arrival time at the spacecraft to the same pulse's arrival time at the SSB is accomplished using time transfer equations. These equations require knowledge of the spacecraft's position and velocity in order to be implemented correctly. In the NKF's measurement scheme, estimated values of spacecraft position and velocity are utilized within the time transfer equation to create the best estimates of pulse arrival times at the SSB. These state estimates are provided by the onboard orbit propagator using Eqs. (8.3) and (8.6) implemented within the vehicle's navigation system, which provides a continuous estimate of the vehicle's dynamics during a pulsar observation.

Figure 8-1 presents a diagram of an Earth-orbiting spacecraft and two pulsars. Unit directions to the pulsars, $\hat{\mathbf{n}}_i$ and $\hat{\mathbf{n}}_j$, as well as the position of the spacecraft with respect to the SSB, $\mathbf{r}_{SC}$, the position of Earth with respect to the SSB, $\mathbf{r}_E$, and the position of the spacecraft with respect to Earth, $\mathbf{r}_{SC/E}$ are shown.

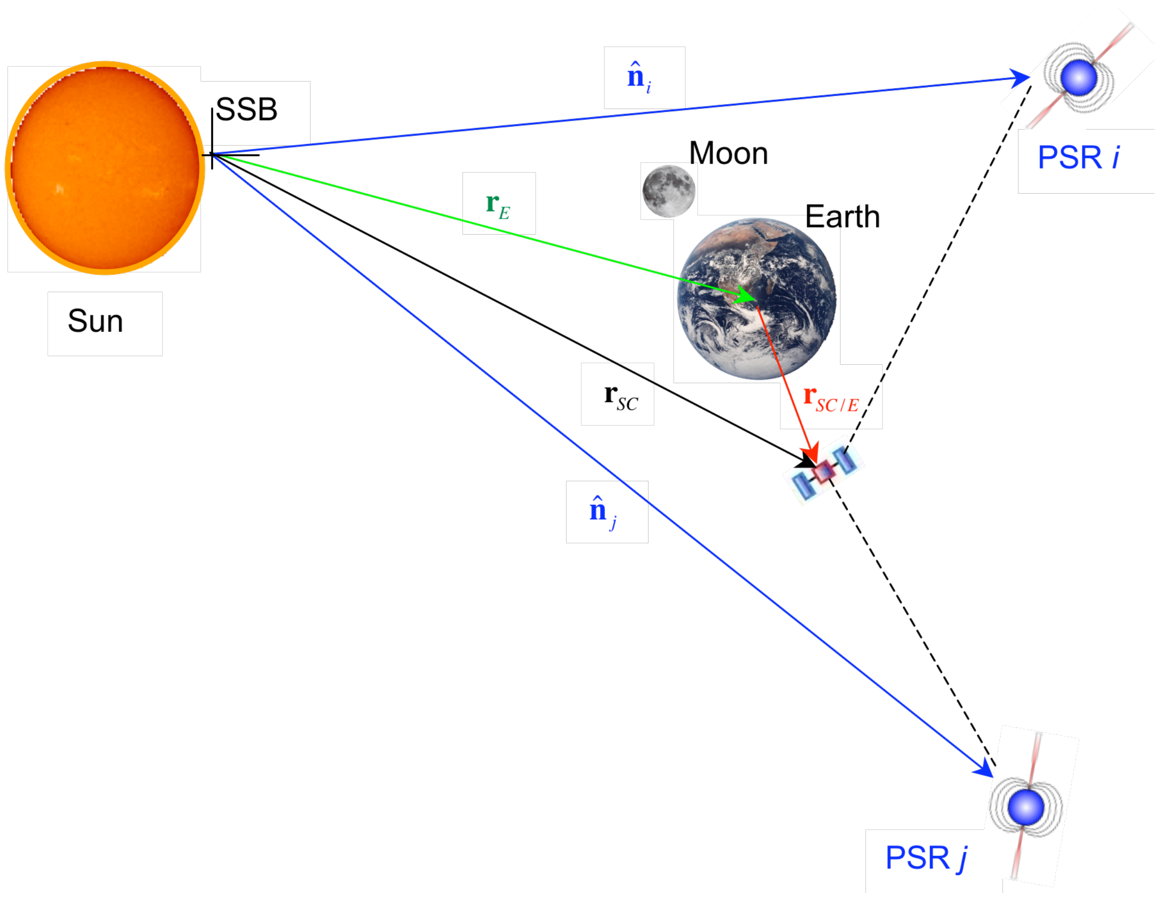

Figure 8-1. Multiple pulsars viewed by Earth-orbiting spacecraft.

8.2.1.1 First Order Measurement

From Chapter 7, to first order, the pulse TOA measured at the spacecraft, t_{SC}, compared to its predicted arrival time at the SSB, t_{SSB}, is shown for the i^{th} pulsar to be,

$$t_{SSB} = t_{SC} + \frac{\hat{\mathbf{n}}_i \cdot \mathbf{r}_{SC}}{c} = t_{SC} + \frac{\hat{\mathbf{n}}_i}{c} \cdot \left(\mathbf{r}_E + \mathbf{r}_{SC/E} \right) \tag{8.65}$$

This expression can be written in terms of spacecraft Earth-relative position, $\mathbf{r}_{SC/E}$, as,

$$ct_{SSB} - ct_{SC} - \hat{\mathbf{n}}_i \cdot \mathbf{r}_E = \hat{\mathbf{n}}_i \cdot \mathbf{r}_{SC/E} \tag{8.66}$$

Eq. (8.66) give a method to represent the desired position of the spacecraft relative to Earth based upon the measured difference in pulse TOA and the known position of Earth within the solar system. The known Earth position could be provided by standard ephemeris tables (ex. JPL ephemeris data [198]).

Using the estimated value of this position, $\tilde{\mathbf{r}}_{SC/E}$, the error in this value, $\delta \mathbf{r}_{SC/E}$, is related to the true value as,

$$\mathbf{r}_{SC/E} = \tilde{\mathbf{r}}_{SC/E} + \delta \mathbf{r}_{SC/E} \tag{8.67}$$

The NKF is used to determine the errors of the spacecraft position. Therefore, the measurement in Eq. (8.66) can be written in terms of the position error as,

$$ct_{SSB} - ct_{SC} - \hat{\mathbf{n}}_i \cdot \left(\mathbf{r}_E + \tilde{\mathbf{r}}_{SC/E} \right) = \hat{\mathbf{n}}_i \cdot \delta \mathbf{r}_{SC/E} \tag{8.68}$$

The form of Eq. (8.68) is the form of the Kalman filter measurement equation of Eq. (8.60), where,

$$\begin{aligned}
\mathbf{y}(t) &= ct_{SSB} \\
\vec{h}(\tilde{\mathbf{x}}) &= ct_{SC} + \hat{\mathbf{n}}_i \cdot \left(\mathbf{r}_E + \tilde{\mathbf{r}}_{SC/E} \right) \\
\mathbf{z}(t) &= \mathbf{y}(t) - \vec{h}(\tilde{\mathbf{x}}) = ct_b - \left[ct_{SC} + \hat{\mathbf{n}}_i \cdot \left(\mathbf{r}_E + \tilde{\mathbf{r}}_{SC/E} \right) \right] \\
\mathbf{H}(\tilde{\mathbf{x}}) \delta \mathbf{x} &= \hat{\mathbf{n}}_i \cdot \delta \mathbf{r}_{SC/E} = \begin{bmatrix} \hat{n}_{i_x} & \hat{n}_{i_y} & \hat{n}_{i_z} & 0 & 0 & 0 \end{bmatrix} \begin{bmatrix} \delta r_{SC/E_x} \\ \delta r_{SC/E_y} \\ \delta r_{SC/E_z} \\ \delta v_{SC/E_x} \\ \delta v_{SC/E_y} \\ \delta v_{SC/E_z} \end{bmatrix}
\end{aligned} \tag{8.69}$$

The measurement noise, $\mathbf{v}(t)$, associated with Eq. (8.69) must be added to assure accurate modeling. This noise would be a function of all unknown measurement errors. For example, this could be chosen as v = 300 m or v = 30 m depending on pulse timing resolution of 1 μs or 100 ns, respectively, or chosen as the range measurement accuracy values for each pulsar in Chapter 3. Thus, using the terms from Eq. (8.69), the first order relationship for a pulsar range measurement would be,

$$\mathbf{z}(t) = \mathbf{y}(t) - \vec{h}(\tilde{\mathbf{x}}) = \mathbf{y}(t) - \mathbf{H}(\tilde{\mathbf{x}})\tilde{\mathbf{x}} = \mathbf{H}(\tilde{\mathbf{x}})\delta\mathbf{x} + \mathbf{v}(t) \tag{8.70}$$

From Eq. (8.69), it can be seen that $\mathbf{z}(t)$ in Eq. (8.70) is actually a scalar value. However, an ensemble of pulsar measurements could be collected together to create a vector of measurements.

This measurement relationship is presented in Figure 8-2. The concept has similarities to methods used by ground-based orbit determination. In this figure, the orbit can be determined via at least three observations by a ground radio telescope from range, ρ_i, and range-rate, $\dot{\rho}_i$, of the vehicle. Combining these separate observations provides a method to measure the orbital elements, or state, information of the vehicle [16, 17, 55]. The pulsar-based method can also produce range measurements relative to the vehicle's primary gravitational body, in this case Earth. These first-order range measurements, $\tilde{\rho}_{i/E} = \left\|\tilde{\mathbf{r}}_{SC_i/E}\right\|$, are generated using the expression of Eq. (8.68) and can be blended with the state dynamics and its errors using the Kalman filter measurement model of Eq. (8.69) to recursively update the estimate of the state errors. Multiple measurements from a single pulsar, or multiple pulsars from different line-of-sight directions, allow the filter to compute the best overall continuous, state solution.

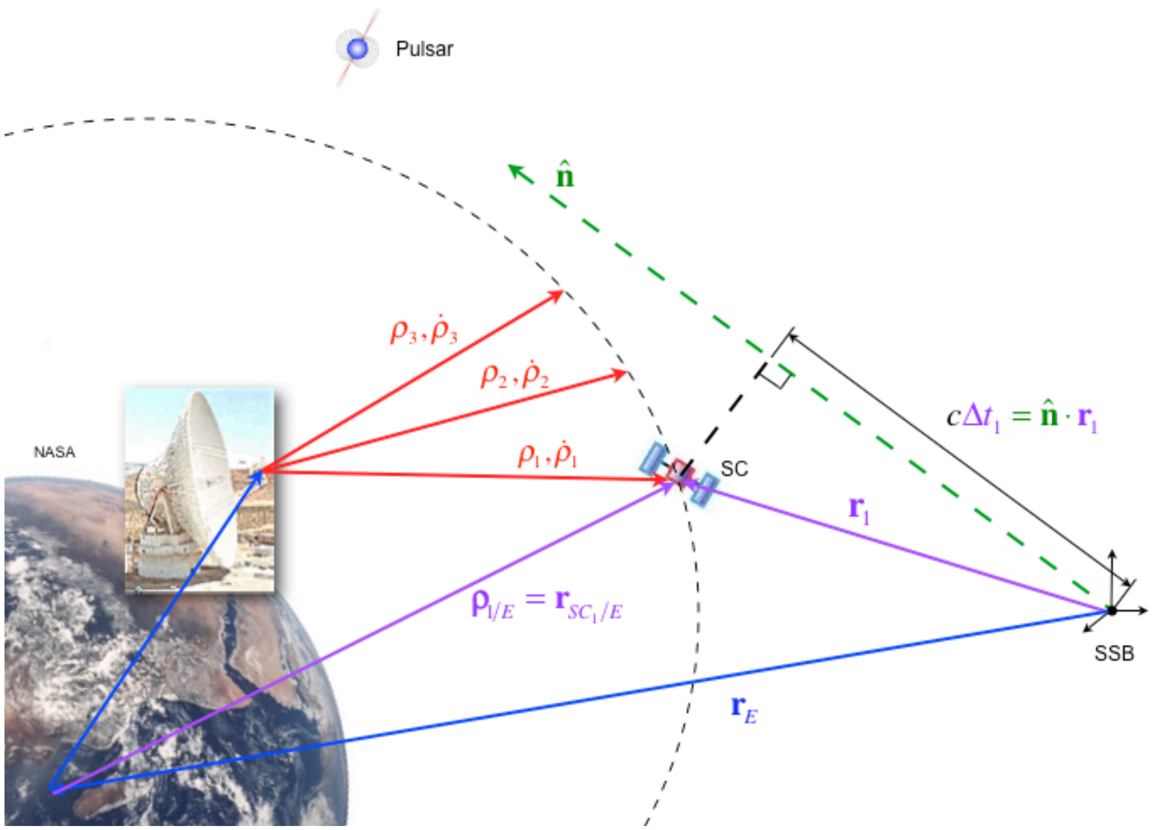

Figure 8-2. Pulsar-based measurement and radar-range measurement comparison.

8.2.1.2 Higher-Order Measurement

The expression of the measurement from Eq. (8.65) is a first order only representation of the pulsar timing measurement and spacecraft position. Increased accuracy can be pursued by including the relativistic effects on the time transfer equation as presented in Chapter 4 and 7. The *proper time* to *coordinate time* correction must account for the clock's time measurement due to its motion and effects from nearby gravitational bodies. Additionally, the relativistic effects of path bending and time transfer within the solar system must be included to adjust the pulse arrival time calculation for these effects. From the higher order measurement equations presented in Chapter 7, the full equation can be written using spacecraft proper time, τ_{SC}, as,

$$
\begin{aligned}
& c\left(t_{SSB} - \tau_{SC} - StdCorr_E\right) - \frac{1}{c}\left[\mathbf{v}_E \cdot \left(\tilde{\mathbf{r}} - \mathbf{r}_E\right)\right] - \left(\hat{\mathbf{n}} \cdot \tilde{\mathbf{r}}\right) \\
& -\frac{1}{D_0}\begin{bmatrix} \frac{1}{2}\left(\hat{\mathbf{n}} \cdot \tilde{\mathbf{r}}\right)^2 - \frac{1}{2}\tilde{r}^2 \\ +\left(\tilde{\mathbf{r}} \cdot \mathbf{V}\Delta t_N\right) - \left(\hat{\mathbf{n}} \cdot \mathbf{V}\Delta t_N\right)\left(\hat{\mathbf{n}} \cdot \tilde{\mathbf{r}}\right) \\ -\left(\mathbf{b} \cdot \tilde{\mathbf{r}}\right) + \left(\hat{\mathbf{n}} \cdot \mathbf{b}\right)\left(\hat{\mathbf{n}} \cdot \tilde{\mathbf{r}}\right) \end{bmatrix} - \frac{2\mu_{Sun}}{c^2}\ln\left|\frac{\hat{\mathbf{n}} \cdot \tilde{\mathbf{r}} + \tilde{r}}{\hat{\mathbf{n}} \cdot \mathbf{b} + b} + 1\right| \\
& = \hat{\mathbf{n}} \cdot \delta\mathbf{r} + \frac{1}{D_0}\begin{bmatrix} \left(\hat{\mathbf{n}} \cdot \tilde{\mathbf{r}}\right)\left(\hat{\mathbf{n}} \cdot \delta\mathbf{r}\right) - \tilde{\mathbf{r}} \cdot \delta\mathbf{r} \\ +\left(\mathbf{V}\Delta t_N\right) \cdot \delta\mathbf{r} - \left(\hat{\mathbf{n}} \cdot \mathbf{V}\Delta t_N\right)\left(\hat{\mathbf{n}} \cdot \delta\mathbf{r}\right) \\ -\left(\mathbf{b} \cdot \delta\mathbf{r}\right) + \left(\hat{\mathbf{n}} \cdot \mathbf{b}\right)\left(\hat{\mathbf{n}} \cdot \delta\mathbf{r}\right) \end{bmatrix} \\
& + \frac{2\mu_{Sun}}{c^2}\left[\frac{\hat{\mathbf{n}} \cdot \delta\mathbf{r} + \frac{\tilde{\mathbf{r}}}{\tilde{r}} \cdot \delta\mathbf{r}}{\left(\hat{\mathbf{n}} \cdot \tilde{\mathbf{r}} + \tilde{r}\right) + \left(\hat{\mathbf{n}} \cdot \mathbf{b} + b\right)}\right] + \frac{1}{c}\left(\mathbf{v}_E \cdot \delta\mathbf{r}\right)
\end{aligned}
\tag{8.71}
$$

This expression can be put into the Kalman filter measurement form as,

$$
\begin{aligned}
& \mathbf{y}(t) = ct_{SSB} \\
& \bar{h}\left(\tilde{\mathbf{x}}\right) = c\left(\tau_{SC} + StdCorr_E\right) + \frac{1}{c}\left[\mathbf{v}_E \cdot \left(\tilde{\mathbf{r}} - \mathbf{r}_E\right)\right] + \left(\hat{\mathbf{n}} \cdot \tilde{\mathbf{r}}\right) \\
& \quad + \frac{1}{D_0}\begin{bmatrix} \frac{1}{2}\left(\hat{\mathbf{n}} \cdot \tilde{\mathbf{r}}\right)^2 - \frac{1}{2}\tilde{r}^2 \\ +\left(\tilde{\mathbf{r}} \cdot \mathbf{V}\Delta t_N\right) - \left(\hat{\mathbf{n}} \cdot \mathbf{V}\Delta t_N\right)\left(\hat{\mathbf{n}} \cdot \tilde{\mathbf{r}}\right) \\ -\left(\mathbf{b} \cdot \tilde{\mathbf{r}}\right) + \left(\hat{\mathbf{n}} \cdot \mathbf{b}\right)\left(\hat{\mathbf{n}} \cdot \tilde{\mathbf{r}}\right) \end{bmatrix} + \frac{2\mu_{Sun}}{c^2}\ln\left|\frac{\hat{\mathbf{n}} \cdot \tilde{\mathbf{r}} + \tilde{r}}{\hat{\mathbf{n}} \cdot \mathbf{b} + b} + 1\right| \\
& \mathbf{z}(t) = \mathbf{y}(t) - \bar{h}\left(\tilde{\mathbf{x}}\right) \\
& \mathbf{H}\left(\tilde{\mathbf{x}}\right)\delta\mathbf{x} = \begin{bmatrix} \begin{bmatrix} \hat{\mathbf{n}} + \frac{1}{D_0}\begin{bmatrix} \left(\hat{\mathbf{n}} \cdot \tilde{\mathbf{r}}\right)\left(\hat{\mathbf{n}}\right) - \tilde{\mathbf{r}} \\ +\left(\mathbf{V}\Delta t_N\right) - \left(\hat{\mathbf{n}} \cdot \mathbf{V}\Delta t_N\right)\left(\hat{\mathbf{n}}\right) \\ -\mathbf{b} + \left(\hat{\mathbf{n}} \cdot \mathbf{b}\right)\left(\hat{\mathbf{n}}\right) \end{bmatrix} \\ + \frac{2\mu_{Sun}}{c^2}\left[\frac{\hat{\mathbf{n}} + \frac{\tilde{\mathbf{r}}}{\tilde{r}}}{\left(\hat{\mathbf{n}} \cdot \tilde{\mathbf{r}} + \tilde{r}\right) + \left(\hat{\mathbf{n}} \cdot \mathbf{b} + b\right)}\right] + \frac{1}{c}\mathbf{v}_E \end{bmatrix}^T & 0 & 0 & 0 \end{bmatrix} \begin{bmatrix} \delta\mathbf{r} \\ \delta\mathbf{v} \end{bmatrix}
\end{aligned}
\tag{8.72}
$$

Using this form, along with its associated measurement errors, allows the NKF to process pulsar-based range measurements with high accuracy.

8.2.2 Pulsar Phase Measurement

As presented in Chapter 6, there is a relationship between the range measurement and the total phase measurement of the pulse cycles for the spacecraft. This total phase is related to range, or distance, by the cycle wavelength. If the estimate of spacecraft position used in the measurement equations of (8.69) or (8.72) is sufficiently accurate that the number of integer phase cycles can be immediately determined between the spacecraft and the inertial reference location, a phase measurement can be used instead of a range value with each of these measurement equations. The fractional phase difference between the phase of the pulse timing model and the measured value at the spacecraft can be added to the difference in full cycle counts to create a measurement of the phase difference that can be implemented within the NKF measurement models. The approach may be directly useful for systems where phase is the chosen as the communicated unit of pulse measurement throughout the system.

8.3 Spacecraft Clock Errors and Measurement

The states chosen for the NKF, as presented previously, are spacecraft position and velocity. Updates to these states provide improved overall navigation information. Measurements of pulsar pulse arrival times are the primary observation used within the system. Since the measured time is critical for improved performance, errors within the spacecraft clock, or pulse timing system, would contribute to any degraded performance of the navigation system. Thus, for many practical applications it may be prudent to add clock states and errors to the state vector, so that any measured pulse arrival time offset that is attributable to the clock time measurement, and not position error, can be determined.

The spacecraft clock's state variable can be represented as τ_{SC}. Consequently, its estimated value can be listed as $\tilde{\tau}_{SC}$ and its errors as $\delta\tau_{SC}$ such that the true clock time can be determined to be,

$$\tau_{SC} = \tilde{\tau}_{SC} + \delta\tau_{SC} \tag{8.73}$$

The error $\delta\tau_{SC}$ is the clock bias state. If the bias is not a fixed value, it will depend on clock drift rate ς_{SC}, whose estimate and error follow as,

$$\varsigma_{SC} = \tilde{\varsigma}_{SC} + \delta\varsigma_{SC} \tag{8.74}$$

Including these two new states, the new estimated state and error-state vectors for the NKF become,

$$\tilde{\mathbf{x}} = \begin{bmatrix} \tilde{\mathbf{r}}_{SC} \\ \tilde{\mathbf{v}}_{SC} \\ \tilde{\tau}_{SC} \\ \tilde{\varsigma}_{SC} \end{bmatrix}; \qquad \delta\mathbf{x} = \begin{bmatrix} \delta\mathbf{r}_{SC} \\ \delta\mathbf{v}_{SC} \\ \delta\tau_{SC} \\ \delta\varsigma_{SC} \end{bmatrix} \tag{8.75}$$

8.3.1 Clock State Dynamics

The dynamics of these two new clock error states can be represented as the following since the bias term is directly related to the drift rate,

$$\begin{aligned} \delta\dot{\tau}_{SC} &= \delta\varsigma_{SC} + \nu_{\tau} \\ \delta\dot{\varsigma}_{SC} &= \qquad\quad \nu_{f} \end{aligned} \tag{8.76}$$

The Jacobian matrix for these new states can be computed directly from Eq. (8.76) as,

$$\mathbf{F}(t)_{clock} = \begin{bmatrix} \dfrac{\partial \dot{\tau}}{\partial \tau} & \dfrac{\partial \dot{\tau}}{\partial \varsigma} \\ \dfrac{\partial \dot{\varsigma}}{\partial \tau} & \dfrac{\partial \dot{\varsigma}}{\partial \varsigma} \end{bmatrix} = \begin{bmatrix} 0 & 1 \\ 0 & 0 \end{bmatrix} \tag{8.77}$$

The process noise matrix comes from the white noise from each state as,

$$\mathbf{Q}(t)_{clock} = \begin{bmatrix} v_{\delta\tau}^2 & 0 \\ 0 & v_{\delta\varsigma}^2 \end{bmatrix} \tag{8.78}$$

The covariance matrix can be written using the error estimate of each state such that,

$$\mathbf{P}_{clock} = \begin{bmatrix} \sigma_{\delta\tau}^2 & 0 \\ 0 & \sigma_{\delta\varsigma}^2 \end{bmatrix} \tag{8.79}$$

8.3.2 Clock Measurement

The clock errors can be measured using the pulsar range equations and the clock error model of Eq. (8.73). Using the first order range equation from Eq. (8.68)

$$ct_{SSB} - ct_{SC} - \hat{\mathbf{n}}_i \cdot \left(\mathbf{r}_E + \tilde{\mathbf{r}}_{SC/E}\right) = \hat{\mathbf{n}}_i \cdot \delta\mathbf{r}_{SC/E} + c\delta\tau_{SC} \tag{8.80}$$

This expression can be represented in Kalman filter measurement form as,

$$\begin{aligned} \mathbf{y}(t) &= ct_{SSB} \\ \vec{h}(\tilde{\mathbf{x}}) &= ct_{SC} + \hat{\mathbf{n}}_i \cdot \left(\mathbf{r}_E + \tilde{\mathbf{r}}_{SC/E}\right) \\ \mathbf{z}(t) &= \mathbf{y}(t) - \vec{h}(\tilde{\mathbf{x}}) = ct_{SSB} - \left[ct_{SC} + \hat{\mathbf{n}}_i \cdot \left(\mathbf{r}_E + \tilde{\mathbf{r}}_{SC/E}\right)\right] \\ \mathbf{H}(\tilde{\mathbf{x}})\delta\mathbf{x} &= \hat{\mathbf{n}}_i \cdot \delta\mathbf{r}_{SC/E} + c\delta\tau_{SC} = \begin{bmatrix} \hat{n}_{i_x} & \hat{n}_{i_y} & \hat{n}_{i_z} & 0 & 0 & 0 & c & 0 \end{bmatrix} \begin{bmatrix} \delta r_{SC/E_x} \\ \delta r_{SC/E_y} \\ \delta r_{SC/E_z} \\ \delta v_{SC/E_x} \\ \delta v_{SC/E_y} \\ \delta v_{SC/E_z} \\ \delta\tau_{SC} \\ \delta\varsigma_{SC} \end{bmatrix} \end{aligned} \tag{8.81}$$

If additional accuracy is required using the relativistic corrections presented in Chapter 7 and the previous Higher-Order Measurement section, the measurement models from Eq. (8.72) can include the spacecraft clock error as needed.

Other higher-order effects could also be considered. Errors due to coordinate time standard corrections, Earth inertial velocity, $\mathbf{v}_E$, or solar system ephemeris data may also contribute to the navigation errors. If these errors are significant compared to the other errors and if they are observable within the measurement system, they could be added as needed to the state vector.

8.4 Visibility Obstruction By Celestial Body

Even though sources are very distant from the solar system, any body that passes between the spacecraft and the source may obstruct a spacecraft detector's view of the source. To avoid this obstruction occurring during a planned source observation, it is necessary to determine the location within an orbit where the detector's visibility of a source is obstructed. For Earth-orbiting spacecraft it is apparent that any source that is not perpendicular to the vehicle's orbit plane may potentially pass behind Earth's limb for some portion of the orbit.

Figure 8-3 provides a diagram of a spacecraft in Earth orbit, as well as the shadow cast by Earth from a pulsar. Earth will block the view of the source while the vehicle is in Earth's shadow. Any celestial body, other spacecraft, or components on the vehicle itself could obscure the view of a source. The size of an object and its distance form the spacecraft's detector affect the amount of obscuration. If a celestial body has an appreciable atmosphere that may absorb X-ray photons, the height of the atmosphere must be added to the diameter of the body when determining source visibility.

To determine whether a body obscures the view of a source, it is necessary to determine the size of the shadow cast by the body and whether the spacecraft's path intersects this shadow [55]. Figure 8-4 provides a diagram of a body and the orbit of a vehicle about this body and the geometry associated with the shadow cast by the body. The angle, ψ, between the vehicle's position relative to the body, $\mathbf{r}_{SC/B}$, and the unit direction to the source, $\hat{\mathbf{n}}$, can be determined from,

$$\cos(\psi) = \hat{\mathbf{n}} \cdot \mathbf{r}_{SC/B} \tag{8.82}$$

The vehicle is within the body's shadow when this angle is within the entrance and exit angles, ψ_{ENT} and ψ_{EXIT} respectively, of the shadow,

$$\psi_{ENT} \leq \psi \leq \psi_{EXIT} \tag{8.83}$$

The offset distance, $\mathbf{d}$, is related to the position and body radius, $\mathbf{R}_B$, as,

$$\mathbf{r}_{SC/B} = \mathbf{R}_B + \mathbf{d} \tag{8.84}$$

Thus the magnitude of this offset is,

$$d = \sqrt{r_{SC/B}^2 - R_B^2} \tag{8.85}$$

Since the shadow can only exist for the angles between $\pi/2$ and $3\pi/2$, Figure 8-4 shows that the entrance and exit angles relate to this distance as,

$$\cos(\pi - \psi_{ENT}) = \frac{d}{r_{SC/B}} \tag{8.86}$$

$$\cos(\psi_{EXIT} - \pi) = \frac{d}{r_{SC/B}} \tag{8.87}$$

Therefore the test from Eq. (8.83) can be rewritten as,

$$\pi - \arccos\left(\frac{\sqrt{r_{SC/B}^2 - R_B^2}}{r_{SC/B}}\right) \leq \arccos\left(\hat{\mathbf{n}} \cdot \mathbf{r}_{SC/B}\right) \leq \pi + \arccos\left(\frac{\sqrt{r_{SC/B}^2 - R_B^2}}{r_{SC/B}}\right) \qquad (8.88)$$

If the computed angle is between these bounds, then the vehicle is within the body's shadow. For Earth, the planetary radius should include Earth's atmosphere height, h_{ATM}, such that $R_B = R_E + h_{ATM}$.

Using the Crab Pulsar and the orbit of the *ARGOS* vehicle on December 26, 1999, Figure 8-5 plots the visibility of the pulsar due to Earth's shadow during four orbits. This plot shows that the Crab Pulsar is visible for approximately 4317 s during the 6102 s orbit. Figure 8-6 plots the visibility of two other pulsars, PSR B1937+21, and PSR B1821+24, during the orbit of *ARGOS* due to Earth's shadow and these two pulsars are obscured from view for some portion of the vehicle's orbit.

Figure 8-7 plots the visibility of all three of these pulsars during four *ARGOS* orbits due to the combined effects of the shadows of Earth, the Sun, and the Moon. This figure shows that during each of these orbits at least one pulsar is visible. Figure 8-8 provides a visibility plot for these three pulsars within the GPS system orbit. Although the GPS spacecraft nearly enters Earth's shadow of the Crab Pulsar, all three pulsars a visible for the entire orbit of this spacecraft. Although visibility durations for a specific source can be determined along a spacecraft orbit, additional visibility limitations such as vehicle component obstruction or detector gimbaled axis limitations may reduce these durations and would require further analysis for a specific implementation.

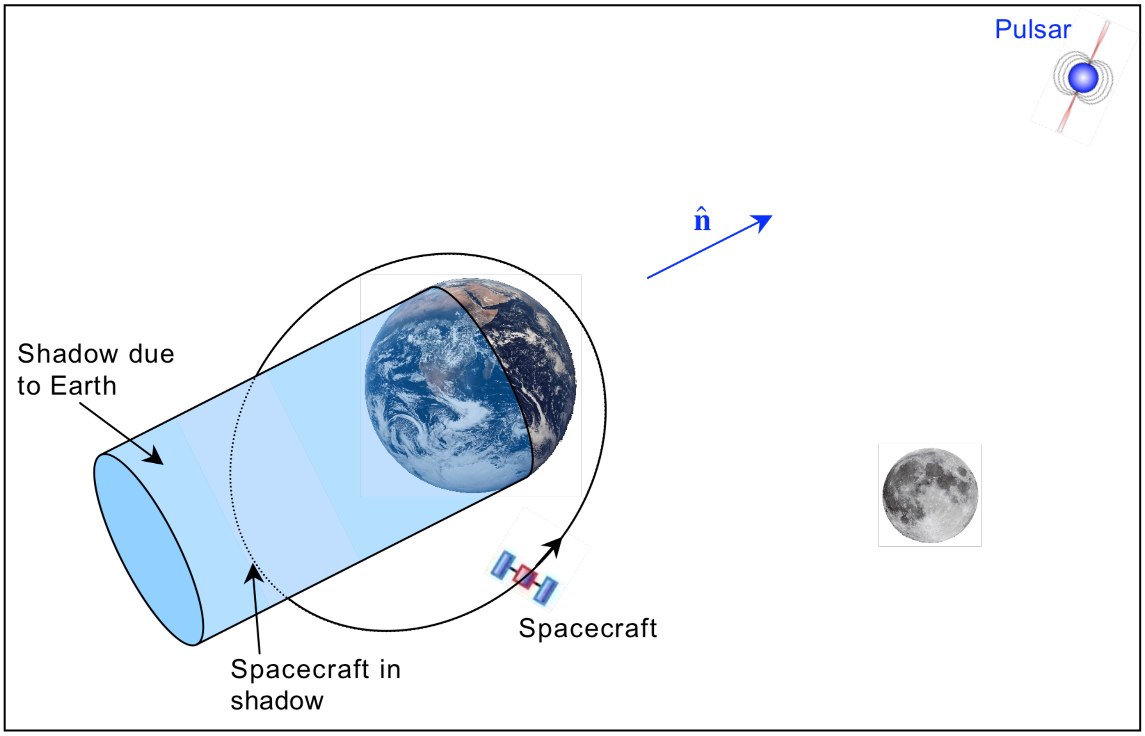

Figure 8-3. Shadow cast by Earth on spacecraft orbit.

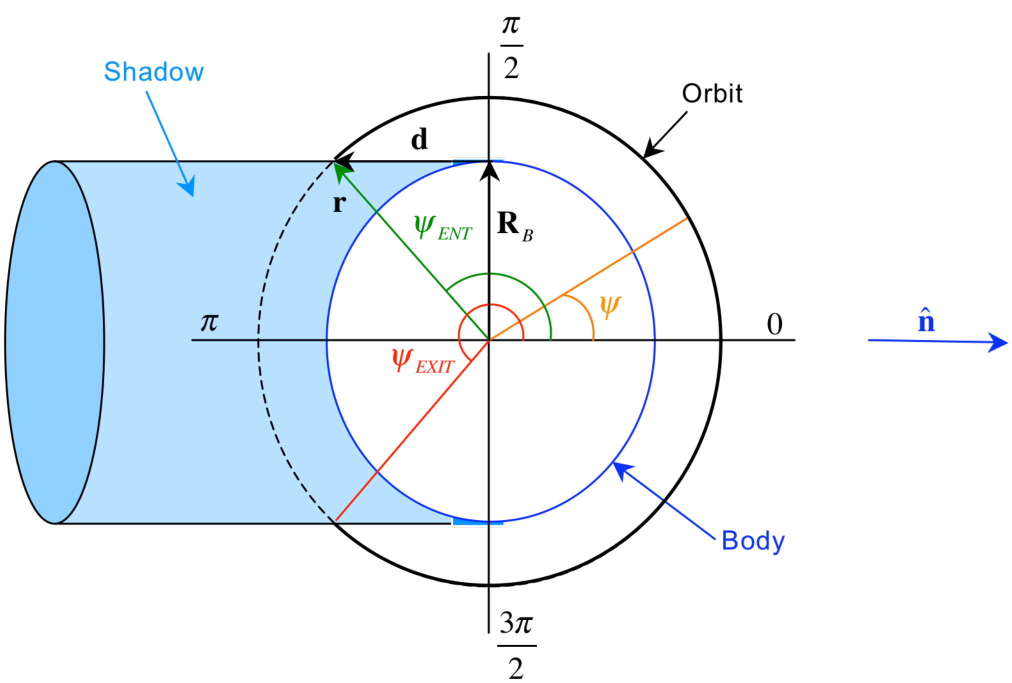

Figure 8-4. Geometry of body shadow with respect to spacecraft orbit.

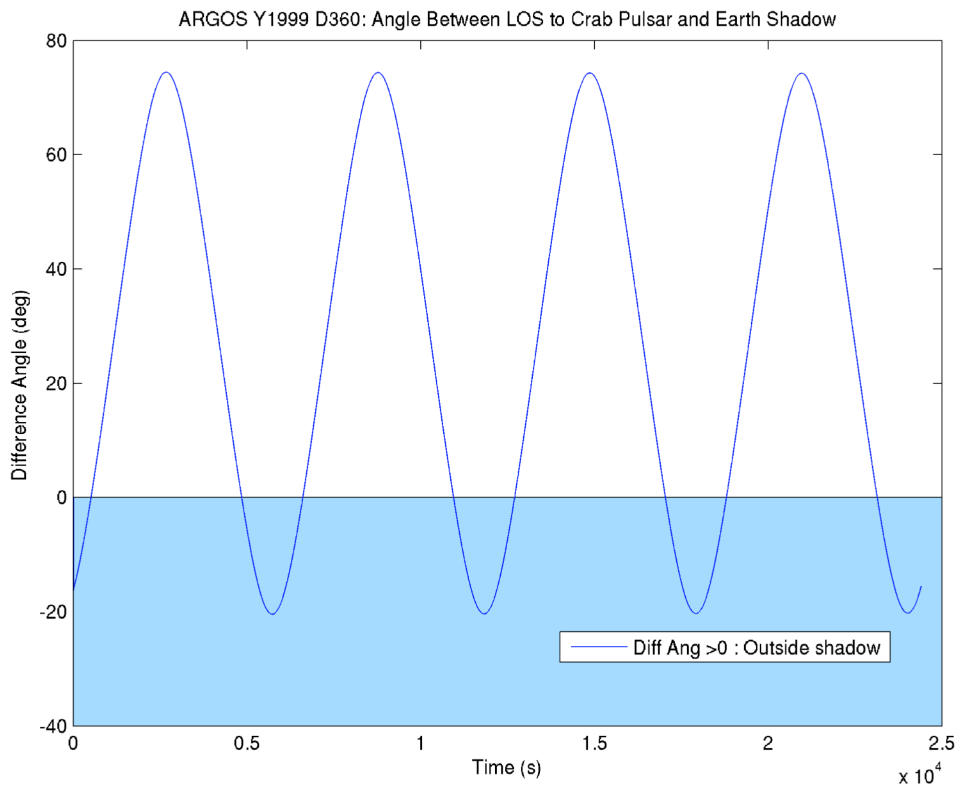

Figure 8-5. Visibility of Crab Pulsar in *ARGOS* orbits about Earth.

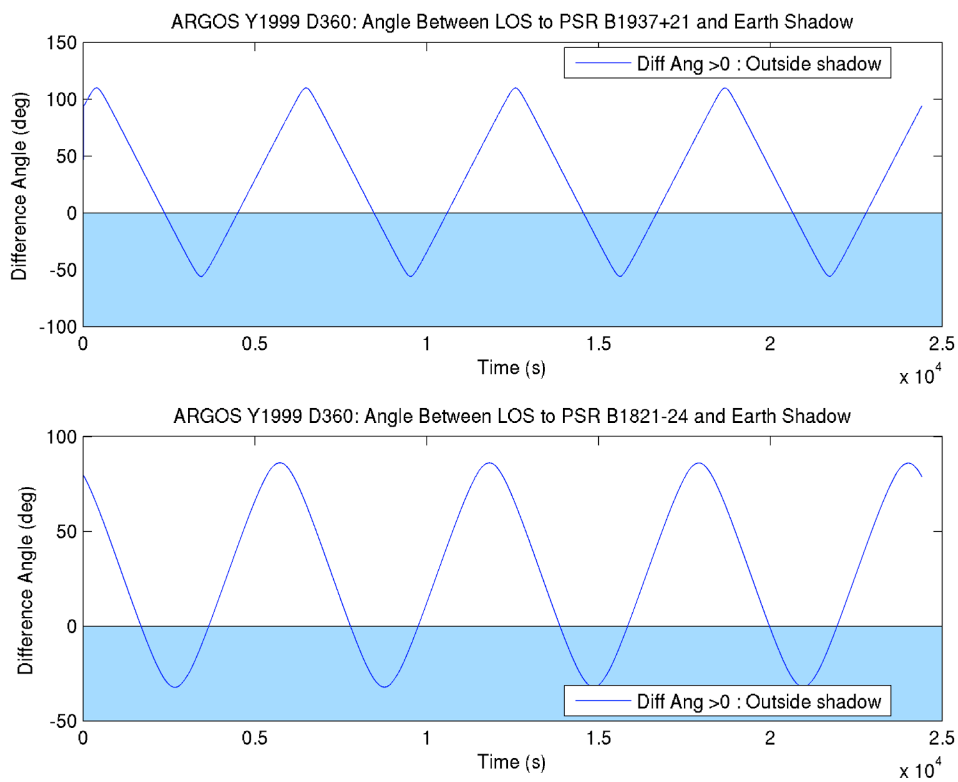

Figure 8-6. Visibility of two pulsars in *ARGOS* orbits about Earth.

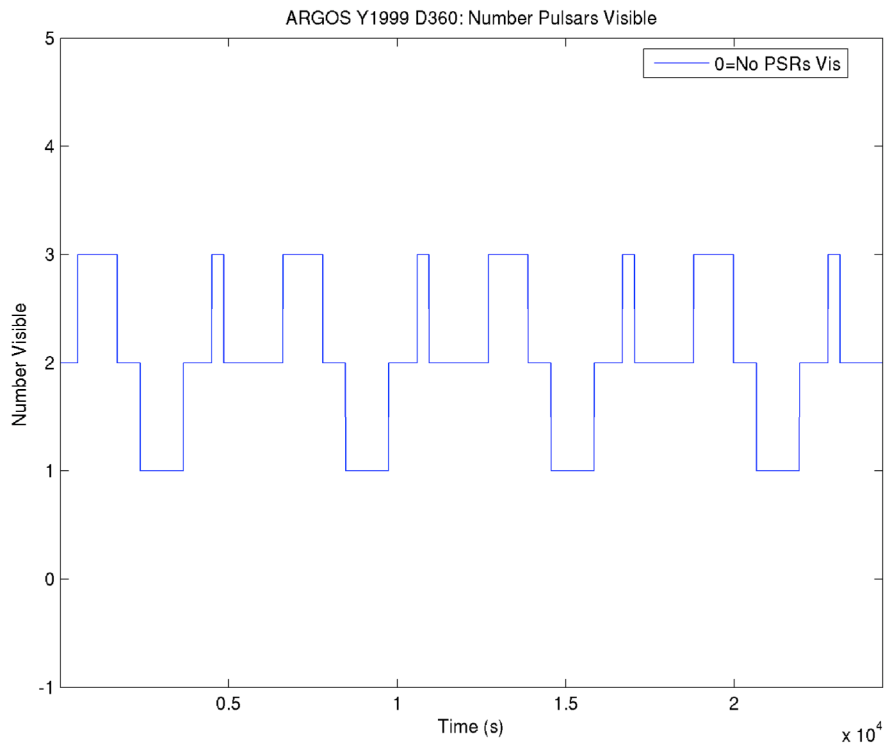

Figure 8-7. Visibility of three pulsars due to shadows from Earth, Sun, and Moon in *ARGOS* orbit.

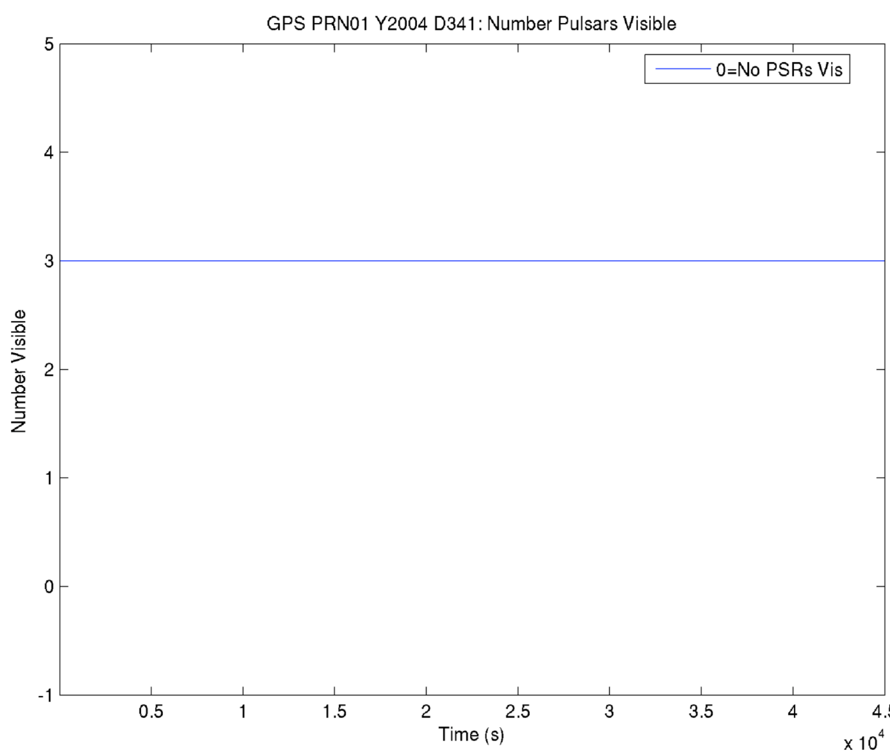

Figure 8-8. Visibility of three pulsars due to shadows from Earth, Sun, and Moon in GPS orbit.

8.5 *Simulation And Results*

8.5.1 Simulation Description

To test the performance of the NKF, a computer simulation was developed that incorporates vehicle dynamics and pulsar-based range measurements. The simulation essentially contains two main components, a numerical orbit propagation routine and the NKF used to correct a navigation solution from the propagator. The numerical orbit propagation routine integrates the vehicle state dynamics in order to provide a continuous position and velocity solution. The NKF then processes simulated range measurements to update the vehicle state dynamics and provide an improved navigation solution. The simulation was coded in the MATLAB® development environment produced by The MathWorks, Inc.

Four existing satellite orbits of *ARGOS*, Laser Geodynamics (LAGEOS-1), GPS Block IIA-16 PRN-01 and DirecTV 2 (DBS 2) were investigated. Initial truth state conditions were chosen from the two-line element sets (TLE) of orbit data provided by NORAD [97]. These TLE sets are read by analytical perturbation orbit propagators, such as the Simplified General Perturbations Number 4 (SGP4) propagator and the Simplified Deep Space Perturbations Number 4 (SDP4) [83, 84]. The TLE data also provided the ballistic coefficients of the spacecraft used in the atmospheric drag computations. A proposed orbit of the NASA Lunar Reconnaissance Orbiter (LRO) was also investigated. This planned mission will orbit the Moon at an altitude of 50 km beginning in 2008 [21]. Table 8-1 lists several orbit parameters for each of the selected spacecraft orbits.

Table 8-1. Spacecraft Orbit Information.

Orbit	Semi-Major Axis (km)	Eccentricity	Period (s)	Inclination (deg)
ARGOS	7217	0.0021	6102	98.8
LAGEOS-1	12275	0.0038	13534	109.8
GPS Block IIA-16 PRN-01	26561	0.0058	43081	56.3
DirecTV 2 (DBS 2)	42166	0.00018	86169	0.027
LRO	1870	0.036	7256	113

The vehicle state dynamics was implemented as Eqs. (8.3) and (8.6). The non-spherical Earth gravitational zonal terms of J_2 through J_6 were implemented [213], and a Harris-Priester model of Earth's atmosphere was utilized [136]. The Moon and Sun were the two third-body effects considered. The solar system position and velocity information was provided by the JPL ephemeris data [198].

A *truth* orbit model was created by integrating the numerical propagator with the initial conditions set from the TLE data values. Two other orbit solutions were created. One of these propagators was used by the NKF and was updated based upon measurement processing within the NKF. The second solution was allowed to run freely and was not corrected at all during the simulation. Each of these two solutions was initialized with state data that included simulated position and velocity error.

The simulated state dynamics for these orbits was integrated using a fourth-order Runge-Kutta method with a fixed time step of 10 s. The numerical solution was validated for each of the Earth orbiting cases using both the SDP4 and the Navy's Position and Partials as functions of Time Version 3 (PPT3) [84, 182] analytical orbit propagators. Although differences between the numerical solution and the analytical solutions for each orbit were small, the analytical model for orbit propagation cannot match the simulation's results exactly due to the higher order perturbation effects considered within the numerical simulation. To demonstrate the accuracy of the numerical solution compared to the analytical solutions, within the LAGEOS-1 orbit Figure 8-9 and Figure 8-10 present the difference between the SDP4 and NKF state dynamics of position and velocity, respectively, for two orbits. Both solutions were begun with the same initial conditions for this test. Comparisons to the PPT3 solution are similar. These plots show that the NKF numerical propagator compares favorably to the analytical orbit solutions.

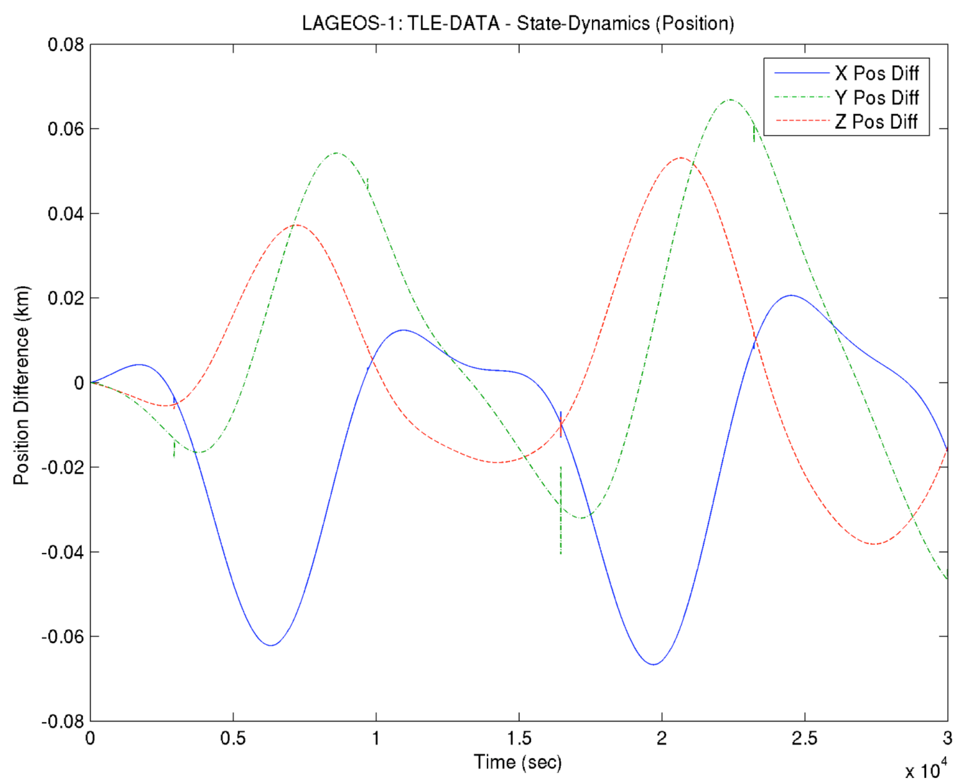

Figure 8-9. Analytical and numerical orbit propagation position differences.

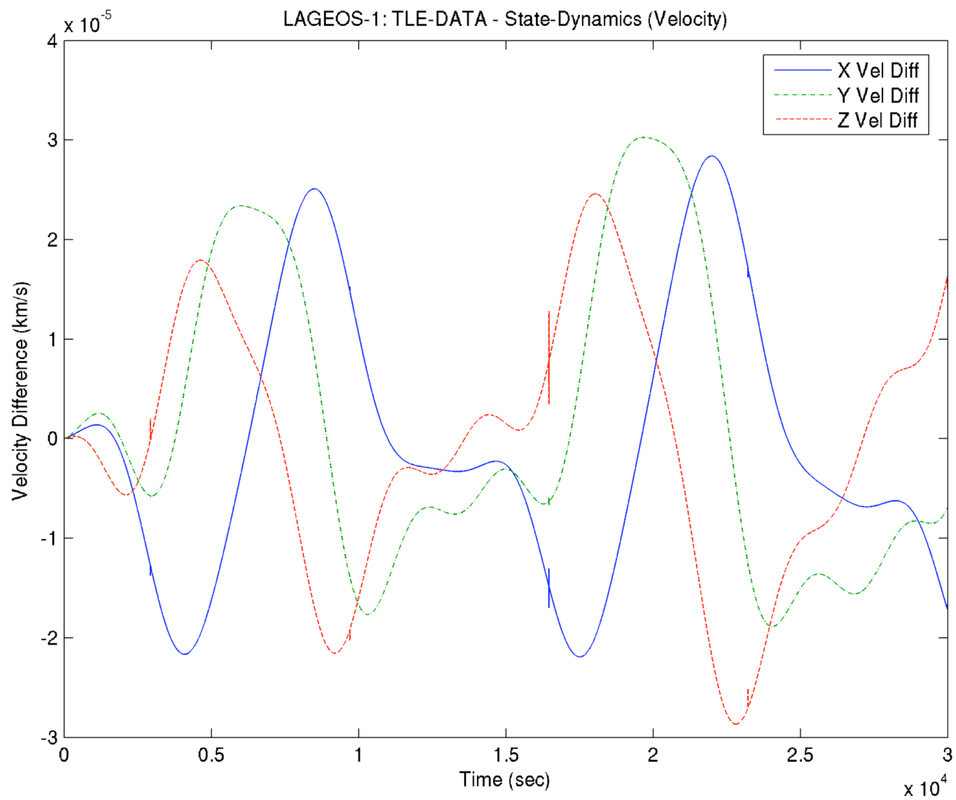

Figure 8-10. Analytical and numerical orbit propagation velocity differences.

With initial errors introduced to the initial conditions, the NKF is started with a solution that does not match the truth solution. This requires the NKF to detect and remove these state errors based upon the simulated range measurements. The performance of the NKF was determined by how well these errors could be detected, and by quantifying the true errors of the NKF after selected periods of operation.

During the state dynamics integration, the state transition matrix, $\mathbf{\Phi}$, was simultaneously computed. The vehicle state estimate and transition matrix were provided to the NKF to process a time-update of the covariance matrix. The initial standard deviations for the covariance matrix were chosen as $\sigma_{\delta \mathbf{r}_0}$ = 250 m and $\sigma_{\delta \mathbf{v}_0}$ = 0.25 m/s for each axis [136]. The one-sigma state process noise was chosen as $\omega_{\delta \mathbf{r}}$ = 0.05 m and $\omega_{\delta \mathbf{v}}$ = 0.05 mm/s, and assumed fixed for the entire simulation run [136]. A *standard* run for each orbit utilized these initial covariance and process noise values along with initial condition errors of 100 m position error and 0.01 m/s velocity error in each axis [136]. Large initial error simulation runs were also investigated. In these runs, larger initial state error of 100 times the standard run errors, at 10 km and 1 m/s, were used. Also, initial standard deviations for the covariance matrix were increased to $\sigma_{\delta \mathbf{r}_0}$ = 10 km and $\sigma_{\delta \mathbf{v}_0}$ = 0.01 km/s for each axis so that the NKF began with a larger error estimate of each state.

To create simulated pulsar-based range measurements, the NKF incorporates the higher order relativistic time transfer expression of Eq. (7.12). Note that currently the highest order Eq. (4.28) cannot be implemented within a navigation system due to the limited knowledge of source position, namely accurate source distance. Simulated error, with a variance equal to the pulsar range measurement accuracy, is added to these simulated measurements to create realistic values. The NKF's processing utilizes the measurement model from Eq. (8.72) to blend the measurement data with the spacecraft dynamics.

The measurement noise, $\mathbf{v}(t)$, associated with Eq. (8.72) was computed based upon the range accuracy of each pulsar based upon the results of the SNR-based calculations in Chapter 3 assuming a 1-m^2 detector. To emulate potential navigation system errors, an additional 2% was added to the range accuracy value for each pulsar. This would incorporate errors due to photon timing, X-ray background, and detector inefficiencies within the measurement. To simulate the random effects of this one-sigma range accuracy, a normalized random number with a standard deviation equal to one was multiplied by the total range accuracy value for each pulsar. Thus, the NKF received and processed a range measurement that included random statistical error, as opposed to a fixed value of error. The relativistic time transfer and range measurement were computed assuming spacecraft coordinate time, although the effects of proper time to coordinate time conversion of Eq. (8.81) will be incorporated in future analysis.

The three top RPSRs of Chapter 3 were chosen as the pulsars available to the NKF. These were primarily chosen due to the knowledge of all their parameters, as most other sources currently have only estimated values. It was assumed that only one pulsar could be detected during a single fixed 500 s observation window. The priority of observation was based upon the measurement accuracies of three RPSRs: B0531+2: 109 m, B1821-24: 325 m, and B1937+21: 344. If the visibility of a pulsar was obscured during an observation, the next pulsar in the priority list was utilized. If none were visible, the measurement cycle was skipped, and the successive cycle would begin. To avoid using only a single pulsar for a long duration within the simulation and increase observability of error in all three axes, after a set amount of time a different pulsar is used for up to six successive measurements. Total navigation solution error is reduced when using multiple pulsars along different line-of-sight vectors.

Table 8-2 provides a listing of the simulation specific information used for each orbit. The duration of the simulation runs is provided and was usually chosen as several multiples of the orbit period. Due to the processing time for the simulation and orbit length, although the total simulation duration may be longer, the number of orbit periods may not be large. However enough orbital periods were completed to represent the performance of the NKF of these spacecraft. The table also provides the times after two orbits and several orbits used to investigate the filter performance. The time to check whether to use additional pulsars is also listed for each vehicle, although *ARGOS* orbit does not require this since the visibility of any source in this orbit is only a fraction of its orbit period.

Table 8-2. Spacecraft Simulation Information.

Orbit	Simulation Duration (s)	Filter Settling Time #1 (s)	Filter Settling Time #2 (s)	Elapsed Time to Check Additional Pulsars (s)
ARGOS	185,000 (~30 orbits)	12,200 (~2 orbits)	124,000 (~20 orbits)	Not Needed
LAGEOS-1	204,000 (~15 orbits)	28,000 (~2 orbits)	163,000 (~12 orbits)	13,500
GPS Block IIA-16 PRN-01	216,000 (~5 orbits)	87,000 (~2 orbits)	173,000 (~4 orbits)	14,000
DirecTV 2 (DBS 2)	431,000 (~5 orbits)	173,000 (~2 orbits)	345,000 (~4 orbits)	25,000
LRO	218,000 (~30 orbits)	15,000 (~2 orbits)	146,000 (~20 orbits)	10,000

Since some orbits have the ability to observe a single pulsar during the entire orbit period, an investigation of the use of a single pulsar for navigation system operation was pursued. If the performance of a single-pulsar navigation system was acceptable, this may allow X-ray detectors to remain fixed on an inertially stabilized spacecraft, thus not requiring a gimbal system. For Earth-orbiting spacecraft that are nadir pointing, this may allow the X-ray detector to view the source only periodically during the orbit. Studies could be pursued to determine if the error growth in the solution is acceptable during the spans between observations. The Crab Pulsar is used as the single source for the GPS and DirecTV orbit simulations presented below.

Although all attempts have been made to make the most up to date, and accurate, estimate of pulsar-based range measurements, it is conceivable that it is difficult to achieve these theoretical values. Perhaps no detector system of current technology may achieve the necessary photon timing or energy resolution, or no pulsar can be shown to produce sufficiently periodic pulsations that can be successfully predicted over the long term. Therefore, a study of the NKF performance of reduced measurement accuracy was pursued. Values of 10 and 100 times the current estimate of measurement accuracy were simulated and performance of these simulation runs are reported.

8.5.2 Simulation Results

For each orbit analysis, the simulation was executed for five distinct runs in each spacecraft orbit. An individual run used a different seeding for the normalized random number generator than the other runs. The data from each run was stored and the average of each of the five runs was computed. This simulation method was used to create a statistical representation of the performance of the algorithms in each orbit. By using five runs, each generated using different random number sets, and then taking the average of these results, the reported values provides a description of the performance independent of any single run.

The primary reported values are the root mean square (RMS) of the error NKF's output, the mean of the NKF covariance estimate of each state, and the mean radial spherical error (MRSE) value of the NKF position error. The RMS value signifies the total error of the filter output with respect to the truth orbit. The covariance estimate provides a representation of the NKF's estimate of its performance and the mean is given since the covariance varies as a sinusoid over the orbit period due to the state dynamics. The MRSE value provides a single value representation of the NKF's performance. The performance values are reported over durations of the entire run, after two orbits, and after a specified number of orbits to demonstrate the performance with zero filter settling time and after a certain amount of filter settling.

Plots of the NKF's output are provided that show the performance of the algorithms over time. Covariance envelope plots are created by graphing the NKF standard deviation (square root of the covariance values) of each state, both the positive and negative values. Overlaid on these plots is the error in the NKF navigation solution output with respect to the truth solution. To show the benefit of the NKF solution, separate plots of the error in the NKF solution and the error in a free-running uncorrected orbit solution are also provided. The free-running uncorrected solution represents a navigation solution that would result if no correction whatsoever were implemented within a navigation system. Since initial error in the solution is introduced within the simulation, the free-running uncorrected solution will diverge significantly from the truth solution over the simulation duration.

Tables of performance values and plots of selected run results are provided. The performance values are reported in the radial, along-track, and cross-track (RAC) axes of the orbit, as the inertial XYZ values can vary significantly for different orbits. Descriptions of the results for each orbit are discussed in detail below.

8.5.2.1 *ARGOS* Orbit Performance Results

Figure 8-11 provides the standard deviation envelope and NKF error plot within the *ARGOS* orbit for the RAC position axes of an example simulation run. Over the duration of the simulation run, the NKF errors remain within the one-sigma standard deviation envelope. Figure 8-12 shows a similar plot for the RAC velocity axes, and the error can also be seen to stay within the standard deviation envelope.

Figure 8-15 shows the graph of the NKF position error magnitude along with the uncorrected orbit solution error magnitude. With both solutions starting with standard run errors in their initial conditions with respect to the truth orbit the plot shows that the NKF error remains bounded and is eventually reduced to a small value (< 100 m), yet the uncorrected solution error continues to grow unbounded, reaching 8 km after 30 orbits.

Table 8-3 lists the performance values for the four different simulation type runs for the *ARGOS* spacecraft orbit. For the standard run type the RMS errors of NKF position solution is less than 120 m per axis for the entire run, whereas after twenty full orbits of this vehicle the RMS error reduces to less than 80 m. The MRSE value after twenty orbits is 81 m. The velocity performance of the NKF for this orbit is on the order of 0.1 m/s. This demonstrates the significant performance achievement of the NKF using pulsar-based range measurements.

If initial error is increased to 100 times the standard simulation run values, for the entire run the RMS value is as high as 1011 m per axis due to high initial errors. However, after twenty orbits the large initial error has been corrected and the RMS error per axis is down to less than 150 m and the MRSE is near that standard run value at 91 m.

Although increasing the measurement error reduces the performance of the NKF position solution, after twenty orbits the MRSE grows to only about 350 m when 10 times the current estimate of measurement error is introduced. The MRSE is about 1100 m for 100 times the current measurement error.

8.5.2.2 LAGEOS-1 Orbit Performance Results

Table 8-4 provides performance values of the four simulation type runs for the LAGEOS-1 orbit. Although nearly twice the orbit radius of the *ARGOS* orbit, it is interesting to note that the NKF position and velocity performance is nearly the same for each orbit. The MRSE value for the standard run and 100 times initial error run are about 100 m after twelve orbits, very similar to *ARGOS* orbit. After twelve orbits, with 10 times the current measurement error, the MRSE value is about 380 m, whereas with as much as 100 times the measurement error, the MRSE value approaches 1 km.

8.5.2.3 GPS Block IIA-16 PRN-01 Orbit Performance Results

Figure 8-13 provides an example standard deviation envelope and NKF error plot within the GPS satellite orbit for the three RAC position axes, and the errors are shown to remain within the envelope. Within approximately one half of the orbit period a majority of the initial simulation error is detected and removed. Figure 8-14 provides a similar plot for the three RAC velocity axes.

A graph of the NKF position error magnitude along with the uncorrected orbit solution error magnitude is provided in Figure 8-16. The graphs in the plot show that the NKF error remains bounded and is eventually reduced to a small value (< 100 m), yet the uncorrected solution error continues to grow unbounded, reaching nearly 19 km within five orbits.

Table 8-5 presents the simulation performance results for the five types of runs that were investigated. The significant performance achievement of the NKF is again demonstrated with these results. After only two GPS orbits, using the pulsar-based range measurements with the NKF, the MRSE value is less than 80 m for both the standard run and 100 times initial error run, and less than 70 m after four orbits. Velocity errors on the order of 10 mm/s are also achieved after some filter settling time.

Providing some type of backup navigation system for GPS satellites is considered an enhancement to its overall system, especially during unforeseen events or catastrophic ground segment failures. Enhancing the ability of GPS satellites to improve their own auto-navigation solution would allow for continuous operation of the system. Although the GPS user range accuracy index (URA) would increase to 8 or 9 with this solution, it would continue to provide a vital navigation service to Earth-based systems until the ground segment can be brought back into full operation [156].

If the NKF can only be supplied range measurements that are 10 or 100 times more pessimistic than the standard simulation values, the RMS error and MRSE would increase for the GPS satellite, although these values are similar to both the *ARGOS* and LAGEOS orbits. With 10 times the measurement error the URA would increase to 10 based upon the 312 m MRSE value, and with 100 times the measurement error the URA would increase to 12 based upon the 1213 m MRSE.

If the X-ray detector affixed to the GPS satellite were able to only view the Crab Pulsar during the entire orbit, after two orbits the MRSE would reduce to about 110 m, with the URA set at 9. Using only a single pulsar may potentially allow reduced complexity within the navigation system if the detector can be mounted on the satellite such that the Crab Pulsar is always in the detector's field of view.

8.5.2.4 DirecTV 2 Orbit Performance Results

Table 8-6 presents the performance values for the DirecTV 2 orbit. The orbit was chosen as a representative geosynchronous orbit that is beneficial for commercial telecommunication spacecraft operators. Again, similar to the *ARGOS*, LAGEOS, and GPS orbits, the NKF position solution can attain RMS errors below 100 m per axis and

MRSE value of less than 110 m after only two orbits for the DirecTV orbit. The NKF velocity solution achieves RMS velocity errors on the order of 10 mm/s. Use of this type of pulsar-based navigation system may help to reduce ground operations cost by allowing the spacecraft to autonomously detect position errors from its nominal orbit, and correct for these small deviations using its onboard control system. The output of the NKF navigation solution could be sent to the vehicle's control system to fire thrusters, such as electrostatic ion or Hall effect thrusters, to maintain its orbit.

As the measurement error is increased, the performance of the NKF in this geosynchronous orbit falls off similarly as the lower Earth orbits. With 10 times the measurement accuracy, after four orbits the MRSE is 338 m and the velocity RMS error is about 30 mm/s. If 100 times measurement error is present in the system, then the position error increases to a MRSE of 1268 m.

As studied in the GPS orbit, if only one pulsar were available for this system during the entire orbit of the DirecTV orbit, the performance of the NKF is still quite remarkable. After only two orbits the MRSE is below 130 m, whereas after four orbits the MRSE is below 125 m. For geosynchronous vehicles that have a portion of the vehicle inertially stabilized, a single pulsar-based navigation system would provide accurate position and velocity solutions.

It is interesting to note that the velocity performance is very good in this GEO orbit, as well as the MEO orbit of GPS, with errors on the order of 10 mm/s even after initial errors as large as 1 m/s. Maintaining an accurate velocity estimate is as important as the position estimate within the NKF. Thus, with these pulsar-based measurements it is significant to see that the NKF is able to blend these range measurements to correct both position and velocity.

8.5.2.5 LRO Orbit Performance Results

The LRO simulations were implemented in a slightly different manner than the previous four orbit types. The orbit dynamics and the NKF for this vehicle were implemented as a selenocentric system. Therefore, it uses the Moon as the primary gravitational effect and Earth as a third-body effect for the orbit propagator and the state transition matrix. The Moon's potential was simulated using its known J_2-J_5 terms [132]. However, orbits about the Moon are a challenge to simulate due to the lumped mass of this object. Future investigations should consider a higher order terms due to the Moon's complex gravitational potential. The pulsar-based measurements were implemented using the same SSB time transfer schemes as the other four orbits, however, the NKF filter interpreted range measurements to be with respect to the Moon's center, and not Earth's center as in the other cases.

Table 8-7 provides the performance of the NKF within the LRO orbit. This orbit about the Moon begins to demonstrate the NKF performance capabilities in deep space. For both the standard run and the run with 100 times initial condition error, the position performance is only slightly larger than the *ARGOS*, LAGEOS-1, GPS, and DirecTV 2 geocentric orbits, with 165 m MRSE for the standard LRO run after sufficient filter settling versus about 100 m for the other runs. The velocity performance for these LRO runs is much more similar to the *ARGOS* LEO case than the other higher Earth orbit cases.

To produce the LRO simulation runs for the 10 times and 100 times of the measurement accuracy, two new considerations were applied. The measurement residual threshold limit was reduced and runs that converged replaced runs where the filter diverged. By reducing the threshold limit from 5 to 2, the LRO NKF essentially ignores measurements that could cause large effects on the state errors. However, this also reduces the total number of measurements processed within each run, as measurements with residuals higher than this limit were ignored. This filter design trade-off must determine the proper threshold limit versus number of measurements to achieve best overall performance. By choosing limit value of 2, many of the measurements that would have produced overly large or poor state adjustments were not processed through this filter, which assisted the NKF's improved performance.

It is important to consider that stability of the NKF is reduced as the measurement accuracy is reduced [65]. Divergence of the state errors can happen if the NKF reduces the estimate of the state covariances to low values while the actual errors are still large. In this scenario, the NKF's solution can diverge causing the state errors to grow unbounded while the NKF covariance estimate remains reasonably small. During simulated LRO runs, this scenario was most evident in the 100 times measurement accuracy runs. To produce the reported performance values, two simulation runs out of the original five were replaced by two runs that produced stable, converging results. These simulation runs used different random number generator seeds in order to produce the new results. Although the current implementation of the LRO NKF could diverge if these original set of measurements were processed, for this analysis it was more important to produce tangible performance results than test the stability of an individual run. In future filter implementations, the stability of the NKF could be improved by using various techniques, such as a fading or finite memory filter, adding process noise, or reviewing and improving the state dynamics and measurement models to ensure best and most realistic performance [65]. In cases where the measurements are not as accurate as the expected dynamics (as in the case of the 100 times of measurement accuracy), the NKF stability must be verified. Another consideration is that part of the divergence was brought about due to the unique combination of the LRO orbit dynamics and the specific geometrical distribution of the three chosen pulsars. Adding additional pulsars along different line-of-sight directions would improve the geometry of the signals (GDOP), which would also improve performance. The reported values of Table 8-7 are those for all the runs that remained stable throughout the simulation duration.

When measurement error is increased by 10 times the standard values, the performance of the NKF for the LRO orbit is on the order of the other runs, with 437 m MRSE for LRO position versus 350 m for the other orbits. The errors for 100 times the measurement accuracy is roughly three times the value of the other orbit runs. This is largely due to the significant along-track error in the LRO orbit runs, which appears to be created by the larger radial velocity error. Future investigations could consider methods to reduce this velocity error, potentially considering producing measurements at a much different rate than the 500 s current rate. This would alter each measurement's individual accuracy, with the intent of improving overall performance.

It is likely that additional filter parameter tuning may be required for the LRO orbit analysis. Increasing the NKF's process noise to compensate for any potential dynamics modeling errors would help improve the performance somewhat. However, increasing this noise also limits the NKF's ability to process good measurements since the covariance values are kept high with higher process noise.

Although lacking the high-order time transfer expressions from this dissertation research, an early analysis compared radar range measurement to first-order pulsar-based range measurements for an interplanetary trajectory to Pluto. This early analysis showed that a pulsar-based system performed well for distant missions [186]. With this LRO mission analysis, most of the results demonstrate the potential benefits of this pulsar-based navigation system for missions above the GPS constellation orbit and for continuous operation perhaps behind the Moon, where radar contact from Earth would be unavailable. Deep space and interplanetary missions would be significant beneficiaries of this navigation system's performance.

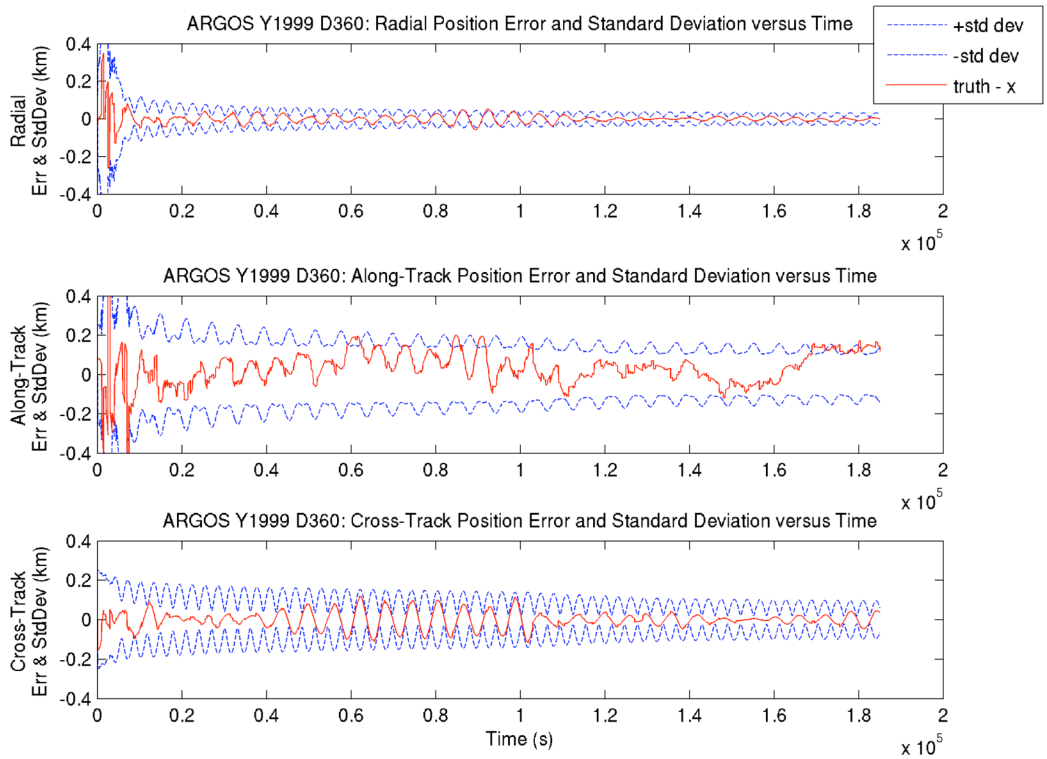

Figure 8-11. Position standard deviation and error for *ARGOS* orbit.

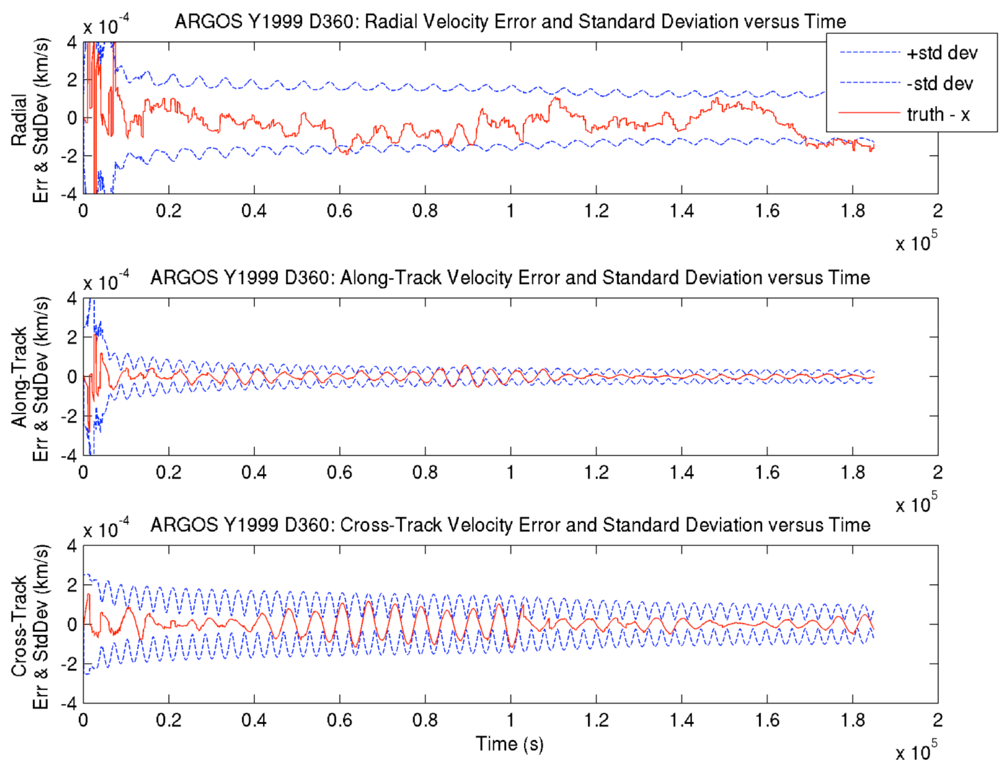

Figure 8-12. Velocity standard deviation and error for *ARGOS* orbit.

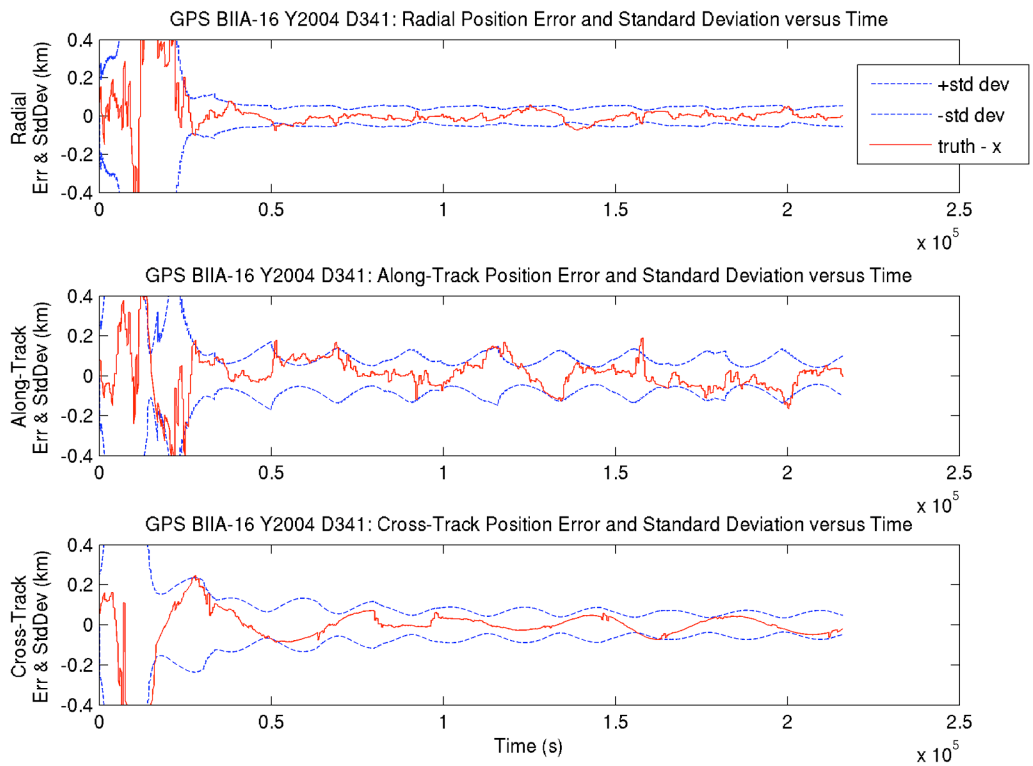

Figure 8-13. Position standard deviation and error for GPS orbit.

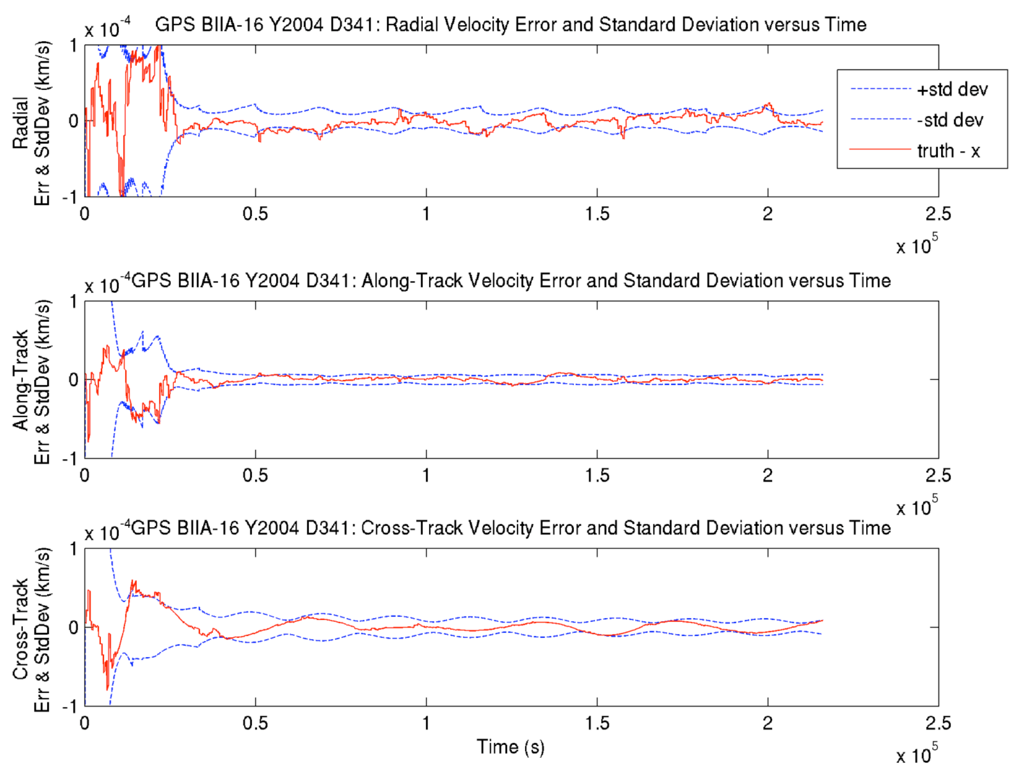

Figure 8-14. Velocity standard deviation and error for GPS orbit.

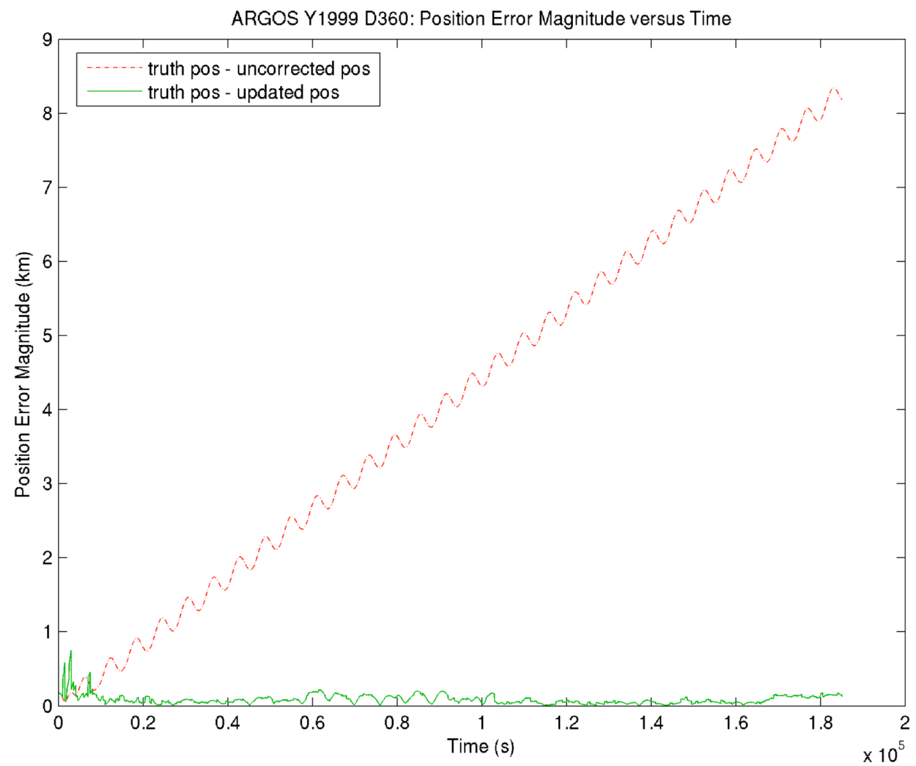

Figure 8-15. Uncorrected and NKF position error magnitude for *ARGOS* orbit.

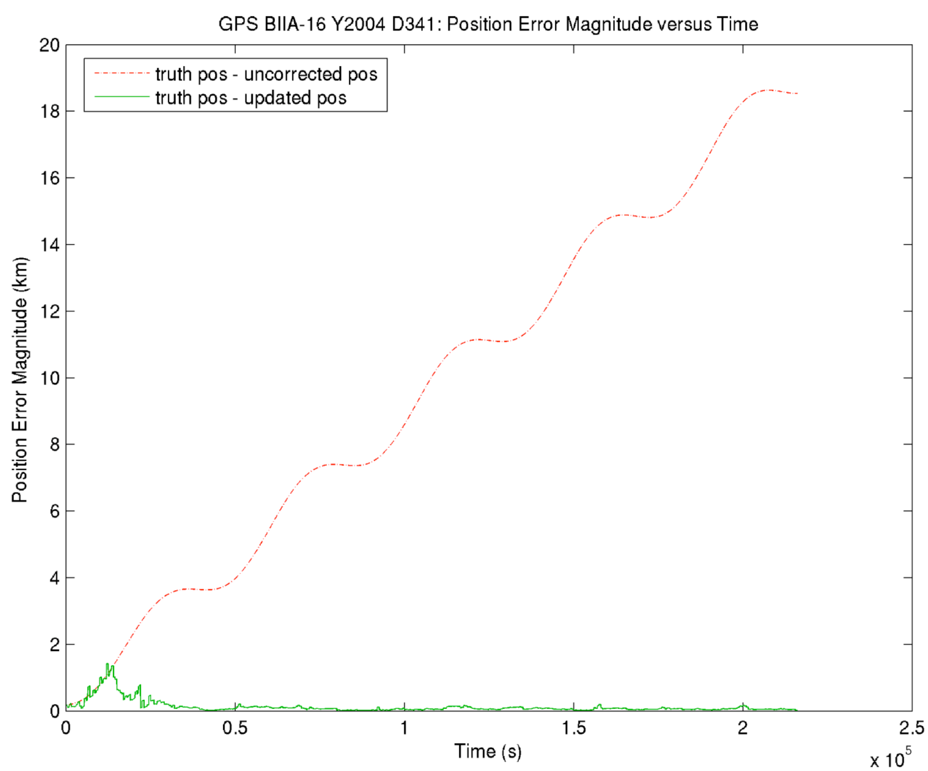

Figure 8-16. Uncorrected and NKF position error for GPS orbit.

Table 8-3. *ARGOS* Simulation Performance Values.

Simulation Type	**Parameter**		**Entire Simulation Run**		**After Two Orbits Filter Settling**		**After Twenty Orbits Filter Settling**	
			NKF Error RMS	NKF Cov. Mean	NKF Error RMS	NKF Cov. Mean	NKF Error RMS	NKF Cov. Mean
Standard Run	Position: (m)	R A C	38 119 54	46 171 96	25 105 53	34 155 91	17 79 27	25 126 69
	Velocity: (m/s)	R A C	0.11 0.034 0.056	0.17 0.044 0.099	0.097 0.026 0.055	0.15 0.034 0.093	0.074 0.017 0.028	0.12 0.025 0.071
	MRSE (m)		130		112		81	
100 Times Initial Error	Position: (m)	R A C	835 854 1011	268 466 324	29 320 240	37 267 178	17 91 38	26 145 85
	Velocity: (m/s)	R A C	1.2 0.52 0.71	0.59 0.19 0.31	0.32 0.030 0.25	0.27 0.038 0.18	0.087 0.018 0.039	0.14 0.026 0.087
	MRSE (m)		1550		354		91	
10 Times Measurement Error	Position: (m)	R A C	106 481 115	165 622 205	99 423 115	148 579 202	87 352 127	127 500 187
	Velocity: (m/s)	R A C	0.46 0.11 0.12	0.58 0.16 0.21	0.39 0.10 0.12	0.53 0.15 0.21	0.32 0.090 0.13	0.46 0.13 0.19
	MRSE (m)		504		444		351	
100 Times Measurement Error	Position: (m)	R A C	127 2853 103	299 3535 246	90 2738 103	273 3439 246	63 2165 101	259 2524 247
	Velocity: (m/s)	R A C	2.9 0.099 0.11	3.6 0.29 0.25	2.8 0.077 0.11	3.5 0.28 0.25	2.2 0.063 0.10	2.6 0.27 0.25
	MRSE (m)		2549		2392		1098	

Table 8-4. LAGEOS-1 Simulation Performance Values.

Simulation Type	Parameter		Entire Simulation Run		After Two Orbits Filter Settling		After Twelve Orbits Filter Settling	
			NKF Error RMS	NKF Cov. Mean	NKF Error RMS	NKF Cov. Mean	NKF Error RMS	NKF Cov. Mean
Standard Run	Position: (m)	R	55	46	18	23	17	20
		A	100	91	53	69	57	63
		C	120	129	110	100	81	74
	Velocity: (m/s)	R	0.047	0.045	0.021	0.027	0.023	0.026
		A	0.019	0.017	0.082	0.010	0.0076	0.0085
		C	0.057	0.060	0.052	0.047	0.037	0.034
	MRSE (m)		169		127		101	
100 Times Initial Error	Position: (m)	R	759	261	19	24	17	20
		A	512	228	54	69	58	64
		C	1426	651	121	106	83	75
	Velocity: (m/s)	R	0.36	0.21	0.021	0.028	0.023	0.026
		A	0.25	0.10	0.0087	0.010	0.0078	0.0086
		C	0.45	0.27	0.058	0.049	0.039	0.035
	MRSE (m)		1691		136		102	
10 Times Measurement Error	Position: (m)	R	149	159	96	112	91	96
		A	424	462	289	382	268	346
		C	187	373	198	369	246	348
	Velocity: (m/s)	R	0.17	0.19	0.11	0.15	0.10	0.14
		A	0.062	0.068	0.045	0.052	0.042	0.044
		C	0.087	0.17	0.092	0.17	0.11	0.16
	MRSE (m)		497		375		378	
100 Times Measurement Error	Position: (m)	R	286	442	223	377	222	344
		A	2201	2635	1745	2403	1339	1877
		C	72	407	73	407	78	406
	Velocity: (m/s)	R	1.0	1.2	0.80	1.1	0.60	0.82
		A	0.11	0.19	0.10	0.17	0.10	0.16
		C	0.033	0.19	0.034	0.19	0.036	0.19
	MRSE (m)		2185		1631		834	

Table 8-5. GPS Block IIA-16 PRN-01 Simulation Performance Values.

Simulation Type	Parameter		Entire Simulation Run		After Two Orbits Filter Settling		After Four Orbits Filter Settling	
			NKF Error RMS	NKF Cov. Mean	NKF Error RMS	NKF Cov. Mean	NKF Error RMS	NKF Cov. Mean
Standard Run	Position: (m)	R	138	103	24	47	23	47
		A	138	149	59	83	55	82
		C	140	135	40	62	31	56
	Velocity: (m/s)	R	0.024	0.023	0.0074	0.012	0.0072	0.012
		A	0.012	0.016	0.0031	0.0055	0.0028	0.0055
		C	0.013	0.020	0.0058	0.0091	0.0045	0.0081
	MRSE (m)		241		77		67	
100 Times Initial Error	Position: (m)	R	1155	419	24	47	23	47
		A	2032	916	59	83	55	82
		C	2545	1025	43	64	33	56
	Velocity: (m/s)	R	0.25	0.16	0.0074	0.012	0.0073	0.012
		A	0.35	0.23	0.0031	0.0055	0.0028	0.0055
		C	0.46	0.27	0.0062	0.0093	0.0048	0.0082
	MRSE (m)		3438		78		68	
10 Times Measurement Error	Position: (m)	R	411	314	82	129	72	124
		A	530	574	267	398	231	376
		C	349	477	264	361	228	328
	Velocity: (m/s)	R	0.093	0.088	0.033	0.050	0.031	0.048
		A	0.041	0.039	0.012	0.018	0.010	0.017
		C	0.050	0.069	0.038	0.053	0.033	0.048
	MRSE (m)		768		388		312	
100 Times Measurement Error	Position: (m)	R	906	866	511	428	507	390
		A	2601	2807	1598	2090	1178	1880
		C	326	1071	373	1055	433	1035
	Velocity: (m/s)	R	0.36	0.41	0.20	0.29	0.14	0.26
		A	0.11	0.11	0.074	0.061	0.073	0.056
		C	0.047	0.16	0.055	0.15	0.064	0.15
	MRSE (m)		2580		1552		1213	
Using Only One Pulsar	Position: (m)	R	148	104	24	45	23	45
		A	144	185	62	124	63	124
		C	181	292	89	233	85	232
	Velocity: (m/s)	R	0.025	0.029	0.0083	0.018	0.0084	0.018
		A	0.013	0.016	0.0029	0.0053	0.0029	0.0052
		C	0.023	0.043	0.013	0.034	0.012	0.034
	MRSE (m)		274		107		103	

Table 8-6. DirecTV 2 Simulation Performance Values.

Simulation Type	Parameter		Entire Simulation Run		After Two Orbits Filter Settling		After Four Orbits Filter Settling	
			NKF Error RMS	NKF Cov. Mean	NKF Error RMS	NKF Cov. Mean	NKF Error RMS	NKF Cov. Mean
Standard Run	Position: (m)	R	166	140	48	78	51	78
		A	235	187	78	99	87	99
		C	192	149	53	75	50	71
	Velocity: (m/s)	R	0.015	0.016	0.0057	0.0086	0.0060	0.0085
		A	0.011	0.012	0.0028	0.0043	0.0030	0.0043
		C	0.012	0.013	0.0040	0.0055	0.0037	0.0051
	MRSE (m)		343		104		108	
100 Times Initial Error	Position: (m)	R	1154	441	48	78	51	78
		A	2934	1187	78	99	87	99
		C	2377	1011	56	76	51	71
	Velocity: (m/s)	R	0.21	0.11	0.0057	0.0086	0.0061	0.0085
		A	0.34	0.19	0.0028	0.0043	0.0030	0.0043
		C	0.27	0.18	0.0043	0.0056	0.0038	0.0052
	MRSE (m)		3946		107		110	
10 Times Measurement Error	Position: (m)	R	428	404	90	178	88	176
		A	512	633	332	431	335	423
		C	403	475	208	307	161	287
	Velocity: (m/s)	R	0.047	0.051	0.022	0.029	0.022	0.028
		A	0.020	0.026	0.0056	0.011	0.0055	0.011
		C	0.028	0.035	0.015	0.022	0.012	0.021
	MRSE (m)		778		377		338	
100 Times Measurement Error	Position: (m)	R	1165	1045	216	422	183	409
		A	2642	2675	1754	1949	1820	1867
		C	1311	1586	1232	1395	896	1281
	Velocity: (m/s)	R	0.20	0.21	0.13	0.13	0.13	0.13
		A	0.062	0.063	0.014	0.029	0.012	0.028
		C	0.094	0.12	0.090	0.10	0.066	0.093
	MRSE (m)		3005		1827		1268	
Using Only One Pulsar	Position: (m)	R	162	140	46	79	41	79
		A	240	252	98	175	93	176
		C	201	286	90	233	90	235
	Velocity: (m/s)	R	0.015	0.020	0.0070	0.014	0.0066	0.014
		A	0.011	0.012	0.0027	0.0044	0.0024	0.0044
		C	0.013	0.023	0.0066	0.017	0.0066	0.017
	MRSE (m)		343		127		123	

Table 8-7. LRO Simulation Performance Values.

Simulation Type	Parameter		Entire Simulation Run		After Two Orbits Filter Settling		After Twenty Orbits Filter Settling	
			NKF Error RMS	NKF Cov. Mean	NKF Error RMS	NKF Cov. Mean	NKF Error RMS	NKF Cov. Mean
Standard Run	Position: (m)	R	63	92	51	75	39	62
		A	207	270	190	243	177	216
		C	37	28	31	24	20	19
	Velocity: (m/s)	R	0.16	0.21	0.14	0.18	0.14	0.16
		A	0.049	0.075	0.044	0.064	0.034	0.053
		C	0.032	0.025	0.027	0.021	0.017	0.016
	MRSE (m)		217		196		165	
100 Times Initial Error	Position: (m)	R	1488	469	106	112	51	76
		A	1647	673	310	304	196	236
		C	634	74	34	30	18	21
	Velocity: (m/s)	R	2.0	0.66	0.21	0.20	0.14	0.17
		A	0.66	0.31	0.091	0.096	0.045	0.065
		C	0.25	0.081	0.030	0.026	0.015	0.018
	MRSE (m)		2300		323		186	
10 Times Measurement Error[a]	Position: (m)	R	134	266	116	243	112	221
		A	935	1438	838	1339	664	1087
		C	151	163	150	157	134	128
	Velocity: (m/s)	R	0.79	1.2	0.71	1.1	0.54	0.89
		A	0.10	0.22	0.097	0.21	0.094	0.19
		C	0.13	0.14	0.13	0.14	0.12	0.11
	MRSE (m)		877		774		437	
100 Times Measurement Error[a]	Position: (m)	R	287	464	287	434	357	379
		A	7632	8264	7868	8326	9766	5875
		C	98	266	98	266	96	265
	Velocity: (m/s)	R	6.6	7.1	6.8	7.2	8.5	5.1
		A	0.18	0.31	0.18	0.30	0.22	0.27
		C	0.085	0.23	0.084	0.23	0.082	0.23
	MRSE (m)		6252		6346		3414	

[a] Measurement residual threshold reduced from 5 to 2.

Chapter 9 Conclusions

"The future influences the present just as much as the past."

– Friedrich Nietzsche

9.1 Results

This dissertation has presented a new spacecraft navigation methodology based upon the use of variable celestial X-ray sources. These sources are shown to be useful for time, attitude, position, and velocity determination. While numerous variable celestial source types can be used to aid spacecraft navigation, this work has emphasized a subset of periodic, stable, and unique sources known as neutron stars, or pulsars. Pulsars emit radiation throughout a broad range of the electromagnetic spectrum from the radio to the gamma-ray bands with periods ranging from a few milliseconds to thousands of seconds. This dissertation examines the class of pulsars that emit in the X-ray band, since these can be detected by X-ray sensors on the order of 1-m^2 that are of practical dimensions for many vehicle designs.

There are significant advantages of these variable celestial sources that are apparent from the discussions within the text. Since these sources are visible for sufficient observation durations due to their vast distances from the solar system, navigation solutions can be computed anywhere in solar system. This spacecraft navigation concept is not limited by the line-of-sight of Earth observation stations or fixed navigation beacons, thus, it can function in many locations where existing methods cannot operate, such as on the far-side of planets and moons. There are numerous sources available, and several of these sources can produce high accuracy measurements. It is projected that with continued sky observations, new sources will be discovered that will provide additional capability.

As with any system, however, limitations remain with this navigation system that must be addressed through either continued research or other augmentation. The accuracy of the line-of-sight data for each source may limit their use over large distances from the inertial origin. The intensity of the signal from many of the sources is low, which requires long observation times. Intrinsic characteristics of sources make their signal processing a challenge. The transient effects of several sources make their availability infrequent. Rare flares and bursts from various sources may potentially produce false identifications. The timing glitches that have been detected in several sources require frequent monitoring of sources and intermittent updates to source almanac data. Most of these issues suggest that the characteristic parameters of sources needs to be further investigated within the astrophysical and astronomical communities in order to determine the best possible known values.

The main focus of this dissertation research has concentrated upon the aspects of position, velocity, and time determination processes, and primarily has investigated LEO, MEO, GEO, and lunar orbits. These were selected because of the wealth of previous research and demonstrations on attitude determination using celestial sources, and the selection of candidate orbits that would allow verification of the produced results. It is anticipated that the navigation performance of interplanetary trajectories would have similar performance since the analysis methods and algorithms are applicable throughout the solar system.

The entire methodology for using variable celestial X-ray sources is developed within the dissertation including information about source location and parameters, source time of arrival modeling and accuracy, and time transfer measurements within an inertial frame that incorporates important general relativistic corrections. With the fundamental pulsar pulse physics as a foundation, various navigation approaches are presented including absolute and relative position, and corrections to estimated navigation solutions.

In terms of absolute position determination, new pulse phase cycle ambiguity algorithms have been presented to solve the lost-in-space problem when a spacecraft has no *a priori* knowledge of its location within the three-dimensions of the solar system. Using a database of X-ray pulsars, with their known angular positions and detailed models of their pulse time of arrival properties, results indicate that by using phase crossings from multiple pulsars, these methods can determine an initial three-dimensional position solution to within several tens of kilometers. Since no prior information about the spacecraft's position is known, these absolute position determination algorithms can be implemented based upon intelligent choices of the suspected orbit, such as geocentric, selenocentric, or heliocentric orbits. After the initial processing mode, this position solution can be refined through an iterative resolution process, or be provided as an initial state to other position update techniques presented in this dissertation. This absolute position determination method is significant since it suggests that pulsars provide a scheme for spacecraft to autonomously determine an estimate of its three-dimensional location.

Results from the delta-correction method when coupled to the recursive extended navigation Kalman filter appear to be even more profound in terms of three-dimensional position and velocity determination. Assuming 500 s observation lengths of individual pulsars, detailed numerical simulations of several candidate LEO, MEO, GEO, and lunar orbits suggest this approach is able to determine a spacecraft's position to within 100 m MRSE and its velocity to within 10 mm/s RMS. Furthermore, comparisons against actual X-ray detector data from the USA experiment indicate that existing technology and pulsar data knowledge can already produce range estimates within one or two orders of magnitude of the simulated results. Assuming improved detector capabilities and photon timing technologies, it is projected that newly developed navigation systems will be able to achieve this simulated navigation performance for many spacecraft missions.

However, even with the challenges imposed by the various stated issues, the potential benefits of the proposed system could be significant and warrant further investigation and research. If only a fraction of the analytical accuracy determined by this research could be achieved, many future spacecraft missions would still be enhanced by the added capability provided by this system. With the currently proposed crewed missions to the Moon and Mars within the next several decades [5], the autonomous navigation capabilities afforded by this new system improves mission survivability and success. Fortunately, this method would not require the enormous infrastructure and cost of producing and implementing navigation beacon satellite constellations centered about these planets or the entire solar system. Also, as space travel to these planetary bodies becomes more frequent, the ability for a spacecraft and its crew to determine their own full navigation solution helps reduce mission cost and improves exploration capabilities.

Hence, this research has illustrated that variable celestial sources that emit in the X-ray band may serve as possible inertially referenced navigation beacons for spacecraft time, attitude, position, and velocity determination throughout the solar system. While the techniques presented have primarily focused upon position and velocity, the additional capability of using these sources for accurate attitude determination, as well as potentially correcting spacecraft clock drift, demonstrate that a full navigation solution is attainable by this system. Although the performance results are significant, it is important to point out that this is only a preliminary investigation into the overall feasibility to variable celestial sources for spacecraft navigation. Additional analyses in terms of detailed mission and system studies must yet be pursued to develop this concept into an operational system.

9.1.1 Navigation System Comparison

A variable celestial source navigation system can be used to complement current day systems that are able to use the GPS, GLONASS (and other human-made global navigation systems) and/or DSN. This system could serve as a back up in the event of failures or catastrophes of human-made systems. Many recent algorithmic techniques implemented for GPS/GLONASS could conceivably be implemented within a navigation system using sources with pulsed radiation, thus research on both systems benefits one another. For spacecraft within Earth orbit above the GPS constellation, such as a highly elliptical orbit, this secondary system could supplement obscured or unavailable GPS data. The benefits of the DSN system providing accurate range and range-rate information from Earth observation stations may also be realized with systems using these sources. Combining measurements from these celestial sources with DSN range observations would reduce errors along the transverse orbit axes.

Although the initial intent of a variable celestial X-ray source-based navigation system would be to complement existing human-made navigation systems and be used in regions where human-made systems are inaccessible, comparisons of the capability between these two types of systems are inevitable. Table 9-1 provides a list of various aspects of both types systems, based upon current known information. Each type of system has advantages and limitations based upon the availability of their signal and the accuracy of the overall solution.

It is projected here that eventually new spacecraft navigation systems will be developed that blend information from each of the GPS/GLONASS, DSN, and X-ray source navigation systems in order to compute the best overall navigation solution. An onboard Kalman filter that propagates an orbit solution and incorporates measurements from each system could produce navigation solutions with greater performance than any of the single systems alone.

Table 9-1. Navigation System Comparison [88, 156, 177].

Characteristic	GPS & GLONASS	DSN	Variable Celestial X-ray Sources
Number of Sources (Design)	24 Satellites	3 Ground Locations	>500
Visible Sources (at spacecraft)	~12 Satellites (LEO)	1 to 2 In View (due to Earth's rotation)	1 – Several (Detector FOV)
Signal Wavelength	GPS L1: 0.1903 m L2: 0.2442 m GLONASS L1: 0.185 – 0.187 m L2: 0.144 – 0.146 m	Older System: 0.0357 m Newer System: 0.1303 m	X-ray Band $10^{-11} – 10^{-8}$ m
Cycle/Pulse Period	GPS L1: 6.35E-10 s L2: 8.15E-10 s GLONASS L1: 6.24E-10 s L2: 8.03E-10 s	Older System: 4.35E-10 s Newer System: 1.19E-10 s	~0.001 – 10^6 s
Solution Accuracy Time Range Position	 ~ 15 ns (1-σ) 0 – 6144 m (URA 0-14) < 100 m (SEP, SPS)	 < 100 µs 2 m per AU 1 – 100 km	 < 1 µs ~ 100 m ~ 100 m (MRSE)
Usable Signal	LEO - MEO	LEO – Heliopause	Interstellar
Issues	Atmospheric Effects Multipath High Power Signal Almanac Required Human-Controlled	Atmospheric Effects Line Of Sight Only Signal Fades with Distance Scheduling & Coordination Human-Controlled	Above Atmosphere Line Of Sight Only Low Intensity Signal Almanac Required Universe-Controlled

9.2 Summary of Contributions

As the various chapters within this dissertation demonstrate, the investigated methods to determine navigation solutions from variable celestial sources have fulfilled the goals set forth in Chapter 1. Although there are still more studies required to investigate its full potential, this research has added to the knowledge of the development of this concept.

Specifically, there are several notable contributions of this work, which include:

- Variable Celestial X-ray Source Catalogue (Chapter 2)

  A comprehensive source catalogue has been assembled from a wide variety of articles and databases, and represents a complete database of X-ray sources with characteristics conducive to spacecraft navigation. Numerous sources are listed in this catalogue and their parameter data can be used to develop the navigation concepts.

- Pulse Time of Arrival Modeling and Range Accuracy (Chapter 3)

  New techniques were developed using the SNR equations to analyze the pulse TOA and its accuracy. These techniques, as well as the new source quality figure of merit, provides methods to evaluate the catalogued sources for different aspects of navigation.

- Solar System Time Transfer Equations (Chapter 4)

  Existing methods of pulsar pulse timing were investigated and a new time transfer equation for use within the entire solar system was derived. This equation demonstrates the theoretical potential of computing photon arrival times at the sub-nanosecond level, and simplified forms of the equation with reduced accuracy are provided.

- Absolute and Relative Position Determination (Chapter 6)

  New algorithms were developed to determine the absolute position of a spacecraft. No current single type of onboard system has the ability to independently compute the absolute position of a deep space vehicle. The methods use phase measurements from multiple pulsars to determine the unknown number of whole phase cycles between a vehicle and a chosen inertial reference location. Once resolved, the phase measurement can be converted to range differences in order to calculate the absolute position of a spacecraft. These new schemes also demonstrate the ability to calculate highly accurate relative position information. With multiple detectors aboard a vehicle, attitude of the vehicle could also be determined using these measured phase differences, although methods using images of these sources similar to optical sources may provide a more direct path to creating new attitude sensors. With additional processing, vehicle velocity can be detected based on phase measurements from multiple sources.

- Delta-Correction Position Estimation (Chapter 7)

  Methods to correct a previously existing estimate of position or orbit solution using measurements from these celestial sources are developed. These schemes provide immediate implementation approaches that can utilize current day technology. The empirical validation of this technique has been demonstrated using actual recorded spacecraft data.

- Navigation Kalman Filter and Performance Analysis (Chapter 8)

  From the delta-correction techniques proposed in Chapter 7 and using the new time transfer equations of Chapter 4, a recursive extended Kalman filter was designed to blend the spacecraft dynamics and the pulsar-based range measurements. Simulations were produced to demonstrate the significant potential of this system. By varying both the error in the initial vehicle state and the pulsar-based range measurement, investigations were pursued to determine which issues contribute to the navigation performance values. The filter design primarily incorporates position and velocity states of the vehicle, but can also include spacecraft clock time states to determine all three parameters.

9.3 Future Research Recommendations

Although this dissertation presents numerous analyses and results on the various aspects of spacecraft navigation, no single unit of research can address all the issues for the scope of a navigation system such as the one described here. Therefore, to assist future research, below are several recommended areas of research to be pursued to further enhance the analysis of utilizing these sources for navigation.

9.3.1 Higher Fidelity Simulation

The orbit dynamics simulation was developed to sufficiently portray all the significant perturbation effects foreseen to impact the chosen mission analyses. Although all attempts were made to ensure the dynamics were as accurate as possible, below are several effects that should be implemented for further analysis.

The current simulation implements a fixed time step for the numerical integration of all orbits. Although the current processing time is reasonable for analysis, investigations of orbits high above Earth or highly elliptical orbits would benefit from integration schemes that can use a variable step integrator in order to reduce processing time. Several such variable step integration schemes are provided in the literature.

High-order gravitational potential models should be provided as an option for the simulated vehicle dynamics. The current use of zonal terms to describe Earth's gravitational potential ignores the sectorial and tesseral term effects. Although these are only higher order effects, the true motion of a space vehicle is affected by even these slight perturbations and over time the simulation would grow in error compared to recorded truth data. Various high order Earth gravitational models exist, such as the NASA Joint Gravitational Model (JGM-2, degree and order 70) and the NASA and

National Imagery and Mapping Agency (NIMA) Earth Gravitational Model (EGM96, degree and order 360). Additionally, higher order gravitational models of other planetary bodies, such as the Moon and Mars, are available or are in development. These models could be incorporated into the simulation for improved overall accuracy.

For near-Earth applications, more accurate atmospheric models would enhance the analysis of vehicles that are significantly affected by drag. More complex models such as the Jacchia-Roberts model or the Russian GOST model could replace the Harris-Priester model used by this simulation. As they become improved, atmospheric models of planets should also be implemented within this simulation for navigation analysis in orbits about those bodies. To remain valid, these more sophisticated atmosphere models require more accurate spacecraft parameters, such as coefficients of drag and mass.

9.3.2 Photon-Level Simulation

The simulation currently produces source pulse TOA measurements based upon specified observations. Future versions of the simulation should pursue the analysis more deeply and implement the measurements of the single photon level arriving at the spacecraft. Although the measurement to the Kalman filter may remain as a single TOA measurement, processing at the finer photon-level may eventually produce deeper integration schemes within the navigation system, potentially leading to improved navigation performance.

9.3.3 Source Observation Scheduling

Due to the importance of coordinating highly accurate pulsar TOA measurements with the availability of the source's signal, new methods of scheduling the observations of sources should be pursued. A predictor program, based on the navigation system's own solution, could be developed to provide the system a means to schedule each source's observation based upon their predicted availability. Additionally, schemes to switch between fixed observations times and indefinite observations for improved accuracy should be investigated. During the development of a vehicle's mission, simulations using these prediction programs could assist in the analysis of when specific sources would be available and how to optimize their observations for best overall navigation solutions.

9.3.4 Doppler Velocity Measurement

Much of the dissertation research has focused on time and position determination from the pulsed radiation of these celestial sources. As a spacecraft advances towards or recedes away from a particular source during its natural orbital revolution about a planetary body, Doppler effects will become apparent in the received signal from the source. This effect is currently removed from the photon arrival times during their transfer to the inertial origin. Alternatively, spacecraft velocity could be measured directly from the observed Doppler effect. Future planned investigations should determine the accuracy of the velocity measurement.

9.3.5 Kalman Filter Models

The existing orbital dynamics models and the Kalman filter state transition matrix provide sufficient fidelity for the analysis pursued within this dissertation. Future implementations of these dynamics will be enhanced to include higher fidelity, with the intent on matching the true dynamics of the space vehicles as closely as possible. As the gravitational potential models are increased from those currently used, in order for the Kalman filter to track this dynamics correctly, the state transition matrix must be appropriately modified to include the effects of those new terms. For example, higher order zonal terms (J_7 and greater) may be included, and the sectorial and tesseral term effects should also be included. If the simplification of using only the first derivative within the state transition matrix is no longer valid for this higher order dynamics, then 2nd order derivative effects must also be added to the state transition matrix. As more higher order perturbation effects are added to the filter dynamics, it is assumed that the improved simulated dynamics will track the true vehicle dynamics to greater precision. These improved dynamics models should allow a reduction in the NKF process noise and covariances, which would improve the overall performance of the filter. Although analytical models are straightforward to implement, testing of these higher order terms are more challenging in the real-world environment. Thus, new methods to test these models while on-orbit must be devised.

9.3.6 Pulsar Observation Models

Existing methods to determine pulsar pulse parameters, such as the pulse timing model parameters, pulse TOAs, and binary orbit parameters, may benefit from the dynamic gain computations of a Kalman filter implementation in contrast to the existing fixed gain weighted least-square techniques. The Kalman filter could include dynamics of the observation station, whether ground-based or space-based, to reduce the effects of these dynamics on determining these parameters. The comparison of a measured pulse profile with a standard template profile may also be implemented directly into a Kalman filter scheme. Any future research into refining the estimates of these important parameters, and implementing these new schemes such that real-time processing can be incorporated into navigation systems, would enhance the development of these systems and assist future astrophysical science observations.

9.3.7 Pulsar Range Measurement Sensitivity

Based upon the SNR equations, the sensitivity of the range measurement accuracy for pulsars could be determined with respect to the individual source parameters. The SNR equation may also be expanded to include specific detector characteristics, such as photon detection efficiency and X-ray background rejection. The sensitivity of source parameters versus detector characteristics could be investigated to determine which terms produce a greater effect on range accuracy.

9.3.8 Multiple Detector Systems

Using a single detector limits the amount of observation time for multiple sources. Systems that utilize multiple detectors, either separate or combined within one unit, can provide additional benefits and improvements to the navigation solution. If enough detectors are onboard a vehicle, simultaneous observations of sources could be generated, and absolute position determination could be accomplished. A system using *coarse* and *fine* resolution detectors, one to provide less accurate, short term, frequent measurements and another to provide high accuracy, long term, infrequent measurements, would generate an overall high quality, continuous navigation solution.

9.3.9 Previous Celestial Source Navigation Methods

Existing methods using visible celestial sources for different aspects of spacecraft navigation could be investigated for use by variable celestial sources. The methods of determining position relative to a planetary body either through source occultation or source elevation angles should be further researched in order to provide viable backup algorithms for verifying navigation solutions. However as noted, aeronomy research must be continued for each of the planetary bodies with appreciable atmospheres for these types of methods to be successful.

9.3.10 Mission Analysis

Further spacecraft mission analysis should be continued to investigate the utility of a navigation system using these variable celestial sources within various orbits, including future interplanetary missions. Missions to support the continued exploration of the Moon and Mars are of particular current interest. While in orbit about these bodies, the loss of contact with spacecraft during a vehicle's occultation behind these bodies is an important opportunity for this proposed system to provide a continuous navigation capability. An interesting orbit to analyze would be the stable Lagrange points (L4 and L5) within the Earth-Moon system for an orbiting variable celestial source base station. Also, the Sun-Earth system L2 Lagrange point, such as that proposed for the James Webb Space Telescope orbit, would be of interest for future astronomy missions. Use of the system proposed here may allow autonomous navigation and control at these distant locations.

For future missions to the outer planets, analysis of the potential performance of this celestial-based navigation system may assist in reducing lifetime mission costs. For missions that may extend beyond the outer planets, used to investigate the outer solar system regions and perhaps traverse the heliopause, applications of this navigation system may only require infrequent vehicle contact with Earth ground stations.

9.3.11 Additional Applications

The use of X-ray pulsars, and other variable X-ray sources, is not limited to single spacecraft navigation. Based upon the research pursued during this dissertation, other technological concepts used for navigation and new applications can be envisioned utilizing these types of sources. Several of these new concepts are described below.

- Differential/Relative Position: An orbiting base station may be used to detect variable source signals and to broadcast pulse arrival times signal errors to other spacecraft. This base station could also be used to monitor and update pulsar almanac information. Ideal orbiting locations for these base stations include geosynchronous orbits, and Sun-Earth and Earth-Moon Lagrange points. Receiving spacecraft are able to navigate with improved information relative to the base station. Relative positioning from a lead vehicle could also be implemented in a satellite formation-flying concept.
- GPS System Time Complement: Pulsar-based systems could be used as time-only reference systems, such as for aiding high-data rate communication between satellites and ground stations.
- Radio-based Systems on Earth and in Space: Although the atmosphere absorbs X-ray signals, navigation systems for Earth applications based upon celestial radio signals could be pursued. Using these sources as celestial clocks and/or navigation aides would be a viable alternative to X-ray sources, as long as an application could support large antennas, such as aboard a large naval vessel or a solar-sail spacecraft.

- Planetary Rovers: With rovers continuing to be suggested for future planetary missions, these celestial sources could provide a navigation system for exploratory mobile vehicles. Upon landing, the rover's base station could monitor pulsar signals and provide a relative positioning system for rovers that navigate over the surface terrain. Planetary bodies with a thin or negligent atmosphere, including Earth's Moon or Mars, are good candidates for this method.
- X-ray Communication: With increased X-ray detector research for development of this navigation system, new methods to transmit and receive modulated X-ray pulses could be pursued. These transmitted modulated signals could carry information. Due to the direct line-of-sight requirements for X-ray photons, secure communication links may be established.
- Enhanced Planetary Ephemeris: If base stations are placed upon planetary bodies and data is compared to measured data on Earth, methods to determine accurate body location could be established. This information would provide improved ephemeris data for these bodies.

9.4 Final Summary

Celestial object navigation methods, which use sources at great distance from Earth, will continue to benefit future space system architectures. X-ray emitting rotation-powered and accretion-powered pulsars represent a small, but important, subset of all possible variable celestial X-ray sources. These unique sources provide pulsed radiation that can be utilized in an X-ray based navigation system for spacecraft. Given their vast distances from Earth, these sources provide good signal coverage for space vehicle operations near Earth, on to the Moon, on to Mars, throughout the solar system, and conceivably, the Galaxy. Although issues with these sources exist that makes their use complicated, further algorithmic and experimental study may address these complications. Also, by complementing existing systems, such as GPS or DSN, this new system can increase the overall navigation performance of many spacecraft missions.

Hence, this dissertation has illustrated the potential of these objects to determine accurate vehicle position, velocity, and time is significant towards increased autonomous vehicle operation. With the capability of generating a *complete* navigation solution, including time, position, velocity, attitude, and attitude rate, variable celestial X-ray sources remain attractive for creating a new celestial-based spacecraft navigation system. Once implemented, this system may eventually be referred to as the *X-ray pulsar positioning system* (XPS) or in more general terms, the *X-ray navigation* (XNAV) system.

Appendices

Appendix A Supplementary Matter

A.1 Constants and Units

Table A-1. Fundamental Constants [16, 183].

Quantity	Symbol	Value	Units
Speed of Light (vacuum)	c	299792458	m/s
Universal Gravitational Constant	G	6.67259×10^{-11}	$m^3/(kg \cdot s^2)$
Planck Constant	h	$6.6260755 \times 10^{-34}$	$J \cdot s$
Thompson Cross-Section	$8\pi r_e^2/3$	6.652×10^{-25}	cm^{-2}
Stefan-Boltzmann Constant	σ	5.67051×10^{-5}	$erg/(cm^2 \cdot K^4 \cdot s)$

Table A-2. Astronomical Constants [16, 183].

Quantity	Symbol	Value	Units
Astronomical Unit	AU	$1.49597870 \times 10^{11}$	m
Light Time 1 AU	$AULTSEC$	499.004782	s
Light Year	ly	9.461×10^{15}	m
Parsec	pc	3.086×10^{16}	m
	pc	3.262	ly
Heliocentric Gravitational Constant	μ_S	$1.32712438 \times 10^{20}$	m^3/s^2
Radius of Sun	R_S	6.96×10^{8}	m
Geocentric Gravitational Constant	μ_E	3.986005×10^{14}	m^3/s^2
Radius of Earth	R_E	6378136	m
Lunar Gravitational Constant	μ_M	4.902799×10^{6}	m
Radius of Moon	R_M	1738000	m

Table A-3. Unit Conversions [183].

Quantity	Units	Conversion Value
Angstrom	Å	$= 1.0\times10^{-10}\ m$
Electron Volt	eV	$= 1.6021917\times10^{-19}\ J$
	eV	$= 1.6021917\times10^{-12}\ erg$
	keV	$= 1.6021917\times10^{-9}\ erg$
Erg (= g•cm^2/s)	erg	$= 1.0\times10^{-7}\ J$
Jansky	Jy	$= 1.0\times10^{-26}\ W/m^2/Hz$
	Jy	$= 1.0\times10^{-23}\ erg/(s\cdot cm^2\cdot Hz)$
Steradian	sr	$= 3.283\times10^{3}\ deg^2$
		$= 4.255\times10^{10}\ arcsec^2$
Proper Motion	mas/yr	$= 1.536282\times10^{-16}\ rad/s$
Arcsecond (arcsec)	as	$= 1/3600\ deg$
		$= 1/(\mathrm{pi}*20)\ rad$
Day	d	$= 24\ hr$
		$= 1440\ min$
		$= 86400\ s$
Julian Year	yr	$= 365.25\ d$
		$= 8766\ hr$
		$= 31557600\ s$

A.1.1 Additional Notes

$1\,Joule \equiv 1\,N\cdot m \equiv 1\,kg\cdot m^2/s^2$

$1\,Watt \equiv 1\,J/s \equiv 1\,kg\cdot m^2/s^3$

In Degrees:Minutes:Seconds (DD:MM:SS): 1 “second” = 1 arcsec

In Hours:Minutes:Seconds (HH:MM:SS): 1”second” = 15 arcsec

A.2 *Time Standards and Coordinates*

Description of systems from Explanatory Supplement to the Astronomical Almanac [183] and Vallado [213].

A.2.1 Terrestrial Time Standards

- TAI: *Temps Atomique International*

  International Atomic Time

  Based upon cycles of a high-frequency electrical circuit maintained in resonance with Cesium-133 atomic transition.
- UT: Universal Time

  Mean solar time at Greenwich
- UT0: Observation of UT at a particular observation/ground station
- UT1: UT0 corrected for polar motion, so time is independent of station location
- UT2: UT1 corrected for seasonal variations
- UTC: Coordinated Universal Time

  Derived from atomic time, follows UT1 within ±0.9s

  Bridge between TAI and UT1

A.2.2 Coordinate Time Standards

- TT: Terrestrial Time

  = TDT (Terrestrial Dynamical Time)

- TCB: *Temps Coordonnée Baricentrique*

  Barycentric Coordinate Time

  Coordinate time for coordinate system with center of mass of solar system

- TCG: *Temps Coordonnée Géocentrique*

  Geocentric Coordinate Time

  Coordinate time for coordinate system with center of mass of Earth

- TDB: *Temps Dynamique Baricentrique*

  Barycentric Dynamical Time

  Independent variable of the equations of motion with respect to the barycenter of the solar system.

- ET: Ephemeris Time

A.3 Coordinate Reference Systems

Description of systems from Explanatory Supplement to the Astronomical Almanac [183] and Vallado [213].

A.3.1 Terrestrial Coordinate Reference Systems

A.3.1.1 Terrestrial Inertial Systems

- GCRS: Geocentric Celestial Reference System

  Family of reference systems

  Intended for applications of framework of general relativity

- ECI: Earth Centered Inertial

  = CIS: Conventional Inertial System

  = IJK: Geocentric Equatorial System

- FK5: Fundamental Katalog System

  Based upon FK5 star catalog

- GCRF: Geocentric Celestial Reference Frame

  Close to FK5, but no nutation

- TEME: True Equator Mean Equinox

  Includes precession but no nutation

- MEME: Mean Equator Mean Equinox

A.3.1.2 Terrestrial-Fixed Non-Inertial Systems

- ITRF: International Terrestrial Reference Frame

  = BF: Body-Fixed Coordinate System

  = ECEF: Earth-Centered Earth-Fixed

  = EFG: Earth-Fixed Greenwich System

- SEZ: South-East-Up

  Observation station local coordinates

  = Topocentric Horizon Coordinate System

- $I_T J_T K_T$: Topocentric-Equatorial Coordinate System

  IJK frame with origin at topocenter, on surface of Earth

A.3.2 Interplanetary Coordinate Reference Systems

A.3.2.1 Interplanetary Inertial Systems

- BCRS: Barycentric Celestial Reference System

  Family of reference systems

  Intended for applications of framework of general relativity

- ICRF: International Celestial Reference Frame

  Equator and equinox of J2000

  Origin at barycenter of solar system

- XYZ: Heliocentric Coordinate System

A.4 X-ray Flux Conversion

A.4.1 X-ray Spectrum

Although the X-ray spectrum is defined broadly, there are no definitive boundary values that are relative to X-ray observation work. In the dissertation text the upper bound is listed as 200 keV. X-rays normally emit by atomic transitions, whereas gamma rays and higher are emitted by nuclear transitions. The positron annihilation line is at 511 keV, so we will use this value for now. So, the approximate range for this spectrum:

Wavelength: $1\times10^{-8} - 2.426\times10^{-11}$ m

Frequency: $3\times10^{16} - 1.236\times10^{20}$ Hz

Quantum Energy: 0.1 – 511 keV

Wavelength is λ, and frequency is ν. Relation is $c \equiv \lambda\nu$. Energy can be in units of Joules, ergs, or electron volts. Relation is $E_{ph} \equiv h\nu \equiv hc/\lambda$. Will use E_{ph} to represent photon energy of photons in a beam (so not to confuse with exponents).

A.4.2 Energy

X-ray sources are measured over a specific energy range. This is typically measured in electron Volts (eV).

X-ray Range in Electromagnetic Spectrum: 0.1 – 511 keV.

Soft X-ray Range: 0.1 – ~4 keV (note ROSAT PSPC = 0.1 – 2.4 keV).

Hard X-ray Range: ~4 – higher keV (could also be to 10 keV, or > 20 keV).

A.4.3 Flux

Flux is *energy per unit area per unit time*. Thus, using flux one can determine accumulated amount of energy received in a given area over a specific time period. Several units are used, including $watts/m^2$ (mks system), $erg/cm^2/s$ (cgs system), $photons/cm^2/s$, and *Crab* (based on flux of Crab Pulsar over the energy range in question). Flux is related to flux density as described below.

Flux density (S_ν) is the flux per unit frequency interval. Sometime flux density (S_E) is defined as the flux per unit energy interval (such as *flux/keV*). The flux density is often measured in *Jansky* (Jy) units. One *Jansky* is defined as 1.0×10^{-26} $\mathrm{Wm^{-2}Hz^{-1}}$= 1.0×10^{-26} $\mathrm{W/m^2/s}$ (mks system) = 1×10^{-23} erg s^{-1} cm^{-2} Hz^{-1} (cgs system).

Flux (F) is simply an integral of the flux density over the frequency or energy range in question: therefore, $F = \int_{\nu_{\min}}^{\nu_{\max}} S_\nu d\nu = \int_{E_{\min}}^{E_{\max}} S_E dE$.

A.4.3.1 Flat Spectrum

If an observation has a flat spectrum, where $S_\nu(\nu) = 1\,\mu\mathrm{Jy}$ for all ν, then a simple flux density conversion from *Jansky* to $erg/cm^2/s$ is the following:

$$1\,\mu Jy = \left(2.4\times10^{-12}\left(erg/cm^2/s\right)/keV\right)\cdot(\text{range in } keV)$$

Ex. Flat spectrum of 0.5 μJy (2—20 keV) => $0.5\cdot2.4\times10^{-12}\cdot(20-2)$ = $1.2\times10^{-12}\cdot(18)$ = 2.16×10^{-11} $erg/cm^2/s$.

Note that most sources, including X-ray sources do not have a flat spectrum, thus flux must be determined using integration of their spectral shape. For much of the catalog work, the full spectrum of each source was not investigated, so it was chosen to use the simple conversion method if flux density was given.

A.4.3.2 Photon Flux

Flux densities are often quoted in units of photons, rather than ergs. The unit of *photons* is a quantum measure, and is unitless. A flux density just needs to be divided by $h\nu$ to convert to photon units. For a spectrum that is a power law in photon energy E_{ph}, this reduces the spectral index by 1. Thus, an energy spectral index of –1 corresponds to a photon spectral index of –2.

A.4.3.3 Crab Flux Unit

Source fluxes are often quoted in units of the flux of the Crab Nebula and Pulsar (combined).

$$1\,Crab(ph/cm^2/s) = \int_{keV_{\min}}^{keV_{\max}} \left(10\mathrm{E}_{ph}{}^{-2.05}\right) e^{(-\sigma\, n_H)} dE_{ph}$$

where this equation is integrated in energy range $\left(keV_{\min} - keV_{\max}\right)$, and n_H is the neutral hydrogen column density, with $n_H = 3\times10^{21}/\mathrm{cm}^2$, and σ is the photoelectric cross section for hydrogen (Thompson cross section). Typically, most sources are measured in terms of milli-Crab (mCrab).

A.4.4 Luminosity

Luminosity is the rate of emission of energy, so it has units of *energy per unit time*. Luminosity is the *total power* emitted from the source. Several units are used, including *watts* (mks system) and erg/s (cgs system).

Assuming isotropic emission from a source, luminosity (L) and flux (F) are related by $L = F \cdot 4\pi d^2$, where d is the distance from the source. If using erg/cm^2/s or ph/cm^2/s, remember to put distance in units of cm, where 1 parsec = 1pc = 3.086×10^{18} cm.

A.4.5 Other Conversions

To get number of photons per second use $Power / E_{ph} = \#\, photon / s$, where power is in units of Watts, and E_{ph} is in units of Joules.

A.4.6 Experiment Conversion Factors

A.4.6.1 ROSAT

Singh's paper states for the ROSAT PSPC a value of: $1\, counts/s = 1\, ct/s = 9.4\times10^{-12}\, erg/cm^2/s$ for energy range (0.1 – 2.4 keV). So using Singh's result, or simply $1\, counts/s = 1\, ct/s = 1\times10^{-11}\, erg/cm^2/s$ for until shown otherwise. This value is not the same for the HRI detector on ROSAT.

A simple, quick calculation of ROSAT counts to flux: $1\, counts/s = 1\, ct/s = 1.44\times10^{-11}\, erg/cm^2/s$ for energy range (0.1 – 2.4 keV), which is very similar to Singh's result. Also approximately for range (0.1 – 2.4 keV): $1.0\times10^{-11}\, erg/cm^2/s = 4.989\times10^{-3}\, photons/cm^2/s \approx 5\times10^{-3}\, photons/cm^2/s$

A.4.6.2 PIMMS

This UNIX tool can be used to convert between various flux units, such as Crab, Jansky, ergs, and photons. The tool is interactive or can read an input file.

For most of analysis chose to use the Crab spectrum as the model spectrum for all sources with unknown flux. As above, this has an exponent of 2.05 and hydrogen column density of 3×10^{21}. Pimms was run from the UNIX command line using the following commands:

- model power 2.05 3E21
- from flux [photons, mJansky, Crab, or erg] [energy range, ex. 2-10]
- instrument flux [photons, mJansky, Crab, or erg] [energy range, ex. 2-10]
- show (shows the set up before running)
- go # (input a value of flux for the "from" category)

Also the above can be put into an input file with an ".xco" extension to run from a file, as in "pimms @input.xco" (don't forget the "@" symbol!!)

WebPIMMS: Runs much like PIMMS, only has a GUI interface. See this at: http://heasarc.gsfc.nasa.gov/Tools/w3pimms.html

Appendix B X-ray Navigation Source Catalogue

B.1 Description

The XNAVSC variable celestial X-ray source catalogue provides parameter listings of sources that have potential application for spacecraft navigation. Chapter 2 provides a complete description of the XNAVSC catalogue and how it was assembled. The catalogue is composed of three main lists – *Simple List*, *Detailed List*, and *2–10 keV Energy List*. Source parameters are listed for each source depending on the type of data needed in each list. Not all parameters are currently available for each source. For those parameters that are either unpublished or unavailable currently, these entries are blank with the catalogue. The sections within this Appendix provide details on the parameter lists within each of these lists, as well as the data from each list.

In addition to the information about each type provided in Chapter 2, Table B-1 provides a listing of the various types of Cataclysmic Variable sources within the XNAVSC, as well as a short description of these types [2, 178].

Table B-1. CV Sources Within the XNAVSC Database.

Object	Description	Number of Sources
CV, AM	AM Her System	2
CV, D	Degenerate/Detached	3
CV, DN	Dwarf Nova	15
CV, IP	Intermediate Polar	29
CV, N	Classical Nova	18
CV, NL	Nova-Like	3
CV, P	Polar	43
CV, RN	Recurrent Nova	1
CV, S	SS Cygni-type	6
CV, U	SU Ursae Majoris-type	5
CV, X	UX Ursae Majoris-type	1
CV, Z	Z Cameloparalis-type	3
Unknown CV Type		12
Total		**141**

B.2 Parameters Within Catalogue Lists

This section provides a description of the three main lists within the XNAVSC. The parameters that are stored within each list are identified, along with a brief description of the parameter and any units that represent the data. For those parameters that have no units, or none are needed, a "N/A" value for Not Applicable is stated.

B.2.1 Simple List Parameters

Table B-2. Parameters for Simple List in XNAVSC.

Parameter	Definition	Units
Install Number	Number of source in order it was installed into catalogue	N/A
Common Names	List of common names used for this source	N/A
Notes	General comments about a source, including type, location, companion, etc.	N/A
Catalogue J-Name	Catalogue specific name composed of catalogued J2000 Right Ascension and Declination position	Jhhmm±ddmm format
J-Name	J2000 frame based name used by external reference catalogues (if different from the Catalogue J-Name)	Reference's format
B-Name	B1950 frame based name used by external references	Bhhmm±dd format
Object Type	Type of object	N/A
Reference Catalog	Number of specific reference used for the object's data	N/A

B.2.2 Detailed List Parameters

Table B-3. Parameters for Detailed List in XNAVSC.

Parameter			Definition	Units
	Install Number		Number of source in order it was installed into catalogue	N/A
Name & Type	Catalogue J-Name		Catalogue specific name composed of catalogued J2000 Right Ascension and Declination position	Jhhmm±ddmm format
	B-Name		B1950 frame based name used by external references	Bhhmm±dd format
	Object Type		Type of object	N/A
	Class		Class of object type	N/A
	Sub-Class		Sub-type of object type class	N/A
Position	RA		J2000 Right Ascension position of object	hh:mm:ss.ssss
	RA Error		Uncertainty of Right Ascension value, as reported by references	arcseconds
	Dec		J2000 Declination position of object	±dd:mm:ss.ssss
	Dec Error		Uncertainty of Declination value, as reported by references	arcseconds
	Gal. Longitude		Galactic Longitude ("LII") of object position (derived from RA and Dec)	0 to 360 degrees
	Gal. Latitude		Galactic Latitude ("BII") of object position (derived from RA and Dec)	-180 to +180 degrees
	Distance From Earth		Distance of object from Earth	kiloparsecs
	Galactic Plane Z-Distance		Distance of object above/below galactic plane	±parsecs
	Proper-Motion RA-Direction		Proper-motion of object in the Right Ascension direction	±arcseconds/year
	Proper-Motion Dec-Direction		Proper-motion of object in the Declination direction	±arcseconds/year
Energy	Soft X-rays <4.5 keV	Energy Range	Energy range of measured X-ray flux of object (4.5 keV is chosen maximum for this range)	kilo electron-Volts
		Flux	X-ray flux of source	photons/cm^2/second
		Flux	X-ray flux of source	ergs/cm^2/second
	Hard X-rays >4.5 keV	Energy Range	Energy range of measured X-ray flux of object	kilo electron-Volts
		Flux	X-ray flux of source	photons/cm^2/second
		Flux	X-ray flux of source	ergs/cm^2/second
	Neutral Hydrogen Column Density		Number of neutral hydrogen atoms in a cylinder of unit cross-sectional area	1/cm^2
	Photon Index		Index parameter for X-ray flux power law model	unitless
	Pulsed Fraction		Fraction of measured flux that is pulsed; ratio of pulsed flux to mean flux	fraction
	Pulse Width (50%)		Width of measured pulse at 50% of height above pulse floor	seconds
	Pulse Width (10%)		Width of measured pulse at 10% of height above pulse floor	seconds
	Magnetic Field		Magnitude of magnetic field of object	Gauss

Stability	Transient Characteristics	Stability of Signal (S = Steady, T = Transient)	N/A
	Stability Code	Code related to stability of object (Bi = Binary System, Bu = Burster, Gl = Glitch, Zsrc = Z-Source)	N/A
	Timing Stability	Stability value of object (currently not used)	N/A
Periodicity	Pulse Period	Duration of full one cycle period of pulse	seconds
	Pulse Period Deriv.	First time derivative of pulse period	seconds/seconds
	Pulse Period 2nd Deriv.	Second time derivative of pulse period	seconds/seconds^2
	Epoch	Date epoch of measured pulse period and period derivatives	Modified Julian Date
	Characteristic Age	Rate of rotation slow down	years
	Binary Orbit Period	Orbit period of objects within binary system	days
	Other Period	Other important period terms (currently not used)	N/A
References	Reference Catalog	Number of specific reference used for the object's data	N/A
	Reference Code	Code for reference information (currently not used)	N/A
	Notes	General comments about a source, including type, location, companion, etc.	N/A

B.2.3 2–10 keV Energy List Parameters

Table B-4. Parameters for 2-10 keV Energy List in XNAVSC.

Parameter			Definition	Units
	Install Number		Number of source in order it was installed into catalogue	N/A
Name & Type	Catalogue J-Name		Catalogue specific name composed of catalogued J2000 Right Ascension and Declination position	Jhhmm±ddmm format
Name & Type	B-Name		B1950 frame based name used by external references	Bhhmm±dd format
Name & Type	Object Type		Type of object	N/A
Name & Type	Class		Class of object type	N/A
Name & Type	Sub-Class		Sub-type of object type class	N/A
Name & Type	Proper-Motion Dec-Direction		Proper-motion of object in the Declination direction	±arcseconds/year
Energy	Soft X-rays <4.5 keV	Energy Range	Energy range of measured X-ray flux of object (4.5 keV is chosen maximum for this range)	kilo electron-Volts
Energy	Soft X-rays <4.5 keV	Flux	X-ray flux of source	photons/cm^2/second
Energy	Soft X-rays <4.5 keV	Flux	X-ray flux of source	ergs/cm^2/second
Energy	Hard X-rays >4.5 keV	Energy Range	Energy range of measured X-ray flux of object	kilo electron-Volts
Energy	Hard X-rays >4.5 keV	Flux	X-ray flux of source	photons/cm^2/second
Energy	Hard X-rays >4.5 keV	Flux	X-ray flux of source	ergs/cm^2/second
2-10 keV X-ray	Energy Range		Energy range of measured X-ray flux of object	kilo electron-Volts
2-10 keV X-ray	Flux		X-ray flux of source	photons/cm^2/second
2-10 keV X-ray	Flux		X-ray flux of source	ergs/cm^2/second

B.3 Catalogue Data Lists

This section provides the actual data lists from the XNAVSC. As these tables of data are quite long, care must be taken by the reader to assure proper alignment of the pages of information. These tables are a text version of the electronic database of the XNAVSC. To reduce the overall pages of the data, some repeated parameters between Lists have been omitted, and are identified within each section below.

B.3.1 Simple List

The following table provides all the data in the *Simple List* of the XNAVSC. All the data from this list is provided. The first page of this table provides the headings of each column of the table. Descriptions of the parameters within this table are provided in Table B-2.

The actual list begins on the following page. Note that is orientated in landscape format.

For the parameter of the *Catalogue J-Name*, this is source name unique to the XNAVSC. For a name that is of format *Jhhmm-ddmm* and written in blue ink, this name has been modified from the original citation's J-name or was derived from the position of the source if only a B-name is known for that source. This *Catalogue J-Name* is only created to produce a consistent naming convention for all the XNAVSC sources, and should not be used as an external name for the source.

Install Number	Common Names	Notes	Catalogue J-Name (Jhhmm-ddmm Format)	J-Name (From References)	B-Name (From References)	Object Type	Reference Catalog
1	Crab Pulsar; PSR B0531+21; 1H 0531+219; Tau X-1; CM Tau		J0534+2200	—	B0531+21	NS	1, 5, 11
2	Vela Pulsar; 4U0833-450		J0835–4510	—	B0833–45	NS	1, 5, 11
3	Geminga; SN 437; PSR J0633+1746; 1E 0630+178; PSR B0630+17 (PSRB0633+17)		J0633+1746	—	B0630+17	NS	1, 5, 11
4	G343.1-02.3; PSR B1706-44; 2CG 342-02		J1709–4428	—	B1706–44	NS	1, 5, 11
5	MSH 15-52; PSR B1509-58; 4U 1510-590	G320.4-1.2	J1513–5908	—	B1509–58	NS	1, 5, 11
6	PSR B1951+32; CTB 80		J1952+3252	—	B1951+32	NS	1, 5, 11
7	PSR B1046-58; Vela Twin		J1048–5832	—	B1046–58	NS	1, 5, 11
8	PSR B1259-63; SS 2883; "Rosetta"	Be-star/bin	J1302–6350	—	B1259–63	NS	1, 5
9	PSR B1823-13	Vela like	J1826–1334	—	B1823–13	NS	1, 5, 11
10	G8.7-0.1; PSR B1800-21		J1803–2137	—	B1800–21	NS	1, 5, 11
11	PSR B1929+10		J1932+1059	—	B1929+10	NS	1, 5, 11, 27
12	PSR J0437-4715	ms Pulsar	J0437–4715	J0437–4715	—	NS	1, 5, 11
13	PSR B1821-24; M 28	ms,in M28	J1824–2452	—	B1821–24	NS	1, 5, 11, 25, 26
14	PSR B0656+14	cooling NS	J0659+1414	—	B0656+14	NS	1, 5, 11
15	PSR B0540-69	Source in LMC	J0540–6919	—	B0540–69	NS	1, 5, 11, 49
16	PSR J2124-33	ms Pulsar	J2124–3358	J2124–3358	—	NS	1, 5, 11
17	PSR B1957+20; Black Widow Pulsar	ms Pulsar	J1959+2048	—	B1957+20	NS	1, 5, 22
18	PSR B0950+08		J0953+0755	—	B0950+08	NS	1, 5, 11, 27
19	PSR B1610-50		J1614–5047	—	B1610–50	NS	1, 5
20	G180.0-1.7		J0538+2817	J0538+2817	—	NS	1, 5, 11
21	PSR J1012+5307	ms Pulsar	J1012+5307	J1012+5307	—	NS	1, 5, 11, 22
22	PSR B1055-52	cooling NS	J1057–5226	—	B1055–52	NS	1, 5, 11
23	PSR B0355+54		J0358+5413	—	B0355+54	NS	1, 5, 11
24	G114.3+0.3; PSR J2337+6151		J2337+6151	—	B2334+61	NS	1, 5, 11

25	PSR J0218+4232	ms Pulsar	J0218+4232	J0218+4232	—	NS	1, 5, 11, 22, 25, 26
26	PSR B0823+26		J0826+2637	—	B0823+26	NS	1, 5, 11, 27
27	PSR J0751+1807	ms Pulsar	J0751+1807	J0751+1807	—	NS	1, 5, 11, 22
28	4U 0142+615		J0142+6100	J0142+61	—	NS	4, 2
29			J0525–6607	J0525–6607	—	NS	4
30	1E 1048.1-5937		J1048–5937	J1048–5937	—	NS	4, 2
31	RX J170849-4009		J1708–4008	J1708–4008	—	NS	4, 2
32	SGR 1806-20; AX J1808.6-2024; SNR G10.0-0.3	SNR:G10.0-0.3	J1808–2024	J1808–2024	—	NS	4, 6
33	1E 1841-045	SNR:Kes 73	J1841–0456	J1841–0456	—	NS	4, 2
34	AX J1845.0-0300	SNR:G29.6	J1845–0256	J1845–0256	—	NS	4, 2
35	SGR1900+14	SNR:G42.8+0.6	J1907+0919	J1907+0919	—	NS	4
36	1E 2259+586	SNR:G109.1-0.1	J2301+5852	J2301+5852	—	NS	4, 2
37	RX J0032.9-7348: B Hyi: HR 98		J0032-7348	J0032.9-7348	—	HMXB	3
38	AX J0049-732		J0049-7310	J0049-732	—	HMXB	3, 32
39	AX J0049-729; RX J0049.1-7250		J0049-7250	J0049-729	—	HMXB	3
40	SMC X-3	Source in SMC	J0052-7226	—	B0050-727	HMXB	3
41	RX J0050.7-7316; AX J 0051-73.3		J0050-7316	J0050.7-7316	—	HMXB	3, 6
42	AX J0051-722; SMC X-3	Source in SMC	J0050-7213	J0051-722	—	HMXB	3
43	2E0050.1-7247; RX J0051.8-7231; 1WAG J0051.8-7231; AV111; SMC 21685	Source in SMC	J0051-7231	J0051.8-7231	—	HMXB	3, 6
44	AX J0051.6-7311; RX J0051.9-7311; SMC 25	Source in SMC	J0051-7310	J0051.9-7311	—	HMXB	3
45	RX J0052.1-7319; SMC X-2	Source in SMC	J0052-7319	J0052.1-7319	—	HMXB	3, 37
46	2E 0051.1-7214; AX J0052.9-7157; RX J0052.9-7158; SMC 46	Source in SMC	J0052-7158	J0052.9-7158	—	HMXB	3
47	SMC X-2	Source in SMC	J0054-7341	—	B0053-739	HMXB	3
48	4U 0053+60; gamma Cas; HD 5394		J0056+6043	—	B0053+604	HMXB	3
49	XTE J0053-724; 1WGA J0053.8-7226		J0053-7226	J0053.8-7226	—	HMXB	3
50	XTE J0054-720		J0054-7204	J0054-720	—	HMXB	3
51	XTE J0055-724; 1SAX J0054.9-7226		J0054-7226	J0055-724	—	HMXB	3

52	J0058-7203; AX J0058-720		J0057-7202	J0058-72.0	—	HMXB	3
53			J0058-7230	J0058.2-7231	—	HMXB	3
54	RX J0059.2-7138		J0059-7138	J0059.2-7138	—	HMXB	3
55	RX J0101.0-7206, CXOU J010102.7-720658		J0101-7206	J0101.0-7206	—	HMXB	3, 32
56	1SAX J0103.2-7209; 1E 0101.5-7225		J0103-7209	J0103-722	—	HMXB	3
57	0107-750		J0109-7444	—	B0103-762	HMXB	3
58	AX J0105-722; RX J0105.3-7210; DEM S128		J0105-7211	J0105-722	—	HMXB	3
59			J0105-7212	J0106.2-7205	—	HMXB	3
60	XTE J0111.2-7317		J0105-7213	J0111.2-7317	—	HMXB	3
61	2S0114+650; LSI+65 010		J0118+6517	—	B0114+650	HMXB	3
62	V635 Cas; 1H 0115+635; 4U 0115+634		J0118+6344	—	B0115+634	HMXB	3, 6
63	4U0115-737; RX J0117.1-7327; SMC X-1	Source in SMC	J0117-7326	—	B0115-737	HMXB	3
64	RX J0117.6-7330		J0117-7330	J0117.6-7330	—	HMXB	3
65	RX J0146.9+6121; LSI+61 235		J0143+6106	J0146.9+6121	—	HMXB	3
66	GT; V615 Cas; LSI+61303		J0240+6113	—	B0236+610	HMXB	3
67	V 0332+53; BQ Cam		J0334+5310	—	B0331+530	HMXB	3
68	4U; X Per; X Persei; Per X-1; HD 24534		J0355+3102	—	B0352+309	HMXB	3
69			J0419+5559	J0421+560	—	HMXB	3
70	RX J0440.9:+4431; BSD 24-491		J0440+4431	J0440.9+4431	—	HMXB	3
71	CAL 9		J0501-7033	J0501.6-7034	—	HMXB	3
72	RX J0502.9-6626; CAL E		J0502-6626	J0502.9-6626	—	HMXB	3
73			J0512-6717	J0512.6-6717	—	HMXB	3
74			J0516-6916	J0516.0-6916	—	HMXB	3
75			J0520-6932	J0520.5-6932	—	HMXB	3
76	SAO57950		J0522+3740	—	B0521+373	HMXB	3
77	RX J0529.8-6556		J0529-6556	J0529.8-6556	—	HMXB	3
78	EXO B053109-6609.2		J0531-6607	—	B053109-6609.2	HMXB	3
79			J0531-6518	J0531.5-6518	—	HMXB	3
80	LMC X-4; 1H 0534-667; 2U 0532-66; 2A; 4U	Source in LMC	J0532-6622	—	B0532-664	HMXB	3, 6
81			J0532-6535	J0532.4-6535	—	HMXB	3

82	RX J0532.5-6551, Sk -65 66		J0532-6551	J0532.5-6551	—	HMXB	3
83			J0535-6700	J0535.0-6700	—	HMXB	3
84	0538-66		J0535-6651	—	B0535-668	HMXB	3
85	A 0535+26; V725 Tau; HD 245770; 1H 0536+263		J0538+2618	—	B0535+262	HMXB	3, 6
86			J0535-6530	J0535.8-6530	—	HMXB	3
87	CAL 70; RX J0538.9-6405; LMC X-3; LMC 306	Source in LMC	J0538-6405	—	B0538-641	HMXB	3
88	CAL 78; 1H 0540-697; RX J0539.6-6944; LMC X-1	Source in LMC	J0539-6944	—	B0540-697	HMXB	3
89			J0541-6936	J0541.4-6936	—	HMXB	3
90			J0541-6832	J0541.5-6833	—	HMXB	3
91			J0544-6633	—	B0544-665	HMXB	3
92	RX J0544.1-7100; 1SAX J0544.1-710		J0544-7100	J0544.1-710	—	HMXB	3
93			J0555+2847	—	B0556+286	HMXB	3
94	SAX J0635.2+0533; PSR J0635+0533		J0635+0533	J0635+0533	—	HMXB	3
95	WGA J0648.0-4418; HD 49798; RX J0648.1-4419		J0648-4418	J0648.0-4419	—	HMXB	3
96	3A 0726-260; 4U 0728-25		J0728-2606	—	B0726-260	HMXB	3
97	SAO235515		J0747-5319	—	B0739-529	HMXB	3
98	SAO250018		J0756-6105	—	B0749-600	HMXB	3
99	RX J0812.4-3114		J0812-3114	J0812.4-3114	—	HMXB	3
100	GS 0834-430; GRS 0831-429		J0835-4311	—	B0834-430	HMXB	3, 6
101	Vela X-1; GX 263+3; HD 77581		J0902-4033	—	B0900-403	HMXB	3
102	GRO J1008-57		J1009-5817	J1008-57	—	HMXB	3
103	TH(alpha) 35-42; 1E 1024.0-5732		J1025-5748	—	B1024.0-5732	HMXB	3
104	4U 1036-56, SAO238130		J1030-5704	—	B1036-565	HMXB	3
105	RX J1037.5-5647; 3A 1036-565; 4U 1036-56; LS 1698		J1037-5647	J1037.5-5647	—	HMXB	3
106	1E1048.1-5937		J1050-5953	—	B1048.1-5937	HMXB	3
107	A 1118-616; Hen 3-640		J1120-6154	—	B1118-615	HMXB	3
108	4U; GPS; Cen X-3; 1H 1118-602		J1121-6037	—	B1119-603	HMXB	3, 6

109	4U 1145-619; V801 Cen; HD 102467; 1H 1144-617		J1148-6212	—	B1145-619	HMXB	3, 6
110	1E 1145.1-6141		J1147-6157	—	B1145.1-6141	HMXB	3
111	GX 301-2, Wra 977; 4U 1223-52; 1H 1221-623		J1226-6246	—	B1223-624	HMXB	3, 6
112			J1242-6012	—	B1239-599	HMXB	3
113			J1247-6038	—	B1244-604	HMXB	3
114			J1249-5907	—	B1246-588	HMXB	3
115	SAO252002		J1242-6303	—	B1249-637	HMXB	3
116	SAO256967		J1239-7522	—	B1253-761	HMXB	3
117	HD1120912		J1254-5710	—	B1255-567	HMXB	3
118	GX 304-1, *2 (MMV); 4U 1258-62; 1H 1257-610		J1301-6136	—	B1258-613	HMXB	3, 6
119	1323-6196; SAX J1324.4-6200		J1324-6200	J1324.4-6200	—	HMXB	3
120	4U 1417-624; 2S 1417-67		J1421-6241	—	B1417-624	HMXB	3
121	SAX J1452.8-5949		J1452-5949	J1452.8-5949	—	HMXB	3
122	1H 1538-522; GX 327+4.5; QV Nor; 4U 1538-52	*12	J1542-5223	—	B1538-522	HMXB	3
123	MX 1553-542		J1557-5424	—	B1553-542	HMXB	3
124			J1554-5519	—	B1555-552	HMXB	3
125	OAO 1657-415		J1700-4140	—	B1657-415	HMXB	3
126	V884 Sco		J1703-3750	—	B1700-377	HMXB	3
127			J1700-4157	J170006-4157	—	HMXB	3
128	EXO 1722-363; GPS 1722-363		J1725-3624	—	B1722-363	HMXB	3
129			J1738-3015	J1739-302	—	HMXB	3
130			J1739-2942	J1739.5-2942	—	HMXB	3
131			J1744-2713	J1744.7-2713	—	HMXB	3
132	AX J1749.2-2725		J1749-2725	J1749.2-2725	—	HMXB	3
133	RX J1750-27; GRO J1750-27		J1749-2638	J1750-27	—	HMXB	3
134			J1810-1052	—	B1807-10	HMXB	3
135	AX J1820.5-1434		J1820-1434	J1820.5-1434	—	HMXB	3, 6
136	RX J1826.1-1450		J1826-1450	J1826.2-1450	—	HMXB	3

137	Sct X-1; 1H 1832-076		J1836-0736	—	B1833-076	HMXB	3, 6
138			J1841-0551	—	B1839-06	HMXB	3
139			J1841-0427	—	B1839-04	HMXB	3
140			J1845+0057	—	B1843+009	HMXB	3
141	AX J1845.0-0300; Kes 75		J1847-0309	—	B1845-03	HMXB	3
142			J1848-0225	—	B1845-024	HMXB	3
143			J1847-0430	—	B1845.0-0433	HMXB	3
144			J1858-0244	—	B1855-02	HMXB	3
145	XTE J1855-026		J1855-0237	J1855-026	—	HMXB	3
146	XTE J1858+034		J1858+0321	J1858+034	—	HMXB	3
147			J1904+0310	—	B1901+03	HMXB	3
148	XTE J1906+09		J1905+0902	J1906+09	—	HMXB	3
149	3A 1907+09; 4U 1907+09; 1H 1909+096		J1909+0949	—	B1907+097	HMXB	3, 6
150	SS 433; V1343 Aql; SNR W50; 1H 1908+047		J1911+0458	—	B1909+048	HMXB	3, 6
151			J1932+5352	—	B1936+541	HMXB	3
152	XTE J1946+274; GRO J1944+26; 3A 1942+274		J1945+2721	J1946+274	B1942+274	HMXB	3
153			J1949+3012	—	B1947+300	HMXB	3
154	GRO J1948+32		J1948+3200	J1948+32	—	HMXB	3
155			J1955+3206	—	B1954+319	HMXB	3
156	Cyg X-1; V1357 Cyg; HD 226868; 1H 1956+350		J1958+3512	—	B1956+350	HMXB	3, 6
157	V1357 Cyg; EXO B2030+375		J2032+3738	—	B2030+375	HMXB	3
158	Cyg X-3; V1521 Cyg		J2032+4057	—	B2030+407	HMXB	3
159			J2030+4751	J2030.5+4751	—	HMXB	3
160	GRO J2058+42		J2059+4143	J2058+42	—	HMXB	3
161	SAX J2103.5+4545		J2103+4545	J2103.5+4545	—	HMXB	3
162	GS 2138+56; Cep X-4; 1H 2138+579		J2139+5703	—	B2138+568	HMXB	3
163	SAO51568		J2201+5010	—	B2202+501	HMXB	3
164	4U 2206+543; 1H 2205+538		J2207+5431	—	B2206+543	HMXB	3, 6
165			J2226+6114	—	B2214+589	HMXB	3
166			J2239+6116	J2239.3+6116	—	HMXB	3

167	XN Per 1992; 4U 0042+32		J0044+3301	—	B0042+323	LMXB	2
168	GRO J0422+32; V518 Per; XN Per 92		J0418+3247	J0422+32	—	LMXB	2
169	4U 0513-40; 1H 0512-401; 2S 0512-400; 2A 0512-399, NGC 1851		J0514-4002	—	B0512-401	LMXB	2
170	CAL 30; 1H 0521-720; RX J0520.4-7157; LMC X-2	Source in LMC	J0520-7157	—	B0521-720	LMXB	2
171			J0532-6926	J0532.7-6926	—	LMXB	2
172	V1055 Ori; 2S 0614+091; 4U 0614+091; 1H 0610+091		J0617+0908	—	B0614+091	LMXB	2, 6, 53
173	Mon X-1; N. Mon 1975, 1917; V616 Mon		J0622-0020	—	B0620-003	LMXB	2
174			J0658-0715	—	B0656-072	LMXB	2
175	EXO 0748-676; UY Vol		J0748-6745	—	B0748-676	LMXB	2
176			J0835+5118	J0835.9+5118	—	LMXB	2
177	GS 0836-429; MX 0836-42		J0837-4253	—	B0836-429	LMXB	2
178			J0920-5512	—	B0918-549	LMXB	2
179	2S 0921-630; 2A; H; V395 Car		J0922-6317	—	B0921-630	LMXB	2
180	MM Vel; XN Vel 1993; GRS 1009-45		J1013-4504	—	B1009-45	LMXB	2
181	KV Uma; J1118+480		J1118+4802	J1118+480	—	LMXB	2
182	GU Mus; GS 1124-684; GRS 1121-684; N Mus 1991		J1126-6840	—	B1124-684	LMXB	2
183	GR Mus; 1H 1254-690; 2S 1254-690		J1257-6917	—	B1254-690	LMXB	2
184	4U 1323-620; EXO 1323.5-6180; 1323-6152		J1326-6208	—	B1323-619	LMXB	2
185	BW Cir; GS 1354-6429; MX 1353-64; Cen X-2		J1358-6444	—	B1354-645	LMXB	2
186	Cen X-4; V822 Cen		J1458-3140	—	B1455-314	LMXB	2
187	Cir X-1; BP Cir; 1H 1516-569; 2S		J1520-5710	—	B1516-569	LMXB	2
188	TrA X-1	*N	J1528-6152	—	B1524-617	LMXB	2
189	3U 1543-47; 4U 1543-45		J1547-4740	—	B1543-475	LMXB	2, 6
190			J1547-6234	—	B1543-624	LMXB	2
191			J1550-5628	J1550-564	—	LMXB	2
192	LU TrA; 1H 1556-605; 1M; 4U 1556-605	*X	J1601-6044	—	B1556-605	LMXB	2
193	UW CrB; MS 1603+2600; 1E 1603.6+2600		J1605+2551	—	B1603.6+2600	LMXB	2

194			J1603-7753	J1603.9-7753	—	LMXB	2
195	GX 331-1; QX Nor; 1H 1608-522; 4U 1608-52		J1612-5225	—	B1608-522	LMXB	2
196	Sco X-1; V818 Sco		J1619-1538	—	B1617-155	LMXB	2, 53
197	NorXR-1; V801Ara; 1H 1624-490; 4U 1624-49		J1628-4911	—	B1624-490	LMXB	2
198	KZ TrA; 4U 1626-67	*4	J1632-6727	—	B1627-673	LMXB	2, 29
199	4U 1630-472		J1634-4723	—	B1630-472	LMXB	2
200			J1636-4749	—	B1632-477	LMXB	2
201	Nor X-1; V801 Ara; 4U 1636-53; 1H 1636-536; MXB 1636-53	*3	J1640-5345	—	B1636-536	LMXB	2, 53
202	GX 340+0		J1645-4536	—	B1642-455	LMXB	2
203	XN Sco 1994; V1033 Sco; GRO J1655-40	?? Name (5/4?)	J1654-3950	J1655-40	—	LMXB	2
204	Her X-1; HZ Her; 1H 1656+354		J1657+3520	—	B1656+354	LMXB	2
205	MXB 1659-29; V2134 Oph	*T	J1702-2956	—	B1658-298	LMXB	2
206	GX 339-4; V821 Ara; 1H 1659-487	*V	J1702-4847	—	B1659-487	LMXB	2
207	Sco X-2; GX 349+2; 1H 1702-363; 4U 1702-36		J1705-3625	—	B1702-363	LMXB	2
208			J1706-4302	—	B1702-429	LMXB	2
209			J1706+2358	—	B1704+240	LMXB	2
210	V2107 Oph; N Oph 1977		J1708-2505	—	B1705-250	LMXB	2
211	4U 1705-44; 1H 1702-437		J1708-4406	—	B1705-440	LMXB	2, 6
212			J1712-4050	—	B1708-408	LMXB	2
213			J1709-2639	J1709-267	—	LMXB	2
214			J1710-2807	J1710-281	—	LMXB	2
215			J1714-3402	—	B1711-339	LMXB	2
216			J1712-3738	J1712.6-3739	—	LMXB	2
217			J1718-3210	—	B1715-321	LMXB	2
218	V2293 Oph; XN Oph 1993; GRO J1719-24		J1719-2501	—	B1716-249	LMXB	2, 6
219			J1718-4029	J171824.2-402934	—	LMXB	2
220			J1723-3739	J1723-376	—	LMXB	2
221			J1727-3544	—	B1724-356	LMXB	2
222			J1727-3048	—	B1724-307	LMXB	2

223	MXB 1728-34; 4U 1728-34; GX 354-0		J1731-3350	—	B1728-337	LMXB	2, 53
224	GX 9+9; V2216 Oph; 1H 1728-169; 4U1728-16		J1731-1657	—	B1728-169	LMXB	2
225	GX 1+4; V2116 Oph; 1H 1728-247	*GF	J1732-2444	—	B1728-247	LMXB	2
226			J1733-3113	—	B1730-312	LMXB	2
227	MXB 1730-335	Rapid Burster	J1733-3323	—	B1730-335	LMXB	2
228			J1733-2202	—	B1730-220	LMXB	2
229	KS 1731-260		J1734-2605	—	B1731-260	LMXB	2, 53
230			J1735-3028	—	B1732-304	LMXB	2
231			J1736-2725	—	B1732-273	LMXB	2
232			J1737-2910	—	B1734-292	LMXB	2
233			J1738-2700	—	B1735-269	LMXB	2
234	V926 Sco; 1H 1735-444; MXB 1735-44	*5	J1738-4427	—	B1735-444	LMXB	2
235			J1738-2829	—	B1735-28	LMXB	2
236			J1739-2943	—	B1736-297	LMXB	2
237			J1739-3059	—	B1737-31	LMXB	2
238			J1740-2818	—	B1737-282	LMXB	2
239			J1742-2746	—	B1739-278	LMXB	2
240			J1742-3030	—	B1739-304	LMXB	2
241	GC X-4		J1743-2926	—	B1740-294	LMXB	2
242			J1743-2944	—	B1740.7-2942	LMXB	2
243			J1744-2900	—	B1741.2-2859	LMXB	2
244	MXB1743-29 ?		J1744-2921	—	B1741-293	LMXB	2
245			J1745-3213	—	B1741-322	LMXB	2
246			J1745-2854	—	B1741.9-2853	LMXB	2
247			J1745-3241	—	B1742-326	LMXB	2
248			J1745-2859	—	B1742.2-2857	LMXB	2
249	GC X-2		J1745-2927	—	B1742-294	LMXB	2
250	A 1742-289		J1745-2901	—	B1742-289	LMXB	2
251			J1745-2900	—	B1742.5-2859	LMXB	2
252			J1745-2846	—	B1742.5-2845	LMXB	2

253			J1745-2903	—	B1742.7-2902	LMXB	2
254			J1746-2854	—	B1742.8-2853	LMXB	2
255			J1746-2853	—	B1742.9-2852	LMXB	2
256	GC X-1		J1746-2931	—	B1742-294	LMXB	2
257			J1746-2851	—	B1742.9-2849	LMXB	2
258			J1746-2844	—	B1743.1-2843	LMXB	2
259			J1746-2853	—	B1743.1-2852	LMXB	2
260	GX+0.2,-0.2		J1746-2853	—	B1743-288	LMXB	2
261			J1747-2959	—	B1744-299	LMXB	2
262	2E 1743.1-2842, GRO J1744-28		J1744-2844	J1744-28	—	LMXB	2
263			J1747-3002	—	B1744-300	LMXB	2
264	GX3+1		J1747-2633	—	B1744-265	LMXB	2
265			J1748-3607	—	B1744-361	LMXB	2
266			J1745-2901	J1745.6-2901	—	LMXB	2
267			J1748-2453	—	B1745-248	LMXB	2
268			J1748-2022	—	B1745-203	LMXB	2
269			J1749-3311	—	B1746-331	LMXB	2
270			J1750-3225	—	B1746.7-3224	LMXB	2
271	NGC 6441; 4U 1746-371; 1H 1746-370		J1750-3703	—	B1746-370	LMXB	2
272			J1750-2125	—	B1747-214	LMXB	2
273			J1750-3117	—	B1747-313	LMXB	2
274			J1748-2828	J1748-288	—	LMXB	2
275			J1748-2021	J1748.9-2021	—	LMXB	2
276	GX+1.1,-1.0		J1752-2830	—	B1749-285	LMXB	2
277			J1750-2902	J1750.8-2900	—	LMXB	2
278			J1752-3137	J1752.3-3138	—	LMXB	2
279	V4134 Sgr; Sco XR-6; 1H 1754-338; 4U 1755-33		J1758-3348	—	B1755-338	LMXB	2, 6
280	XTE J1755-324		J1755-3228	J1755-324	—	LMXB	2
281	1H 1758-250; 4U 1758-25; GX 5-1		J1801-2504	—	B1758-250	LMXB	2, 53
282			J1801-2544	—	B1758-258	LMXB	2

283	GX 9+1		J1801-2031	—	B1758-205	LMXB	2
284			J1806-2435	—	B1803-245	LMXB	2
285			J1806-2435	J1806-246	—	LMXB	2
286	SAX J1808.4-3658, XTE J1808-369		J1808-3658	J1808.4-3658	—	LMXB	2, 46, 47, 52
287	J1810.7-2609		J1810-2609	J1810.8-2609	—	LMXB	2
288	GX 13+1; 1811-1710		J1814-1709	—	B1811-171	LMXB	2
289			J1815-1205	—	B1812-12	LMXB	2
290	NP Ser; GX 17+2; 4U 1813-14		J1816-1402	—	B1813-140	LMXB	2, 53
291	J1819-254		J1819-2525	J1819.3-2525	—	LMXB	2
292	NGC 6624; 1H 1820-303; 4U 1820-30; 1820-3023		J1823-3021	—	B1820-303	LMXB	2, 53
293	V691 CrA; 1H 1822-371; 2A 1822-371		J1825-3706	—	B1822-371	LMXB	2
294			J1825-0000	—	B1822-000	LMXB	2
295	GS 1826-238		J1829-2347	—	B1826-238	LMXB	2
296			J1835-3258	—	B1832-330	LMXB	2
297	Ser X-1; MM Ser; 4U 1837+04; MXB 1837+05	*DS	J1839+0502	—	B1837+049	LMXB	2, 6
298			J1849-0303	—	B1846-031	LMXB	2
299	NGC 6712; 1H 1850-087; 1820-3023		J1853-0842	—	B1850-087	LMXB	2
300			J1856+0519	J1856+053	—	LMXB	2
301			J1858+2239	J1859+226	—	LMXB	2
302			J1908+0010	—	B1905+000	LMXB	2
303	Aql XR-1; V1333 Aql; 4U 1908+005		J1911+0035	—	B1908+005	LMXB	2, 53
304			J1915+1058	—	B1915+105	LMXB	2
305	V1405 Aql; 4U 1915-05; 1H 1916-053		J1918-0514	—	B1916-053	LMXB	2
306			J1920+1441	—	B1918+146	LMXB	2
307			J1942-0354	—	B1940-04	LMXB	2
308	V1408 Aql; 4U 1957+11; 1H 1956+115		J1959+1142	—	B1957+115	LMXB	2, 6
309	QZ Vul; N Vul 1988; GS 2000+25	,*B	J2002+2514	—	B2000+251	LMXB	2
310	XTE J2012+381		J2012+3811	J2012+381	—	LMXB	2
311	V404 Cyg; N Cyg 89; GS 2023+338		J2024+3352	—	B2023+338	LMXB	2

312	XTE J2123-058		J2123-0547	J2123-058	—	LMXB	2
313	M15; AC211; 1H 2128+120; 4U 2127+11		J2129+1210	—	B2127+119	LMXB	2, 6
314	V1727 Cyg; 4U 2129+47; 1H 2131+473		J2131+4717	—	B2129+470	LMXB	2, 6
315	Cyg X-2; V1341 Cyg; 1H 2142+380		J2144+3819	—	B2142+380	LMXB	2
316			J2320+6217	—	B2318+620	LMXB	2
317	RX J0720.4-3125; 1ES 0718-31.3		J0720-3125	—	B0718-3118	NS	2, 6, 43
318	RX J1838.4-0301; SNR G28.8+1.5		J1838-0301	J1838.4-0301	—	NS	2, 6
319	PG1232+379; WD; AM CVn; HZ 29		J1234+3737	—	—	CV	6, 7
320	GP Com; G 61-29		J1305+1801	—	—	CV	6, 7
321	47 Tuc; NGC 104; X 0021.8-7221		J0024-7204	—	—	CV	6, 7
322	LB 1800; V347 Pup; 4U		J0610-4844	—	—	CV	6, 7
323	V348 Pup; H 0710-360; 1H 0709-360		J0712-3605	—	—	CV	6, 7
324	HT Cas; 0107+598		J0110+6004	—	—	CV	6, 7
325	SS Aur; 1H 0613+479		J0613+4744	—	—	CV	6, 7
326	U Gem; H 0752+222; 1H 0801+213		J0755+2200	—	—	CV	6, 7
327	Z Cha		J0807-7632	—	—	CV	6, 7
328	Z Cam		J0825+7306	—	—	CV	6, 7
329	AC Cnc; H 0850+13		J0844+1252	—	—	CV	6, 7
330	SY Cnc; BD+18 2101		J0901+1753	—	—	CV	6, 7
331	X Leo; 0951+119		J0951+1152	—	—	CV	6, 7
332	OY Car		J1006-7014	—	—	CV	6, 7
333	TW Vir; PG1142-041		J1145-0426	—	—	CV	6, 7
334	AH Her; PG 1642+253		J1644+2515	—	—	CV	6, 7
335	V426 Oph; 1805+058		J1807+0551	—	—	CV	6, 7
336	WZ Sge; 2005+175		J2007+1742	—	—	CV	6, 7
337	SS Cyg; 1H 2140+433		J2142+4335	—	—	CV	6, 7
338	RU Peg; 2211+124		J2214+1242	—	—	CV	6, 7
339	V709 Cas; RX J0028.8+5917; 4U 0027+59; 1H 0025+588		J0028+5917	—	—	CV	6, 7
340	H 0204-023; 1H 0201-029		J0203-0243	—	—	CV	6

341	TT Ari; BD+14 34; 1H 0157+1421		J0206+1517	—	—	CV	6
342	1H 0253+193; XY Ari; MBM 12		J0256+1926	—	—	CV	6, 7
343	GK Per; N Per 1901		J0331+4354	—	—	CV	6, 7
344	H 0349+17; V471 Tau; BD +16 516		J0350+1714	—	—	CV	6
345	V1062 Tau; 1H 0459+246		J0502+2445	—	—	CV	6
346	Col1; UU Col; RX J0512-3241		J0512-3241	—	—	CV	6, 7
347	2A 0526-328; TV Col; 1H 0527-328		J0529-3249	—	—	CV	6, 7
348	TW Pic; H0534-581; 1H 0538-577		J0534-5801	—	—	CV	6, 7
349	TX Col; 1H 0542-407		J0543-4101	—	—	CV	6, 7
350	Aur1; V405 Aur; RX J0558+5353		J0558+5353	—	—	CV	6, 7
351	Men1; 1H 0551-819; H 0616-818		J0611-8149	—	—	CV	6
352	BG Cmi; 3A 0729+103		J0731+0956	—	—	CV	6, 7
353	Car1; RX J0744.9-5257		J0744-5257	—	—	CV	6
354	PQ Gem; RX J0751+1444; RE J0751+144		J0751+1444	—	—	CV	6, 7
355	RX J0757.0+6306; 1RXS J075700.5+630602		J0757+6305	—	—	CV	6
356	Pyx2; WX Pyx; 1E 0830.9-2238		J0833-2248	—	—	CV	6
357	VZ Pyx1; 1H 0857-242; 1H 0857-242		J0859-2428	—	—	CV	6, 7
358	DO Dra; YY Dra; E1140.8+7158; PG 1140+719; 3A 1148+719; PG 1140+719		J1143+7141	—	—	CV	6, 7
359	RX J1238-38		J1238-3845	—	—	CV	6
360	EX Hya; 4U 1249-28; 1H 1251-291		J1252-2914	—	—	CV	6, 7
361	V795 Her; SVS 2613; PG 1711+336		J1712+3331	—	—	CV	6, 7
362	Oph3; RX J1712.6-2414		J1712-2414	—	—	CV	6, 7
363	V533 Her; N Her 1963		J1814+4151	—	—	CV	6, 7
364	V1223 Sgr; 4U1849-31; 1H 1853-312		J1855-3109	—	—	CV	6, 7
365	AE Aqr; 2037-010		J2040-0052	—	—	CV	6, 7
366	FO Aqr; H2215-086		J2217-0821	—	—	CV	6, 7
367	RX J2353.0-3852		J2353-3851	—	—	CV	6, 7
368	AH Eri		J0422-1321	—	—	CV	6, 7
369	KR Aur		J0615+2835	—	—	CV	6, 7

370	BZ Cam; 0623+71		J0629+7104	—	—	CV	6, 7
371	CP Pup; N Pup 1942		J0811-3521	—	—	CV	6, 7
372	H 0928+500; 0928+5004; 1H 0927+501		J0932+4950	—	—	CV	6, 7
373	RW Sex; BD-7 3007		J1019-0841	—	—	CV	6, 7
374	T Leo; BD+4 2506a; 1H 1130+043; PG 135+036		J1138+0322	—	—	CV	6, 7
375	GQ Mus; N Mus 1983		J1152-6712	—	—	CV	6, 7
376	T CrB; HD 143454; 1559+259		J1559+2555	—	—	CV	6
377	U Sco; N Sco 1987; 1619-178		J1622-1752	—	—	CV	6, 7
378	V1017 Sgr; N Sgr 1919; 1832-294		J1832-2923	—	—	CV	6, 7
379	V603 Aql; N Aql 1918; 1846+005		J1848+0035	—	—	CV	6, 7
380	H 1933+510; 1H 1929+509		J1934+5107	—	—	CV	6, 7
381	EC 19314-5915; V345 Pav; 1H 1930-589		J1935-5850	—	—	CV	6
382	V794 Aql; 2017-037		J2017-0339	—	—	CV	6, 7
383	V Sge; 2020+211; 2018+209		J2020+2106	—	—	CV	6, 7
384	HR Del; N Del 1967		J2042+1909	—	—	CV	6, 7
385	UX Uma; 1334+521		J1336+5154	—	—	CV	6, 7
386	V2301 Oph; 1H 1752+081		J1800+0810	—	—	CV	6, 7
387	RX J0132.7-6554; Hyi		J0132-6554	—	—	CV	6, 7
388	BL Hyi; H 0139-68; 1H 0136-681		J0141-6753	—	—	CV	6, 7
389	RX J0203.8+2959; Tri		J0203+2959	—	—	CV	6, 7
390	WW Hor; EXO 0234-523		J0236-5219	—	—	CV	6, 7
391	EF Eri; 3A; 2A 0311-227; 1H 0311-227		J0314-2235	—	—	CV	6, 7
392	VY For; EXO 032957-2606.9		J0332-2556	—	—	CV	6, 7
393	Cae1; RS Cae; RX J0453-4213		J0453-4213	—	—	CV	6, 7
394	V1309 Ori; RX J0515+0104; RX J0515.6+0105		J0515+0104	—	—	CV	6, 7
395	Pic1; UW Pic; RX J0531-4624		J0531-4624	—	—	CV	6, 7
396	H 0538+608; BY Cam; 1H 0533+607		J0542+6051	—	—	CV	6
397	RX J0719.2+6557; 1RXS J071913.4+655734		J0719+6557	—	—	CV	6
398	VV Pup; 1E 0812-1854		J0815-1903	—	—	CV	6, 7
399	EU Cnc; M 67; 0851+118		J0851+1146	—	—	CV	6, 7

400	Hya4; MN Hya; RX 0929.1-2404		J0929-2405	—	—	CV	6, 7
401	RE J1002-19; Hya		J1002-1925	—	—	CV	6, 7
402	Leo; RX J1015.5+0904		J1015+0904	—	—	CV	6, 7
403	E 1013-477; KO Vel; 1H 1006-472		J1015-4758	—	—	CV	6, 7
404	FH UMa; UMa 9; RX J1047.1+6335		J1047+6335	—	—	CV	6, 7
405	EK Uma; 1E1048.5+5421; 1H 1046+547		J1051+5404	—	—	CV	6, 7
406	AN Uma; PG 1101+453		J1104+4503	—	—	CV	6, 7
407	ST Lmi; CW 1103+254		J1105+2506	—	—	CV	6, 7
408	AR UMa; 1ES 1113+432; 1H 1120+423		J1115+4258	—	—	CV	6, 7
409	DP Leo; 1E 1114+182		J1117+1757	—	—	CV	6, 7
410	Cen3; RX J1141.3-6410		J1141-6410	—	—	CV	6
411	EU Uma; RE J1149+28		J1149+2845	—	—	CV	6, 7
412	EV Uma; RX J1307+535; RE J1307+535		J1307+5351	—	—	CV	6, 7
413	E 1405-451; V834 Cen; 1H 1404-450		J1409-4517	—	—	CV	6
414	MR Ser; PG 1550+191		J1552+1856	—	—	CV	6, 7
415	RX J1724.0+4114		J1727+4114	—	—	CV	6
416	Her5; V884 Her; RX J1802.1+1804; WGA J1802.1+1804		J1802+1804	—	—	CV	6, 7
417	H 1816+49; AM Her; 1H 1814+498		J1816+4952	—	—	CV	6, 7
418	V347 Pav; RX J1844-74; RE J1844-74		J1844-7418	—	—	CV	6, 7
419	EP Dra; 1H 1903+689; H 1907+690		J1907+6908	—	—	CV	6
420	RX J1914.4+2456		J1914+2456	—	—	CV	6, 7
421	QS Tel; RX J1938.6-4912; RE J1938.6-4912		J1938-4612	—	—	CV	6, 7
422	QQ Vul; E2003+225; H 2005+22		J2005+2239	—	—	CV	6, 7
423	V349 Pav; Drissen V211b		J2008-6527	—	—	CV	6, 7
424	RX J2022.6-3954; V4738 Sgr		J2022-3954	—	—	CV	6
425	HU Aqr; RX J2107.9-0518; RE J2107.9-0518		J2107-0517	—	—	CV	6, 7
426	V1500 Cyg; N Cyg 1975; 2109+479		J2111+4809	—	—	CV	6, 7
427	RX J2115.7-5840; EUVE J2115-58.6		J2115-5840	—	—	CV	6, 7
428	CE Gru; Grus IV		J2137-4342	—	—	CV	6, 7

429	AX J2315-592; IRAS 23128-5919		J2315-5910	—	—	CV	6
430	T Pyx; HV 3348; 1H 0908-326		J0904-3222	—	—	CV	6, 7
431	WX Hyi; 0208-635		J0209-6318	—	—	CV	6, 7
432	VW Hyi; AN 11.1932		J0409-7118	—	—	CV	6, 7
433	YZ Cnc		J0810+2808	—	—	CV	6, 7
434	SU Uma; PG 0808+627; 1H 0811+625		J0812+6236	—	—	CV	6, 7
435	V436 Cen; 1E 1111-3724		J1114-3740	—	—	CV	6, 7
436	EK TrA; 1509-649		J1514-6505	—	—	CV	6
437	IX Vel; CPD-48 1577		J0815-4913	—	—	CV	6, 7
438	EI Uma; PG 0834+488; 1H 0832+488		J0838+4838	—	—	CV	6, 7
439	BV Cen		J1331-5458	—	—	CV	6, 7
440	AB Dra		J1949+7744	—	—	CV	6, 7
441	EY Cyg		J1954+3221	—	—	CV	6, 7
442	V3885 Sgr; CD-4214462; 1944-421		J1947-4200	—	—	CV	6, 7
443	WW Cet; 1H 2357-126		J0011-1128	—	—	CV	6, 7
444	RX And; 1E 0101+4101		J0104+4117	—	—	CV	6, 7
445	HL Cma; 1E 0643-1648		J0645-1651	—	—	CV	6, 7
446	Tau3; RX J0459.7+1929		J0459+1926	—	—	CV	6
447	RX J0502.8+1624		J0502+1624	—	—	CV	6
448	Lanning 10; V363 Aur		J0533+3659	—	—	CV	6, 7
449	RX J1326.9+4532; DE CVn		J1326+4532	—	—	CV	6
450	LY Hya2; 1329-294		J1331-2940	—	—	CV	6, 7
451	LX Ser; 1536+190		J1538+1852	—	—	CV	6, 7
452	V825 Her; PG 1717+413		J1718+4115	—	—	CV	6, 7
453	V380 Oph; 1747+061		J1750+0605	—	—	CV	6, 7
454	V827 Her; Nova Her 1991; 1844+122		J1846+1222	—	—	CV	6
455	V1974 Cyg; N Cyg 1992		J2030+5237	—	—	CV	6, 7
456	Cyg6; RX J2123.7+4217		J2123+4217	—	—	CV	6
457	A0538-66; X 0535-668		J0538-6652	—	—	HMXB	6
458	GS 1843-02; GRO J1849-03; X1845-024		J1849-0318	—	—	HMXB	6

459	V Tuc; HD 5148		J0051-7159	—	—	LMXB	6, 8
460	U Cep; HD 5679		J0102+8152	—	—	LMXB	6, 8
461	DS And; NGC 752		J0157+3804	—	—	LMXB	6, 8
462	DO Cas; HD 16506		J0241+6033	—	—	LMXB	6, 8
463	RZ Cas; HR 815; HD 17138; 1E 0244+694		J0248+6938	—	—	LMXB	6, 8
464	Beta Per; Algol		J0308+4057	—	—	LMXB	6, 8
465	Lambda Tau; SAO 93719		J0400+1229	—	—	LMXB	6, 8
466	IM Aur; HD 33853; BV 267		J0515+4624	—	—	LMXB	6, 8
467	AR Aur; HR 1728		J0518+3346	—	—	LMXB	6, 8
468	AW Cam; HD 48049; BV 412; SAO 013951		J0647+6937	—	—	LMXB	6, 8
469	S Cnc; HD74307; BD19 2090		J0843+1902	—	—	LMXB	6, 8
470	TX UMa; HD 43033		J1045+4533	—	—	LMXB	6, 8
471	TT Hya; MS 1110-262; HD 97528		J1113-2627	—	—	LMXB	6, 8
472	Z Dra; BD+73 0533		J1145+7215	—	—	LMXB	6, 8
473	1E 1247.0-0548; SAO 138983		J1249-0604	—	—	LMXB	6
474	SS Cen; HD 114720		J1313-6409	—	—	LMXB	6, 8
475	Delta Lib; HD 132742; INCA 2609		J1500-0831	—	—	LMXB	6, 8
476	U CrB; HD 136175		J1518+3138	—	—	LMXB	6, 8
477	TW Dra; SAO 016767; HV 3274		J1533+6354	—	—	LMXB	6, 8
478	Alpha CrB; Alphekka; HR 5793; HD 139006		J1534+2642	—	—	LMXB	6, 8
479	R Ara; HD 149730; SAO 244037		J1639-5659	—	—	LMXB	6, 8
480	V1010 Oph; HD 151676; HR 6240; SAO 160116		J1649-1540	—	—	LMXB	6, 8
481	AI Dra; CSV 101620		J1656+5241	—	—	LMXB	6, 8
482	V846 Oph; HD 316070		J1739-2851	—	—	LMXB	6, 8
483	XZ Sgr; HD 168710; HV 3074		J1822-2514	—	—	LMXB	6, 8
484	BS Sct; NGC 6705; SVS 91		J1852-0614	—	—	LMXB	6, 8
485	RS Vul; HD 180949; SAO 087035		J1917+2226	—	—	LMXB	6, 8
486	BE Vul; HD340201; SVS 475; SAO 088663		J2025+2722	—	—	LMXB	6, 8
487	DF Peg; SAO 107496		J2154+1433	—	—	LMXB	6, 8
488	DI Peg; SAO 108667		J2332+1458	—	—	LMXB	6, 8

489	1E 1740.7-2942; Great Annihilator		J1744-2943	—	—	LMXB	6
490	EXO 1846-031		J1849-0308	—	—	LMXB	6
491	Zeta And; HR 215; BD23 0106; SAO 074267; HR 215		J0047+2416	—	—	LMXB	6, 8
492	CF Tuc; HD 5303		J0053-7439	—	—	LMXB	6, 8
493	UV Psc, HD 7700; SAO 109778		J0116+0648	—	—	LMXB	6, 8
494	BI Cet; HD 8358; 1ES0120+004		J0122+0042	—	—	LMXB	6, 8
495	AR Psc; HD 8357; 1H 0123+075		J0122+0725	—	—	LMXB	6, 8
496	TZ Tri A; HR 642A		J0212+3018	—	—	LMXB	6, 8
497	LX Per; SAO 38651		J0313+4806	—	—	LMXB	6, 8
498	1E 0315.7-1955		J0318-1944	—	—	LMXB	6
499	UX Ari; H 0324+28		J0325+2842	—	—	LMXB	6, 8
500	IX Per; HD 22124		J0335+3201	—	—	LMXB	6, 8
501	V711 Tau; HR 1099; 1H 0327+000		J0336+0035	—	—	LMXB	6, 8
502	V837 Tau; HD 22403; BD25 0580		J0337+2559	—	—	LMXB	6, 8
503	RZ Eri; HD 30050		J0443-1039	—	—	LMXB	6, 8
504	HR 1623; 12 Cam; 1H 0501+592		J0506+5901	—	—	LMXB	6
505	1E0505.0-0527; MS0505.0-0527		J0507-0524	—	—	LMXB	6
506	Alpha Aur; HD 34029; 1E 0513+459; Capella A+B		J0516+4559	—	—	LMXB	6, 8
507	AB Dor; HD 36705; 1E052840-6429		J0528-6527	—	—	LMXB	6
508	CQ Aur; HD 250810		J0603+3119	—	—	LMXB	6, 8
509	SV Cam; EXO 0630+823; H 0630+82		J0641+8216	—	—	LMXB	6, 8
510	VV Mon; BD-5 1935		J0703-0544	—	—	LMXB	6, 8
511	SS Cam; HV 3100		J0716+7320	—	—	LMXB	6, 8
512	AR Mon; HD 57364		J0720-0515	—	—	LMXB	6, 8
513	AE Lyn; HD 65626; HR 3119; SAO 026634		J0802+5716	—	—	LMXB	6, 8
514	RU Cnc; 0834+237		J0837+2333	—	—	LMXB	6, 8
515	RZ Cnc; HD 73343; SAO 60954		J0839+3147	—	—	LMXB	6, 8
516	TY Pyx; HD 77137; RE 0859-274		J0859-2749	—	—	LMXB	6, 8

517	WY Cnc; CSV 1397; S 4751		J0901+2641	—	—	LMXB	6, 8
518	XY UMa; SAO 27143		J0909+5429	—	—	LMXB	6, 8
519	LR Hya; HD 91816; SAO 156090		J1036-1154	—	—	LMXB	6, 8
520	1E 1127.9-1502; MS 1127.8-1502; HD100022; SAO156720		J1130-1519	—	—	LMXB	6
521	EXO 113348-3746; V858 Cen; SAO 202618		J1136-3802	—	—	LMXB	6
522	RW Uma; 11353+525		J1140+5159	—	—	LMXB	6
523	93 Leo; HD 102509; SAO 81998		J1147+2013	—	—	LMXB	6, 8
524	DK Dra; HR 4665; HD 106677; 1ES 1213+728		J1215+7233	—	—	LMXB	6, 8
525	IL Com; HD 108102; MS 1222+258		J1225+2533	—	—	LMXB	6, 8
526	HZ Com; BD+25 2511		J1229+2431	—	—	LMXB	6, 8
527	UX Com; BV 295		J1301+2837	—	—	LMXB	6, 8
528	RS CVn; HD 114519; 13083+382		J1310+3556	—	—	LMXB	6, 8
529	BL CVn; HD 115782; SAO 063466		J1318+3326	—	—	LMXB	6, 8
530	BH CVn; HR 5110		J1334+3710	—	—	LMXB	6, 8
531	RV Lib; HD 128171		J1435-1802	—	—	LMXB	6, 8
532	SS Boo; BD+39 2849		J1513+3834	—	—	LMXB	6, 8
533	TZ CrB; sigma CrB; RE 1614+335		J1614+3351	—	—	LMXB	6, 8
534	WW Dra; HD 150708; HV 3398		J1639+6042	—	—	LMXB	6, 8
535	epsilon UMi; HD 153751		J1645+8202	—	—	LMXB	6, 8
536	V792 Her; HD 155638; H 1708+49		J1710+4857	—	—	LMXB	6, 8
537	V824 Ara; HD 155555; EXO 171224-6653.9		J1717-6656	—	—	LMXB	6, 8
538	V965 Sco; HD 158393; SAO 208895; 1727-336		J1730-3339	—	—	LMXB	6, 8
539	Z Her; Hyades; INCA 1189		J1758+1508	—	—	LMXB	6, 8
540	MM Her; HD 341475; SAO 085600		J1758+2208	—	—	LMXB	6, 8
541	V772 Her Aab; HD 175590A; SAO 085723		J1805+2126	—	—	LMXB	6, 8
542	PW Her; S 4777		J1810+3157	—	—	LMXB	6, 8
543	AW Her; HD 348635; SVS 163		J1825+1817	—	—	LMXB	6, 8
544	V1430 Aql; 1E 1919+0427		J1921+0432	—	—	LMXB	6
545	V1817 Cyg; HR 7428; HD 184398/9		J1931+5543	—	—	LMXB	6, 8

546	V1764 Cyg HD 185151		J1936+2753	—	—	LMXB	6, 8
547	CG Cyg; BD+34 4217		J2058+3510	—	—	LMXB	6, 8
548	ER Vul; HD 200391; SAO 089396; 1 ES 2100+276		J2102+2748	—	—	LMXB	6, 8
549	HR 8170; HD 203454		J2121+4020	—	—	LMXB	6, 8
550	AD Cap; CSV 5452; HD206046		J2139-1600	—	—	LMXB	6, 8
551	FF Aqr; SAO 145804; BD -3 5357		J2200-0244	—	—	LMXB	6, 8
552	RT Lac; HD 209318; SAO 051563		J2201+4353	—	—	LMXB	6, 8
553	AR Lac; HD 210334; 1H 2207+455		J2208+4544	—	—	LMXB	6, 8
554	RT And; BD+52 3383a		J2311+5301	—	—	LMXB	6, 8
555	SZ Psc; HD 219113; INCA 1263; SAO 128041		J2313+0240	—	—	LMXB	6, 8
556	KT Peg; HD 222317; SAO 091405		J2339+2814	—	—	LMXB	6, 8
557	HR 9024; 2350+364		J2349+3625	—	—	LMXB	6, 8
558	1H 2354+285; II Pegasi; A 0000+28		J2355+2838	—	—	LMXB	6
559	HV 1554; RX J0527.8-6954		J0527-6921	—	—	LMXB	6
560	CAL 87; LHG 87; 1E; LMC 363	Source in LMC	J0546-7108	—	—	LMXB	6, 7
561	B0056.8-7164; N67?		J0058-7135	—	—	LMXB	6
562	OAO; V861 Sco; HD 152667		J1656-4049	—	—	LMXB	6
563	RX J0002+6246; G117.7+0.6		J0002+6246	—	—	NS	6
564	PSR J0117+5914; PSR B0114+58		J0117+5914	—	B0114+58	NS	6, 11
565	PSR J0631+10		J0628+1038	—	—	NS	6
566	G290.1-08; 2EG 1103-6106; PSR J1105-6107		J1105-6107	—	—	NS	6, 11
567	SNR 332.4-00.4; AX J161730-505505; 1E 161348-5055; PSR J161730-5055; RCW 103		J1617-5055	—	—	NS	6, 11
568	M4; PSR B1620-26		J1623-2631	—	B1620-26	NS	6, 1
569	PSR 1642-03; PSR J1645-0317		J1645-0317	—	—	NS	6
570	1RXS J170849.0-400910		J1708-4009	—	—	NS	6
571	PSR J1740-3015; PSR B 1737-30		J1740-3015	—	—	NS	6
572	4U 1743-29; 1H 1744-293		J1748-2924	—	—	LMXB	6, 53
573	AX J1811.5-1926; SNR G11.2-0.3		J1811-1926	—	—	NS	6, 11

574	PSR J1917+1353; PSR B1915+13		J1917+1353	—	—	NS	6
575	PSR B1937+21		J1939+2134	—	B1937+21	NS	6, 11, 25, 26
576	1WGA J1958.2+3232		J1958+3232	—	—	HMXB	6
577	PSR J2322+2057		J2322+2057	—	—	NS	6, 1
578	Beta Ceti; 0044-180		J0043-1759	—	—	NS	6
579	RX J1856.5-3754		J1856-3754	—	—	NS	6
580	BG Psc; HD 9902; EXO 013425+2027		J0137+2042	—	—	LMXB	6
581	MS 0244.8-0042; SAO 130113		J0247+0037	—	—	LMXB	6
582	sigma Gem; HD 62044; 1H 0741+289		J0743+2853	—	—	LMXB	6
583	2A 1052+606; DM Uma; 1H 1051+607; SAO 015338		J1055+6028	—	—	LMXB	6
584	HU Vir; HD 106225		J1213-0904	—	—	LMXB	6
585	KN UMa; RX J1239.8+5511; GSC 3844.0317		J1239+5511	—	—	LMXB	6
586	PG 1413+010		J1416+0046	—	—	LMXB	6
587	MS 1520.2+2548; UV CrB; SAO 83795		J1522+2537	—	—	LMXB	6
588	MS 1520.7-0625; GX Lib; SAO 140499		J1523-0636	—	—	LMXB	6
589	DR Dra; 29 Dra; HD 160538; 1733+742		J1732+7413	—	—	LMXB	6
590	UU Sge		J1942+1705	—	—	LMXB	6
591	HK Lac; 22049+472		J2204+4714	—	—	LMXB	6
592	H 2311+77; HD 220140; 1H 2313+783; EXO 23180+7873		J2319+7900	—	—	LMXB	6
593	lambda And; HD 222107; 1H 2336+462		J2337+4627	—	—	LMXB	6
594	V773 Tau; HD 283447		J0414+2812	—	—	TTS	6
595	LkCa 7; 041636+2743		J0419+2749	—	—	TTS	6
596	BP Tau; 04161+2859		J0419+2906	—	—	TTS	6
597	T Tau; 04190+1924		J0421+1932	—	—	TTS	6
598	HDE 283572; SAO 76567		J0421+2818	—	—	TTS	6
599	RY Tau; 04188+2819		J0421+2826	—	—	TTS	6
600	DF Tau; 04240+2535		J0427+2542	—	—	TTS	6
601	DH Tau; 04267+2626X1		J0429+2632	—	—	TTS	6

602	UX TauA; 04271+1807X2		J0430+1813	—	—	TTS	6
603	TAP 40; 042835+1700		J0431+1706	—	—	TTS	6
604	TAP 41; 042916+1751		J0432+1757	—	—	TTS	6
605	V826 Tau; 0429+179		J0432+1801	—	—	TTS	6
606	V827 Tau; 0429+182		J0432+1820	—	—	TTS	6
607	GI Tau; 04305+2414X1		J0433+2421	—	—	TTS	6
608	GK Tau; 04305+2414X2		J0433+2421	—	—	TTS	6
609	V830 Tau; 0430+274		J0433+2434	—	—	TTS	6
610	AA Tau; 04318+2422		J0434+2428	—	—	TTS	6
611	DN Tau; 04324+2408		J0435+2414	—	—	TTS	6
612	GM Aur; 04519+3017		J0455+3021	—	—	TTS	6
613	SU Aur; 04528+3029		J0455+3034	—	—	TTS	6
614	TAP 57 NW; 045251+3016		J0456+3021	—	—	TTS	6
615	V836 Tau; 0500+253		J0503+2523	—	—	TTS	6
616	RW Aur A; IRAS 05046+3020		J0507+3024	—	—	TTS	6
617	V1321 Ori; Par 1724		J0535-0508	—	—	TTS	6
618	WD 0232+035; Feige 24		J0235+0344	—	—	WD	6
619	RE 2013+400		J2013+4002	—	—	WD	6
620	RX J2117.1+3412; PG 1159; V2027 Cyg		J2117+3412	—	—	WD	6
621	1E0035.4-7230; SMC 13	Source in SMC	J0037-7214	—	—	???	6, 7
622	M33 X-8		J0133+3039	—	—	???	6
623	1H 0538-641; LMC X-3	Source in LMC	J0538-6404	—	—	HMXB	6
624	R140a2 (WN6); 30 Doradus; HD 269919a		J0538-6905	—	—	???	6
625	GRS 1758-258		J1801-2547	—	—	???	6
626	Nova Aql 1992; GRS 1915+105		J1915+1056	—	—	???	6
627	PSR J1907+0919; SGR 1900+14		J1907+0918	—	—	???	6
628	ROSAT 58; Einstein 69; M31		J0042+4115	—	—	???	6
629	ROSAT 60; Einstein 71; M31		J0042+4116	—	—	???	6
630	PSR B1257+12		J1300+1240	—	B1257+12	???	6, 1
631	PSR B1534+12; PSR J1537+1155		J1537+1155	—	B1534+12	???	6, 1

632	Terzan 5; XB 1745-25; PSR 1744-24A		J1748-2446	—	B1744-24A	LMXB	6, 54
633	GS 1843+009; GPS 1840+01		J1845+0050	—	—	???	6
634	PSR J2019+2425		J2019+2425	—	—	???	6, 1
635	FF And; Gliese 29.1; RE 0042+353		J0042+3533	—	—	???	6
636	V405 And; BY Dra; RX J0222.4+4729		J0222+4729	—	—	???	6
637	CC Eri; HD 16157		J0234-4347	—	—	???	6
638	YY Gem; Castor C; 1H 0729+316		J0734+3152	—	—	???	6
639	YZ CMi; GJ 285; 1H 0743+037		J0744+0333	—	—	???	6
640	EQ Vir		J1334-0820	—	—	???	6
641	CM Dra; GLIESE 630.1; 1634+571		J1634+5709	—	—	???	6
642	AU Mic; HD 197481; SAO 212402		J2045-3120	—	—	???	6
643	HD 218738; SAO 52753		J2309+4757	—	—	???	6
644	HD 185510; 1H 1934-063		J1939-0603	—	—	???	6
645	1ES 1328+244; FK Com; HD 117555		J1330+2413	—	—	???	6
646	RE 0720-318; EUVE J0720-317		J0720-3146	—	—	???	6
647	QR And; RX J0019.8+2156		J0019+2156	—	—	???	6, 7
648	RX J0513.9-6951; HV 5682; LMC 65	Source in LMC	J0513-6951	—	—	LMXB	6, 7
649	CAL 83; LHG 83; LMC 348	Source in LMC	J0543-6822	—	—	LMXB	6, 7
650	MR Vel; RX J0925-4758		J0925-4758	—	—	???	6, 7
651	AG Dra; BD+67 922; 1601+669		J1601+6648	—	—	???	6
652	eta Car; HD 93308; 1045-597		J1045-5941	—	—	???	6
653	EZ CMa; HD 50896; 0654-239		J0654-2355	—	—	???	6
654	HD 193793; V1687 Cyg		J2020+4354	—	—	???	6
655	YY Eri; 0409-106		J0412-1028	—	—	???	6
656	W Uma; 0943+560		J0943+5557	—	—	???	6
657	XY Leo; 0959+176		J1001+1724	—	—	???	6
658	44i Boo; HD 133640		J1503+4739	—	—	???	6
659	RE J2037+753; VW Cep; 1H 2041+756		J2037+7535	—	—	???	6
660	1E 2119.7+1655		J2122+1708	—	—	???	6
661	MS 1211.8+1206; AH Vir; SAO 100003		J1214+1149	—	—	???	6

662	V829 Her; 1E 1653.9+3515		J1655+3510	—	—	???	6
663	MS 1806.0+6944		J1805+6945	—	—	???	6
664	RE0044+09; BD+08 102		J0044+0932	—	—	?	6
665	RX J0103.8-7254; 1J 0103-762; SMC 106	Source in SMC	J0103-7254	—	—	?	6
666	M33 X-7		J0133+3032	—	—	?	6
667	theta1 Ori C; HD 37022; HR 1895; 0538-054		J0535-0523	—	—	?	6
668	PSR J0537-6910; N157B; SNR 0539-69.1	Source in LMC	J0537-6909	—	—	NS	6, 11
669	1E 1751+7046; ET Dra; BD70 959		J1750+7045	—	—	?	6
670	RR Tel; HV 3181; 2004-557		J2004-5543	—	—	?	6
671	2E 206; AX J0051.6-7311	Source in SMC	J0051-7310	—	—	HMXB	9, 10
672	XTE J0052-723	Source in SMC	J0052-7220	—	—	HMXB	9, 10
673	AX J0043-737	Source in SMC	J0042-7340	—	—	HMXB	9, 10
674	AX J0049.5-7323; RX J0049.7-7323	Source in SMC	J0049-7323	—	—	HMXB	9, 10
675		Source in SMC	J0052-7233	—	—	HMXB	10
676	XMMU J005605.2-722200	Source in SMC	J0056-7222	—	—	HMXB	10
677	CXOU J005750.3-720756	Source in SMC	J0057-7207	—	—	HMXB	10
678		Source in SMC	J0057-7219	—	—	HMXB	10
679	AX J0057.4-7325	Source in SMC	J0057-7325	—	—	HMXB	9, 10
680	CXOU J010043.1-721134	Source in SMC	J0100-7211	—	—	NS	10, 17, 32
681		Source in SMC	J0101-7211	—	—	HMXB	10
682	2E 0101.5-7225; AX J0103-722	Source in SMC	J0103-7208	—	—	HMXB	9, 10
683	XTE J0103-728	Source in SMC	J0103-7241	—	—	NS	10
684		Source in SMC	J0119-7311	—	—	NS	10
685	PSR J0030+0451		J0030+0451	J0030+0451	—	NS	11
686	PSR J0205+6449	in SNR 3C 58	J0205+6449	J0205+6449	—	NS	11
687	PSR J1024-0719		J1024-0719	J1024-0719	—	NS	11
688	PSR J1119-6127	SNR G292.2-0.5	J1119-6127	J1119-6127	—	NS	11, 21
689	PSR J1124-5916	SNR G292.0+1.8	J1124-5916	J1124-5916	—	NS	11, 19
690	PSR J1420-6048	Kookaburra	J1420-6048	J1420-6048	—	NS	11

691	PSR J1744-1134		J1744-1134	J1744-1134	—	NS	11
692	PSR B1757-24		J1800-2450	—	B1757-24	NS	11
693	PSR J1846-0258	in SNR Kes 75 (G29.7-0.3)	J1846-0258	J1846-0258	—	NS	11, 20
694	PSR B1853+01		J1856+0113	—	B1853+01	NS	11
695	PSR J2229+6114		J2229+6114	J2229+6114	—	NS	11
696	XTE J0929-314		J0929-3123	—	—	LMXB	12, 29
697	XTE 1751-305		J1751-3037	—	—	LMXB	13, 29, 48, 51
698	XTE J1807-294		J1806-2924	—	—	LMXB	14, 30, 44, 50
699	XTE J1814-338		J1813-3346	—	—	LMXB	15, 31, 45
700	PSR J0111-7317; XTE J0111-732; (HFP2000) 446		J0111-7316	J0111-7317	—	HMXB	16, 32
701	GS 1843+00; Ginga		J1845+0051	—	B1843+00	HMXB	16
702	J0537.7-7034; in LMC	Source in LMC	J0537-7034	J0537.7-7034	—	LMXB	16
703	Granat B1743-290		J1746-2903	—	B1743-290	LMXB	16
704	SAX J1747.0-2853; XB 1743-29		J1747-2852	J1747.0-2853	—	LMXB	16
705	GRB 970228; J0501.7+1146		J0501+1146	J0501.7+1146	—	NS	16
706	PSR J1845-0434; PSR B1842-04		J1845-0434	J1845-0434	B1842-04	NS	16
707	RX J0356.5-3641; EUVE J0356-36.6; 1E 0354.6-3650		J0356-3641	J0356.5-3641	—	LMXB	16
708	B0240-002; APG 37; NGC 1068		J0242-0000	—	B0240-002	AGN	16
709	ESO 434-40		J0947-3056	—	B0945-307	AGN	16
710	NGC 4507		J1235-3954	—	B1232-396	AGN	16
711	NGC 4945		J1305-4928	—	B1304-497	AGN	16
712	Cen A; NGC 5128		J1325-4301	—	B1322-427	AGN	16
713	NGC 7582		J2318-4222	—	B2315-426	AGN	16
714	3C273		J1229+0203	—	B1226+023	QSO	16
715	SAX 1744.7-2916		J1744-2916	J1744.7-2916	—	?	16
716	Granat B1747-347		J1750-3412	—	B1747-341	?	16
717	J0153+7442		J0153+7442	J0153+7442	—	CV	7

718	J0439-6809		J0439-6809	J0439-6809	—	CV	7
719	V1425 Aql; N Aql 1995		J1905-0142	—	—	CV	7
720	PSR J1930+1852	in SNR G54.1+03	J1930+1852	—	—	NS	18
721	47 Tuc C; PSR B0021-72C; PSR J0023-7204C		J0023-7204	J0023-7204C	B0021-72C	NS	23, 24
722	47 Tuc D; PSR B0021-72D; PSR J0024-7204D		J0024-7204D	J0024-7204D	B0021-72D	NS	23, 24
723	47 Tuc E; PSR B0021-72E; PSR J0024-7205E		J0024-7205	J0024-7205E	B0021-72E	LMXB	23, 24
724	47 Tuc F; PSR B0021-72F; PSR J0024-7204F		J0024-7204F	J0024-7204F	B0021-72F	NS	23, 24
725	47 Tuc G; PSR B0021-72G; J0024-7204G		J0024-7204G	J0024-7204G	B0021-72G	NS	23, 24
726	47 Tuc H; PSR B0021-72H; PSR J0024-7204H		J0024-7204H	J0024-7204H	B0021-72H	LMXB	23, 24
727	47 Tuc I; PSR B0021-72I; PSR J0024-7204I		J0024-7204I	J0024-7204I	B0021-72I	LMXB	23, 24
728	47 Tuc J; PSR B0021-72J; PSR J0023-7203J		J0023-7203	J0023-7203J	B0021-72J	LMXB	23, 24
729	47 Tuc L; PSR B0021-72L; PSR J0024-7204L		J0024-7204L	J0024-7204L	B0021-72L	NS	23, 24
730	47 Tuc M; PSR B0021-72M; PSR J0023-7205M		J0023-7205	J0023-7205M	B0021-72M	NS	23, 24
731	47 Tuc N; PSR B0021-72N; PSR J0024-7204N		J0024-7204N	J0024-7204N	B0021-72N	NS	23, 24
732	47 Tuc O; PSR B0021-72O; PSR J0024-7204O		J0024-7204O	J0024-7204O	B0021-72O	LMXB	23, 24
733	47 Tuc Q; PSR B0021-72Q; PSR J0024-7204Q		J0024-7204Q	J0024-7204Q	B0021-72Q	LMXB	23, 24
734	47 Tuc S; PSR B0021-72S; PSR J0024-7204S		J0024-7204S	J0024-7204S	B0021-72S	LMXB	23, 24
735	47 Tuc T; PSR B0021-72T; PSR J0024-7204T		J0024-7204T	J0024-7204T	B0021-72T	LMXB	23, 24
736	47 Tuc U; PSR B0021-72U; PSR J0024-7203U		J0024-7203	J0024-7203U	B0021-72U	LMXB	23, 24
737	6397A; PSR B1736-53; PSR J1740-5340		J1740-5340	J1740-5340	B1736-53	LMXB	23, 24, 28
738	PSR B2224+65; PSR J2225+6535	Guitar Nebula	J2225+6535	—	B2224+65	NS	27
739	PSR J2043+2740		J2043+2740	J2043+2740	—	NS	27
740	4U 0628-28; PSR B0628-28; PSR J0630-2834		J0630-2834	—	B0628-28	NS	27
741	PSR 1813-36; PSR 1817-3618		J1817-3618	—	B1813-36	NS	27
742	1XMMU J005921.0-722317	Source in SMC	J0059-7223	—	—	HMXB	32
743	1XMMU J004723.7-731226	Source in SMC	J0047-7312	—	—	HMXB	32
744	maybe: RX J0051.8-7310	Source in SMC	J0051-7310B	—	—	NS	33
745	maybe: RX J0051.8-7310	Source in SMC	J0051-7310C	—	—	NS	33
746	XTE J0055-727	Source in SMC	J0055-7242	—	—	NS	32

747	maybe RX J0055.4-7210	Source in SMC	J0055-7210	—	—	NS	32
748	RX J0054.9-7245, AX J0054.8-7244, CXOU J005455.6-724510, XMMU J005455.4-724512	Source in SMC	J0054-7245	—	—	HMXB	32
749		Source in SMC	J0053-7227	—	—	NS	32
750	RX J0055.2-7238	Source in SMC	J0055-7238	—	—	NS	32
751	XTE SMC95	Source in SMC	J0053-7249	—	—	HMXB	34
752	AX J1845-0258; PSR 1844-0258, PSR 1845-0258	in SNR G29.6+0.1	J1844-0257	—	—	NS	35
753	XTE J1859+083		J1859+0815	—	—	NS	36
754	RX J0420.0-5022		J0420-5022	—	—	NS	38
755	XTE J1543-568		J1544-5645	—	—	NS	39
756	AX J1740.2-2848		J1740-2847	—	—	HMXB	40
757	RX J1605.3+3249		J1605+3249	—	—	NS	41
758	RBS1223; RX J130848.6+212708		J1308+2127	—	—	NS	42
759	RX J0806.4-4123		J0806-4122	—	—	NS	43

B.3.2 Detailed List

The following table provides data from the *Detailed List* of the XNAVSC. All the data from this list is provided, except for the *References* section, since this information is repeated from the *Simple List*. Descriptions of the parameters within this table are provided in Table B-3.

The actual list begins on the following page. This is the largest list of the XNAVSC. Therefore, data from a single source spans a total of six pages. The format of the layout of this list is in a column orientation. All the rows from a column in this list are printed first with as many columns that will fit on a page. Then the next set of rows from the columns that fit on a page is printed. This is repeated until the list is completed. A reader may wish to print out these pages and place them in a row orientation. The best approach for this would be to locate all the pages where the new headings for the columns begin and then set out the six pages for those sets of sources.

For the parameter of the *Catalogue J-Name*, this is source name unique to the XNAVSC. For a name that is of format *Jhhmm-ddmm* and written in blue ink, this name has been modified from the original citation's J-name or was derived from the position of the source if only a B-name is known for that source. This *Catalogue J-name* is only created to produce a consistent naming convention for all the XNAVSC sources, and should not be used as an external name for the source.

For the Galactic coordinates of Longitude (LII) and Latitude (BII), those written in blue ink have been computed directly from the Right Ascension and Declination values. Otherwise these coordinates are from the source's citation.

X-ray flux values written in blue ink are “derived” values from a given source’s citation. This may mean that X-ray detector photon counts were converted to energy flux. For some sources this may mean that the source was not directly observed in the “derived” energy range, so there is no assurance that the source is visible within this X-ray range.

Install Number	NAME and TYPE				
	Catalogue J-Name	B-Name	Object	Class	Sub-Class
1	J0534+2200	B0531+21	NS	RPSR	SNR
2	J0835-4510	B0833–45	NS	RPSR	SNR
3	J0633+1746	B0630+17	NS	RPSR	
4	J1709–4428	B1706–44	NS	RPSR	SNR
5	J1513–5908	B1509–58	NS	RPSR	SNR
6	J1952+3252	B1951+32	NS	RPSR	SNR
7	J1048–5832	B1046–58	NS	RPSR	
8	J1302–6350	B1259–63	NS	RPSR	
9	J1826–1334	B1823–13	NS	RPSR	
10	J1803–2137	B1800–21	NS	RPSR	SNR
11	J1932+1059	B1929+10	NS	RPSR	
12	J0437–4715	—	NS	RPSR	
13	J1824–2452	B1821–24	NS	RPSR	
14	J0659+1414	B0656+14	NS	RPSR	
15	J0540–6919	B0540–69	NS	RPSR	SNR
16	J2124–3358	—	NS	RPSR	
17	J1959+2048	B1957+20	NS	RPSR	
18	J0953+0755	B0950+08	NS	RPSR	
19	J1614–5047	B1610–50	NS	RPSR	
20	J0538+2817	—	NS	RPSR	
21	J1012+5307	—	NS	RPSR	
22	J1057–5226	B1055–52	NS	RPSR	
23	J0358+5413	B0355+54	NS	RPSR	
24	J2337+6151	B2334+61	NS	RPSR	SNR
25	J0218+4232	—	NS	RPSR	
26	J0826+2637	B0823+26	NS	RPSR	
27	J0751+1807	—	NS	RPSR	
28	J0142+6100	—	NS	AXP	
29	J0525–6607	—	NS	AXP	
30	J1048–5937	—	NS	AXP	
31	J1708–4008	—	NS	AXP	
32	J1808–2024	—	NS	SGR	SNR
33	J1841–0456	—	NS	AXP	SNR
34	J1845–0256	—	NS	AXP	SNR
35	J1907+0919	—	NS	SGR	SNR
36	J2301+5852	—	NS	AXP	SNR
37	J0032-7348	—	HMXB		
38	J0049-7310	—	HMXB	HMNS	HMBP

39	J0049-7250	—	HMXB	HMNS	APSR
40	J0052-7226	B0050-727	HMXB		
41	J0050-7316	—	HMXB	HMNS	APSR
42	J0050-7213	—	HMXB	HMNS	APSR
43	J0051-7231	—	HMXB	HMNS	APSR
44	J0051-7310	—	HMXB		
45	J0052-7319	—	HMXB	HMNS	HMBP
46	J0052-7158	—	HMXB		
47	J0054-7341	B0053-739	HMXB	HMNS	APSR
48	J0056+6043	B0053+604	HMXB		
49	J0053-7226	—	HMXB	HMNS	APSR
50	J0054-7204	—	HMXB	HMNS	APSR
51	J0054-7226	—	HMXB	HMNS	APSR
52	J0057-7202	—	HMXB	HMNS	APSR
53	J0058-7230	—	HMXB		
54	J0059-7138	—	HMXB	HMNS	APSR
55	J0101-7206	—	HMXB		
56	J0103-7209	—	HMXB	HMNS	HMBP
57	J0109-7444	B0103-762	HMXB		
58	J0105-7211	—	HMXB	HMNS	APSR
59	J0105-7212	—	HMXB		
60	J0105-7213	—	HMXB	HMNS	HMBP
61	J0118+6517	B0114+650	HMXB	HMNS	APSR
62	J0118+6344	B0115+634	HMXB	HMNS	APSR
63	J0117-7326	B0115-737	HMXB	HMNS	APSR
64	J0117-7330	—	HMXB	HMNS	APSR
65	J0143+6106	—	HMXB	HMNS	APSR
66	J0240+6113	B0236+610	HMXB		
67	J0334+5310	B0331+530	HMXB	HMNS	HMBP
68	J0355+3102	B0352+309	HMXB	HMNS	APSR
69	J0419+5559	—	HMXB		
70	J0440+4431	—	HMXB	HMNS	APSR
71	J0501-7033	—	HMXB		
72	J0502-6626	—	HMXB	HMNS	APSR
73	J0512-6717	—	HMXB		
74	J0516-6916	—	HMXB		

75	J0520-6932	—	HMXB		
76	J0522+3740	B0521+373	HMXB		
77	J0529-6556	—	HMXB	HMNS	APSR
78	J0531-6607	B053109-6609.2	HMXB	HMNS	APSR
79	J0531-6518	—	HMXB		
80	J0532-6622	B0532-664	HMXB	HMNS	APSR
81	J0532-6535	—	HMXB		
82	J0532-6551	—	HMXB		
83	J0535-6700	—	HMXB		
84	J0535-6651	B0535-668	HMXB	HMNS	HMBP
85	J0538+2618	B0535+262	HMXB	HMNS	APSR
86	J0535-6530	—	HMXB		
87	J0538-6405	B0538-641	HMXB		
88	J0539-6944	B0540-697	HMXB		
89	J0541-6936	—	HMXB		
90	J0541-6832	—	HMXB		
91	J0544-6633	B0544-665	HMXB		
92	J0544-7100	—	HMXB	HMNS	APSR
93	J0555+2847	B0556+286	HMXB		
94	J0635+0533	—	HMXB	HMNS	HMBP
95	J0648-4418	—	HMXB	HMNS	HMBP
96	J0728-2606	B0726-260	HMXB	HMNS	APSR
97	J0747-5319	B0739-529	HMXB		
98	J0756-6105	B0749-600	HMXB		
99	J0812-3114	—	HMXB	HMNS	APSR
100	J0835-4311	B0834-430	HMXB	HMNS	APSR
101	J0902-4033	B0900-403	HMXB	HMNS	APSR
102	J1009-5817	—	HMXB	HMNS	HMBP
103	J1025-5748	B1024.0-5732	HMXB	HMNS	APSR
104	J1030-5704	B1036-565	HMXB		
105	J1037-5647	—	HMXB	HMNS	APSR
106	J1050-5953	B1048.1-5937	HMXB	HMNS	HMBP
107	J1120-6154	B1118-615	HMXB	HMNS	HMBP
108	J1121-6037	B1119-603	HMXB	HMNS	APSR

109	J1148-6212	B1145-619	HMXB	HMNS	APSR
110	J1147-6157	B1145.1-6141	HMXB	HMNS	APSR
111	J1226-6246	B1223-624	HMXB	HMNS	APSR
112	J1242-6012	B1239-599	HMXB	HMNS	HMBP
113	J1247-6038	B1244-604	HMXB		
114	J1249-5907	B1246-588	HMXB		
115	J1242-6303	B1249-637	HMXB		
116	J1239-7522	B1253-761	HMXB		
117	J1254-5710	B1255-567	HMXB		
118	J1301-6136	B1258-613	HMXB	HMNS	APSR
119	J1324-6200	—	HMXB	HMNS	APSR
120	J1421-6241	B1417-624	HMXB	HMNS	APSR
121	J1452-5949	—	HMXB	HMNS	APSR
122	J1542-5223	B1538-522	HMXB	HMNS	APSR
123	J1557-5424	B1553-542	HMXB	HMNS	APSR
124	J1554-5519	B1555-552	HMXB		
125	J1700-4140	B1657-415	HMXB	HMNS	APSR
126	J1703-3750	B1700-377	HMXB		
127	J1700-4157	—	HMXB	HMNS	HMBP
128	J1725-3624	B1722-363	HMXB	HMNS	APSR
129	J1738-3015	—	HMXB		
130	J1739-2942	—	HMXB		
131	J1744-2713	—	HMXB		
132	J1749-2725	—	HMXB	HMNS	APSR
133	J1749-2638	—	HMXB	HMNS	APSR
134	J1810-1052	B1807-10	HMXB		
135	J1820-1434	—	HMXB	HMNS	APSR
136	J1826-1450	—	HMXB		
137	J1836-0736	B1833-076	HMXB	HMNS	APSR
138	J1841-0551	B1839-06	HMXB		
139	J1841-0427	B1839-04	HMXB	HMNS	HMBP
140	J1845+0057	B1843+009	HMXB	HMNS	HMBP
141	J1847-0309	B1845-03	HMXB		

142	J1848-0225	B1845-024	HMXB	HMNS	HMBP
143	J1847-0430	B1845.0-0433	HMXB		
144	J1858-0244	B1855-02	HMXB	HMNS	HMBP
145	J1855-0237	—	HMXB	HMNS	APSR
146	J1858+0321	—	HMXB	HMNS	APSR
147	J1904+0310	B1901+03	HMXB		
148	J1905+0902	—	HMXB	HMNS	APSR
149	J1909+0949	B1907+097	HMXB	HMNS	APSR
150	J1911+0458	B1909+048	HMXB	HMBH	
151	J1932+5352	B1936+541	HMXB		
152	J1945+2721	B1942+274	HMXB	HMNS	APSR
153	J1949+3012	B1947+300	HMXB		
154	J1948+3200	—	HMXB	HMNS	APSR
155	J1955+3206	B1954+319	HMXB		
156	J1958+3512	B1956+350	HMXB	HMBH	
157	J2032+3738	B2030+375	HMXB	HMNS	HMBP
158	J2032+4057	B2030+407	HMXB		
159	J2030+4751	—	HMXB		
160	J2059+4143	—	HMXB	HMNS	APSR
161	J2103+4545	—	HMXB	HMNS	APSR
162	J2139+5703	B2138+568	HMXB	HMNS	APSR
163	J2201+5010	B2202+501	HMXB		
164	J2207+5431	B2206+543	HMXB	HMNS	APSR
165	J2226+6114	B2214+589	HMXB		
166	J2239+6116	—	HMXB		
167	J0044+3301	B0042+323	LMXB		
168	J0418+3247	—	LMXB		
169	J0514-4002	B0512-401	LMXB	LMNS	XBRST
170	J0520-7157	B0521-720	LMXB	LMNS	ZSRC
171	J0532-6926	—	LMXB		
172	J0617+0908	B0614+091	LMXB	LMNS	ATOLL
173	J0622-0020	B0620-003	LMXB		

174	J0658-0715	B0656-072	LMXB		
175	J0748-6745	B0748-676	LMXB	LMNS	XBRST
176	J0835+5118	—	LMXB	LMNS	XBRST
177	J0837-4253	B0836-429	LMXB	LMNS	XBRST
178	J0920-5512	B0918-549	LMXB		
179	J0922-6317	B0921-630	LMXB		
180	J1013-4504	B1009-45	LMXB		
181	J1118+4802	—	LMXB	LMNS	ATOLL
182	J1126-6840	B1124-684	LMXB		
183	J1257-6917	B1254-690	LMXB	LMNS	XBRST
184	J1326-6208	B1323-619	LMXB	LMNS	XBRST
185	J1358-6444	B1354-645	LMXB		
186	J1458-3140	B1455-314	LMXB	LMNS	XBRST
187	J1520-5710	B1516-569	LMXB	LMNS	ATOLL
188	J1528-6152	B1524-617	LMXB		
189	J1547-4740	B1543-475	LMXB	LMBH	
190	J1547-6234	B1543-624	LMXB		
191	J1550-5628	—	LMXB		
192	J1601-6044	B1556-605	LMXB		
193	J1605+2551	B1603.6+2600	LMXB		
194	J1603-7753	—	LMXB	LMNS	XBRST
195	J1612-5225	B1608-522	LMXB	LMNS	ATOLL
196	J1619-1538	B1617-155	LMXB	LMNS	ZSRC
197	J1628-4911	B1624-490	LMXB		
198	J1632-6727	B1627-673	LMXB	LMNS	APSR
199	J1634-4723	B1630-472	LMXB		
200	J1636-4749	B1632-477	LMXB		
201	J1640-5345	B1636-536	LMXB	LMNS	ATOLL
202	J1645-4536	B1642-455	LMXB	LMNS	ZSRC
203	J1654-3950	—	LMXB		
204	J1657+3520	B1656+354	LMXB	LMNS	APSR
205	J1702-2956	B1658-298	LMXB	LMNS	XBRST
206	J1702-4847	B1659-487	LMXB		

207	J1705-3625	B1702-363	LMXB	LMNS	ZSRC
208	J1706-4302	B1702-429	LMXB	LMNS	ATOLL
209	J1706+2358	B1704+240	LMXB		
210	J1708-2505	B1705-250	LMXB		
211	J1708-4406	B1705-440	LMXB	LMNS	ATOLL
212	J1712-4050	B1708-408	LMXB		
213	J1709-2639	—	LMXB	LMNS	XBRST
214	J1710-2807	—	LMXB	LMNS	XBRST
215	J1714-3402	B1711-339	LMXB		
216	J1712-3738	—	LMXB	LMNS	XBRST
217	J1718-3210	B1715-321	LMXB	LMNS	XBRST
218	J1719-2501	B1716-249	LMXB	LMBH	
219	J1718-4029	—	LMXB	LMNS	XBRST
220	J1723-3739	—	LMXB	LMNS	XBRST
221	J1727-3544	B1724-356	LMXB		
222	J1727-3048	B1724-307	LMXB	LMNS	ATOLL
223	J1731-3350	B1728-337	LMXB	LMNS	ATOLL
224	J1731-1657	B1728-169	LMXB	LMNS	ATOLL
225	J1732-2444	B1728-247	LMXB	LMNS	APSR
226	J1733-3113	B1730-312	LMXB		
227	J1733-3323	B1730-335	LMXB	LMNS	XBRST
228	J1733-2202	B1730-220	LMXB		
229	J1734-2605	B1731-260	LMXB	LMNS	ATOLL
230	J1735-3028	B1732-304	LMXB	LMNS	XBRST
231	J1736-2725	B1732-273	LMXB		
232	J1737-2910	B1734-292	LMXB		
233	J1738-2700	B1735-269	LMXB	LMNS	XBRST
234	J1738-4427	B1735-444	LMXB	LMNS	ATOLL
235	J1738-2829	B1735-28	LMXB		
236	J1739-2943	B1736-297	LMXB		
237	J1739-3059	B1737-31	LMXB		
238	J1740-2818	B1737-282	LMXB		
239	J1742-2746	B1739-278	LMXB		
240	J1742-3030	B1739-304	LMXB		
241	J1743-2926	B1740-294	LMXB		
242	J1743-2944	B1740.7-2942	LMXB		

243	J1744-2900	B1741.2-2859	LMXB		
244	J1744-2921	B1741-293	LMXB	LMNS	XBRST
245	J1745-3213	B1741-322	LMXB		
246	J1745-2854	B1741.9-2853	LMXB	LMNS	XBRST
247	J1745-3241	B1742-326	LMXB		
248	J1745-2859	B1742.2-2857	LMXB		
249	J1745-2927	B1742-294	LMXB	LMNS	XBRST
250	J1745-2901	B1742-289	LMXB	LMNS	XBRST
251	J1745-2900	B1742.5-2859	LMXB		
252	J1745-2846	B1742.5-2845	LMXB		
253	J1745-2903	B1742.7-2902	LMXB		
254	J1746-2854	B1742.8-2853	LMXB		
255	J1746-2853	B1742.9-2852	LMXB		
256	J1746-2931	B1742-294	LMXB	LMNS	XBRST
257	J1746-2851	B1742.9-2849	LMXB		
258	J1746-2844	B1743.1-2843	LMXB		
259	J1746-2853	B1743.1-2852	LMXB		
260	J1746-2853	B1743-288	LMXB	LMNS	XBRST
261	J1747-2959	B1744-299	LMXB		
262	J1744-2844	—	LMXB	LMNS	APSR
263	J1747-3002	B1744-300	LMXB	LMNS	XBRST
264	J1747-2633	B1744-265	LMXB	LMNS	ATOLL
265	J1748-3607	B1744-361	LMXB		
266	J1745-2901	—	LMXB	LMNS	XBRST
267	J1748-2453	B1745-248	LMXB	LMNS	XBRST
268	J1748-2022	B1745-203	LMXB		
269	J1749-3311	B1746-331	LMXB		
270	J1750-3225	B1746.7-3224	LMXB		
271	J1750-3703	B1746-370	LMXB	LMNS	ATOLL
272	J1750-2125	B1747-214	LMXB	LMNS	XBRST
273	J1750-3117	B1747-313	LMXB		
274	J1748-2828	—	LMXB		
275	J1748-2021	—	LMXB	LMNS	XBRST

276	J1752-2830	B1749-285	LMXB		
277	J1750-2902	—	LMXB	LMNS	XBRST
278	J1752-3137	—	LMXB	LMNS	XBRST
279	J1758-3348	B1755-338	LMXB		
280	J1755-3228	—	LMXB		
281	J1801-2504	B1758-250	LMXB	LMNS	ZSRC
282	J1801-2544	B1758-258	LMXB		
283	J1801-2031	B1758-205	LMXB	LMNS	ATOLL
284	J1806-2435	B1803-245	LMXB		
285	J1806-2435	—	LMXB	LMNS	ATOLL
286	J1808-3658	—	LMXB	LMNS	APSR
287	J1810-2609	—	LMXB	LMNS	XBRST
288	J1814-1709	B1811-171	LMXB	LMNS	ATOLL
289	J1815-1205	B1812-12	LMXB	LMNS	XBRST
290	J1816-1402	B1813-140	LMXB	LMNS	ZSRC
291	J1819-2525	—	LMXB		
292	J1823-3021	B1820-303	LMXB	LMNS	ATOLL
293	J1825-3706	B1822-371	LMXB		
294	J1825-0000	B1822-000	LMXB		
295	J1829-2347	B1826-238	LMXB	LMNS	XBRST
296	J1835-3258	B1832-330	LMXB	LMNS	XBRST
297	J1839+0502	B1837+049	LMXB	LMNS	XBRST
298	J1849-0303	B1846-031	LMXB		
299	J1853-0842	B1850-087	LMXB	LMNS	XBRST
300	J1856+0519	—	LMXB		
301	J1858+2239	—	LMXB		
302	J1908+0010	B1905+000	LMXB	LMNS	XBRST
303	J1911+0035	B1908+005	LMXB	LMNS	ATOLL
304	J1915+1058	B1915+105	LMXB	LMNS	XBRST
305	J1918-0514	B1916-053	LMXB	LMNS	XBRST
306	J1920+1441	B1918+146	LMXB		
307	J1942-0354	B1940-04	LMXB	LMNS	XBRST
308	J1959+1142	B1957+115	LMXB	LMBH	
309	J2002+2514	B2000+251	LMXB		
310	J2012+3811	—	LMXB		
311	J2024+3352	B2023+338	LMXB		
312	J2123-0547	—	LMXB	LMNS	ATOLL
313	J2129+1210	B2127+119	LMXB	LMNS	XBRST
314	J2131+4717	B2129+470	LMXB	LMNS	XBRST

315	J2144+3819	B2142+380	LMXB	LMNS	ZSRC
316	J2320+6217	B2318+620	LMXB		
317	J0720-3125	B0718-3118	NS	AXP	
318	J1838-0301	—	NS	AXP	
319	J1234+3737	—	CV	CV,AM	
320	J1305+1801	—	CV	CV,AM	
321	J0024-7204	—	CV	CV,D	
322	J0610-4844	—	CV	CV,D	
323	J0712-3605	—	CV	CV,D	
324	J0110+6004	—	CV	CV,DN	
325	J0613+4744	—	CV	CV,DN	
326	J0755+2200	—	CV	CV,DN	
327	J0807-7632	—	CV	CV,DN	
328	J0825+7306	—	CV	CV,DN	
329	J0844+1252	—	CV	CV,DN	
330	J0901+1753	—	CV	CV,DN	
331	J0951+1152	—	CV	CV,DN	
332	J1006-7014	—	CV	CV,DN	
333	J1145-0426	—	CV	CV,DN	
334	J1644+2515	—	CV	CV,DN	
335	J1807+0551	—	CV	CV,DN	
336	J2007+1742	—	CV	CV,DN	
337	J2142+4335	—	CV	CV,DN	
338	J2214+1242	—	CV	CV,DN	
339	J0028+5917	—	CV	CV,IP	
340	J0203-0243	—	CV	CV,IP	
341	J0206+1517	—	CV	CV,IP	
342	J0256+1926	—	CV	CV,IP	
343	J0331+4354	—	CV	CV,IP	
344	J0350+1714	—	CV	CV,IP	
345	J0502+2445	—	CV	CV,IP	
346	J0512-3241	—	CV	CV,IP	
347	J0529-3249	—	CV	CV,IP	
348	J0534-5801	—	CV	CV,IP	
349	J0543-4101	—	CV	CV,IP	
350	J0558+5353	—	CV	CV,IP	
351	J0611-8149	—	CV	CV,IP	
352	J0731+0956	—	CV	CV,IP	
353	J0744-5257	—	CV	CV,IP	
354	J0751+1444	—	CV	CV,IP	
355	J0757+6305	—	CV	CV,IP	
356	J0833-2248	—	CV	CV,IP	
357	J0859-2428	—	CV	CV,IP	
358	J1143+7141	—	CV	CV,IP	
359	J1238-3845	—	CV	CV,IP	

360	J1252-2914	—	CV	CV,IP	
361	J1712+3331	—	CV	CV,IP	
362	J1712-2414	—	CV	CV,IP	
363	J1814+4151	—	CV	CV,IP	
364	J1855-3109	—	CV	CV,IP	
365	J2040-0052	—	CV	CV,IP	
366	J2217-0821	—	CV	CV,IP	
367	J2353-3851	—	CV	CV,IP	
368	J0422-1321	—	CV	CV,N	
369	J0615+2835	—	CV	CV,N	
370	J0629+7104	—	CV	CV,N	
371	J0811-3521	—	CV	CV,N	
372	J0932+4950	—	CV	CV,N	
373	J1019-0841	—	CV	CV,N	
374	J1138+0322	—	CV	CV,N	
375	J1152-6712	—	CV	CV,N	
376	J1559+2555	—	CV	CV,N	
377	J1622-1752	—	CV	CV,N	
378	J1832-2923	—	CV	CV,N	
379	J1848+0035	—	CV	CV,N	
380	J1934+5107	—	CV	CV,N	
381	J1935-5850	—	CV	CV,N	
382	J2017-0339	—	CV	CV,N	
383	J2020+2106	—	CV	CV,N	
384	J2042+1909	—	CV	CV,N	
385	J1336+5154	—	CV	CV,NL	
386	J1800+0810	—	CV	CV,NL	
387	J0132-6554	—	CV	CV,P	
388	J0141-6753	—	CV	CV,P	
389	J0203+2959	—	CV	CV,P	
390	J0236-5219	—	CV	CV,P	
391	J0314-2235	—	CV	CV,P	
392	J0332-2556	—	CV	CV,P	
393	J0453-4213	—	CV	CV,P	
394	J0515+0104	—	CV	CV,P	
395	J0531-4624	—	CV	CV,P	
396	J0542+6051	—	CV	CV,P	
397	J0719+6557	—	CV	CV,P	
398	J0815-1903	—	CV	CV,P	
399	J0851+1146	—	CV	CV,P	
400	J0929-2405	—	CV	CV,P	
401	J1002-1925	—	CV	CV,P	
402	J1015+0904	—	CV	CV,P	
403	J1015-4758	—	CV	CV,P	
404	J1047+6335	—	CV	CV,P	

405	J1051+5404	—	CV	CV,P	
406	J1104+4503	—	CV	CV,P	
407	J1105+2506	—	CV	CV,P	
408	J1115+4258	—	CV	CV,P	
409	J1117+1757	—	CV	CV,P	
410	J1141-6410	—	CV	CV,P	
411	J1149+2845	—	CV	CV,P	
412	J1307+5351	—	CV	CV,P	
413	J1409-4517	—	CV	CV,P	
414	J1552+1856	—	CV	CV,P	
415	J1727+4114	—	CV	CV,P	
416	J1802+1804	—	CV	CV,P	
417	J1816+4952	—	CV	CV,P	
418	J1844-7418	—	CV	CV,P	
419	J1907+6908	—	CV	CV,P	
420	J1914+2456	—	CV	CV,P	
421	J1938-4612	—	CV	CV,P	
422	J2005+2239	—	CV	CV,P	
423	J2008-6527	—	CV	CV,P	
424	J2022-3954	—	CV	CV,P	
425	J2107-0517	—	CV	CV,P	
426	J2111+4809	—	CV	CV,P	
427	J2115-5840	—	CV	CV,P	
428	J2137-4342	—	CV	CV,P	
429	J2315-5910	—	CV	CV,P	
430	J0904-3222	—	CV	CV,RN	
431	J0209-6318	—	CV	CV,S	
432	J0409-7118	—	CV	CV,S	
433	J0810+2808	—	CV	CV,S	
434	J0812+6236	—	CV	CV,S	
435	J1114-3740	—	CV	CV,S	
436	J1514-6505	—	CV	CV,S	
437	J0815-4913	—	CV	CV,U	
438	J0838+4838	—	CV	CV,U	
439	J1331-5458	—	CV	CV,U	
440	J1949+7744	—	CV	CV,U	
441	J1954+3221	—	CV	CV,U	
442	J1947-4200	—	CV	CV,X	
443	J0011-1128	—	CV	CV,Z	
444	J0104+4117	—	CV	CV,Z	
445	J0645-1651	—	CV	CV,Z	
446	J0459+1926	—	CV		
447	J0502+1624	—	CV		
448	J0533+3659	—	CV		
449	J1326+4532	—	CV		

450	J1331-2940	—	CV		
451	J1538+1852	—	CV		
452	J1718+4115	—	CV		
453	J1750+0605	—	CV		
454	J1846+1222	—	CV		
455	J2030+5237	—	CV		
456	J2123+4217	—	CV		
457	J0538-6652	—	HMXB	HMNS	APSR
458	J1849-0318	—	HMXB	HMNS	APSR
459	J0051-7159	—	LMXB	ALGOL	
460	J0102+8152	—	LMXB	ALGOL	
461	J0157+3804	—	LMXB	ALGOL	
462	J0241+6033	—	LMXB	ALGOL	
463	J0248+6938	—	LMXB	ALGOL	
464	J0308+4057	—	LMXB	ALGOL	
465	J0400+1229	—	LMXB	ALGOL	
466	J0515+4624	—	LMXB	ALGOL	
467	J0518+3346	—	LMXB	ALGOL	
468	J0647+6937	—	LMXB	ALGOL	
469	J0843+1902	—	LMXB	ALGOL	
470	J1045+4533	—	LMXB	ALGOL	
471	J1113-2627	—	LMXB	ALGOL	
472	J1145+7215	—	LMXB	ALGOL	
473	J1249-0604	—	LMXB	ALGOL	
474	J1313-6409	—	LMXB	ALGOL	
475	J1500-0831	—	LMXB	ALGOL	
476	J1518+3138	—	LMXB	ALGOL	
477	J1533+6354	—	LMXB	ALGOL	
478	J1534+2642	—	LMXB	ALGOL	
479	J1639-5659	—	LMXB	ALGOL	
480	J1649-1540	—	LMXB	ALGOL	
481	J1656+5241	—	LMXB	ALGOL	
482	J1739-2851	—	LMXB	ALGOL	
483	J1822-2514	—	LMXB	ALGOL	
484	J1852-0614	—	LMXB	ALGOL	
485	J1917+2226	—	LMXB	ALGOL	
486	J2025+2722	—	LMXB	ALGOL	
487	J2154+1433	—	LMXB	ALGOL	
488	J2332+1458	—	LMXB	ALGOL	
489	J1744-2943	—	LMXB	LMBH	
490	J1849-0308	—	LMXB	LMBH	
491	J0047+2416	—	LMXB	RS CVn	
492	J0053-7439	—	LMXB	RS CVn	
493	J0116+0648	—	LMXB	RS CVn	
494	J0122+0042	—	LMXB	RS CVn	

495	J0122+0725	—	LMXB	RS CVn	
496	J0212+3018	—	LMXB	RS CVn	
497	J0313+4806	—	LMXB	RS CVn	
498	J0318-1944	—	LMXB	RS CVn	
499	J0325+2842	—	LMXB	RS CVn	
500	J0335+3201	—	LMXB	RS CVn	
501	J0336+0035	—	LMXB	RS CVn	
502	J0337+2559	—	LMXB	RS CVn	
503	J0443-1039	—	LMXB	RS CVn	
504	J0506+5901	—	LMXB	RS CVn	
505	J0507-0524	—	LMXB	RS CVn	
506	J0516+4559	—	LMXB	RS CVn	
507	J0528-6527	—	LMXB	RS CVn	
508	J0603+3119	—	LMXB	RS CVn	
509	J0641+8216	—	LMXB	RS CVn	
510	J0703-0544	—	LMXB	RS CVn	
511	J0716+7320	—	LMXB	RS CVn	
512	J0720-0515	—	LMXB	RS CVn	
513	J0802+5716	—	LMXB	RS CVn	
514	J0837+2333	—	LMXB	RS CVn	
515	J0839+3147	—	LMXB	RS CVn	
516	J0859-2749	—	LMXB	RS CVn	
517	J0901+2641	—	LMXB	RS CVn	
518	J0909+5429	—	LMXB	RS CVn	
519	J1036-1154	—	LMXB	RS CVn	
520	J1130-1519	—	LMXB	RS CVn	
521	J1136-3802	—	LMXB	RS CVn	
522	J1140+5159	—	LMXB	RS CVn	
523	J1147+2013	—	LMXB	RS CVn	
524	J1215+7233	—	LMXB	RS CVn	
525	J1225+2533	—	LMXB	RS CVn	
526	J1229+2431	—	LMXB	RS CVn	
527	J1301+2837	—	LMXB	RS CVn	
528	J1310+3556	—	LMXB	RS CVn	
529	J1318+3326	—	LMXB	RS CVn	
530	J1334+3710	—	LMXB	RS CVn	
531	J1435-1802	—	LMXB	RS CVn	
532	J1513+3834	—	LMXB	RS CVn	
533	J1614+3351	—	LMXB	RS CVn	
534	J1639+6042	—	LMXB	RS CVn	
535	J1645+8202	—	LMXB	RS CVn	
536	J1710+4857	—	LMXB	RS CVn	
537	J1717-6656	—	LMXB	RS CVn	
538	J1730-3339	—	LMXB	RS CVn	
539	J1758+1508	—	LMXB	RS CVn	

540	J1758+2208	—	LMXB	RS CVn	
541	J1805+2126	—	LMXB	RS CVn	
542	J1810+3157	—	LMXB	RS CVn	
543	J1825+1817	—	LMXB	RS CVn	
544	J1921+0432	—	LMXB	RS CVn	
545	J1931+5543	—	LMXB	RS CVn	
546	J1936+2753	—	LMXB	RS CVn	
547	J2058+3510	—	LMXB	RS CVn	
548	J2102+2748	—	LMXB	RS CVn	
549	J2121+4020	—	LMXB	RS CVn	
550	J2139-1600	—	LMXB	RS CVn	
551	J2200-0244	—	LMXB	RS CVn	
552	J2201+4353	—	LMXB	RS CVn	
553	J2208+4544	—	LMXB	RS CVn	
554	J2311+5301	—	LMXB	RS CVn	
555	J2313+0240	—	LMXB	RS CVn	
556	J2339+2814	—	LMXB	RS CVn	
557	J2349+3625	—	LMXB	RS CVn	
558	J2355+2838	—	LMXB	RS CVn	
559	J0527-6921	—	LMXB		LMXB-SSXS
560	J0546-7108	—	LMXB		LMXB-SSXS
561	J0058-7135	—	LMXB		
562	J1656-4049	—	LMXB		
563	J0002+6246	—	NS	RPSR	SNR
564	J0117+5914	B0114+58	NS	RPSR	SNR
565	J0628+1038	—	NS	RPSR	SNR
566	J1105-6107	—	NS	RPSR	SNR
567	J1617-5055	—	NS	RPSR	SNR
568	J1623-2631	B1620-26	NS	RPSR	SNR
569	J1645-0317	—	NS	RPSR	SNR
570	J1708-4009	—	NS	RPSR	SNR
571	J1740-3015	—	NS	RPSR	SNR
572	J1748-2924	—	LMXB	LMNS	ATOLL
573	J1811-1926	—	NS	RPSR	SNR
574	J1917+1353	—	NS	RPSR	SNR
575	J1939+2134	B1937+21	NS	RPSR	SNR
576	J1958+3232	—	HMXB	HMNS	APSR
577	J2322+2057	—	NS	RPSR	SNR
578	J0043-1759	—	NS		
579	J1856-3754	—	NS		
580	J0137+2042	—	LMXB	RS CVn	
581	J0247+0037	—	LMXB	RS CVn	
582	J0743+2853	—	LMXB	RS CVn	
583	J1055+6028	—	LMXB	RS CVn	
584	J1213-0904	—	LMXB	RS CVn	

585	J1239+5511	—	LMXB	RS CVn	
586	J1416+0046	—	LMXB	RS CVn	
587	J1522+2537	—	LMXB	RS CVn	
588	J1523-0636	—	LMXB	RS CVn	
589	J1732+7413	—	LMXB	RS CVn	
590	J1942+1705	—	LMXB	RS CVn	
591	J2204+4714	—	LMXB	RS CVn	
592	J2319+7900	—	LMXB	RS CVn	
593	J2337+4627	—	LMXB	RS CVn	
594	J0414+2812	—	TTS		
595	J0419+2749	—	TTS		
596	J0419+2906	—	TTS		
597	J0421+1932	—	TTS		
598	J0421+2818	—	TTS		
599	J0421+2826	—	TTS		
600	J0427+2542	—	TTS		
601	J0429+2632	—	TTS		
602	J0430+1813	—	TTS		
603	J0431+1706	—	TTS		
604	J0432+1757	—	TTS		
605	J0432+1801	—	TTS		
606	J0432+1820	—	TTS		
607	J0433+2421	—	TTS		
608	J0433+2421	—	TTS		
609	J0433+2434	—	TTS		
610	J0434+2428	—	TTS		
611	J0435+2414	—	TTS		
612	J0455+3021	—	TTS		
613	J0455+3034	—	TTS		
614	J0456+3021	—	TTS		
615	J0503+2523	—	TTS		
616	J0507+3024	—	TTS		
617	J0535-0508	—	TTS		
618	J0235+0344	—	WD		
619	J2013+4002	—	WD		
620	J2117+3412	—	WD		
621	J0037-7214	—	???		BHC
622	J0133+3039	—	???		BHC
623	J0538-6404	—	HMXB	HMBH	
624	J0538-6905	—	???		BHC
625	J1801-2547	—	???		BHC
626	J1915+1056	—	???		BHC
627	J1907+0918	—	???		MGTR
628	J0042+4115	—	???		BP
629	J0042+4116	—	???		BP

630	J1300+1240	B1257+12	???		BP
631	J1537+1155	B1534+12	???		BP
632	J1748-2446	B1744-24A	LMXB	LMNS	XBRST
633	J1845+0050	—	???		BP
634	J2019+2425	—	???		BP
635	J0042+3533	—	???		BY
636	J0222+4729	—	???		BY
637	J0234-4347	—	???		BY
638	J0734+3152	—	???		BY
639	J0744+0333	—	???		BY
640	J1334-0820	—	???		BY
641	J1634+5709	—	???		BY
642	J2045-3120	—	???		BY
643	J2309+4757	—	???		BY
644	J1939-0603	—	???		CHRM
645	J1330+2413	—	???		FK
646	J0720-3146	—	???		PCB
647	J0019+2156	—	???		SSXS
648	J0513-6951	—	LMXB		LMXB-SSXS
649	J0543-6822	—	LMXB		LMXB-SSXS
650	J0925-4758	—	???		SSXS
651	J1601+6648	—	???		SSXS
652	J1045-5941	—	???		VXS
653	J0654-2355	—	???		W-R
654	J2020+4354	—	???		W-R
655	J0412-1028	—	???		WU
656	J0943+5557	—	???		WU
657	J1001+1724	—	???		WU
658	J1503+4739	—	???		WU
659	J2037+7535	—	???		WU
660	J2122+1708	—	???		WU
661	J1214+1149	—	???		WUM
662	J1655+3510	—	???		WUM
663	J1805+6945	—	???		WUM
664	J0044+0932	—	?		
665	J0103-7254	—	?		
666	J0133+3032	—	?		
667	J0535-0523	—	?		
668	J0537-6909	—	NS	RPSR	SNR
669	J1750+7045	—	?		
670	J2004-5543	—	?		
671	J0051-7310	—	HMXB	HMNS	HMBP
672	J0052-7220	—	HMXB	HMNS	HMBP
673	J0042-7340	—	HMXB	HMNS	HMBP
674	J0049-7323	—	HMXB	HMNS	APSR

675	J0052-7233	—	HMXB	HMNS	HMBP
676	J0056-7222	—	HMXB	HMNS	HMBP
677	J0057-7207	—	HMXB	HMNS	HMBP
678	J0057-7219	—	HMXB	HMNS	HMBP
679	J0057-7325	—	HMXB	HMNS	HMBP
680	J0100-7211	—	NS	AXP	SNR
681	J0101-7211	—	HMXB	HMNS	HMBP
682	J0103-7208	—	HMXB	HMNS	APSR
683	J0103-7241	—	NS	RPSR	SNR
684	J0119-7311	—	NS	RPSR	SNR
685	J0030+0451	—	NS	RPSR	SNR
686	J0205+6449	—	NS	RPSR	SNR
687	J1024-0719	—	NS	RPSR	SNR
688	J1119-6127	—	NS	RPSR	SNR
689	J1124-5916	—	NS	RPSR	SNR
690	J1420-6048	—	NS	RPSR	SNR
691	J1744-1134	—	NS	RPSR	SNR
692	J1800-2450	B1757-24	NS	RPSR	SNR
693	J1846-0258	—	NS	RPSR	SNR
694	J1856+0113	B1853+01	NS	RPSR	SNR
695	J2229+6114	—	NS	RPSR	SNR
696	J0929-3123	—	LMXB	LMNS	APSR
697	J1751-3037	—	LMXB	LMNS	APSR
698	J1806-2924	—	LMXB	LMNS	APSR
699	J1813-3346	—	LMXB	LMNS	APSR
700	J0111-7316	—	HMXB	HMNS	APSR
701	J1845+0051	B1843+00	HMXB	HMNS	HMBP
702	J0537-7034	—	LMXB		
703	J1746-2903	B1743-290	LMXB		
704	J1747-2852	—	LMXB		
705	J0501+1146	—	NS	SGR	XBRST
706	J1845-0434	B1842-04	NS	RPSR	SNR
707	J0356-3641	—	LMXB		
708	J0242-0000	B0240-002	AGN	Seyfert 2	
709	J0947-3056	B0945-307	AGN	Seyfert 2	
710	J1235-3954	B1232-396	AGN	Seyfert 2	
711	J1305-4928	B1304-497	AGN	Seyfert 2	
712	J1325-4301	B1322-427	AGN		
713	J2318-4222	B2315-426	AGN	Seyfert 2	
714	J1229+0203	B1226+023	QSO		
715	J1744-2916	—	?		
716	J1750-3412	B1747-341	?		
717	J0153+7442	—	CV	CV,NL	IP
718	J0439-6809	—	CV		CV-SSXS
719	J1905-0142	—	CV	CV,N	IP

720	J1930+1852	—	NS	RPSR	SNR
721	J0023-7204	B0021-72C	NS	RPSR	SNR
722	J0024-7204D	B0021-72D	NS	RPSR	SNR
723	J0024-7205	B0021-72E	LMXB	LMNS	LMBP
724	J0024-7204F	B0021-72F	NS	RPSR	SNR
725	J0024-7204G	B0021-72G	NS	RPSR	SNR
726	J0024-7204H	B0021-72H	LMXB	LMNS	LMBP
727	J0024-7204I	B0021-72I	LMXB	LMNS	LMBP
728	J0023-7203	B0021-72J	LMXB	LMNS	LMBP
729	J0024-7204L	B0021-72L	NS	RPSR	SNR
730	J0023-7205	B0021-72M	NS	RPSR	SNR
731	J0024-7204N	B0021-72N	NS	RPSR	SNR
732	J0024-7204O	B0021-72O	LMXB	LMNS	LMBP
733	J0024-7204Q	B0021-72Q	LMXB	LMNS	LMBP
734	J0024-7204S	B0021-72S	LMXB	LMNS	LMBP
735	J0024-7204T	B0021-72T	LMXB	LMNS	LMBP
736	J0024-7203	B0021-72U	LMXB	LMNS	LMBP
737	J1740-5340	B1736-53	LMXB	LMNS	LMBP
738	J2225+6535	B2224+65	NS	RPSR	SNR
739	J2043+2740	—	NS	RPSR	SNR
740	J0630-2834	B0628-28	NS	RPSR	SNR
741	J1817-3618	B1813-36	NS	RPSR	SNR
742	J0059-7223	—	HMXB	HMNS	HMBP
743	J0047-7312	—	HMXB	HMNS	HMBP
744	J0051-7310B	—	NS		
745	J0051-7310C	—	NS		
746	J0055-7242	—	NS		
747	J0055-7210	—	NS		
748	J0054-7245	—	HMXB	HMNS	HMBP
749	J0053-7227	—	NS		
750	J0055-7238	—	NS		
751	J0053-7249	—	HMXB	HMNS	HMBP
752	J1844-0257	—	NS	AXP	SNR
753	J1859+0815	—	NS		
754	J0420-5022	—	NS	RPSR	
755	J1544-5645	—	NS		
756	J1740-2847	—	HMXB	HMNS	HMBP
757	J1605+3249	—	NS		
758	J1308+2127	—	NS		
759	J0806-4122	—	NS		

					POSITION
RA (J2000) (hh:mm:ss)	RA Error (arcsec)	Dec (J2000) (dd:mm:ss)	Dec Error (arcsec)	Gal. Longitude ("LII") (deg)	Gal. Latitude ("BII") (deg)
05:34:31.973	0.0751	+22:00:52.06	0.0600	184.55755	-5.78427
08:35:20.67	0.299	-45:10:35.7	0.299	263.5521	-2.7873
06:33:54.02	0.600	+17:46:11.5	0.499	195.1339	4.2652
17:09:42.16	1.200	-44:28:56	2.99	343.0996	-2.6824
15:13:55.61	1.349	-59:08:08	1.00	320.3209	-1.1617
19:52:58.298	0.135	+32:52:40.4	0.160	68.76518	2.82311
10:48:13.0	2.991	-58:32:12.6	0.120	287.4273	0.5757
13:02:47.67	0.299	-63:50:08.6	0.100	304.1836	-0.9916
18:26:13.16	0.150	-13:34:47.1	0.800	18.0006	-0.6912
18:03:51.35	0.450	-21:37:07.2	0.499	8.3952	0.1461
19:32:13.899	0.0299	+10:59:31.99	0.0699	47.38142	-3.88437
04:37:15.7102	0.00299	-47:15:07.998	0.00600	253.394088	-41.963944
18:24:32.00833	0.000899	-24:52:10.74	0.0120	7.7968	-5.5776
06:59:48.122	0.0150	+14:14:21.53	0.0100	201.10763	8.25824
05:40:11.04	0.450	-69:19:55.1	0.499	279.7175	-31.5158
21:24:43.862	0.0600	-33:58:43.91	0.0800	10.92539	-45.43756
19:59:36.76988	0.000751	+20:48:15.1217	0.000600	59.196946	-4.697474
09:53:09.315	0.0010	+07:55:36.15	0.0200	228.90798	43.69662
16:14:15.4	4.497	-50:47:18	4.00	332.223	0.1734
05:38:25.06	0.600	+28:17:11	4.99	179.7182	-1.6856
10:12:33.4326	0.00600	+53:07:02.66	0.0100	160.34701	50.85778
10:57:58.84	0.450	-52:26:56.2	0.299	285.9839	6.6492
03:58:53.704	0.0600	+54:13:13.58	0.0299	148.19	0.81078
23:37:05.78	0.299	+61:51:01.8	0.100	114.2839	0.2334
02:18:06.35	0.150	+42:32:17.5	0.100	139.508	-17.5268
08:26:51.309	0.0299	+26:37:25.57	0.0699	196.96211	31.74226
07:51:09.1582	0.0105	+18:07:38.71	0.0499	202.72961	21.08587
01:42:00	15	+61:00:00	1	129.024	-1.272
05:25:55	75	-66:07:00	20	276.136	-33.251
10:48:06	15	-59:37:00	1	287.906	-0.392
17:08:46.5	13.5	-40:08:53	10	346.4801	0.0369
18:08:39	15	-20:24:39	15	9.996	-0.241
18:41:19	30	-04:56:13	3	27.3857	-0.0055
18:45:53.3	1.5	-02:56:42	1	29.6786	-0.1093
19:07:14	15	+09:19:19	25	43.02	0.767
23:01:07.9	15	+58:52:46	1	109.0868	-0.995
00:32:56.1		-73:48:19.		304.7018	-43.2593
00:49:29.6		-73:10:56.		303.1273	-43.9453

00:49:02.5		-72:50:52.		303.1787	-44.2793
00:52:06.1		-72:26:06.		302.8615	-44.6932
00:50:44.7		-73:16:05.		303.0011	-43.8601
00:50:55.8		-72:13:55.		302.9866	-44.8963
00:51:47.7		-72:31:29		302.8943	-44.6035
00:51:51.4		-73:10:38.		302.8898	-43.951
00:52:13.9		-73:19:13.		302.853	-43.8079
00:52:54.0		-71:58:08.		302.7715	-45.1589
00:54:33.4		-73:41:04.		302.6303	-43.442
00:56:42.3		+60:43:00.		123.5764	-2.1485
00:53:55.0		-72:26:47.		302.6691	-44.6806
00:54:36.		-72:04:00		302.587	-45.06
00:54:56.17		-72:26:27.6		302.5608	-44.6847
00:57:48.4		-72:02:42.		302.237	-45.0747
00:58:12.7		-72:30:45.		302.2172	-44.6064
00:59:11.3		-71:38:45.		302.062	-45.4693
01:01:01.1		-72:06:57.		301.8921	-44.9931
01:03:13.9		-72:09:14.0		301.6557	-44.9451
01:09:06.1		-74:44:40.		301.3616	-42.3299
01:05:08.9		-72:11:44.		301.4532	-44.8933
01:06:15.1		-72:05:25.		301.3225	-44.9917
01:11:08.4		-73:16:46.		300.9714	-43.7737
01:18:02.8		+65:17:19.		125.7105	2.5605
01:18:31.9		+63:44:24.		125.9237	1.0257
01:17:05.2		-73:26:35.		300.4148	-43.5596
01:17:41.4		-73:30:49.		300.3697	-43.4838
01:43:32.6		+61:06:26.		129.1854	-1.1303
02:40:31.6		+61:13:45.		135.6752	1.0859
03:34:59.9		+53:10:23.		146.0521	-2.1941
03:55:23.0		+31:02:45.		163.0811	-17.1364
04:19:46.0		+55:59:24.		149.1895	4.1328
04:40:59.9		+44:31:51.		159.8478	-1.2684
05:01:23.9		-70:33:33.		281.935	-34.5281
05:02:51.6		-66:26:25.		277.0366	-35.4697
05:12:41.8		-67:17:23.		277.7909	-34.3419
05:16:00.1		-69:16:09.		280.0508	-33.6342

05:20:30.3		-69:32:04.		280.2659	-33.1926
05:22:35.2		+37:40:34.		170.0532	0.7103
05:29:48.4		-65:56:51.		275.8764	-32.8797
05:31:13.		-66:07:06.		276.059	-32.718
05:31:36.1		-65:18:16.		275.0917	-32.7657
05:32:49.2		-66:22:14.		276.3353	-32.5297
05:32:25.3		-65:35:09.		275.4141	-32.6524
05:32:32.6		-65:51:40.8		275.738	-32.6116
05:35:05.9		-67:00:16.		277.0529	-32.2375
05:35:40.5		-66:51:53.		276.8817	-32.1959
05:38:54.57		+26:18:56.8		181.445	-2.6435
05:35:53.8		-65:30:34.		275.2839	-32.3015
05:38:56.4		-64:05:01.		273.5757	-32.0819
05:39:38.7		-69:44:36.		280.2032	-31.516
05:41:22.2		-69:36:29.		280.0259	-31.3823
05:41:37.1		-68:32:32.		278.7807	-31.4689
05:44:15.5		-66:33:50.		276.4462	-31.3756
05:44:06.3		-71:00:50.		281.6298	-30.9992
05:55:54.7		+28:47:06.		181.2834	1.8584
06:35:17.4		+05:33:20.9		206.1475	-1.0437
06:48:04.6		-44:18:54.4		253.7053	-19.1408
07:28:53.4		-26:06:28.		240.281	-4.0509
07:47:23.5		-53:19:58.		266.3128	-13.7262
07:56:15.8		-61:05:59.		274.0311	-16.2096
08:12:28.4		-31:14:51.		249.578	1.5431
08:35:53		-43:11:21.2		262.019	-1.518
09:02:06.9		-40:33:17.		263.0584	3.9299
10:09:46.		-58:17:32.		282.998	-1.822
10:25:56.6		-57:48:42.		284.5154	-0.2389
10:30:22.5		-57:04:39.		284.642	0.6983
10:37:35.2		-56:47:59.		285.3529	1.4326
10:50:07.9		-59:53:16.		288.2572	-0.5181
11:20:57.2		-61:54:58.		292.4984	-0.8912
11:21:15.2		-60:37:24.		292.0904	0.336

11:48:01.8		-62:12:29.4		295.6148	-0.2406
11:47:28.6		-61:57:14.		295.4899	-0.0098
12:26:37.6		-62:46:13.		300.0981	-0.0351
12:42:01.7		-60:12:05.4		301.7619	2.6489
12:47:35.		-60:38:36.		302.459	2.225
12:49:36.		-59:07:18.		302.696	3.749
12:42:50.4		-63:03:32.		301.9582	-0.2034
12:39:15.0		-75:22:12.		302.1439	-12.5169
12:54:37.0		-57:10:06.		303.3649	5.7007
13:01:16.4		-61:36:14.2		304.1013	1.2455
13:24:26.3		-62:00:53.		306.793	0.6094
14:21:12.9		-62:41:54.		313.0212	-1.5985
14:52:49.3		-59:49:18.		317.645	-0.4634
15:42:23.3		-52:23:10.		327.4195	2.1637
15:57:49.2		-54:24:52.		327.9449	-0.8569
15:54:22.0		-55:19:44.		326.9767	-1.239
17:00:47.9		-41:40:23.		344.3538	0.3111
17:03:56.7		-37:50:39.		347.7543	2.1737
17:00:05.3		-41:57:44.		344.0445	0.2372
17:25:55.		-36:24:42.		351.472	-0.547
17:38:53.		-30:15:36.		358.103	0.546
17:39:30.1		-29:42:07.		358.6467	0.7305
17:44:45.4		-27:13:47.		1.3565	1.0528
17:49:10.1		-27:25:16.		1.701	0.1157
17:49:12.0		-26:38:50.		2.3682	0.508
18:10:42.		-10:52:00		18.6	3.932
18:20:29.5		-14:34:24.		16.4719	0.0699
18:26:14.9		-14:50:29.		16.8875	-1.2854
18:36:28.6		-07:36:21		24.4625	-0.1608
18:41:42.		-05:51:00		26.618	-0.508
18:41:48.		-04:27:00		27.874	0.11
18:45:30.		+00:57:00		33.101	1.754
18:47:24.		-03:09:00		29.668	-0.539

18:48:17.7		-02:25:13.		30.4197	-0.4046
18:47:41.		-04:30:12.		28.496	-1.219
18:58:00.		-02:44:00		31.245	-2.705
18:55:42.		-02:37:00		31.088	-2.141
18:58:36.		+03:21:00		36.729	-0.064
19:04:12.		+03:10:30.		37.213	-1.387
19:05:20.		+09:02:30.		42.556	1.054
19:09:37.9		+09:49:49.		43.7437	0.4761
19:11:49.5		+04:58:58.1		39.694	-2.2443
19:32:52.3		+53:52:45.		85.8499	15.9024
19:45:38.		+27:21:38.0		63.2	1.398
19:49:35.6		+30:12:31.		66.099	2.0831
19:48:00.		+32:00:00		67.475	3.282
19:55:43.3		+32:06:03.		68.397	1.926
19:58:21.68		+35:12:05.8		71.335	3.0668
20:32:15.3		+37:38:15.		77.1519	-1.2418
20:32:25.7		+40:57:28.		79.8454	0.7003
20:30:30.6		+47:51:46.		85.2292	5.0473
20:59:00.		+41:43:00		83.55	-2.724
21:03:33.		+45:45:00.		87.124	-0.68
21:39:34.		+57:03:36.		99.067	3.363
22:01:38.2		+50:10:04.		97.2476	-4.0413
22:07:57		+54:31:05.8		100.605	-1.107
22:26:33.1		+61:14:17.		106.3881	3.11
22:39:20.90		+61:16:26.8		107.7346	2.3623
00:44:50.4		+33:01:17.		121.3377	-29.8299
04:18:29.9		+32:47:24.		165.4873	-12.4798
05:14:06.6		-40:02:37.		244.5096	-35.0361
05:20:29.2		-71:57:36.		283.0935	-32.6902
05:32:42.8		-69:26:18.		279.9393	-32.1547
06:17:07.3	1	+09:08:13.	1	200.8774	-3.3635
06:22:44.5		-00:20:45.		209.338	-6.2226

06:58:27.		-07:15:50.		220.195	-1.756
07:48:33.8		-67:45:09.		279.9781	-19.8109
08:35:56.		+51:18:36.		167.531	36.933
08:37:23.		-42:53:09.		261.942	-1.117
09:20:26.8		-55:12:24.		275.8525	-3.8446
09:22:34.7		-63:17:42.		281.8356	-9.3398
10:13:36.		-45:04:35.		275.878	9.345
11:18:10.85		+48:02:12.9		157.6605	62.3205
11:26:26.7		-68:40:33.		295.3006	-7.0727
12:57:37.2		-69:17:21.		303.4819	-6.424
13:26:36.1		-62:08:10.		307.0281	0.4557
13:58:09.7		-64:44:05.		309.9774	-2.7796
14:58:22.0		-31:40:08.		332.2426	23.8811
15:20:40.9		-57:10:01.		322.1185	0.0375
15:28:17.2		-61:52:58.		320.3193	-4.4272
15:47:08.5		-47:40:09.4		330.9185	5.4261
15:47:54.8		-62:34:05.		321.7572	-6.3364
15:50:58.78		-56:28:35.0		325.8826	-1.827
16:01:02.3		-60:44:17.		324.1392	-5.9314
16:05:45.8		+25:51:45.		42.7503	46.7786
16:03:54.		-77:53:06.		312.429	-18.731
16:12:43.0		-52:25:23.		330.9263	-0.8505
16:19:55.1		-15:38:25.		359.0943	23.7843
16:28:02.4		-49:11:25.		334.9201	-0.2566
16:32:16.8		-67:27:43.		321.7876	-13.0924
16:34:00.4		-47:23:39.		336.9081	0.2519
16:36:28.		-47:49:37.		336.869	-0.346
16:40:55.5		-53:45:05.		332.915	-4.818
16:45:47.7		-45:36:40.		339.5881	-0.0794
16:54:00.137		-39:50:44.90		344.98189	2.45597
16:57:49.8		+35:20:33.		58.1492	37.5231
17:02:06.3		-29:56:45.		353.8264	7.2661
17:02:49.5		-48:47:23.		338.9394	-4.3267

17:05:44.5		-36:25:22.		349.1039	2.7486
17:06:15.3		-43:02:10.		343.8865	-1.3185
17:06:34.6		+23:58:18.		45.1517	32.9903
17:08:14.6		-25:05:29.		358.5875	9.0568
17:08:54.7		-44:06:02.		343.3224	-2.3416
17:12:23.		-40:50:36.		346.327	-0.928
17:09:30.2		-26:39:27.		357.4705	7.9112
17:10:12.3		-28:07:54.		356.3571	6.922
17:14:19.2		-34:02:58.		352.0568	2.7457
17:12:34.		-37:38:36.		348.935	0.928
17:18:47.4		-32:10:40.		354.1277	3.0644
17:19:36.9		-25:01:03.		0.1424	6.991
17:18:24.13		-40:29:30.4		347.2774	-1.6512
17:23:38.		-37:39:42.		350.182	-0.873
17:27:39.		-35:44:04.		352.23	-0.46
17:27:33.2		-30:48:07.		356.3199	2.2981
17:31:57.4		-33:50:05.		354.3022	-0.1501
17:31:44.2		-16:57:42.		8.5128	9.0377
17:32:02.2		-24:44:44.		1.9372	4.7948
17:33:32.		-31:13:00		356.678	0.1
17:33:24.1		-33:23:16.		354.8409	-0.1583
17:33:57.		-22:02:07.		4.467	5.887
17:34:13.0		-26:05:09.		1.0743	3.6555
17:35:47.6		-30:28:56.		357.558	0.9897
17:36:02.		-27:25:33.		0.1627	2.592
17:37:25.		-29:10:48.		358.846	1.393
17:38:16.		-27:00:16.		0.785	2.398
17:38:58.3		-44:27:00.		346.0543	-6.9939
17:38:34.		-28:29:00		359.569	1.553
17:39:33.		-29:43:26.		358.634	0.71
17:39:56.		-30:59:00		357.611	-0.03
17:40:57.		-28:18:36.		359.995	1.201
17:42:37.		-27:46:59.		0.636	1.167
17:42:44.		-30:30:51.		358.328	-0.292
17:43:47.		-29:26:00		359.367	0.082
17:43:54.7		-29:44:43.		359.1156	-0.1054

17:44:25.4		-29:00:45.		359.7983	0.1834
17:44:49.		-29:21:06.		359.554	-0.067
17:45:02.		-32:13:38.		357.126	-1.608
17:45:01.		-28:54:06.		359.961	0.131
17:45:29.		-32:41:39.		356.776	-1.933
17:45:26.6		-28:59:00.		359.9396	0.0084
17:45:37.		-29:27:00		359.561	-0.267
17:45:37.0		-29:01:07.		359.9293	-0.0423
17:45:40.7		-29:00:11.		359.9496	-0.0457
17:45:42.9		-28:46:53.		0.143	0.0629
17:45:52.9		-29:03:22.		359.9274	-0.1113
17:46:00.0		-28:54:49.		0.0626	-0.0592
17:46:04.9		-28:53:13.		0.0946	-0.0606
17:46:06.2		-29:31:06.		359.5578	-0.3931
17:46:09.7		-28:51:04.		0.1343	-0.057
17:46:19.2		-28:44:07.		0.2513	-0.0264
17:46:19.5		-28:53:43.		0.1152	-0.1105
17:46:47.		-28:53:41.		0.168	-0.196
17:47:25.7		-29:59:43.		359.2993	-0.8864
17:44:33.1		-28:44:29.		0.044	0.3012
17:47:25.9		-30:02:31.		359.2598	-0.9112
17:47:56.0		-26:33:49.		2.2938	0.7937
17:48:13.4		-36:07:53.		354.1214	-4.1922
17:45:36.		-29:01:34.		359.921	-0.043
17:48:56.		-24:53:40.		3.84	1.462
17:48:53.5		-20:22:02.		7.7242	3.795
17:49:50.6		-33:11:55.		356.8162	-2.9763
17:50:03.5		-32:25:43.		357.5017	-2.6211
17:50:12.7		-37:03:08.		353.5309	-5.0052
17:50:25.7		-21:25:21.		6.9996	2.9469
17:50:45.5		-31:17:32.		358.5552	-2.1677
17:48:05.06		-28:28:25.8		0.6756	-0.2221
17:48:53.4		-20:21:43.		7.7285	3.798

17:52:16.		-28:30:22.		1.119	-1.028
17:50:24.		-29:02:18.		0.453	-0.948
17:52:24.		-31:37:42.		358.444	-2.64
17:58:40.0	1	-33:48:27.	1	357.2154	-4.8723
17:55:28.6		-32:28:39.		358.0393	-3.6314
18:01:08.2		-25:04:45.		5.0772	-1.0185
18:01:12.7		-25:44:26.		4.5108	-1.3607
18:01:32.3		-20:31:44.		9.0768	1.1537
18:06:50.2		-24:35:15.		6.1407	-1.9039
18:06:51.		-24:35:06.		6.144	-1.905
18:08:27.54		-36:58:44.3		355.385	-8.1483
18:10:44.5		-26:09:01.		5.1973	-3.4312
18:14:31.1		-17:09:26.		13.5158	0.108
18:15:12.		-12:05:00.		18.056	2.383
18:16:01.4		-14:02:11.		16.4321	1.2776
18:19:21.48		-25:25:36.0		6.7564	-4.7977
18:23:40.6		-30:21:41.		2.7881	-7.9139
18:25:46.8		-37:06:19.		356.8501	-11.2908
18:25:22.1		-00:00:44.		29.9911	5.8191
18:29:27.		-23:47:29.		9.275	-6.081
18:35:44.0		-32:58:55.		1.5395	-11.3679
18:39:56.9		+05:02:08.7		36.1168	4.8445
18:49:17.1		-03:03:44.		29.9611	-0.9174
18:53:04.9		-08:42:20.		25.3556	-4.3199
18:56:39.		+05:19:48.		38.269	1.272
18:58:41.58		+22:39:29.4		54.0461	8.6075
19:08:27.0		+00:10:08.		35.0246	-3.7072
19:11:16.0		+00:35:06.		35.7184	-4.143
19:15:17.		+10:58:06.		45.396	-0.228
19:18:48.0		-05:14:09.		31.36	-8.4631
19:20:17.		+14:41:39.		49.26	0.435
19:42:38.		-03:54:00		35.301	-13.163
19:59:23.9	1	+11:42:29	1	51.3072	-9.3299
20:02:49.6		+25:14:12.		63.3668	-2.9989
20:12:37.80		+38:11:01.1		75.3885	2.2467
20:24:03.8		+33:52:04.		73.1192	-2.0911
21:23:14.54		-05:47:52.9		46.483	-36.1994
21:29:58.3		+12:10:03.		65.013	-27.3122
21:31:26.2	1	+47:17:24.	1	91.5774	-3.0365

21:44:41.2		+38:19:18.		87.3285	-11.3163
23:20:34.1		+62:17:33.		112.5852	1.2602
07:20:24.96		-31:25:50.2		244.158	-8.1645
18:38:27.02		-03:01:14.4		28.762	1.5076
12:34:54.4	1	+37:37:43		140.2384	78.9382
13:05:43.4	1	+18:01:02		323.5429	80.3123
00:24:06.2	1	-72:04:57		305.8936	-44.8882
06:10:33.6	2	-48:44:27		256.4227	-26.5455
07:12:32.9	1	-36:05:40		247.6826	-11.682
01:10:13.2	1	+60:04:36		125.2749	-2.7096
06:13:22.4	1	+47:44:26		166.0063	13.7997
07:55:05.3	1	+22:00:06		199.223	23.3948
08:07:28.6	1	-76:32:02		289.187	-22.0824
08:25:13.2	1	+73:06:40		141.3819	32.6286
08:44:27.2	1	+12:52:32		213.7396	30.8183
09:01:03.4	1	+17:53:56		210.0109	36.4413
09:51:01.6	1	+11:52:30		223.6988	45.119
10:06:22.3	1	-70:14:05		289.7655	-11.7066
11:45:21.2	1	-04:26:07		273.6054	54.6296
16:44:09.8	1	+25:15:01		44.8498	38.2364
18:07:51.8	1	+05:51:48		33.2365	12.3508
20:07:36.2	1	+17:42:15		57.5361	-7.9288
21:42:42.5	1	+43:35:10		90.5585	-7.11
22:14:02.5	1	+12:42:11		74.0379	-34.8276
00:28:48.9	3	+59:17:22		120.0417	-3.4553
02:03:42.1		-02:43:48.6		161.3461	-60.0971
02:06:53	1	+15:17:42	1	148.527	-43.795
02:56:08.8	>15	+19:26:35		159.2495	-34.4885
03:31:11.8	1	+43:54:17		150.9552	-10.1041
03:50:24.5		+17:14:48.1		172.4809	-27.9384
05:02:27.4		+24:45:22.1		178.0778	-10.3143
05:12:13.1	2	-32:41:39		235.6437	-34.0919
05:29:25.5	2	-32:49:05		236.7897	-30.6043
05:34:50.8	1	-58:01:42		266.4239	-32.7782
05:43:20.3	1	-41:01:56		246.7701	-29.7298
05:58:00.3	1	+53:53:58		159.2051	14.3163
06:11:44.07		-81:49:24.1		293.7816	-28.2401
07:31:29	1	+09:56:22		208.479	13.362
07:44:57.9		-52:57:12.9		265.7946	-13.8776
07:51:17.3	1	+14:44:23		206.0609	19.7696
07:57:00.3		+63:05:56		153.4806	31.3509
08:33:06.3		-22:48:43.9		245.1894	10.0969
08:59:20	1	-24:28:56		250.253	13.883
11:43:38.34	1	+71:41:20.4		130.3043	44.456
12:38:05.00		-38:45:54.5		300.0821	24.0327

12:52:24.5	1	-29:14:58		303.1861	33.6218
17:12:56.1	1	+33:31:21		56.6597	34.1242
17:12:35.9	1	-24:14:41		359.8664	8.7417
18:14:20.4	1	+41:51:21		69.1883	24.2735
18:55:02.3	1	-31:09:49		4.958	-14.3549
20:40:09.1	1	-00:52:16		46.9325	-23.5491
22:17:55.5	1	-08:21:05		53.0001	-49.1582
23:53:00.6	>15	-38:51:45		345.3585	-73.0782
04:22:38.1	1	-13:21:29		208.3127	-38.968
06:15:44	1	+28:35:08		183.574	5.562
06:29:34.1	1	+71:04:36		143.5956	23.8184
08:11:46	1	-35:21:05		252.926	-0.835
09:32:15	1	+49:50:53		168.05	45.969
10:19:56.6	1	-08:41:56		251.8735	38.7176
11:38:27	1	+03:22:07		263.493	60.525
11:52:02.4	1	-67:12:20		297.2118	-4.9958
15:59:30.16		+25:55:12.6		42.3738	48.1647
16:22:30.7	1	-17:52:42		357.6686	21.8692
18:32:04.3	1	-29:23:13		4.4905	-9.1084
18:48:54.5	1	+00:35:03		33.1635	0.8292
19:34:36.6	1	+51:07:37		83.3796	14.5015
19:35:42.99		-59:08:21.8		337.927	-28.6252
20:17:34.2	1	-03:39:50		39.6987	-20.8014
20:20:14.8	1	+21:06:08		62.0526	-8.6028
20:42:20.3	1	+19:09:39		63.4302	-13.972
13:36:41.1	1	+51:54:49		107.0295	63.795
18:00:35.6	1	+08:10:12		34.5432	14.9895
01:32:42	>15	-65:54:32		296.307	-50.685
01:41:00.4	1	-67:53:29		295.9227	-48.5567
02:03:48.	>15	+29:59:00		141.087	-30.325
02:36:11.6	1	-52:19:14		272.2286	-58.1074
03:14:13.1	1	-22:35:42		212.9374	-57.4057
03:32:04.6	1	-25:56:57		220.4064	-54.2061
04:53:25.5	2	-42:13:41		246.7589	-39.1244
05:15:41.4	1	+01:04:40		200.4843	-20.6376
05:31:35.4	1	-46:24:08		252.583	-32.6665
05:42:48.9		+60:51:28		151.8343	15.6893
07:19:14	1	+65:57:48	1	150.026	27.407
08:15:06.8	1	-19:03:18		239.6522	8.7131
08:51:27	>15	+11:46:58		215.733	31.922
09:29:07.1	1	-24:05:05		254.5945	19.2605
10:02:11.71	1	-19:25:37.5	1	256.9775	27.9705
10:15:34.7	>15	+09:04:42		231.5895	49.0492
10:15:58.4	2	-47:58:11		277.8785	7.1952
10:47:09.9	2	+63:35:13		143.1496	48.3738

10:51:35.2	1	+54:04:36		153.866	55.2481
11:04:25.8	1	+45:03:14		165.8266	62.1484
11:05:39.8	1	+25:06:28		211.8033	66.2142
11:15:44.9	1	+42:58:23		167.4532	64.9672
11:17:16	1	+17:57:41		230.897	66.457
11:41:23		-64:10:15		295.392	-2.33
11:49:55.7	1	+28:45:08		202.536	76.3281
13:07:53.9	1	+53:51:30		117.5647	63.098
14:09:07.4	1	-45:17:16	1	316.9787	15.4546
15:52:47.3	1	+18:56:27		31.7154	47.7086
17:27:06.2		+41:14:11		66.3685	32.7739
18:02:06.5	2	+18:04:43		44.1149	18.7962
18:16:13.4	1	+49:52:03		77.8644	25.8758
18:44:47.8	1	-74:18:33		320.3744	-25.5957
19:07:06.4		+69:08:39.7		100.079	23.8575
19:14:25.7	1	+24:56:40		57.7263	6.4013
19:38:35.6	1	-46:12:57		352.4536	-27.0658
20:05:42	>15	+22:39:58		61.532	-4.92
20:08:55.8	1	-65:27:43		330.6144	-32.5073
20:22:37.5		-39:54:12		1.3135	-33.8517
21:07:58.2	1	-05:17:39		44.7628	-32.638
21:11:36.5	1	+48:09:02		89.8229	-0.0731
21:15:41	1	-58:40:54		337.025	-41.442
21:37:56.5	1	-43:42:14		356.7006	-47.9393
23:15:18.4		-59:10:27		323.6812	-53.9096
09:04:41.5	1	-32:22:47		257.207	9.7068
02:09:50.8	1	-63:18:41		288.8848	-51.6253
04:09:11.3	1	-71:17:41		284.8881	-38.1338
08:10:56.7	1	+28:08:33		194.084	28.8091
08:12:28.2	1	+62:36:23		153.9609	33.1365
11:14:00.2	1	-37:40:49		282.4255	21.281
15:14:01.1	1	-65:05:42	1	317.225	-6.2584
08:15:19.1	1	-49:13:21		264.9296	-7.8898
08:38:22.1	1	+48:38:01		170.882	37.3577
13:31:19.6	1	-54:58:34		308.6844	7.4495
19:49:06.5	1	+77:44:23		109.9736	23.4862
19:54:40.7	1	+32:21:55		68.5096	2.2515
19:47:40.5	1	-42:00:26		357.4767	-27.7624
00:11:24.7	1	-11:28:44		90.0051	-71.7433
01:04:35.5	1	+41:17:58		125.5868	-21.5045
06:45:17	2	-16:51:35		227.375	-8.924
04:59:43.1		+19:26:35.2		182.0812	-13.9636
05:02:50.4		+16:24:31.7		185.0811	-15.1153
05:33:33.4	1	+36:59:32		171.8325	2.1451
13:26:54.3		+45:32:55		104.2808	70.2737

13:31:53.8	1	-29:40:59		313.3392	32.3698
15:38:00.2	1	+18:52:02		29.7772	50.9706
17:18:37.1	1	+41:15:50		66.1219	34.3557
17:50:13.7	1	+06:05:28		31.4254	16.3759
18:46:31.3		+12:22:00.6		43.4352	6.6789
20:30:31.7	1	+52:37:51		89.1339	7.8191
21:23:45.7		+42:17:52.2		87.1221	-5.6898
05:38:57.9		-66:52:28.2		276.8568	-31.8734
18:49:00	60	-03:18:00	60	29.717	-0.962
00:51:46.8		-71:59:53		302.8945	-45.1302
01:02:17.9		+81:52:32.6		123.3376	19.0125
01:57:46		+38:04:29.2		137.055	-22.971
02:41:23.9		+60:33:12.1		136.0486	0.5127
02:48:35.3		+69:38:02.7		132.8589	9.0527
03:08:10.1		+40:57:20.5		148.9764	-14.9003
04:00:40.9		+12:29:25.8		178.3719	-29.3753
05:15:29.7		+46:24:21.9		162.1345	4.6331
05:18:18.9		+33:46:04		172.7671	-2.2331
06:47:28.9		+69:37:45.1		145.5089	24.9684
08:43:56.14		+19:02:03		206.9704	33.0453
10:45:20.5		+45:33:58.5		168.1404	58.9497
11:13:12.6		-26:27:54.4		277.0819	31.4294
11:45:29.4		+72:15:58.6		129.8301	43.9679
12:49:38.7		-06:04:44.3		302.1181	56.7899
13:13:38.1		-64:09:05		305.349	-1.3839
15:00:58.6		-08:31:07.9		348.8683	42.5109
15:18:11.4		+31:38:49.8		49.9512	57.8656
15:33:51		+63:54:24.5		99.066	44.968
15:34:40.8		+26:42:57.4		41.8713	53.7743
16:39:44.7		-56:59:38.3		330.352	-6.8285
16:49:27.7		-15:40:04.3		3.7605	18.1617
16:56:18.1		+52:41:54.4		80.1976	38.4926
17:39:40.4		-28:51:11.7		359.3853	1.1503
18:22:06.9		-25:14:23.2		7.2132	-5.2624
18:52:05.9		-06:14:37.9		27.4449	-2.9889
19:17:40		+22:26:28.7		55.832	4.596
20:25:33.6		+27:22:09.8		67.9648	-6.0799
21:54:43.4		+14:33:28.6		71.6231	-30.2096
23:32:14.8		+14:58:09		96.0102	-43.7242
17:44:02.7		-29:43:25		359.1492	-0.1187
18:49:06		-03:08:00		29.877	-0.909
00:47:20.33		+24:16:01.8		121.7366	-38.5951
00:53:04.9		-74:39:07.2		302.7845	-42.4758
01:16:55.12		+06:48:42.1		134.1489	-55.5041
01:22:50.7		+00:42:55.4		139.3769	-61.1496

01:22:56.8		+07:25:09		136.5071	-54.62
02:12:22.6		+30:18:13.4		142.9761	-29.3984
03:13:22.37		+48:06:31.3		145.9923	-8.3058
03:18:03.82		-19:44:13.8		208.4792	-55.6919
03:25:35.3		+28:42:55		159.3585	-23.045
03:35:01		+32:01:02.1		158.929	-19.188
03:36:47.1		+00:35:25		184.9079	-41.5678
03:37:11.04		+25:59:27.9		163.3993	-23.5724
04:43:45.8		-10:39:56		207.9846	-33.1486
05:06:12.14		+59:01:16.8		150.9514	10.8308
05:07:28.7		-05:24:02.1		205.5986	-25.5431
05:16:40.9		+45:59:29		162.5931	4.5615
05:28:44.8		-65:27:02.5		275.3032	-33.0455
06:03:53.7		+31:19:41.3		179.9257	4.6177
06:41:18.1		+82:16:10.1		131.5698	26.5223
07:03:18.3		-05:44:10.1		219.3876	0.0148
07:16:25.2		+73:20:02.7		141.7124	27.6841
07:20:48.5		-05:15:35.6		220.9784	4.098
08:02:36.1		+57:16:28		160.327	32.0471
08:37:30.13		+23:33:41.6		201.2788	33.1259
08:39:08.54		+31:47:44.5		191.7649	35.6475
08:59:42		-27:49:01		252.954	11.836
09:01:55.8		+26:41:28		199.4695	39.3083
09:09:56.2		+54:29:26.7		162.7166	41.6749
10:36:01.8		-11:54:34.8		258.4084	38.9842
11:30:24.8		-15:19:19.6		275.6612	43.2181
11:36:16.23		-38:02:11.4		286.9928	22.4976
11:40:46.35		+51:59:53.4		146.2343	61.8145
11:47:59.14		+20:13:08.2		235.0034	73.9319
12:15:41.6		+72:33:05.3		126.6644	44.3168
12:25:02.3		+25:33:38.7		226.2937	83.8823
12:29:41		+24:31:15		239.767	84.454
13:01:31.2		+28:37:40.5		67.4608	87.3144
13:10:36.91		+35:56:05.6		99.2633	80.2952
13:18:52		+33:26:18.7		81.437	81.351
13:34:47.5		+37:10:57.1		83.3268	76.408
14:35:48.5		-18:02:10.5		335.0993	38.2305
15:13:32.8		+38:34:06.5		63.1589	58.2762
16:14:40.8		+33:51:27		54.6654	46.1412
16:39:03.8		+60:42:01.7		90.8602	39.454
16:45:57.7		+82:02:13.9		114.9962	31.0487
17:10:25.6		+48:57:57.5		75.4077	36.3859
17:17:25.7		-66:56:56.4		324.9006	-16.2966
17:30:33.36		-33:39:15.9		354.2932	0.1922
17:58:07		+15:08:17.9		40.868	18.491

17:58:38.5		+22:08:48.3		47.7805	21.1075
18:05:49.8		+21:26:47		47.7578	19.298
18:10:26.4		+31:57:41.5		58.659	22.0693
18:25:38.6		+18:17:39.3		46.675	13.7707
19:21:48.49		+04:32:56.9		40.4638	-4.6492
19:31:13.5		+55:43:55.5		87.5128	16.8742
19:36:42.6		+27:53:03.4		62.6805	3.3751
20:58:13.4		+35:10:30.4		78.4648	-6.8658
21:02:24.9		+27:48:48		73.3443	-12.299
21:21:01.5		+40:20:53.5		85.3687	-6.703
21:39:48.7		-16:00:21.6		36.8147	-44.3628
22:00:36.42		-02:44:26.9		56.2573	-42.4572
22:01:30.5		+43:53:24.6		93.406	-9.0264
22:08:39.8		+45:44:40		95.5559	-8.298
23:11:10.1		+53:01:34.3		108.0577	-6.9253
23:13:23.7		+02:40:21.0		80.6635	-51.9658
23:39:29.8		+28:14:36.1		104.2233	-32.0014
23:49:40.96		+36:25:31.0		109.2831	-24.8043
23:55:03.3		+28:38:03		108.2297	-32.6228
05:27:53.8		-69:21:15		279.9171	-32.5863
05:46:45.1	12	-71:08:54		281.759	-30.7716
00:58:36.9		-71:35:53		302.1236	-45.5189
16:56:35.98		-40:49:24.4		344.531	1.4571
00:02:54.1		+62:46:23		117.4131	0.4225
01:17:38.70		+59:14:37.9		126.2831	-3.4573
06:28:40.5	1	+10:38:15	40	200.8842	-0.1468
11:05:26.07		-61:07:52.1		290.4896	-0.8465
16:17:30.2		-50:55:04		332.5029	-0.275
16:23:38.2228		-26:31:53.71		350.97626	15.95997
16:45:02.045		-03:17:58.35		14.11406	26.06154
17:08:46.6		-40:09:27		346.4727	0.0311
17:40:33.73		-30:15:41.9		358.2945	0.2385
17:48:12		-29:24:00		359.8956	-0.7221
18:11:29.22	1	-19:25:27.6	60	11.1814	-0.3479
19:17:39.771		+13:53:57.05		48.2598	0.62407
19:39:38.5600084	0.000012	+21:34:59.13548	0.00014	57.508884	-0.289593
19:58:13.8	1	+32:32:58.7	1	69.0562	1.7066
23:22:22.36		+20:57:03.0		96.5148	-37.31
00:43:35.37		-17:59:11.8		111.3302	-80.6811
18:56:35.41		-37:54:08		358.6061	-17.2118
01:37:08.84		+20:42:00.4		137.1274	-40.9083
02:47:25.5		+00:37:27.5		172.81	-50.6612
07:43:17.2		+28:53:03		191.1867	23.2694
10:55:43.55		+60:28:09.7		145.359	51.3229
12:13:20.69		-09:04:46.9		287.3159	52.6332

12:39:53.8		+55:11:34		126.4244	61.8571
14:16:07.79		+00:46:16.1		344.0876	56.717
15:22:25.1		+25:37:34.8		39.1178	56.2778
15:23:26.4		-06:36:24.9		356.0233	40.1052
17:32:41.21		+74:13:38.5		105.4927	31.3534
19:42:10.2	1	+17:05:15	1	53.891	-3.0263
22:04:56.61		+47:14:04.5		95.9228	-6.7175
23:19:27.7		+79:00:02.8		118.4635	16.9354
23:37:33.9		+46:27:50		109.9049	-14.5309
04:14:12.92		+28:12:12.3		168.2168	-16.34
04:19:41.30		+27:49:38.8		169.3674	-15.7256
04:19:15.83		+29:06:26.9		168.3358	-14.9149
04:21:59.43		+19:32:06.4		176.2297	-20.8868
04:21:58.85		+28:18:06.5		169.3659	-15.0323
04:21:57.41		+28:26:35.6		169.255	-14.9398
04:27:02.80		+25:42:22.3		172.1468	-15.9423
04:29:41.51		+26:32:59.8		171.899	-14.9387
04:30:03.99		+18:13:49.4		178.6093	-20.2636
04:31:27.2		+17:06:25		179.7629	-20.7147
04:32:09.28		+17:57:23.3		179.1692	-20.0514
04:32:15		+18:01:42		179.125	-19.989
04:32:14.56		+18:20:15.0		178.8682	-19.7954
04:33:34.02		+24:21:18.2		174.2137	-15.7127
04:33:34.41		+24:21:07.2		174.2171	-15.7136
04:33:13		+24:34:18		173.989	-15.633
04:34:55.45		+24:28:53.7		174.3207	-15.3952
04:35:27.37		+24:14:59.5		174.5855	-15.4518
04:55:10.2		+30:21:58		172.5661	-8.1958
04:55:59.38		+30:34:01.5		172.5167	-7.9328
04:56:02.2		+30:21:03		172.6949	-8.0582
05:03:06.60		+25:23:19.6		177.6504	-9.8193
05:07:49.57		+30:24:05.2		174.2042	-6.0029
05:35:04.21		-05:08:13.2		208.7476	-19.3149
02:35:07		+03:44:13		165.962	-50.268
20:13:10.2		+40:02:44		77.0032	3.1829
21:17:07		+34:12:24		80.352	-10.407
00:37:19.8	1	-72:14:14		304.4488	-44.8495
01:33:50.9		+30:39:36.8		133.6102	-31.3306
05:38:55.6		-64:04:57		273.5745	-32.0834
05:38:41.8		-69:05:14		279.4493	-31.6743
18:01:00		-25:47:26.4		4.4436	-1.3441
19:15:11.5		+10:56:44.7		45.3656	-0.2189
19:07:21.1	2	+09:18:41	2	43.0242	0.7359
00:42:52.6		+41:15:39.7		121.2019	-21.582
00:42:55		+41:16:02.6		121.2102	-21.5759

13:00:02.99		+12:40:56.9		311.3004	75.4141
15:37:09		+11:55:48		19.842	48.344
17:48:02.2534	0.0165	-24:46:37.7	0.5	3.83604	1.69622
18:45:36	1	+00:50:00	120	33.008	1.679
20:19:31.96		+24:25:15.4		64.746	-6.6242
00:42:48.7		+35:33:12		120.9578	-27.2853
02:22:26.03		+47:29:19.3		138.4637	-12.6202
02:34:22.57		-43:47:46.9		258.4808	-63.4143
07:34:36.3		+31:52:28		187.4557	22.4762
07:44:39.5		+03:33:01		215.8567	13.4539
13:34:43.1		-08:20:56		320.9108	53.0054
16:34:20.40		+57:09:42.8		86.5649	40.9126
20:45:09.9		-31:20:04		12.6628	-36.8024
23:09:56.5		+47:57:30.3		105.9015	-11.5289
19:39:38.82		-06:03:49.5		32.9711	-13.4715
13:30:47		+24:13:58.8		17.024	80.678
07:20:47.2		-31:46:58		244.5115	-8.2534
00:19:50	1	+21:56:54		113.304	-40.332
05:13:50.8	1	-69:51:47		280.7964	-33.6881
05:43:34.2	1	-68:22:22		278.564	-31.3058
09:25:46.3	1	-47:58:17		271.3556	1.885
16:01:41.01		+66:48:10.1		100.2877	40.9712
10:45:03.59		-59:41:04.3		287.5969	-0.6296
06:54:13.04		-23:55:42.0		234.7568	-10.0832
20:20:46		+43:54:55		81.011	4.167
04:12:08.85		-10:28:10.0		203.502	-40.0405
09:43:45.47		+55:57:09.1		158.9224	45.9024
10:01:40.43		+17:24:32.7		217.7973	49.7407
15:03:45.7		+47:39:00		80.3667	57.0718
20:37:18.7		+75:35:44		109.2183	20.058
21:22:04.5		+17:08:22.1		67.8703	-22.6577
12:14:23.6		+11:49:21.9		271.5406	72.3975
16:55:47.8		+35:10:56.9		57.866	37.9074
18:05:36.1		+69:45:16.9		100.0522	29.2747
00:44:01.32		+09:32:57.8		119.8733	-53.2783
01:03:53.5		-72:54:48		301.6568	-44.1841
01:33:33.8		+30:32:12.8		133.5673	-31.4634
05:35:16.47		-05:23:23.1		209.0108	-19.3841
05:37:36.7		-69:09:41.3		279.5492	-31.7617
17:50:25.12		+70:45:36.4		101.2778	30.5094
20:04:18.46		-55:43:32.3		342.1629	-32.2416
00:51:49.2		-73:10:30		302.8935	-43.9532
00:52:11		-72:20:18		302.852	-44.79
00:42:35		-73:40:30		303.789	-43.439
00:49:43.8		-73:23:02		303.1009	-43.7438

00:52:55		-72:33:00		302.776	-44.578
00:56:05		-72:22:01		302.437	-44.757
00:57:50		-72:07:57		302.238	-44.987
00:57:36		-72:19:35		302.273	-44.794
00:57:27		-73:25:31		302.339	-43.696
01:00:43.14		-72:11:33.8		301.9301	-44.9175
01:01:21		-72:11:18		301.862	-44.919
01:03:12.8		-72:08:59		301.6573	-44.9494
01:03:13		-72:41:39		301.706	-44.406
01:19:51		-73:11:49		300.094	-43.774
00:30:27.43		+04:51:39.7		113.1412	-57.6113
02:05:37.92		+64:49:42.8		130.7192	3.0845
10:24:38.77		-07:19:19.0		251.7018	40.5159
11:19:14.30		-61:27:49.5		292.1513	-0.5369
11:24:39.1		-59:16:20		292.0383	1.7515
14:20:08.24		-60:48:16.4		313.5412	0.227
17:44:29.39		-11:34:54.6		14.7939	9.1798
18:00:59.8		-24:50:57		5.2613	-0.877
18:46:24.5		-02:58:28		29.7116	-0.2382
18:56:10.89		+01:13:20.6		34.5606	-0.4978
22:29:05.28		+61:14:09.3		106.6475	2.9487
09:29:18		-31:23:06		260.1	14.209
17:51:13.49	0.75	-30:37:23.4	0.6	359.1819	-1.912
18:06:59.8		-29:24:30		1.9353	-4.2726
18:13:39.03		-33:46:22.3		358.7461	-7.5885
01:11:08.4		-73:16:46		300.9714	-43.7737
18:45:36.9		+00:51:45		33.0359	1.6888
05:37:43.0		-70:34:15		281.1905	-31.5749
17:46:20.8		-29:03:28.6		359.9787	-0.1991
17:47:02.6		-28:52:58.9		0.2073	-0.2385
05:01:46.8		+11:46:51		188.9139	-17.9413
18:45:34.8		-04:34:35		28.1919	-0.7855
03:56:28		-36:41:42		238.65	-49.986
02:42:40.83		-00:00:48.4		171.6457	-51.6181
09:47:40.2		-30:56:54		262.7439	17.2343
12:35:37		-39:54:19		299.64	22.865
13:05:26.1		-49:28:15		305.2681	13.3374
13:25:27.62		-43:01:08.8		309.5159	19.4173
23:18:23.5		-42:22:35		348.0663	-65.6928
12:29:06		+02:03:09		289.944	64.36
17:44:42		-29:16:54		359.6	-0.009
17:50:45.2		-34:12:11.7		356.0475	-3.6518
01:53:04.		+74:42:44		127.044	12.335
04:39:49.7	1	-68:09:02	1	279.8683	-37.0961
19:05:26.6	1	-01:42:03	1	33.0135	-3.8913

19:30:30.13		+18:52:14.1		54.0962	0.2652
00:23:50.3511	0.003	-72:04:31.486	0.001	305.923459	-44.892185
00:24:13.8776	0.003	-72:04:43.8323	0.0009	305.880632	-44.893314
00:24:11.1013	0.006	-72:05:20.131	0.003	305.883479	-44.882814
00:24:03.8519	0.003	-72:04:42.799	0.001	305.898634	-44.891679
00:24:07.956	0.015	-72:04:39.683	0.007	305.8915	-44.8933
00:24:06.6989	0.0105	-72:04:06.789	0.003	305.895649	-44.902116
00:24:07.932	0.015	-72:04:39.664	0.005	305.8915	-44.8933
00:23:59.4040	0.0015	-72:03:58.7720	0.0009	305.909184	-44.902916
00:24:03.770	0.03	-72:04:56.90	0.01	305.89795	-44.88779
00:23:54.485	0.045	-72:05:30.72	0.01	305.91256	-44.87672
00:24:09.1835	0.0135	-72:04:28.875	0.007	305.889908	-44.896526
00:24:04.6492	0.0075	-72:04:53.751	0.003	305.896564	-44.888825
00:24:16.488	0.015	-72:04:25.149	0.007	305.87705	-44.89894
00:24:03.9	0.6	-72:04:43.4	0.6	305.8985	-44.8915
00:24:08.541	0.03	-72:04:38.91	0.02	305.89047	-44.89365
00:24:09.8325	0.0075	-72:03:59.667	0.003	305.890454	-44.904673
17:40:44.589	0.06	-53:40:40.9	0.1	338.16487	-11.96671
22:25:52.36		+65:35:33.8		108.6364	6.8454
20:43:43.6		+27:40:56		70.6123	-9.1512
06:30:49.53		-28:34:43.6		236.9523	-16.7577
18:17:05.76		-36:18:05.5		356.8006	-9.3743
00:59:21.05		-72:23:17.1		302.0896	-44.7272
00:47:23.7		-73:12:26.9		303.3373	-43.9176
00:51:51.2	7	-73:10:32	7	302.8902	-43.9527
00:51:51.2	7	-73:10:32	7	302.8902	-43.9527
00:55:21.6		-72:42:00		302.5237	-44.4251
00:55:27.9	0.6	-72:10:58	0.6	302.4967	-44.9421
00:54:55.6	0.6	-72:45:10	0.6	302.5702	-44.373
00:53:23.8	0.6	-72:27:15	0.6	302.7243	-44.6733
00:55:17.9	3	-72:38:53	3	302.5285	-44.4772
00:53:26.4		-72:49:15.6		302.7253	-44.3064
18:44:50.59		-02:57:58.5		29.5405	0.1132
18:59:06		+08:15:00		41.1466	2.0625
04:20:02.36		-50:22:49.5		258.1362	-44.385
15:44:01		-56:45:54		324.9512	-1.4612
17:40:11.6		-28:47:48		359.4938	1.0839
16:05:18.66		+32:49:19.7		52.8811	47.9916
13:08:48.17		+21:27:07.5		338.7309	83.0823
08:06:22.8		-41:22:33		257.4258	-4.9849

Distance From Earth (kpc)	**Galactic Plane Z-Distance (pc)**	**Proper Motion RA-direction (arcsec/yr)**	**Proper Motion Dec-direction (arcsec/yr)**	**Energy Range (keV)**	**SOFT X-RAYS Flux (photons/cm^2/s)**	**Flux (erg/cm^2/s)**
2.00				0.5 - 2.4	9.66E-01	1.995E-09
0.25				0.1 - 2.4	8.36E-03	1.675E-11
0.16				0.1 - 2.4	2.05E-03	4.109E-12
1.82				0.5 - 2.4	1.73E-03	3.563E-12
4.30				0.5 - 2.4	4.27E-03	8.812E-12
2.50				0.5 - 2.4	1.78E-03	3.682E-12
2.98				0.5 - 2.4	1.99E-04	4.107E-13
2.00				0.5 - 2.4	9.02E-04	1.862E-12
4.12				0.5 - 2.4	5.85E-04	1.208E-12
3.94				0.5 - 2.4	2.99E-04	6.180E-13
0.17				0.5 - 2.4	1.40E-04	2.891E-13
0.18				0.1 - 2.4	9.32E-04	1.868E-12
5.50				0.5 - 2.4	2.33E-04	4.800E-13
0.28				0.1 - 2.4	6.90E-03	1.382E-11
47.3				0.5 - 2.4	2.69E-03	5.553E-12
0.25				0.1 - 2.4	1.49E-04	2.993E-13
1.53				0.5 - 2.4	1.47E-04	3.038E-13
0.26		-0.00209	0.02946	0.1 - 2.4	6.48E-05	1.299E-13
7.26						
1.50				0.5 - 2.4	9.89E-04	2.041E-12
0.52				0.1 - 2.4	2.44E-05	4.898E-14
0.50				0.1 - 2.4	4.68E-03	9.389E-12
2.07				0.5 - 2.4	8.62E-05	1.779E-13
2.46				0.5 - 2.4	4.84E-05	1.000E-13
5.70				0.1 - 2.4	7.21E-05	1.446E-13
0.38				0.1 - 2.4	1.95E-05	3.912E-14
2.02				0.1 - 2.4	4.07E-05	8.153E-14
1.5	-11			0.1 - 2	2.86E-01	5.199E-10
10.6	93			0.1 - 2	2.29E-02	4.165E-11
10	3			0.1 - 2	4.59E-02	8.356E-11
14.5						
7	32			0.1 - 2	3.28E-02	5.969E-11
8.5	10			0.1 - 2	5.78E-03	1.052E-11
6.2	-108			0.1 - 2	2.03E-02	3.695E-11
60						

65				0.1 - 2.4	6.09E-04	1.22E-12
60				0.1 – 2	1.44E-02	2.60E-11
				0.15 - 2.4	5.43E-03	1.09E-11
				0.2 - 2	7.18E-03	1.31E-11
				0.2 - 2	2.393E-05 - 2.393E-04	4.356E-14 - 4.356E-13
60						
				0.2 - 2	1.19E-05	2.16E-14
3.5						
				0.1 - 2.4	2.777E-03 - 8.331E-03	5.566E-12 - 1.670E-11

50				0.1 - 2.4	1.60E-01	3.2E-10
				0.1 - 2.4	2.78E-05	5.57E-14
				0.1 - 2.4	8.33E-05	1.67E-13
				0.1 - 2.4	1.11E-04	2.23E-13
2.6				0.05 - 2	8.24E-02	1.5E-10
				0.1 - 2.4	1.39E-03	2.78E-12
				0.1 - 2.4	1.75E-03	3.5E-12
				0.2 - 4.5	3.856E-03 - 3.856E-02	1.03E-11 - 1.03E-10
8.5				0.1 - 2.4	2.28E-03	4.56E-12

1.5				0.2 - 2	1.52E-02	2.76E-11
5.3						
2.4				0.1 - 2.4	1.50E-03	3E-12
20						
8.5						

2				0.1 - 2.4	3.60E-04	7.224E-13
3.7						
2.5						
2.5						
				0.1 - 2.4	2.43E-01	4.866E-10

4						
				0.3 - 3.2	4.570E-04	1.05E-12

8.5						

				0.9 - 4.0	2.49E-04	7.50E-13
				0.9 - 4.0	3.732E-04 - 6.469E-02	1.125E-12 - 1.951E-10
				0.9 - 4.0	4.976E-04	1.50E-12
				0.9 - 4.0	4.976E-04	1.50E-12
				0.9 - 4.0	4.976E-04	1.50E-12
				0.9 - 4.0	4.976E-04	1.50E-12
				0.9 - 4.0	4.976E-04	1.50E-12

3				0.1 - 2.4	1.55E-01	3.108E-10
4						
				0.5 - 2	1.546E-02	2.90E-11
7				0.1 - 2.4	3.47E-01	6.962E-10
7				0.05 - 2	7.09E-01	1.29E-09
9.4				0.5 - 4.5	1.85E-01	5.07E-10
1						

0.3	-43			0.1 - 2.4	8.43E-03	1.69E-11
5.2	135			0.1 - 2.4	2.50E-03	5E-12
0.832				0.1 - 4	8.65E-05	2.2E-13
0.075				0.1 - 3.5	2.46E-03	5.9E-12
4.60				0.5 - 2.5	1.19E-03	2.5E-12
0.38						
0.19				0.1 - 1.2	3.75E-04	5E-13
				0.1 - 2.4	1.18E-03	2.36E-12
0.075				0.1 - 3.5	1.13E-03	2.7E-12
0.125				0.2 - 4	7.47E-04	1.9E-12
0.3				1.5 - 4	4.18E-04	1.6E-12
				0.1 - 0.5	8.29E-03	6E-12
				0.1 - 2.4	9.90E-04	1.985E-12
0.355				0.1 - 4	6.29E-05	1.6E-13
82						
0.14				0.1 - 3.5	6.67E-03	1.6E-11
0.25				0.1 - 4	1.42E-04	3.6E-13
0.20						
0.08				0.1 - 3.5	6.67E-04	1.6E-12
0.125				0.1 - 4	1.14E-03	2.9E-12
0.25				0.1 - 3.5	1.00E-02	2.4E-11
				0.1 - 2.4	4.39E-03	8.8E-12
0.125				0.1 - 3.5	5.42E-03	1.3E-11
0.2						
0.49						
0.045						
1.1						
0.74				0.1 - 2.4	7.54E-04	1.512E-12
0.16				0.1 - 3.5	2.71E-03	6.5E-12
0.5						
				0.1 - 2.4	1.05E-03	2.103E-12
				0.1 - 2.4	8.98E-03	1.8E-11
0.5						
				0.1 - 2.4	1.28E-03	2.56E-12
0.4						
				0.1 - 2.4	7.57E-04	1.518E-12
1.6				0.2 - 3.5	1.67E-02	4E-11
0.25						
0.15				0.1 - 2.4	2.93E-03	5.873E-12
				0.1 - 2.4	2.23E-04	4.459E-13

0.125				0.1 - 3.5	2.71E-02	6.5E-11
0.433				0.1 - 2.4	5.99E-05	1.2E-13
				0.1 - 2.4	4.74E-03	9.5E-12
1.5						
0.4						
0.08				0.1 - 4	2.75E-03	7E-12
0.3						
				0.1 - 2.4	9.05E-04	1.813E-12
				0.1 - 4	2.99E-04	7.6E-13
0.18				0.2 - 4.5	7.71E-04	2.06E-12
0.83				0.1 - 2.4	3.83E-04	7.668E-13
0.7				0.1 - 3.5	5.84E-04	1.4E-12
0.15				0.1 - 3.5	9.59E-04	2.3E-12
0.136				0.1 - 2.4	3.29E-03	6.586E-12
				0.1 - 2.4	2.00E-05	4E-14
1.18				0.1 - 4	8.65E-05	2.2E-13
				0.2 - 4.5	5.68E-05	1.518E-13
0.38				0.1 - 3.5	3.13E-03	7.5E-12
0.6						
0.2				0.1 - 4	2.01E-03	5.1E-12
1.3				0.1 - 3.5	1.67E-04	4E-13
0.81				0.2 - 4	1.18E-04	3E-13
0.345				0.2 - 4	2.24E-04	5.7E-13
0.15						
0.3				0.1 - 2.4	1.38E-03	2.763E-12
0.13				0.1 - 4	3.93E-03	1E-11
0.6				0.1 - 2.4	2.69E-03	5.394E-12
0.43				0.1 - 2.4	1.11E-04	2.23E-13
0.1				0.18 - 0.5	2.76E-02	2E-11
0.52				0.05 - 2	2.79E-03	5.071E-12
0.44				0.1 - 2.4	3.49E-05	7E-14
0.5				0.1 - 2.4	1.90E-03	3.812E-12
0.3				0.1 - 2.4	3.62E-03	7.261E-12
0.19						
0.1				0.1 - 2.4	9.35E-04	1.873E-12
0.144				0.5 - 4.5	6.56E-03	1.8E-11
				0.1 - 2.4	1.63E-03	3.263E-12
				0.1 - 2.4	2.98E-03	5.978E-12
				0.1 - 2.4	5.71E-03	1.145E-11
				0.1 - 4	1.57E-04	4E-13
				0.1 - 0.5	4.84E-04	3.5E-13

				0.1 - 2.4	5.53E-03	1.109E-11
0.3				0.1 - 4	2.83E-04	7.2E-13
0.216				0.05 - 2	5.41E-02	9.854E-11
0.088				0.2 - 4.5	3.54E-01	9.458E-10
0.38						
				0.1 - 2.4	7.33E-04	1.47E-12
				0.1 - 2.4	1.66E-02	3.335E-11
0.705	630			0.1 - 2.4	9.28E-03	1.859E-11
0.086				0.1 - 4	1.57E-03	4E-12
0.142						
0.25				0.1 - 2.4	6.49E-03	1.3E-11
				0.1 - 2.4	1.25E-02	2.509E-11
0.1				0.1 - 0.28	7.12E-01	3.1E-10
				0.1 - 2.4	4.67E-03	9.357E-12
0.3						
				0.1 - 2.4	3.34E-04	6.7E-13
0.4						
0.215				0.1 - 2.5	4.89E-03	1E-11
0.4				0.1 - 2.4	2.76E-04	5.535E-13
0.19				0.1 - 2.4	1.65E-03	3.299E-12
0.25				0.1 - 2.4	2.57E-04	5.144E-13
1.2				0.2 - 4	1.97E-04	5E-13
0.25				0.1 - 2.4	1.90E-03	3.804E-12
2.5				0.2 - 4.5	4.61E-05	1.232E-13
0.12				0.1 - 3.5	7.51E-04	1.8E-12
0.1				0.1 - 3.5	5.84E-04	1.4E-12
0.13				0.1 - 3.5	5.00E-04	1.2E-12
0.14				0.1 - 3.5	5.25E-03	1.26E-11
0.075				0.1 - 3.5	2.75E-03	6.6E-12
				0.1 - 2.4	9.24E-04	1.851E-12
0.95				0.1 - 2.4	1.58E-03	3.173E-12
0.1				0.1 - 2.4	2.82E-03	5.646E-12
0.3				0.1 - 3.5	1.67E-03	4E-12
0.2				0.1 - 4	1.06E-03	2.7E-12
0.14				0.1 - 3.5	6.67E-04	1.6E-12
0.13				0.1 - 3.5	2.92E-03	7E-12
0.2				0.1 - 3.5	2.67E-03	6.4E-12
0.08				0.1 - 3.5	4.63E-03	1.11E-11
				0.1 - 2.4	2.15E-04	4.299E-13
				0.1 - 2.4	3.30E-04	6.623E-13
1				0.1 - 4	4.33E-05	1.1E-13
				0.1 - 2.4	7.10E-04	1.423E-12

				0.1 - 2.4	1.55E-05	3.1E-14
0.63				0.1 - 4	9.44E-05	2.4E-13
2.8				2 - 2.4	2.00E-02	7E-11
2.3				0.1 - 2.4	9.98E-05	2E-13
				0.1 - 2.4	4.40E-04	8.818E-13
50				0.2 - 4.5	1.00E+00	2.67E-09
5						
0.7143				0.1 - 2.4	2.35E-05	4.7E-14
0.2083				0.1 - 2.4	1.79E-03	3.5814E-12
0.4167				0.1 - 2.4	3.75E-05	7.52E-14
0.2273				0.1 - 2.4	6.10E-05	1.222E-13
0.0781				0.1 - 2.4	7.88E-03	1.5792E-11
0.0278				0.1 - 2.4	3.99E-02	7.99E-11
0.1111				0.1 - 2.4	1.41E-05	2.82E-14
0.4348				0.1 - 2.4	1.41E-04	2.82E-13
0.1351				0.1 - 2.4	2.81E-05	5.64E-14
0.3448				0.1 - 2.4	6.10E-05	1.222E-13
0.4762				0.1 - 2.4	1.08E-04	2.162E-13
0.2564				0.1 - 2.4	4.41E-04	8.836E-13
0.1852				0.1 - 2.4	7.97E-05	1.598E-13
0.5555				0.1 - 2.4	1.08E-04	2.162E-13
				0.3 - 3.5	5.30E-05	1.271E-13
0.5				0.1 - 2.4	1.08E-04	2.162E-13
0.0833				0.1 - 2.4	2.98E-03	5.9784E-12
0.5				0.1 - 2.4	2.77E-04	5.546E-13
0.25				0.1 - 2.4	5.30E-04	1.0622E-12
0.0263				0.1 - 2.4	2.35E-04	4.7E-13
0.1667				0.1 - 2.4	8.21E-04	1.645E-12
0.0741				0.1 - 2.4	1.87E-03	3.7506E-12
0.2381				0.1 - 2.4	5.68E-04	1.1374E-12
0.5802				0.1 - 2.4	7.50E-05	1.504E-13
0.2632				0.1 - 2.4	1.08E-04	2.162E-13
1				0.1 - 2.4	2.81E-05	5.64E-14
0.3448				0.1 - 2.4	9.38E-05	1.88E-13
0.3125				0.1 - 2.4	3.28E-05	6.58E-14
0.4348				0.1 - 2.4	6.24E-04	1.2502E-12
0.2				0.1 - 2.4	7.97E-05	1.598E-13
10						
0.031				0.1 - 2.4	9.76E-03	1.9552E-11
0.054				0.1 - 2.4	4.74E-03	9.494E-12
0.125				0.1 - 2.4	4.46E-03	8.93E-12
0.06				0.1 - 2.4	7.04E-03	1.41E-11

0.017				0.1 - 2.4	2.04E-02	4.089E-11
0.075				0.1 - 2.4	4.64E-03	9.306E-12
0.13				0.1 - 2.4	3.47E-03	6.956E-12
0.42				0.2 - 4.5	2.81E-04	7.5E-13
0.05				0.1 - 2.4	3.08E-02	6.1758E-11
0.048				0.1 - 2.4	1.45E-03	2.914E-12
0.036				0.1 - 2.4	1.14E-01	2.28044E-10
0.055				0.1 - 2.4	2.02E-02	4.042E-11
0.143				0.1 - 2.4	7.50E-04	1.504E-12
0.18				0.1 - 2.4	2.33E-03	4.668E-12
0.0545				0.3 - 3.5	2.80E-04	6.721E-13
0.013				0.1 - 2.4	1.18E-01	2.3688E-10
0.02				0.1 - 3.5	8.34E-03	2E-11
0.22				0.1 - 2.4	1.88E-04	3.76E-13
0.074				0.1 - 2.4	1.92E-03	3.854E-12
0.38				0.1 - 2.4	6.57E-04	1.316E-12
0.255				0.1 - 2.4	3.28E-04	6.58E-13
0.525				0.1 - 2.4	5.63E-04	1.128E-12
0.038				0.1 - 2.4	6.57E-03	1.316E-11
0.3				0.1 - 2.4	7.97E-04	1.598E-12
0.395				0.1 - 2.4	4.69E-04	9.4E-13
0.055				0.1 - 2.4	8.96E-03	1.7954E-11
0.16				0.1 - 2.4	4.69E-05	9.4E-14
0.1				0.1 - 2.4	1.41E-03	2.82E-12
0.034				0.1 - 2.4	3.00E-04	6.016E-13
0.11				0.3 - 3.5	3.67E-04	8.8E-13
0.165				0.1 - 2.4	1.04E-03	2.089E-12
0.15				0.15 - 2.8	1.65E-01	3.56E-10
0.036				0.1 - 2.4	5.49E-03	1.0998E-11
0.13				0.1 - 2.4	7.93E-03	1.5886E-11
0.086				0.1 - 2.4	3.80E-03	7.614E-12
0.055				0.1 - 2.4	1.13E-03	2.256E-12
0.35				0.1 - 2.4	8.91E-04	1.786E-12
0.18				0.1 - 2.4	3.75E-03	7.52E-12
0.3				0.1 - 2.4	3.28E-04	6.58E-13
0.053				0.1 - 2.4	1.27E-02	2.5474E-11
0.27				0.1 - 2.4	6.58E-04	1.31816E-12
0.22				0.1 - 2.4	2.81E-04	5.64E-13
0.021				0.1 - 2.4	4.85E-02	9.7196E-11
0.18				0.1 - 2.4	2.67E-03	5.358E-12
0.071				0.1 - 2.4	6.80E-03	1.363E-11
0.31				0.1 - 2.4	1.60E-03	3.196E-12
0.039				0.1 - 2.4	2.62E-02	5.2546E-11
0.4				0.1 - 2.4	8.91E-04	1.786E-12
0.1				0.1 - 2.4	1.74E-03	3.478E-12

0.19				0.1 - 2.4	6.57E-04	1.316E-12
0.0417				0.1 - 2.4	8.86E-03	1.7766E-11
0.285				0.1 - 2.4	7.04E-04	1.41E-12
0.315				0.1 - 2.4	7.50E-04	1.504E-12
				0.1 - 2.4	6.31E-04	1.265E-12
0.302				0.1 - 2.4	7.04E-04	1.41E-12
0.39				0.1 - 2.4	3.28E-04	6.58E-13
0.063				0.1 - 2.4	5.16E-04	1.034E-12
0.046				0.1 - 2.4	1.36E-02	2.7166E-11
0.029				0.1 - 2.4	4.08E-03	8.178E-12
0.25				0.1 - 2.4	1.67E-03	3.3424E-12
0.3				0.1 - 2.4	1.59E-03	3.1772E-12
0.205				0.1 - 2.4	6.57E-04	1.316E-12
0.047				0.1 - 2.4	3.62E-02	7.2568E-11
0.095				0.1 - 2.4	9.38E-04	1.88E-12
0.125				0.1 - 2.4	1.14E-02	2.2936E-11
0.025				0.1 - 2.4	1.64E-03	3.29E-12
0.175				0.1 - 2.4	4.64E-03	9.306E-12
0.029				0.1 - 2.4	5.44E-02	1.09E-10
50						
1.95				0.5 - 3	1.74E-04	4E-13
3				0.1 - 2.4	6.57E-04	1.316E-12
2.12	-0.13			0.1 - 2.4	1.55E-05	3.1E-14
6.56				0.1 - 2.4	2.39E-04	5.10E-13
7.0						
4.5				0.6 - 2	3.61E-04	7E-13
1.8				0.1 - 2.4	4.99E-06	1E-14
2.9	1.27			0.1 - 2.4	2.74E-05	5.5E-14
3.28	0.01			0.1 - 2.4	1.15E-05	2.3E-14
7.8						
4.07	0.04			0.1 - 2.4	1.32E-04	2.64E-13
3.6		-0.128	-0.486			
				0.1 - 2.4	4.99E-07	1E-15
0.78				0.1 - 2.4	2.99E-06	6E-15
				0.2 - 4	5.90E-03	1.5E-11
				0.1 - 2.4	1.82E-02	3.639E-11
0.165				0.1 - 2.4	7.03E-04	1.409E-12
				0.3 - 3.5	4.84E-04	1.16E-12
0.059						
0.13						
				0.1 - 2.4	2.14E-03	4.289E-12

0.09				0.1 - 2.4	7.40E-04	1.484E-12
0.4				0.18 - 2.5	5.08E-03	1.04E-11
				0.3 - 3.5	1.51E-04	3.62E-13
				0.3 - 3.5	1.51E-04	3.62E-13
0.088				0.1 - 2.4	1.11E-02	2.23E-11
0.15				0.18 - 2.5	1.47E-02	3E-11
0.15				0.1 - 2.4	7.30E-03	1.463E-11
0.03				0.44 - 2.8	2.11E-02	4.6E-11
0.026				0.1 - 2.4	4.90E-02	9.822E-11
				0.1 - 2.4	7.50E-04	1.503E-12
				0.2 - 4.5	2.69E-04	7.18E-13
				0.2 - 4.5	1.15E-04	3.077E-13
0.14				0.2 - 4.5	4.48E-04	1.197E-12
				0.2 - 4.5	4.30E-03	1.149E-11
				0.2 - 4.5	1.79E-04	4.787E-13
				0.2 - 4.5	1.15E-04	3.077E-13
				0.2 - 4.5	3.20E-04	8.548E-13
				0.2 - 4.5	6.66E-04	1.778E-12
				0.2 - 4.5	2.18E-04	5.812E-13
				0.2 - 4.5	1.66E-04	4.445E-13
				0.2 - 4.5	4.61E-04	1.231E-12
				0.2 - 4.5	5.63E-04	1.504E-12
				0.2 - 4.5	4.86E-04	1.299E-12
				0.2 - 4.5	4.86E-04	1.299E-12
				0.2 - 4.5	3.33E-04	8.89E-13
				0.2 - 4.5	2.94E-04	7.864E-13
				0.2 - 4.5	2.43E-04	6.496E-13
				0.2 - 4.5	1.28E-04	3.419E-13
				0.2 - 4.5	7.17E-04	1.915E-12
				0.2 - 4.5	3.33E-04	8.89E-13
				0.2 - 4.5	1.41E-04	3.761E-13
				0.2 - 4.5	1.02E-04	2.735E-13
				0.1 - 2.4	1.69E-03	3.394E-12
0.09						
				0.1 - 2.4	3.69E-03	7.402E-12
				0.1 - 2.4	1.82E-03	3.64E-12
68				0.1 - 2.4	1.36E-03	2.726E-12
				0.1 - 2.4	5.74E-03	1.15E-11
50				0.1 - 2.4	5.94E-02	1.19E-10
				0.2 - 4.5	1.17E-01	3.118E-10
10						
12.5						
12				0.1 - 2.4	3.49E-04	7E-13
				0.2 - 4	2.36E-05	5.994E-14
				0.2 - 4	1.32E-04	3.351E-13

0.62				0.1 - 2.4	5.49E-06	1.1E-14
0.68				0.1 - 2.4	8.88E-06	1.78E-14
				0.1 - 2.4	2.02E-03	4.047E-12
5						
0.91				0.1 - 2.4	8.93E-06	1.79E-14
0.0213				0.05 - 2	1.43E-02	2.612E-11
0.03				0.1 - 2.4	1.10E-03	2.211E-12
0.0114				0.05 - 2	1.66E-01	3.014E-10
0.0147				0.04 - 2	1.03E-02	1.87E-11
0.006				0.15 - 4	3.74E-03	9.5E-12
0.0164				0.05 - 2	5.35E-04	9.733E-13
0.0147				0.05 - 2	1.39E-03	2.53E-12
0.088				0.05 - 2	5.94E-02	1.081E-10
0.0194				0.1 - 2.4	9.62E-03	1.928E-11
				0.1 - 2.4	1.82E-03	3.647E-12
				0.1 - 2.4	8.97E-04	1.797E-12
0.136				0.1 - 2.4	1.06E-03	2.123E-12
2.38				0.1 - 2.4	9.38E-03	1.88E-11
55						
55						
2				0.1 - 2.4	3.99E-03	8E-12
				0.1 - 2.4	5.25E-03	1.052E-11
2.6						
				0.1 - 2.4	4.01E-04	8.038E-13
1.34						
0.055				0.1 - 4	5.67E-04	1.44E-12
0.556				0.1 - 4	1.44E-03	3.67E-12
0.052				0.1 - 4	1.04E-03	2.64E-12
0.013				0.1 - 4	1.22E-03	3.09E-12
0.0238				0.1 - 4	3.78E-03	9.6E-12
0.4127				0.3 - 3.5	7.17E-05	1.72E-13
				0.3 - 3.5	3.45E-04	8.28E-13
				0.3 - 3.5	7.38E-05	1.77E-13
				0.3 - 3.5	5.75E-05	1.38E-13
0.055				0.4 - 2.4	9.39E-04	1.8894E-12
50						
				0.1 - 2.4	3.10E-04	6.21E-13
0.44				0.1 - 2.4	1.19E-02	2.39E-11
47.3				0.1 - 2	3.30E-04	6E-13
				0.1 - 2.4	7.72E-04	1.547E-12
60						

60						
60						
57						
60						
0.23				0.1 - 2.4	9.98E-05	2.00E-13
2.6				0.8 - 10	4.61E-03	2.00E-11
0.35				0.1 - 2.4	1.09E-05	1.12E-14
5				0.7 - 5.0	4.31E-05	2.00E-13
4.8				2 - 8	1.59E-03	9.49E-12
2						
0.357				0.1 - 2.4	1.06E-05	9.23E-15
5						
19						
3.2						
3						
6	1200					
8						
8						
8						
				0.1 - 2.4	0.023	4.61E-11
				0.1 - 2.4	0.0023	4.61E-12

5						
4.5		0.0078	-0.0032	0.5 - 2.5	9.92E-08	1.64E-16
4.5		0.0077	-0.0026	0.5 - 2.5	4.97E-07	8.23E-16
4.5		0.0091	-0.0039	0.5 - 2.5	9.92E-07	1.64E-15
4.5		0.0066	-0.0037	0.5 - 2.5	7.88E-07	1.30E-15
4.5				0.5 - 2.5	3.14E-07	5.19E-16
4.5				0.5 - 2.5	3.14E-07	5.19E-16
4.5				0.5 - 2.5	3.95E-07	6.54E-16
4.5		0.0046	-0.0037	0.5 - 2.5	4.97E-07	8.23E-16
4.5				0.5 - 2.5	6.26E-07	1.04E-15
4.5				0.5 - 2.5	3.14E-07	5.19E-16
4.5				0.5 - 2.5	3.95E-07	6.54E-16
4.5				0.5 - 2.5	9.92E-07	1.64E-15
4.5				0.5 - 2.5	3.14E-07	5.19E-16
4.5				0.5 - 2.5	3.95E-07	6.54E-16
4.5				0.5 - 2.5	2.49E-07	4.13E-16
4.5				0.5 - 2.5	4.97E-07	8.23E-16
2.2	-0.45			0.5 - 2.5	6.92E-06	1.37E-14
60						
60						
60						
60						
60						
60						
60						
60						
60						
63						
15						
3.9				0.1 – 2.4	2.66E-03	6.90E-13
8.5						
1				0.1 – 2.4	1.06E-02	9.00E-12
				0.1 – 2.4	3.51E-03	2.90E-12
				0.1 – 2.4	2.79E-03	2.90E-12

ENERGY					
Energy Range (keV)	**HARD X-RAYS Flux (photons/cm^2/s)**	**Flux (erg/cm^2/s)**	**Neutral Hydrogen Column Density - N_H** (1/cm^2)	**Photon Index (Power Law Model) - Γ or α**	**Pulsed Fraction**
2 - 10	1.54E+00	9.93E-09	3.00E+21		0.70000
2 - 10	1.59E-03	1.03E-11	4.00E+20		0.10000
2 - 10	1.23E-05	7.94E-14	1.30E+20		0.33113
2 - 10	1.59E-04	1.03E-12	3.45E+21		
2 - 10	1.62E-02	1.05E-10	1.27E+22		0.64565
2 - 10	3.15E-04	2.04E-12	3.40E+21		
2 - 10	3.86E-05	2.50E-13	4.00E+21		
			3.60E+21		
2 - 10	2.63E-03	1.70E-11	4.00E+22		
2 - 10	2.75E-05	1.78E-13	1.30E+22		
0.2 – 10	1.14E-04	4.07E-13	1.00E+20		0.31623
2 - 10	6.65E-05	4.30E-13	8.00E+20	2.35	0.27542
2 - 10	1.93E-04	1.25E-12	2.90E+21		0.98000
2 - 10	3.17E-05	2.05E-13	1.70E+20		0.14791
2 - 10	5.15E-03	3.33E-11	4.60E+21	1.92	0.67000
2 - 10	1.28E-05	8.26E-14	3.50E+20		0.28184
			4.50E+21		0.60000
0.2 – 10	4.81E-05	1.10E-13	2.90E+20	1.75	0.68000
2 - 10	1.24E-07	8.00E-16	6.00E+20		
2 - 10	1.93E-06	1.25E-14	6.00E+19		0.75?
2 - 10	1.64E-06	1.06E-14	2.60E+20		0.14125
2 - 10	1.79E-05	1.16E-13	2.00E+20		
2 - 10	6.26E-06	4.05E-14	2.00E+21		
2 - 10	6.65E-05	4.30E-13	2.00E+21	0.61	0.73000
2 - 10	9.27E-07	6.00E-15	4.00E+20	1.50	
2 - 10	6.63E-06	4.29E-14	4.40E+21		0.70000
0.5 - 10	1.63E-03	5.97E-12			
2 - 10	5.984E-04	3.872E-12			
2 - 10	1.197E-04	7.744E-13			

2 - 10	1.496E-03 - 2.693E-02	9.680E-12 - 1.742E-10			
2 - 10	<2.992E-03 - 1.496E-02	<1.936E-11 - 9.680E-11			
0.7 - 10	9.242E-04	3.60E-12			
2 - 10	7.780E-03	5.034E-11			
2 - 10	2.992E-05 - 2.693E-02	1.936E-13 - 1.742E-10			
2 - 10					
2 - 10	7.181E-05 - 1.406E-02	4.646E-13 - 9.099E-11			0.27
2 - 10	<2.992E-03 - 2.095E-02	<1.936E-11 - 1.355E-10			
2 - 10	1.496E-02 - 3.291E-02	9.680E-11 - 2.130E-10			
2 - 10	4.189E-03	2.710E-11			
2 - 10	1.137E-02	7.357E-11			
2 - 10	2.992E-03	1.936E-11			
0.7 - 10	5.776E-04	2.25E-12			
2 - 10	2.992E-04	1.936E-12			
2 - 10	6.882E-03	4.453E-11			
2 - 10	2.992E-04	1.936E-12			
2 - 10	4.488E-02	2.904E-10			
2 - 10	1.197E-02	7.744E-11			
2 - 10	<5.984E-03 - 1.047E+00	<3.872E-11 - 6.776E-09			
2 - 10	1.496E-03 - 1.706E-01	9.680E-12 - 1.104E-09			
2 - 10	2.992E-02	1.936E-10			
0.2 - 5	8.336E-04	2.32E-12			
2 - 10	<1.496E-03 - 3.740E+00	<9.680E-12 - 2.420E-08			
2 - 10	<2.693E-02 - 1.107E-01	<1.742E-10 - 7.163E-10			
2 - 10	5.984E+00	3.872E-08			
2 - 10	2.992E-03	1.936E-11			
2 - 10	1.706E-02	1.104E-10			
2 - 10	2.095E-04	1.355E-12			

2 - 10	2.992E-03	1.936E-11			
2 - 10	5.087E-04	3.291E-12			
2 - 10	2.992E-03	1.936E-11			
2 - 10	<8.977E-03 - 1.795E-01	<5.808E-11 - 1.162E-09			0.05
2 - 10	<2.992E-05 - 5.386E-01	<1.936E-13 - 3.485E-09			
2 - 10	<8.977E-03 - 8.378E+00	<5.808E-11 - 5.421E-08			
2 - 10	<5.087E-03 - 1.317E-01	<3.291E-11 - 8.518E-10			
2 - 10	8.977E-03 - 7.480E-02	5.808E-11 - 4.840E-10			
2 - 10	5.386E-03	3.485E-11			
2 - 10	4.189E-04 - 1.077E-03	2.710E-12 - 6.970E-12			
2 - 10	3.291E-03	2.130E-11			
2 - 10	1.646E-03	1.065E-11			
2 - 10	8.977E-05	5.808E-13			
2 - 10	3.591E-03 - 1.406E-02	2.323E-11 - 9.099E-11			
2 - 10	2.095E-03	1.355E-11			
2 - 10	2.095E-03	1.355E-11			
2 - 10	1.795E-03	1.162E-11			
2 - 10	8.977E-02 - 8.977E-01	5.808E-10 - 5.808E-09			
2 - 10	5.984E-03 - 3.291E+00	3.872E-11 - 2.130E-08			
2 - 10	3.591E+00	2.323E-08			
2 - 10	9.874E-03	6.389E-11			
2 - 10	5.087E-04	3.291E-12			
2 - 10	<2.992E-04 - 2.992E-03	<1.936E-12 - 1.936E-11			
2 - 10	2.992E-04 - 2.095E-01	1.936E-12 - 1.355E-09			
2 - 10	2.992E-02 - 9.336E-01	1.936E-10 - 6.040E-09			

2 - 10	1.197E-02 - 2.992E+00	7.744E-11 - 1.936E-08			0.64
2 - 10	1.197E-02 - 1.197E-01	7.744E-11 - 7.744E-10			
2 - 10	2.693E-02 - 2.992E+00	1.742E-10 - 1.936E-08			
2 - 10	8.977E-03 - 4.787E-02	5.808E-11 - 3.098E-10			
2 - 10	<7.181E-02 - 2.992E-01	<4.646E-10 - 1.936E-09			
2 - 10	<7.181E-02 - 8.977E-01	<4.646E-10 - 5.808E-09			
2 - 10	6.583E-03	4.259E-11			
2 - 10	1.795E-03	1.162E-11			
2 - 10	2.394E-03	1.549E-11			
2 - 10	8.977E-04 - 5.984E-01	5.808E-12 - 3.872E-09			
2 - 10	1.197E-03	7.744E-12			
2 - 10	5.984E-03 - 1.287E-01	3.872E-11 - 8.325E-10			
2 - 10	1.197E-04	7.744E-13			
2 - 10	<8.977E-03 - 8.977E-02	<5.808E-11 - 5.808E-10			
2 - 10	8.079E-02	5.227E-10			
2 - 10	5.087E-03	3.291E-11			
2 - 10	1.197E-02 - 1.257E-01	7.744E-11 - 8.131E-10			
2 - 10	<3.291E-02 - 3.291E-01	<2.130E-10 - 2.130E-09			
2 - 10	1.197E-03	7.744E-12			
2 - 10	5.984E-04 - 1.496E-02	3.872E-12 - 9.680E-11			
2 - 10	8.65E-01	7.57E-09			
2 - 10	5.984E-03	3.872E-11			
2 - 10	1.795E-04	1.162E-12			
2 - 10	4.069E-03	2.633E-11			
2 - 10	8.079E-02	5.227E-10			
2 - 10	<5.984E-03 - 2.992E-01	<3.872E-11 - 1.936E-09			
2 - 10	2.992E-03	1.936E-11			
2 - 10	8.977E-04	5.808E-12			
2 - 10	4.787E-03 - 5.984E-01	3.098E-11 - 3.872E-09			
2 - 10	2.992E-03	1.936E-11			
2 - 10	7.480E-03	4.840E-11			
2 - 10	1.197E-03 - 9.874E-02	7.744E-12 - 6.389E-10			
2 - 10	2.992E-03	1.936E-11			

2 - 10	2.992E-03 - 1.317E-01	1.936E-11 - 8.518E-10			
0.7 - 10	2.599E-01	1.01E-09			
2 - 10	5.984E-03	3.872E-11			
2 - 10	1.795E-02	1.162E-10			
2 - 10	7.480E-02	4.840E-10			
2 - 10	<5.984E-03 - 2.603E-01	<3.872E-11 - 1.684E-09			
2 - 10	2.095E-03	1.355E-11			
2 - 10	1.197E-02 - 8.229E-01	7.744E-11 - 5.324E-09			
2 - 10	5.984E-03 - 2.992E-02	3.872E-11 - 1.936E-10			
2 - 10	2.095E-03	1.355E-11			
2 - 60	<1.268E-02 - 3.170E-01	<1.404E-10 - 3.509E-09			
2 - 10	<2.992E-02 - 2.513E-01	<1.936E-10 - 1.626E-09			
20 - 75	6.266E-02 - 1.230E-01	3.594E-09 - 7.054E-09			
2 - 10	<4.488E-03 - 2.394E-01	<2.904E-11 - 1.549E-09			
2 - 10	7.032E-01 - 3.950E+00	4.550E-09 - 2.556E-08			
2 - 10	<1.496E-03 - 4.189E+00	<9.680E-12 - 2.710E-08			
2 - 10	2.693E-01 - 1.287E+00	1.742E-09 - 8.325E-09			
2 - 10	1.197E-04	7.744E-13			
2 - 10	9.575E-01	6.195E-09			
2 - 10	5.984E-02	3.872E-10			
2 - 10	<1.795E-02 - 2.992E-01	<1.162E-10 - 1.936E-09			
2 - 10	2.095E-03	1.355E-11			
2 - 10	1.795E-03 - 1.646E-02	1.162E-11 - 1.065E-10			
2 - 10	1.496E-03	9.680E-12			
2 - 10	4.787E-02	3.098E-10			
2 - 10	1.496E-03 - 1.646E-01	9.680E-12 - 1.065E-09			
20 - 300	2.246E+01	2.03E-06			
2 - 10	8.977E-03 - 1.795E-02	5.808E-11 - 1.162E-10			
2 - 10	2.693E-02 - 1.317E-01	1.742E-10 - 8.518E-10			
2 - 10	1.496E-03	9.680E-12			
2 - 10	1.496E-01	9.680E-10			
2 - 10	5.984E-05 - 1.496E+02	3.872E-13 - 9.680E-07			

2 - 10	5.984E-02 - 2.394E-01	3.872E-10 - 1.549E-09			
2 - 10	2.992E-04 - 1.795E-01	1.936E-12 - 1.162E-09			
2 - 10	<1.795E-02	<1.162E-10			
2 - 10	2.992E-03 - 1.646E-01	1.936E-11 - 1.065E-09			
2 - 10	2.992E-02	1.936E-10			
2 - 10	8.977E-03	5.808E-11			
1 - 10	3.940E+00	1.74E-08			
2 - 12	1.40E-01	9.68E-10			
2 - 10	<1.197E-02 - 8.977E+00	<7.744E-11 - 5.808E-08			
2 - 10	7.48E-02	4.840E-10			
2 - 10	2.095E-02	1.355E-10			
2 - 10	1.496E-02 - 3.591E-01	9.680E-11 - 2.323E-09			
2 - 10	2.992E-04 - 5.984E+01	1.936E-12 - 3.872E-07			
2 - 10	1.496E-02 - 8.977E+00	9.680E-11 - 5.808E-08			
2 - 10	<1.496E-02 - 2.843E+00	<9.680E-11 - 1.839E-08			
2 - 10	<2.992E-03 - 4.488E+01	<1.936E-11 - 2.904E-07			
2 - 10	1.047E-01	6.776E-10			
2 - 10	1.795E+00 - 2.095E+01	1.162E-08 - 1.355E-07			
2 - 10	4.787E-02	3.098E-10			
2 - 10	4.787E-01	3.098E-09			
2 - 10	<2.992E-03 - 2.992E-01	<1.936E-11 - 1.936E-09			
2 - 10	4.189E+01	2.710E-07			
2 - 10	1.646E-01	1.065E-09			
2 - 10	7.480E-02	4.840E-10			
2 - 10	<5.984E-03 - 4.189E+00	<3.872E-11 - 2.710E-08			
2 - 10	3.890E-02	2.517E-10			
2 - 10	6.583E-01	4.259E-09			
2 - 10	1.496E+00	9.680E-09			
2 - 12	5.61E+00	3.87E-08			
2 - 10	4.488E-02 - 1.496E-01	2.904E-10 - 9.680E-10			
2 - 10	<1.496E-02 - 2.394E-01	<9.680E-11 - 1.549E-09			
2 - 10	4.488E-03 - 2.693E+00	2.904E-11 - 1.742E-08			

2 - 10	2.469E+00	1.597E-08			
2 - 10	1.346E-01	8.712E-10			
2 - 10	<1.496E-03 - 3.291E-02	<9.680E-12 - 2.130E-10			
2 - 10	<5.984E-03 - 1.077E+01	<3.872E-11 - 6.970E-08			
2 - 10	2.992E-02 - 8.378E-01	1.936E-10 - 5.421E-09			
2 - 10	9.575E-02	6.195E-10			
2 - 10	4.488E-01	2.904E-09			
2 - 10	5.984E-03	3.872E-11			
2 - 10	4.787E-02 - 3.890E-01	3.098E-10 - 2.517E-09			
2 - 9	9.26E-02	5.760E-10			
2 - 10	8.378E-02	5.421E-10			
20 - 100	4.551E+00	2.90E-07			
2 - 10	4.189E+00	2.710E-08			
2 - 10	2.095E-01	1.355E-09			
2 - 10	9.575E-02	6.195E-10			
2 - 10	4.488E-02	2.904E-10			
2 - 10	4.488E-01	2.904E-09			
2 - 10	8.977E-01	5.808E-09			
2 - 10	2.992E-01	1.936E-09			
2 - 10	2.693E+00	1.742E-08			
2 - 10	<2.992E-04 - 5.984E-01	<1.936E-12 - 3.872E-09			
2 - 10	<2.992E-02 - 3.890E-01	<1.936E-10 - 2.517E-09			
2 - 10	<2.992E-02 - 3.291E-01	<1.936E-10 - 2.130E-09			
2 - 10	2.992E-02	1.936E-10			
2 - 10	<1.496E-02 - 1.496E-01	<9.680E-11 - 9.680E-10			
2 - 10	1.017E-02	6.582E-11			
2 - 10	2.992E-02	1.936E-10			
2 - 10	4.787E-01	3.098E-09			
2 - 10	<1.197E-03 - 1.691E+00	<7.744E-12 - 1.094E-08			
2 - 10	5.984E-03	3.872E-11			
2 - 10	7.780E-02	5.034E-10			
2 - 10	8.977E-03	5.808E-11			
2 - 60	1.09E+01	1.21E-07			
2 - 10	2.693E-02	1.742E-10			
2 - 10	8.977E-02	5.808E-10			
2 - 10	1.197E-02 - 8.977E-02	7.744E-11 - 5.808E-10			

2 - 10	<4.488E-03 - 8.977E-01	<2.904E-11 - 5.808E-09			
2 - 10	<1.496E-02 - 7.780E-02	<9.680E-11 - 5.034E-10			
2 - 10	<5.984E-03 - 2.304E+00	<3.872E-11 - 1.491E-08			
2 - 10	2.095E-02	1.355E-10			
2 - 10	<5.984E-03 - 8.977E-03	<3.872E-11 - 5.808E-11			
2 - 10	1.346E-01	8.712E-10			
2 - 10	<2.693E-02 - 5.984E+00	<1.742E-10 - 3.872E-08			
2 - 10	2.992E-03 - 1.496E-02	1.936E-11 - 9.680E-11			
2 - 10	1.795E-01 - 5.386E-01	1.162E-09 - 3.485E-09			
2 - 10	1.496E-03 - 3.591E-02	9.680E-12 - 2.323E-10			
2 - 10	<2.992E-03 - 1.197E-01	<1.936E-11 - 7.744E-10			
2 - 10	1.795E-02	1.162E-10			
8 - 20	6.995E+00	1.365E-07			
2 - 10	1.197E-02	7.744E-11			
2 - 10	1.197E+00	7.744E-09			
2 - 10	<7.480E-02 - 8.229E-01	<4.840E-10 - 5.324E-09			
3 - 10	8.215E-04 - 4.107E-03	6.776E-12 - 3.388E-11			
2 - 10	2.992E-04 - 3.291E-01	1.936E-12 - 2.130E-09			
2 - 10	2.992E-04 - 5.386E-01	1.936E-12 - 3.485E-09			
2 - 10	8.079E-02	5.227E-10			
2 - 10	2.992E-04	1.936E-12			
2 - 10	9.575E-02	6.195E-10			
2 - 10	2.095E-01	1.355E-09			
2 - 10	4.488E-03 - 5.984E-02	2.904E-11 - 3.872E-10			
2 - 10	1.915E+00	1.239E-08			
2 - 10	8.977E-02	5.808E-10			

2 - 10	1.795E-01	1.162E-09			
2 - 10	3.890E-01	2.517E-09			
2 - 26	4.85E+00	4.30E-08			
2 - 10	2.992E-01	1.936E-09			
2 - 12	6.31E-01	4.36E-09			
2 - 10	3.740E+00	2.420E-08			
2 - 10	5.984E-02	3.872E-10			
2 - 10	2.095E+00	1.355E-08			
2 - 10	5.984E-03 - 2.992E+00	3.872E-11 - 1.936E-08			
2 - 12	1.54E+00	1.07E-08			
2 - 10	3.291E-01	2.130E-09	1.22E+21	2.2	0.041
2 - 10	4.787E-02	3.098E-10			
2 - 10	1.047E+00	6.776E-09			
2 - 10	4.488E-02	2.904E-10			
2 - 10	2.095E+00	1.355E-08			
2 - 12	3.504E-03 - 4.555E+01	2.420E-11 - 3.146E-07			
2 - 10	7.480E-01	4.840E-09			
2 - 10	2.992E-02 - 7.480E-02	1.936E-10 - 4.840E-10			
2 - 10	7.480E-02 - 1.855E-01	4.840E-10 - 1.200E-09			
2 - 10	8.977E-02	5.808E-10			
2 - 10	6.732E-01	4.356E-09			
2 - 10	8.977E-01	5.808E-09			
2 - 10	2.095E-02	1.355E-10			
2 - 10	2.095E-01	1.355E-09			
2 - 10	1.795E+00	1.162E-08			
2 - 10	2.992E-02	1.936E-10			
2 - 10	<2.992E-04 - 3.890E+00	<1.936E-12 - 2.517E-08			
2 - 10	8.977E-01	5.808E-09			
2 - 10	7.480E-02	4.840E-10			
2 - 10	<1.496E-02 - 1.346E-01	<9.680E-11 - 8.712E-10			
2 - 10	<1.496E-01	<9.680E-10			
2 - 10	8.977E-02	5.808E-10			
2 - 10	<1.496E-03 - 3.291E+01	<9.680E-12 - 2.130E-07			
2 - 10	4.787E-01	3.098E-09			
2 - 10	1.197E-03 - 5.984E+01	7.744E-12 - 3.872E-07			
2 - 10	3.291E-01	2.130E-09			
2 - 10	1.795E-02	1.162E-10			
2 - 10	2.693E-02	1.742E-10			

2 - 10	1.346E+00	8.712E-09			
2 - 10	7.181E-03	4.646E-11			
2 - 10	1.14E-02	7.4E-11			
0.5 - 25	4.43E-03	2.1168E-11			
2 - 20	4.65E-04	3.8E-12			
2 - 20	7.34E-04	6E-12			
2 - 20	4.89E-05	4E-13			
2 - 20	2.13E-03	1.74E-11			
2 - 20	1.10E-04	9E-13			
2 - 20	3.91E-04	3.2E-12			
2 - 10	1.30E-02	8.4E-11			
2 - 20	4.77E-04	3.9E-12			
2 - 10	2.94E-03	1.9E-11			
0.5 - 25	6.27E-04	3E-12			
2 - 10	4.02E-03	2.6E-11			
2 - 10	6.18E-03	4E-11			
2 - 10	7.73E-05	5E-13			
2 - 10	2.78E-03	1.8E-11			
2 - 10	4.64E-03	3.00E-11			
2 - 10	4.33E-03	2.8E-11			
0.5 - 25	3.94E-03	1.8816E-11			
2 - 10	3.09E-03	2E-11			
1 - 20	7.32E-03	4E-11			
2 - 10	3.25E-03	2.1E-11			

2 - 10	2.01E-02	1.3E-10			
2 - 10	7.73E-05	5E-13			
2 - 10	9.27E-03	6E-11			
2 - 10	4.64E-04	3E-12			
2 - 10	4.33E-03	2.8E-11			
0.5 - 25	4.43E-03	2.1168E-11			
0.5 - 25	3.94E-03	1.8816E-11			
2 - 10	5.56E-03	3.6E-11			
2 - 10	6.65E-03	4.3E-11			
2 - 10	2.16E-04	1.4E-12			

2 - 10	6.18E-04	4E-12			
2 - 10	3.40E-03	2.2E-11			
2 - 6	6.03E-04	3.2E-12			
2 - 10	2.63E-03	1.7E-11			
2 - 10	3.56E-03	2.3E-11			
2 - 10	6.18E-04	4E-12			
2 - 10	4.33E-04	2.8E-12			
2 - 10	3.56E-03	2.3E-11			
2 - 20	5.87E-04	4.8E-12			
					0.4
					0.26
2 - 20	9.29E-04	7.6E-12			

20 - 100	2.21E-02	1.41E-09			
1 - 100	1.41E-05	1.12E-13			
2 - 10	3.09E-05	2E-13			

2 - 10	6.18E-06	4E-14			
2 - 10	1.24E-05	8E-14			
2 - 10	1.48E-05	9.6E-14			
					0.1
2 - 10	6.57E-07	4.25E-15	2.57E+21		
			3.90E+21		
2 - 10	1.00E-04	6.47E-13	8.55E+21		
2 - 10	1.37E-03	8.86E-12	6.80E+21		
0.8 - 10	4.19E-02	1.7E-10			0.3
2 - 10	1.90E-03	1.23E-11	1.38E+22		
2 - 10	4.99E-05	4.10E-13	2.10E+22	1.21	0.86
2 - 10	4.28E-01	2.77E-09			
2 - 10	9.24E-02	5.98E-10			

10 - 20	1.55E-02	3.43E-10			
2 - 10	7.73E-01	5.00E-09			
2 - 10	1.98E-03	1.28E-11			
					0.4
					0.5

2 - 10	6.86E-02	4.44E-10			0.07
2 - 10	2.47E-05	1.6E-13			
2 - 10	6.18E-05	4E-13			
2 - 10	1.62E-02	1.05E-10			
0.5 - 12	4.12E-03	1.6E-11			
3 - 12	1.51E-01	1.34E-09			
2 - 10	7.93E-05	5.13E-13	6.90E+21		

0.2 - 10	1.69E-04	6.04E-13	3.00E+20	2.85	0.33
2 - 10	1.96E-05	1.27E-13	2.15E+21		
2 - 10	2.32E-03	1.50E-11	3.00E+21		
2 - 10	1.37E-06	8.86E-15	2.00E+20		
2 - 10	7.33E-05	4.74E-13	1.50E+22		0?
2 - 10	1.70E-03	1.10E-11	3.17E+21	1.60	
2 - 10	7.26E-04	4.70E-12	2.20E+22	1.60	
2 - 10	9.95E-07	6.44E-15	1.00E+20		
2 - 10	1.22E-04	7.90E-13	3.50E+22		
2 - 10	6.03E-03	3.90E-11	4.70E+22		
2 - 10	1.86E-04	1.20E-12	2.57E+21		
2 - 10	2.01E-04	1.30E-12	6.30E+21		
2 - 10	1.05E-02	7.10E-11	1.00E+22	1.70	0.05
2 - 10	1.81E-01	1.17E-09	9.8E+21	1.44	0.055
2 - 10	1.18E-01	8.29E-10	6.30E+21	1.96	0.075
0.5 - 10	9.97E-02	3.66E-10			0.12
2 - 10	1.98E-02	1.28E-10			
2 - 10	4.76E-02	3.08E-10			
2 - 10	4.00E-04	2.59E-12			
2 - 10	1.56E-02	1.01E-10			
2 - 10	1.44E+01	9.32E-08			
2 - 10	3.20E-04	2.05E-12			
2 - 10	2.40E-03	1.55E-11			
2 - 10	7.60E-03	4.92E-11			
2 - 10	4.00E-03	2.59E-11			
2 - 10	4.00E-03	2.59E-11			
2 - 10	2.50E-02	1.62E-10			
2 - 10	8.00E-03	5.18E-11			
40 - 80	1.01E-03	8.97E-11			
2 - 10	6.64E-03	4.30E-11			
2 - 10	1.76E-03	1.14E-11			

2 - 10	2.16E-04	1.70E-12			0.27
			1.00E+21	1.5	
0.2 – 10	3.30E-06	1.41E-14		1.73	
0.2 – 10	2.26E-06	1.10E-14		1.5	
0.2 – 10	2.17E-05	5.37E-14		2.73	
0.2 – 10	4.24E-07	1.51E-15			
0.2 – 6	2.55E-04	7.89E-13	9.00E+20	1.10	0.50
0.2 – 6	1.04E-03	3.48E-12	2.30E+21	0.74	0.47
2 – 15	1.14E-03	8.50E-12	1.00E+21	2.00	
2 – 15	9.21E-04	6.90E-12	1.00E+21	2.00	
0.5 – 10	2.80E-04	9.98E-13			
0.5 – 10	1.89E-04	6.73E-13			
2 – 10	5.75E-03	4.51E-11	1.82E+22	1.41	0.80
			1.00E+23		
2 – 10	3.12E-02	2.00E-10			
			1.70E+20		
2 – 10	1.92E-02	1.23E-10			0.6
2 – 10	3.76E-04	3.47E-12	3.16E+22	0.70	
			1.10E+20		
			1.00E+20		
			2.50E+20		

			STABILITY		
Pulse Width (50%) (s)	**Pulse Width (10%)** (s)	**Magnetic Field (Gauss)**	**Transient Characteristics**	**Stability Code**	**Timing Stability**
1.67E-03		3.79E+12	S	Gl	
		3.38E+12	S	Gl	
		1.63E+12	S		
		3.13E+12	S	Gl	
		1.54E+13	S		
		4.86E+11	S	Gl	
		3.48E+12	S		
		3.33E+11	S	Bi	
		2.79E+12	S	Gl	
		4.29E+12	S	Gl	
		5.18E+11	S		
		5.81E+08	S	Bi	
5.50E-05		2.25E+09	S		
		4.66E+12	S		
		4.97E+12	S		
		4.68E+08	S		
		1.67E+08	S	Bi	
		2.44E+11	S		
		1.08E+13	S		
		7.33E+11	S		
		2.81E+08	S	Bi	
		1.08E+12	S		
		8.39E+11	S	Gl	
		9.86E+12	S		
3.50E-04		4.23E+08	S	Bi	
		9.64E+11	S		
		1.69E+08	S	Bi	
		2.60E+14			
		6.30E+14			
		9.50E+14			
		8.00E+14			
		1.40E+15			
		8.07E+14			
		1.20E+14			
				Bi	
				Bi	

			T	Bi	
			T	Bi	
			T	Bi	
			T	Bi	
			T	Bi	
			T	Bi	
			T	Bi	
			T	Bi	
			T	Bi	
				Bi	
			T	Bi	
			T	Bi	
			T	Bi	
			T	Bi	
				Bi	
			T	Bi	
			T	Bi	
				Bi	
			T	Bi	
			T	Bi	
				Bi	
			T	Bi	
			T	Bi	
			T	Bi	
				Bi	
			T	Bi	
			T	Bi	
				Bi	
			T	Bi	
			T	Bi	
			T	Bi	
			T	Bi	
				Bi	
			T	Bi	
				Bi	
			T	Bi	

			T	Bi	
				Bi	
			T	Bi	
			T	Bi	
				Bi	
				Bi	
				Bi	
				Bi	
			T	Bi	
			T	Bi	
			T	Bi	
				Bi	
				Bi	
				Bi	
				Bi	
				Bi	
				Bi	
			T	Bi	
				Bi	
				Bi	
				Bi	
			T	Bi	
				Bi	
				Bi	
			T	Bi	
			T	Bi	
				Bi	
			T	Bi	
			T	Bi	
				Bi	
			T	Bi	
		3.81E+14		Bi	
			T	Bi	
		2.40E+12		Bi	

			T	Bi	
				Bi	
			T	Bi	
				Bi	
			T	Bi	
			T	Bi	
				Bi	
				Bi	
				Bi	
			T	Bi	
			T	Bi	
			T	Bi	
			T	Bi	
				Bi	
			T	Bi	
				Bi	
				Bi	
				Bi	
				Bi	
			T	Bi	
			T	Bi	
				Bi	
				Bi	
			T	Bi	
			T	Bi	
			T	Bi	
			T	Bi	
				Bi	
			T	Bi	
			T	Bi	
			T	Bi	
			T	Bi	
			T	Bi	

			T	Bi	
			T	Bi	
			T	Bi	
			T	Bi	
			T	Bi	
			T	Bi	
			T	Bi	
		2.10E+12	T	Bi	
				Bi	
				Bi	
			T	Bi	
			T	Bi	
			T	Bi	
				Bi	
				Bi	
			T	Bi	
				Bi	
				Bi	
			T	Bi	
			T	Bi	
			T	Bi	
				Bi	
			T	Bi	
				Bi	
			T	Bi	
			T	Bi	
			T	Bi	
				Bi, Bu	
				Bi	
				Bi	
		1.70E+08		Bi	
			T	Bi	

			T	Bi	
			T	Bi, Bu	
			T	Bi, Bu	
			T	Bi, Bu	
				Bi	
				Bi	
			T	Bi	
			T	Bi	
			T	Bi	
				Bi, Bu	
				Bi, Bu	
			T	Bi	
			T	Bi, Bu	
			T	Bi	
			T	Bi	
			T	Bi	
				Bi	
			T	Bi	
				Bi	
				Bi	
			T	Bi, Bu	
			T	Bi	
		2.35E+09		Bi	
				Bi	
		3.00E+12		Bi	
			T	Bi	
				Bi	
		5.50E+08		Bi	
				Bi. Zsrc	
			T	Bi	
				Bi	
			T	Bi, Bu	
			T	Bi	

				Bi	
				Bi	
				Bi	
			T	Bi	
				Bi	
				Bi	
			T	Bi, Bu	
			T	Bi, Bu	
			T	Bi	
			T	Bi, Bu	
				Bi, Bu	
			T	Bi	
				Bi, Bu	
			T	Bi, Bu	
				Bi	
				Bi	
		4.50E+08		Bi	
				Bi	
				Bi	
			T	Bi	
			T	Bi, Bu	
			T	Bi	
		2.30E+08	T	Bi, Bu	
				Bi, Bu	
			T	Bi	
				Bi	
				Bi, Bu	
				Bi	
			T	Bi	
				Bi	
			T	Bi	
				Bi	
			T	Bi	
				Bi	
			T	Bi	
				Bi	

				Bi	
			T	Bi, Bu	
			T	Bi	
			T	Bi, Bu	
				Bi	
				Bi	
			T	Bi, Bu	
			T	Bi, Bu	
				Bi	
				Bi	
				Bi	
				Bi	
				Bi	
				Bi, Bu	
				Bi	
				Bi	
				Bi	
			T	Bi, Bu	
				Bi	
			T	Bi, Bu	
				Bi, Bu	
				Bi	
			T	Bi	
			T	Bi, Bu	
			T	Bi, Bu	
			T	Bi	
				Bi	
				Bi	
				Bi	
			T	Bi, Bu	
				Bi	
			T	Bi	
			T	Bi, Bu	

			T	Bi	
			T	Bi, Bu	
				Bi, Bu	
				Bi	
			T	Bi	
		2.18E+09		Bi	
				Bi	
				Bi	
			T	Bi	
			T	Bi	
		4.00E+08	T	Bi, Bu	
			T	Bi, Bu	
				Bi	
				Bi, Bu	
		2.38E+09		Bi	
			T	Bi	
		6.19E+08		Bi	
				Bi	
				Bi	
			T	Bi, Bu	
				Bi, Bu	
				Bi, Bu	
			T	Bi	
				Bi, Bu	
			T	Bi	
			T	Bi	
				Bi, Bu	
		2.10E+08	T	Bi	
			T	Bi, Bu	
				Bi, Bu	
			T	Bi	
				Bi, Bu	
		1.00E+08		Bi	
			T	Bi	
			T	Bi	
			T	Bi	
			T	Bi	
				Bi, Bu	
				Bi, Bu	

				Bi	
				Bi	
		1.00E+14			
		1.01E+03			
			T		
			T		
		1.90E+06	T		
		3.00E+05			
		3.00E+05	S		
		8.00E+12			

		6.00E+05	T		
		1.00E+05			
		7.00E+12			
		6.80E+13			
		2.30E+12	T		
		3.80E+13			
		3.60E+13			
		1.90E+13			

		4.40E+13			
		3.00E+13			
		2.30E+13			
		2.45E+13			
		1.00E+08			
		5.60E+13			
		6.70E+13			
			T		

		1.00E+11	T	Bi	
			T	Bi	
				Bi	
				Bi	
				Bi	
				Bi	
				Bi	
				Bi	
				Bi	
				Bi	
				Bi	
				Bi	
				Bi	
				Bi	
				Bi	
				Bi	
				Bi	
				Bi	
				Bi	
				Bi	
				Bi	
				Bi	
				Bi	
				Bi	
				Bi	
				Bi	
				Bi	
				Bi	
				Bi	
				Bi	
				Bi	
				Bi	
				Bi	
				Bi	
				Bi	
				Bi	
				Bi	

				Bi	
				Bi	
				Bi	
				Bi	
				Bi	
				Bi	
				Bi	
				Bi	
				Bi	
				Bi	
				Bi	
				Bi	
				Bi	
				Bi	
				Bi	
				Bi	
				Bi	
				Bi	
				Bi	
				Bi	
				Bi	
				Bi	
				Bi	
				Bi	
				Bi	
				Bi	
				Bi	
				Bi	
				Bi	
				Bi	
				Bi	
				Bi	
				Bi	
				Bi	
				Bi	
				Bi	
				Bi	
				Bi	
				Bi	
				Bi	
				Bi	
				Bi	
				Bi	
				Bi	
				Bi	

				Bi	
				Bi	
				Bi	
				Bi	
				Bi	
				Bi	
				Bi	
				Bi	
				Bi	
				Bi	
				Bi	
				Bi	
				Bi	
				Bi	
				Bi	
				Bi	
				Bi	
				Bi	
				Bi	
				Bi	
				Bi	
				Bi	
				Bi	
		7.76E+11			
		5.50E+12			
		1.00E+12			
		6.31E+12			
		3.02E+09			
		8.32E+11			
		1.70E+13			
		1.76E+08		Bi	
		2.00E+12			
		1.20E+12			
2.10E-05		4.07E+08			
			T	Bi	
		1.29E+08			
				Bi	
				Bi	
				Bi	
				Bi	
				Bi	

				Bi	
				Bi	
				Bi	
				Bi	
				Bi	
				Bi	
				Bi	
				Bi	
				Bi	
			T		
				Bi	
		2.00E+14			
				Bi	
				Bi	

		4.60E+10		Bi	
		9.55E+09		Bi	
				Bi, Bu	
				Bi	
		1.00E+08		Bi	
				Bi	
				Bi	
			T		
		1.00E+12			
				Bi	
				Bi	
				Bi	
			T	Bi	

				Bi	
				Bi	
				Bi	
				Bi	
				Bi	
				Bi	
			T	Bi	
			T		
		4.47E+08			
		3.60E+12			
		4.10E+13			
		1.00E+13			
		2.40E+12			
		4.80E+13		Gl?	
		4.07E+12			
			T	Bi	
			T	Bi	
0.0015			T	Bi	
			T	Bi	
			T	Bi	
			T	Bi	
				Bi	
				Bi	
			T	Bi, Bu	
			T	Bu	
				Bi	

		1.00E+13	S		
		4.00E+08			
		8.00E+08			
		8.00E+08		Bi	
		7.00E+08			
		7.00E+08			
		5.00E+08		Bi	
		6.00E+08		Bi	
		2.00E+08		Bi	
		7.00E+08			
		3.00E+08			
		5.00E+08			
		7.00E+08		Bi	
		7.00E+08		Bi	
				Bi	
		2.20E+09		Bi	
		9.00E+08		Bi	
				Bi	
				Bi	
				Bi	
				Bi?	
				Bi?	
			T		
				Bi?	
				Bi	
				Bi?	
				Bi?	
			T	Bi	
		8.00E+14			
			T		
				Bi	

		PERIODICITY				
Pulse Period (s)	**Pulse Period Deriv. (s/s)**	**Pulse Period 2nd Deriv. (s/s/s)**	**Epoch** (MJD)	**Characteristic Age (t_c = P/2Pdot) (yrs)**	**Binary Orbit Period (d)**	**Other Period**
0.0334	4.2096E-13	-2.799E-25	48743.00000	1.256E+03		—
0.08929	1.2468E-13		49672.00000	1.132E+04		—
0.23709	1.097E-14	-1.47236E-26	43946.00000	3.420E+05		—
0.10245	9.304E-14		48861.30000	1.746E+04		—
0.15023	1.5402E-12	-1.31164E-23	48355.00000	1.552E+03		—
0.03953	5.85E-15		47005.18800	1.074E+05		—
0.12365	9.592E-14		48658.00000	2.042E+04		—
0.04776	2.27E-15		49500.00000	3.327E+05	1236.72359	—
0.10145	7.495E-14		48650.00000	2.143E+04		—
0.13361	1.3432E-13		48700.00000	1.578E+04		—
0.22651	1.16E-15		48381.00000	3.105E+06		—
0.00575	2E-20		48825.00000	1.600E+09	5.741042329	—
0.00305	1.60E-18		47953.50000	2.992E+07		—
0.38487	5.503E-14		48423.00000	1.109E+05		—
0.05037	4.7906E-13	-1.77347E-25	48256.00000	1.667E+03		—
0.00493	1.08E-20		49113.00000	7.300E+09		—
0.0016	1.2E-20		48196.00000	1.510E+09	0.381966639	—
0.253065	2.30E-16		52403.00000	1.741E+07		—
0.2316	4.9254E-13		48658.00000	7.447E+03		—
0.14315	3.66E-15		49444.36720	6.194E+05		—
0.00525	1.4E-20		49220.00000	5.702E+09	0.604672713	—
0.1971	5.83E-15		43555.61720	5.358E+05		—
0.15638	4.39E-15		48382.00000	5.636E+05		—
0.49524	1.9191E-13		48419.00000	4.093E+04		—
0.00232	8E-20		49150.60860	4.909E+08	2.02885	—
0.53066	1.72E-15		48383.00000	4.920E+06		—
0.00347	8E-21		49301.00000	6.887E+09	0.263144268	—
8.6880590	2.34E-12			5.883E+04		
8.1000000						
6.4497690	2.2E-11			4.645E+03		
10.9994427	1.9237E-11			9.059E+03		
7.4765510	2.8E-11			4.231E+03		
11.7657300	4.133E-11			4.510E+03		
6.9713000						
5.1591300	1.09E-10			7.499E+02		
6.9789485	4.883E-13			2.264E+05		
9.1321						

74.676						
323.2					0.059	
91.1					5.000	
8.88163	3.00E-10					
15.3	-1.26E-08					
2.374						
46.63					5.792	
169.3						
58.969					2.708	
280.4						
2.7632						
304						
345.2						
3.343						
31.0294						
10008					0.483	
3.6145107	5.90E-11				1.013	
0.716					0.162	
22.07						
1404.2						
					1.102	
4.4					1.427	
835					24.167	
202.5						
4.0635						

69.5						
13.7					1.058	
13.502932	8.07E-06				0.058	
					10.042	
0.069					0.696	
103.29	-6.00E-08				4.625	
					0.071	
					0.176	
96.08						
0.0338						
13.1789					0.065	
103.2					1.438	
31.8851					3.333	
12.327396					4.583	
283					0.373	
93.5					5.625	
0.061						
862						
6.4498	2.2000E-11			4.64E+03		
405						
4.81793					0.087	

293.4464					7.813	
298					0.235	
697.63	3.20E-07				1.733	
191						
272.267					5.542	
170.84						
17.6					1.755	
437.4						
529					0.155	
9.3					1.275	
38					0.433	
					0.142	
714.5						
413						
220.38						
4.45					1.242	
152.26						
111.194	3.30E-09					
81.1						
29.5						
6.9713						

94.8					10.042	
361					0.254	
221						
89.17						
437.649	5.00E-07				0.349	
					0.546	
15.8					3.333	
18.7					1.45 - 2.92	
					0.208	
41.8					1.917	
					0.008	
198					4.583	
358.61					0.528	
66.2						
392						
					10.917	
					0.213	
					0.340	
0.00305					5.20000	
					0.323	

					0.159	
					9.008	
					0.171	
					0.433	
					0.164	
					0.122	
					0.629	
					16.600	
					1.123	
					1.540	
					0.379	
					0.077	
0.00323					0.788	
					0.875	
7.7					0.029	
0.00345					0.158	
					2.620	
1.24					1.700	
					0.296	
					0.618	

					0.91 - 0.9375	
					0.521	
					0.0544	
					0.613	
0.00276						
					0.175	
114					14.167	
0.0038						
					0.194	

0.467					11.834	
					0.238	
					0.515	

					0.18125	
0.00303						
0.00249392	4.35E-18				0.084	
					24.700	
0.00327						
0.00363					0.008	
					0.232	
					0.9375	
					0.014	
0.00364					0.792	
					0.035	
					0.3887	
					0.344	
					6.475	
					0.248	
					0.713	
					0.218259	

					9.842	
8.39115	1.00E-16					
5.4479	-4.43633E-11					
1028.7325	-3.20E-12				0.01227	
					0.0323386	
120.2						
					0.23193	
8460					0.101666667	
21.83					0.07365	
					0.18280	
					0.17690	
					0.0744992	
					0.28984	
					0.30048	
30					0.38000	
160					0.16440	
					0.06312	
					0.18267	
24					0.258116	
745.8					0.285314	
27.8682					0.056666667	
66					0.27512973	
					0.370833333	
323.2					0.22500	
					0.022917	
1020					0.13755	
206.298					0.25256	
351.341	-2.70E-11				1.99680	
554.635					0.52118	
3726					0.414583333	
863.5					0.14375	
1911??					0.22900	
7188					0.25830	
1920					0.58330	
269.5						
1040.4					0.12720	
913.2					0.1347486	
					0.15000	
834.3					0.22917	
					0.05625	
1557.5					0.25	
3108					0.07332	
529.31					0.16538	
2144					0.248148148	

4021.62	4.54E-11				0.06823	
4847.7312					0.6151	
927					0.14208	
63.633032	4.00E-13				0.2098	
745.506	2.30E-11				0.1402323	
33.0767335	4.00E-14				0.411666667	
1254.451	2.20E-11				0.20206	
5246						
2500					0.23910	
120					0.16280	
					0.13900	
					0.06143	
					0.41830	
					0.24507	
					0.05882	
					0.05923	
					227.500	
					1.23440	
					5.714	
3682.8					0.138154	
					0.146	
					0.198096	
					0.23	
					0.51420	
					0.214165	
					0.1966713	
					0.07845	
					0.05405	
275					0.07890	
276						
					0.08020	
4861.2??					0.05627	
					0.15860	
5702.4					0.07080	
					0.33542	
					0.09268	
12002.4	3.30E-09				0.13842	
					0.68207	
					0.069747	
					0.08710	
					0.14125	
					0.07429	
					0.05547	
4086					0.20600	
2400						

					0.07948		
					0.07975		
113.9					0.07909		
3477.6					0.08050		
5388.144192					0.062363		
					0.131516		
					0.06260		
					0.055340278		
					0.07049		
					0.0788709		
					0.0832837		
					0.078504167		
					0.128927		
					0.0627		
					0.07265625		
567.7							
					0.097189		
					0.1545252		
					0.110833333		
					78.0176		
					0.08682		
					0.139613		
					0.076944444		
					0.075416667		
5360							
					0.14334		
					0.074813		
14.07					0.074271		
25.703	2.76E-06				0.86924		
					0.07635		
					0.06250		
					0.06360		
					0.19393		
					0.26810		
					0.610116		
					0.15198		
					240		
					0.2163		
					0.76500		
35.7					0.209893		
					0.21450		
					0.32125		
					0.36410		

					0.13700	
					0.1584328	
					0.20583	
					0.16	
					0.297645	
					0.08125	
0.069212	5.01E-10				16.6680	
94.9					242.18	
					0.87092	
					2.49310	
					1.01050	
					0.68470	
					1.19520	
					2.86730	
					3.95295	
					1.2473	
					4.13470	
					0.77130	
					9.48530	
					3.06320	
					6.95340	
					1.35740	
					1.31	
					2.47870	
					2.32730	
					3.45220	
					2.80680	
					17.3599	
					4.42510	
					0.66140	
					1.19880	
					3.12676	
					3.27549	
					3.8210	
					4.47766	
					1.5520	
					14.26	
					0.71181	
					17.7692	
241747.2						
					0.86105	
44933.184						

1057968						
1273008.96						
682992						
					4.70000	
556235.424						
114566.4					1.32600	
245462.4						
163296						
2712960						
705888					8.17000	
					8.82000	
691200					104.023	
44460						
912384						
51241.248					0.59307	
522768.384						
416707.2						
					21.20812	
878083.2						
875664					10.1700	
1869957.792						
286848					3.19860	
71657.568						
41384.736					0.47900	
271710.72						
					2.30000	
					1.04300	
					7.32825	
4752000						
5508000						
70848					0.96160	
					3.55830	
314702.496						
413960.544					4.80000	
1614962.88						
					2.61321	
926394.624						
657169.632						
100975.68					1.14000	
399999.168						
					39.4809	
2338848					27.5384	
145298.88					1.68170	
2674918.08						
342316.8						

685670.4						
75988.8						
248918.4						
					8.80076	
					0.873712	
9404985.6						
3445459.2						
54530.7552						
59978.88					0.6981	
					3.243347	
255744						
795549.6					9.208	
438394.896						
171350.208					1.9832	
54339.552						
341712						
526348.8						
2008800						
					6.72400	
					0.39262	
					0.44268	
38.2	-6.51E-09				7.84825	
0.241						
0.101443723	5.84E-15					
0.28775	1.05E-13					
0.063191253	1.58E-14					
0.069338	1.40E-13					
0.011075761	9.77E-19	-2.30E-27	47187.50415		191.443	
0.387688791	1.78E-15		40621.54			
10.00759						
0.606643258	4.66E-11		48673			
0.0034						
0.064667	4.40E-14			24000		
0.194626341	7.20E-15		42301.5			
0.001557807	1.05E-19	-3.78E-32	52328			
721						
0.0048	4.00E-21					
					7.60000	
					2.63000	
					19.6045	
					7.49200	
898560						

					7.1	
					0.33417	
					9.63000	
					11.1300	
2721600					905.900	
					0.465069102	
					24.43	
					2.766	
4654368					20.5212	
≤ d 2.96 ??					51.075 ??	
487296						
656640						
241920						
133747.2						
565056						
734400						
622080						
233280						
289440						
104544						
349920						
313632						
622080						
397440						
238464						
708480						
570240						
1036800						
257472						
406080						
603936						
432000						
490691.52						
					4.2319	
					0.71	
821						
					0.17193	
9149760					10.000	
					1.70491	
					2.75960	
5.161297854	1.23E-10					
76.923						
3.01856						

0.0062	3.30E-20				66.5400	
0.037	2.42E-18				0.42000	
0.011563148	-1.90E-20		48270		0.075646117	
29.5056	-2.80493E-08					
0.00393	2.00E-21					
					2.17000	
					0.46543	
					1.56100	
					0.81428	
					2.78000	
					3.96000	
					1.26840	
					4.865	
					3.033	
					20.6	
					2.40029	
40003.2					1.26245	
					0.66042	
					0.76278	
					1.04360	
					3.50000	
					554	
5148576					85.1	
					3.76600	
					2900	
					0.32150	
					0.33364	
					0.28410	
					0.2678158	
					0.2783152	
					0.45789	
					0.40800	
					0.35800	
					0.358	
36002.016						
8640000						
					3.45310	
					15.422	
0.016114775	5.12E-14			5000		
1207872						
					387	
172.4						
4.782						
0.087						
755.5						

82.4						
140.1						
152.1						
564.83						
101.4						
8.02	2.57E-11					
455						
343						
6.848						
2.165						
0.00487	1.00E-20					
0.06568	1.93E-13			5380		
0.00516	2.99E-21					
0.40764	4.02E-12	3.59E-23	51173	1606		
0.13531	7.45E-13			2900		
0.06818	8.32E-14					
0.00407	7.13E-21					
0.1249	1.28E-13					
0.324818968	7.10E-12		51991.08778	723		
0.2674	2.08E-13					
0.05162	7.80E-14					
0.005402332	2.69E-18		52396		0.03026326	
0.002297171	1.58E-18				0.0294599	
0.005245943					0.027829236	
0.00318148					0.178125	
31						
29.5						
					0.1403	
					0.2558	

0.136855047	7.51E-13		52280	2900		
0.00575678	-4.985E-20					
0.005357573	-3.330E-21					
0.003536329	9.852E-20				2.256844818	
0.002623579	6.451E-20					
0.004040379	-4.215E-20					
0.003210341	-1.620E-21				2.3576965	
0.003484992	-4.590E-20				0.229792249	
0.002100634	-9.787E-21				0.120664939	
0.004346168	-1.219E-19					
0.003676643	-3.832E-20					
0.003053954	-2.186E-20					
0.002643343	3.032E-20				0.135974304	
0.004033181	3.410E-20				1.18908405	
0.00758848	2.947E-19				1.12617678	
0.004342827	9.524E-20				0.429105683	
0.003650329	1.68E-19		51749.71082		1.35405939	
0.683						
0.096						
1.244						
0.387						
201.9			51834.633			
263			51832.684			
16.5718	1.26E-08					
25.4904	-1.95E-08					
18.37						
34.08						
503.6						
138.04						
701.6						
95.2						
6.97						
9.801			52859.78			
22.69						
27.12						
729						

B.3.3 2–10 keV Energy List

The following table provides all the data in the *2–10 keV Energy List* of the XNAVSC. To reduce the overall size of this table, only the *Installation Number*, the *J-name*, and the converted *2–10 keV X-ray Flux* columns are provided for this list, as all other columns are repeated in the other lists. The first page of this table provides the headings of each column of the table. Descriptions of the parameters within this table are provided in Table B-4.

For the parameter of the *Catalogue J-Name*, this is source name unique to the XNAVSC. For a name that is of format *Jhhmm-ddmm* and written in blue ink, this name has been modified from the original citation's J-name or was derived from the position of the source if only a B-name is known for that source. This *Catalogue J-Name* is only created to produce a consistent naming convention for all the XNAVSC sources, and should not be used as an external name for the source.

X-ray flux values written in blue ink are "derived" values from a given source's citation. This may mean that X-ray detector photon counts were converted to energy flux. For some sources this may mean that the source was not directly observed in the "derived" energy range, so there is no assurance that the source is visible within this X-ray range.

Install Number	Catalogue J-Name	2-10 keV X-ray		
		Energy Range (keV)	Flux (photons/cm^2/s)	Flux (erg/cm^2/s)
1	J0534+2200	2 - 10	1.54E+00	9.93E-09
2	J0835-4510	2 - 10	1.59E-03	1.03E-11
3	J0633+1746	2 - 10	1.23E-05	7.94E-14
4	J1709–4428	2 - 10	1.59E-04	1.03E-12
5	J1513–5908	2 - 10	1.62E-02	1.05E-10
6	J1952+3252	2 - 10	3.15E-04	2.04E-12
7	J1048–5832	2 - 10	3.86E-05	2.50E-13
8	J1302–6350	2 - 10	5.10E-04	3.30E-12
9	J1826–1334	2 - 10	2.63E-03	1.70E-11
10	J1803–2137	2 - 10	2.75E-05	1.78E-13
11	J1932+1059	2 – 10	4.30E-05	2.78E-13
12	J0437–4715	2 - 10	6.65E-05	4.30E-13
13	J1824–2452	2 - 10	1.93E-04	1.25E-12
14	J0659+1414	2 - 10	3.17E-05	2.05E-13
15	J0540–6919	2 - 10	5.15E-03	3.33E-11
16	J2124–3358	2 - 10	1.28E-05	8.26E-14
17	J1959+2048	2 - 10	8.31E-05	5.38E-13
18	J0953+0755	2 - 10	9.60E-06	6.53E-14
19	J1614–5047			
20	J0538+2817	2 - 10	1.24E-07	8.00E-16
21	J1012+5307	2 - 10	1.93E-06	1.25E-14
22	J1057–5226	2 - 10	1.64E-06	1.06E-14
23	J0358+5413	2 - 10	1.79E-05	1.16E-13
24	J2337+6151	2 - 10	6.26E-06	4.05E-14
25	J0218+4232	2 - 10	6.65E-05	4.30E-13
26	J0826+2637	2 - 10	9.27E-07	6.00E-15
27	J0751+1807	2 - 10	6.63E-06	4.29E-14
28	J0142+6100	2 - 10	1.73E-01	1.12E-09
29	J0525–6607			
30	J1048–5937	2 - 10	1.39E-02	8.98E-11
31	J1708–4008	2 - 10	2.78E-02	1.80E-10
32	J1808–2024	2 - 10	6.35E-04	4.11E-12
33	J1841–0456	2 - 10	1.99E-02	1.29E-10
34	J1845–0256	2 - 10	3.50E-03	2.27E-11
35	J1907+0919			
36	J2301+5852	2 - 10	1.23E-02	7.96E-11
37	J0032-7348	2 - 10	5.98E-04	3.87E-12
38	J0049-7310	2 - 10	1.20E-04	7.74E-13
39	J0049-7250	2 - 10	1.50E-03	9.68E-12
40	J0052-7226	2 - 10	2.99E-03	1.94E-11
41	J0050-7316	2 - 10	3.91E-04	2.53E-12

42	J0050-7213	2 - 10	7.78E-03	5.03E-11
43	J0051-7231	2 - 10	2.99E-05	1.94E-13
44	J0051-7310			
45	J0052-7319	2 - 10	1.41E-02	9.10E-11
46	J0052-7158	2 - 10	2.93E-03	1.90E-11
47	J0054-7341	2 - 10	2.99E-03	1.94E-11
48	J0056+6043	2 - 10	1.50E-02	9.68E-11
49	J0053-7226	2 - 10	4.19E-03	2.71E-11
50	J0054-7204	2 - 10	1.14E-02	7.36E-11
51	J0054-7226	2 - 10	2.99E-03	1.94E-11
52	J0057-7202	2 - 10	2.44E-04	1.58E-12
53	J0058-7230			
54	J0059-7138	2 - 10	4.35E-03	2.82E-11
55	J0101-7206	2 - 10	2.99E-04	1.94E-12
56	J0103-7209	2 - 10	1.45E-05	9.38E-14
57	J0109-7444	2 - 10	6.88E-03	4.45E-11
58	J0105-7211	2 - 10	2.99E-04	1.94E-12
59	J0105-7212	2 - 10	7.21E-06	4.67E-14
60	J0105-7213	2 - 10	4.49E-02	2.90E-10
61	J0118+6517	2 - 10	1.20E-02	7.74E-11
62	J0118+6344	2 - 10	5.98E-03	3.87E-11
63	J0117-7326	2 - 10	1.50E-03	9.68E-12
64	J0117-7330	2 - 10	2.99E-02	1.94E-10
65	J0143+6106	2 - 10	1.50E-03	9.70E-12
66	J0240+6113	2 - 10	3.48E-04	2.25E-12
67	J0334+5310	2 - 10	1.50E-03	9.68E-12
68	J0355+3102	2 - 10	2.69E-02	1.74E-10
69	J0419+5559	2 - 10	5.98E+00	3.87E-08
70	J0440+4431	2 - 10	2.99E-03	1.94E-11
71	J0501-7033			
72	J0502-6626	2 - 10	1.71E-02	1.10E-10
73	J0512-6717			
74	J0516-6916	2 - 10	2.10E-04	1.36E-12
75	J0520-6932			
76	J0522+3740	2 - 10	2.99E-03	1.94E-11
77	J0529-6556	2 - 10	5.09E-04	3.29E-12
78	J0531-6607	2 - 10	2.99E-03	1.94E-11
79	J0531-6518			
80	J0532-6622	2 - 10	8.98E-03	5.81E-11
81	J0532-6535	2 - 10	1.50E-05	9.71E-14
82	J0532-6551	2 - 10	4.50E-05	2.91E-13
83	J0535-6700	2 - 10	5.99E-05	3.88E-13
84	J0535-6651	2 - 10	2.99E-05	1.94E-13
85	J0538+2618	2 - 10	8.98E-03	5.81E-11
86	J0535-6530	2 - 10	7.51E-04	4.86E-12

87	J0538-6405	2 - 10	5.09E-03	3.29E-11
88	J0539-6944	2 - 10	8.98E-03	5.81E-11
89	J0541-6936			
90	J0541-6832			
91	J0544-6633	2 - 10	5.39E-03	3.49E-11
92	J0544-7100	2 - 10	4.19E-04	2.71E-12
93	J0555+2847	2 - 10	3.29E-03	2.13E-11
94	J0635+0533	2 - 10	1.65E-03	1.07E-11
95	J0648-4418	2 - 10	8.98E-05	5.81E-13
96	J0728-2606	2 - 10	3.59E-03	2.32E-11
97	J0747-5319	2 - 10	2.10E-03	1.36E-11
98	J0756-6105	2 - 10	2.10E-03	1.36E-11
99	J0812-3114	2 - 10	1.80E-03	1.16E-11
100	J0835-4311	2 - 10	8.98E-02	5.81E-10
101	J0902-4033	2 - 10	5.98E-03	3.87E-11
102	J1009-5817	2 - 10	3.59E+00	2.32E-08
103	J1025-5748	2 - 10	1.65E-03	1.07E-11
104	J1030-5704	2 - 10	9.87E-03	6.39E-11
105	J1037-5647	2 - 10	5.09E-04	3.29E-12
106	J1050-5953	2 - 10	2.99E-04	1.94E-12
107	J1120-6154	2 - 10	2.99E-04	1.94E-12
108	J1121-6037	2 - 10	2.99E-02	1.94E-10
109	J1148-6212	2 - 10	1.20E-02	7.74E-11
110	J1147-6157	2 - 10	1.20E-02	7.74E-11
111	J1226-6246	2 - 10	2.69E-02	1.74E-10
112	J1242-6012	2 - 10	8.98E-03	5.81E-11
113	J1247-6038	2 - 10	7.18E-02	4.65E-10
114	J1249-5907	2 - 10	7.18E-02	4.65E-10
115	J1242-6303	2 - 10	6.58E-03	4.26E-11
116	J1239-7522	2 - 10	1.80E-03	1.16E-11
117	J1254-5710	2 - 10	2.39E-03	1.55E-11
118	J1301-6136	2 - 10	8.98E-04	5.81E-12
119	J1324-6200	2 - 10	1.20E-03	7.74E-12
120	J1421-6241	2 - 10	5.98E-03	3.87E-11
121	J1452-5949	2 - 10	1.20E-04	7.74E-13
122	J1542-5223	2 - 10	8.98E-03	5.81E-11
123	J1557-5424	2 - 10	8.08E-02	5.23E-10
124	J1554-5519	2 - 10	5.09E-03	3.29E-11
125	J1700-4140	2 - 10	1.20E-02	7.74E-11
126	J1703-3750	2 - 10	3.29E-02	2.13E-10
127	J1700-4157	2 - 10	1.20E-03	7.74E-12
128	J1725-3624	2 - 10	5.98E-04	3.87E-12
129	J1738-3015	2 - 10	8.65E-01	7.57E-09
130	J1739-2942	2 - 10	5.98E-03	3.87E-11
131	J1744-2713	2 - 10	1.80E-04	1.16E-12

132	J1749-2725	2 - 10	4.07E-03	2.63E-11
133	J1749-2638	2 - 10	8.08E-02	5.23E-10
134	J1810-1052	2 - 10	5.98E-03	3.87E-11
135	J1820-1434	2 - 10	2.99E-03	1.94E-11
136	J1826-1450	2 - 10	8.98E-04	5.81E-12
137	J1836-0736	2 - 10	4.79E-03	3.10E-11
138	J1841-0551	2 - 10	2.99E-03	1.94E-11
139	J1841-0427	2 - 10	7.48E-03	4.84E-11
140	J1845+0057	2 - 10	1.20E-03	7.74E-12
141	J1847-0309	2 - 10	2.99E-03	1.94E-11
142	J1848-0225	2 - 10	2.99E-03	1.94E-11
143	J1847-0430	2 - 10	1.10E-01	7.11E-10
144	J1858-0244	2 - 10	5.98E-03	3.87E-11
145	J1855-0237	2 - 10	1.80E-02	1.16E-10
146	J1858+0321	2 - 10	7.48E-02	4.84E-10
147	J1904+0310	2 - 10	5.98E-03	3.87E-11
148	J1905+0902	2 - 10	2.10E-03	1.36E-11
149	J1909+0949	2 - 10	1.20E-02	7.74E-11
150	J1911+0458	2 - 10	5.98E-03	3.87E-11
151	J1932+5352	2 - 10	2.10E-03	1.36E-11
152	J1945+2721	2 - 10	1.06E-02	6.84E-11
153	J1949+3012	2 - 10	2.99E-02	1.94E-10
154	J1948+3200	2 - 10	7.31E-01	4.73E-09
155	J1955+3206	2 - 10	4.49E-03	2.90E-11
156	J1958+3512	2 - 10	7.03E-01	4.55E-09
157	J2032+3738	2 - 10	1.50E-03	9.68E-12
158	J2032+4057	2 - 10	2.69E-01	1.74E-09
159	J2030+4751	2 - 10	1.20E-04	7.74E-13
160	J2059+4143	2 - 10	9.58E-01	6.20E-09
161	J2103+4545	2 - 10	5.98E-02	3.87E-10
162	J2139+5703	2 - 10	1.80E-02	1.16E-10
163	J2201+5010	2 - 10	2.10E-03	1.36E-11
164	J2207+5431	2 - 10	1.80E-03	1.16E-11
165	J2226+6114	2 - 10	1.50E-03	9.68E-12
166	J2239+6116	2 - 10	4.79E-02	3.10E-10
167	J0044+3301	2 - 10	1.50E-03	9.68E-12
168	J0418+3247	2 - 10	2.09E+02	1.35E-06
169	J0514-4002	2 - 10	8.98E-03	5.81E-11
170	J0520-7157	2 - 10	2.69E-02	1.74E-10
171	J0532-6926	2 - 10	1.50E-03	9.68E-12
172	J0617+0908	2 - 10	1.50E-01	9.68E-10
173	J0622-0020	2 - 10	5.98E-05	3.87E-13
174	J0658-0715	2 - 10	5.98E-02	3.87E-10
175	J0748-6745	2 - 10	2.99E-04	1.94E-12
176	J0835+5118	2 - 10	1.80E-02	1.16E-10

177	J0837-4253	2 - 10	2.99E-03	1.94E-11
178	J0920-5512	2 - 10	2.99E-02	1.94E-10
179	J0922-6317	2 - 10	8.98E-03	5.81E-11
180	J1013-4504	2 - 10	2.01E+00	1.30E-08
181	J1118+4802	2 - 10	1.35E-01	8.70E-10
182	J1126-6840	2 - 10	1.20E-02	7.74E-11
183	J1257-6917	2 - 10	7.48E-02	4.84E-10
184	J1326-6208	2 - 10	2.10E-02	1.36E-10
185	J1358-6444	2 - 10	1.50E-02	9.68E-11
186	J1458-3140	2 - 10	2.99E-04	1.94E-12
187	J1520-5710	2 - 10	1.50E-02	9.68E-11
188	J1528-6152	2 - 10	1.50E-02	9.68E-11
189	J1547-4740	2 - 10	2.99E-03	1.94E-11
190	J1547-6234	2 - 10	1.05E-01	6.78E-10
191	J1550-5628	2 - 10	1.80E+00	1.16E-08
192	J1601-6044	2 - 10	4.79E-02	3.10E-10
193	J1605+2551	2 - 10	2.16E-04	1.40E-12
194	J1603-7753	2 - 10	4.79E-01	3.10E-09
195	J1612-5225	2 - 10	2.99E-03	1.94E-11
196	J1619-1538	2 - 10	4.19E+01	2.71E-07
197	J1628-4911	2 - 10	1.65E-01	1.07E-09
198	J1632-6727	2 - 10	7.48E-02	4.84E-10
199	J1634-4723	2 - 10	5.98E-03	3.87E-11
200	J1636-4749	2 - 10	3.89E-02	2.52E-10
201	J1640-5345	2 - 10	6.58E-01	4.26E-09
202	J1645-4536	2 - 10	1.50E+00	9.68E-09
203	J1654-3950	2 - 10	5.39E+00	3.49E-08
204	J1657+3520	2 - 10	4.49E-02	2.90E-10
205	J1702-2956	2 - 10	1.50E-02	9.68E-11
206	J1702-4847	2 - 10	4.49E-03	2.90E-11
207	J1705-3625	2 - 10	2.47E+00	1.60E-08
208	J1706-4302	2 - 10	1.35E-01	8.71E-10
209	J1706+2358	2 - 10	1.50E-03	9.68E-12
210	J1708-2505	2 - 10	5.98E-03	3.87E-11
211	J1708-4406	2 - 10	2.99E-02	1.94E-10
212	J1712-4050	2 - 10	9.58E-02	6.20E-10
213	J1709-2639	2 - 10	4.49E-01	2.90E-09
214	J1710-2807	2 - 10	5.98E-03	3.87E-11
215	J1714-3402	2 - 10	4.79E-02	3.10E-10
216	J1712-3738	2 - 10	9.52E-02	6.16E-10
217	J1718-3210	2 - 10	8.38E-02	5.42E-10
218	J1719-2501	2 - 10	4.89E+01	3.16E-07
219	J1718-4029	2 - 10	4.19E+00	2.71E-08
220	J1723-3739	2 - 10	2.10E-01	1.36E-09
221	J1727-3544	2 - 10	9.58E-02	6.20E-10

222	J1727-3048	2 - 10	4.49E-02	2.90E-10
223	J1731-3350	2 - 10	4.49E-01	2.90E-09
224	J1731-1657	2 - 10	8.98E-01	5.81E-09
225	J1732-2444	2 - 10	2.99E-01	1.94E-09
226	J1733-3113	2 - 10	2.69E+00	1.74E-08
227	J1733-3323	2 - 10	2.99E-04	1.94E-12
228	J1733-2202	2 - 10	2.99E-02	1.94E-10
229	J1734-2605	2 - 10	2.99E-02	1.94E-10
230	J1735-3028	2 - 10	2.99E-02	1.94E-10
231	J1736-2725	2 - 10	1.50E-02	9.68E-11
232	J1737-2910	2 - 10	1.02E-02	6.58E-11
233	J1738-2700	2 - 10	2.99E-02	1.94E-10
234	J1738-4427	2 - 10	4.79E-01	3.10E-09
235	J1738-2829	2 - 10	1.20E-03	7.74E-12
236	J1739-2943	2 - 10	5.98E-03	3.87E-11
237	J1739-3059	2 - 10	7.78E-02	5.03E-10
238	J1740-2818	2 - 10	8.98E-03	5.81E-11
239	J1742-2746	2 - 10	9.08E+00	5.88E-08
240	J1742-3030	2 - 10	2.69E-02	1.74E-10
241	J1743-2926	2 - 10	8.98E-02	5.81E-10
242	J1743-2944	2 - 10	1.20E-02	7.74E-11
243	J1744-2900	2 - 10	4.49E-03	2.90E-11
244	J1744-2921	2 - 10	1.50E-02	9.68E-11
245	J1745-3213	2 - 10	5.98E-03	3.87E-11
246	J1745-2854	2 - 10	2.10E-02	1.36E-10
247	J1745-3241	2 - 10	5.98E-03	3.87E-11
248	J1745-2859	2 - 10	1.45E-04	9.39E-13
249	J1745-2927	2 - 10	1.35E-01	8.71E-10
250	J1745-2901	2 - 10	2.69E-02	1.74E-10
251	J1745-2900	2 - 10	2.99E-03	1.94E-11
252	J1745-2846	2 - 10	2.18E-04	1.41E-12
253	J1745-2903	2 - 10	2.90E-04	1.88E-12
254	J1746-2854	2 - 10	2.90E-04	1.88E-12
255	J1746-2853	2 - 10	2.90E-04	1.88E-12
256	J1746-2931	2 - 10	1.80E-01	1.16E-09
257	J1746-2851	2 - 10	2.90E-04	1.88E-12
258	J1746-2844	2 - 10	1.50E-03	9.68E-12
259	J1746-2853	2 - 10	2.90E-04	1.88E-12
260	J1746-2853	2 - 10	2.99E-03	1.94E-11
261	J1747-2959	2 - 10	1.80E-02	1.16E-10
262	J1744-2844	2 - 10	3.80E+01	2.46E-07
263	J1747-3002	2 - 10	1.20E-02	7.74E-11
264	J1747-2633	2 - 10	1.20E+00	7.74E-09
265	J1748-3607	2 - 10	7.48E-02	4.84E-10
266	J1745-2901	2 - 10	1.39E-03	9.00E-12

267	J1748-2453	2 - 10	2.99E-04	1.94E-12
268	J1748-2022	2 - 10	2.99E-04	1.94E-12
269	J1749-3311	2 - 10	8.08E-02	5.23E-10
270	J1750-3225	2 - 10	2.99E-04	1.94E-12
271	J1750-3703	2 - 10	9.58E-02	6.20E-10
272	J1750-2125	2 - 10	2.10E-01	1.36E-09
273	J1750-3117	2 - 10	4.49E-03	2.90E-11
274	J1748-2828	2 - 10	1.92E+00	1.24E-08
275	J1748-2021	2 - 10	8.98E-02	5.81E-10
276	J1752-2830	2 - 10	1.80E-01	1.16E-09
277	J1750-2902	2 - 10	3.89E-01	2.52E-09
278	J1752-3137	2 - 10	4.22E+00	2.73E-08
279	J1758-3348	2 - 10	2.99E-01	1.94E-09
280	J1755-3228	2 - 10	6.06E-01	3.92E-09
281	J1801-2504	2 - 10	3.74E+00	2.42E-08
282	J1801-2544	2 - 10	5.98E-02	3.87E-10
283	J1801-2031	2 - 10	2.10E+00	1.36E-08
284	J1806-2435	2 - 10	5.98E-03	3.87E-11
285	J1806-2435	2 - 10	1.48E+00	9.57E-09
286	J1808-3658	2 - 10	3.29E-01	2.13E-09
287	J1810-2609	2 - 10	4.79E-02	3.10E-10
288	J1814-1709	2 - 10	1.05E+00	6.78E-09
289	J1815-1205	2 - 10	4.49E-02	2.90E-10
290	J1816-1402	2 - 10	2.10E+00	1.36E-08
291	J1819-2525	2 - 10	3.37E-03	2.18E-11
292	J1823-3021	2 - 10	7.48E-01	4.84E-09
293	J1825-3706	2 - 10	2.99E-02	1.94E-10
294	J1825-0000	2 - 10	7.48E-02	4.84E-10
295	J1829-2347	2 - 10	8.98E-02	5.81E-10
296	J1835-3258	2 - 10	9.86E-03	6.38E-11
297	J1839+0502	2 - 10	6.73E-01	4.36E-09
298	J1849-0303	2 - 10	8.98E-01	5.81E-09
299	J1853-0842	2 - 10	2.10E-02	1.36E-10
300	J1856+0519	2 - 10	2.10E-01	1.36E-09
301	J1858+2239	2 - 10	1.80E+00	1.16E-08
302	J1908+0010	2 - 10	2.99E-02	1.94E-10
303	J1911+0035	2 - 10	2.99E-04	1.94E-12
304	J1915+1058	2 - 10	8.98E-01	5.81E-09
305	J1918-0514	2 - 10	7.48E-02	4.84E-10
306	J1920+1441	2 - 10	1.50E-02	9.68E-11
307	J1942-0354	2 - 10	1.50E-01	9.68E-10
308	J1959+1142	2 - 10	8.98E-02	5.81E-10
309	J2002+2514	2 - 10	1.50E-03	9.68E-12
310	J2012+3811	2 - 10	4.79E-01	3.10E-09
311	J2024+3352	2 - 10	1.20E-03	7.74E-12

312	J2123-0547	2 - 10	3.29E-01	2.13E-09
313	J2129+1210	2 - 10	1.80E-02	1.16E-10
314	J2131+4717	2 - 10	2.69E-02	1.74E-10
315	J2144+3819	2 - 10	1.35E+00	8.71E-09
316	J2320+6217	2 - 10	7.18E-03	4.65E-11
317	J0720-3125	2 - 10	4.55E-03	2.95E-11
318	J1838-0301	2 - 10	1.35E-03	8.73E-12
319	J1234+3737	2 - 10	3.81E-05	2.46E-13
320	J1305+1801	2 - 10	1.13E-03	7.30E-12
321	J0024-7204	2 - 10	6.57E-04	4.25E-12
322	J0610-4844	2 - 10	1.14E-02	7.40E-11
323	J0712-3605	2 - 10	1.63E-03	1.06E-11
324	J0110+6004	2 - 10	4.14E-04	2.68E-12
325	J0613+4744	2 - 10	6.37E-04	4.12E-12
326	J0755+2200	2 - 10	6.54E-04	4.23E-12
327	J0807-7632	2 - 10	4.36E-05	2.82E-13
328	J0825+7306	2 - 10	1.90E-03	1.23E-11
329	J0844+1252	2 - 10	1.00E-01	6.47E-10
330	J0901+1753	2 - 10	5.35E-04	3.46E-12
331	J0951+1152	2 - 10	2.77E-05	1.79E-13
332	J1006-7014	2 - 10	9.80E-05	6.34E-13
333	J1145-0426	2 - 10	3.06E-03	1.98E-11
334	J1644+2515	2 - 10	3.49E-04	2.26E-12
335	J1807+0551	2 - 10	1.30E-02	8.40E-11
336	J2007+1742	2 - 10	4.25E-04	2.75E-12
337	J2142+4335	2 - 10	5.02E-04	3.25E-12
338	J2214+1242	2 - 10	2.94E-03	1.90E-11
339	J0028+5917	2 - 10	2.37E-03	1.53E-11
340	J0203-0243	2 - 10	2.31E-04	1.50E-12
341	J0206+1517	2 - 10	2.49E-03	1.61E-11
342	J0256+1926	2 - 10	4.02E-03	2.60E-11
343	J0331+4354	2 - 10	6.18E-03	4.00E-11
344	J0350+1714	2 - 10	7.73E-05	5.00E-13
345	J0502+2445	2 - 10	2.78E-03	1.80E-11
346	J0512-3241	2 - 10	4.07E-04	2.63E-12
347	J0529-3249	2 - 10	4.64E-03	3.00E-11
348	J0534-5801	2 - 10	4.33E-03	2.80E-11
349	J0543-4101	2 - 10	5.67E-04	3.67E-12
350	J0558+5353	2 - 10	4.85E-03	3.14E-11
351	J0611-8149	2 - 10	1.45E-03	9.40E-12
352	J0731+0956	2 - 10	3.09E-03	2.00E-11
353	J0744-5257	2 - 10	6.91E-04	4.47E-12
354	J0751+1444	2 - 10	3.52E-03	2.28E-11
355	J0757+6305	2 - 10	4.09E-04	2.65E-12
356	J0833-2248	2 - 10	7.66E-03	4.96E-11

357	J0859-2428	2 - 10	3.25E-03	2.10E-11
358	J1143+7141	2 - 10	1.58E-03	1.02E-11
359	J1238-3845	2 - 10	1.20E-04	7.79E-13
360	J1252-2914	2 - 10	2.01E-02	1.30E-10
361	J1712+3331	2 - 10	3.23E-05	2.09E-13
362	J1712-2414	2 - 10	2.56E-03	1.66E-11
363	J1814+4151	2 - 10	7.73E-05	5.00E-13
364	J1855-3109	2 - 10	9.27E-03	6.00E-11
365	J2040-0052	2 - 10	4.64E-04	3.00E-12
366	J2217-0821	2 - 10	4.33E-03	2.80E-11
367	J2353-3851	2 - 10	4.89E-04	3.16E-12
368	J0422-1321	2 - 10	1.32E-04	8.52E-13
369	J0615+2835	2 - 10	3.29E-04	2.13E-12
370	J0629+7104	2 - 10	2.07E-04	1.34E-12
371	J0811-3521	2 - 10	2.68E-04	1.73E-12
372	J0932+4950	2 - 10	1.63E-03	1.06E-11
373	J1019-0841	2 - 10	4.40E-04	2.85E-12
374	J1138+0322	2 - 10	1.78E-03	1.15E-11
375	J1152-6712	2 - 10	1.08E-05	6.99E-14
376	J1559+2555	2 - 10	3.81E-05	2.46E-13
377	J1622-1752	2 - 10	2.43E-05	1.57E-13
378	J1832-2923			
379	J1848+0035	2 - 10	1.44E-03	9.29E-12
380	J1934+5107	2 - 10	1.45E-03	9.40E-12
381	J1935-5850			
382	J2017-0339	2 - 10	8.85E-04	5.73E-12
383	J2020+2106	2 - 10	7.66E-05	4.96E-13
384	J2042+1909	2 - 10	5.20E-05	3.36E-13
385	J1336+5154	2 - 10	9.86E-05	6.38E-13
386	J1800+0810	2 - 10	5.56E-03	3.60E-11
387	J0132-6554	2 - 10	7.45E-04	4.82E-12
388	J0141-6753	2 - 10	1.73E-03	1.12E-11
389	J0203+2959	2 - 10	1.45E-03	9.40E-12
390	J0236-5219	2 - 10	5.99E-05	3.88E-13
391	J0314-2235	2 - 10	6.65E-03	4.30E-11
392	J0332-2556	2 - 10	1.69E-03	1.09E-11
393	J0453-4213	2 - 10	1.89E-05	1.22E-13
394	J0515+0104	2 - 10	1.03E-03	6.64E-12
395	J0531-4624	2 - 10	1.96E-03	1.27E-11
396	J0542+6051			
397	J0719+6557	2 - 10	5.05E-04	3.27E-12
398	J0815-1903	2 - 10	2.16E-04	1.40E-12
399	J0851+1146			
400	J0929-2405	2 - 10	8.80E-04	5.70E-12
401	J1002-1925	2 - 10	1.61E-03	1.04E-11

402	J1015+0904	2 - 10	3.08E-03	2.00E-11
403	J1015-4758	2 - 10	6.91E-05	4.47E-13
404	J1047+6335	2 - 10	5.84E-03	3.78E-11
405	J1051+5404	2 - 10	2.99E-03	1.93E-11
406	J1104+4503	2 - 10	6.18E-04	4.00E-12
407	J1105+2506	2 - 10	3.28E-02	2.12E-10
408	J1115+4258	2 - 10	1.51E-01	9.78E-10
409	J1117+1757	2 - 10	3.40E-03	2.20E-11
410	J1141-6410	2 - 10	3.96E-04	2.56E-12
411	J1149+2845	2 - 10	8.96E-03	5.80E-11
412	J1307+5351	2 - 10	5.01E-03	3.24E-11
413	J1409-4517	2 - 10	6.91E-04	4.47E-12
414	J1552+1856	2 - 10	7.24E-04	4.68E-12
415	J1727+4114	2 - 10	3.50E-03	2.27E-11
416	J1802+1804	2 - 10	6.75E-03	4.37E-11
417	J1816+4952	2 - 10	2.63E-03	1.70E-11
418	J1844-7418	2 - 10	2.52E-03	1.63E-11
419	J1907+6908	2 - 10	3.56E-03	2.30E-11
420	J1914+2456	2 - 10	1.80E-04	1.17E-12
421	J1938-4612	2 - 10	6.18E-04	4.00E-12
422	J2005+2239	2 - 10	4.33E-04	2.80E-12
423	J2008-6527	2 - 10	1.49E-04	9.64E-13
424	J2022-3954	2 - 10	8.91E-04	5.77E-12
425	J2107-0517	2 - 10	1.39E-04	8.98E-13
426	J2111+4809	2 - 10	8.67E-05	5.61E-13
427	J2115-5840	2 - 10	1.03E-03	6.64E-12
428	J2137-4342			
429	J2315-5910	2 - 10	3.56E-03	2.30E-11
430	J0904-3222	2 - 10	1.97E-05	1.27E-13
431	J0209-6318	2 - 10	5.23E-04	3.39E-12
432	J0409-7118	2 - 10	2.68E-04	1.73E-12
433	J0810+2808	2 - 10	2.29E-04	1.48E-12
434	J0812+6236	2 - 10	2.41E-03	1.56E-11
435	J1114-3740	2 - 10	1.26E-03	8.16E-12
436	J1514-6505	2 - 10	4.99E-04	3.23E-12
437	J0815-4913	2 - 10	8.53E-04	5.52E-12
438	J0838+4838	2 - 10	1.52E-03	9.85E-12
439	J1331-5458	2 - 10	7.66E-04	4.96E-12
440	J1949+7744	2 - 10	8.28E-04	5.36E-12
441	J1954+3221			
442	J1947-4200	2 - 10	3.06E-04	1.98E-12
443	J0011-1128	2 - 10	1.34E-03	8.67E-12
444	J0104+4117	2 - 10	1.23E-03	7.92E-12
445	J0645-1651	2 - 10	2.12E-03	1.37E-11
446	J0459+1926	2 - 10	1.16E-04	7.51E-13

447	J0502+1624	2 - 10	1.78E-04	1.15E-12
448	J0533+3659	2 - 10	1.91E-05	1.23E-13
449	J1326+4532	2 - 10	3.83E-04	2.48E-12
450	J1331-2940	2 - 10	8.37E-06	5.42E-14
451	J1538+1852	2 - 10	4.16E-05	2.69E-13
452	J1718+4115			
453	J1750+0605			
454	J1846+1222	2 - 10	9.92E-02	6.42E-10
455	J2030+5237	2 - 10	5.39E-05	3.49E-13
456	J2123+4217	2 - 10	2.38E-04	1.54E-12
457	J0538-6652	2 - 10	4.27E-01	2.76E-09
458	J1849-0318	2 - 10	2.37E-01	1.54E-09
459	J0051-7159	2 - 10	1.27E-05	8.21E-14
460	J0102+8152	2 - 10	9.67E-04	6.25E-12
461	J0157+3804	2 - 10	2.03E-05	1.31E-13
462	J0241+6033	2 - 10	3.29E-05	2.13E-13
463	J0248+6938	2 - 10	4.26E-03	2.75E-11
464	J0308+4057	2 - 10	2.16E-02	1.39E-10
465	J0400+1229	2 - 10	7.61E-06	4.93E-14
466	J0515+4624	2 - 10	7.61E-05	4.93E-13
467	J0518+3346	2 - 10	1.52E-05	9.82E-14
468	J0647+6937	2 - 10	3.29E-05	2.13E-13
469	J0843+1902	2 - 10	5.83E-05	3.77E-13
470	J1045+4533	2 - 10	2.38E-04	1.54E-12
471	J1113-2627	2 - 10	4.30E-05	2.79E-13
472	J1145+7215	2 - 10	5.83E-05	3.77E-13
473	J1249-0604	2 - 10	2.43E-05	1.57E-13
474	J1313-6409	2 - 10	5.83E-05	3.77E-13
475	J1500-0831	2 - 10	1.61E-03	1.04E-11
476	J1518+3138	2 - 10	1.50E-04	9.68E-13
477	J1533+6354	2 - 10	2.86E-04	1.85E-12
478	J1534+2642	2 - 10	1.27E-04	8.21E-13
479	J1639-5659	2 - 10	4.43E-04	2.87E-12
480	J1649-1540	2 - 10	1.01E-03	6.53E-12
481	J1656+5241	2 - 10	3.07E-04	1.98E-12
482	J1739-2851	2 - 10	4.05E-05	2.62E-13
483	J1822-2514	2 - 10	5.83E-05	3.77E-13
484	J1852-0614	2 - 10	1.52E-05	9.82E-14
485	J1917+2226	2 - 10	5.07E-05	3.28E-13
486	J2025+2722	2 - 10	1.77E-05	1.15E-13
487	J2154+1433	2 - 10	3.37E-04	2.18E-12
488	J2332+1458	2 - 10	4.30E-05	2.79E-13
489	J1744-2943	2 - 10	6.48E-06	4.20E-14
490	J1849-0308	2 - 10	3.09E-05	2.00E-13
491	J0047+2416	2 - 10	5.27E-03	3.41E-11

492	J0053-7439	2 - 10	2.56E-03	1.66E-11
493	J0116+0648	2 - 10	2.41E-03	1.56E-11
494	J0122+0042	2 - 10	3.80E-03	2.46E-11
495	J0122+0725	2 - 10	1.10E-02	7.13E-11
496	J0212+3018	2 - 10	2.51E-03	1.62E-11
497	J0313+4806	2 - 10	1.87E-03	1.21E-11
498	J0318-1944	2 - 10	1.20E-04	7.76E-13
499	J0325+2842	2 - 10	1.66E-02	1.08E-10
500	J0335+3201	2 - 10	7.83E-04	5.07E-12
501	J0336+0035	2 - 10	6.16E-02	3.98E-10
502	J0337+2559	2 - 10	1.09E-02	7.06E-11
503	J0443-1039	2 - 10	4.05E-04	2.62E-12
504	J0506+5901	2 - 10	1.26E-03	8.14E-12
505	J0507-0524	2 - 10	1.29E-04	8.31E-13
506	J0516+4559	2 - 10	6.37E-02	4.12E-10
507	J0528-6527	2 - 10	3.83E-03	2.48E-11
508	J0603+3119	2 - 10	1.02E-04	6.57E-13
509	J0641+8216	2 - 10	1.04E-03	6.71E-12
510	J0703-0544	2 - 10	3.55E-04	2.30E-12
511	J0716+7320	2 - 10	1.77E-04	1.15E-12
512	J0720-0515	2 - 10	3.04E-04	1.97E-12
513	J0802+5716	2 - 10	3.55E-03	2.30E-11
514	J0837+2333	2 - 10	4.30E-04	2.79E-12
515	J0839+3147	2 - 10	2.53E-04	1.64E-12
516	J0859-2749	2 - 10	4.84E-03	3.13E-11
517	J0901+2641	2 - 10	2.53E-05	1.64E-13
518	J0909+5429	2 - 10	7.61E-04	4.93E-12
519	J1036-1154	2 - 10	1.62E-04	1.05E-12
520	J1130-1519	2 - 10	1.68E-04	1.09E-12
521	J1136-3802	2 - 10	5.62E-04	3.63E-12
522	J1140+5159	2 - 10	8.25E-02	5.34E-10
523	J1147+2013	2 - 10	2.96E-03	1.92E-11
524	J1215+7233	2 - 10	4.28E-03	2.77E-11
525	J1225+2533	2 - 10	2.05E-03	1.33E-11
526	J1229+2431	2 - 10	6.10E-04	3.95E-12
527	J1301+2837	2 - 10	4.81E-04	3.11E-12
528	J1310+3556	2 - 10	2.03E-03	1.31E-11
529	J1318+3326	2 - 10	1.77E-04	1.15E-12
530	J1334+3710	2 - 10	6.86E-03	4.44E-11
531	J1435-1802	2 - 10	3.55E-04	2.30E-12
532	J1513+3834	2 - 10	1.52E-04	9.82E-13
533	J1614+3351	2 - 10	2.62E-02	1.69E-10
534	J1639+6042	2 - 10	1.44E-03	9.33E-12
535	J1645+8202	2 - 10	3.67E-03	2.38E-11
536	J1710+4857	2 - 10	8.64E-04	5.59E-12

537	J1717-6656	2 - 10	1.42E-02	9.15E-11
538	J1730-3339	2 - 10	4.81E-04	3.11E-12
539	J1758+1508	2 - 10	9.40E-04	6.08E-12
540	J1758+2208	2 - 10	3.55E-04	2.30E-12
541	J1805+2126	2 - 10	4.78E-03	3.10E-11
542	J1810+3157	2 - 10	3.80E-04	2.46E-12
543	J1825+1817	2 - 10	4.05E-04	2.62E-12
544	J1921+0432	2 - 10	3.41E-04	2.21E-12
545	J1931+5543	2 - 10	3.80E-04	2.46E-12
546	J1936+2753	2 - 10	1.77E-04	1.15E-12
547	J2058+3510	2 - 10	2.79E-04	1.80E-12
548	J2102+2748	2 - 10	7.34E-03	4.75E-11
549	J2121+4020	2 - 10	2.20E-03	1.43E-11
550	J2139-1600	2 - 10	9.02E-04	5.84E-12
551	J2200-0244	2 - 10	8.59E-04	5.56E-12
552	J2201+4353	2 - 10	3.55E-04	2.30E-12
553	J2208+4544	2 - 10	1.96E-02	1.27E-10
554	J2311+5301	2 - 10	5.07E-04	3.28E-12
555	J2313+0240	2 - 10	6.16E-03	3.98E-11
556	J2339+2814	2 - 10	8.86E-04	5.73E-12
557	J2349+3625	2 - 10	2.51E-03	1.62E-11
558	J2355+2838	2 - 10	2.94E-02	1.90E-10
559	J0527-6921	2 - 10	6.18E-06	4.00E-14
560	J0546-7108	2 - 10	1.24E-05	8.00E-14
561	J0058-7135	2 - 10	1.48E-05	9.60E-14
562	J1656-4049	2 - 10	8.80E-05	5.70E-13
563	J0002+6246	2 - 10	3.55E-04	2.30E-12
564	J0117+5914	2 - 10	6.57E-07	4.25E-15
565	J0628+1038	2 - 10	1.49E-04	9.57E-13
566	J1105-6107	2 - 10	1.00E-04	6.47E-13
567	J1617-5055	2 - 10	1.37E-03	8.86E-12
568	J1623-2631	2 - 10	2.70E-06	1.74E-14
569	J1645-0317	2 - 10	1.48E-05	9.57E-14
570	J1708-4009	2 - 10	1.88E-02	1.21E-10
571	J1740-3015	2 - 10	6.21E-06	4.02E-14
572	J1748-2924			
573	J1811-1926	2 - 10	1.90E-03	1.23E-11
574	J1917+1353	2 - 10	7.13E-05	4.61E-13
575	J1939+2134	2 - 10	4.99E-05	4.10E-13
576	J1958+3232	2 - 10	2.70E-07	1.74E-15
577	J2322+2057	2 - 10	1.62E-06	1.05E-14
578	J0043-1759	2 - 10	2.60E-03	1.68E-11
579	J1856-3754	2 - 10	9.83E-03	6.36E-11
580	J0137+2042	2 - 10	3.80E-04	2.46E-12
581	J0247+0037	2 - 10	2.22E-04	1.44E-12

582	J0743+2853	2 - 10	4.28E-01	2.77E-09
583	J1055+6028	2 - 10	9.24E-02	5.98E-10
584	J1213-0904	2 - 10	1.16E-03	7.48E-12
585	J1239+5511	2 - 10	4.00E-04	2.59E-12
586	J1416+0046	2 - 10	2.68E-03	1.74E-11
587	J1522+2537	2 - 10	6.93E-05	4.48E-13
588	J1523-0636	2 - 10	6.93E-05	4.48E-13
589	J1732+7413	2 - 10	5.99E-03	3.88E-11
590	J1942+1705	2 - 10	7.77E-03	5.02E-11
591	J2204+4714	2 - 10	3.94E-03	2.55E-11
592	J2319+7900	2 - 10	1.07E-02	6.92E-11
593	J2337+4627	2 - 10	2.65E-02	1.71E-10
594	J0414+2812	2 - 10	4.05E-04	2.62E-12
595	J0419+2749	2 - 10	1.15E-04	7.43E-13
596	J0419+2906	2 - 10	4.91E-05	3.18E-13
597	J0421+1932	2 - 10	1.91E-04	1.24E-12
598	J0421+2818	2 - 10	1.84E-03	1.19E-11
599	J0421+2826	2 - 10	7.64E-05	4.95E-13
600	J0427+2542	2 - 10	4.91E-05	3.18E-13
601	J0429+2632	2 - 10	1.37E-04	8.84E-13
602	J0430+1813	2 - 10	2.84E-04	1.84E-12
603	J0431+1706	2 - 10	9.31E-05	6.02E-13
604	J0432+1757	2 - 10	7.09E-05	4.59E-13
605	J0432+1801	2 - 10	1.97E-04	1.27E-12
606	J0432+1820	2 - 10	2.40E-04	1.56E-12
607	J0433+2421	2 - 10	2.08E-04	1.34E-12
608	J0433+2421	2 - 10	2.08E-04	1.34E-12
609	J0433+2434	2 - 10	1.42E-04	9.20E-13
610	J0434+2428	2 - 10	1.26E-04	8.12E-13
611	J0435+2414	2 - 10	1.04E-04	6.71E-13
612	J0455+3021	2 - 10	5.47E-05	3.54E-13
613	J0455+3034	2 - 10	3.06E-04	1.98E-12
614	J0456+3021	2 - 10	1.42E-04	9.20E-13
615	J0503+2523	2 - 10	6.02E-05	3.90E-13
616	J0507+3024	2 - 10	4.36E-05	2.82E-13
617	J0535-0508	2 - 10	9.13E-04	5.90E-12
618	J0235+0344			
619	J2013+4002	2 - 10	1.99E-03	1.29E-11
620	J2117+3412	2 - 10	9.83E-04	6.36E-12
621	J0037-7214	2 - 10	7.34E-04	4.75E-12
622	J0133+3039	2 - 10	3.10E-03	2.01E-11
623	J0538-6404	2 - 10	3.21E-02	2.08E-10
624	J0538-6905	2 - 10	5.00E-02	3.23E-10
625	J1801-2547	2 - 10	1.27E-01	8.21E-10
626	J1915+1056	2 - 10	7.73E-01	5.00E-09

627	J1907+0918	2 - 10	1.98E-03	1.28E-11
628	J0042+4115	2 - 10	1.04E-05	6.72E-14
629	J0042+4116	2 - 10	5.81E-05	3.76E-13
630	J1300+1240	2 - 10	2.96E-06	1.92E-14
631	J1537+1155	2 - 10	4.80E-06	3.10E-14
632	J1748-2446	2 - 10	1.09E-03	7.06E-12
633	J1845+0050	2 - 10	6.86E-02	4.44E-10
634	J2019+2425	2 - 10	4.82E-06	3.12E-14
635	J0042+3533	2 - 10	8.67E-03	5.61E-11
636	J0222+4729	2 - 10	5.94E-04	3.84E-12
637	J0234-4347	2 - 10	1.01E-01	6.51E-10
638	J0734+3152	2 - 10	6.24E-03	4.04E-11
639	J0744+0333	2 - 10	1.65E-03	1.07E-11
640	J1334-0820	2 - 10	3.24E-04	2.10E-12
641	J1634+5709	2 - 10	8.42E-04	5.45E-12
642	J2045-3120	2 - 10	3.60E-02	2.33E-10
643	J2309+4757	2 - 10	5.20E-03	3.36E-11
644	J1939-0603	2 - 10	9.83E-04	6.36E-12
645	J1330+2413	2 - 10	4.84E-04	3.13E-12
646	J0720-3146	2 - 10	5.72E-04	3.70E-12
647	J0019+2156	2 - 10	5.07E-03	3.28E-11
648	J0513-6951	2 - 10	2.47E-05	1.60E-13
649	J0543-6822	2 - 10	6.18E-05	4.00E-13
650	J0925-4758	2 - 10	2.16E-03	1.39E-11
651	J1601+6648	2 - 10	2.84E-03	1.83E-11
652	J1045-5941	2 - 10	1.62E-02	1.05E-10
653	J0654-2355	2 - 10	2.17E-04	1.40E-12
654	J2020+4354	2 - 10	1.58E-03	1.02E-11
655	J0412-1028	2 - 10	2.50E-04	1.62E-12
656	J0943+5557	2 - 10	6.34E-04	4.10E-12
657	J1001+1724	2 - 10	4.58E-04	2.96E-12
658	J1503+4739	2 - 10	5.37E-04	3.48E-12
659	J2037+7535	2 - 10	1.66E-03	1.08E-11
660	J2122+1708	2 - 10	3.29E-05	2.13E-13
661	J1214+1149	2 - 10	1.58E-04	1.02E-12
662	J1655+3510	2 - 10	3.39E-05	2.19E-13
663	J1805+6945	2 - 10	2.64E-05	1.71E-13
664	J0044+0932	2 - 10	5.10E-04	3.30E-12
665	J0103-7254	2 - 10	2.39E-01	1.55E-09
666	J0133+3032	2 - 10	1.67E-04	1.08E-12
667	J0535-0523	2 - 10	6.43E-03	4.16E-11
668	J0537-6909	2 - 10	7.93E-05	5.13E-13
669	J1750+7045	2 - 10	4.17E-04	2.70E-12
670	J2004-5543			
671	J0051-7310			

672	J0052-7220			
673	J0042-7340			
674	J0049-7323			
675	J0052-7233			
676	J0056-7222			
677	J0057-7207			
678	J0057-7219			
679	J0057-7325			
680	J0100-7211	2 - 10	6.37E-05	4.12E-13
681	J0101-7211			
682	J0103-7208			
683	J0103-7241			
684	J0119-7311			
685	J0030+0451	2 - 10	1.96E-05	1.27E-13
686	J0205+6449	2 - 10	2.32E-03	1.50E-11
687	J1024-0719	2 - 10	1.37E-06	8.86E-15
688	J1119-6127	2 - 10	7.33E-05	4.74E-13
689	J1124-5916	2 - 10	1.70E-03	1.10E-11
690	J1420-6048	2 - 10	7.26E-04	4.70E-12
691	J1744-1134	2 - 10	9.95E-07	6.44E-15
692	J1800-2450	2 - 10	1.22E-04	7.90E-13
693	J1846-0258	2 - 10	6.03E-03	3.90E-11
694	J1856+0113	2 - 10	1.86E-04	1.20E-12
695	J2229+6114	2 - 10	2.01E-04	1.30E-12
696	J0929-3123	2 - 10	1.05E-02	7.10E-11
697	J1751-3037	2 - 10	1.81E-01	1.17E-09
698	J1806-2924	2 - 10	1.18E-01	8.29E-10
699	J1813-3346	2 - 10	3.88E-02	2.51E-10
700	J0111-7316	2 - 10	1.98E-02	1.28E-10
701	J1845+0051	2 - 10	4.76E-02	3.08E-10
702	J0537-7034	2 - 10	1.24E-02	8.04E-11
703	J1746-2903	2 - 10	4.00E-04	2.59E-12
704	J1747-2852	2 - 10	1.56E-02	1.01E-10
705	J0501+1146	2 - 10	1.44E+01	9.32E-08
706	J1845-0434	2 - 10	3.20E-04	2.05E-12
707	J0356-3641	2 - 10	1.24E-03	8.04E-12
708	J0242-0000	2 - 10	2.40E-03	1.55E-11
709	J0947-3056	2 - 10	7.60E-03	4.92E-11
710	J1235-3954	2 - 10	4.00E-03	2.59E-11
711	J1305-4928	2 - 10	4.00E-03	2.59E-11
712	J1325-4301	2 - 10	2.50E-02	1.62E-10
713	J2318-4222	2 - 10	8.00E-03	5.18E-11
714	J1229+0203	2 - 10	3.54E-02	2.29E-10
715	J1744-2916	2 - 10	6.64E-03	4.30E-11
716	J1750-3412	2 - 10	1.76E-03	1.14E-11

717	J0153+7442			
718	J0439-6809			
719	J1905-0142			
720	J1930+1852	2 - 10	2.16E-04	1.70E-12
721	J0023-7204	2 - 10	2.71E-08	1.75E-16
722	J0024-7204D	2 - 10	1.36E-07	8.78E-16
723	J0024-7205	2 - 10	2.71E-07	1.75E-15
724	J0024-7204F	2 - 10	2.16E-07	1.39E-15
725	J0024-7204G	2 - 10	8.58E-08	5.54E-16
726	J0024-7204H	2 - 10	8.58E-08	5.54E-16
727	J0024-7204I	2 - 10	1.08E-07	6.97E-16
728	J0023-7203	2 - 10	1.36E-07	8.78E-16
729	J0024-7204L	2 - 10	1.71E-07	1.11E-15
730	J0023-7205	2 - 10	8.58E-08	5.54E-16
731	J0024-7204N	2 - 10	1.08E-07	6.97E-16
732	J0024-7204O	2 - 10	2.71E-07	1.75E-15
733	J0024-7204Q	2 - 10	8.58E-08	5.54E-16
734	J0024-7204S	2 - 10	1.08E-07	6.97E-16
735	J0024-7204T	2 - 10	6.82E-08	4.40E-16
736	J0024-7203	2 - 10	1.36E-07	8.78E-16
737	J1740-5340	2 - 10	4.64E-06	3.34E-14
738	J2225+6535	2 - 10	1.57E-06	1.08E-14
739	J2043+2740	2 - 10	1.23E-06	8.96E-15
740	J0630-2834	2 - 10	4.49E-06	2.55E-14
741	J1817-3618	2 - 10	1.60E-07	1.03E-15
742	J0059-7223	2 - 10	1.43E-04	1.12E-12
743	J0047-7312	2 - 10	7.70E-04	6.51E-12
744	J0051-7310B	2 - 10	1.05E-03	6.78E-12
745	J0051-7310C	2 - 10	8.49E-04	5.50E-12
746	J0055-7242			
747	J0055-7210			
748	J0054-7245	2 - 10	1.05E-04	6.72E-13
749	J0053-7227			
750	J0055-7238	2 - 10	7.08E-05	4.53E-13
751	J0053-7249	2 – 10	5.75E-03	4.51E-11
752	J1844-0257			
753	J1859+0815	2 – 10	3.12E-02	2.00E-10
754	J0420-5022	2 - 10	1.77E-04	1.13E-12
755	J1544-5645	2 – 10	1.92E-02	1.23E-10
756	J1740-2847	2 – 10	3.76E-04	3.47E-12
757	J1605+3249	2 - 10	8.41E-04	5.31E-12
758	J1308+2127	2 - 10	2.66E-04	1.68E-12
759	J0806-4122	2 - 10	3.21E-04	2.03E-12

B.4 Catalogue Specific References

The reference articles and databases utilized specifically by the XNAVSC are provided in Table B-5. There are a total of 54 references used within this catalogue. These reference numbers are those that pertain specifically to the XNAVSC and are not to be confused with the numbers of the references used for this dissertation.

Table B-5. XNAVSC References.

XNAVSC Reference Number	Reference Citation
[1]	Becker, W., and Trümper, J., "The X-ray luminosity of rotation-powered neutron stars," *Astronomy and Astrophysics*, Vol. 326, October 1997, pp. 682-691.
[2]	Liu, Q. Z., van Paradijs, J., and van den Heuvel, E. P. J., "A catalogue of low-mass X-ray binaries," *Astronomy and Astrophysics*, Vol. 368, March 2001, pp. 1021-1054.
[3]	Liu, Q. Z., van Paradijs, J., and van den Heuvel, E. P. J., "A catalogue of high-mass X-ray binaries," *Astronomy and Astrophysics Supplement Series*, Vol. 147, November 2000, pp. 25-49.
[4]	ATNF, "ATNF Pulsar Catalogue," [online database], Australian Telescope National Facility, URL: http://www.atnf.csiro.au/research/pulsar/psrcat/ [cited 22 December 2003].
[5]	Princeton, "Princeton University Pulsar Group Pulsar Catalog," [online database], Princeton University, URL: http://pulsar.princeton.edu/pulsar/catalog.shtml [cited 4 May 2003].
[6]	Kim, Y. H., *X-ray Source Tables*, Saddleback College, 2002 (unpublished).
[7]	Ritter, H., and Kolb, U., "Catalogue of cataclysmic binaries, low-mass X-ray binaries and related objects (Sixth edition)," *Astronomy and Astrophysics Supplement Series*, Vol. 129, April 1998, pp. 83-85.
[8]	Singh, K. P., Drake, S. A., and White, N. E., "RS CVn Versus Algol-Type Binaries: A Comparative Study of Their X-Ray Emission," *Astronomical Journal*, Vol. 111, No. 6, June 1996, pg. 2415.
[9]	Mereghetti, S., "The Zoo of X-ray Pulsars," *Frontier Objects in Astrophysics and Particle Physics, Vulcano Workshop, Italian Physical Society*, Eds. F. Giovannelli and G. Mannocchi, Vulcano, Italy, 21-27 May 2000, pg. 239.
[10]	Corbet, R., Coe, M., Edge, W., Laycock, S., Markwardt, C., and Marshall, F. E., "X-ray Pulsars in the SMC," [online database], URL: http://lheawww.gsfc.nasa.gov/users/corbet/pulsars/ [cited 30 October 2004].
[11]	Possenti, A., Cerutti, R., Colpi, M., and Mereghetti, S., "Re-examining the X-ray versus spin-down luminosity correlation of rotation powered pulsars," *Astronomy and Astrophysics*, Vol. 387, June 2002, pp. 993-1002.
[12]	Remillard, R. A., Swank, J., and Strohmayer, T., "XTE J0929-314," *International Astronomical Union Circular*, Vol. 7893, May 2002, pg. 1.
[13]	Markwardt, C. B., and Swank, J. H., "XTE J1751-305," *International Astronomical Union Circular*, Vol. 7867, April 2002, pg. 1.
[14]	Markwardt, C. B., Juda, M., and Swank, J. H., "XTE J1807-294," *International Astronomical Union Circular*, Vol. 8095, March 2003, pg. 2.
[15]	Krauss, M. I., Dullighan, A., Chakrabarty, D., van Kerkwijk, M. H., and Markwardt, C. B., "XTE J1814-338," *International Astronomical Union Circular*, Vol. 8154, June 2003, pg. 3.

[16]	Meliani, M. T., "A Catalogue of X-ray sources in the sky region between delta = -73deg. and delta = +27 deg," *Publications of the Astronomical Society of Australia*, Vol. 16, August 1999, pp. 175-205.
[17]	Lamb, R. C., Prince, T. A., Macomb, D. J., and Majid, W. A., "CXOU J010043.1-721134," *International Astronomical Union Circular*, Vol. 8220, October 2003, pg. 1.
[18]	Camilo, F., Lorimer, D. R., Bhat, N. D. R., Gotthelf, E. V., Halpern, J. P., Wang, Q. D., Lu, F. J., and Mirabal, N., "Discovery of a 136 Millisecond Radio and X-Ray Pulsar in Supernova Remnant G54.1+0.3," *Astrophysical Journal*, Vol. 574, July 2002, pp. L71-L74.
[19]	Camilo, F., Manchester, R. N., Gaensler, B. M., Lorimer, D. R., and Sarkissian, J., "PSR J1124-5916: Discovery of a Young Energetic Pulsar in the Supernova Remnant G292.0+1.8," *Astrophysical Journal*, Vol. 567, March 2002, pp. L71-L75.
[20]	Mereghetti, S., Bandiera, R., Bocchino, F., and Israel, G. L., "BeppoSAX Observations of the Young Pulsar in the Kes 75 Supernova Remnant," *Astrophysical Journal*, Vol. 574, August 2002, pp. 873-878.
[21]	Pivovaroff, M. J., Kaspi, V. M., Camilo, F., Gaensler, B. M., and Crawford, F., "X-Ray Observations of the New Pulsar-Supernova Remnant System PSR J1119-6127 and Supernova Remnant G292.2-0.5," *Astrophysical Journal*, Vol. 554, June 2001, pp. 161-172.
[22]	Becker, W., and Trümper, J., "The X-ray emission properties of millisecond pulsars," *Astronomy and Astrophysics*, Vol. 341, January 1999, pp. 803-817.
[23]	Grindlay, J. E., Camilo, F., Heinke, C. O., Edmonds, P. D., Cohn, H., and Lugger, P., "Chandra Study of a Complete Sample of Millisecond Pulsars in 47 Tucanae and NGC 6397," *Astrophysical Journal*, Vol. 581, December 2002, pp. 470-484.
[24]	Freire, P. C., Camilo, F., Lorimer, D. R., Lyne, A. G., Manchester, R. N., and D'Amico, N., "Timing the millisecond pulsars in 47 Tucanae," *Monthly Notices of the Royal Astronomical Society*, Vol. 326, September 2001, pp. 901-915.
[25]	Kuiper, L., and Hermsen, W., "X-ray and Gamma-ray Observations of Millisecond Pulsars," *X-ray and Gamma-ray Astrophysics of Galactic Sources*, 8 December 2003.
[26]	Nicastro, L., Cusumano, G., Löhmer, O., Kramer, M., Kuiper, L., Hermsen, W., Mineo, T., and Becker, W., "BeppoSAX Observation of PSR B1937+21," *Astronomy and Astrophysics*, Vol. 413, January 2004, pp. 1065-1072.
[27]	Zavlin, V. E., and Pavlov, G. G., "X-Ray Emission from the Old Pulsar B0950+08," *Astrophysical Journal*, Vol. 616, November 2004, pp. 452-462.
[28]	D'Amico, N., Possenti, A., Manchester, R. N., Sarkissian, J., Lyne, A. G., and Camilo, F., "An Eclipsing Millisecond Pulsar with a Possible Main-Sequence Companion in NGC 6397," *Astrophysical Journal*, Vol. 561, November 2001, pp. L89-L92.
[29]	Galloway, D. K., Chakrabarty, D., Morgan, E. H., and Remillard, R. A., "Discovery of a High-Latitude Accreting Millisecond Pulsar in an Ultracompact Binary," *Astrophysical Journal*, Vol. 576, September 2002, pp. L137-L140.
[30]	Markwardt, C. B., Smith, E., and Swank, J. H., "XTE J1807-294," *International Astronomical Union Circular*, Vol. 8080, February 2003, pg. 2.
[31]	Markwardt, C. B., and Swank, J. H., "XTE J1814-338," *International Astronomical Union Circular*, Vol. 8144, June 2003, pg. 1.
[32]	Majid, W. A., Lamb, R. C., and Macomb, D. J., "X-Ray Pulsars in the Small Magellanic Cloud," *Astrophysical Journal*, Vol. 609, July 2004, pp. 133-143.
[33]	Lamb, R. C., Macomb, D. J., Prince, T. A., and Majid, W. A., "Discovery of 16.6 and 25.5 Second Pulsations from the Small Magellanic Cloud," *Astrophysical Journal*, Vol. 567, March 2002, pp. L129-L132.
[34]	Laycock, S., Corbet, R. H. D., Perrodin, D., Coe, M. J., Marshall, F. E., and Markwardt, C., "Discovery of a new transient X-ray pulsar in the Small Magellanic Cloud," *Astronomy and Astrophysics*, Vol. 385, April 2002, pp. 464-470.
[35]	Gaensler, B. M., Gotthelf, E. V., and Vasisht, G., "A New Supernova Remnant Coincident with the Slow X-Ray Pulsar AX J1845-0258," *Astrophysical Journal*, Vol. 526, November 1999, pp. L37-L40.
[36]	Marshall, F. E., in 't Zand, J. J. M., Strohmayer, T., and Markwardt, C. B., "XTE J1859+083," *International Astronomical Union Circular*, Vol. 7240, August 1999, pg. 2.

[37]	Lamb, R. C., Prince, T. A., Macomb, D. J., and Finger, M. H., "RX J0052.1-7319," *International Astronomical Union Circular*, Vol. 7081, January 1999, pg. 4.
[38]	Haberl, F., Pietsch, W., and Motch, C., "RX J0420.0-5022: an isolated neutron star candidate with evidence for 22.7 s X-ray pulsations," *Astronomy and Astrophysics*, Vol. 351, November 1999, pp. L53-L57.
[39]	Takeshima, T., Marshall, F. E., and in 't Zand, J., "XTE J1543-568," *International Astronomical Union Circular*, Vol. 7369, February 2000, pg. 2.
[40]	Sakano, M., and Koyama, K., "AX J1740.2-2848," *International Astronomical Union Circular*, Vol. 7364, February 2000, pg. 2.
[41]	Motch, C., Haberl, F., Zickgraf, F. J., Hasinger, G., and Schwope, A. D., "The isolated neutron star candidate RX J1605.3+3249," *Astronomy and Astrophysics*, Vol. 351, November 1999, pp. 177-184.
[42]	Schwope, A. D., Hasinger, G., Schwarz, R., Haberl, F., and Schmidt, M., "The isolated neutron star candidate RBS1223 (1RXS J130848.6+212708)," *Astronomy and Astrophysics*, Vol. 341, January 1999, pp. L51-L54.
[43]	Haberl, F., Motch, C., and Pietsch, W., "Isolated Neutron Stars in the ROSAT Survey," *Astronomische Nachrichten*, Vol. 319, January 1998, pg. 97.
[44]	Campana, S., Ravasio, M., Israel, G. L., Mangano, V., and Belloni, T., "XMM-Newton Observation of the 5.25 Millisecond Transient Pulsar XTE J1807-294 in Outburst," *Astrophysical Journal*, Vol. 594, September 2003, pp. L39-L42.
[45]	Strohmayer, T. E., Markwardt, C. B., Swank, J. H., and in't Zand, J., "X-Ray Bursts from the Accreting Millisecond Pulsar XTE J1814-338," *Astrophysical Journal*, Vol. 596, October 2003, pp. L67-L70.
[46]	Chakrabarty, D., and Morgan, E. H., "The two-hour orbit of a binary millisecond X-ray pulsar," *Nature*, Vol. 394, 23 July 1998, pp. 346-348.
[47]	Wijnands, R., "An XMM-Newton Observation during the 2000 Outburst of SAX J1808.4-3658," *Astrophysical Journal*, Vol. 588, May 2003, pp. 425-429.
[48]	Markwardt, C. B., Swank, J. H., Strohmayer, T. E., in 't Zand, J. J. M., and Marshall, F. E., "Discovery of a Second Millisecond Accreting Pulsar: XTE J1751-305," *Astrophysical Journal*, Vol. 575, August 2002, pp. L21-L24.
[49]	Kaaret, P., Marshall, H. L., Aldcroft, T. L., Graessle, D. E., Karovska, M., Murray, S. S., Rots, A. H., Schulz, N. S., and Seward, F. D., "Chandra Observations of the Young Pulsar PSR B0540-69," *Astrophysical Journal*, Vol. 546, January 2001, pp. 1159-1167.
[50]	Kirsch, M. G. F., Mukerjee, K., Breitfellner, M. G., Djavidnia, S., Freyberg, M. J., Kendziorra, E., and Smith, M. J. S., "Studies of orbital parameters and pulse profile of the accreting millisecond pulsar XTE J1807-294," *Astronomy and Astrophysics*, Vol. 423, August 2004, pp. L9-L12.
[51]	Miller, J. M., Wijnands, R., Méndez, M., Kendziorra, E., Tiengo, A., van der Klis, M., Chakrabarty, D., Gaensler, B. M., and Lewin, W. H. G., "XMM-Newton Spectroscopy of the Accretion-driven Millisecond X-Ray Pulsar XTE J1751-305 in Outburst," *Astrophysical Journal*, Vol. 583, February 2003, pp. L99-L102.
[52]	Wijnands, R., and van der Klis, M., "A millisecond pulsar in an X-ray binary system," *Nature*, Vol. 394, 23 July 1998, pp. 344-346.
[53]	White, N. E., and Zhang, W., "Millisecond X-Ray Pulsars in Low-mass X-Ray Binaries," *Astrophysical Journal*, Vol. 490, November 1997, pg. L87.
[54]	Nice, D. J., and Thorsett, S. E., "Pulsar PSR 1744-24A - Timing, eclipses, and the evolution of neutron star binaries," *Astrophysical Journal*, Vol. 397, September 1992, pp. 249-259.

Appendix C TOA Observations and Spacecraft Orbit Data

C.1 ARGOS Barycentered and Non-Barycentered TOAs

Information is provided on several observations of the Crab Pulsar made by the USA experiment on *ARGOS*. A discussion is provided on how to create phase difference measurements using an observation at the vehicle where position is unknown.

Table C-1 provides a list of Crab Pulsar observations, as well as the TOA for each observation measured by transferring the photon arrival times to the SSB using the *ARGOS* navigation information. Table C-2 provides the measured TOAs for the same observations but assuming the position of the spacecraft is located at the geocenter. No spacecraft navigation information is used to produce these geocenter-based TOAs, only Earth position relative to SSB and the recorded arrival time of photons at the spacecraft. The table also provides measured TOAs for this set of observations at *ARGOS*, where no time transfer at all is used to correct the photon arrival times. The TOAs listed in these tables were created by comparing the folded profile to the standard template profile of the Crab Pulsar.

Table C-1. Crab Pulsar Observations by USA on *ARGOS*.

Observation Number	Observation Date	Duration (s)	SSB Barycentered TOA (MJD)	Expected Error (10^{-6} s)
1	1999 Nov 28 13:13:14.67	1209.635954	51510.5569987267372	3.73
2	1999 Dec 18 12:38:56.03	382.659762	51530.5334426842310	11.25
3	1999 Dec 19 08:54:05.78	483.573335	51531.3772976203982	9.98
4	2000 Jan 03 13:29:45.06	381.745011	51546.5684437619566	14.55
5	2000 Jan 03 15:09:48.94	462.948790	51546.6379248843878	10.13
6	2000 Jan 03 16:50:00.20	488.675447	51546.7075021853379	13.92

Table C-2. Geocenter-Based TOAs and *ARGOS*-Based TOAs.

Observation Number	Geocenter to SSB TOA (MJD)	Expected Error (10^{-6} s)	No Time Transfer TOA (MJD)	Expected Error (10^{-6} s)
1	51510.5569984666872	11.14	51510.5516072401006	25.62
2	51530.5334422425440	34.99	51530.5277840136696	17.81
3	51531.3772974026506	7.93	51531.3716434666494	15.98
4	51546.5684434401846	17.32	51546.5630758781772	41.62
5	51546.6379249412712	24.02	51546.6325593182410	66.14
6	51546.7075018385294	37.95	51546.7021387089699	29.60

The data in Table C-1 and Table C-2 provide information on TOAs created using different assumptions of detector location. It can be seen that these TOAs have large expected errors, which would result in large position estimate errors. This may be a result of the pulse template being defined for the SSB and not at either the geocenter or the *ARGOS* positions. The TOAs for the geocenter are known to be in error since the pulses were detected on the vehicle and not at Earth-center, so these values must be corrected for this offset error. Since this error is related directly to the offset of the vehicle position with respect to Earth, determining this difference provides the desired position.

Below is a series of steps that corrects the above information to determine accurate position.

- Compute geocenter to SSB TOA using SSB template: TOA_{GEO}
- Using pulsar template model, determine any phase fraction between TOA and integer cycle: $\phi_{GEO} = \Phi_{GEO} - round\left(\Phi_{GEO}\right)$

- Determine number of cycles, such as:
  - Assume $N_{GEO} = 0$
  - Use spacecraft near Earth: $N_{GEO} = \pm 1$
  - Use other methods within dissertation to determine ambiguous cycles
- Correct geocenter-based TOA to SSB TOA:

  $$TOA_{SSB} \approx TOA_{GEO_{corrected}} = TOA_{GEO} - \left(N_{GEO} + \phi_{GEO}\right)P$$

- Using non-time transferred profile on spacecraft determine TOA at spacecraft:

  $$TOA_{SC} = MJD0_{NoBary} - \delta\tau_{NoBary}$$

- Determine delta-time from these measurements and compare to position:

  $$dt_{SC} = \frac{\hat{\mathbf{n}} \cdot \mathbf{r}_{SC/E}}{c} = \left(TOA_{GEO_{corrected}} - TOA_{SC}\right) - \frac{\hat{\mathbf{n}} \cdot \mathbf{r}_{E}}{c}$$

Improved results for the above were found when modifying the spacecraft TOA by:

$$TOA_{SC} = MJD0_{NoBary} - \delta\tau_{NoBary} + \left(\phi_{GEO} P\right)$$

This is not completely understood at this time, but may be related to methods of determining the geocenter-based TOA.

Table C-3 provides data used to correct the TOAs for the above observations. The values of the unknown cycles, N, were chosen by hand for these single pulsar examples. An actual system would have to determine these using the methods described in this dissertation. Using the known location of Earth at the TOA time, the difference of these two arrival times can be compared to determine the phase difference between the two locations. Since *ARGOS* navigation provides this data directly, this can be compared to the computed results. Table C-4 provides this data, along with the measured Doppler effect $(\hat{\mathbf{n}} \cdot \mathbf{v}_E)$, which indicates amount of smearing of pulse profile at spacecraft and potential quality of phase difference measurement. The table shows that Doppler effect can affect the measured results. However, observation #4 shows very large Doppler, but fairly small errors. Observation #3 provides the best results and has the least expected error in all the TOA measurements of Table C-1 and Table C-2. The TOAs with large expected error may contribute to the errors computed in Table C-4.

The least confident algorithm is the expression for the TOA_{SC}, since Earth position is known well, and $TOA_{GEO_{corrected}}$ compared well with the true TOA values from Table C-1. Additional research should be completed to determine the correct computation of this value. Barycentered pulse timing models were used in these tests. In future work, creating models that exist at the geocenter and using an inertial frame origin at geocenter may reduce errors and computations.

Table C-3. Corrected TOAs and Integer Cycles.

Observation Number	Cycles	$TOA_{GEO_{corrected}}$ (MJD)	TOA_{SC} (MJD)
1	-1	51510.55699872404	51510.55160716116
2	-1	51530.53344268298	51530.52778432857
3	-1	51531.37729761945	51531.37164344235
4	-1	51546.56844376143	51546.56307617072
5	0	51546.63792488415	51546.63255964142
6	-1	51546.70750218459	51546.70213899849

Table C-4. Comparison of Measured and Actual Phase Differences.

Observation Number	Doppler Effect (km/s)	$\Delta\phi_{meas}$	$\Delta\phi_{truth}$	Phase Error	Range Error (km)
1	1.37	-0.41353552760884	-0.32839378530425	0.085	855
2	-1.44	-0.31372734668821	-0.42938761882579	-0.116	-1161
3	0.126	-0.41886773125163	-0.41974694328832	0.00088	-9
4	-4.74	-1.06915135332274	-1.06223427267455	0.0069	69
5	-4.78	-0.39887068722268	-0.01767531215233	38	3828
6	-4.77	-0.94820501914336	-0.90815067628982	0.040	402

C.2 Spacecraft Orbit Data

The Two-Line Element (TLE) sets provided by NORAD were used to determine spacecraft orbit information for various sections of this dissertation [97]. The TLE sets used during the dissertation analysis are provided below.

ARGOS

1 25634U 99008A   99360.46769266 .00000242 00000-0 13979-3 0 2228

2 25634 98.7653 305.9904 0010182 97.0149 263.2181 14.17835610 43356

LAGEOS-1

1 08820U 76039A   03365.88757026 -.00000010 00000-0 10000-3 0   248

2 08820 109.8375 249.2939 0044229 259.2681 100.3073 6.38664526389689

GPS Block IIA-16 PRN-01

1 22231U 92079A   04341.32034493 -.00000065 +00000-0 +00000-0 0 01957

2 22231 056.2538 046.2019 0061186 264.6021 094.7448 02.00570114088222

DirecTV 2 (DBS 2)

1 23192U 94047A   05002.12423223 -.00000093 +00000-0 +10000-3 0 06272

2 23192 000.0210 096.9411 0001908 193.3646 115.4913 01.00271524048246

Orbit information of the LRO's planned mission was provided by Dave Folta and Mark Beckman of NASA GSFC. This data is preliminary information for a mission planned to be launched and orbit the Moon in 2008. Below is the first epoch in the data file, which provides ECI position and velocity information of the vehicle in its orbit about the Moon.

LRO

Time:	1 Jun 2008 12:00:00.000		
Position (m):	280653.751729	192906.946167	116373.703572
Velocity (m/s):	0.130996	1.297566	-0.995554

Appendix D State Dynamics and Kalman Filter Equations

D.1 *State Dynamics and Observations*

The following sections provide a description of a system of equations representing time-varying state variables $\mathbf{x} = \vec{x}(t) = \{x_1, x_2, x_{3,} \cdots, x_n\}$, where $\mathbf{x}$ is the vector of individual states, x_i. The time-dependent dynamics of this system may be represented as linear or non-linear based upon the physical nature of the system. Equations for both types of systems are discussed. For systems where the chosen state variables are represented as the whole value states, dynamics necessary to describe the propagation of the errors within the states is also presented. External observations that are used to correct estimated values of the whole value states, as well as determine any errors associated with these states, are presented. A summary of all the dynamics of the states, their errors, and their observations is provided at the end of this section [65, 189].

D.1.1 Linear System Equations

D.1.1.1 State Dynamics

Given a set of states, $\mathbf{x}$, which are the whole value of each state that vary *linearly* with time, the dynamics over time can be represented as follows [39, 65, 176],

$$\dot{\mathbf{x}}(t) = \mathbf{A}(t)\mathbf{x}(t) + \mathbf{B}(t)\mathbf{u}(t) + \mathbf{N}(t)\boldsymbol{\omega}(t) \tag{D.1}$$

In Eq. (D.1), $\dot{\mathbf{x}} = d\mathbf{x}(t)/dt$ represents the first time derivative of each state. Higher order derivatives can be included in the system by continually introducing state variables that represent the first order derivative of another variable, such that only first order equations are represented. An example of this is the acceleration of a body. The position of the body is typically of interest, and position can be chosen as a state variable. In order to express the dynamics of a body, its acceleration in an inertial frame relating the motion of the body to the external forces is required. If velocity is introduced as a second set of state variables, then the first time derivative of velocity is acceleration, and the first time derivative of position is velocity. Thus, choosing position and velocity as the state variables, the full motion of the body can be represented as a first order system of equations.

The remaining terms in Eq. (D.1) are as follows. $\mathbf{A}(t)$ is the matrix that linearly maps the dynamics of the state variables, $\dot{\mathbf{x}}$, with each state. The $\mathbf{u}(t)$ vector is the *control input* vector, determined by the system's available control parameters, and $\mathbf{B}(t)$ is the matrix that maps these input variables into the state dynamics. The $\boldsymbol{\omega}(t)$ vector is the *random forcing function*, or *noise*, which may be affecting the system, and $\mathbf{N}(t)$ is the matrix that maps this noise into the state variables.

Eq. (D.1) represents the full linear dynamics of the whole value states. This system of equations can be integrated, either analytically or numerically, to determine the solution of the states with respect to time.

D.1.1.2 Observations

If external observations, or measurements, are provided and are observable, the relationship of this observation vector, $\mathbf{y}(t)$, to the state variables can be represented as,

$$\mathbf{y}(t)=\mathbf{C}(t)\mathbf{x}(t)+\mathbf{D}(t)\mathbf{u}(t)+\mathbf{M}(t)\boldsymbol{\omega}(t)+\boldsymbol{\nu}(t) \tag{D.2}$$

In this equation, $\mathbf{C}(t)$ is the matrix that linearly maps the states into the observations, the $\mathbf{D}(t)$ matrix maps the control input vector into the observations, $\mathbf{M}(t)$ maps the state noise into the observations, and the vector $\boldsymbol{\nu}(t)$ is the measurement noise associated with each observation.

The linear system represented by Eqs. (D.1) and (D.2) describes the full dynamics and observations of a system. With these two equations, a system is said to be in *state-space* form.

D.1.1.3 State Errors

If a system includes errors associated with the estimated values, whether known or unknown, then the state errors can also be represented by the dynamics and observations equations. Assuming the state vector $\mathbf{x}(t)$ is the true value of the states, then the estimated values of these states are represented using the symbol, $\tilde{\mathbf{x}}(t)$, a *tilde* over the state. The errors of the estimated states with respect to the true state values are then written as $\delta\mathbf{x}(t)$. Since the errors are assumed small, they relate estimates to the true values in a linear fashion as in,

$$\mathbf{x}(t)=\tilde{\mathbf{x}}(t)+\delta\mathbf{x}(t) \tag{D.3}$$

(Note that some texts and articles use capital “x”, $\mathbf{X}(t)$, to represent whole value states, and small “x” to represent the error-states. This can get confusing when writing these equations by hand, or when reading some small fonts. To avoid confusion, $\mathbf{x}(t)$ will refer to the whole value states, and an explicit $\delta\mathbf{x}(t)$ will be used to represent the error in the states.)

D.1.1.3.1 Error-State Dynamics

Taking the derivative of Eq. (D.3) with respect to time yields,

$$\dot{\mathbf{x}}(t) = \dot{\tilde{\mathbf{x}}}(t) + \delta\dot{\mathbf{x}}(t) \tag{D.4}$$

The dynamics of the errors within the states can be found by substituting Eq. (D.4) into Eq. (D.1), such that,

$$\delta\dot{\mathbf{x}}(t) = \left[\mathbf{A}(t)\tilde{\mathbf{x}}(t) - \dot{\tilde{\mathbf{x}}}(t)\right] + \mathbf{A}(t)\delta\mathbf{x}(t) + \mathbf{B}(t)\mathbf{u}(t) + \mathbf{N}(t)\boldsymbol{\omega}(t) \tag{D.5}$$

In many operational cases, the term in brackets may be estimated as zero, and the error-states equation reduces to,

$$\delta\dot{\mathbf{x}}(t) = \mathbf{A}(t)\delta\mathbf{x}(t) + \mathbf{B}(t)\mathbf{u}(t) + \mathbf{N}(t)\boldsymbol{\omega}(t) \tag{D.6}$$

D.1.1.3.2 Error-State Observations

In order to process observations using error-states, a measurement residual is introduced that is the difference of observation and whole value states as,

$$\mathbf{z}(t) = \mathbf{y}(t) - \mathbf{C}(t)\mathbf{x}(t) \tag{D.7}$$

Therefore, using Eq. (D.2) the full measurement residual equation is,

$$\mathbf{z}(t) = \mathbf{D}(t)\mathbf{u}(t) + \mathbf{M}(t)\boldsymbol{\omega}(t) + \boldsymbol{\nu}(t) \tag{D.8}$$

By using the estimated and error-states, this measurement residual equation can be written as,

$$\begin{aligned} \mathbf{z}(t) &= \mathbf{y}(t) - \mathbf{C}(t)\tilde{\mathbf{x}}(t) \\ &= \mathbf{C}(t)\delta\mathbf{x}(t) + \mathbf{D}(t)\mathbf{u}(t) + \mathbf{M}(t)\boldsymbol{\omega}(t) + \boldsymbol{\nu}(t) \end{aligned} \tag{D.9}$$

D.1.2 Non-Linear System Equations

The previous section presented algorithms that represent systems where the states vary *linearly* with respect to their dynamics and observations. For many real-world systems however, this relationships is actually *non-linear,* and cannot be accurately represented by the state-space form of Eqs. (D.1) and (D.2). This is often the case when the dynamics is a function of the states in a complex manner [ex. $\dot{x}_j = x_i^{\,2}$, $\dot{x}_j = \cos(x_i)$]. This section provides method to represent these non-linear systems in forms that can be solved without the use of complicated non-linear techniques [98].

Assume the non-linear system can be represented by the state vector and input control vector as,

$$\dot{\mathbf{x}}(t) = \vec{f}\left(\mathbf{x}(t), \mathbf{u}(t), t\right) + \boldsymbol{\eta}(t) \tag{D.10}$$

In this equation, $\vec{f}$ is a non-linear function of the state vector and control input vector, and perhaps time. The second term in Eq. (D.10) is the noise associated with the state dynamics.

To begin the error-state analysis, assume that there is zero control input, $\mathbf{u} = \mathbf{0}$, and the noise is negligible, $\boldsymbol{\eta}(t) \approx \mathbf{0}$. Using the estimated state vector and the error-states as in Eq. (D.4), the non-linear dynamics of Eq. (D.10) can be expanded in Taylor series form about the estimated state as the following,

$$\dot{\mathbf{x}} = \dot{\tilde{\mathbf{x}}} + \delta\dot{\mathbf{x}} = \vec{f}(\tilde{\mathbf{x}}) + \frac{\partial \vec{f}(\tilde{\mathbf{x}})}{\partial \mathbf{x}}\delta\mathbf{x} + \frac{1}{2!}\frac{\partial^2 \vec{f}(\tilde{\mathbf{x}})}{\partial \mathbf{x}^2}(\delta\mathbf{x})^2 + H.O.T. \tag{D.11}$$

In this equation, *H.O.T.* refers to *higher-order terms* within the Taylor series expansion that can be combined together or ignored with acceptable truncation error. Terms of second order and higher can be expressed [160],

$$\frac{1}{2!}\frac{\partial^2 \bar{f}(\tilde{\mathbf{x}})}{\partial \mathbf{x}^2}(\delta\mathbf{x})^2 + H.O.T. = \frac{1}{2!}\frac{\partial^2 \bar{f}_i}{\partial x_j \partial x_k}\delta x_j \delta x_k + \frac{1}{3!}\frac{\partial^3 \bar{f}_i}{\partial x_j \partial x_k \partial x_m}\delta x_j \delta x_k \delta x_m + \cdots \tag{D.12}$$

Assuming second and higher-order terms are all represented as $\boldsymbol{\upsilon}$, the error-state dynamics for a non-linear system can then be written from Eqs. (D.11) as,

$$\delta\dot{\mathbf{x}} = \frac{\partial \bar{f}(\tilde{\mathbf{x}})}{\partial \mathbf{x}}\delta\mathbf{x} + \boldsymbol{\upsilon} \tag{D.13}$$

To further solve the error-state dynamics, introduce the error-state dynamics matrix, $\mathbf{F}$, referred to as the *Jacobian* matrix, as

$$\mathbf{F}(t) = \frac{\partial \bar{f}(\tilde{\mathbf{x}})}{\partial \mathbf{x}} \tag{D.14}$$

such that the error-state dynamics from Eq. (D.13) is represented as,

$$\delta\dot{\mathbf{x}} = \mathbf{F}(t)\delta\mathbf{x} + \boldsymbol{\upsilon} \tag{D.15}$$

To find the solution to Eq. (D.15) and the relationship of the $\mathbf{F}$ matrix, first assume no noise, $\boldsymbol{\upsilon} = \mathbf{0}$, and a solution of the form,

$$\delta\mathbf{x} = \mathbf{\Phi}(t,t_0)\delta\mathbf{x}_0 \tag{D.16}$$

In this expression, the *state transition matrix*, $\mathbf{\Phi}$, represents the dynamics of the error-states from $t_0 \to t$. Using Eqs. (D.13) through (D.16), this dynamics can be represented as,

$$\begin{aligned}\delta\dot{\mathbf{x}} &= \dot{\mathbf{\Phi}}(t,t_0)\delta\mathbf{x}_0 + \mathbf{\Phi}(t,t_0)\delta\dot{\mathbf{x}}_0 \\ &\cong \dot{\mathbf{\Phi}}(t,t_0)\delta\mathbf{x}_0 \\ &= \mathbf{F}(t)\mathbf{\Phi}(t,t_0)\delta\mathbf{x}_0\end{aligned} \tag{D.17}$$

Here the time derivative of the initial error-states is assumed small $(\delta\dot{\mathbf{x}} \approx \mathbf{0})$. The error-state-transition matrix can then be represented from Eq. (D.17) as,

$$\begin{aligned}\dot{\mathbf{\Phi}}(t,t_0) &= \mathbf{F}(t)\mathbf{\Phi}(t,t_0) \\ \mathbf{\Phi}(t_0,t_0) &= \mathbf{I}\end{aligned} \tag{D.18}$$

Other important identities for the state-transition matrix are,

$$\begin{aligned}\mathbf{\Phi}(t,t_0) &= \mathbf{\Phi}^{-1}(t_0,t) \\ \mathbf{\Phi}(t_{k+1},t_0) &= \mathbf{\Phi}(t_{k+1},t_k)\mathbf{\Phi}(t_k,t_0)\end{aligned} \tag{D.19}$$

D.1.2.1 Truncated Error Terms

In the above analysis, higher-order Taylor series terms, as well as the noise, of each state was assumed zero during the dynamics. For some systems this assumption can produce truncation error, which can be potentially significant. Assuming these higher order terms are constant over small time steps, $\delta\tau$, their solution from Eq. (D.13) becomes,

$$\delta\mathbf{x}_{H.O.T} = \boldsymbol{\upsilon}\delta\tau \tag{D.20}$$

A more general expression for these terms can be expressed as [213],

$$\boldsymbol{\omega} = \int_{t_0}^{t} \mathbf{\Phi}(t,t_0)\boldsymbol{\upsilon}dt \tag{D.21}$$

The term $\boldsymbol{\omega}$ is referred to as the *process noise* and represents the uncertainty in the error-state dynamics.

D.1.2.2 Error-State Dynamics

The full dynamics of the error-states can be expressed in linear form using Eqs. (D.13) through (D.21) as,

$$\delta\dot{\mathbf{x}}(t) = \mathbf{F}(t)\delta\mathbf{x}(t) + \mathbf{L}(t)\mathbf{u}(t) + \mathbf{G}(t)\boldsymbol{\omega}(t) \tag{D.22}$$

The matrix $\mathbf{L}(t)$ represents the mapping of the control input variables into the dynamics of the error-states, in which case,

$$\mathbf{L}(t) = \frac{\partial \bar{f}(\tilde{\mathbf{x}})}{\partial \mathbf{u}} \tag{D.23}$$

In this equation, matrix $\mathbf{G}(t)$ has been added for completeness, specifically for situations where process noise is connected to different states.

D.1.2.3 Error-State Discrete Dynamics

The above algorithms are sufficient for *continuous* systems, where time varies continuously from one time point to the next. In many systems, especially real-time operating systems, *discrete* time points are utilized for processing loops. For these discrete time-step systems, the dynamics and observations must be valid from one time point to another.

Using the second identity in Eq. (D.19), the error-state dynamics can be written in a common form used in discrete time systems,

$$\delta\mathbf{x}(t_{k+1}) = \mathbf{\Phi}(t_{k+1}, t_k)\delta\mathbf{x}(t_k) \tag{D.24}$$

Given the error-state vector estimate at time point t_k, Eq. (D.24) can be used to determine the dynamics between $t_k \rightarrow t_{k+1}$ in order to compute the error-state vector estimate at time point t_{k+1}. By similarly determining the discrete time dynamics of the remaining terms in Eq. (D.22), the following equation represents the full dynamics of the error-state in discrete time,

$$\delta\mathbf{x}_{k+1} = \mathbf{\Phi}(t_{k+1}, t_k)\delta\mathbf{x}_k + \mathbf{\Lambda}(t_{k+1}, t_k)\mathbf{u}_k + \mathbf{\Gamma}(t_{k+1}, t_k)\boldsymbol{\omega}_k \tag{D.25}$$

In Eq. (D.25), a notation simplification is used for $\delta\mathbf{x}(t_k) = \delta\mathbf{x}_k$. $\mathbf{\Gamma}(t_{k+1}, t_k)$ and $\mathbf{\Lambda}(t_{k+1}, t_k)$ are the discrete time representations of the continuous matrices $\mathbf{G}(t)$ and $\mathbf{L}(t)$ from $t_k \rightarrow t_{k+1}$, respectively.

For a non-linear system the state-transition matrix is determined using numerical integration of its dynamics from Eq. (D.18). However, in the cases where the system is *near-linear* approximations to the integration can be made to the dynamics when the Jacobian matrix $\mathbf{F}$ can be considered constant over the integration interval $\Delta t = t_{k+1} - t_k$ such that

$$\mathbf{\Phi}\left(t_{k+1}, t_k\right) = e^{\mathbf{F}\Delta t} \cong \mathbf{I} + \mathbf{F}\Delta t + \frac{1}{2!}\left[\mathbf{F}\Delta t\right]^2 + \frac{1}{3!}\left[\mathbf{F}\Delta t\right]^3 \cdots \tag{D.26}$$

Use of Eq. (D.26) must be carefully considered to insure valid results from this approximation.

D.1.2.4 Measurement Using Error-States

Similar to the state dynamics, the observations may also have a non-linear relationship with the whole-value states and the control input vector. Thus the measurement may have the following representation,

$$\mathbf{y}(t) = \vec{h}\left(\mathbf{x}(t), \mathbf{u}(t), t\right) + \boldsymbol{\nu}(t) \tag{D.27}$$

In this equation, $\vec{h}$ is a non-linear function of the state vector and control input vector, and perhaps time. The measurement noise associated with each observation is represented as $\boldsymbol{\nu}$.

Using the estimated and error-states as in Eq. (D.3), the measurement of Eq. (D.27) can be represented using Taylor series expansion as,

$$\mathbf{y}(t) = \vec{h}(\tilde{\mathbf{x}}) + \frac{\partial \vec{h}(\tilde{\mathbf{x}})}{\partial \mathbf{x}} \delta\mathbf{x} + \frac{1}{2!} \frac{\partial^2 \vec{h}(\tilde{\mathbf{x}})}{\partial \mathbf{x}^2} (\delta\mathbf{x})^2 + H.O.T. + \boldsymbol{\nu}(t) \tag{D.28}$$

Using the representation of the measurement difference as in Eq. (D.7) and only the first order terms from Eq. (D.28) yields,

$$\mathbf{z}(t)=\mathbf{y}(t)-\bar{h}(\tilde{\mathbf{x}})=\frac{\partial\bar{h}(\tilde{\mathbf{x}})}{\partial\mathbf{x}}\delta\mathbf{x}+\boldsymbol{\nu}(t) \tag{D.29}$$

Thus, a new matrix of measurement partial derivatives can be introduced as,

$$\mathbf{H}(\tilde{\mathbf{x}})=\frac{\partial\bar{h}(\tilde{\mathbf{x}})}{\partial\mathbf{x}} \tag{D.30}$$

The measurement difference can therefore be written as,

$$\mathbf{z}(t)=\mathbf{H}(\tilde{\mathbf{x}})\delta\mathbf{x}+\boldsymbol{\nu}(t) \tag{D.31}$$

This measurement difference, $\mathbf{z}(t)$, is often referred to as the *measurement residual*. This can be represented in discrete form as,

$$\mathbf{z}_{k+1}=\mathbf{H}_{k+1}\delta\mathbf{x}_{k+1}+\boldsymbol{\nu}_{k+1} \tag{D.32}$$

D.1.3 Dynamics Summary

This section provides a summary of the state-space form of the above dynamics and observations, for both linear and non-linear systems. The terms that are continuous functions of time have their (t) dropped for simplicity.

Linear Systems

Whole Value States

$$\dot{\mathbf{x}} = \mathbf{Ax} + \mathbf{Bu} + \mathbf{N\omega}$$
$$\mathbf{y} = \mathbf{Cx} + \mathbf{Du} + \mathbf{M\omega} + \boldsymbol{\nu}$$

Error-States

$$\delta\dot{\mathbf{x}} = \left[\mathbf{A}\tilde{\mathbf{x}} - \dot{\tilde{\mathbf{x}}}\right] + \mathbf{A}\delta\mathbf{x} + \mathbf{Bu} + \mathbf{N\omega}$$
$$\mathbf{z} = \mathbf{C}\delta\mathbf{x} + \mathbf{Du} + \mathbf{M\omega} + \boldsymbol{\nu}$$

Non-Linear Systems

Whole Value States

$$\dot{\mathbf{x}} = \vec{f}\left(\mathbf{x}, \mathbf{u}, t\right) + \boldsymbol{\eta}$$
$$\mathbf{y} = \vec{h}\left(\mathbf{x}, \mathbf{u}, t\right) + \boldsymbol{\nu}$$

Error-States

$$\delta\dot{\mathbf{x}} = \mathbf{F}\delta\mathbf{x} + \mathbf{Lu} + \mathbf{G\omega}$$
$$\mathbf{z} = \mathbf{H}\delta\mathbf{x} + \boldsymbol{\nu}$$

Discrete Systems

$$\delta\dot{\mathbf{x}} = \mathbf{F\Phi}\left(t, t_0\right)\delta\mathbf{x}_0$$
$$\delta\mathbf{x}_{k+1} = \mathbf{\Phi}\left(t_{k+1}, t_k\right)\delta\mathbf{x}_k + \mathbf{\Lambda}\left(t_{k+1}, t_k\right)\mathbf{u}_k + \mathbf{\Gamma}\left(t_{k+1}, t_k\right)\boldsymbol{\omega}_k$$
$$\mathbf{z}_{k+1} = \mathbf{H}_{k+1}\delta\mathbf{x}_{k+1} + \boldsymbol{\nu}_{k+1}$$

D.2 Kalman Filter Equations

This section describes the processing algorithms of the Kalman filter. This type of filter can be used to blend the dynamics of a set of variables with their observations in a recursive, or repeated sequentially, manner. Based upon the dynamics and the estimated knowledge of accuracy within the system, an optimal gain can be determined that is used to generate corrections to the state variables [29, 65, 91, 213, 221, 237].

A discussion on probability and statistics that is needed for the Kalman filter equation derivations is presented first. The discrete Kalman filter is presented next, and then the continuous Kalman filter algorithms follow. Subsets of each form are presented, which depend on the known dynamics of the system.

It is interesting to note that the discrete form of the Kalman filter was developed prior to the continuous form, whereas most analytical processes are developed in the reverse order. This is because for many practical applications only the discrete form is really applicable. The continuous form is presented here for completeness. The spacecraft navigation Kalman filter, discussed within the dissertation, utilizes the discrete form of the filter.

D.2.1 Random Variables and Statistics

Take X to be a random variable, a variable that can take on a random set of values. The value of this variable is recorded for N different samples. The *sample average,* or *sample mean,* of this random variable is expressed as [29],

$$\bar{X} = \frac{X_1 + X_2 + X_3 + \cdots + X_N}{N} = \frac{1}{N}\sum_{i=1}^{N} X_i \qquad \text{(D.33)}$$

Here the *over-bar* of the variable represents this average, or mean. For an infinite number (or large amount) of samples, the random variable could have n possible realizable values of $x_1, x_2, x_3, \cdots, x_n$. For each sample there is an associated probability, p_i, that it will be chosen, such that over N trials there is an expected occurrence of each value of $p_1 N x_1$'s, $p_2 N x_2$'s, etc. With these values of the random variable and their probabilities, the sample average can be expressed as,

$$\bar{X} = \frac{p_1 N x_1 + p_2 N x_2 + p_3 N x_3 + \cdots + p_n N x_n}{N} \tag{D.34}$$

Based on this equation, the *expected* value of X is can be found using the *expectation* operator, E, as

$$\begin{aligned} \bar{X} &= \text{Expected value of } X \\ &= E(X) \equiv \begin{cases} \sum_{i=1}^{n} p_i x_i = \dfrac{1}{N} \sum_{i=1}^{N} X_i & \text{Discrete Form} \\ \int_{-\infty}^{\infty} x f_x(x)\, dx & \text{Continuous Form} \end{cases} \end{aligned} \tag{D.35}$$

In the continuous form of the expectation in Eq. (D.35), $f_x(x)$ is known as the *probability density function* of X. Important properties of this function are [29],

$$\begin{aligned} &i)\ f_x(x) \text{ is a non-negative function} \\ &ii)\ \int_{-\infty}^{\infty} f_x(x)\, dx = 1 \end{aligned} \tag{D.36}$$

The expectation operator, E, is referred to as the *first moment* of X, and represents the mean value of X. The *mean expected squared value*, or *second moment*, of X is defined as [65],

$$E\left(X^2\right) \equiv \begin{cases} \dfrac{1}{N} \sum_{i=1}^{N} X_i^2 & \text{Discrete Form} \\ \int_{-\infty}^{\infty} x^2 f_x(x)\, dx & \text{Continuous Form} \end{cases} \tag{D.37}$$

The square root of $E\left(X^2\right)$ in Eq. (D.37) is referred to as the *root mean square* (RMS) of X. In discrete form, this is expressed as

$$RMS(X) = \sqrt{E\left(X^2\right)} \cong \sqrt{\frac{1}{N}\sum_{i=1}^{N} X_i^2} \tag{D.38}$$

The *variance* of a random variable is the *second moment about the mean*, or a measure of dispersion (or deviation) of X about its mean [29],

$$\text{Variance of } X = \sigma_X^2 \equiv E\left[\left(X - E(X)\right)^2\right] \tag{D.39}$$

This can be expanded in terms of the expectations as,

$$\begin{aligned}\sigma_X^2 &\equiv E\left[\left(X - E(X)\right)^2\right] = E\left(X^2\right) - 2\left[E(X)\right]^2 + \left[E(X)\right]^2 \\ &= E\left(X^2\right) - \left[E(X)\right]^2\end{aligned} \tag{D.40}$$

The expression for variance can therefore also be written as,

$$\text{Variance of } X = \sigma_X^2 \equiv \begin{cases} \dfrac{1}{N}\displaystyle\sum_{i=1}^{N} X_i^2 - \left(\dfrac{1}{N}\displaystyle\sum_{i=1}^{N} X_i\right)^2 & \text{Discrete Form} \\ \displaystyle\int_{-\infty}^{\infty} \left(x - E(X)\right)^2 f_x(x)\,dx & \text{Continuous Form} \end{cases} \tag{D.41}$$

The *standard deviation* of the random variable X is defined as the square root of the variance, or,

$$\sigma_X \equiv \sqrt{\text{Variance of } X} = \sqrt{\sigma_X^2} \tag{D.42}$$

From their definitions, a relationship exists between the root mean square of X and its variance. From Eqs. (D.38) and (D.40), the relationship for the root mean square is the square of the sum of the variance and the mean value squared, or,

$$\begin{aligned}RMS(X) &= \sqrt{E\left(X^2\right)} = \sqrt{\left(E\left(X^2\right) - \left[E(X)\right]^2\right) + \left[E(X)\right]^2} \\ &= \sqrt{\sigma_X^2 + \bar{X}^2}\end{aligned} \tag{D.43}$$

D.2.2 Covariance Matrix

The above representations can also be implemented when investigating the statistics of two or more random variables. The *covariance* between two random variables X and Y is the product of their deviations from their mean values as,

$$\begin{aligned}\text{Covariance of } X \text{ and } Y = \sigma_{XY}^2 &= E\left[\left(X - E(X)\right)\left(Y - E(Y)\right)\right] \\ &= E(XY) - \left[E(X)E(Y)\right]\end{aligned} \tag{D.44}$$

If $\mathbf{x}$ is now a vector of several random variables, the mean vector, $\mathbf{m}$, of this set of variables is the mean of each element as,

$$E(\mathbf{x}) = \mathbf{m} \tag{D.45}$$

The covariance of this vector is a matrix of covariances between each element in the vector. This *covariance matrix*, $\mathbf{P}$, is represented as,

$$\mathbf{P} = E\left[\left(\mathbf{x} - E(\mathbf{x})\right)\left(\mathbf{x} - E(\mathbf{x})\right)^T\right] = E\left[(\mathbf{x} - \mathbf{m})(\mathbf{x} - \mathbf{m})^T\right] \tag{D.46}$$

The covariance can also be used to represent the error of an estimated vector of state variables relative to their true state values [65]. The covariance matrix can be written in this case as,

$$\mathbf{P} = E\left[(\tilde{\mathbf{x}} - \mathbf{x})(\tilde{\mathbf{x}} - \mathbf{x})^T\right] = E\left[(\mathbf{x} - \tilde{\mathbf{x}})(\mathbf{x} - \tilde{\mathbf{x}})^T\right] = E\left[(\delta\mathbf{x})(\delta\mathbf{x})^T\right] \tag{D.47}$$

The covariance matrix in the form of Eq. (D.47) represents the estimates of the errors within each state, and can be used to determine how well each sate has been determined. The variance of each specific state variable within the vector $\mathbf{x}$ is provided along the diagonal of the covariance matrix. The standard deviation of the variances of $\mathbf{x}$ are from $\mathbf{P}$ as,

$$\text{std dev}(\mathbf{x}) = \left\{\sigma_1, \sigma_2, \sigma_3, \cdots, \sigma_n\right\} = \sqrt{diag(\mathbf{P})} \tag{D.48}$$

The covariance matrix is a symmetric matrix, since $\sigma_{xy} = \sigma_{yx}$. Therefore, for all instances $\mathbf{P} = \mathbf{P}^T$.

The covariance matrix is associated with the states that are defined in a specified reference frame. To transform the covariance matrix into another reference frame use,

$$\mathbf{P}_b = \mathbf{T}_a^b \mathbf{P}_a \mathbf{T}_a^{bT} \tag{D.49}$$

In Eq. (D.49), the transformation matrix $\mathbf{T}_a^b$ transforms vectors in frame *a* into frame *b* $\left(\mathbf{b} = \mathbf{T}_a^b \mathbf{a}\right)$.

D.2.3 Discrete Kalman Filter Equations

Based upon the statistics discussed above, the Kalman filter algorithms are presented below. The discrete form of the blending routines is presented through the development of the dynamics and measurement processing algorithms.

D.2.3.1 Covariance Dynamics

Given that the covariance matrix represents the error estimates of each state, as in Eq. (D.47), the propagation of this matrix presents the error estimates of each state over time. Assuming there is no control input $(\mathbf{u} = \mathbf{0})$, for the discrete form of the dynamics equation, Eq. (D.25), the covariance matrix at time t_{k+1} can be found from,

$$\begin{aligned}
\mathbf{P}_{k+1}^{-} &= E\left[(\delta\mathbf{x})(\delta\mathbf{x})^T\right] = E\left[\left(\mathbf{\Phi}_k \delta\mathbf{x}_k + \mathbf{\Gamma}_k \boldsymbol{\omega}_k\right)\left(\mathbf{\Phi}_k \delta\mathbf{x}_k + \mathbf{\Gamma}_k \boldsymbol{\omega}_k\right)^T\right] \\
&= E\left[\mathbf{\Phi}_k \delta\mathbf{x}_k \delta\mathbf{x}_k^T \mathbf{\Phi}_k^T + \mathbf{\Phi}_k \delta\mathbf{x}_k \boldsymbol{\omega}_k^T \mathbf{\Gamma}_k^T + \mathbf{\Gamma}_k \boldsymbol{\omega}_k \delta\mathbf{x}_k^T \mathbf{\Phi}_k^T + \mathbf{\Gamma}_k \boldsymbol{\omega}_k \boldsymbol{\omega}_k^T \mathbf{\Gamma}_k^T\right] \\
&= \mathbf{\Phi}_k E\left[\delta\mathbf{x}_k \delta\mathbf{x}_k^T\right]\mathbf{\Phi}_k^T + \mathbf{\Phi}_k E\left[\delta\mathbf{x}_k \boldsymbol{\omega}_k^T\right]\mathbf{\Gamma}_k^T \\
&\quad + \mathbf{\Gamma}_k E\left[\boldsymbol{\omega}_k \delta\mathbf{x}_k^T\right]\mathbf{\Phi}_k^T + \mathbf{\Gamma}_k E\left[\boldsymbol{\omega}_k \boldsymbol{\omega}_k^T\right]\mathbf{\Gamma}_k^T
\end{aligned} \tag{D.50}$$

The minus superscript $(-)$ is utilized to represent the update to the covariance matrix due to time propagation only (*a priori*), and prior to any measurement update, which is described below. In Eq. (D.50) the symbols from Eq. (D.25) have been simplified as $\mathbf{\Phi}_k = \mathbf{\Phi}\left(t_{k+1}, t_k\right)$ and $\mathbf{\Gamma}_k = \mathbf{\Gamma}\left(t_{k+1}, t_k\right)$.

The expectations of the error-states and the noise are represented as,

$$\mathbf{P}_k = E\left[\delta\mathbf{x}_k \delta\mathbf{x}_k^T\right] \tag{D.51}$$

$$\mathbf{Q}_k = E\left[\boldsymbol{\omega}_k \boldsymbol{\omega}_k^T\right] \tag{D.52}$$

The $\mathbf{Q}$ matrix is referred to as the *process noise* matrix for the system, and is related to how well the dynamics of the state variables are known. High process noise is interpreted by the filter as poor knowledge of the dynamics. The noise of the individual states, $\boldsymbol{\omega}$, is assumed to be uncorrelated with respect to time (*white noise*). The noise is also assumed to be uncorrelated with respect to the states such that,

$$E\left[\delta\mathbf{x}_k \boldsymbol{\omega}_k^T\right] = \mathbf{0} \tag{D.53}$$

Using the terms from Eqs. (D.51)–(D.53), the dynamics of the covariance matrix from Eq. (D.50) becomes,

$$\mathbf{P}_{k+1}^{-} = \mathbf{\Phi}_k \mathbf{P}_k \mathbf{\Phi}_k^T + \mathbf{\Gamma}_k \mathbf{Q}_k \mathbf{\Gamma}_k^T \tag{D.54}$$

D.2.3.2 Measurement Update

A similar approach as the covariance dynamics can be applied to the processing of the filter's covariance matrix estimate of state errors due to external observations, or measurements. The primary contribution of R. Kalman's work was the computation of the optimal gain used to produce the best estimate of the new error-states after a measurement update [91]. A simple derivation of the measurement update algorithms is presented below for both linear and non-linear systems.

D.2.3.2.1 Linear System

Assuming zero control input, $\mathbf{u} = \mathbf{0}$, and state noise is not observable, a measurement as in Eq. (D.2) can be represented in discrete time as,

$$\mathbf{y}_{k+1} = \mathbf{C}_{k+1}\mathbf{x}_{k+1} + \boldsymbol{\nu}_{k+1} \tag{D.55}$$

Using the estimated state, a gain, $\mathbf{K}$, can be chosen that can be applied to the difference of the observation and the state-based estimate of the observation in order to correct errors within the estimate of the state. This is represented using Eq. (D.55) as,

$$\begin{aligned}\tilde{\mathbf{x}}_{k+1}^{+} &= \tilde{\mathbf{x}}_{k+1}^{-} + \mathbf{K}_{k+1}\left(\mathbf{y}_{k+1} - \mathbf{C}_{k+1}\tilde{\mathbf{x}}_{k+1}^{-}\right) \\ &= \tilde{\mathbf{x}}_{k+1}^{-} + \mathbf{K}_{k+1}\mathbf{C}_{k+1}\left(\mathbf{x}_{k+1} - \tilde{\mathbf{x}}_{k+1}^{-}\right) + \mathbf{K}_{k+1}\boldsymbol{\nu}_{k+1}\end{aligned} \tag{D.56}$$

Here the plus superscript $(+)$ is used to represent the state estimates after the measurement update (*a posteriori*). This equation can also be represented using the measurement and error-state expression of Eq. (D.9) as,

$$\tilde{\mathbf{x}}_{k+1}^{+} = \tilde{\mathbf{x}}_{k+1}^{-} + \mathbf{K}_{k+1}\mathbf{z}_{k+1} = \tilde{\mathbf{x}}_{k+1}^{-} + \mathbf{K}_{k+1}\mathbf{C}_{k+1}\delta\mathbf{x}_{k+1}^{-} + \mathbf{K}_{k+1}\boldsymbol{\nu}_{k+1} \tag{D.57}$$

Using this measurement update for the estimated states, the update to the covariance matrix can be determined. The updated form of the error estimate can be expressed as,

$$\delta\mathbf{x}_{k+1}^{+} = \mathbf{x}_{k+1} - \tilde{\mathbf{x}}_{k+1}^{+} \tag{D.58}$$

The new covariance is generated based upon this error estimate of Eq. (D.58) as,

$$\mathbf{P}_{k+1}^{+} = E\left[\left(\delta\mathbf{x}_{k+1}^{+}\right)\left(\delta\mathbf{x}_{k+1}^{+}\right)^{T}\right] = E\left[\left(\mathbf{x}_{k+1} - \tilde{\mathbf{x}}_{k+1}^{+}\right)\left(\mathbf{x}_{k+1} - \tilde{\mathbf{x}}_{k+1}^{+}\right)^{T}\right] \tag{D.59}$$

Substituting the updated error estimate from Eq. (D.56) and the measurement from Eq. (D.55) into this covariance update equation yields,

$$\mathbf{P}_{k+1}^{+} = E\left[\begin{pmatrix} \mathbf{x}_{k+1} - \tilde{\mathbf{x}}_{k+1}^{-} - \mathbf{K}_{k+1}\mathbf{C}_{k+1}\delta\mathbf{x}_{k+1}^{-} \\ -\mathbf{K}_{k+1}\mathbf{v}_{k+1} \end{pmatrix}\begin{pmatrix} \mathbf{x}_{k} - \tilde{\mathbf{x}}_{k}^{-} - \mathbf{K}_{k+1}\mathbf{C}_{k+1}\delta\mathbf{x}_{k+1}^{-} \\ -\mathbf{K}_{k+1}\mathbf{v}_{k+1} \end{pmatrix}^{T}\right]$$
$$= E\left[\begin{pmatrix} \delta\mathbf{x}_{k+1}^{-} - \mathbf{K}_{k+1}\mathbf{C}_{k+1}\delta\mathbf{x}_{k+1}^{-} \\ -\mathbf{K}_{k+1}\mathbf{v}_{k+1} \end{pmatrix}\begin{pmatrix} \delta\mathbf{x}_{k+1}^{-} - \mathbf{K}_{k+1}\mathbf{C}_{k+1}\delta\mathbf{x}_{k+1}^{-} \\ -\mathbf{K}_{k+1}\mathbf{v}_{k+1} \end{pmatrix}^{T}\right] \tag{D.60}$$

Working the expectation operator through this equation, as was done in Eq. (D.50), and assuming the *a priori* state-errors are uncorrelated with respect to measurement noise such that $E\left(\delta\mathbf{x}_{k+1}^{-}\mathbf{v}_{k+1}^{T}\right) = \mathbf{0}$, yields the final relationship for a measurement update to the covariance matrix,

$$\mathbf{P}_{k+1}^{+} = \left(\mathbf{I} - \mathbf{K}_{k+1}\mathbf{C}_{k+1}\right)\mathbf{P}_{k+1}^{-}\left(\mathbf{I} - \mathbf{K}_{k+1}\mathbf{C}_{k+1}\right)^{T} + \mathbf{K}_{k+1}\mathbf{R}_{k+1}\mathbf{K}_{k+1}^{T} \tag{D.61}$$

The measurement noise covariance matrix, $\mathbf{R}$, is the expectation of the measurement noise, as

$$\mathbf{R} = E\left[\mathbf{v}\mathbf{v}^{\mathbf{T}}\right] \tag{D.62}$$

This measurement noise is often assumed to be white noise, with zero mean, or

$$E\left(\mathbf{v}\right) = \mathbf{0} \tag{D.63}$$

To determine the optimal gain for this process, the trace of the covariance matrix of Eq. (D.61) is differentiated with respect to the variable gain, $\mathbf{K}_{k+1}$ [29, 91], as in,

$$\frac{d\left[trace\left(\mathbf{P}_{k+1}^{+}\right)\right]}{d\mathbf{K}_{k+1}} = -2\left(\mathbf{C}_{k+1}\mathbf{P}_{k+1}^{-}\right)^{T} + 2\mathbf{K}_{k+1}\left(\mathbf{C}_{k+1}\mathbf{P}_{k+1}^{-}\mathbf{C}_{k+1}^{T} + \mathbf{R}_{k+1}\right) = \mathbf{0} \tag{D.64}$$

Solving this expression yields the optimal gain as

$$\mathbf{K}_{k+1_{opt}} = \mathbf{P}_{k+1}^{-}\mathbf{C}_{k+1}^{T}\left(\mathbf{C}_{k+1}\mathbf{P}_{k+1}^{-}\mathbf{C}_{k+1}^{T} + \mathbf{R}_{k+1}\right)^{-1} \tag{D.65}$$

This gain is often referred to as the *Kalman* gain. Substituting this gain back into Eq. (D.61) yields three alternative update equations,

$$\mathbf{P}_{k+1}^{+} = \mathbf{P}_{k+1}^{-} - \mathbf{P}_{k+1}^{-}\mathbf{C}_{k+1}^{T}\left(\mathbf{C}_{k+1}\mathbf{P}_{k+1}^{-}\mathbf{C}_{k+1}^{T} + \mathbf{R}_{k+1}\right)^{-1}\mathbf{C}_{k+1}\mathbf{P}_{k+1}^{-} \tag{D.66}$$

or,

$$\mathbf{P}_{k+1}^{+} = \mathbf{P}_{k+1}^{-} - \mathbf{K}_{k+1_{opt}}\left(\mathbf{C}_{k+1}\mathbf{P}_{k+1}^{-}\mathbf{C}_{k+1}^{T} + \mathbf{R}_{k+1}\right)\mathbf{K}_{k+1_{opt}}^{T} \tag{D.67}$$

or,

$$\mathbf{P}_{k+1}^{+} = \left(\mathbf{I} - \mathbf{K}_{k+1_{opt}}\mathbf{C}_{k+1}\right)\mathbf{P}_{k+1}^{-} \tag{D.68}$$

The Eq. (D.68) is the most commonly used expression for the covariance measurement update, however, all of Eqs. (D.66)–(D.68) can be used with the optimal Kalman gain. An alternative form, referred to as the *Joseph's form* [65] can be used with either the optimal gain or any sub-optimal gain. This form is exactly Eq. (D.61) with any selected gain.

Some filter designers also choose to implement additional terms with the system such that the *memory* of older measurements fades over time allowing newer measurements to be considered with equal weight. These *fading memory* filters help avoid ignoring important current measurements [65].

With properly modeled state dynamics and measurements, the Kalman filter should converge upon a solution after time propagation and measurement updates. However, due to poorly modeled state dynamics, or significantly high process noise, a Kalman filter solution to the state-error estimates can diverge away from the true solution. Proper consideration of true state dynamics, including any significant perturbation effects from nominal dynamics, as well as true measurement models, must be maintained to reduce or eliminate the chance of filter divergence.

If little or no process noise is used with the system, processing many high quality measurements $(\mathbf{R} \approx \text{small})$ will drive the covariance estimate to small values. Very small valued covariance estimates and low measurement noise produces a small matrix within the parentheses of Eq. (D.65), which produces an unreliable computation of the optimal gain matrix of Eq. (D.64). This often results in less and less consideration, or weight, given to future measurements. Designing Kalman filters and selecting its parameters are often a trade-off between exact modeling of the dynamics and accurate representation of the process and measurement noise while assuring all measurements are considered with the system. Some filter designers often choose to retain higher process noise terms to avoid this issue of driving the covariance estimates to very small values.

Numerical stability of the Kalman filter equations can be a concern due to the calculation of the matrix inverse in Eq. (D.65). Several alternative forms of determining the covariance matrix, $\mathbf{P}$, and the Kalman gain, $\mathbf{K}$, have been developed that improve the overall stability of the Kalman filter process. These methods primarily involve factoring these matrices into decomposed forms and processing the filter on these new matrices. The *Cholesky decomposition* method creates a new matrix that is the square root of the covariance matrix [29, 65]

$$\mathbf{P} = \mathbf{S}\mathbf{S}^T; \quad \mathbf{S} = \sqrt{\mathbf{P}} \tag{D.69}$$

Routines for time propagation and measurement update process the covariance square root matrix $\mathbf{S}$, instead of $\mathbf{P}$. Alternatively, Bierman proposes a factorization into a unit-diagonal upper-triangular matrix $\mathbf{U}$, and a diagonal matrix $\mathbf{D}$, such that [26],

$$\mathbf{P} = \mathbf{U}\mathbf{D}\mathbf{U}^T \tag{D.70}$$

The Kalman filter routines are written for these factored matrices, instead of the full covariance matrix, in order to maintain numerical stability.

D.2.3.2.2 Non-Linear System

For a system that has non-linear dynamics or measurements, the Kalman filter routines are modified slightly from the linear case. This type of filter that takes into account the non-linear effects is referred to as an *Extended* Kalman filter. The discrete form of the covariance dynamics has the same form as the linear case, as,

$$\mathbf{P}_{k+1}^{-} = \mathbf{\Phi}_k \mathbf{P}_k \mathbf{\Phi}_k^T + \mathbf{\Gamma}_k \mathbf{Q}_k \mathbf{\Gamma}_k^T \tag{D.71}$$

However, the filter measurement equations change slightly due to the different observation matrix, $\mathbf{H}$, for a non-linear system. The state update equation (*a posteriori*) becomes from Eq. (D.32) and (D.57)

$$\tilde{\mathbf{x}}_{k+1}^{+} = \tilde{\mathbf{x}}_{k+1}^{-} + \mathbf{K}_{k+1}\mathbf{z}_{k+1} = \tilde{\mathbf{x}}_{k+1}^{-} + \mathbf{K}_{k+1}\mathbf{H}_{k+1}\delta\mathbf{x}_{k+1}^{-} + \mathbf{K}_{k+1}\boldsymbol{\upsilon}_{k+1} \tag{D.72}$$

The optimal Kalman gain also changes to,

$$\mathbf{K}_{k+1_{opt}} = \mathbf{P}_{k+1}^{-}\mathbf{H}_{k+1}^{T}\left(\mathbf{H}_{k+1}\mathbf{P}_{k+1}^{-}\mathbf{H}_{k+1}^{T} + \mathbf{R}_{k+1}\right)^{-1} \tag{D.73}$$

This changes the covariance update equation from Eq. (D.68) to

$$\mathbf{P}_{k+1}^{+} = \left(\mathbf{I} - \mathbf{K}_{k+1_{opt}}\mathbf{H}_{k+1}\right)\mathbf{P}_{k+1}^{-} \tag{D.74}$$

The Joseph's form of this update becomes,

$$\mathbf{P}_{k+1}^{+} = \left(\mathbf{I} - \mathbf{K}_{k+1}\mathbf{H}_{k+1}\right)\mathbf{P}_{k+1}^{-}\left(\mathbf{I} - \mathbf{K}_{k+1}\mathbf{H}_{k+1}\right)^{T} + \mathbf{K}_{k+1}\mathbf{R}_{k+1}\mathbf{K}_{k+1}^{T} \tag{D.75}$$

D.2.4 Continuous Kalman Filter Equations

The *continuous* form of the Kalman filter routines is different from the discrete form, primarily through the realization of the time propagation routines. These are presented below for both the linear and non-linear systems.

D.2.4.1.1 Linear System

The continuous form of the time propagation for the covariance matrix of a linear system is referred to as the *linear variance equation* [65]. This is represented as,

$$\dot{\mathbf{P}}(t) = \mathbf{A}(t)\mathbf{P}(t) + \mathbf{P}(t)\mathbf{A}(t)^T + \mathbf{N}(t)\mathbf{Q}(t)\mathbf{N}(t)^T; \quad \mathbf{P}(t_0) = \mathbf{P}_0 \tag{D.76}$$

The Kalman gain is determined to be,

$$\mathbf{K}(t) = \mathbf{P}(t)\mathbf{C}(t)^T \mathbf{R}(t)^{-1} \tag{D.77}$$

The measurement equation of the covariance is a blend of the Eqs. (D.76) and (D.77),

$$\begin{aligned}\dot{\mathbf{P}}(t) = \mathbf{A}(t)\mathbf{P}(t) + \mathbf{P}(t)\mathbf{A}(t)^T + \mathbf{N}(t)\mathbf{Q}(t)\mathbf{N}(t)^T \\ - \mathbf{P}(t)\mathbf{C}(t)^T \mathbf{R}(t)^{-1} \mathbf{C}(t)\mathbf{P}(t)\end{aligned} \tag{D.78}$$

This is referred to as the *matrix Ricatti equation*.

D.2.4.1.2 Non-Linear System

For a continuous non-linear system, the Kalman filter equations are changed from Eqs. (D.76)-(D.78) due to the different dynamics and observations matrices. For time propagation, the covariance update is [65],

$$\dot{\mathbf{P}}(t) = \mathbf{F}(t)\mathbf{P}(t) + \mathbf{P}(t)\mathbf{F}(t)^T + \mathbf{G}(t)\mathbf{Q}(t)\mathbf{G}(t)^T; \quad \mathbf{P}(t_0) = \mathbf{P}_0 \tag{D.79}$$

The Kalman gain equation becomes,

$$\mathbf{K}(t) = \mathbf{P}(t)\mathbf{H}(t)^T \mathbf{R}(t)^{-1} \tag{D.80}$$

The measurement equation for the non-linear system case is then,

$$\dot{\mathbf{P}}(t) = \mathbf{F}(t)\mathbf{P}(t) + \mathbf{P}(t)\mathbf{F}(t)^T + \mathbf{G}(t)\mathbf{Q}(t)\mathbf{G}(t)^T - \mathbf{P}(t)\mathbf{H}(t)^T \mathbf{R}(t)^{-1} \mathbf{H}(t)\mathbf{P}(t) \tag{D.81}$$

D.2.5 Measurement Testing

Although most observations, or measurements, are assumed valid, spurious or erroneous measurements may occur due to sensor malfunction or data processing issues. If these erroneous measurements are improperly tagged with a measurement noise that appears to show optimistic performance, the processing of these erroneous measurements through the Kalman filter can severely impact the filter's performance. It is prudent to test individual measurements prior to their incorporation into the filter to avoid these negative situations.

A method to test an individual measurement is to use the filter's estimate of its performance to evaluate a measurement. If the filter "believes" it is performing well, by having reduced covariance values, out-lying measurements that are many times the filter's own estimate of its performance can be ignored. The *innovations* of the filter are determined from the optimal Kalman gain calculations of Eqs. (D.65) or (D.73). This innovations term, $\boldsymbol{\alpha}$, for the non-linear case is,

$$\boldsymbol{\alpha}_{k+1} = \mathbf{H}_{k+1}\mathbf{P}_{k+1}^{-}\mathbf{H}_{k+1}^{T} + \mathbf{R}_{k+1} \tag{D.82}$$

Assuming there are N individual states and M measurements, for a specific individual measurement z_i as,

$$\mathbf{z} = \begin{bmatrix} z_1 \\ z_2 \\ \vdots \\ z_i \\ \vdots \\ z_M \end{bmatrix}; \; z_i = \mathbf{z}(i) \tag{D.83}$$

An individual measurement from Eq. (D.32) can be represented as,

$$z_i = \mathbf{H}(i,1:N)\delta\mathbf{x}_{Nx1} \tag{D.84}$$

In Eq. (D.84), the i^{th} row of the measurement matrix $\mathbf{H}$ is used. A test of this individual measurement compared to the innovations can be made such that if the following is true the measurement is valid; otherwise it is marked as invalid and not processed through the filter,

$$z_i \le m\alpha_i \tag{D.85}$$

The innovations for this measurement are the i^{th} diagonal element from Eq. (D.82) as $\alpha_i = \boldsymbol{\alpha}_{k+1}(i,i)$. The scalar m is the proportional value of the innovations chosen as an acceptable value for the test. As long as the measurement is m-times less than the filter's innovations, the filter can process this measurement. Typical values of m are 3, 4, or 5. Since the value of z_i is often referred to as the *measurement residual,* Eq. (D.85) is referred to as the *measurement residual test*.

D.2.6 Kalman Filter Algorithm Summary

This section provides a summary of the algorithms used by Kalman filters for both linear and non-linear systems. These routines assume zero control input $(\mathbf{u}=\mathbf{0})$. The terms that are continuous functions of time have their (t) dropped for simplicity.

Linear Kalman Filter

Discrete Form

Time Propagation

$\dot{\mathbf{\Phi}}(t_k,t_0)=\mathbf{A}(t)\mathbf{\Phi}(t_k,t_0)$ — State Transition Matrix

$\tilde{\mathbf{x}}_{k+1}^{-}=\mathbf{\Phi}_k\tilde{\mathbf{x}}_k^{-};\quad \tilde{\mathbf{x}}(t_0)=\tilde{\mathbf{x}}_0$ — Whole Value State Estimate

$\mathbf{P}_{k+1}^{-}=\mathbf{\Phi}_k\mathbf{P}_k\mathbf{\Phi}_k^T+\mathbf{\Gamma}_k\mathbf{Q}_k\mathbf{\Gamma}_k^T$ — Error-Covariance

Measurement Update

$\mathbf{z}_{k+1}=\mathbf{y}_{k+1}-\mathbf{C}_{k+1}\tilde{\mathbf{x}}_{k+1}^{-}$ — Measurement Residual

$\boldsymbol{\alpha}_{k+1}=\mathbf{C}_{k+1}\mathbf{P}_{k+1}^{-}\mathbf{C}_{k+1}^T+\mathbf{R}_{k+1}$ — Innovations

If $\mathbf{z}_{k+1}\le m\boldsymbol{\alpha}_{k+1}$ — Measurement Residual Test

$\mathbf{K}_{k+1_{opt}}=\mathbf{P}_{k+1}^{-}\mathbf{C}_{k+1}^T\left(\boldsymbol{\alpha}_{k+1}\right)^{-1}$ — Optimal Kalman Gain

$\mathbf{P}_{k+1}^{+}=\left(\mathbf{I}-\mathbf{K}_{k+1_{opt}}\mathbf{C}_{k+1}\right)\mathbf{P}_{k+1}^{-}$ — Error Covariance Update

$\tilde{\mathbf{x}}_{k+1}^{+}=\tilde{\mathbf{x}}_{k+1}^{-}+\mathbf{K}_{k+1_{opt}}\mathbf{z}_{k+1}$ — Whole Value State Update

End

Continuous Form

Time Propagation

$\dot{\tilde{\mathbf{x}}}=\mathbf{A}\tilde{\mathbf{x}};\quad \tilde{\mathbf{x}}(t_0)=\tilde{\mathbf{x}}_0$ — Whole Value State

$\dot{\mathbf{P}}=\mathbf{AP}+\mathbf{PA}^{\mathbf{T}}+\mathbf{NQN}^T;\quad \mathbf{P}(t_0)=\mathbf{P}_0$ — Error-Covariance

Measurement Update

$\mathbf{K}=\mathbf{PC}^T\mathbf{R}^{-1}$ — Kalman Gain

$\dot{\tilde{\mathbf{x}}}=\mathbf{A}\tilde{\mathbf{x}}+\mathbf{K}\left[\mathbf{y}-\mathbf{C}\tilde{\mathbf{x}}\right]$ — Whole Value State

$\dot{\mathbf{P}}=\mathbf{AP}+\mathbf{PA}^{\mathbf{T}}+\mathbf{NQN}^{\mathbf{T}}-\mathbf{PC}^{\mathbf{T}}\mathbf{R}^{-1}\mathbf{CP}$ — Error-Covariance

Non-Linear Kalman Filter

Discrete Form

Time Propagation

$\dot{\tilde{\mathbf{x}}}_{k+1}^{-} = \vec{f}\left(\tilde{\mathbf{x}}_k^{+}, t\right)$ Whole Value State Estimate

$\mathbf{F} = \dfrac{\partial \vec{f}\left(\tilde{\mathbf{x}}_{k+1}^{-}, t\right)}{\partial \mathbf{x}}$ State Jacobian Matrix

Near-Linear

$\delta\mathbf{x}_{k+1}^{-} = \mathbf{\Phi}_k \delta\mathbf{x}_k^{+}$ Error-State Estimate

$\mathbf{\Phi}_k = \mathbf{I} + \mathbf{F}\Delta t + \frac{1}{2!}\left[\mathbf{F}\Delta t\right]^2 + \frac{1}{3!}\left[\mathbf{F}\Delta t\right]^3 \cdots$ State Transition Matrix

Full Non-Linear (Extended)

$\delta\mathbf{x}_{k+1}^{-} = \mathbf{0}$ Error-State Estimate

$\dot{\mathbf{\Phi}}\left(t, t_0\right) = \mathbf{F\Phi}\left(t, t_0\right); \quad \mathbf{\Phi}\left(t_0, t_0\right) = \mathbf{I}$ State Transition Matrix

$\mathbf{P}_{k+1}^{-} = \mathbf{\Phi}_k \mathbf{P}_k \mathbf{\Phi}_k^T + \mathbf{\Gamma}_k \mathbf{Q}_k \mathbf{\Gamma}_k^T$ Error-Covariance

Measurement Update

$\mathbf{z}_{k+1} = \mathbf{y}_{k+1} - \mathbf{H}_{k+1}\tilde{\mathbf{x}}_{k+1}^{-}$ Measurement Residual

$\boldsymbol{\alpha}_{k+1} = \mathbf{H}_{k+1}\mathbf{P}_{k+1}^{-}\mathbf{H}_{k+1}^T + \mathbf{R}_{k+1}$ Innovations

If $\mathbf{z}_{k+1} \le m\boldsymbol{\alpha}_{k+1}$ Measurement Residual Test

$\mathbf{K}_{k+1_{opt}} = \mathbf{P}_{k+1}^{-}\mathbf{H}_{k+1}^T\left(\boldsymbol{\alpha}_{k+1}\right)^{-1}$ Optimal Kalman Gain

$\mathbf{P}_{k+1}^{+} = \left(\mathbf{I} - \mathbf{K}_{k+1_{opt}}\mathbf{H}_{k+1}\right)\mathbf{P}_{k+1}^{-}$ Error Covariance Update

Near-Linear

$\delta\mathbf{x}_{k+1}^{+} = \delta\mathbf{x}_{k+1}^{-} + \mathbf{K}_{k+1_{opt}}\left(\mathbf{z}_{k+1} - \mathbf{H}_{k+1}\delta\mathbf{x}_{k+1}^{-}\right)$ Error-State Update

Full Non-Linear (Extended)

$\delta\mathbf{x}_{k+1}^{+} = \mathbf{K}_{k+1_{opt}}\mathbf{z}_{k+1}$ Error-State Update

$\tilde{\mathbf{x}}_{k+1}^{+} = \tilde{\mathbf{x}}_{k+1}^{-} + \delta\mathbf{x}_{k+1}^{+}$ Whole Value State Update

End

Continuous Form

Time Propagation

$\dot{\tilde{\mathbf{x}}} = \vec{f}\left(\tilde{\mathbf{x}}, t\right)$ Whole Value State

$\mathbf{F} = \dfrac{\partial \vec{f}\left(\tilde{\mathbf{x}}, t\right)}{\partial \mathbf{x}}$ State Jacobian Matrix

$\delta\dot{\mathbf{x}} = \mathbf{F}\delta\mathbf{x}$ Error-State

$\dot{\mathbf{P}} = \mathbf{F}\mathbf{P} + \mathbf{P}\mathbf{F}^T + \mathbf{G}\mathbf{Q}\mathbf{G}^T; \quad \mathbf{P}\left(t_0\right) = \mathbf{P}_0$ Error-Covariance

Measurement Update

$\mathbf{H} = \dfrac{\partial \vec{h}\left(\tilde{\mathbf{x}}, t\right)}{\partial \mathbf{x}}$ Measurement Matrix

$\mathbf{K} = \mathbf{P}\mathbf{H}^T\mathbf{R}^{-1}$ Kalman Gain

$\dot{\tilde{\mathbf{x}}} = \vec{f}\left(\tilde{\mathbf{x}}, t\right) + \mathbf{K}\left[\mathbf{y} - \mathbf{H}\tilde{\mathbf{x}}\right]$ Whole Value State

$\dot{\mathbf{P}} = \mathbf{F}\mathbf{P} + \mathbf{P}\mathbf{F}^T + \mathbf{G}\mathbf{Q}\mathbf{G}^T - \mathbf{P}\mathbf{H}^T\mathbf{R}^{-1}\mathbf{H}\mathbf{P}$ Error-Covariance

D.2.7 Error Measures

Several methods exist to determine the statistical measure of the magnitude of the filter states as they vary in time. Several of these are discussed below.

From the Kalman filter itself, the filter's covariance matrix provides the statistical estimate measured for each state. This value helps determine how well the filter has determined its solution. However, unless these values have zero mean, this value does not fully represent error from truth.

If the true values of filter states are known, and the filter estimates are differenced from these values, then the RMS of these state differences can be computed over different durations of the filter operation [11]. Computing the RMS value provides additional information about the filter's performance, since the RMS includes the mean value of this truth minus state difference. If the mean value of this difference is non-zero, this information is represented within the RMS value.

D.2.7.1 Mean Radial Spherical Error

The mean radial spherical error (MRSE) represents the radius of a sphere within which the computed error between a measured quantity and its expected value should reside. The probability that the error lies in this sphere is 61% [133].

A covariance matrix of the errors can be assembled by determining the variance of each state error during the filter's operation as,

$$\begin{aligned}\sigma_{\delta x}^2 &\equiv E\left[\left(\delta x - E(\delta x)\right)^2\right] = E\left(\delta x^2\right) - \left[E(\delta x)\right]^2 \\ &= E\left(\delta x^2\right) - \delta\overline{x}\end{aligned} \tag{D.86}$$

The covariance matrix, $\mathbf{P}_{\delta x}$, is based upon the variances and covariances of all the error states combined together. If only the three position states are considered, the 3x3 sub-matrix from the covariance matrix can be produced. The eigenvalues of this covariance sub-matrix are the squares of each of the three primary error axes in space, and can be labeled as, σ_1^2, σ_2^2, and σ_3^2. The MRSE is the norm-2 magnitude of these eigenvalues, or

$$MRSE = \sqrt{\sigma_1^2 + \sigma_2^2 + \sigma_3^2} \tag{D.87}$$

Appendix E X-ray Detectors

E.1 Detector Types

Variable celestial sources that produce X-ray emissions have been detected by a variety of methods on previous spacecraft missions. These detectors are designed using the principles of measuring the energy that is released when the X-ray energy photons collide with atoms within the detector material. The amount of energy released is considered proportional to the number of photons detected. Two-dimensional arrays within the detectors have been used to assist in the determination of where the photon entered the detector grid. Several types of detectors are described below, along with their attributes and limitations [59]. Some types are better for source image detection due to their accurate photon position determination within the grid. Others are more beneficial for pulse timing due to their accurate photon arrival determination.

- Proportional Counters.

  Description: These photon counting devices are typically windowed chambers filled with an inert gas. Low and high electric fields are produced within the gas using electrodes. Assembling a mesh of electrodes allows two-dimensional position determination of the photon arrival. As an X-ray photon enters the gas chamber, they may interact with the gas molecules releasing a photoelectron. This photoelectron is then multiplied many times when it is near the anode wire and ionized gas. The magnitude of the number of electron-positive ion pairs produced is proportional to the X-ray photon energy. Collimators may be added in front of the detector window to reject X-ray background photons [59].

  Limitations: Gas proportional counters are limited due to the lifetime of the gas and damage to the anode wires within the chambers.

  Timing: Microsecond-level photon arrival timing is possible. Timing is limited by the positive ion mobility and anode-cathode spacing.

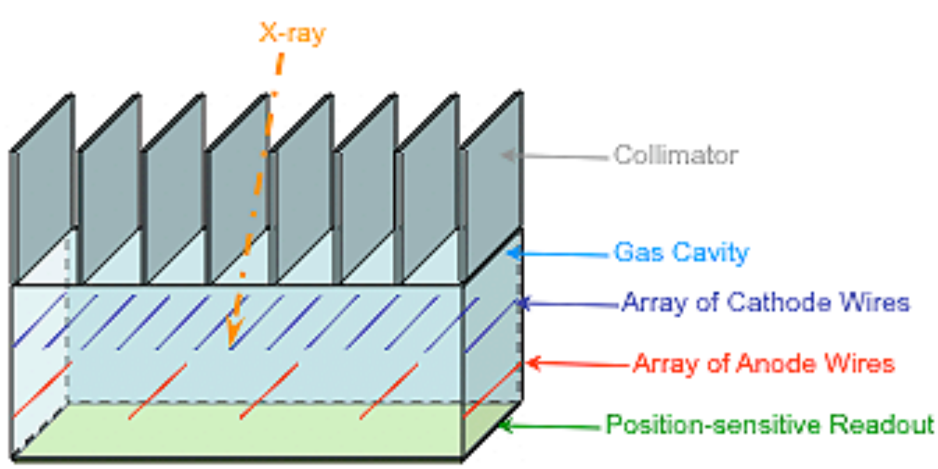

Figure E-1. Gas proportional counter X-ray detector diagram.

- Microchannel Plates

Description: These devices are composed of tightly packed individual channels. The channels are typically glass tubes, about 10 mm in diameter. As an X-ray photon enters the device they interact with the channel plate glass and electrodes via the photoelectric effect. The electrons produced in this interaction are then detected on a position sensitive plate. The device provides distortionless imaging with very high spatial resolution. Z-plate (chevrons) configurations are used to suppress ion feedback and channel electrons onto the read-out electronics [59].

Limitations: The channel plates can be complex to manufacture. The plates also require very low pressure or vacuum to be effective (10^{-5} Torr).

Timing: Nanosecond-level photon arrival timing is possible.

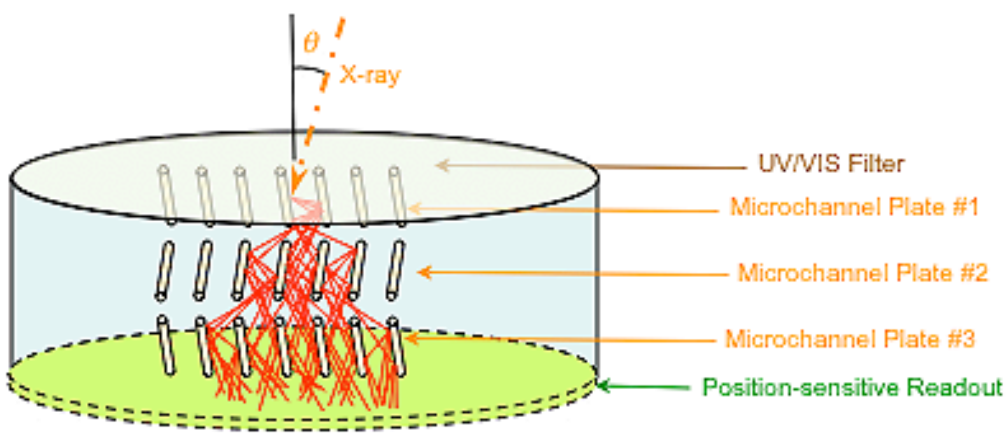

Figure E-2. Microchannel plate X-ray detector diagram [59].

- Scintillators

  Description: These devices are composed of crystals or similar materials. As an X-ray photon enters the device X-ray energy is converted to visible light. This light is used to excite electrons. These devices have been typically used in balloon-supported telescopes in the hard X-ray range of 20–200 keV [59].

  Limitations: This type of device is more efficient at higher X-ray energy.

  Timing: Unsure.

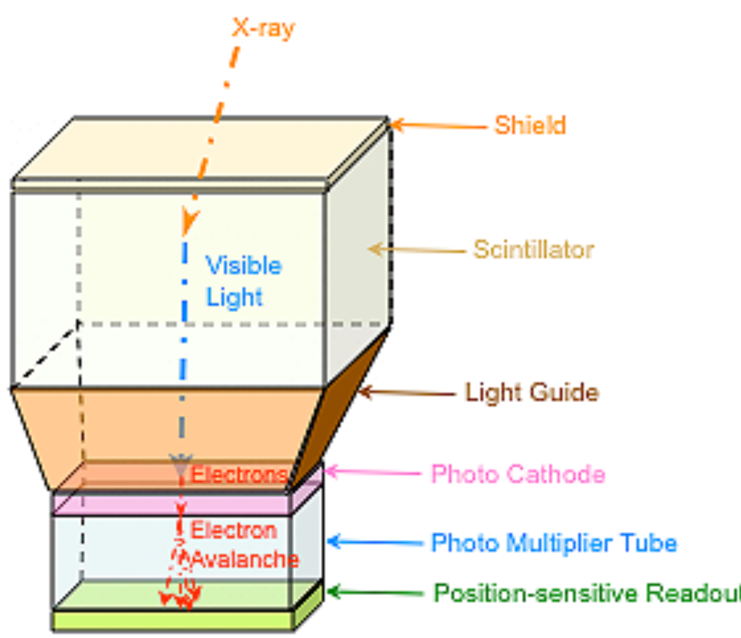

Figure E-3. Scintillator X-ray detector diagram [59].

- Calorimeters

Description: These devices are composed of super-cooled solid matter. As X-ray photons enter the absorbent solid material, the temperature pulse induced in the material is measured. The amount of temperature rise is dependent on the energy of the photons. The material must be kept near 0° K. The types of devices can detect a single photon [59].

Limitations: Due to the required cryo-cooling, the detector power usage is high and must utilize a significant amount of supporting electronics and hardware. The absorber is typically very small, on the order of 1-mm^3, so the detector area is small. This requires optics in order to increase the effective area.

Timing: Nanosecond-level or lower photon arrival timing is possible.

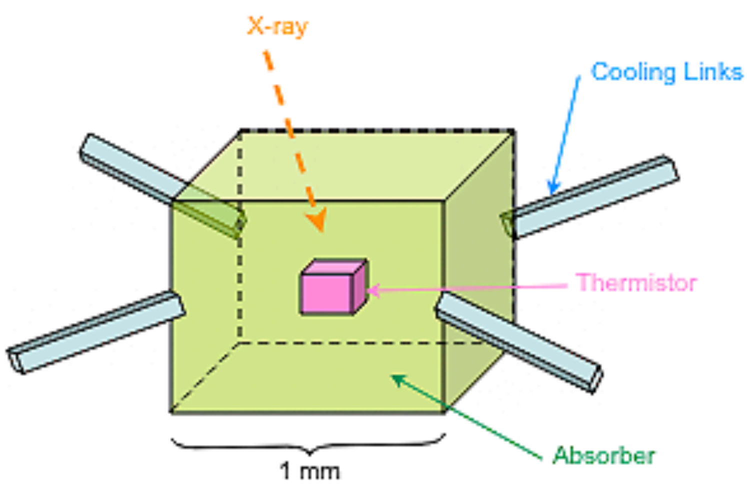

Figure E-4. Calorimeter X-ray detector diagram.

- Charge-Coupled Device (CCD) Semiconductors

Description: These devices are of an array of individual pixels composed of charge-coupled semiconductors. The metal-oxide-silicon capacitors are charge by the energy of arriving X-ray photons. These capacitors are periodically read and cleared by electronics. Due to the pixel array configuration, these devices provide a high quality imaging capability. The array of pixels allows good two-dimensional positioning of arriving photons [59].

Limitations: Each time a pixel is read, deep depletion is required to clear the remaining energy. Some devices may require backlit illumination.

Timing: Microsecond-level photon arrival timing is possible. Timing is limited by the read-out electronics and the deep depletion methods.

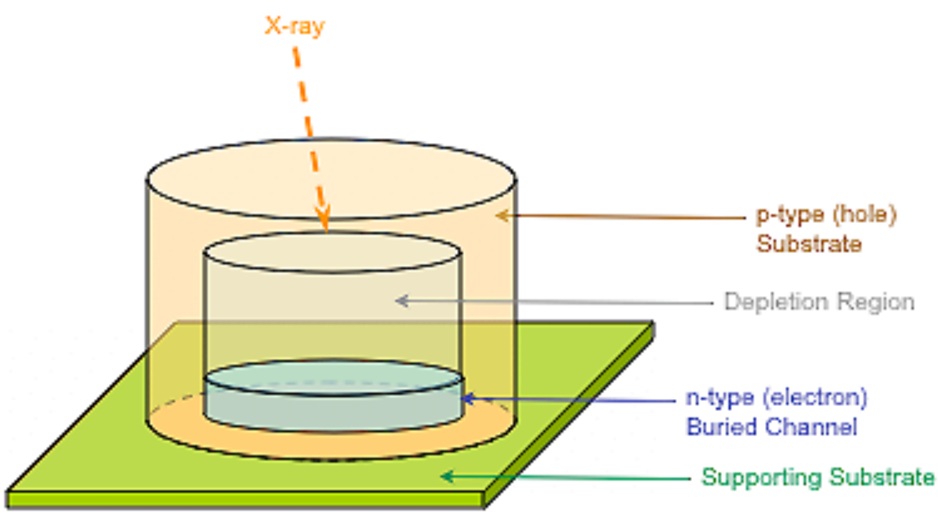

Figure E-5. CCD semiconductor X-ray detector diagram.

- Solid State Semiconductors

  Description: These devices are solid-state semiconductors that are assumed non-calorimetric and non-scintillation types. They are composed of a volume of semi-conducting material separated by doping of other matter. X-ray photons interact with the atoms of the semiconductor and electron-hole pairs are created. The multiplication of these pairs allows a measure of the X-ray energy of the arriving photons [59].

  Limitations: These devices are limited by the purity of the material used. Achieving low X-ray energies are difficult, and may require cooling.

  Timing: Microsecond-level photon arrival timing is possible.

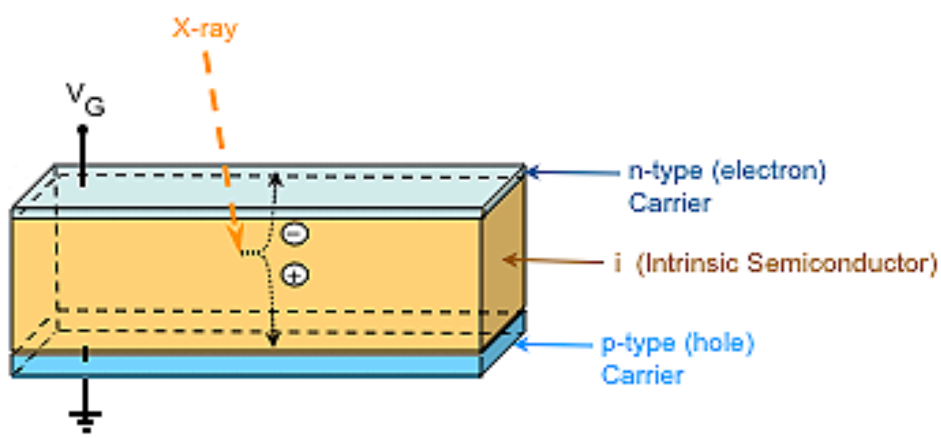

Figure E-6. Solid state semiconductor X-ray detector diagram.

Table E-1 through Table E-3 provide a comparison of the characteristics of the various X-ray detector types. Each type has advantages and limitations, and these design trade-offs have been typically chosen based upon the requirements of a specific X-ray astronomy mission.

Table E-1. Characteristics Of Detector Types (Part A).

Characteristic / Detector Type	Technology State (Manufacturing)	Power Usage	Mass	Quantum Efficiency	Detector Size
Proportional Gas Counters	Mature		High (40 kg)		Large (1000s cm^2)
Microchannel Plates	Mature	Medium (10s Watts)		Soft X-rays: Low (~20%) Hard X-rays: Med (~40%)	
Scintillators	Fairly New			Soft X-rays: Low (~25%) Hard X-rays: High (~90%)	
Calorimeters	New (1980s)	High (100s Watts)		High (95%)	Small (0.01 cm^2)
CCD Semiconductor	New (1980s)	Low		Soft X-rays: Low (~25%) Hard X-rays: High (~90%)	
Solid State Semiconductor	New (late 1980s)	Low (1 W per 100 cm^2)		High (80%)	Large (1000s cm^2)

Table E-2. Characteristics Of Detector Types (Part B).

Characteristic / Detector Type	Spatial Resolution	Energy Range	Energy Resolution	Photon Timing
Proportional Gas Counters		Soft X-rays: Good (0.1-20 keV) Hard X-rays: Poor (> 20 keV)	Medium	Medium (~ µs)
Microchannel Plates	High (~30 mm)	Soft X-rays: Good (0.1-10 keV)	Poor	Very Good (< ns, maybe 10 ps)
Scintillators	Medium	Soft X-rays: Poor (0.1-20 keV) Hard X-rays: Good (> 20 keV)	Medium	
Calorimeters			High (3 eV @ 6 keV)	Very Good (< ns)
CCD Semiconductor	High (~15 mm)		Poor (~1 keV)	Poor (> ms)
Solid State Semiconductor		Hard X-rays: Good (2-100 keV)		Medium (~ µs)

Table E-3. Characteristics Of Detector Types (Part C).

Characteristic / Detector Type	Imaging Capable	Active Cooling Required	Optics Required	Background Rejection
Proportional Gas Counters	Yes	No	No (collimator)	High
Microchannel Plates	Yes	No (but needs vacuum)	No (Lobster-eye Optics)	Good
Scintillators	Yes	Medium (Strongly temperature dependent)	No	Good
Calorimeters	Poor (Cant be packed close together due to heat)	Yes	Yes (Detector very small)	
CCD Semiconductor	Yes	Some (180° K)	No	
Solid State Semiconductor	Yes		No	

E.2 Conceptual Detector System Designs

X-ray detector systems are well known and have successfully flown on many orbital missions, as shown in Chapter 2. Various detectors, such as the one used by the USA experiment, are gas-filled proportional counters with collimators used to sense the arrival of X-ray photons. Newer semiconductor sensor technology, such as those based on silicon, can be used as detectors situated at the base of a collimated container. A coded-aperture mask or focusing X-ray optics may be used to help image the X-ray sources within the field of view. To improve navigation performance with several simultaneous measurements, multiple detectors, either within the same sensor unit or positioned at strategic locations upon the spacecraft surface, could be used to detect multiple sources over the same time epoch.

Figure E-7 shows a concept sensor system for X-ray pulsar-based navigation. The unit is comprised of a set of five detection sub-units, however, any number of individual sub-units may be utilized depending on the application. Using multiple detection units in a single system allows for simultaneous observation of different X-ray sources. Each detection unit may include a coded-aperture mask, a containment structure, a thin collimator, a silicon-strip detector positioned directly beneath the collimator, and supporting electronics for each detector. The five detection units are positioned with one in a zenith position (up), and four positioned around this unit at 45° angles to zenith, although their orientation angles may be optimized depending on the application. The containment boxes shown have dimensions of 10 cm long, 10 cm wide, and 30 cm high, which allows a 100-cm^2 detection area but could be adjusted proportionately. The containment chambers are positioned to reduce overall system size, and the photons paths within each chamber intersect for this system. The intersecting X-ray photons, however, should not collide or interact with one another. This system may be fixed to spacecraft structure or mounted on a gimbaled mechanism to allow for direct pointing to specific sources. Alternatively, each sub-unit could be actuated independently so that they could each be oriented towards a specific source.

Aside from the physical X-ray detector, the system would require electronics to process the arriving photon information. Methods to time the photon arrival to high accuracy must be devised for high performing systems. Additionally, significant data processing is required for use of the photon arrival time within a navigation system. This data processing would require onboard computers with sufficient processing potential to produce accurate navigation solutions.

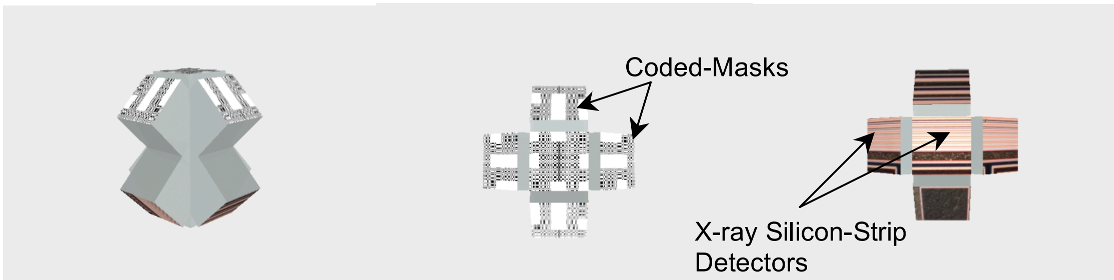

Figure E-7. Side, top, and bottom views of conceptual multiple X-ray detector system.

Bibliography

[1] *The Astronomical Almanac for the year 2001*, U. S. Government Printing Office, 2000.

[2] AAVSO, "Types of Variable Stars," [online database], The American Association of Variable Star Observers, URL: http://www.aavso.org/vstar/types.shtml [cited 7 March 2005].

[3] Abdel-Hafez, M. F., Lee, Y. J., Williamson, W. R., Wolfe, J. D., and Speyer, J. L., "A High-Integrity and Efficient GPS Integer Ambiguity Resolution Method," *Journal of the Institute of Navigation*, Vol. 50, No. 4, 2003, pp. 295-310.

[4] Abidin, H., "On the Construction of the Ambiguity Search Space for On-The-Fly," *Journal of the Institute of Navigation*, Vol. 40, No. 3, 1993, pp. 321-338.

[5] Aldridge, E. C. P. J., Fiorina, C. S., Jackson, M. P., Leshin, L. A., Lyles, L. L., Spudis, P. D., Tyson, N. d., Walker, R. S., and Zuber, M. T., "Report of the President's Commission on Implementation of United States Space Exploration Policy," U. S. Government Printing Office, 2004.

[6] Allan, D. W., "Statistics of Atomic Frequency Standards," *Proceedings of the IEEE*, Vol. 54, No. 2, February 1966, pp. 221-230.

[7] Allan, D. W., "Millisecond Pulsar Rivals Best Atomic Clock Stability," *41st Annual Frequency Control Symposium*, IEEE, Philadelphia PA, 1987, pp. 2-11.

[8] Arzoumanian, Z., Nice, D. J., Taylor, J. H., and Thorsett, S. E., "Timing behavior of 96 radio pulsars," *Astrophysical Journal*, Vol. 422, February 1994, pp. 671-680.

[9] Ashby, N., "Relativity in the Global Positioning System," *Living Reviews in Relativity*, Vol. 6, 28 January 2003, pp. 1-45.

[10] Ashby, N., and Allan, D. W., "Coordinate Time On and Near the Earth," *Physical Review Letters*, Vol. 53, No. 19, November 1984, pg. 1858.

[11] Atkinson, K. E., *An Introduction to Numerical Analysis*, Second ed., John Wiley and Sons, New York, 1989.

[12] ATNF, "ATNF Pulsar Catalogue," [online database], Australian Telescope National Facility, URL: http://www.atnf.csiro.au/research/pulsar/psrcat/ [cited 22 December 2003].

[13] Baade, W., and Zwicky, F., "Cosmic Rays from Super-novae," *Proceedings of the National Academy of Science*, Vol. 20, No. 5, January 1934, pp. 259-263.

[14] Baade, W., and Zwicky, F., "On Super-novae," *Proceedings of the National Academy of Science*, Vol. 20, No. 5, January 1934, pp. 254-259.

[15] Backer, D. C., and Hellings, R. W., "Pulsar Timing and General Relativity," *Annual Review of Astronomy and Astrophysics*, Vol. 24, January 1986, pp. 537-575.

[16] Bate, R. R., Mueller, D. D., and White, J. E., *Fundamentals of Astrodynamics*, Dover Publications Inc., New York, 1971.

[17] Battin, R. H., *An Introduction to the Mathematics and Methods of Astrodynamics*, Revised ed., American Institute of Aeronautics and Astronautics, Washington, DC, 1999.

[18] Bauer, W., "Spectrum Applet," [online], 1999, URL: http://lectureonline.cl.msu.edu/~mmp/applist/Spectrum/s.htm [cited March 7 2005].

[19] Becker, W., and Trümper, J., "The X-ray luminosity of rotation-powered neutron stars," *Astronomy and Astrophysics*, Vol. 326, October 1997, pp. 682-691.

[20] Becker, W., and Trümper, J., "The X-ray emission properties of millisecond pulsars," *Astronomy and Astrophysics*, Vol. 341, January 1999, pp. 803-817.

[21] Beckman, M., and Folta, D., "Mission Design of the First Robotic Lunar Exploration Program Mission: The Lunar Reconnaissance Orbiter," *AAS/AIAA Astrodynamics Specialists Conference*, Paper AAS 05-300, Lake Tahoe CA, August 7-11 2005.

[22] Bell, J. F., "Radio Pulsar Timing," *Advances in Space Research*, Vol. 21, No. 1/2, January 1998, pp. 137-147.

[23] Bergeron, J. Ed., *Proceedings of 21st General Assembly*, Transactions of the International Astronomical Union, Vol. XXI B. Reidel, Dordrecht, 1992.

[24] Bhattacharya, D., "Millisecond Pulsars," *X-ray Binaries*, W. H. G. Lewin, J. van Paradijs, and E. P. J. van den Heuvel Eds., Cambridge University Press, Cambridge UK, 1995, pp. 223-251.

[25] Bhattacharya, D., and Srinivasan, G., "The Magnetic Fields of Neutron Stars and Their Evolution," *X-ray Binaries*, W. H. G. Lewin, J. van Paradijs, and E. P. J. van den Heuvel Eds., Cambridge University Press, Cambridge UK, 1995, pp. 495-522.

[26] Bierman, G. J., *Factorization Methods for Discrete Sequential Estimation*, Academic, New York, 1977.

[27] Bildsten, L., Chakrabarty, D., Chiu, J., Finger, M. H., Koh, D. T., Nelson, R. W., Prince, T. A., Rubin, B. C., Scott, D. M., Stollberg, M., Vaughan, B. A., Wilson, C. A., and Wilson, R. B., "Observations of Accreting Pulsars," *Astrophysical Journal Supplement Series*, Vol. 113, December 1997, pg. 367.

[28] Blandford, R., and Teukolsky, S. A., "Arrival-Time Analysis for a Pulsar in a Binary System," *Astrophysical Journal*, Vol. 205, April 1976, pp. 580-591.

[29] Brown, R. G., and Hwang, P. Y. C., *Introduction to Random Signals and Applied Kalman Filtering*, Third ed., John Wiley and Sons, New York, 1997.

[30] Caltech, "Caltech Astronomy: Palomar Observatory," [online], URL: http://www.astro.caltech.edu/palomar/ [cited 7 March 2005].

[31] Camilo, F., Manchester, R. N., Gaensler, B. M., Lorimer, D. R., and Sarkissian, J., "PSR J1124-5916: Discovery of a Young Energetic Pulsar in the Supernova Remnant G292.0+1.8," *Astrophysical Journal*, Vol. 567, March 2002, pp. L71-L75.

[32] Camilo, F., Lorimer, D. R., Bhat, N. D. R., Gotthelf, E. V., Halpern, J. P., Wang, Q. D., Lu, F. J., and Mirabal, N., "Discovery of a 136 Millisecond Radio and X-Ray Pulsar in Supernova Remnant G54.1+0.3," *Astrophysical Journal*, Vol. 574, July 2002, pp. L71-L74.

[33] Campana, S., Ravasio, M., Israel, G. L., Mangano, V., and Belloni, T., "XMM-Newton Observation of the 5.25 Millisecond Transient Pulsar XTE J1807-294 in Outburst," *Astrophysical Journal*, Vol. 594, September 2003, pp. L39-L42.

[34] Caraveo, P. A., and Mignani, R. P., "A new HST measurement of the Crab Pulsar proper motion," *Astronomy and Astrophysics*, Vol. 344, April 1999, pp. 367-370.

[35] CDS, "SIMBAD Astronomical Database," [online database], Centre de Données astronomiques de Strasbourg, URL: http://simbad.harvard.edu/cgi-bin/WSimbad.pl [cited 2002-2005].

[36] Chakrabarty, D., and Morgan, E. H., "The two-hour orbit of a binary millisecond X-ray pulsar," *Nature*, Vol. 394, 23 July 1998, pp. 346-348.

[37] Chandrasekhar, S., *Stellar Structure and Stellar Atmospheres*, University of Chicago Press, Chicago IL, 1989.

[38] Charles, P. A., and Seward, F. D., *Exploring the X-ray Universe*, Cambridge University Press, Cambridge UK, 1995.

[39] Chen, C.-T., *Linear System Theory and Design*, Oxford University Press, New York, 1999.

[40] Chester, T. J., and Butman, S. A., "Navigation Using X-ray Pulsars," *NASA Technical Reports N81-27129*, 1981, pp. 22-25.

[41] Chlohessy, W. H., and Wiltshire, R. S., "Terminal Guidance System for Satellite Rendezvous," *Journal of Aerospace Sciences*, Vol. 27, No. 9, 1960, pp. 653-658, 674.

[42] Chobotov, V. A. Ed., *Orbital Mechanics*, Education Series. American Institute of Aeronautics and Astronautics, Washington, DC, 1991.

[43] Corbet, R., Coe, M., Edge, W., Laycock, S., Markwardt, C., and Marshall, F. E., "X-ray Pulsars in the SMC," [online database], URL: http://lheawww.gsfc.nasa.gov/users/corbet/pulsars/ [cited 30 October 2004].

[44] Cordova, F. A.-D., "Cataclysmic Variable Stars," *X-ray Binaries*, W. H. G. Lewin, J. van Paradijs, and E. P. J. van den Heuvel Eds., Cambridge University Press, Cambridge UK, 1995, pp. 331-389.

[45] Culhane, J. L., and Sanford, P. W., *X-ray Astronomy*, Charles Scribner's Sons, New York, 1981.

[46] Cunningham, L. E., "On the Computation of the Spherical Harmonic Terms Needed During the Numerical Integration of the Orbital Motion of an Artificial Satellite," *Celestial Mechanics*, Vol. 2, 1970, pp. 207-216.

[47] D'Amico, N., Possenti, A., Manchester, R. N., Sarkissian, J., Lyne, A. G., and Camilo, F., "An Eclipsing Millisecond Pulsar with a Possible Main-Sequence Companion in NGC 6397," *Astrophysical Journal*, Vol. 561, November 2001, pp. L89-L92.

[48] Department of Defense and Department of Transportation, "2001 Federal Radionavigation Systems," United States Government, 2001.

[49] Department of Defense: Command Control Communications and Intelligence, "Global Positioning System Standard Positioning Service Performance Standard," United States Government, 2001.

[50] Downs, G. S., "Interplanetary Navigation Using Pulsating Radio Sources," *NASA Technical Reports N74-34150*, October 1974, pp. 1-12.

[51] Downs, G. S., and Reichley, P. E., "Techniques for Measuring Arrival Times of Pulsar Signals I: DSN Observations from 1968 to 1980," NASA Jet Propulsion Laboratory, California Institute of Technology, Pasadena CA, NASA Technical Reports NASA-CR-163564, 15 August 1980.

[52] Duncan, R. C., and Thompson, C., "Formation of Very Strongly Magnetized Neutron Stars - Implications for Gamma-ray Bursts," *Astrophysical Journal*, Vol. 392, June 1992, pp. L9-L13.

[53] Einstein, A., *The Meaning of Relativity*, Princeton University Press, Princeton NJ, 1984.

[54] Epstein, R., "The binary pulsar - Post-Newtonian timing effects," *Astrophysical Journal*, Vol. 216, August 1977, pp. 92-100.

[55] Escobal, P. R., *Methods of Orbit Determination*, Krieger Publishing Company, Malabar FL, 1965.

[56] Fabbiano, G., "Normal Galaxies and their X-ray Binary Populations," *X-ray Binaries*, W. H. G. Lewin, J. van Paradijs, and E. P. J. van den Heuvel Eds., Cambridge University Press, Cambridge UK, 1995, pp. 390-418.

[57] Fairhead, L., and Bretagnon, P., "An analytical formula for the time transformation TB-TT," *Astronomy and Astrophysics*, Vol. 229, March 1990, pp. 240-247.

[58] Folta, D. C., Gramlin, C. J., Long, A. C., Leung, D. S. P., and Belur, S. V., "Autonomous Navigation Using Celestial Objects," *American Astronautical Society (AAS) Astrodynamics Specialist Conference*, AAS Paper 99-439, August 1999, pp. 2161-2177.

[59] Fraser, G. W., *X-ray Detectors in Astronomy*, Cambridge University Press, Cambridge UK, 1989.

[60] Freire, P. C., Camilo, F., Lorimer, D. R., Lyne, A. G., Manchester, R. N., and D'Amico, N., "Timing the millisecond pulsars in 47 Tucanae," *Monthly Notices of the Royal Astronomical Society*, Vol. 326, September 2001, pp. 901-915.

[61] Frommert, H., and Kronberg, C., "The First Known Variable Stars," [online database], URL: http://www.seds.org/~spider/spider/Vars/vars.html [cited 7 March 2005].

[62] Frommert, H., and Kronberg, C., "The First Known Variable Stars," [online database], URL: http://www.seds.org/~spider/spider/Vars/vars.html [cited 7 March 2005].

[63] Fukushima, T., "Time ephemeris," *Astronomy and Astrophysics*, Vol. 294, February 1995, pp. 895-906.

[64] Galloway, D. K., Chakrabarty, D., Morgan, E. H., and Remillard, R. A., "Discovery of a High-Latitude Accreting Millisecond Pulsar in an Ultracompact Binary," *Astrophysical Journal*, Vol. 576, September 2002, pp. L137-L140.

[65] Gelb, A. Ed., *Applied Optimal Estimation*. The M.I.T. Press, Cambridge MA, 1974.

[66] Giacconi, R., and Gursky, H. Eds., *X-ray Astronomy*, Astrophysics and Space Science Library, Vol. 43. D. Reidel Publishing Company, Boston MA, 1974.

[67] Giacconi, R., Gursky, H., Paolini, F. R., and Rossi, B. B., "Evidence for X Rays From Sources Outside the Solar System," *Physical Review Letters*, Vol. 9, No. 11, December 1962, pp. 439-443.

[68] Gounley, R., White, R., and Gai, E., "Autonomous Satellite Navigation by Stellar Refraction," *Journal of Guidance, Control, and Dynamics*, Vol. 7, No. 2, 1984, pp. 129-134.

[69] Griffin, M. D., and French, J. R., *Space Vehicle Design*, American Institute of Aeronautics and Astronautics, Washington, DC, 1991.

[70] Grindlay, J. E., Camilo, F., Heinke, C. O., Edmonds, P. D., Cohn, H., and Lugger, P., "Chandra Study of a Complete Sample of Millisecond Pulsars in 47 Tucanae and NGC 6397," *Astrophysical Journal*, Vol. 581, December 2002, pp. 470-484.

[71] Gunckel, T. L., "Orbit Determination Using Kalman's Method," *Navigation: Journal of the Institute of Navigation*, Vol. 10, No. 3, 1963.

[72] Hanson, J. E., "Principles of X-ray Navigation," Doctoral Dissertation, Department of Aeronautics and Astronautics, Stanford University, 1996.

[73] Hatch, R., and Euler, H.-J., "Comparison of Several AROF Kinematic Techniques," *Proceeding of Institute of Navigation GPS-94*, Salt Lake City UT, September 1994, pp. 363-370.

[74] Haugan, M. P., "Post-Newtonian arrival-time analysis for a pulsar in a binary system," *Astrophysical Journal*, Vol. 296, September 1985, pp. 1-12.

[75] HEASARC, "HEASARC Observatories," [online database], High Energy Astrophysics Science Archive Research Center NASA/GSFC/SAO, URL: http://heasarc.gsfc.nasa.gov/docs/observatories.html [cited 1 July 2003].

[76] HEASARC, "HEASARC: WebPIMMS - A Portable Mission Count Rate Simulator," [online], URL: http://heasarc.gsfc.nasa.gov/Tools/w3pimms.html [cited 21 January 2003].

[77] HEASARC, "Master Radio Catalog," [online database], NASA/HEASARC, URL: http://heasarc.gsfc.nasa.gov/W3Browse/all/radio.html [cited 2004].

[78] HEASARC, "Master X-ray Catalog," [online database], NASA/HEASARC, URL: http://heasarc.gsfc.nasa.gov/W3Browse/master-catalog/xray.html [cited 2004].

[79] Hellings, R. W., "Relativistic Effects in Astronomical Timing Measurements," *Astronomical Journal*, Vol. 91, March 1986, pp. 650-659.

[80] Hewish, A., Bell, S. J., Pilkington, J. D., Scott, P. F., and Collins, R. A., "Observation of a Rapidly Pulsating Radio Source," *Nature*, Vol. 217, 24 February 1968, pp. 709-713.

[81] Hobbs, G., Manchester, R., Teoh, A., and Hobbs, M., "The ATNF Pulsar Catalog," *IAU Symposium*, Vol. 218, 1 January 2004, pg. 139.

[82] Hogg, H. S., "Variable Stars," *Astrophysics and Twentieth-Century Astronomy to 1950: Part A*, *The General History of Astronomy*, Owen Gingerich Ed., The General History of Astronomy, Vol. 4A, Cambridge, 1984, pp. 73-89.

[83] Hoots, F. R., and Roehrich, R. L., "Spacetrack Report No. 3, Model for Propagation of NORAD Element Sets," Department of Defense, Defense Documentation Center, December 1980.

[84] Hoots, F. R., Schumacher, P. W. J., and Glover, R. A., "History of Analytical Orbit Modeling in the U.S. Space Surveillance System," *Journal of Guidance, Control, and Dynamics*, Vol. 27, No. 2, pp. 174-185.

[85] Hwang, P. Y. C., "Kinematic GPS: Resolving Integer Ambiguities On The Fly," *Proceedings IEEE PLANS-90*, Las Vegas NV, 1990, pp. 579-586.

[86] IAU, "IAU Specifications for Nomenclature," [online], URL: http://vizier.u-strasbg.fr/Dic/iau-spec.htx [cited 1 December 2004].

[87] Irwin, A. W., and Fukushima, T., "A numerical time ephemeris of the Earth," *Astronomy and Astrophysics*, Vol. 348, August 1999, pp. 642-652.

[88] Jet Propulsion Laboratory, "About The Deep Space Network," [online], California Institute of Technology, NASA, 2005, URL: http://deepspace.jpl.nasa.gov/dsn/ [cited 14 June 2005].

[89] Jordan, J. F., "Navigation of Spacecraft on Deep Space Missions," *Journal of Navigation*, Vol. 40, January 1987, pp. 19-29.

[90] Kaaret, P., Marshall, H. L., Aldcroft, T. L., Graessle, D. E., Karovska, M., Murray, S. S., Rots, A. H., Schulz, N. S., and Seward, F. D., "Chandra Observations of the Young Pulsar PSR B0540-69," *Astrophysical Journal*, Vol. 546, January 2001, pp. 1159-1167.

[91] Kalman, R. E., "A New Approach to Linear Filtering and Prediction Problems," *Transactions of the American Society of Mechanical Engineering - Journal of Basic Engineering*, Vol. 82, No. D, 1960, pp. 35-45.

[92] Kane, H. K., "Ancient Hawai'i," [online], 1997, URL: http://www.hawaiiantrading.com/herb-kane/ah-book/index.html [cited 12 June 2005].

[93] Kaplan, M. H., *Modern Spacecraft Dynamics and Control*, John Wiley and Sons, New York, 1976.

[94] Kaspi, V. M., "Applications of Pulsar Timing," Doctoral Dissertation, Department of Physics, Princeton University, 1994.

[95] Kaspi, V. M., "High-Precision Timing of Millisecond Pulsars and Precision Astrometry," *International Astronomical Union Symposium 166: Astronomical and Astrophysical Objectives of Sub-Milliarcsecond Optical Astrometry*, Eds. E. Hog and P. Kenneth Seidelmann, Vol. 166, August 1994, pp. 163-174.

[96] Kaspi, V. M., Taylor, J. H., and Ryba, M. F., "High-Precision Timing of Millisecond Pulsars. III: Long-Term Monitoring of PSRs B1855+09 and B1937+21," *Astrophysical Journal*, Vol. 428, June 1994, pp. 713-728.

[97] Kelso, T. S., "NORAD Two-Line Element Sets Historical Archives," [online database], Celestrak, URL: http://www.celestrak.com/NORAD/archives/request.asp [cited 22 December 2004].

[98] Khalil, H. K., *Nonlinear Systems*, Second ed., Prentice Hall, 1996.

[99] Kim, Y. H., *X-ray Source Tables*, Saddleback College, 2002 (unpublished).

[100] King, A., "Accretion in Close Binaries," *X-ray Binaries*, W. H. G. Lewin, J. van Paradijs, and E. P. J. van den Heuvel Eds., Cambridge University Press, Cambridge UK, 1995, pp. 419-456.

[101] Kirsch, M. G. F., Mukerjee, K., Breitfellner, M. G., Djavidnia, S., Freyberg, M. J., Kendziorra, E., and Smith, M. J. S., "Studies of orbital parameters and pulse profile of the accreting millisecond pulsar XTE J1807-294," *Astronomy and Astrophysics*, Vol. 423, August 2004, pp. L9-L12.

[102] Kopeikin, S. M., "Millisecond and Binary Pulsars as Nature's Frequency Standards - Part I. A Generalized Statistical Model of Low-Frequency Timing Noise," *Monthly Notices of the Royal Astronomical Society*, Vol. 288, June 1997, pp. 129-137.

[103] Kopeikin, S. M., "Millisecond and Binary Pulsars as Nature's Frequency Standards - Part II. The Effects of Low-Frequency Timing noise on Residuals and Measured Parameters," *Monthly Notices of the Royal Astronomical Society*, Vol. 305, May 1999, pp. 563-590.

[104] Krauss, M. I., Dullighan, A., Chakrabarty, D., van Kerkwijk, M. H., and Markwardt, C. B., "XTE J1814-338," *International Astronomical Union Circular*, Vol. 8154, June 2003, pg. 3.

[105] Kuiper, L., and Hermsen, W., "X-ray and Gamma-ray Observations of Millisecond Pulsars," *X-ray and Gamma-ray Astrophysics of Galactic Sources*, 8 December 2003.

[106] Landau, H., and Euler, H.-J., "On-The-Fly Ambiguity Resolution for Precise Differential Positioning," *Proceedings Institutes of Navigation GPS-92*, Albuquerque NM, September 1992, pp. 607-613.

[107] Larson, W. J., and Wertz, J. R. Eds., *Space Mission Analysis and Design*, 3rd Edition, Space Technology Series. Microcosm Press and Kluwer Academic Publishers (Jointly), Boston MA, 1999.

[108] LBL, "The Electromagnetic Spectrum," [online], URL: http://www.lbl.gov/MicroWorlds/ALSTool/EMSpec/EMSpec2.html [cited 7 March 2005].

[109] Lewin, W. H. G., Paradijs, J. V., and Taam, R. E., "X-ray Bursts," *X-ray Binaries*, W. H. G. Lewin, J. van Paradijs, and E. P. J. van den Heuvel Eds., Cambridge University Press, Cambridge UK, 1995, pp. 175-232.

[110] Liu, Q. Z., van Paradijs, J., and van den Heuvel, E. P. J., "A catalogue of high-mass X-ray binaries," *Astronomy and Astrophysics Supplement Series*, Vol. 147, November 2000, pp. 25-49.

[111] Liu, Q. Z., van Paradijs, J., and van den Heuvel, E. P. J., "A catalogue of low-mass X-ray binaries," *Astronomy and Astrophysics*, Vol. 368, March 2001, pp. 1021-1054.

[112] Lommen, A. N., "Precision Multi-Telescope Timing of Millisecond Pulsars: New Limits on the Gravitational Wave Background and other results from the Pulsar Timing Array," PhD Dissertation, Astrophysics, University of California, Berkeley CA, 2001.

[113] Lorimer, D. R., "Binary and Millisecond Pulsars at the New Millennium," *Living Reviews in Relativity*, Vol. 4, June 2001, pg. 5.

[114] Lyne, A. G., and Graham-Smith, F., *Pulsar Astronomy*, Cambridge University Press, Cambridge UK, 1998.

[115] Lyne, A. G., Jordan, C. A., and Roberts, M. E., "Jodrell Bank Crab Pulsar Timing Results," [online], URL: http://www.jb.man.ac.uk/~pulsar/crab.html [cited 13 August 2002].

[116] Majid, W. A., Lamb, R. C., and Macomb, D. J., "X-Ray Pulsars in the Small Magellanic Cloud," *Astrophysical Journal*, Vol. 609, July 2004, pp. 133-143.

[117] Maldonado, A. L., Baylocq, M., and Hannan, G., "Autonomous Spacecraft Navigation - Extended Kalman Filter Estimation of Classical Orbital Parameters," *Guidance and Control Conference*, American Institute of Aeronautics and Astronautics, Seattle, WA, August 20-22 1984.

[118] Manchester, R. N., and Taylor, J. H., *Pulsars*, W.H. Freeman and Company, San Francisco CA, 1977.

[119] Manchester, R. N., Lyne, A. G., Camilo, F., Bell, J. F., Kaspi, V. M., D'Amico, N., McKay, N. P. F., Crawford, F., Stairs, I. H., Possenti, A., Kramer, M., and Sheppard, D. C., "The Parkes multi-beam pulsar survey - I. Observing and data analysis systems, discovery and timing of 100 pulsars," *Monthly Notices of the Royal Astronomical Society*, Vol. 328, November 2001, pp. 17-35.

[120] Markley, F. L., "Approximate Cartesian State Transition Matrix," *Journal of Astronautical Sciences*, Vol. 34, No. 2, 1986, pp. 161-169.

[121] Markwardt, C. B., and Swank, J. H., "XTE J1751-305," *International Astronomical Union Circular*, Vol. 7867, April 2002, pg. 1.

[122] Markwardt, C. B., and Swank, J. H., "XTE J1814-338," *International Astronomical Union Circular*, Vol. 8144, June 2003, pg. 1.

[123] Markwardt, C. B., Juda, M., and Swank, J. H., "XTE J1807-294," *International Astronomical Union Circular*, Vol. 8095, March 2003, pg. 2.

[124] Markwardt, C. B., Smith, E., and Swank, J. H., "XTE J1807-294," *International Astronomical Union Circular*, Vol. 8080, February 2003, pg. 2.

[125] Markwardt, C. B., Swank, J. H., Strohmayer, T. E., in 't Zand, J. J. M., and Marshall, F. E., "Discovery of a Second Millisecond Accreting Pulsar: XTE J1751-305," *Astrophysical Journal*, Vol. 575, August 2002, pp. L21-L24.

[126] Martin, C. F., Torrence, M. H., and Misner, C. W., "Relativistic Effects on an Earth-Orbiting Satellite in the Barycenter Coordinate System," *Journal of Geophysical Research*, Vol. 90, No. B11, September 1985, pp. 9403-9410.

[127] Matsakis, D. N., Taylor, J. H., and Eubanks, T. M., "A Statistic for Describing Pulsar and Clock Stabilities," *Astronomy and Astrophysics*, Vol. 326, October 1997, pp. 924-928.

[128] Melbourne, W. G., "Navigation Between the Planets," *Scientific American*, Vol. 234, No. 6, 1976, pp. 58-74.

[129] Meliani, M. T., "A Catalogue of X-ray sources in the sky region between delta = -73deg. and delta = +27 deg," *Publications of the Astronomical Society of Australia*, Vol. 16, August 1999, pp. 175-205.

[130] Melvin, P. J., "A Kalman Filter For Orbit Determination with Applications to GPS and Stellar Navigation," *Advances in Astronautical Sciences, Spaceflight Mechanics Conference*, Paper AAS 96-145, Proceedings of American Astronautical Society (AAS), 1996.

[131] Mereghetti, S., Bandiera, R., Bocchino, F., and Israel, G. L., "BeppoSAX Observations of the Young Pulsar in the Kes 75 Supernova Remnant," *Astrophysical Journal*, Vol. 574, August 2002, pp. 873-878.

[132] Meyer, K. W., Buglia, J. J., and Desai, P. N., "Lifetimes of Lunar Orbits," *NASA Technical Paper 3394*, March 1994, pp. 1-35, Langley Research Center, Hampton VA.

[133] Mikhail, E. M., *Observations and Least Squares*, IEP-A Dun-Donnelley, New York, 1976.

[134] Miller, J. M., Wijnands, R., Méndez, M., Kendziorra, E., Tiengo, A., van der Klis, M., Chakrabarty, D., Gaensler, B. M., and Lewin, W. H. G., "XMM-Newton Spectroscopy of the Accretion-driven Millisecond X-Ray Pulsar XTE J1751-305 in Outburst," *Astrophysical Journal*, Vol. 583, February 2003, pp. L99-L102.

[135] Misner, C. W., Thorne, K. S., and Wheeler, J. A., *Gravitation*, W. H. Freeman and Company, San Francisco, 1973.

[136] Montenbruck, O., and Gill, E., *Satellite Orbits*, Springer-Verlag, Berlin, 2000.

[137] Moyer, T. D., "Transformation from Proper Time on Earth to Coordinate Time in Solar System Barycentric Space-Time Frame of Reference - Part One," *Celestial Mechanics*, Vol. 23, January 1981, pp. 33-56.

[138] Moyer, T. D., "Transformation from Proper Time on Earth to Coordinate Time in Solar System Barycentric Space-Time Frame of Reference - Part Two," *Celestial Mechanics*, Vol. 23, January 1981, pp. 57-68.

[139] MSFC, "ASM Accreting Pulsars," [online database], NASA/MSFC, URL: http://gammaray.msfc.nasa.gov/batse/pulsar/asm_pulsars.html [cited 30 October 2004].

[140] Murray, C. A., *Vectorial Astrometry*, Adam Hilger Ltd, Bristol UK, 1983.

[141] Nagase, F., "Accretion-powered X-ray pulsars," *Publications of the Astronomical Society of Japan*, Vol. 41, January 1989, pp. 1-79.

[142] NAIC, "Arecibo Observatory Home," [online], URL: http://www.naic.edu/ [cited March 7 2005].

[143] NASA, "The Hubble Project - Technology," [online], URL: http://hubble.nasa.gov/technology/optics.php [cited March 7 2005].

[144] NASA, "RXTE Guest Observatory Facility," [online], URL: http://heasarc.gsfc.nasa.gov/docs/xte/xte_1st.html [cited 1 August 2002].

[145] NASA/HEASARC/RXTE, "Types of Sources in the ASM Catalogue," [online], URL: http://heasarc.gsfc.nasa.gov/docs/xte/learning_center/ASM/source_types.html [cited 15 July 2003].

[146] NASA/PSU/G.Pavlov, "Chandra Photo Album: Vela Pulsar 06 Jun 2000," [online], URL: http://chandra.harvard.edu/photo/2000/vela/ [cited 7 March 2005].

[147] NASA/SAO/CXC, "Chandra Photo Album Crab Nebula 28 Sep 1999," [online], URL: http://chandra.harvard.edu/photo/0052/ [cited March 7 2005].

[148] Nelson, R. A., *Handbook on Relativistic Time Transfer*, Satellite Engineering Research Corporation, 2003 (unpublished).

[149] Nelson, R. A., "Relativistic Effects in Satellite Time and Frequency Transfer and Dissemination," *ITU Handbook on Satellite Time and Frequency Transfer and Dissemination*, International Telecommunication Union, Geneva, (to be published), pp. 1-30.

[150] Newton, I., *Philosophiae Naturalis Principia Mathematica (Mathematical Principles of Natural Philosophy)*, Josephi Streater, London, 1687.

[151] Nicastro, L., Cusumano, G., Löhmer, O., Kramer, M., Kuiper, L., Hermsen, W., Mineo, T., and Becker, W., "BeppoSAX Observation of PSR B1937+21," *Astronomy and Astrophysics*, Vol. 413, January 2004, pp. 1065-1072.

[152] Nice, D. J., and Thorsett, S. E., "Pulsar PSR 1744-24A - Timing, eclipses, and the evolution of neutron star binaries," *Astrophysical Journal*, Vol. 397, September 1992, pp. 249-259.

[153] Nordtvedt, K., Jr., and Will, C. M., "Conservation Laws and Preferred Frames in Relativistic Gravity. Part II. Experimental Evidence to Rule Out Preferred-Frame Theories of Gravity," *Astrophysical Journal*, Vol. 177, November 1972, pp. 775-792.

[154] NRAO, "NRAO Green Bank Telescopes," [online], URL: http://www.gb.nrao.edu [cited 7 March 2005].

[155] Oppenheimer, J. R., and Volkoff, G. M., "On Massive Neutron Cores," *Physical Review*, Vol. 55, February 1939, pp. 374-381.

[156] Parkinson, B. W., and Spilker, J. J. Eds., *Global Positioning System: Theory and Applications, Volume I*. American Institute of Aeronautics and Astronautics, Washington, DC, 1996.

[157] Parkinson, B. W., and Spilker, J. J. Eds., *Global Positioning System: Theory and Applications, Volume II*. American Institute of Aeronautics and Astronautics, Washington, DC, 1996.

[158] Possenti, A., Cerutti, R., Colpi, M., and Mereghetti, S., "Re-examining the X-ray versus spin-down luminosity correlation of rotation powered pulsars," *Astronomy and Astrophysics*, Vol. 387, June 2002, pp. 993-1002.

[159] Princeton, "Princeton University Pulsar Group Pulsar Catalog," [online database], Princeton University, URL: http://pulsar.princeton.edu/pulsar/catalog.shtml [cited 4 May 2003].

[160] Prussing, J. E., and Conway, B. A., *Orbital Mechanics*, Oxford University Press, Oxford UK, 1993.

[161] Rappaport, S., *Pulsar SNR Discussion*, Massachusetts Institute of Technology, October 2004 (personal communication).

[162] Rawley, L. A., Taylor, J. H., and Davis, M. M., "Fundamental Astrometry and Millisecond Pulsars," *Astrophysical Journal*, Vol. 326, March 1988, pp. 947-953.

[163] Rawley, L. A., Taylor, J. H., Davis, M. M., and Allan, D. W., "Millisecond pulsar PSR 1937+21 - A highly stable clock," *Science*, Vol. 238, November 1987, pp. 761-765.

[164] Ray, P. S., Wood, K. S., Wolff, M. T., Lovellette, M. N., Sheikh, S., Moon, D. S., Eikenberry, S. S., Roberts, M., Bloom, E. D., Tournear, D., Saz Parkinson, P., and Reilly, K., "Absolute Timing of the Crab Pulsar: X-ray, Radio, and Optical Observations," *Bulletin of the American Astronomical Society*, American Astronomical Society, Vol. 201, December 2002, pg. 1298.

[165] Ray, P. S., Wood, K. S., Wolff, M. T., Lovellette, M. N., Sheikh, S., Moon, D. S., Eikenberry, S. S., Roberts, M., Lyne, A., Jordon, C., Bloom, E. D., Tournear, D., Saz Parkinson, P., and Reilly, K., "Absolute Timing Calibration of the USA Experiment Using Pulsar Observations," *American Astronomical Society (AAS) High Energy Astrophysics Division (HEAD)*, Vol. 7, 1 March 2003.

[166] Ray, P. S., Wood, K. S., Fritz, G., Hertz, P., Kowalski, M., Johnson, W. N., Lovellette, M. N., Wolff, M. T., Yentis, D., Bandyopadhyay, R. M., Bloom, E. D., Giebels, B., Godfrey, G., Reilly, K., Parkinson, P. S., Shabad, G., Michelson, P., Roberts, M., Leahy, D. A., Cominsky, L., Scargle, J., Beall, J., Chakrabarty, D.,

and Kim, Y., "The USA X-ray Timing Experiment," *X-ray Astronomy: Stellar Endpoints, AGN, and the Diffuse X-ray Background*, American Institute of Physics (AIP) Proceedings, Vol. 599, 1 December 2001, pp. 336-345.

[167] Reichley, P., Downs, G., and Morris, G., "Use of Pulsar Signals as Clocks," *NASA Jet Propulsion Laboratory Quarterly Technical Review*, Vol. 1, No. 2, July 1971, pp. 80-86.

[168] Reichley, P. E., Downs, G. S., and Morris, G. A., "Time-Of-Arrival Observations of Eleven Pulsars," *Astrophysical Journal*, Vol. 159, January 1970, pp. L35-L40.

[169] Remillard, R. A., Swank, J., and Strohmayer, T., "XTE J0929-314," *International Astronomical Union Circular*, Vol. 7893, May 2002, pg. 1.

[170] Richter, G. W., and Matzner, R. A., "Gravitational deflection of light at 1 1/2 PPN order," *Astrophysics and Space Science*, Vol. 79, September 1981, pp. 119-127.

[171] Richter, G. W., and Matzner, R. A., "Second-order contributions to gravitational deflection of light in the parameterized post-Newtonian formalism," *Physical Review D*, Vol. 26, No. 6, September 1982, pp. 1219-1224.

[172] Richter, G. W., and Matzner, R. A., "Second-order contributions to gravitational deflection of light in the parameterized post-Newtonian formalism. II. Photon orbits and deflections in three dimensions," *Physical Review D*, Vol. 26, No. 10, November 1982, pp. 2549-2556.

[173] Richter, G. W., and Matzner, R. A., "Second-order contributions to relativistic time delay in the parameterized post-Newtonian formalism," *Physical Review D*, Vol. 28, No. 12, December 1983, pp. 3007-3012.

[174] Ritter, H., and Kolb, U., "Catalogue of cataclysmic binaries, low-mass X-ray binaries and related objects (Sixth edition)," *Astronomy and Astrophysics Supplement Series*, Vol. 129, April 1998, pp. 83-85.

[175] Roth, G. D., "An Historical Exploration of Modern Astronomy," *Compendium of Practical Astronomy*, G. D. Roth Ed., Springer Verlag, 1994, pp. 425-435.

[176] Rugh, W. J., *Linear System Theory*, Second ed., Prentice Hall, Upper Saddle River, New Jersey, 1996.

[177] Russian Federation Ministry of Defense, "GLONASS," [online], 2002, URL: http://www.glonass-center.ru/frame_e.html [cited 7 March 2005].

[178] Samus, N. N., and Durlevich, O. V., "General Catalogue of Variable Stars," *VizieR Online Data Catalog*, Vol. 2250, November 2004.

[179] Samus, N. N., and Durlevich, O. V., "General Catalogue of Variable Stars (GCVS) Variability Types and Distribution Statistics of Designated Variable

Stars According to their Types of Variability," [online database], URL: http://www.sai.msu.su/groups/cluster/gcvs/gcvs/iii/vartype.txt [cited 7 March 2005].

[180] SAO, "6 m telescope short description," [online], URL: http://www.sao.ru/Doc-en/Telescopes/bta/descrip.html [cited 7 March 2005].

[181] SAO, "Special Astrophysical Observatory Russian Academy of Sciences Radiotelescope RATAN-600," [online], URL: http://www.sao.ru/ratan/ [cited 7 March 2005].

[182] Schumacher, P. W., and Glover, R. A., "Analytic Orbit Model for U.S. Naval Space Surveillance: An Overview," *1995 AAS/AIAA Astrodynamics Specialist Conference*, AAS Paper 95-427, American Astronautical Society, Halifax, Nova Scotia, Canada, August 14-17, 1995.

[183] Seidelmann, P. K., *Explanatory Supplement to the Astronomical Almanac*, University Science Books, Sausalito CA, 1992.

[184] Shapiro, I. I., "Fourth Test of General Relativity," *Physical Review Letters*, Vol. 13, No. 26, December 1964, pp. 789-791.

[185] Shearer, A., and Golden, A., "Implications of the Optical Observations of Isolated Neutron Stars," *Astrophysical Journal*, Vol. 547, February 2001, pp. 967-972.

[186] Sheikh, S. I., *The Use of Pulsars for Interplanetary Navigation*, University of Maryland, College Park, MD, 2000 (unpublished).

[187] Sheikh, S. I., *Crab Comparison Plot Description*, University of Maryland, College Park, MD, 2002 (unpublished).

[188] Sheikh, S. I., *Derivation of Relativistic Corrections and Time Transfer for Spacecraft Clock Proper Time within the Solar System Barycenter Frame*, University of Maryland, College Park, MD, 2004 (unpublished).

[189] Sheikh, S. I., *Absolute and Relative Position Determination Using Variable Celestial Sources*, University of Maryland, College Park, MD, 2005 (unpublished).

[190] Sheikh, S. I., *Navigation Kalman Filter*, University of Maryland, College Park, MD, 2005 (unpublished).

[191] Sheikh, S. I., and Pines, D. J., "Recursive Estimation of Spacecraft Position Using X-ray Pulsar Time of Arrival Measurements," *ION 61st Annual Meeting*, Institute of Navigation, Boston MA, 27-29 June 2005.

[192] Sheikh, S. I., Pines, D. J., Wood, K. S., Ray, P. S., Lovellette, M. N., and Wolff, M. T., "The Use of X-ray Pulsars for Spacecraft Navigation," *14th AAS/AIAA*

Space Flight Mechanics Conference, Paper AAS 04-109, Maui HI, February 8-12 2004.

[193] Sheikh, S. I., Pines, D. J., Wood, K. S., Ray, P. S., Lovellette, M. N., and Wolff, M. T., "Spacecraft Navigation Using X-ray Pulsars," *Journal of Guidance, Control, and Dynamics*, In press [anticipated 2005 publication].

[194] Shklovskii, I. S., "Possible Causes of the Secular Increase in Pulsar Periods," *Soviet Astronomy*, Vol. 13, No. 4, February 1970, pp. 562-565.

[195] Sidi, M. J., *Spacecraft Dynamics and Control*, Cambridge University Press, Cambridge UK, 1997.

[196] Singh, K. P., Drake, S. A., and White, N. E., "RS CVn Versus Algol-Type Binaries: A Comparative Study of Their X-Ray Emission," *Astronomical Journal*, Vol. 111, No. 6, June 1996, pg. 2415.

[197] Sobel, D., *Longitude: The True Story of a Lone Genius Who Solved the Greatest Scientific Problem of His Time*, Penguin Books, New York, 1995.

[198] Standish, E. M., "NASA JPL Planetary and Lunar Ephemerides," [online database], NASA, URL: http://ssd.jpl.nasa.gov/eph_info.html [cited 1 December 2004].

[199] Standish, E. M., "Time scales in the JPL and CfA ephemerides," *Astronomy and Astrophysics*, Vol. 336, August 1998, pp. 381-384.

[200] Strohmayer, T. E., Markwardt, C. B., Swank, J. H., and in't Zand, J., "X-Ray Bursts from the Accreting Millisecond Pulsar XTE J1814-338," *Astrophysical Journal*, Vol. 596, October 2003, pp. L67-L70.

[201] Stumpff, P., "On the Computation of Barycentric Radial Velocities with Classical Perturbation Theories," *Astronomy and Astrophysics*, Vol. 56, April 1977, pp. 13-23.

[202] Stumpff, P., "The Rigorous Treatment of Stellar Aberration and Doppler Shift, and the Barycentric Motion of the Earth," *Astronomy and Astrophysics*, Vol. 78, September 1979, pp. 229-238.

[203] Taylor, J. H., "Millisecond Pulsars: Nature's Most Stable Clocks," *Proceedings of the IEEE*, Vol. 79, No. 7, July 1991, pp. 1054-1062.

[204] Taylor, J. H., "Pulsar Timing and Relativistic Gravity," *Philosophical Transactions of the Royal Society of London*, Vol. 341, January 1992, pp. 117-134.

[205] Taylor, J. H., and Stinebring, D. R., "Recent Progress in the Understanding of Pulsars," *Annual Review of Astronomy and Astrophysics*, Vol. 24, January 1986, pp. 285-327.

[206] Taylor, J. H., and Weisberg, J. M., "Further Experimental Tests of Relativistic Gravity Using the Binary Pulsar PSR 1913+16," *Astrophysical Journal*, Vol. 345, October 1989, pp. 434-450.

[207] Taylor, J. H., Manchester, R., and Nice, D. J., "TEMPO Software Package," [online], URL: http://pulsar.princeton.edu/tempo/ [cited 10 November 2002].

[208] Taylor, J. H., Manchester, R. N., and Lyne, A. G., "Catalog of 558 Pulsars," *Astrophysical Journal Supplement Series*, Vol. 88, October 1993, pp. 529-568.

[209] Thomas, J. B., "Reformulation of the Relativistic Conversion Between Coordinate Time and Atomic Time," *Astronomical Journal*, Vol. 80, No. 5, May 1975, pp. 405-411.

[210] Thompson, C., and Duncan, R. C., "The Soft Gamma Repeaters as Very Strongly Magnetized Neutron Stars. II. Quiescent Neutrino, X-Ray, and Alfven Wave Emission," *Astrophysical Journal*, Vol. 473, December 1996, pp. 322-342.

[211] Thompson, D. J., "Pulse period of several well known pulsars," [online], URL: http://heasarc.gsfc.nasa.gov/docs/objects/pulsars/pulsars_lc.html [cited 7 March 2005].

[212] Thomson, W. T., *Introduction to Space Dynamics*, Dover, Mineola NY, 1986.

[213] Vallado, D. A., *Fundamentals of Astrodynamics and Applications*, Second ed., Space Technology Library, Kluwer Academic Publishers, Boston MA, 2001.

[214] van der Klis, M., "Rapid Aperiodic Variability in X-ray Binaries," *X-ray Binaries*, W. H. G. Lewin, J. van Paradijs, and E. P. J. van den Heuvel Eds., Cambridge University Press, Cambridge UK, 1995, pp. 252-307.

[215] Verbunt, F., and van den Heuvel, E. P. J., "Formation and Evolution of Neutron Stars and Black Holes in Binaries," *X-ray Binaries*, W. H. G. Lewin, J. van Paradijs, and E. P. J. van den Heuvel Eds., Cambridge University Press, Cambridge UK, 1995, pp. 457-494.

[216] Voges, W., Aschenbach, B., Boller, T., Bräuninger, H., Briel, U., Burkert, W., Dennerl, K., Englhauser, J., Gruber, R., Haberl, F., Hartner, G., Hasinger, G., Pfeffermann, E., Pietsch, W., Predehl, P., Schmitt, J., Trümper, J., and Zimmermann, U., "Rosat All-Sky Survey Faint Source Catalogue," *International Astronomical Union Circular*, Vol. 7432, May 2000, pg. 3.

[217] Voges, W., Aschenbach, B., Boller, T., Bräuninger, H., Briel, U., Burkert, W., Dennerl, K., Englhauser, J., Gruber, R., Haberl, F., Hartner, G., Hasinger, G.,

Kürster, M., Pfeffermann, E., Pietsch, W., Predehl, P., Rosso, C., Schmitt, J. H. M. M., Trümper, J., and Zimmermann, H. U., "The ROSAT all-sky survey bright source catalogue," *Astronomy and Astrophysics*, Vol. 349, September 1999, pp. 389-405.

[218] Wallace, K., "Radio Stars, What They Are and The Prospects for their Use in Navigational Systems," *Journal of Navigation*, Vol. 41, No. 3, September 1988, pp. 358-374.

[219] Weeks, C. J., and Bowers, M. J., "Analytical Models of Doppler Data Signatures," *Journal of Guidance, Control, and Dynamics*, Vol. 18, No. 6, 1995, pp. 1287-1291.

[220] Weinberg, S., *Gravitation and Cosmology: Principles and Applications of the General Theory of Relativity*, John Wiley and Sons, New York, 1972.

[221] Wertz, J. R. Ed., *Spacecraft Attitude Determination and Control*. Kluwer Academic Publishers, Boston MA, 1978.

[222] White, N. E., and Zhang, W., "Millisecond X-Ray Pulsars in Low-mass X-Ray Binaries," *Astrophysical Journal*, Vol. 490, November 1997, pg. L87.

[223] White, N. E., Nagase, F., and Parmar, A. N., "The Properties of X-ray Binaries," *X-ray Binaries*, W. H. G. Lewin, J. van Paradijs, and E. P. J. van den Heuvel Eds., Cambridge University Press, 1995.

[224] Wie, B., *Space Vehicle Dynamics and Control*, American Institute of Aeronautics and Astronautics, Reston VA, 1998.

[225] Wijnands, R., "An XMM-Newton Observation during the 2000 Outburst of SAX J1808.4-3658," *Astrophysical Journal*, Vol. 588, May 2003, pp. 425-429.

[226] Wijnands, R., and van der Klis, M., "A millisecond pulsar in an X-ray binary system," *Nature*, Vol. 394, 23 July 1998, pp. 344-346.

[227] Wikipedia, "Astronomical Object," [online], URL: http://www.answers.com/topic/astronomical-object/ [cited 15 March 2005].

[228] Will, C. M., and Nordtvedt, K., Jr., "Conservation Laws and Preferred Frames in Relativistic Gravity. Part I. Preferred-Frame Theories and an Extended PPN Formalism," *Astrophysical Journal*, Vol. 177, November 1972, pp. 757-774.

[229] Wood, K. S., "Navigation Studies Utilizing The NRL-801 Experiment and the ARGOS Satellite," *Small Satellite Technology and Applications III*, Ed. B. J. Horais, International Society of Optical Engineering (SPIE) Proceedings, Vol. 1940, 1993, pp. 105-116.

[230] Wood, K. S., "USA Observations," [online database], NRL/USA, URL: http://xweb.nrl.navy.mil/usa/index.html [cited 21 January 2003].

[231] Wood, K. S., Determan, J. R., Ray, P. S., Wolff, M. T., Budzien, S. A., Lovellette, M. N., and Titarchuk, L., "Using the Unconventional Stellar Aspect (USA) Experiment on ARGOS to Determine Atmospheric Parameters by X-ray Occultation," *Optical Spectroscopic Techniques, Remote Sensing, and Instrumentation for Atmospheric and Space Research IV*, Eds. A. M. Larar and M. G. Mlynczak, International Society of Optical Engineering (SPIE) Proceedings, Vol. 4485, January 2002, pp. 258-265.

[232] Wood, K. S., Kowalski, M., Lovellette, M. N., Ray, P. S., Wolff, M. T., Yentis, D. J., Bandyopadhyay, R. M., Fewtrell, G., and Hertz, P. L., "The Unconventional Stellar Aspect (USA) Experiment on ARGOS," *American Institute of Aeronautics and Astronautics (AIAA) Space Conference and Exposition*, AIAA Paper 2001-4664, Albuquerque NM, August 2001.

[233] Wood, K. S., Meekins, J. F., Yentis, D. J., Smathers, H. W., McNutt, D. P., Bleach, R. D., Friedman, H., Byram, E. T., Chubb, T. A., and Meidav, M., "The *HEAO* A-1 X-ray source catalog," *Astrophysical Journal Supplement Series*, Vol. 56, December 1984, pp. 507-649.

[234] Wood, K. S., Fritz, G., Hertz, P., Johnson, W. N., Lovellette, M. N., Wolff, M. T., Bloom, E., Godfrey, G., Hanson, J., Michelson, P., Taylor, R., and Wen, H., "The USA Experiment on the ARGOS Satellite: A Low Cost Instrument for Timing X-Ray Binaries," *The Evolution of X-ray Binaries*, American Institute of Physics (AIP) Proceedings, Vol. 308, January 1994, pp. 561-564.

[235] Wood, K. S., Fritz, G. G., Hertz, P. L., Johnson, W. N., Kowalski, M. P., Lovellette, M. N., Wolff, M. T., Yentis, D. J., Bloom, E., Cominsky, L., Fairfield, K., Godfrey, G., Hanson, J., Lee, A., Michelson, P. F., Taylor, R., and Wen, H., "USA Experiment on the ARGOS Satellite: A Low-cost Instrument for Timing X-ray Binaries," *EUV, X-Ray, and Gamma-Ray Instrumentation for Astronomy V*, Eds. O. H. Siegmund and J. V. Vallerga, International Society of Optical Engineering (SPIE) Proceedings, Vol. 2280, September 1994, pp. 19-30.

[236] Wright, J. R., "Sequential Orbit Determination with Auto-Correlated Gravity Modeling Errors," *Journal of Guidance and Control*, Vol. 4, No. 3, May-June 1981, pp. 304-309.

[237] Zarchan, P., and Musoff, H., *Fundamentals of Kalman Filtering*, American Institute of Aeronautics and Astronautics, Washington, DC, 2000.